NNT : 0000AIXM0000

THÈSE DE DOCTORAT

Soutenue à Aix-Marseille Université
le 13 février 2024 par

Florian Wernert

L'organisation du cytosquelette axonal et son rôle dans la régulation de l'endocytose

Discipline
Biologie Santé

Spécialité
Neurosciences

École doctorale
ED 62

Laboratoire/Partenaires de recherche
Équipe Neurocyto de l'institut de l'Institut de Neurophysiopathologie (INP UMR 7051)

En partenariat avec Stéphane Vassilopoulos et Satish Moparthi de l'Institut de Myologie, Paris

Composition du jury

Marie-Claude POTIER ICM, Paris	Rapporteuse
Thierry GALLI IPNP, Paris	Rapporteur
François DEVRED INP, Marseille	Président du jury
Christophe LETERRIER INP, Marseille	Directeur de thèse
Marie-Jeanne PAPANDREOU INP, Marseille	Membre invitée
Stéphane VASSILOPOULOS Institut de Myologie, Paris	Membre invité

Affidavit

Je soussigné, Florian Wernert, déclare par la présente que le travail présenté dans ce manuscrit est mon propre travail, réalisé sous la direction scientifique de Christophe Leterrier et Marie-Jeanne Papandréou, dans le respect des principes d'honnêteté, d'intégrité et de responsabilité inhérents à la mission de recherche. Les travaux de recherche et la rédaction de ce manuscrit ont été réalisés dans le respect à la fois de la charte nationale de déontologie des métiers de la recherche et de la charte d'Aix-Marseille Université relative à la lutte contre le plagiat.

Ce travail n'a pas été précédemment soumis en France ou à l'étranger dans une version identique ou similaire à un organisme examinateur.

Fait à Marseille, le 13 décembre 2023

Liste de publications et/ou brevets et participation aux conférences

1) Liste des publications et/ou brevet réalisées dans le cadre du projet de thèse :

   1. *The actin-spectrin submembrane scaffold restricts endocytosis along proximal axons.*
      Florian Wernert, Satish Moparthi, Jeanne Lainé, Gilles Moulay, Fanny Boroni-Rueda, Florence Pelletier, Nicolas Jullien, Sofia Benkhelifa-Ziyat, Marie-Jeanne Papandréou, Christophe Leterrier and Stéphane Vassilopoulos.

      En préparation

   2. *Clathrin packets move in slow axonal transport and deliver functional payloads to synapses.*
      Archan Ganguly, Rohan Sharma, Nicholas P. Boyer, Florian Wernert, Sébastien Phan, Daniela Boassa, Leonardo Parra, Utpal Das, Ghislaine Caillol, Xuemei Han, John R. Yates III, Mark H. Ellisman, Christophe Leterrier, and Subhojit Roy.

      Publié le 15 Septembre 2021 dans Neuron
      https://doi.org/10.1016/j.neuron.2021.08.016

   3. *Presynapses contain distinct actin nanostructures.*
      Dominic Bingham, Channa Elise Jakobs, Florian Wernert, Fanny Boroni-Rueda, Nicolas Jullien, Eva-Maria Schentarra, Karoline Friedl, Julie Da Costa Moura, Danique Michelle van Bommel, Ghislaine Caillol, Yuki Ogawa, Marie-Jeanne Papandréou, and Christophe Leterrier.

      Publié le 14 aout 2023 dans Journal of Cell Biology
      https://doi.org/10.1083/jcb.202208110

2) Participation aux conférences et écoles d'été au cours de la période de thèse :

   1. Participation à l'école thématique Microscopy For Biology, du 5 au 12 Novembre 2021.
   2. Présentation orale au Séminaire R&D de l'institut Marseille Imaging, *Exploring the functional relationship between the axonal cytoskeleton and endocytosis through super-resolution microscopy*, 28 septembre 2022, Marseille.
   3. Présentation orale au Séminaire Neurodays, *MPS and the membrane access regulation in the context of endocytosis*, 16 novembre 2023, Marseille.

Résumé

Les fonctions physiologiques des neurones sont rendues possibles par l'établissement de compartiments distincts et de processus cellulaires spécialisés lors du développement cellulaire. Au sein des neurones, l'endocytose médiée par la clathrine présente des caractéristiques uniques dans des compartiments tels que les dendrites et les boutons présynaptiques. Cependant, encore peu de choses sont connues sur la façon dont les composants membranaires et extracellulaires sont internalisés le long de l'axone.

Dans ce travail de thèse, je me suis intéressé aux structures cellulaires à manteau de clathrine et à l'endocytose le long du segment initial de l'axone (AIS), ainsi qu'à leur relation avec l'échafaudage périodique d'actine/spectrine qui longe la membrane plasmique de l'axone.

L'utilisation de technique de microscopie de super-résolution et microscopie électronique sur réplique de platine (PREM) sur des neurones d'hippocampes de rat en culture primaire révèlent que les puits de clathrine se forment dans des clairières circulaires formées par le réseau des spectrines au niveau du segment initial de l'axone.

En ciblant l'actine, la clathrine ou les spectrines avec différentes perturbations chimiques ou des shRNAs, j'ai pu observer des effets distincts sur l'organisation des puits de clathrine axonaux, suggérant que l'échafaudage de spectrine du cytosquelette régule l'accès à la membrane pour la formation des puits de clathrine.

L'exploration de ces effets par des la visualisation de l'endocytose de cargo, de la clathrine et du cytosquelette en microscopie sur cellules vivantes ou fixées m'a permis de révéler que la plupart des puits de clathrine de l'AIS ont une durée de vie longue, et sont étroitement régulés par l'échafaudage d'actine et de spectrine qui contrôle l'accès à la membrane cellulaire. Enfin, la mise en œuvre d'un protocole de stimulation synaptique utilisant du NMDA a permis de révéler que ces puits de clathrine inactifs à l'AIS sont capables d'endocytose et peuvent être activés pour réguler l'excitabilité neuronale.

Pris dans leur ensemble, ces résultats mettent en lumière la façon dont le cytosquelette axonal participe à la régulation des échanges à la membrane plasmique au sein d'un compartiment clé pour l'excitabilité et la physiologie neuronale.

Mots clés : segment initial de l'axone (AIS), cytosquelette périodique sous-membranaire (MPS), endocytose médiée par la clathrine (CME), puits de clathrine (CCP), vésicule à manteau de clathrine (CCV), spectrine, SMLM, PREM, SIM.

Abstract

The physiological functions of neurons are made possible by the establishment of distinct compartments and specialized cellular processes during cell development. Within neurons, clathrin-mediated endocytosis shows unique features in compartments such as dendrites and presynaptic boutons, however still little is known about how membrane and extracellular components are internalized along the axon.

In this thesis work, I focused on clathrin-coated structures and endocytosis along the axon initial segment (AIS), and their relationship to the periodic actin/spectrin scaffold that runs along the axon plasma membrane.

The use of super-resolution microscopy and platinum replica electron microscopy (PREM) techniques on primary cultured rat hippocampal neurons reveals that clathrin pits form in circular clearings over the spectrin mesh at the initial segment of the axon.

By targeting actin, clathrin or spectrins with different drugs or shRNAs I was able to observe distinct effects on the organization of axonal clathrin pits, suggesting that the cytoskeletal spectrin scaffold regulates membrane access for clathrin pits formation.

Exploring these effects through cargo endocytosis experiments and immunolabeling of clathrin and cytoskeleton in live and fixed cell microscopy, I revealed that most AIS clathrin wells are long-lived and tightly regulated by the actin and spectrin scaffold that intermediates their access to the cell membrane. Finally, applying a synaptic transmission stimulation protocol that uses NMDA revealed that these inactive clathrin pits at the AIS are capable of endocytosis and can be activated to regulate neuronal excitability. Taken altogether, these results shed light on how the axonal cytoskeleton participates in the regulation of excitability physiology.

Keywords: axon initial segment (AIS), membrane-associated periodic skeleton (MPS), clathrin-mediated endocytosis (CME), clathrin-coated pit (CCP), clathrin-coated vesicle (CCV), spectrin, SMLM, PREM, SIM.

Remerciements

L'adage dit qu'il faut un village pour élever un enfant, après ces 4 ans de doctorat je veux bien étendre cet adage pour affirmer qu'il faut le soutien continu de toute une communauté humaine pour faire naitre une thèse.

Mes premiers remerciements vont évidemment à l'équipe Neurocyto dans laquelle j'ai effectué mon doctorat. Marie-Jeanne pour avoir fait briller mes yeux devant la beauté du cytosquelette neuronal en cours magistral et m'avoir intéressé à regarder de plus près ce que faisait l'équipe Neurocyto, pour ton franc-parler, ton humour détonnant et bien sûr pour les spécialités culinaires grecques ramenées au labo. Christophe, pour m'avoir fait confiance en stage et soutenu pour le concours de l'école doctorale, cette réussite est aussi collective que les travaux de thèse qui ont suivi. Pour ton engagement très au-delà des heures de bureau, ton soutien, la qualité de tes retours, et la façon saine dont tu pratiques le mentorat des étudiant.e.s et postdocs de l'équipe, même dans les circonstances les plus stressantes. Comme j'ai eu l'occasion de le vendre à toutes les personnes souhaitant rejoindre l'équipe après moi, en plus de ta compétence pointue inégalée en tant que chercheur, tes qualités d'encadrant sont visibles dans l'atmosphère sereine de coopération et les liens amicaux développés entre les membres de l'équipe. Tu es un exemple inspirant pour l'apprenti-chercheur que je suis. Nico pour ta compétence sans bornes dès qu'il s'agit d'aller éditer des gènes et pour tous tes retours constructifs lors des présentations de travaux. Karo et Dom, mes camarades du premier batch de doctorants label Neurocyto, d'avoir construit ensemble l'ouverture de l'équipe aux thésard.e.s. Ghislaine, Fanny, Florence pour tout ce que vous m'avez appris et transmis dès le stage, pour tous les coups de main non prévus et les rattrapages in extremis d'erreurs de manip, Florence, pour ta contribution importante dans les expériences rapportés dans cette thèse et pour garder aussi bien sur les rails l'organisation du labo quand les coups de folie des doctorant.e.s la font dévier. Sofia, Ciarán, Terry, Christopher, Louiza, le batch doctorant.e.s et postdocs Neurocyto 2^{e} génération auprès duquel j'ai pu réaliser tout ce que j'avais appris au labo en vous aidant à prendre votre départ ici, pour les bières, les karaokés, les journal-club, les images de cellules partagées juste pour le plaisir des yeux, et tous les moments amicaux construits ensemble, l'environnement de travail que chacun.e de nous contribue à construire dans l'équipe est vraiment précieux. Stéphane pour notre collaboration à long terme, tes retours et ton implication dans le projet et l'article, Satish for your patience during the fine-tuning experiments for the correlative and PREM experiments on neurons, working with you was great.

Le travail de thèse n'aurait pas eu la même saveur sans la bonne humeur de l'aile verte du labo partagée avec Audrey, Laurie, Louise, Angélique, Delphine, Yván, Pedro, Maud et Jehanne. Et les autres liens construits au labo avec Abigaëlle, Guillaume, Victoria, pour les moments amicaux partagés hors labo et le soutien mutuel dans l'adversité des expériences qui ne fonctionnent pas. Laure, Mourad et Montse pour le support apporté dans vos spécialités respectives, et même en dehors pour la vidéo Laure !

Dans le reste de l'INP, Géraldine et l'équipe d'animation pour créer ensemble des moments où l'on peut parler d'autre chose que de la recherche ! François, Michel, Santi pour vos retours scientifiques lors des séminaires de labo et pour aider à faire de l'INP l'institut qu'il est. Guylaine, Christian, Hanta, Laurence pour le soutien dans tous ce qui relève des arcanes de l'administration du labo !

À AMU, merci à l'équipe du Master qui ont contribué à m'élever vers le doctorat et le jury de l'école doctoral pour avoir misé sur le projet que j'ai défendu. Un immense merci à Isabelle et toute l'équipe de Neuroschool pour toute l'organisation et la coordination du parcours pédagogique des thésard.e.s, la qualité des événements et formations proposées, et les coups de main divers face aux imprévus de thèse. Merci à mes camarades doctorant.e.s avec qui nous avons partagé le mandat de représentants auprès de l'ED, Lionel, Louise, Victoria, pour le boulot fait en commun pour nos camarades doctorant.e.s. Évidemment un immense merci à Aurélie Auffray à l'ED, notre Wonder Woman pour résoudre des situations qui ne rentrent pas dans les cases de l'administration, et au Pr. Mège pour laisser suffisamment de souplesse administrative quand nécessaire. Un immense merci à mes camarades de Master à qui je dois énormément dans mon parcours jusqu'au concours de l'ED, Hugo, Louison, Emma, Flo, Alex, Florence, Iseline, merci pour tout le temps pris avec moi pour contribuer à arriver au niveau. Merci aux 3 promos d'étudiant.e.s de L3 à qui j'ai eu le privilège d'enseigner à quel point la modélisation mathématique et la programmation en Python, c'est moins compliqué et beaucoup plus sympa que ce qu'ils s'imaginent ! Vous m'avez fait progresser autant que j'espère vous avoir fait avancer, et j'ai été touché de voir certain.e.s d'entre vous entrer en doctorat cette année. Merci Elysa à l'INT pour le dépannage de NMDA lors des expériences pilotes.

Merci à David Rousseau, Daniel Sage et toute la team du GdR ImaBio et DeepScopie pour les formations pointues et les conseils précieux sur l'analyse des images de microscopie. J'espère avoir la chance d'apprendre encore de vous dans la suite de mon parcours scientifique. Merci aux proches chercheur.se.s qui ont contribué à me montrer à quel point la recherche c'est chouette, à l'UNIS Estelle, Jean-Marc, Fabien, Oussama et Christian, hors de la communauté neuro Ambre et Roxanne.

Merci à la communauté amicale en dehors de la recherche qui a aussi contribué à équilibrer ma vie pendant ces années de doctorat, Ninon pour ton soutien pendant le Master, Devin, Clemish, JP, Lucie,

Alexia, Skip, Florian, Hélène, vous êtes de chouettes amis. Merci Camille d'être dans ma vie et me laisser exister dans la tienne, pour les liens que l'on tisse et nos compagnons non-humains, merci Sofia (encore) pour ton soutien, pour être qui tu es et me rappeler que je peux être qui je suis.

Merci à mes parents de supporter du mieux qu'ils peuvent les zigzags, fantaisies, fulgurances et autres atypies de l'humain conçu il y a quelques décennies. Merci mamie Yvette de me montrer qu'on peut rester dans une attitude d'ouverture et de curiosité tout au long de sa vie, j'espère réussir à en faire autant à ton âge.

Table des matières

Introduction

1 Architecture des neurones

1.1 Spécialisation morphologique et fonctionnelle

Les neurones sont des cellules extrêmement spécialisées dans le transport rapide et l'intégration de l'information dans le réseau nerveux qu'ils constituent. Le système nerveux central (SNC) est constitué de plusieurs centaines de milliards de ces neurones, organisées de façon particulièrement dense. Ces neurones se différencient morphologiquement et fonctionnellement et se regroupent en structures possédant elles-mêmes une organisation de plus haut niveau propre à la fonction qu'elles remplissent au sein du réseau. Ces neurones assemblés en noyaux et zones spécialisés établissent également des liens finement régulés entre eux. On peut ainsi retrouver dans le SNC une structuration fine à plusieurs échelles : de la morphologie cellulaire individuelle, à l'agencement cellulaire spécifique propre à chaque noyau et zone, jusqu'aux projections axonales reliant les différentes structures du cerveau et de la moelle épinière. À l'échelle de la cellule individuelle, pour accomplir leur fonction de transmission et d'intégration de l'information, les neurones disposent d'une morphologie unique en compartiments spatialement distincts, chacun hautement spécialisé dans l'accomplissement de fonctions particulières.

Parmi les compartiments spécialisés on retrouve des prolongements neuronaux (neurites) tels que les dendrites et l'axone. L'axone prend naissance à partir du cône d'émergence, il comprend le segment initial axonal (*axon initial segment* : AIS), des branchements éventuels, les boutons synaptiques et la terminaison axonale (**Figure 1-1**).

Les dendrites sont des prolongements ramifiés de forme conique dont la base large prend naissance au soma et la largeur diminue à mesure que l'on s'éloigne de celui-ci, ils sont spécialisés dans la réception et l'intégration de l'information et on y retrouve la majorité des récepteurs aux neurotransmetteurs concentrés à la postsynapse. Leur longueur est très variable en fonction du type neuronal, de quelques micromètres à quelques dizaines de micromètres dans le SNC, ils peuvent s'allonger sur plusieurs dizaines de centimètres pour les neurones sensoriels du système nerveux périphérique (SNP). Ils présentent souvent des épines dendritiques, protubérances spécialisées dans la formation des postsynapses excitatrices au contact des axones.

L'axone prend racine après quelques micromètres de cône d'émergence rattaché au soma, c'est un prolongement tubulaire longitudinal, composé à son départ de l'AIS, compartiment impliqué dans l'initiation du potentiel d'action (PA), et qui est parfois plus large que la partie plus distale de l'axone. Dans le prolongement de l'AIS se trouve le tube axonal, de forme cylindrique et de diamètre quasi-constant pour une même cellule : son diamètre moyen dans le SNC est de 1µm, mais peut varier de 0.1 à 10 µm suivant le type neuronal. Sa longueur est particulièrement variable, de quelques micromètres à plusieurs dizaines de centimètres pour les motoneurones contrôlant les extrémités les plus éloignées des corps cellulaires dans la moelle spinale. Il permet la transmission du PA jusqu'aux synapses qu'il forme au contact des dendrites et du soma d'autres neurones.

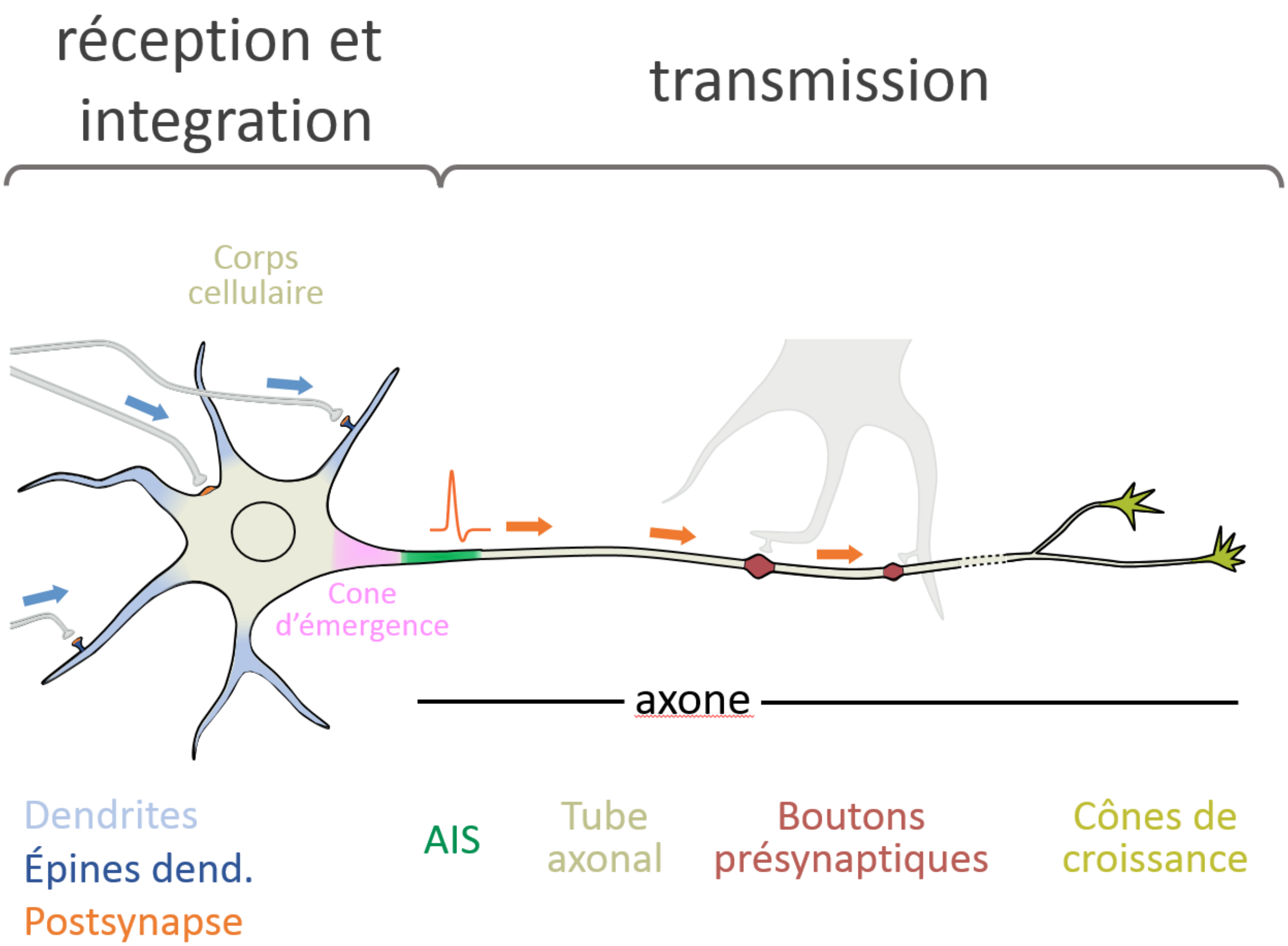

Figure 1-1 : Organisation des compartiments neuronaux et spécialisation fonctionnelle. En bleu, les dendrites prennent naissance sur le corps cellulaire du neurone et forment des épines dendritiques (en bleu foncé) au contact des afférences d'un autre neurone. Les afférences d'autres neurones (flèches bleues) forment des synapses (en orange) aux épines dendritiques et directement sur le soma. En vert vif, l'AIS prend naissance au cône d'émergence (en rose) et il initie le PA (en orange) qui est transmis le long de l'axone. L'arrivée du PA aux boutons présynaptiques (en rouge) pourra provoquer

provoquer la dépolarisation du neurone et conduire à l'exocytose de neurotransmetteurs. Adapté depuis Papandréou & Leterrier, 2018, *Mol. Cell. Neurosci.*

Les synapses sont le compartiment spécialisé dans la transmission de l'information d'un neurone à l'autre. L'arrivée du PA à une synapse entraine une ouverture des canaux sodiques sensibles au potentiel, une dépolarisation rapide s'ensuit, ce qui entraine l'entrée présynaptique d'ion calcium par les canaux calciques sensibles au potentiel (VGCC) Ces ions vont alors activer la chaine transductive SNARE-synaptotagmine conduisant à l'exocytose, dans la fente synaptique, des vésicules chargées en neurotransmetteurs.

Chacun de ces éléments est nécessaire à la transmission de l'information au sein d'une cellule, de sa réception jusqu'à sa retransmission vers un autre neurone du réseau.

1.2 Le cytosquelette support de la spécialisation neuronale

La spécialisation des compartiments cellulaires neuronaux s'appuie sur le cytosquelette, un échafaudage intracellulaire de protéines assurant le support, le maintien, la résistance mécanique et la plasticité des compartiments dans le temps.

Parmi les composants moléculaires du cytosquelette on retrouve les microtubules, l'actine et les filaments intermédiaires.

1.2.1 Microtubules

Les microtubules sont de longues structures formées par l'assemblage en ressort de dimères α et β tubuline (Goodson & Jonasson, 2018, *Cold Spring Harb. Perspect. Biol.*). Ils prennent la forme de tubes creux dont le périmètre est constitué de 13 protofilaments composés de chaines de dimères α/β tubuline et leur diamètre extérieur mesure 25 nm en moyenne. Leurs deux extrémités sont spatialement polarisées et qualifiées de *plus end* (extrémité côté β-tubuline) ou *minus end* (extrémité côté α-tubuline). Ils sont retrouvés dans toutes les cellules eucaryotes où ils constituent la structure profonde du cytosquelette et sont impliqués dans la croissance cellulaire, la mobilité, la division cellulaire et le maintien morphologique de la cellule. Dans les neurones, ils sont un acteur majeur du transport vésiculaire et jouent le rôle de support physique au déplacement des moteurs moléculaires dans l'axone et les dendrites. Les microtubules axonaux ont la particularité d'être orientés plus end vers le coté le plus distal de l'axone, tandis que dans les dendrites de neurones matures les microtubules peuvent être orientés dans les deux sens (Barlan & Gelfand, 2017, *Cold Spring Harb. Perspect. Biol.*; Goodson & Jonasson, 2018, *Cold Spring Harb. Perspect. Biol.*; Kapitein & Hoogenraad, 2011, *Mol.*

Cell. Neurosci.). Dans les neurones en développement les microtubules coopèrent avec l'actine et les spectrines dans les phases d'exploration, de croissance et de consolidation de la membrane plasmique (Ghisleni et al., 2020, *Nat. Commun.*).

La caractéristique la plus étonnante des microtubules est le contraste entre leur rôle de maintien structurel supposant de la stabilité et sa dynamique d'assemblage/désassemblage qualifiée d'instabilité dynamique (*dynamic instability*). En effet, sous l'effet de l'hydrolyse du GTP lié aux monomères de tubuline, son extrémité *plus end* subit des cycles d'assemblage (croissance ou *rescue*) et de désassemblage partiel (*catastrophe*) éventuellement suivi de récupération (*rescue*). L'extrémité *minus end* est soumis au même phénomène mais avec moins d'amplitude dans les variations de longueur, et moins fréquemment (Goodson & Jonasson, 2018, *Cold Spring Harb. Perspect. Biol.*).

1.2.2 Neurofilaments

Les neurofilaments sont en dehors du périmètre des travaux rapportés dans cette thèse, mais constituent un élément du cytosquelette neuronal qui ne peut être négligé, ce paragraphe les présentera donc dans un aspect assez général. Pour un aperçu plus complet la revue de Yuan et al. peut constituer un bon point de départ (Yuan et al., 2017, *Cold Spring Harb. Perspect. Biol.*).

Les neurofilaments sont d'autres structures d'échafaudage, de maintenance structurelle et de régulation du diamètre axonal présentes dans les neurites (Yuan et al., 2017, *Cold Spring Harb. Perspect. Biol.*). Ils constituent le sous-type neuronal de la famille des filaments intermédiaires et 3 types de neurofilaments de différent poids moléculaire sont connus et qualifiés de *low* (L), *medium* (M), ou *high* (H) en fonction de leur poids. Ils sont composés de monomères NF-L, NF-M ou NF-H qui s'assemblent parallèlement en hétérodimères, puis les dimères en tétramères antiparallèles. 8 tétramères parallèles forment l'unité de base de chaque neurofilament (*unit-length filament*) et l'assemblage longitudinal de ces unités conduit à la formation du filament (**Figure 1-2**).

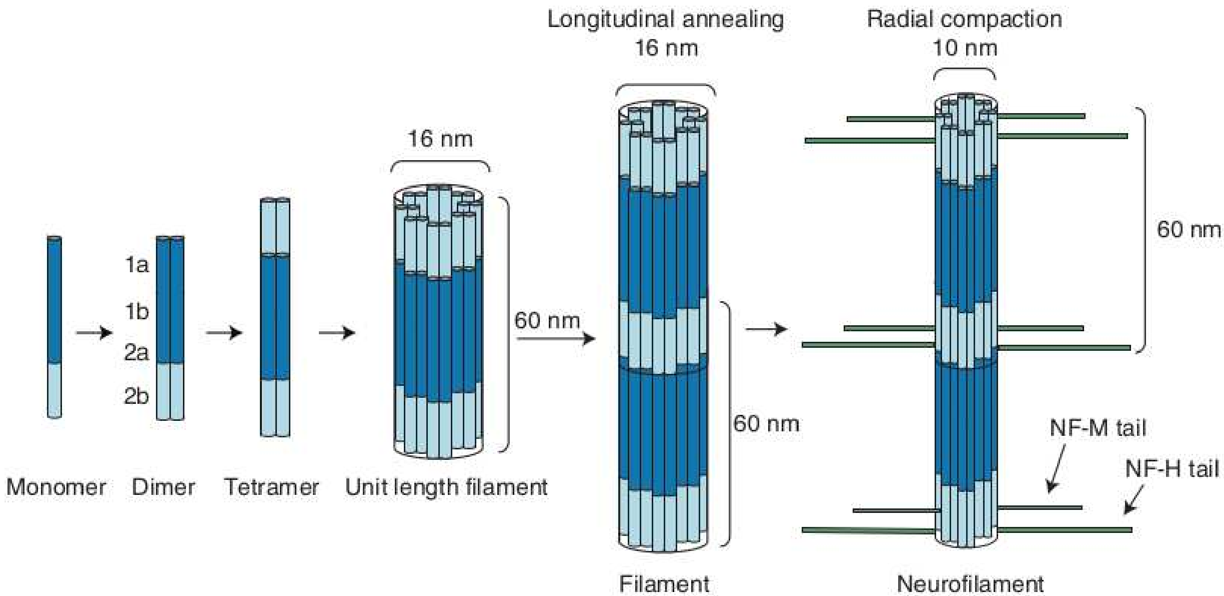

Figure 1-2: Assemblage des neurofilaments. Les monomères NF dimérisent parallèlement sur les domaines partagés par tous les types de NF, puis tétramérisent de façon antiparallèle au niveau de leurs domaines 1a 1b et 2a. 8 tétramères assemblés parallèlement en tube constituent l'unité de longueur filamentaire (*unit length filament* : ULF) de l'élongation d'un neurofilament et ces ULF s'assemblent entre elles par leurs domaines 2b. Au fur et à mesure de l'élongation du neurofilament, son diamètre tubulaire initial de 16 nm se compacte jusqu'à atteindre 10 nm pour un neurofilament mature. Adapté depuis Yuan et al., 2017, *Cold Spring Harb. Perspect. Biol.*

On retrouve les neurofilaments dans l'axone, parallèles aux microtubules et reliés à ceux-ci par des *cross-linkers* proches du centre de l'axone, et branchés latéralement au réseau d'actine à proximité de la membrane plasmique interne (**Figure 1-3**).

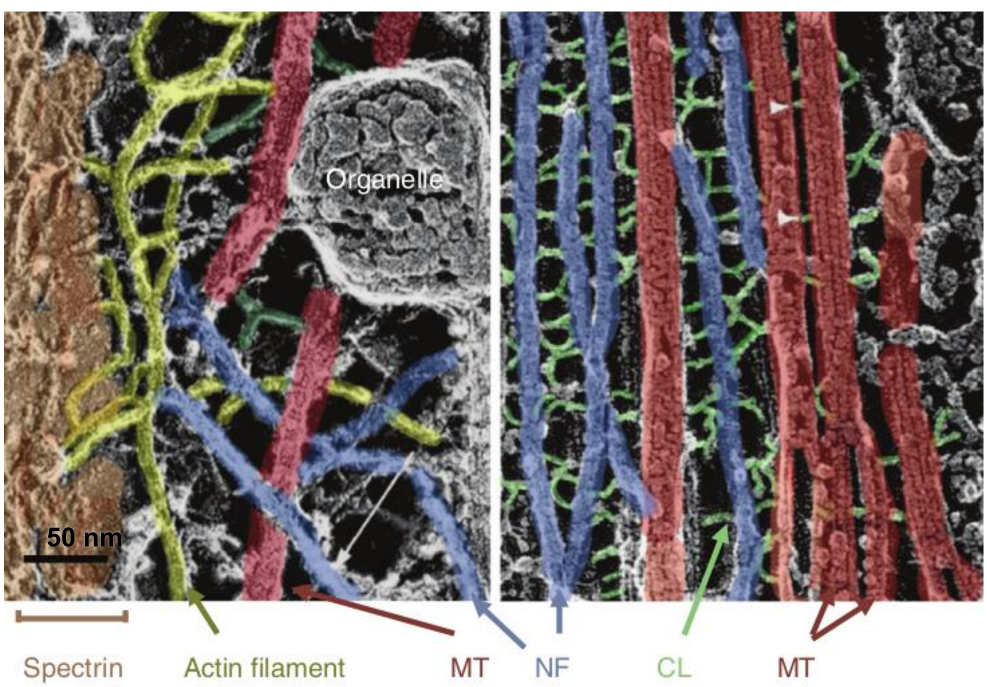

Figure 1-3 : Neurofilaments et cytosquelette observés en microscopie électronique après cryofracture. En fausses couleurs, on voit à droite la partie la plus centrale de l'axone où les neurofilaments (NF, en bleu) sont parallèles aux microtubules (MT, en rouge) et reliés à ces derniers via des crosslinkers (CL, en vert). À gauche on voit la partie sous-membranaire de l'axone, ici les neurofilaments sont branchés vers l'actine sous-membranaire (en jaune, à gauche). Adapté depuis Yuan et al., 2017, *Cold Spring Harb. Perspect. Biol.*

Enfin plus récemment, les neurofilaments sont un sujet d'intérêt comme marqueurs biologiques de maladies neurodégénératives comme la sclérose latérale amyotrophique, la maladies Charcot-Marie Tooth ou l'ataxie héréditaire (Herrmann & Aebi, 2016, *Cold Spring Harb. Perspect. Biol.*; Hohmann & Dehghani, 2019, *Cells*; Yuan et al., 2017, *Cold Spring Harb. Perspect. Biol.*).

1.2.3 Actine

L'actine se présente sous forme de monomères globulaires (actine G) pouvant s'autoassembler en filaments (actine F) longitudinaux ou branchés (Rottner et al., 2017, *J. Cell Sci.*). C'est la protéine la plus représentée dans une grande majorité de cellules eucaryotes et elle est impliquée dans des fonctions cellulaires majeures telles que le développement, la motilité, la contractilité et la maintenance de la structure cellulaire (Dominguez & Holmes, 2011, *Annu. Rev. Biophys.*). Dans les neurones, l'actine constitue la structure sous-membranaire à l'origine de la résistance mécanique des neurites tout en permettant, par sa structure dynamique, la plasticité requise par les phénomènes de renforcement ou dépression synaptique.

Les filaments d'actine ont deux extrémités dites « pointue » et « barbée » (**Figure 1-4**) identifiables en microscopie électronique et aux caractéristiques dynamiques distinctes : on observe en particulier plus de réorganisation rapide de l'actine à l'extrémité barbée et davantage de stabilité du côté pointu.

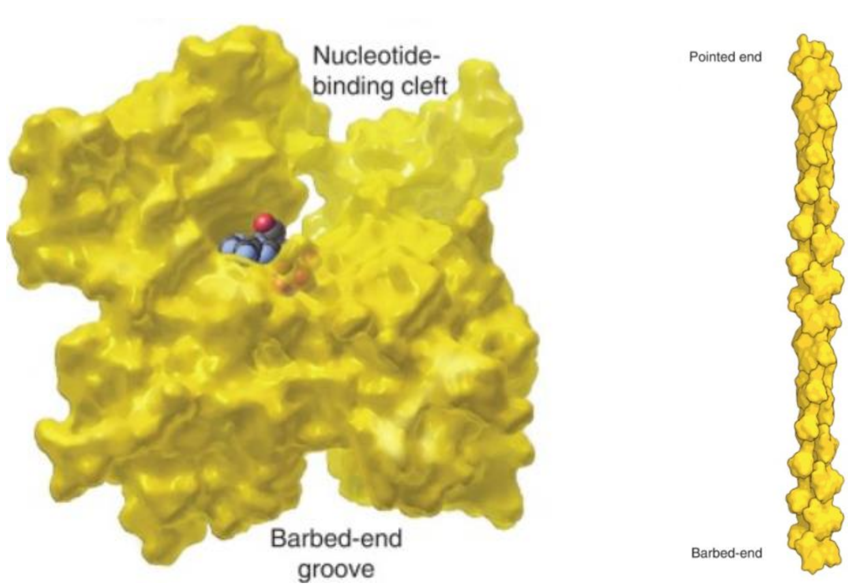

Figure 1-4 : Structure de l'actine G et F. À gauche on voit un monomère d'actine G et son nucléotide d'ATP dans sa fente coté pointu (*nucleotide-binding cleft*). À droite on voit un assemblage de monomères d'actine assemblés en filament avec ses deux extrémités, pointue en haut et barbée en bas. Adapté depuis Pollard, 2016, *Cold Spring Harb. Perspect. Biol.*

Dans le neurone en développement et en association avec les microtubules, l'actine est impliquée dans l'établissement d'une polarisation du neurone en compartiments distincts, les phénomènes de réorganisation dynamique de l'actine et des microtubules conduisent en particulier à l'apparition du cône de croissance axonal (**Figure 1-5**) et de protubérances dendritiques (**Figure 1-6**, Hlushchenko et al., 2016, *Cytoskeleton*; Lei et al., 2016, *Curr. Opin. Neurobiol.*; Pollard, 2016, *Cold Spring Harb. Perspect. Biol.*).

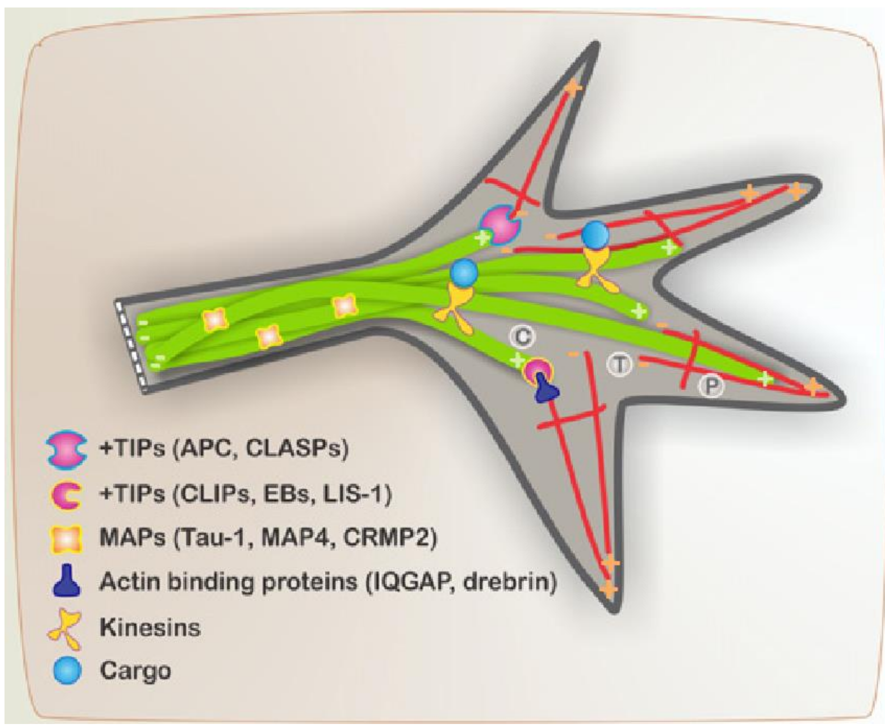

Figure 1-5 : Coopération de l'actine et des microtubules au cône de croissance axonal. Les extrémités « plus » des microtubules (vert) envahissent le cône de croissance, les filaments d'actine (rouge) font avancer la membrane plasmique en s'allongeant du coté barbé (+ orange). Les moteurs moléculaires kinésines (tripodes jaunes) transportent sur les microtubules les cargos (bleu) supportant la croissance de l'axone. Adapté depuis Neukirchen & Bradke, 2011, *Semin. Cell Dev. Biol.*

Aux lamellipodes et dans les filopodes lors du développement axonal et dendritique, l'extrémité barbée est tournée vers la membrane et l'extrémité pointue démarre au voisinage des microtubules. Les phases de croissance se déroulent en vagues de flux et reflux d'actine et d'envahissement par les microtubules lors du reflux. Lors de ces vagues, l'assemblage rapide d'actine à l'extrémité barbée et l'établissement d'un lien moléculaire fort entre celle-ci et les protéines transmembranaires d'adhésion focale vont transmettre la force mécanique de l'actine à la membrane et la déplacer. Les protéines d'adhésion focale vont s'ancrer à leur nouvelle position dans la matrice extracellulaire, à la suite de quoi leur lien moléculaire avec l'actine va alors devenir suffisamment faible pour que l'actine reflue, laissant ainsi l'espace disponible pour l'envahissement par les microtubules qui vont « consolider » le chemin gagné pendant la vague d'actine. En plus d'être à l'origine de la croissance des neurites et la polarisation neuronale, des travaux suggèrent que ce processus pourrait aussi servir de senseur mécanique dirigeant la croissance des protubérances (Stricker et al., 2010, *J. Biomech.*).

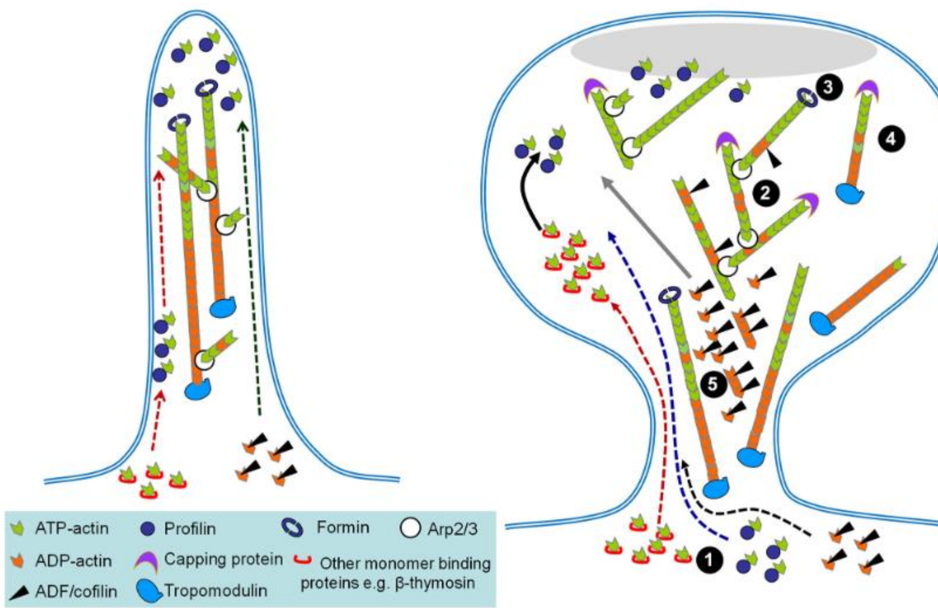

Figure 1-6 : L'actine aux protubérances dendritiques. À gauche, on voit l'élongation longitudinale de l'actine dans un filopode. À droite, on voit l'organisation mixte branchée (2 et 3) et longitudinale (4 et 5) des monomères d'actine (1) dans une épine dendritique. Adapté depuis Lei et al., 2016, *Curr. Opin. Neurobiol.*

Les filaments d'actine peuvent s'assembler en structures de différents types selon les complexes de nucléation à l'origine du filament. Ainsi, dans les neurones, les filaments d'actine linéaire sont initiés depuis un site formine et branchés à 70 degrés lorsqu'ils sont nucléés depuis un complexe l'Arp2/3 (**Figure 1-6** et **Figure 1-8**).

La profiline seule séquestre les monomères d'actine G et inhibe la formation des filaments (Sohn & Goldschmidt-Clermont, 1994, *BioEssays*), cependant, lorsqu'elle s'associe aux formines (Paul & Pollard, 2009, *Cell Motil.*) ou à l'Arp2/3 (May, 2001, *Cell. Mol. Life Sci. CMLS*) , elle peut devenir promotrice de la nucléation de l'actine en filaments en accélérant l'échange de nucléotides d'ADP par de l’ATP sur les monomères d’actine G (**Figure 1-7**, Ferron et al., 2007, *EMBO J.*; Pinto-Costa & Sousa, 2020, *Cytoskeleton*; Pollard, 2016, *Cold Spring Harb. Perspect. Biol.*). Sous l’effet de cette catalyse et en présence d’autres facteurs promoteurs comme les motifs Ena-VASP avec les formines (filaments longitudinaux) ou WASP avec Arp2/3 (filaments branchés), l’assemblage en filament de l’actine G-ATP devient énergétiquement beaucoup plus favorable (**Figure 1-8**, Pollard, 2016, *Cold Spring Harb. Perspect. Biol.*).

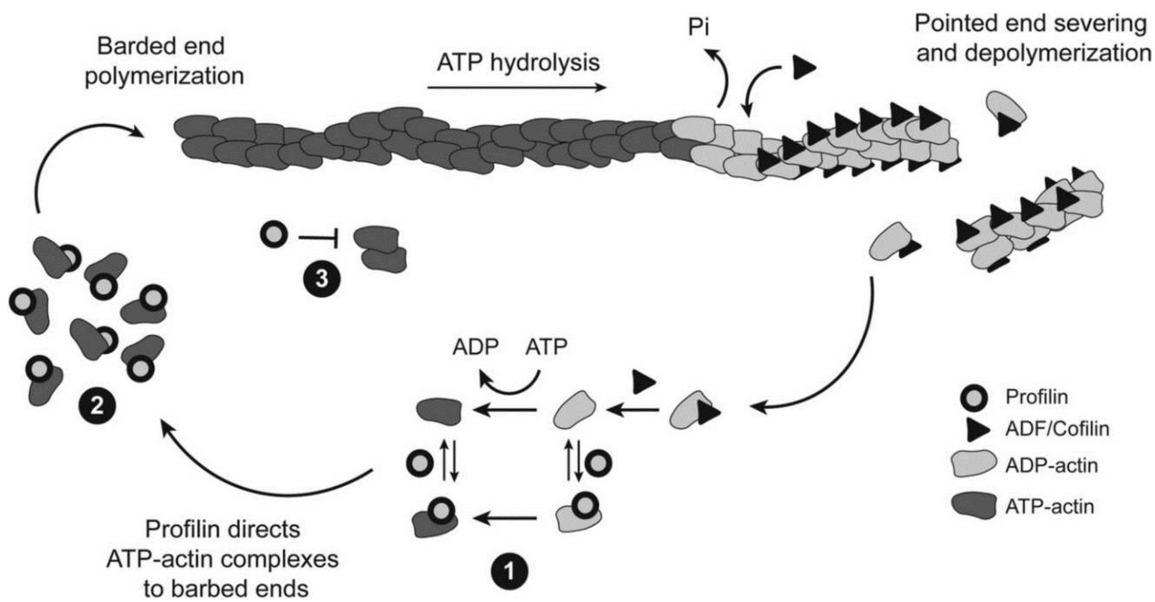

Figure 1-7 : Interactions actine/profiline dans la croissance des filaments. L’actine-ADP coté pointu se dépolymérise, la profiline séquestre les monomères d’actine (3) et favorise l’échange ADP/ATP (1), les monomères d’actine-ATP polymérisent du côté barbé du filament (2). Adapté depuis Pinto-Costa & Sousa, 2020, *Cytoskeleton*.

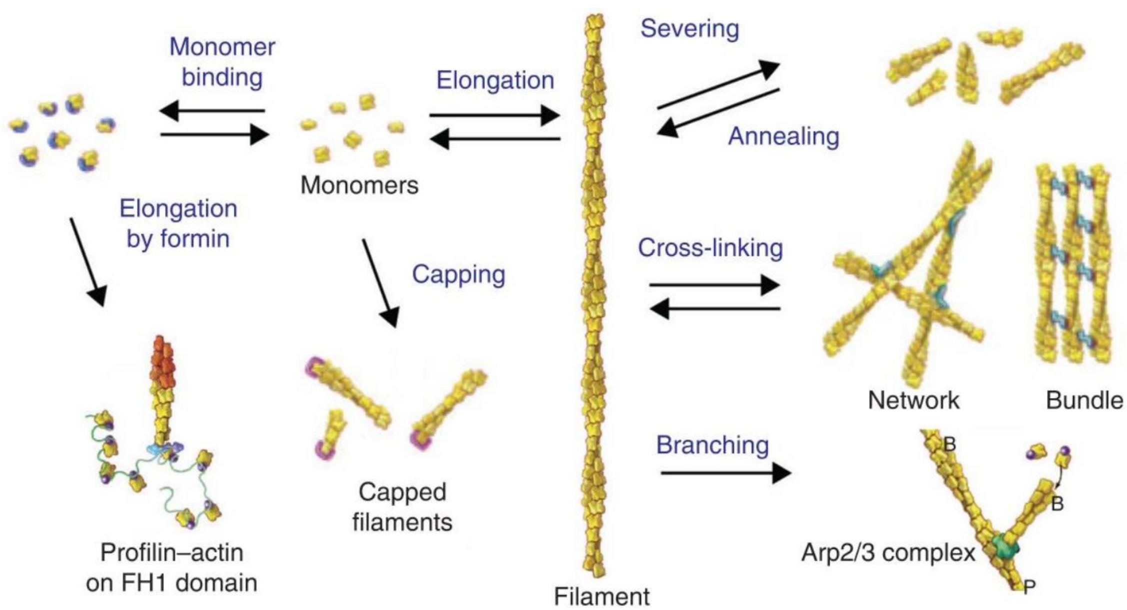

Figure 1-8 : Assemblages d'actine et coopération moléculaire. Dans la moitié gauche, les mécanismes moléculaires impliquant les formines et la profiline qui conduisent à une élongation longitudinale. Dans la moitié droite sont montrés des assemblages branchés de filaments d'actine en coopération avec le complexe Arp2-3. Adapté depuis Pollard, 2016, *Cold Spring Harb. Perspect. Biol.*

Dans les axones, la polarisation pointue/barbée établie par les filaments d'actine permet aux moteurs moléculaires de type myosine d'assurer le transport vésiculaire vers la membrane des cargos arrivant sur les microtubules (Arnold & Gallo, 2014, *J. Neurochem.*; Rottner et al., 2017, *J. Cell Sci.*; Titus, 2018, *Cold Spring Harb. Perspect. Biol.*).

Au-delà de ce cette vision « classique » de l'actine dans les phénomènes de croissance, exploration et motilité cellulaire, des observations plus récentes de structures d'actine différenciées suivant le compartiment neuronal ont renouvelé notre connaissance sur les mécanismes moléculaires liés à l'actine. Les avancées en microscopie sur cellules vivantes en particulier ont permis d'observer des structures très dynamique d'actine nommées « hotspots » et « trails » qui contribuent au transport lent de l'actine axonale (Ganguly et al., 2015, *J. Cell Biol.*).

2 Le MPS dans les neurones

2.1 L'étude du cytosquelette

Au cours de la dernière décennie, le développement technologique en microscopie et la mise au point de nouvelles sondes fluorescentes a permis une avancée considérable de notre connaissance du cytosquelette, en particulier dans les neurones (Leterrier, 2021, *Curr. Opin. Neurobiol.*).

En 2013 en particulier, l'utilisation de la microscopie STORM a conduit à révéler l'existence d'une structure périodique sous membranaire (*submembranous periodic structure* : MPS) d'actine et de spectrines dans l'axone (**Figure 2-1**, Xu et al., 2013, *Science*), ainsi qu'un agencement périodique moins systématique mais notable dans les dendrites.

Depuis cette étude princeps sur des neurones d'hippocampe de rat mis en culture, le MPS a pu être observé dans les axones de tous les autres sous-types neuronaux chez le rat et dans les cellules bipolaires rétiniennes de la souris (D'Este et al., 2016, *Sci. Rep.*), dans les neurones mis en culture d'autres espèces vertébrées (neurone de poulet en culture primaire et motoneurone iPSC Humain) et in-vivo sur des modèles invertébrés (*C. elegans* et *Drosophilia* dans He et al., 2016, *Proc. Natl. Acad. Sci.*). Le MPS a été également observé dans des cellules gliales dans lesquelles ses caractéristiques sont équivalentes à celles présentes dans les dendrites, et il est depuis reconnu comme un acteur majeur de la morphogénèse neuronale.

2.2 Les structures d'actine

2.2.1 Anneaux périodiques d'actine axonale

Dans l'axone, l'actine forme des anneaux sous membranaires perpendiculaires au tube axonal et observés tout au long de celui-ci. Ces anneaux sont espacés périodiquement de 190 nm et sont reliés entre eux par des tétramères de spectrine parallèles au tube axonal et perpendiculaires aux anneaux (**Figure 2-2**).

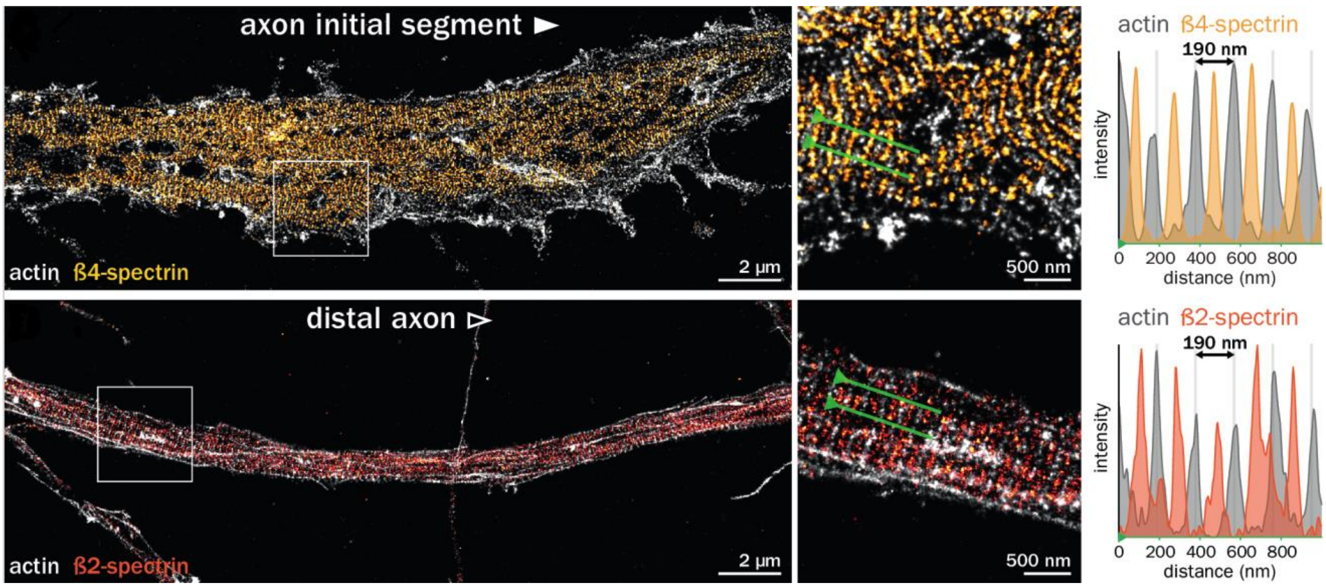

Figure 2-1 : Organisation périodique de l'actine et des spectrines dans l'axone. DNA-PAINT 2 couleurs actine/β4-spectrine et actine/β2-spectrine à l'axone. En haut on peut voir la périodicité de l'actine en gris et de la β4-spectrine en jaune, à l'AIS. En bas, on peut voir la périodicité de l'actine en gris et de la β2-spectrine en rouge, à l'axone distal. À droite, sont présentés les profils d'intensité des zones délimitées en vert sur les agrandissements, pour les marquages actine/β4-spectrine en haut et actine/β2-spectrine en bas. L'anticorps spectrine reconnaît l'extrémité C-terminale de la β4-spectrine et de la β2-spectrin, c'est à dire le centre du tétramère de spectrine, on retrouve ainsi sur les profils le pic d'intensité des spectrines décalé d'une demi-période par rapport à l'actine. Adapté depuis Leterrier, 2021, *Curr. Opin. Neurobiol.*

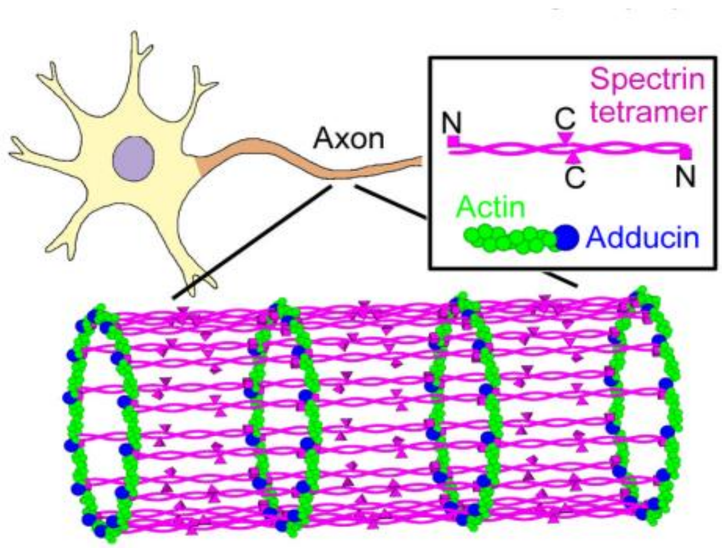

Figure 2-2 : Premier modèle d'organisation du MPS axonal. Les anneaux périodiques d'actine, les tétramères de spectrine et les « linkers » d'adducine sont montrés respectivement en vert, en magenta et en bleu. Adapté depuis Xu et al., 2013, *Science*.

Depuis l'étude princeps (**Figure 2-2**), d'autres travaux ont permis de révéler en microscopie électronique sur réplique de platine (*platinum replica electron microscopy* : PREM), l'ultrastructure des anneaux d'actine axonale intercalées par les tétramères de spectrines du MPS (Vassilopoulos et al., 2019, *Nat. Commun.*). La technique *d'Immunogold* (Ig) sur des échantillons *unroofés* (voir les méthodes en **4.1.2** et **4.2.1.2**) et traités pour être observables en PREM a permis de connaître à quelle ultrastructure reconnaissable était associé le marquage Ig-actine et d'observer ainsi pour la première fois les anneaux d'actine axonale sous-membranaire avec une résolution et un contexte ne pouvant être atteints en microscopie fluorescente. Cette même technique utilisée pour marquer les spectrines a confirmé leur agencement longitudinal perpendiculaire aux anneaux d'actine axonale (**Figure 2-3**).

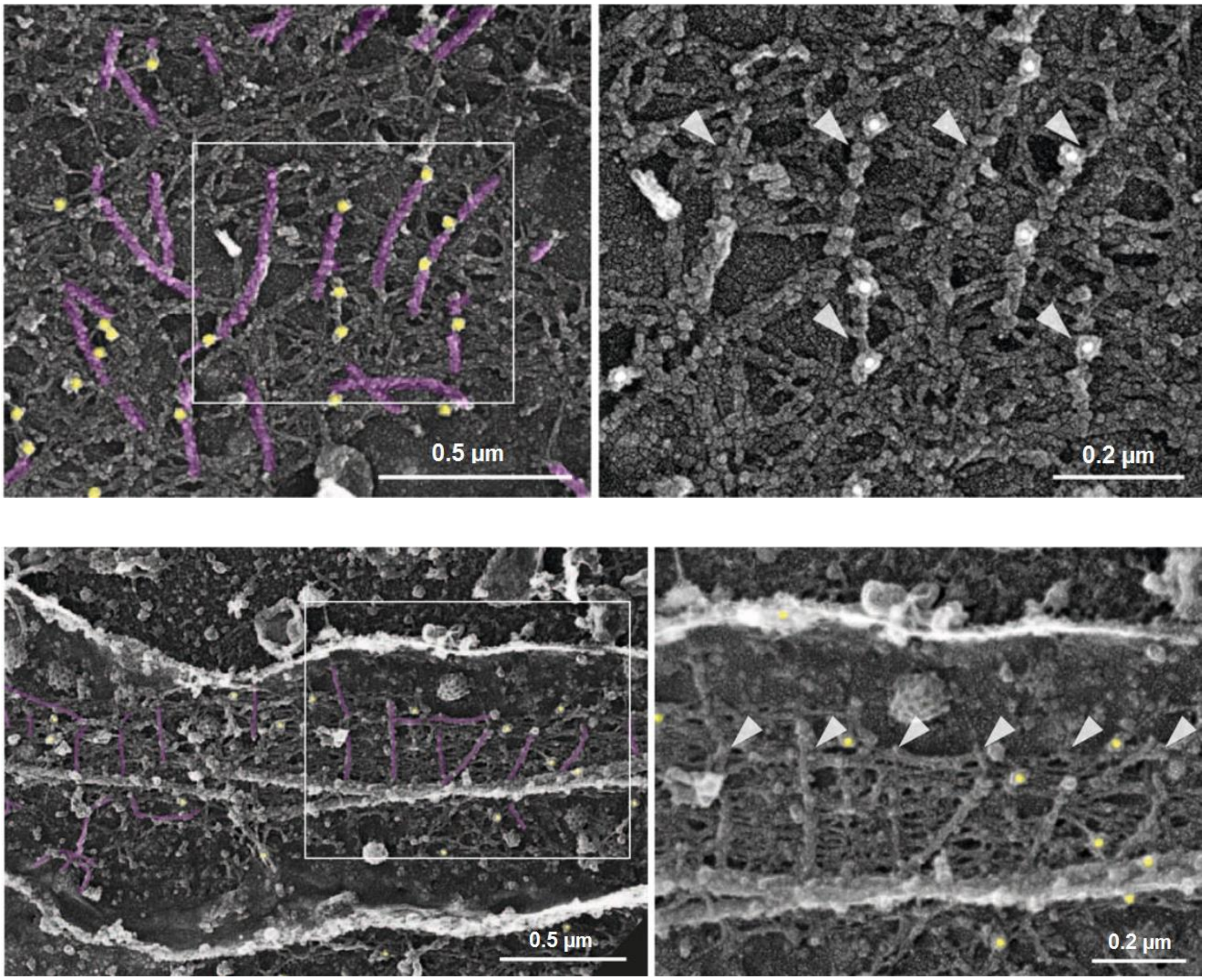

Figure 2-3 : Anneaux d'actine du MPS en PREM. En haut à gauche est montré l'immunogold d'actine en fausses couleurs avec l'actine en magenta et les billes d'or en jaune. En haut à droite, les têtes de flèche désignent les filaments d'actine périodique. En bas à gauche, est montré l'immunogold α2/β2/β4 spectrine en fausses couleurs. En bas à droite, les têtes de flèches désignent les tetramères de spectrine perpendiculaires aux anneaux d'actine périodique. Adapté depuis Vassilopoulos et al., 2019, Nat. Commun.

2.2.2 Actine dendritique périodique et longitudinale

On peut retrouver de façon moins systématique des anneaux périodiques d'actine sous-membranaire dans les segments dendritiques ainsi qu'aux épines dendritiques (**Figure 2-4**, Bär et al., 2016, *Sci. Rep.*; D'Este et al., 2015, *Cell Rep.*; Han et al., 2017, *Proc. Natl. Acad. Sci.*).

Dans les segments dendritiques, l'organisation de l'actine est dépendante de l'activité neuronale. Ainsi l'actine peut être organisée en anneaux périodiques (activité moindre), en fibres longitudinales (activité forte), et dans toute la continuité entre ces deux pôles (Lavoie-Cardinal et al., 2020, *Sci. Rep.*).

Aux épines dendritiques, les travaux récents rapportent la présence d'anneaux d'actine périodique à la base des épines, sans que leur présence n'impliquent l'absence d'actine longitudinale parallèle à la racine (**Figure 2-5**). La tête des épines dendritiques est très densément enrichie d'actine branchée (Bingham et al., 2023, *J. Cell Biol.*; Korobova & Svitkina, 2010, *Mol. Biol. Cell*) et les motifs périodiques du MPS y sont absents (**Figure 2-5**, Bär et al., 2016, *Sci. Rep.*). Enfin les filopodes dendritiques récapitulent les différentes structures longitudinales et branchées des épines dont ils précèdent la formation.

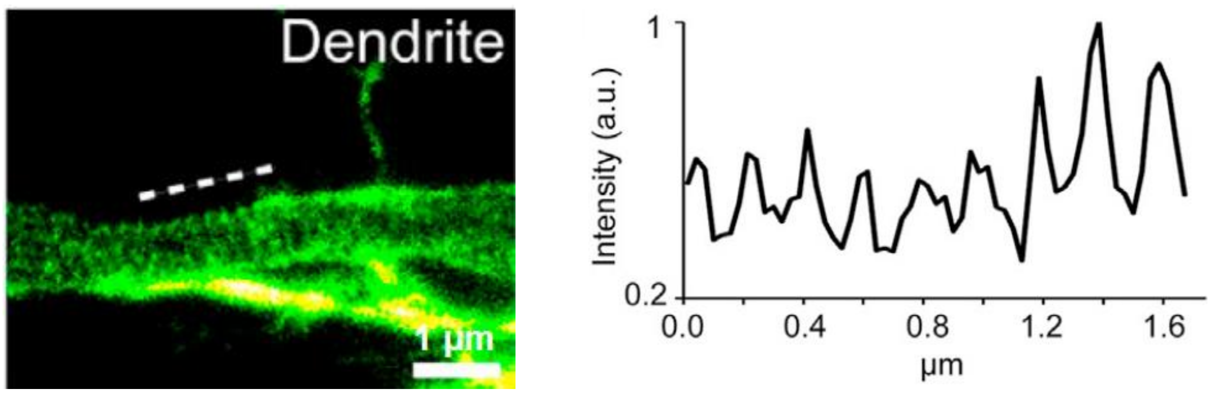

Figure 2-4 : Périodicité de l'actine aux segments dendritiques. À gauche est montré le motif périodique de l'actine en anneaux sur une dendrite en microscopie STED. À droite, le profil d'intensité de fluorescence est mesuré sur le segment de dendrite indiqué par la ligne discontinue sur l'image de microscopie. On observe bien une périodicité sur ce profil sans atteindre la régularité de la périodicité des profils axonaux. Adapté depuis D'Este et al., 2015, *Cell Rep.*

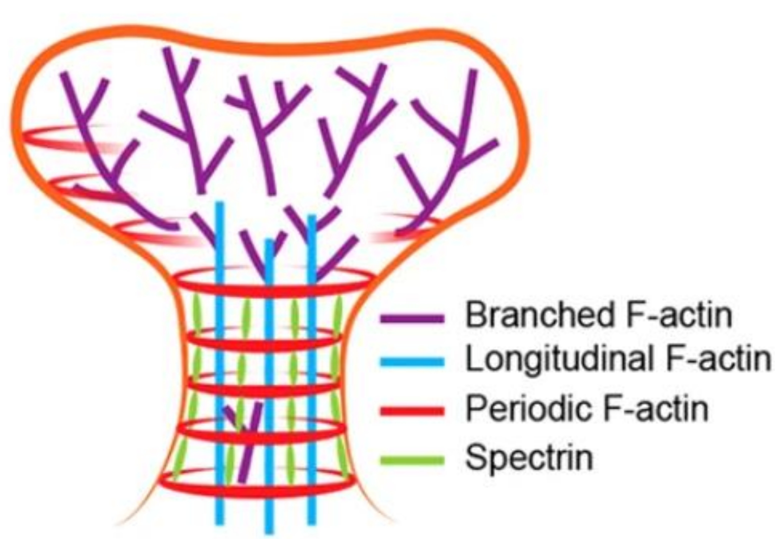

Figure 2-5 : Modèle d'organisation du MPS aux épines dendritiques. L'actine forme des anneaux périodique à la base des épines mais pas à la tête, on retrouve des structures longitudinales d'actine et de spectrine parallèles à la base de l'épine, ainsi que de l'actine branchée dans sa tête. Adapté depuis Bär et al., 2016, *Sci. Rep.*

2.2.3 Actine au soma

Au soma les composants du MPS forment partiellement des maillages polygonaux sous la membrane plasmique, similaire au maillage des érythrocytes mais avec une périodicité qui reste similaire à celle des axones et des dendrites, alors que dans les érythrocytes la période de ce maillage est de 70 à 90 nm. La publication de Han et al., 2017, *Proc. Natl. Acad. Sci.* observe que la proportion de maillage régulier des spectrines sous-membranaires au soma est drastiquement réduite par l'utilisation de latrunculine ou de cytochalasine D, toutes deux ciblant l'actine (Han et al., 2017, *Proc. Natl. Acad. Sci.*). Ce résultat suggère que l'actine est impliquée dans ce maillage sous membranaire.

2.2.4 D'autres structures d'actine neuronale

En plus des anneaux périodiques, d'autres nouvelles structures d'actine axonale ont été observées et caractérisées récemment, les « hotspots » et « trails » (**Figure 2-6**, Chakrabarty et al., 2018, *J. Cell Biol.*; Ganguly et al., 2015, *J. Cell Biol.*). Ce sont des structures dont la dynamique d'assemblage et désassemblage se compte en minutes. Les hotspots d'actine prennent forme autour d'endosomes stationnaires et les trails s'allongent en antérograde et rétrograde depuis les hotspots, avant que l'ensemble ne se désassemble au bout de quelques minutes. Le mouvement moyen est antérograde et ces structures très dynamiques d'actine sont à ce jour considérées comme jouant une fonction de transport lent indépendant des mécanismes connus des moteurs moléculaires (Chakrabarty et al., 2018, *J. Cell Biol.*; Pollard & Goldman, 2018, *Cold Spring Harb. Perspect. Biol.*).

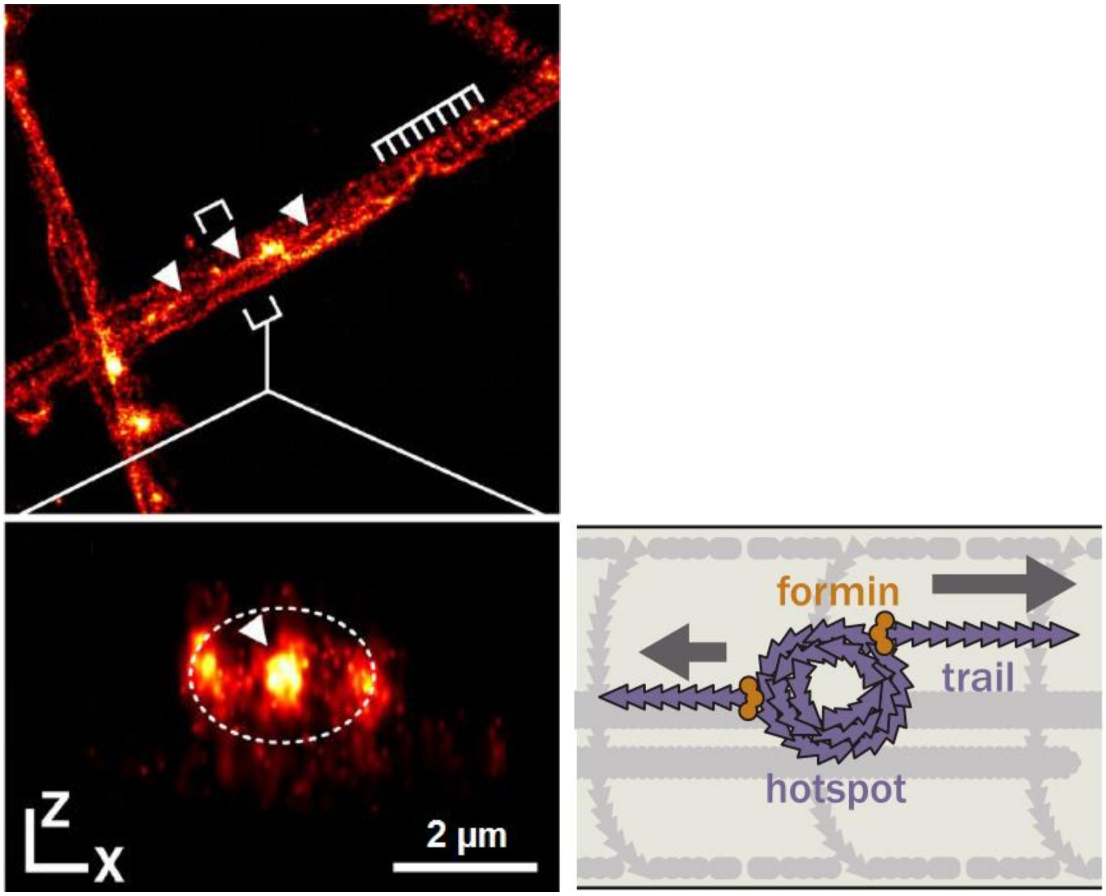

Figure 2-6 : Hotspot et trails d'actine axonale en STORM. En haut la tête de flèche centrale indique le hotspot, les 2 autres têtes de flèche indiquent les extrémités des trails du côté antérograde et rétrograde, la ligne graduée indique les anneaux périodiques d'actine. En bas à gauche projection XZ du hotspot. À droite est montré un modèle des deux structures. Panneau gauche adapté depuis Ganguly et al., 2015, *J. Cell Biol.* et panneau de droite adapté depuis Leterrier, 2021, *Curr. Opin. Neurobiol.*

Toujours dans les avancées concernant l'actine, des travaux récemment publiés dans l'équipe et auxquels j'ai contribué (Bingham et al., 2023, *J. Cell Biol.*) montrent la présence de 3 structures distinctes d'actine dans la zone non périodique à proximité de la zone active présynaptique : une structure en mailles branchées située directement à la zone active (ZA) agirait en régulatrice de l'exocytose, une structure en « rails » longitudinaux perpendiculaires à la zone active permettraient le transport vésiculaire du pool de réserve vers la ZA et une structure en *corrals* périsynaptiques servirait d'échafaudage au pool de vésicules synaptiques de réserve et pourrait également jouer un rôle dans le maintien d'une réserve de membrane endocytable à la périphérie de la zone active (**Figure 2-7**).

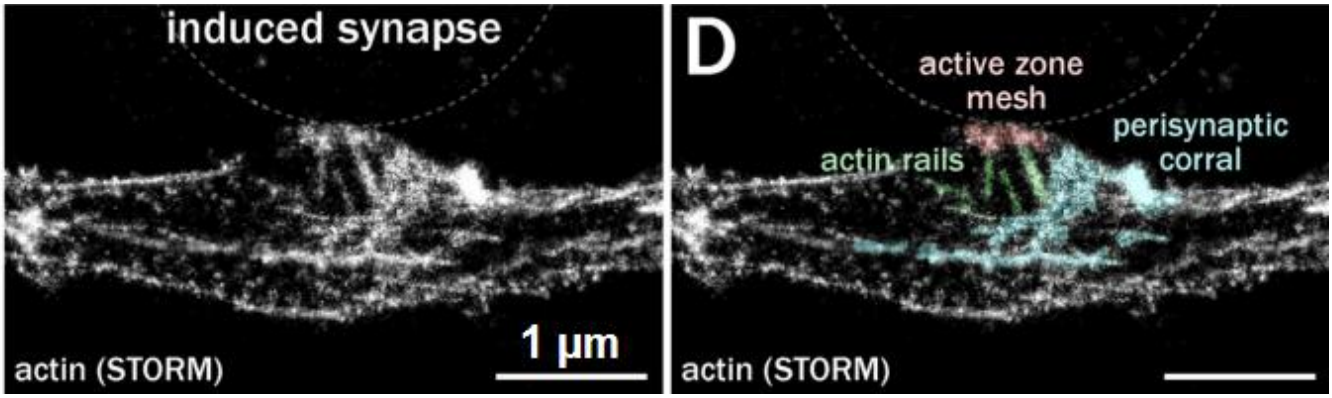

Figure 2-7 : Nouvelles structures d'actine découvertes à la présynapse. Il s'agit d'une présynapse induite par billes sur des neurones d'embryon de rat mis en culture primaires. À gauche on observe le marquage de l'actine en microscopie super-résolue STORM qui montre une organisation de en structures spécialisées à la présynapse. À droite il s'agit de la même image avec les structures d'actine identifiées en fausses couleurs : le maillage de la ZA, les rails et les coraux périsynaptiques sont respectivement présentés en rouge, en vert et en bleu. Adapté depuis Bingham et al., 2023, *J. Cell Biol.*

2.3 Structures de spectrines

Les anneaux d'actine du MPS sont séparés par des tétramères de spectrine, ce qui explique leur espacement de ≈190 nm (**Figure 2-8**). Les spectrines sont des protéines majeures du cytosquelette et sont présentes de façon ubiquitaire dans les cellules eucaryotes. Elles assurent en premier lieu une fonction d'échafaudage et de maintien structurel des membranes cellulaires. Elles se présentent sous la forme de tétramères composés par l'assemblage antiparallèle de dimères α et β (Lorenzo et al., 2023, *Nat. Rev. Neurosci.*).

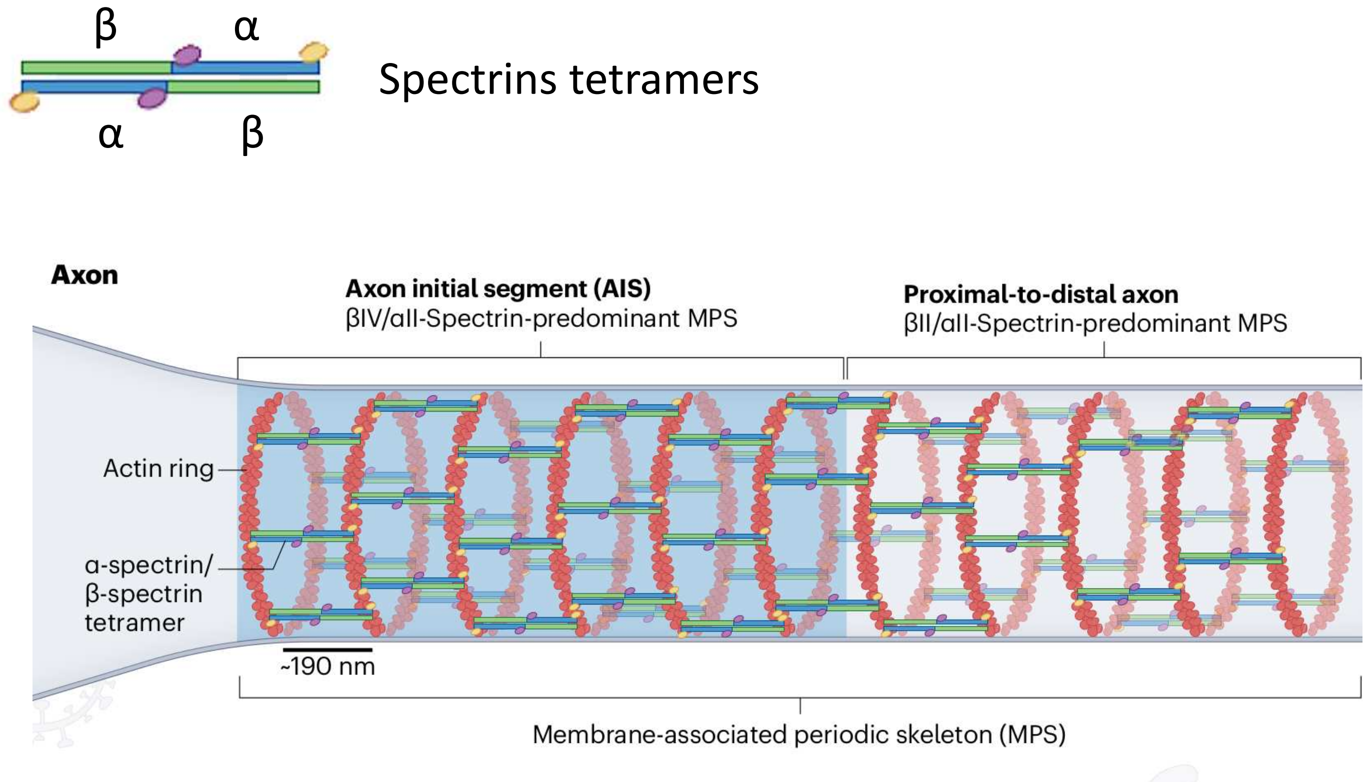

Figure 2-8 : Maillage périodique d'anneaux d'actine et de tétramères de spectrines à l'axone. En haut, les α et β spectrine s'assemblent en dimères puis en tétramères antiparallèles, en bas ces tétramères forment un maillage perpendiculaire aux anneaux d'actine axonale et contribuent à espacer les anneaux d'actine à une période de ≈190 nm. Le modèle présenté ici est reconnaissable sur l'échantillon présenté dans la **Figure 2-3**. Adapté depuis Lorenzo et al., 2023, *Nat. Rev. Neurosci.*

2.3.1 Caractérisation des sous-unités α et β

Sous leur forme canonique, chacune des sous-unités est caractérisée par la présence de 20 et 17 domaines répétés spectrine (*spectrin repeats* : SR) respectivement pour les sous-unités α et β, plus un domaine SR partiel pour chacun des deux types de sous-unité (**Figure 2-9**). Les spectrines β possèdent un domaine d'homologie pleckstrine (*pleckstrin homology* : PH) du coté C-terminal qui leur permet de s'ancrer aux phospholipides sur la face interne de la membrane. Du coté N-terminal, elles présentent deux domaines CH pouvant lier l'actine et un domaine de liaison à l'ankyrine (*ankyrin binding domain* ABD) est présent à l'interface des SR 14 et 15. Les sous-unités α possèdent également un double hélice de type EF à l'extrémité C-terminale.

Dans le cytosquelette neuronal, on retrouve les formes α2, β1, β2 β3 et β4 spectrine, avec une organisation spécifique en tétramères α2/β4 à l'AIS et α2/β2 dans le reste de l'axone. La β4-spectrine canonique est dite Σ1 et possède un épissage alternatif dit ΣVI qui ne présente pas de domaine d'homologie calponine (*calponin homology* : CH) et possède seulement 9 SR. En dépit de son impossibilité à s'ancrer aux anneaux d'actine de par l'absence de domaine CH, un phénotype KO pan-β4-spectrine par CRISPR-Cas9 ciblant un exon commun aux 2 isotypes peut être restauré par l'expression par transfection de l'isotype ΣVI seul (R. Yang et al., 2019, *Proc. Natl. Acad. Sci. U. S. A.*). Ce résultat met en lumière le rôle critique de l'ankyrine-G dans l'organisation fonctionnelle des spectrines à l'AIS.

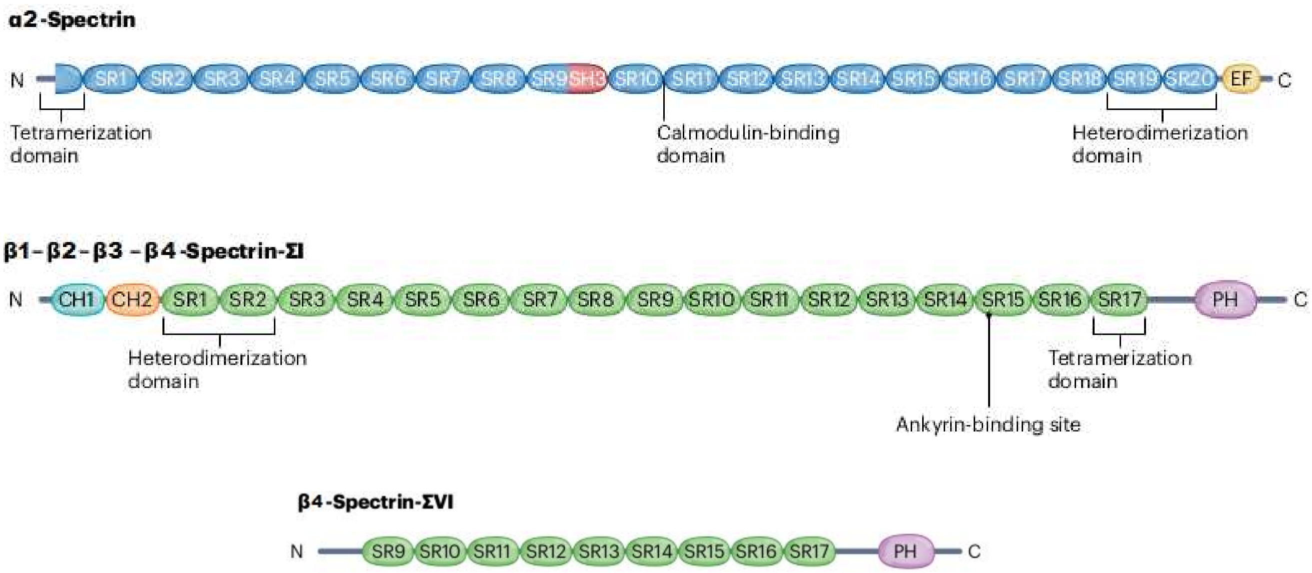

Figure 2-9 : Caractérisation des spectrines et de leurs sous-domaines. En haut est montrée la spectrine α2, au milieu les spectrines β1 à β4-Σ1 et en bas, le variant β4-Σ6. SR : spectrin repeats, CH : calmodulin homology, PH : pleckstrin homology, EF : motif « main EF ». Adapté depuis Lorenzo et al., 2023, *Nat. Rev. Neurosci.*

2.3.2 Hétérodimérisation α/β et tetramérisation

Les sous unités α et β s'assemblent par covalence en hétérodimères antiparallèles au niveau des SR 19 et 20 pour les α, SR 1 et 2 pour les β. Les hétérodimères tétramérisent par paire au niveau de leurs domaines SR partiels côté C-terminal pour les sous-unités β et côté N-terminal pour les α (**Figure 2-10**).

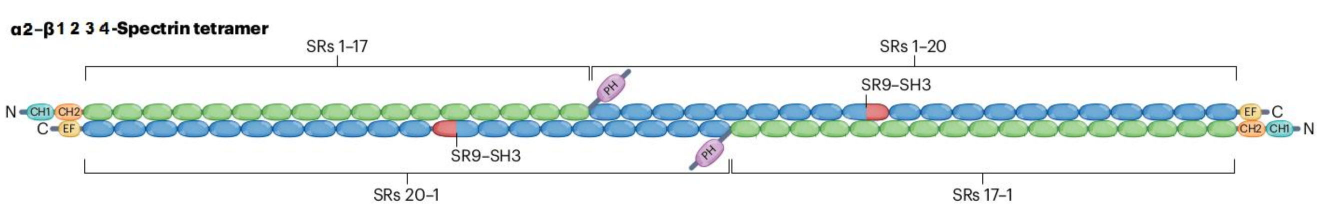

Figure 2-10 : Composition des tétramères de spectrine. Les α2-spectrines sont montrées en bleu et les β1/β2/β3/β4 spectrines en vert. (Lorenzo et al., 2023, *Nat. Rev. Neurosci.*)

2.3.3 Interactions moléculaires possibles

Dans les cellules et en condition physiologique, ces tétramères prennent une forme longitudinale et leurs différents domaines d'homologie PH et CH vont favoriser leurs interactions avec des composants spécifiques.

L'assemblage des sous-unités spectrines en dimères puis en tétramère antiparallèle fait présenter les domaines CH des sous-unités β aux deux extrémités C et N du tétramère. La présence de ces domaines donne aux tétramères de spectrine la capacité à se lier aux filaments d'actine à leurs extrémités et former un maillage périodique avec celles-ci (Yin et al., 2020, *Front. Cell Dev. Biol.*).

Par contraste avec les domaines CH et du fait de l'assemblage des sous unités, les domaines PH pouvant lier les phospholipides membranaires vont se retrouver davantage localisés au centre des tétramères de spectrine.

2.4 L'assemblage des composants du MPS axonal, structure et fonction

2.4.1 Le réseau anneaux d'actine / tétramères de spectrine

Dans les axones, ces caractéristiques particulières des tétramères de spectrines leur permettent de se lier avec les anneaux d'actine et de produire ainsi un échafaudage sous-membranaire périodique dont le motif se répétera dans le sens longitudinal de l'axone tous les 190 nanomètres.

Le domaine pouvant lier l'ankyrine est nécessaire pour le développement du MPS à l'AIS et pour le fonctionnement normal de ce dernier (R. Yang et al., 2019, *Proc. Natl. Acad. Sci. U. S. A.*). En effet, l'ankyrine G forme un échafaudage reliant les faisceaux de microtubules du cytosquelette profond au réseau sous-membranaire périodique d'actine-spectrines. En plus d'établir ce lien entre cytosquelette profond et sous-membranaire, l'ankyrine G sert également à stabiliser les canaux ioniques membranaires sensibles au potentiel et responsables de l'initiation du PA et elle doit nécessairement être associée avec la β4-spectrine pour jouer ce rôle de stabilisation (Figure 2-11, Liu et al., 2020, *eLife*; Yang et al., 2019, *Proc. Natl. Acad. Sci. U. S. A.*).

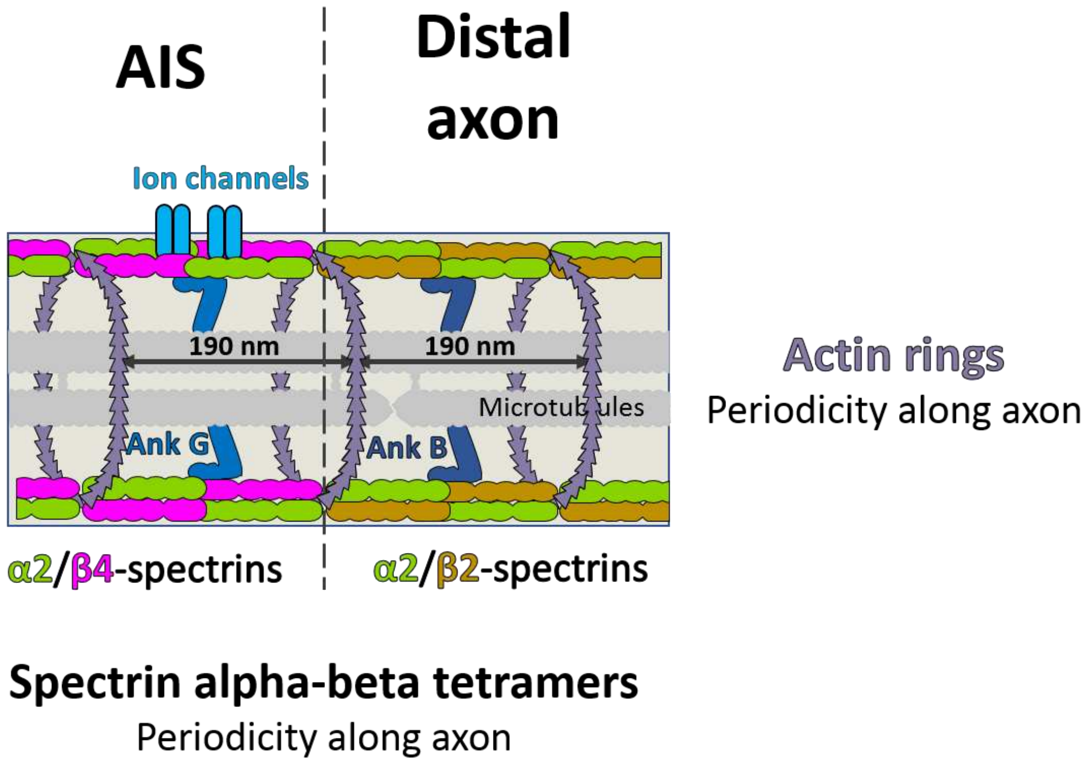

Figure 2-11 : Modèle de l'assemblage périodique α2-β2/β4-spectrine et anneaux d'actine avec leurs autres partenaires moléculaires axonaux. L'ankyrine G et B, les microtubules et les canaux ioniques sont montrés respectivement en bleu foncé, gris et bleu clair. Adapté depuis Leterrier, 2021, Curr. Opin. Neurobiol.

Dans le reste de l'axone hors AIS, le MPS est composé de tétramères α2/β2-spectrine qui relient les anneaux d'actine toujours perpendiculairement à ces derniers et parallèlement au tube axonal, de plus l'ankyrine B prend ici la place de la G comme échafaudage reliant la composante sous-membranaire aux faisceaux profonds de microtubules. On retrouve également de l'adducine à la jonction actine-spectrine dans l'axone distal, qui stabilise la polymérisation des anneaux d'actine. Au-delà de son rôle structurel et de morphogénèse, l'actine du MPS serait aussi impliquée dans le maintien à long-terme des microtubules axonaux (Qu et al., 2017, *Mol. Biol. Cell*).

Dans les dendrites, cet assemblage périodique α2/β2-spectrine peut parfois se retrouver également, bien que moins fréquemment et de façon plus localisée sur de petits « patchs » localisés de périodicité. On retrouve ces patchs dans 10 à 30 % des segments dendritiques (**Figure 2-12**, J. He et al., 2016, *Proc. Natl. Acad. Sci.*; Xu et al., 2013, *Science*) et la simple surexpression des β2-spectrine dans les neurones suffit à rendre le MPS présent et périodique de façon similaire à l'axone dans la totalité des dendrites.

En complément avec ce résultat, l'étude de Zhong et al., 2014 dans *eLife* a pu mettre en lumière le rôle de l'ankyrine B dans la régulation négative de l'expression des β2-spectrines dans les dendrites. La suppression de l'ankyrine-B conduit à un résultat similaire à la surexpression des β2-spectrines, avec un MPS présent dans les dendrites et présentant une périodicité aussi importante qu'à l'axone en condition contrôle.

Ces résultats mettent en lumière un équilibre finement régulé entre la quantité d'expression des β2-spectrines et la quantité d' ankyrine B inhibitrice de leur assemblage aux dendrites (Zhong et al., 2014, *eLife*). Cet équilibre fin expression/inhibition semble donc particulièrement important dans la différenciation fonctionnelle des neurites en axone et dendrites, l'étude des conséquences fonctionnelles de la dérégulation de cet équilibre commence à être étudié (Lorenzo et al., 2019, *Proc. Natl. Acad. Sci.*; Zhou et al., 2019, *Science*).

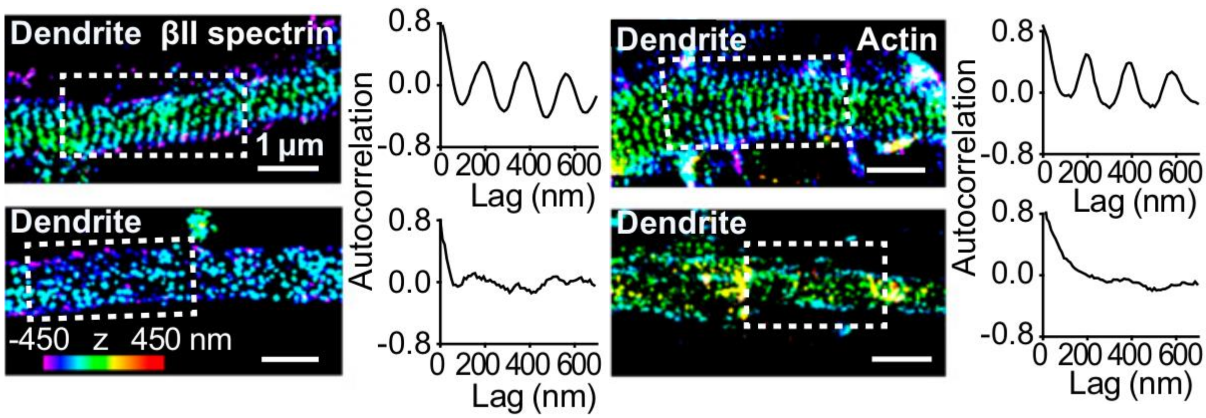

Figure 2-12 : Variabilité de la périodicité du cytosquelette dendritique. Le marquage β2-spectrine est montré à gauche et celui d'actine à droite. Sur des échantillons non-traités, on peut voir en haut le MPS régulier et en bas le MPS absent ou irrégulier. La profondeur est codée en couleur. À droite de chaque illustration est montré le profil d'autocorrelation pour la zone délimitée en pointillés blanc sur chaque image. Adapté depuis He et al., 2016, Proc. Natl. Acad. Sci.

Le rôle le plus établi de l'assemblage sous-membranaire d'actine-spectrine est sa contribution aux propriétés mécanique de l'axone. Dégrader les β2-spectrines du MPS entraine de nombreuses ruptures axonales lors des mouvement du nématode C. Elegans (Hammarlund et al., 2007, *J. Cell Biol.*) et l'application d'échelons contrôlés de stress mécanique à des axones de ganglions dorsaux de poulet montre une moindre résistance de ces derniers est moindre lors de l'application de perturbateurs chimiques de l'actine ou des spectrines (Dubey et al., 2020, *eLife*)

Dans les synapses, plusieurs études conduisent à aux observations suivantes ; la périodicité du MPS d'actine-spectrine s'interrompt que ce soit au niveau axonal (présynaptique) ou dendritique (postsynaptique) et on peut observer la présence d'anneaux d'actine périodique à la base des épines axonales mais pas à leurs têtes où se trouve la zone de densité postsynaptique (*postsynaptic density :* PSD.

Lors de travaux de l'équipe sur la structure du MPS, l'observation a été faite que des composants moléculaires associés à l'endocytose était présents de façon consistante dans l'axone, dans des cultures de neurones matures sans stimulation électrique ou chimique externe. Cette observation avait de quoi surprendre dans la mesure où l'axone est plus connu pour ses propriétés d'initiation du PA à l'AIS et sa conduction jusqu'aux présynapses. De plus, à l'axone, les cycles rapides d'exocytose/endocytose sont habituellement observés aux présynapses mais peu d'études rapportent à ce jour l'observation de ce type de phénomène dans le tube axonal. Seule une étude récente (Fréal et al., 2023) suggère la possibilité d'une endocytose de canaux sodiques à l'AIS qui réguleraient à la baisse l'excitabilité neuronale lors d'un protocole de dépression de long terme (*long term depression* : LTD). Ce faisceau d'indices et d'observations m'a conduit à vouloir étudier de plus près les liens structurels et fonctionnels pouvant exister entre le MPS axonal et l'endocytose.

3 L'endocytose

L'endocytose est le mécanisme physiologique par lequel une cellule forme une vésicule cytosolique *de novo* depuis sa membrane plasmique. Le phénomène consiste en une invagination interne de la membrane, puis son étirement jusqu'à former une quasi-sphère et enfin la scission de la lumière reliant cette sphère à la membrane (**Figure 3-1**, Doherty & McMahon, 2009, *Annu. Rev. Biochem.*).

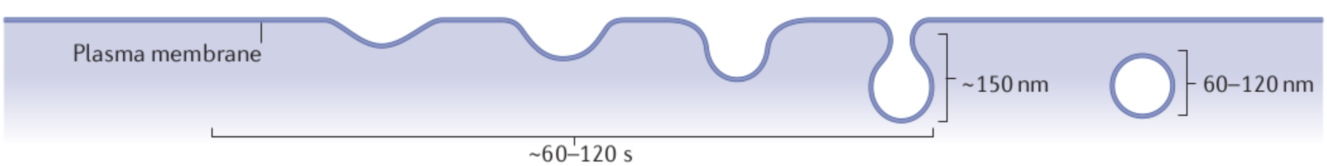

Figure 3-1 : Mécanisme général d'endocytose. De gauche à droite, on peut voir le décours temporel de la formation d'une vésicule en invaginant la membrane plasmique jusqu'à la scission. Adapté depuis Kaksonen & Roux, 2018, *Nat. Rev. Mol. Cell Biol.*

Ce processus d'endocytose peut entrer en jeu pour réaliser différentes fonctions nécessaires à la cellule. Il peut s'agir de faire entrer dans la cellule un composé soluble présent dans le milieu extracellulaire, de recycler de la membrane ayant été fusionnée lors de l'exocytose de granules ou de vésicules, de réguler à la baisse la disponibilité de certains récepteurs membranaires après leur activation par un ligand, de réguler la pression osmotique entre les compartiments intra et extracellulaires (Rauch & Farge, 2000, *Biophys. J.*). En plus des fonctions physiologiques, le mécanisme de l'endocytose peut aussi être la porte d'entrée de virus dans l'organisme, par endocytose directe ou médiée par un récepteur, l'une n'était pas exclusive de l'autre comme cela fut récemment montré pour le SARS-CoV-2 (Jackson et al., 2022, *Nat. Rev. Mol. Cell Biol.*).

3.1 Types d'endocytose et leurs mécanismes moléculaires

Suivant les spécificités de chaque type cellulaire, on peut retrouver différents mécanismes permettant à la cellule d'effectuer de l'endocytose, ces mécanismes peuvent être répartis dans 2 familles : l'endocytose médiée par la clathrine (*clathrin mediated endocytosis* : CME) et l'endocytose indépendante de la clathrine (*clathrin independent endocytosis* : CIE). Une revue détaillée de tous les mécanismes d'endocytose connus à ce jour serait très au-delà du périmètre des travaux rapportés dans cette thèse, par souci de concision ce chapitre ne va donc détailler que les mécanismes et observations relevant de la CME.

3.1.1 L'endocytose médiée par la clathrine

L'endocytose médiée par la clathrine est le type d'endocytose qui a été le plus étudié, et se décompose selon les étapes suivantes (**Figure 3-2**, Kaksonen & Roux, 2018, *Nat. Rev. Mol. Cell Biol.*) :

Elle commence (1) par l'assemblage à la membrane de protéines initiatrices (FCHO, puis eps15 et l'intersectine) qui vont recruter (2) de façon coordonnée un des acteurs majeurs de la CME, les complexes de protéines adaptatrices de clathrine (*adaptor protein complex* : AP). Ces complexes ont eux-mêmes la capacité de se lier à la membrane cellulaire et à des trimères de clathrine avec lesquels ils assemblent l'échafaudage moléculaire ayant la force nécessaire pour courber la membrane plasmique et former une vésicule depuis celle-ci (3, 4). Enfin une protéine de scission va venir serrer jusqu'à la couper la lumière rattachant la proto-vésicule à la membrane plasmique (5). Une fois la vésicule ainsi formée et libre dans le cytosol, le manteau de clathrine se désassemble rapidement (6) et la vésicule et son contenu peuvent être transportés vers d'autres compartiments cellulaires (7).

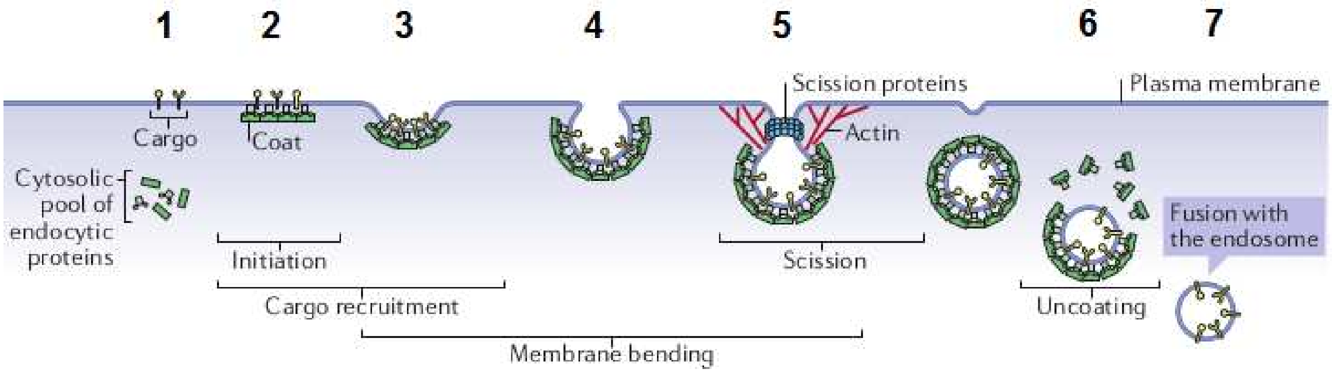

Figure 3-2 : Modèle canonique de l'endocytose médiée par la clathrine. De gauche à droite on peut voir le décours temporel de la formation d'une CCV. Les protéines initiatrices de la CME s'assemblent à la membrane et recrutent le manteau de clathrine, l'assemblage de la clathrine génère suffisament de force pour invaginer la membrane et former une vésicule, puis des protéines de scission séparent la CCV de la membrane plasmique. Immédiatement après, le manteau de clathrine de la vésicule est désassemblé et la vésicule suit la voie de recyclage vers les endosomes. Adapté depuis Kaksonen & Roux, 2018, *Nat. Rev. Mol. Cell Biol.*

3.1.2 Les complexes de protéines adaptatrices

Les protéines adaptatrices associées à la CME sont AP-1 au réseau trans-Golgi (*trans-Golgi network* : TGN) et aux endosomes de recyclage, AP2 à la membrane plasmique et AP3 aux endosomes non-matures. Ce sont des hétérotétramères dont les deux chaines lourdes α/γ/δ/ε/ζ et β ont la capacité de se lier aux phospholipides de la membrane cellulaire en leur extrémité N-terminale, elles ont également une région *clathrin-box* sur un domaine « charnière » (*hinge domain*, voir **Figure 3-3**) à l'autre extrémité de la sous-unité β. Ce domaine présente une centaine de résidus et comprend un motif hautement conservé de 5 résidus pouvant lier la clathrine (Tom Kirchhausen et al., 2014, *Cold Spring Harb. Perspect. Biol.*; Miele et al., 2004, *Nat. Struct. Mol. Biol.*; Park & Guo, 2014, *Biosci. Rep.*; ter Haar et al., 2000, *Proc. Natl. Acad. Sci. U. S. A.*). Les AP disposent également de domaines σ et μ plus petits et plus internes à la structure, le domaine μ présentant une articulation leur permettant de trier et lier les cargos à leur extrémité C-terminale après que le tétramère ait changé de conformation en position dite « ouverte » (**Figure 3-3**).

À la membrane plasmique on retrouve la forme AP2, et les neurones ont un isotype spécifique d'AP3 qui serait impliqué dans la maturation des vésicules synaptiques en amont de l'exocytose, ce qui contribuerait à réguler cette dernière (Danglot & Galli, 2007, *Biol. Cell*).

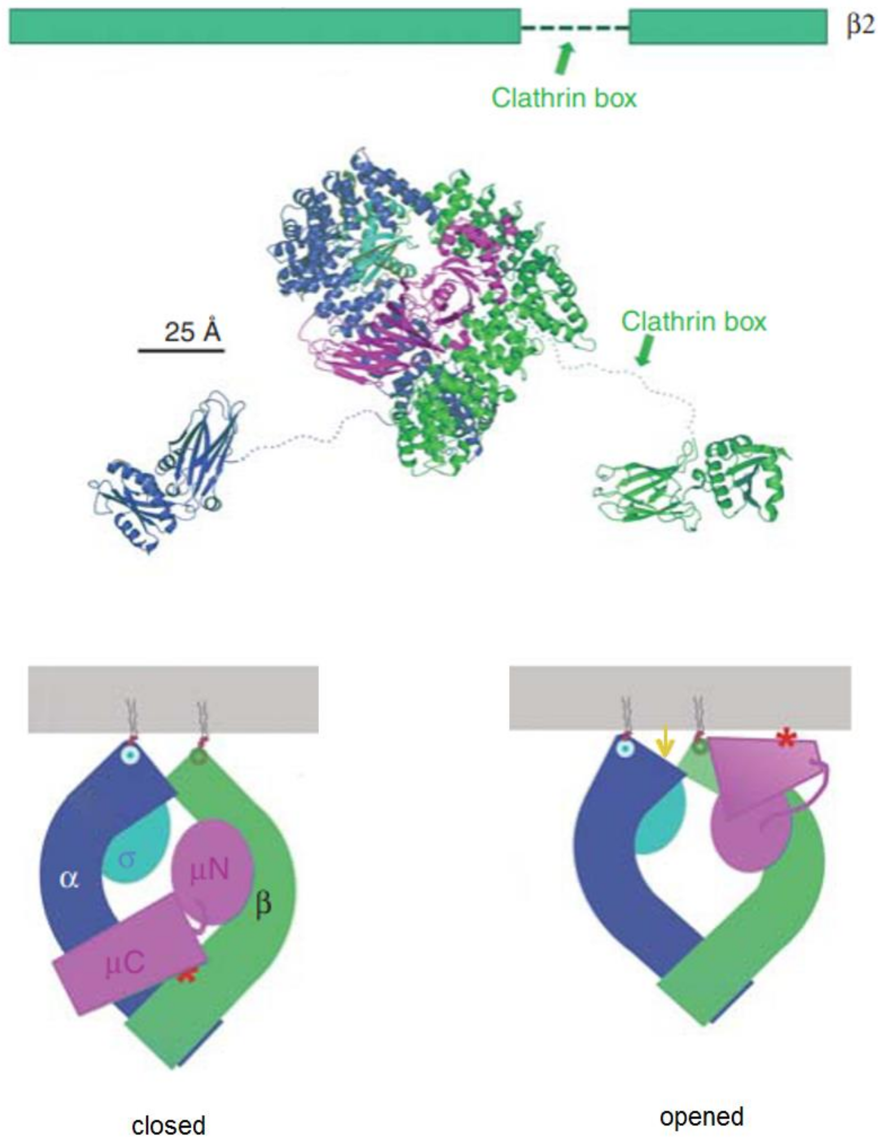

Figure 3-3 : Structure et conformations du complexe AP2. En haut et au milieu la flèche indique la région *clathrin-box,* respectivement sur la présentation linéaire de la sous-unité β2 et sur la structure tridimensionnelle du complexe AP2. En bas sont présentées les conformations fermée (à gauche) et ouverte (à droite) du complexe AP2, dans le conformation ouverte on peut observer le déplacement de la partie C-terminale du sous-domaine μ (astérisque rouge) vers la membrane et le déplacement des domaines liant les phospholipides membranaires aux sous-unités α et β laisse apparaitre le motif de capture du cargo (flèche jaune). Adapté depuis Tom Kirchhausen et al., 2014, *Cold Spring Harb. Perspect. Biol.*

3.1.3 La clathrine

La clathrine est un trimère (T. Kirchhausen, 2000, *Annu. Rev. Biochem.*) composé de 3 chaines lourdes légèrement incurvées qui se rassemblent à leur extrémité C-terminale en un point nodal dit « vertex », les extrémités N-terminales se terminent par un petit repliement, cet assemblage présente une forme proche d'un triskèle vue de dessus (**Figure 3-4**). Une chaine légère lie la partie proximale de chacune des 3 chaines lourdes, parallèlement à celles-ci. Le rôle des chaines légères n'est pas encore complètement élucidé, mais les études existantes leur attribuent un rôle dans de régulation de l'assemblage des triskèles aux membranes cellulaires en venant limiter les degrés de liberté des orientations possibles des chaines lourdes, côté vertex. La présence des chaines légères permet également d'inhiber l'autoassemblage des triskèles de clathrine au pH cytosolique, et n'autorise l'assemblage qu'en présence des protéines adaptatrices dont les charges viennent s'opposer à l'inhibition des chaines légères (Das et al., 2021, *Front. Cell Dev. Biol.*; Greene et al., 2000, *Traffic Cph. Den.*; Redlingshöfer & Brodsky, 2021, *Cells Dev.*).

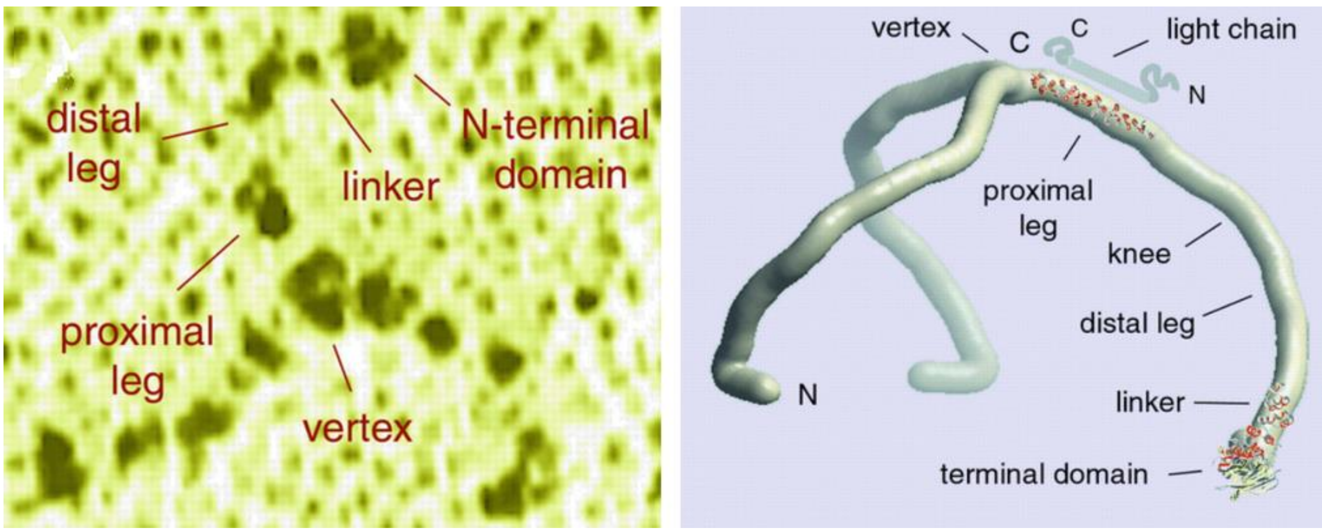

Figure 3-4 : Structure du trimère de clathrine. À gauche : vue de dessus en microscopie électronique sur tranche fine. À droite : structure tridimensionnelle et sous-domaines des jambes de clathrine. Adapté depuis T. Kirchhausen, 2000, *Annu. Rev. Biochem.*

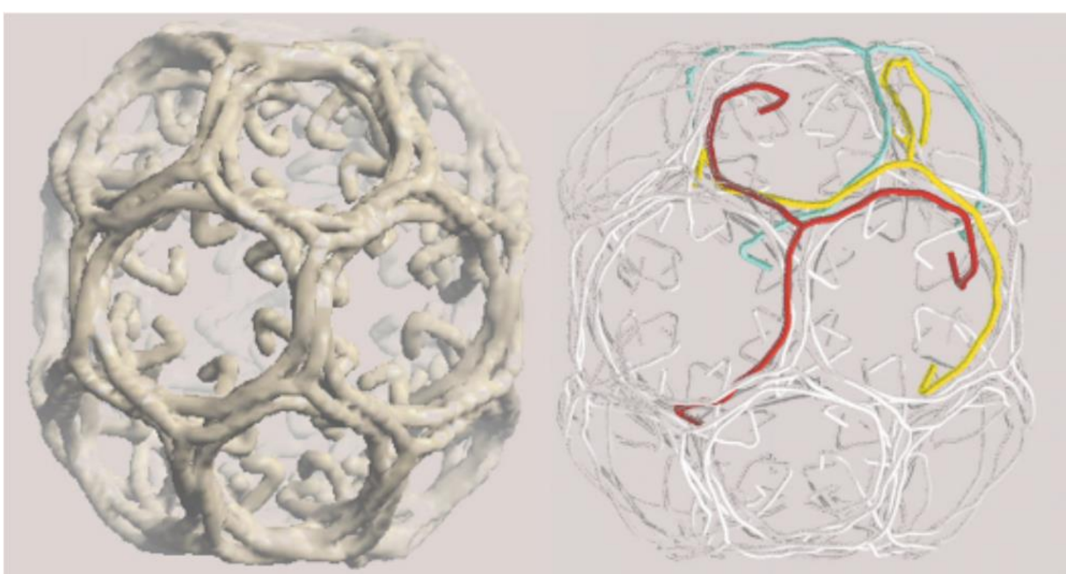

Figure 3-5 : Structure de l'assemblage des triskèles de clathrine en manteau autour d'une vésicule. Les triskèles peuvent former des faces hexagonales ou pentagonales, à droite 3 triskèles distincts sont représentés en rouge, jaune et cyan. Adapté depuis T. Kirchhausen, 2000, *Annu. Rev. Biochem.*

3.1.4 L'assemblage clathrine-AP2

Chez les mammifères, la protéine adaptatrice AP2 est la seule des 4 protéines de sa famille à pouvoir générer des vésicules à manteau de clathrine (*clathrin-coated vesicle* : CCV) à la membrane plasmique neuronale (Danglot & Galli, 2007, *Biol. Cell*; Robinson, 2004, *Trends Cell Biol.*), cette caractéristique lui fait jouer un rôle central dans le recyclage vésiculaire présynaptique. Avec la clathrine qu'elle recrute, ces deux protéines vont former un manteau au maillage composite pentagonal et hexagonal à la membrane (**Figure 3-5**), et effectuer les étapes d'endocytose mentionnées en section 3.1.1. Dans l'assemblage AP2-clathrine c'est la dynamine qui vient effectuer la constriction et la scission de la vésicule et la détacher ainsi de la membrane (**Figure 3-6**).

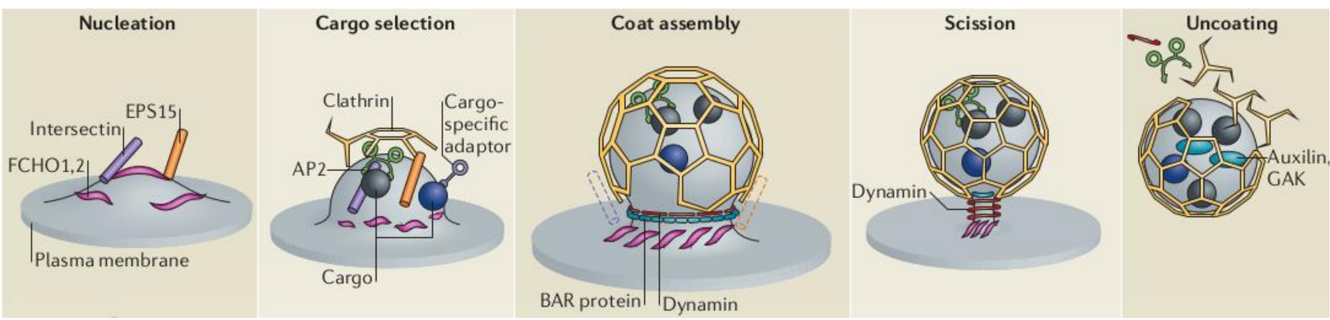

Figure 3-6 : Processus moléculaire de la CME chez les mammifères. FCHO se lie aux lipides membranaires et recrute l'intersectine et EPS15, puis ces deux dernières recrutent AP2 qui capture le cargo et recrute les trimères de clathrine, au fur et à mesure que la clathrine est recrutée elle s'assemble en manteau et contribue à générer la force nécessaire pour créer une protusion sphérique de membrane, enfin la dynamine forme une constriction à la base de la vésicule jusqu'à sa scission de la membrane plasmique. Une fois détachée de la membrane, des auxilines recrutent des phosphatases qui débarassent la vésicule de son manteau de clathrine en quelques secondes (K. He et al., 2020, *J. Cell Biol.*). Adapté depuis McMahon & Boucrot, 2011, *Nat. Rev. Mol. Cell Biol.*

3.1.5 Endocytose complète ou avortée

La présence d'un cargo extracellulaire à la membrane ou d'un récepteur transmembranaire n'est pas nécessaire pour que l'assemblage conduisant à l'endocytose ait lieu. En présence d'une concentration locale suffisante des protéines requises pour l'initiation, celles-ci peuvent s'assembler de façon stochastique et éventuellement conduire à une complétion de l'endocytose (Cocucci et al., 2012, *Cell*; Ehrlich et al., 2004, *Cell*; Loerke et al., 2009, *PLoS Biol.*). Bien que ces événements aléatoires arrivant à complétion existent, dans la majorité de ces cas ils se retrouvent rapidement limités par la disponibilité des molécules nécessaires à la complétion. Dans ce cas, l'assemblage du manteau AP2-clathrine s'arrête et en quelques secondes à quelques dizaines de secondes celui-ci peut se désassembler, on parle alors d'endocytose « avortée » (*abortive endocytosis*, Loerke et al., 2009, *PLoS Biol.*).

3.1.6 Autres assemblages de clathrine, questions ouvertes et travaux récents

3.1.6.1 Aire ou courbure constante ?

Suite aux premiers travaux ayant mis en évidence les structures en mailles de clathrine précédant l'endocytose (Pearse, 1975, *J. Mol. Biol.*), il a aussi été observé des étendues aplaties de mailles de clathrine (plaques) dans de nombreux types cellulaires non-neuronaux (**Figure 3-8**, J. Heuser, 1980, *J. Cell Biol.*). La présence simultanée à la membrane plasmique de ces plaques étendues et de dômes courbés de surface réduite suggère une vésicule en formation. Plusieurs décennies de travaux (Robinson, 2015, *Traffic*) sur ces structures ont conduit à l'élaboration de deux modèles possibles décrivant le rôle potentiel du maillage de clathrine lors de l'endocytose, l'endocytose à aire constante et l'endocytose à courbure constante (**Figure 3-7**, Avinoam et al., 2015, *Science*). Dans le modèle à aire constante, toute la surface de membrane qui va composer la CCV est d'abord recouverte d'un maillage quasi-plan de clathrine, puis la courbure membranaire a lieu sans ajout supplémentaire de clathrine et la vésicule est formée. Ce modèle suppose qu'une aire suffisamment grande de membrane doit être couverte pour pouvoir générer la force nécessaire à la courbure. Dans le modèle à courbure constante, la courbure membranaire commence dès les premiers assemblages de clathrine et les trimères de clathrine sont ajoutés au fur et à mesure que la vésicule se forme. Ce modèle suppose que les CCV ne peuvent émerger depuis les larges plaques de clathrine.

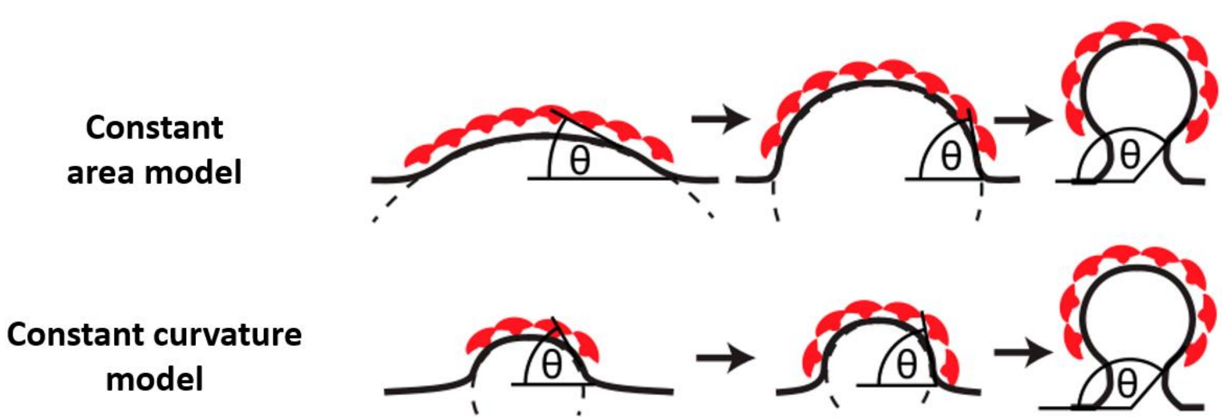

Figure 3-7 : Modèles de courbure membranaire dans l'endocytose. Sont présentés en haut le modèle d'endocytose à aire constante, en bas le modèle d'endocytose à courbure constante. La membrane plasmique est représentée en noir et le manteau de clathrine en rouge. Adapté depuis Redlingshöfer et al., 2020, Proc. Natl. Acad. Sci.

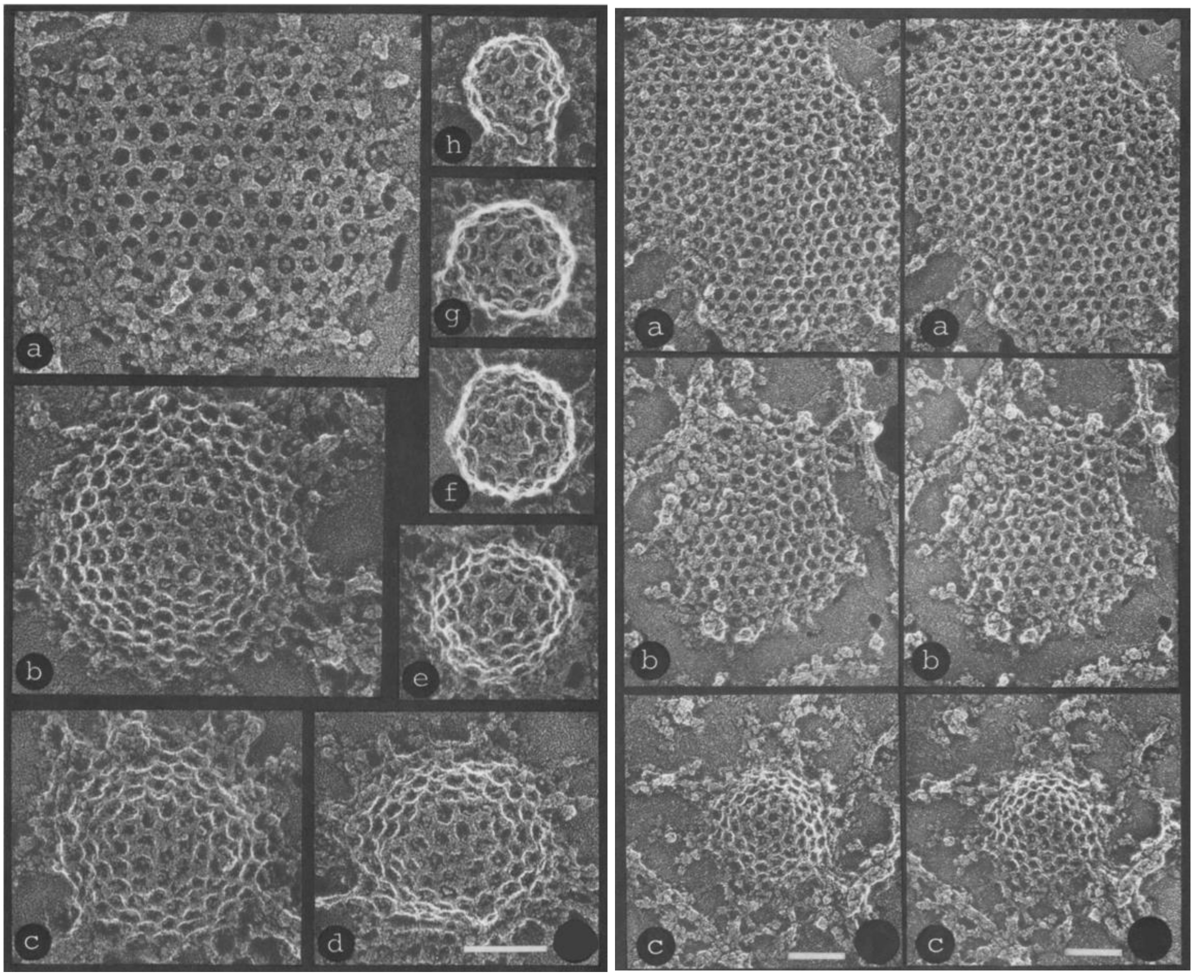

Figure 3-8 : Observations historiques en PREM des plaques membranaires de clathrine. À gauche on observe la diversité de courbure des structures de clathrine membranaire trouvées au sein d'un échantillon, triée de la plus plate (a) aux plus courbées (f, g, h). À droite des paires d'image en stéréoscopie montrent le relief des structures de clathrine à différentes courbures, de la plus plate (a) à une courbure quasi hémisphérique (c). Adapté depuis J. Heuser, 1980, J. Cell Biol.

Les synthèses des travaux récents suggèrent que ces deux modèles ne sont pas mutuellement exclusifs et qu'une diversité de voies conduisant à la production d'une CCV existerait. Les paramètres biophysiques de tension et courbure membranaire propres à chaque type cellulaire et son environnement proche seraient déterminants pour définir la voie structurelle par laquelle les CCV se forment (**Figure 3-9**, Sochacki & Taraska, 2019, *Trends Cell Biol.*).

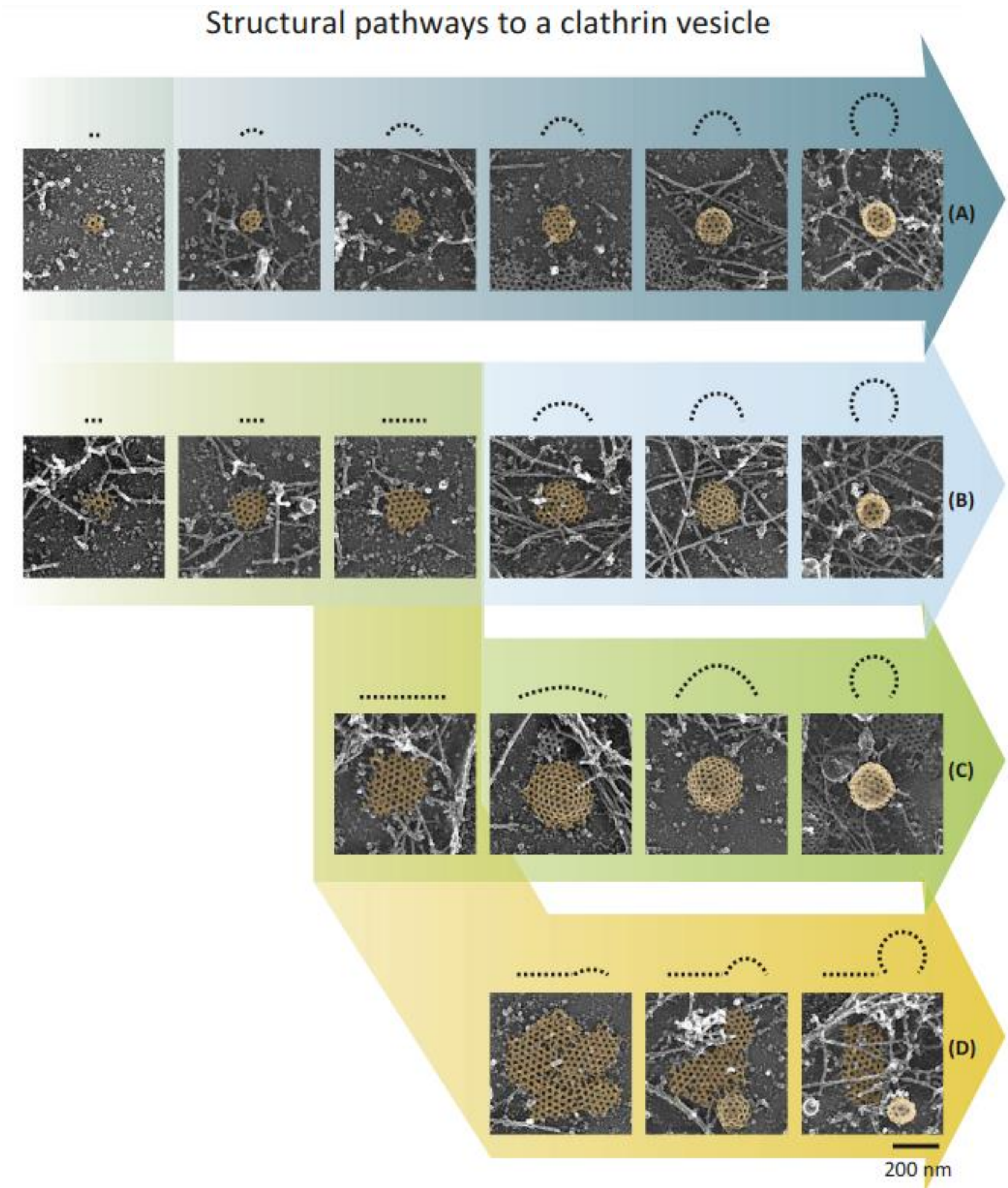

Figure 3-9 : Diversité des voies structurelles possibles conduisant à la formation d'une CCV. La flèche (A) montre la voie dite « classique », une vésicule unique se forme depuis un assemblage progressif de triskèles de clathrine à la membrane et déforme progressivement cette dernière. La flèche (B) montre un assemblage d'abord plan à la membrane, qui s'incurve à mi-chemin du recrutement de la clathrine pour finalement former la CCV. La flèche (C) montre un assemblage de clathrine plan à la membrane qui ne s'incurve qu'une fois le recrutement de la clathrine completé. La flèche (D) montre la formation d'une CCV directement depuis un large assemblage de clathrine plan à la membrane et en ne « consommant » qu'une partie de la clathrine présente dans celui-ci. La couleur des différentes flèches met en relief la diversité des chemins possibles entre ces différentes voies et ainsi la variabilité des processus de formation de CCV. Adapté depuis Sochacki & Taraska, 2019, *Trends Cell Biol.*

Enfin, récemment deux études ont montré que la présence d'épissages alternatifs de la chaine lourde (Moulay et al., 2020, *J. Cell Biol.*) ou légère (Redlingshöfer et al., 2020, *Proc. Natl. Acad. Sci.*) de clathrine peuvent influencer de façon majeure la courbure des chaines lourdes des triskèles, modulant ainsi leur propriétés mécaniques et l'équilibre biophysique lors de leur assemblage. Dans un modèle cellulaire de myotubes, l'exon 31 de la chaine lourde de clathrine est présent dans un des 2 épissages possibles, et une modification antisens de celui-ci conduit à une diminution des assemblages de clathrine en plaques et une augmentation des assemblages en puits. À l'inverse, la surexpression du même exon dans des myoblastes qui présentent peu de plaques et beaucoup de puits permet d'inverser la distribution et leur faire produire majoritairement des plaques. Ce résultat laisse penser que la distribution hétérogène des plaques dans les différents types cellulaires serait à minima partiellement expliquée par le type d'isoforme exprimée (Moulay et al., 2020, *J. Cell Biol.*). Dans des neurones de souris la composition hétérogène des mailles de clathrine avec des isotypes neuronaux *a* et *b* de la chaine légère contribue à favoriser la formation de CCV par comparaison avec des mailles de clathrine composées d'isotypes non-neuronaux ou bien présentant une composition homogène avec un seul des deux isotypes neuronaux. Les expériences en électrophysiologie montrent que l'isotype neuronal *a* favorise le recyclage vésiculaire et l'isotype neuronal *b* le régule à la baisse. Ceci suggère que l'endocytose neuronale nécessite d'une part d'avoir une efficacité accrue comparée aux autres types cellulaires, et d'autre part de pouvoir être finement régulée à la hausse ou à la baisse en fonction de l'équilibre entre les isotypes neuronaux *a* et *b* (Redlingshöfer et al., 2020, *Proc. Natl. Acad. Sci.*). Enfin une dernière étude récente suggère que les plaques aplaties de clathrine sont bien plus flexibles et diverses qu'initialement envisagé et qu'elles peuvent former des CCV sans apport externe d'énergie et sans modification dans la composition des trimères. L'étude souligne aussi le rôle de la tension membranaire générée spécifiquement par les phospholipides associés aux protéines d'adhésion focales dans la création des plaques (Sochacki et al., 2021, *Dev. Cell*).

3.1.6.2 De l'actine aux CCP en formation dans les cellules mammifères ?

Des échafaudages d'actine sont nécessaires à la CME dans les levures, mais ceci reste sujet à débat dans les cellules mammifères (Almeida-Souza et al., 2018, *Cell*; Merrifield & Kaksonen, 2014, *Cold*

Spring Harb. Perspect. Biol.). L'état des connaissances actuelles laisse penser que l'actine est requise pour la CME dans les levures car par leur morphologie cellulaire, leur tension membranaire est plus élevée que pour les cellules de mammifères et la membrane demande donc davantage de force pour être invaginée pour former une vésicule. L'actine branchée observée autour des CCV en formation dans les levures jouerait donc un rôle d'échafaudage pour contrebalancer la tension membranaire là où la force de l'association AP2/clathrine serait suffisante dans les cellules de mammifères (Boulant et al., 2011, *Nat. Cell Biol.*). Toutefois une étude réalisée sur des fibroblastes montre qu'un assemblage d'actine est recruté à la base de la vésicule peu de temps après l'initiation de sa constriction par la dynamine (Merrifield et al., 2002, *Nat. Cell Biol.*). La compréhension actuelle est que le phénomène d'endocytose n'est pas uniforme à tous les types cellulaires et présente des spécialisations en fonction des contraintes spécifiques à chacun des types (Almeida-Souza et al., 2018, *Cell*), la tension membranaire semblant être un facteur déterminant (Merrifield & Kaksonen, 2014, *Cold Spring Harb. Perspect. Biol.*).

3.2 L'endocytose dans le neurone

Après avoir décrit les aspects moléculaires généraux de la CME, puis identifié l'existence d'isotypes neuronaux de la clathrine suggérant une modulation fine de l'endocytose neuronale, et pour entrer à présent dans les spécificités fonctionnelles de la CME dans les neurones (Moulay et al., 2020, *J. Cell Biol.*; Redlingshöfer et al., 2020, *Proc. Natl. Acad. Sci.*) un détour s'impose par le phénomène complémentaire de celle-ci: l'exocytose.

3.2.1 Exocytose, mécanismes et intérêt

Un aspect particulièrement étudié et connu des neurones est leur capacité d'exocytose synaptique rapide lors du déclenchement d'un PA. L'exocytose est le phénomène de fusion de vésicules intracellulaires à la membrane plasmique et grâce auquel le contenu vésiculaire se retrouve libéré dans l'espace extracellulaire (Doherty & McMahon, 2009, *Annu. Rev. Biochem.*). Ce phénomène universel aux cellules eucaryotes est compris comme une spécialisation fonctionnelle parallèle à leur organisation en compartiments qui leur permet une communication qui ne soit pas purement diffusive et donc liée uniquement à la concentration globale d'un composé dans le cytosol (**Figure 3-10**, Guček et al., 2012, *Neurochem. Res.*). Ainsi une cellule peut conserver une réserve de petits compartiments renfermant une concentration importante d'un composé à proximité du site de transduction dont il est effecteur au lieu de nécessiter une concentration importante du composé dans le volume total du cytosol pour déclencher la voie de transduction.

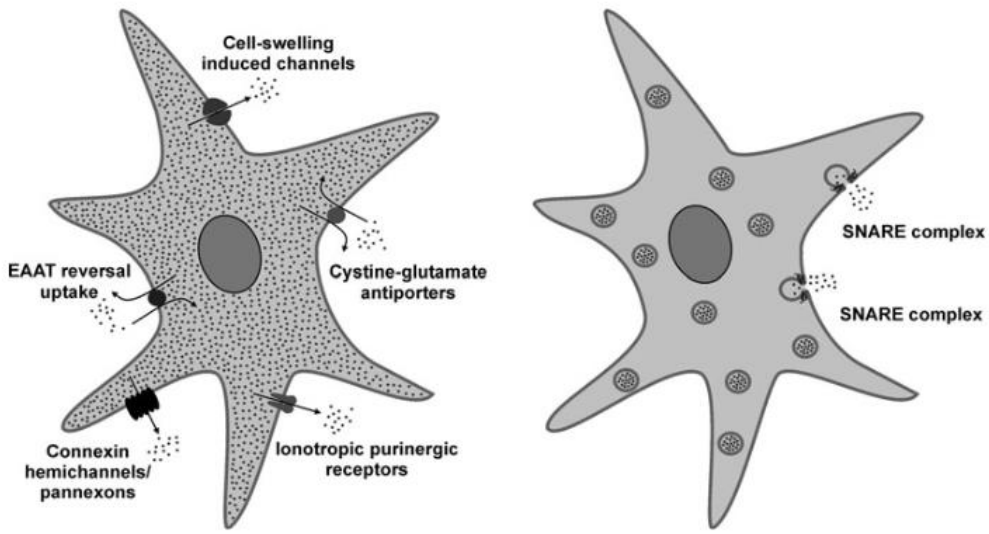

Figure 3-10 : Avantage d'une communication non-diffusive dans une cellule astrocytaire. À gauche : la concentration d'un composé est la même partout dans le cytosol et elle est régulée globalement par des mécanismes de canaux et pompes membranaires. À droite : des concentrations locales de composés peuvent exister dans des compartiments membranaires dédiés, ces composés peuvent être libérés par fusion membranaire des compartiments. Adapté depuis Guček et al., 2012, *Neurochem. Res.*

3.2.2 Le cycle exocytose/endocytose dans la transmission synaptique

Dans les neurones, des synapses peuvent se former par contact direct entre axone et dendrite ou soma, ou par l'intermédiaire d'une épine dendritique. La présynapse est le côté émetteur du message et se trouve sur l'axone, où plusieurs centaines d'entre elles peuvent être présentes. Une réserve locale de vésicules remplies de neurotransmetteurs s'y trouve et peut être déversée dans la fente synaptique par exocytose. Du coté post-synaptique on retrouve une organisation locale spécialisée (*post-synaptic density* : PSD) et cette zone est enrichie en récepteurs membranaires sensibles aux neurotransmetteurs. Cette dynamique sophistiquée de transmission rapide et modulation d'information cellule à cellule nécessite la présence de mécanismes d'exocytose et d'endocytose particulièrement efficaces et dont l'équilibre est finement régulé.

3.2.2.1 Exocytose présynaptique

L'exocytose est ainsi le mécanisme par lequel un neurone présynaptique transforme le signal électrique du PA en message chimique transmis à un neurone postsynaptique par la fusion de vésicules chargées en neurotransmetteurs dans la fente synaptique, elle permet l'effection d'une voie de transduction intercellulaire dans un temps se comptant en millisecondes (Sabatini & Regehr, 1999, *Annu. Rev. Physiol.*). Cette effection rapide de la voie de signalisation synaptique demande une réserve considérable de vésicules chargées de neurotransmetteurs prêtes à être fusionnées à la synapse (**Figure 3-11**). L'organisation intracellulaire de la présynapse reflète cette nécessité, on y retrouve une réserve de vésicules prêtes à être exocytées immédiatement lors de l'arrivée d'un PA (*readily releasable pool* : RRP), un pool de recyclage contenant des vésicules rechargées en neurotransmetteurs mais pas encore rendues sensibles à l'arrivée du PA (*priming*) pour suppléer rapidement à celles du RRP lors d'une stimulation physiologique prolongée (*recycling pool*), et un pool dit « de réserve » (*reserve pool*) dont les vésicules ne sont pas disponibles immédiatement pour l'exocytose mais peuvent maturer et être libérées en cas de stimulation intense (Rizzoli & Betz, 2005, *Nat. Rev. Neurosci.*, Danglot & Galli, 2007, *Biol. Cell*).

Figure 3-11 : Modèle des différents pools de vésicules synaptiques. Les vésicules du pool de libération immédiate (RRP, en vert) sont à proximité immédiate de la fente synaptique et sont les premières mobilisées lors d'une exocytose. Le pool de réserve contient la plus grande part des vésicules d'une synapse (en rouge), plus en retrait de la membrane. Ces vésicules sont mobilisées lentement en cas de stimulation intense ou prolongée. Les vésicules du pool de recyclage (en jaune) sont plus nombreuses que celles du RRP et moins nombreuses qu'au pool de réserve, elles sont présentes de façon diffuse entre ces deux pools et sont mobilisables en cas de stimulation physiologique d'intensité modérée. Adapté depuis Danglot & Galli, 2007, *Biol. Cell*.

Comme l'exocytose est dépendante de la disponibilité des vésicules synaptiques et des stimuli nerveux qui peuvent se prolonger sur des durées bien supérieures à celles de la déplétion du RRP, un mécanisme de recyclage vésiculaire est nécessaire pour pouvoir rapidement rendre disponibles de nouvelles vésicules exocytables et maintenir la transmission synaptique dans le temps (Rizzoli & Betz, 2005, *Nat. Rev. Neurosci.*; Südhof, 2004, *Annu. Rev. Neurosci.*). Une partie de ce mécanisme de recyclage présynaptique est assuré par la CME.

3.2.3 L'endocytose présynaptique

Lors de l'exocytose à la zone active (ZA) de la synapse, les vésicules peuvent se comporter de différentes façons (**Figure 3-12**), elles peuvent partiellement fusionner avec la membrane et créer ainsi une lumière par laquelle les neurotransmetteurs sont libérés dans la fente synaptique, puis s'en détacher et soit être dirigées rapidement vers le pool de réserve (*kiss and run*), soit être immédiatement recyclées et remplies à nouveau de neurotransmetteurs puis *primées* avant d'être à nouveau exocytées au RRP (*kiss and stay*). Ces deux mécanismes seraient indépendants de la CME mais leur nature très transitoire rend leur étude particulièrement ardue et les déterminants de ces mécanismes sont peu connus. L'état des connaissances sur ce sujet (Chanaday et al., 2019, *J. Neurosci.*) indique des résultats variables en fonction des conditions expérimentales de la physiologie propre à l'espèce animale et au type neuronal étudié : la question de l'importance de leur présence est encore débattue à ce jour. L'existence d'une voie d'endocytose ultrarapide (*ultrafast endocytosis*) indépendante de la CME et située en périphérie de la ZA présynaptique sous certaines conditions d'excitation a été suggérée et ouvre de nouvelles questions sur le recyclage synaptique (Watanabe et al., 2013, *Nature*).

La CME est historiquement la voie canonique du recyclage vésiculaire synaptique et c'est dans ce contexte que les résultats de mes travaux sont interprétés, sans nier l'existence probable de mécanismes composites d'endocytose impliquant à la fois CME et les formes d'endocytose plus récemment observées. Dans cette voie canonique, les vésicules exocytées sont entièrement fusionnées à la membrane plasmique et libèrent ainsi leur contenu dans la fente synaptique, puis la membrane est recyclée par CME en périphérie de la ZA (Bingham et al., 2023, *J. Cell Biol.*; J. E. Heuser & Reese, 1973, *J. Cell Biol.*) et reforme ainsi une vésicule qui peut être dirigée soit vers le pool de recyclage pour une réutilisation rapide, soit vers un endosome présynaptique qui stocke localement une réserve de membrane depuis laquelle des vésicules peuvent être reformées.

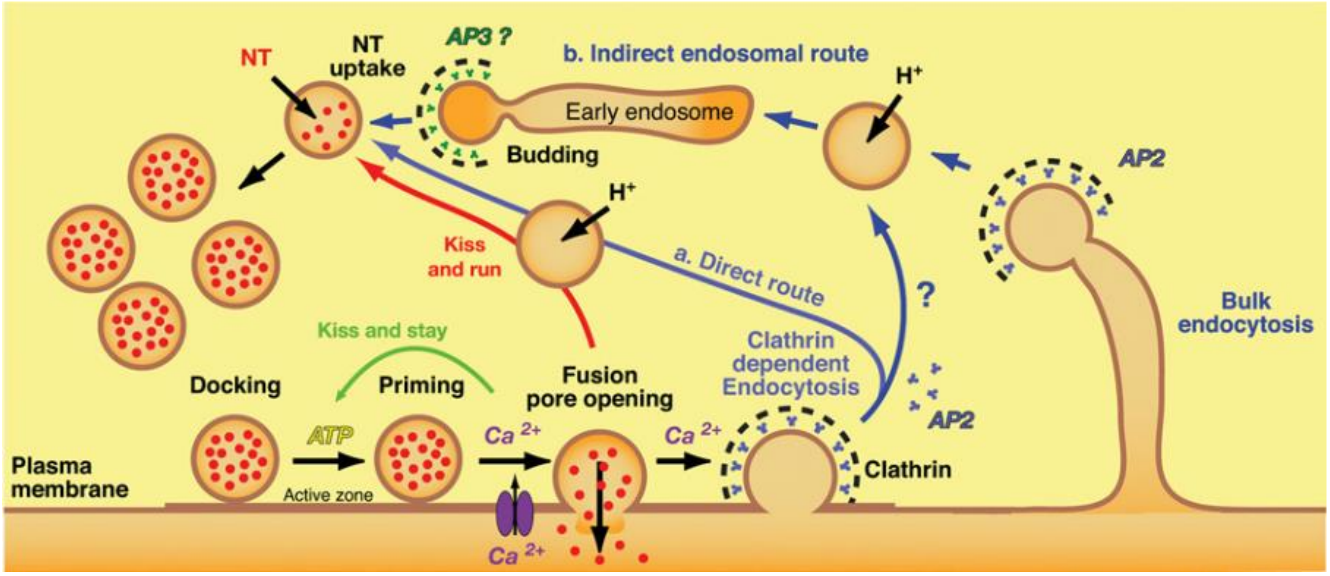

Figure 3-12 : Modèles des différentes voies de recyclage vésiculaire à la synapse. De gauche à droite, dans le sens anti-horaire, les vésicules du pool de recyclage sont maturées (chargées en neurotransmetteur NT), puis accrochées à la membrane et « primées » (rendues disponibles à l'exocytose). Lors d'une stimulation, le flux entrant de calcium active la chaine de signalisation qui conduit à la fusion vésiculaire à la membrane synaptique. Avant la fusion totale avec la membrane plasmique ces vésicules fusionnées peuvent alors soit être recyclées pour réutilisation immédiate par le mécanisme de « kiss and stay », pour être recyclées et re-maturées rapidement via le kiss and run, ou endocytées et re-maturées rapidement par la voie directe de la CME. Les vésicules endocytées par CME peuvent aussi prendre la voie indirecte et être dirigées vers des endosomes depuis lesquels de nouvelles vésicules pourront être crées et maturées. Adapté depuis Danglot & Galli, 2007, *Biol. Cell*.

3.2.4 L'endocytose de récepteurs

Plus d'une décennie après la découverte de la CME présynaptique, le mécanisme de régulation par CME des récepteurs membranaires fut d'abord décrit sur le récepteur couplé aux protéines G β-adrénergique de grenouille (**Figure 3-13**, Chuang & Costa, 1979, *Proc. Natl. Acad. Sci. U. S. A.*) puis observé directement sur le récepteur humain (Ferguson et al., 1996, *Science*; von Zastrow & Kobilka, 1992, *J. Biol. Chem.*). Ces travaux évoquent également 2 voies possibles pour les récepteurs à la suite de leur endocytose, ils peuvent être gardés momentanément en vésicule ou adressés dans un endosome regroupant plusieurs contenus vésiculaires. Ces récepteurs pourront plus tard être à nouveau recyclés depuis les endosomes et transportés à nouveau à la membrane plasmique, ou bien encore être ciblés pour être dégradés dans les lysosomes.

3.2.4.1 L'endocytose de récepteurs postsynaptiques pour réguler l'excitabilité

Dans la même période, le récepteur GABA-A fut le premier récepteur ionotropique postsynaptique dont la régulation par CME fut mise en évidence dans des neurones corticaux de poulet (Tehrani & Barnes Jr., 1991, *J. Neurochem.*) et de rat (Jalilian Tehrani & Barnes Jr., 1993, *J. Neurochem.* **Figure 3-13**).

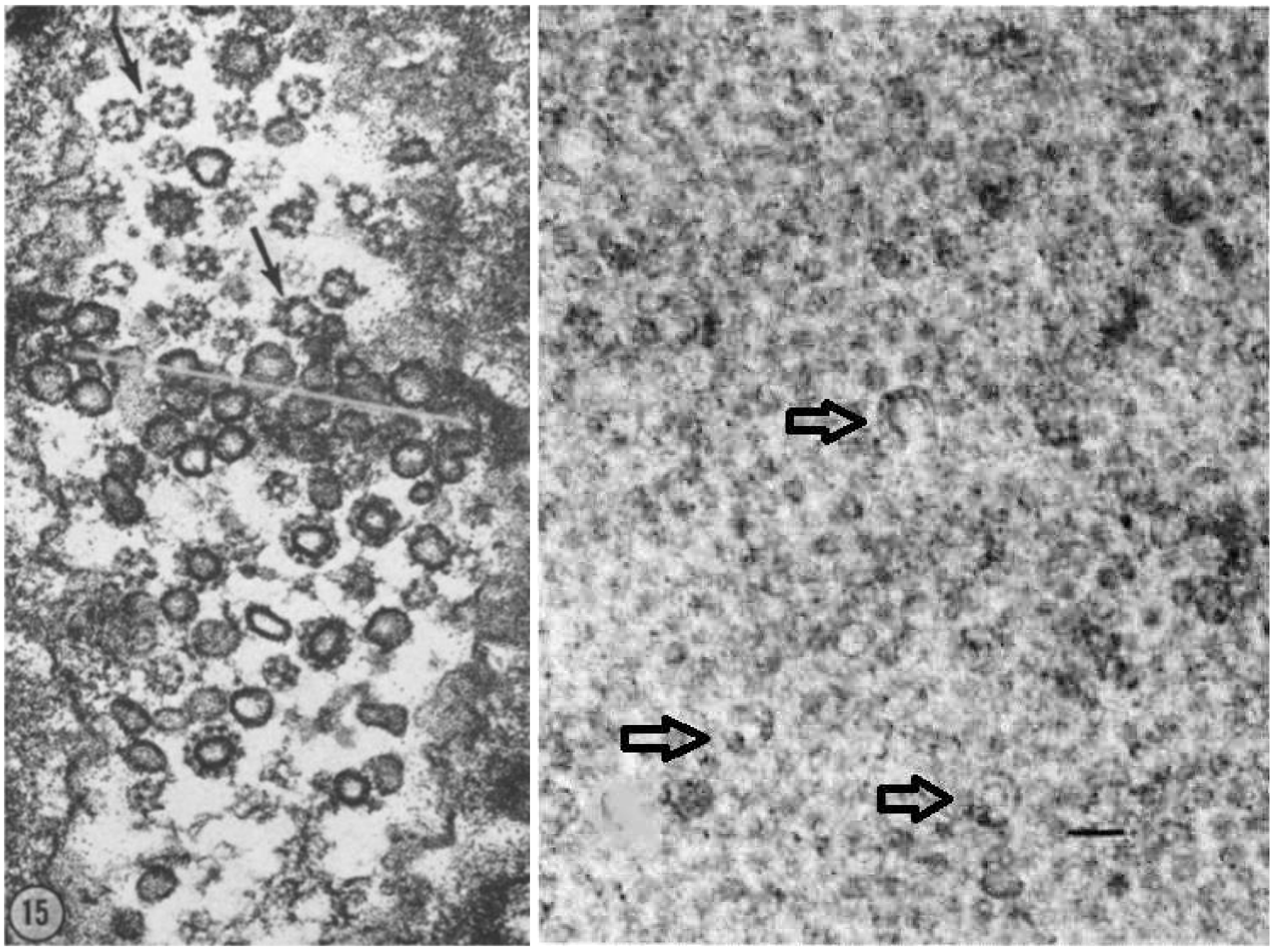

Figure 3-13 : Observations historiques de recyclage présynaptique et d'endocytose de récepteurs postsynaptiques. À gauche l'existence possible du recyclage de vésicules synaptiques a été déduit depuis l'observation de vésicules à manteau à la jonction neuromusculaire de grenouille stimulée (J. E. Heuser & Reese, 1973, *J. Cell Biol.*). Droite : Vésicules à manteau de clathrine ayant internalisé le récepteur GABA-A, isolées depuis des cerveaux de rats après stimulation GABA-A ou benzodiazépines et observées en microscopie électronique sur tranches ultrafines. Adapté depuis Jalilian Tehrani & Barnes Jr., 1993, *J. Neurochem.*

Toujours à la même période, plusieurs travaux en microscopie (Liao et al., 1999, *Nat. Neurosci.*) et électrophysiologie (Isaac et al., 1995, *Neuron*) ont conduit à faire l'hypothèse de l'existence de synapses glutamatergiques « silencieuses » (Malenka & Nicoll, 1997, *Neuron*) de par l'observation d'absence à la membrane de récepteurs AMPA nécessaires pour initier la réponse postsynaptique des récepteurs NMDA (**Figure 3-14**). Ces récepteurs sont présents dans la cellule et peuvent être externalisés à la membrane postsynaptique en induisant une potentiation de long-terme (*long-term potentiation* : LTP). L'existence de ces synapses silencieuses et de l'endocytose des récepteurs postsynaptiques dans les dendrites est désormais bien établie et reconnue comme une contributrice importante de la régulation à la hausse ou à la baisse de l'excitabilité postsynaptique (Blanpied et al., 2002, *Neuron*; Carroll et al., 2001, *Nat. Rev. Neurosci.*).

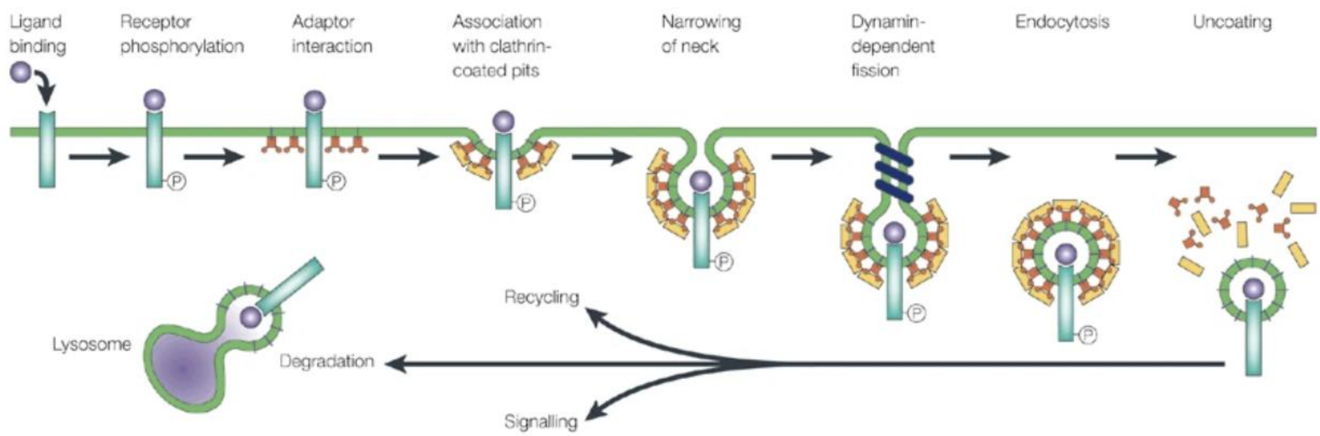

Figure 3-14 : Mécanisme de régulation de l'activité d'un récepteur membranaire par CME et voies possibles post-endocytose. Suite à l'activation de la voie de transduction du ligand, la CME est initiée et réalisée comme décrit précédemment **Figure 3-2** et **Figure 3-6**, puis le récepteur peut être recyclé et transporté à nouveau à la membrane, il peut aussi servir à activer une voie de transduction plus en aval, ou être dégradé par acidification dans un lysosome. Adapté depuis Carroll et al., 2001, *Nat. Rev. Neurosci.*

3.2.4.2 Internalisation de composés extracellulaires et pinocytose

Comme mentionné dans les parties précédentes, la CME peut aussi avoir lieu de façon aspécifique d'un cargo membranaire particulier et faire ainsi entrer dans la cellule des composés solubles du milieu extracellulaire présents à la membrane au moment son invagination (Kaksonen & Roux, 2018, *Nat. Rev. Mol. Cell Biol.*), du fait de leur petite taille ces composés sont ainsi internalisés passivement en même temps que le milieu extracellulaire dans lequel ils se trouvaient. On parle alors de pinocytose ou d'endocytose de phase fluide, celle-ci possède deux voies, dépendante ou indépendante de la clathrine. Cette endocytose non-spécifique d'un ligand ou d'un récepteur sera utilisée expérimentalement dans l'article principal en partie 0.

3.3 Des interactions entre la CME et le MPS ?

Dans des types cellulaires non-neuronaux mais présentant des assemblages similaires à ceux que l'on retrouve dans le MPS des neurones, des travaux récents suggèrent qu'il pourrait exister un lien fonctionnel entre les composantes du MPS et l'endocytose.

3.3.1 Ankyrine-G/β2-spectrine dans cellules cylindriques de l'épithélium

Dans leurs travaux publiés en 2015 Jenkins et al. s'intéressent aux membranes latérales des cellules épithéliales cylindriques (**Figure 3-15**, Jenkins et al., 2015, *Sci. Adv.*). Ces cellules présentent des microdomaines sous-membranaires composés d'assemblage mobiles de spectrine et d'ankyrine-G et dont le déplacement nécessite la présence des microtubules. Leurs expériences de suppression du domaine de liaison à l'ankyrine-G (*ankyrin binding domain* : ABD) sur les spectrines ou en KO ankyrine-G montrent une diminution de hauteur de la membrane latérale, sauf en présence d'inhibiteurs de l'endocytose. Dans leur ensemble, ces expériences indiquent que les microdomaines sous-membranaires mobiles de spectrine/ankyrine-G inhiberaient l'endocytose aux membranes latérales, ce qui permettrait ainsi la morphogénèse et le maintien desdites membranes.

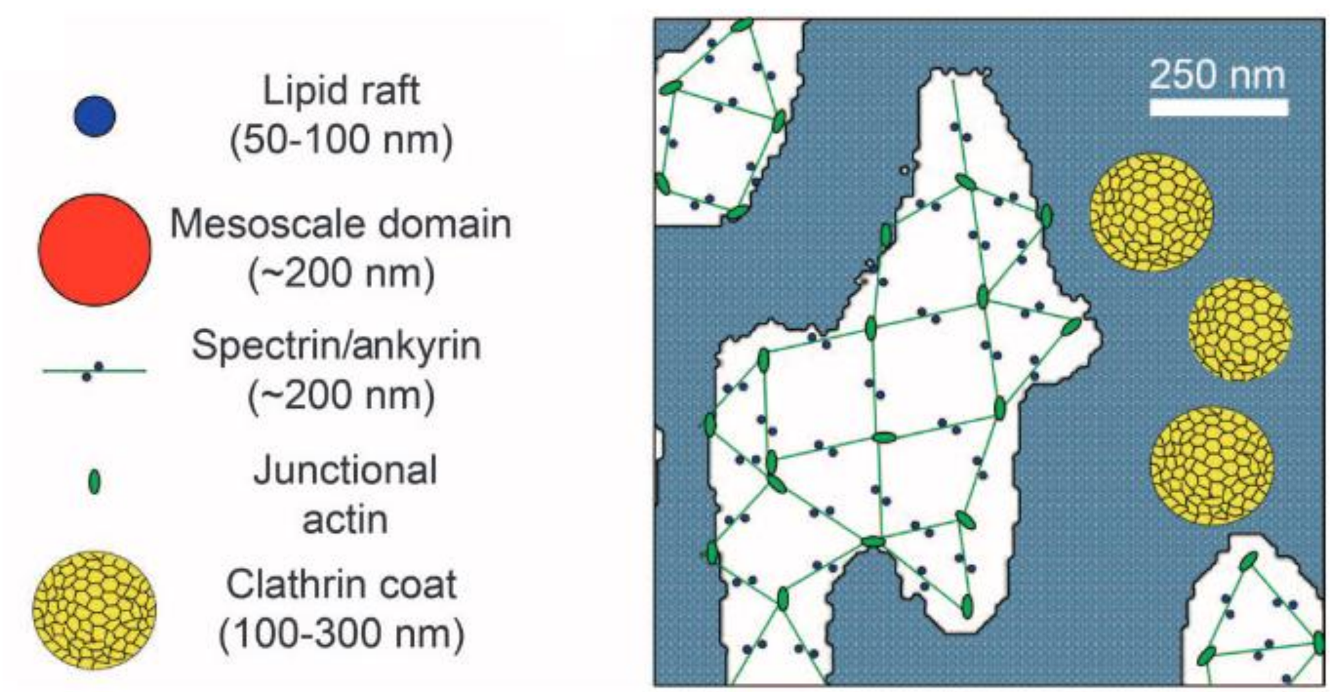

Figure 3-15 : Modèle des interactions sous-membranaires entre composants du cytosquelette et de l'endocytose dans les cellules épithéliales. À la membrane latérale, les manteaux de clathrine ne sont retrouvés qu'en dehors des microdomaines mobiles présentant un maillage actine/spectrine/ankyrine. Adapté depuis Jenkins et al., 2015, *Sci. Adv.*

3.3.2 Le réseau spectrine/acto-myosine définit des zones incluant la CME

En caractérisant les liens et la dynamique du complexe actine-myosine et de la β2-spectrine dans les adaptations membranaires de fibroblastes, Ghisleni, Galli et al. ont fait l'observation que la distribution des protéines associées à l'endocytose (Clathrine et AP2) semblait être mutuellement exclusive avec les structures de β2-spectrine (Ghisleni et al., 2020, *Nat. Commun.*). Les autrices de cette publication ajoutent qu'en plus de cette distribution en microdomaines exclusifs, la durée de vie moyenne de la CME est corrélée avec les densités de β2-spectrine et avec l'état d'association forte ou faible entre actine et β2-spectrine, lui-même correspondant à différentes phases de remodelage de la membrane plasmique. Elles suggèrent enfin un modèle d'interdépendance à 4 composants impliquant phospho-myosines, spectrines, endocytose et activité contractile de l'actine-myosine.

3.3.3 Des composants de la CME présents à l'axone en dehors de la synapse

Lors d'une étude précédente réalisée dans l'équipe (Vassilopoulos et al., 2019, *Nat. Commun.*) portant sur la composition des filaments d'actine axonale du MPS en microscopie corrélative STORM/PREM sur des neurones de rat *unroofés*, des structures identifiées comme des CCP furent observées à la face interne de la membrane axonale et celles-ci présentaient une certaine cohérence relativement au MPS. Dans l'axone les CCPs étaient presque systématiquement circonscrits dans « clairières » dénuées de maillage sous-membranaire, faiblement denses en électron (**Figure 3-16**, zones sombres en arrière-plan des CCPs indiqués par des flèches blanches).

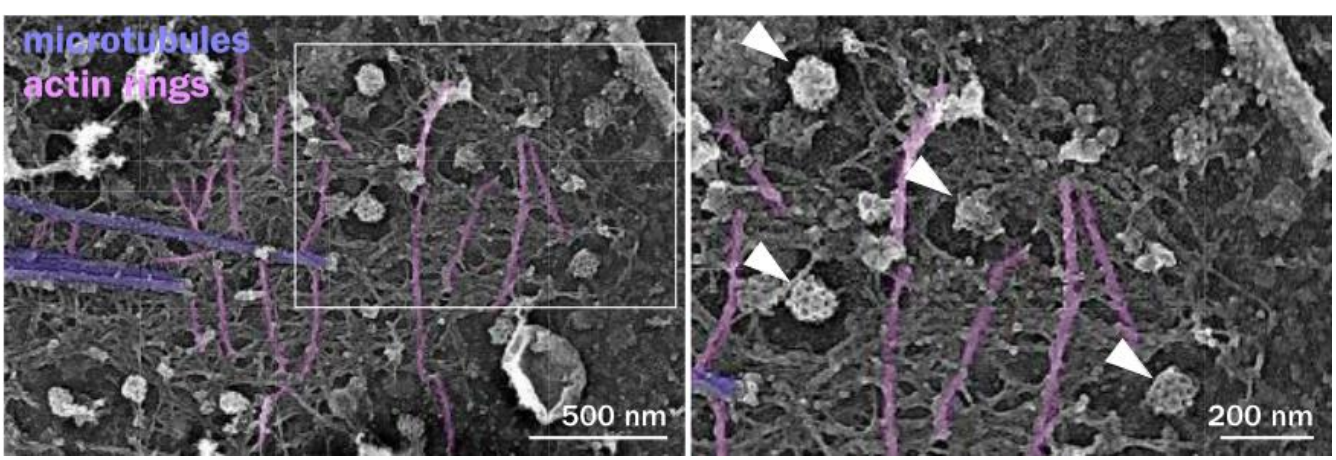

Figure 3-16 : Structures de clathrine axonale au sein du MPS. Observations en PREM après unroofing, les microtubules sont montrées en violet, l'actine en magenta, il s'agit de fausses couleurs dans les deux cas. Les marqueurs indiquent les structures identifiées comme des CCP dans des microdomaines dénués de MPS. Adapté depuis Vassilopoulos et al., 2019, *Nat. Commun.*

Ainsi, plusieurs indices récents peuvent laisser penser qu'il existerait un lien entre plusieurs des composants majeurs du cytosquelette ou du MPS neuronal et le processus cellulaire d'endocytose. C'est sur la base de ces observations préliminaires que le projet de recherche rapporté par cette thèse fut initié.

Méthodologie de la recherche

4 Visualiser et étudier le cytosquelette et l'endocytose

Pour étudier les deux composantes cellulaires que cette thèse aborde, des moyens de rendre visible l'endocytose et de perturber le cytosquelette et l'endocytose sont nécessaires. Les méthodes dans leurs aspects strictement techniques sont décrites dans le manuscrit de chaque article, et ce chapitre se concentre à replacer celles-ci dans le contexte de la thèse et à expliquer leur utilisation.

4.1 Méthodes biologiques

4.1.1 Marqueurs/sondes d'endocytose

4.1.1.1 Endocytose de transferrine

Pour pouvoir rendre l'endocytose observable et quantifiable, une méthode éprouvée est d'incuber les cellules en présence d'un cargo associé à une sonde fluorescente qui sera endocyté par les cellules. Ce marqueur peut entrer dans la cellule par le biais de la liaison à un récepteur, c'est le cas de la transferrine (Tf) qui est couramment utilisée de par la présence de son récepteur dans un grand nombre de types cellulaires chez les vertébrés (Kawabata, 2019, *Free Radic. Biol. Med.*), incluant les neurones (Johnsen et al., 2019, *Prog. Neurobiol.*). L'internalisation du récepteur lié à la Tf contribue à réguler l'homéostasie du fer intracellulaire, et cette endocytose est dépendante de la clathrine (Qian & Ke, 2019, *Biol. Rev.*). Dans l'article principal associé à cette thèse, plusieurs expériences utilisent de la Tf couplée à une sonde fluorescente Alexa Fluor comme marqueur de la CME. Ces expériences permettent en particulier de visualiser l'endocytose dans les fibroblastes Rat2, et de comparer les proportions de CME du récepteur Tf dans les compartiments dendritiques, somatiques et axonaux sur des échantillons fixés après un temps d'incubation de la sonde fluorescente.

4.1.1.2 Endocytose de phase fluide

La robustesse de la méthode par endocytose de Tf est dépendante de la proportion de récepteurs Tf exprimés par la cellule ou le compartiment que l'on souhaite étudier. Dans les cellules compartimentées comme les neurones, cette dépendance à la présence des récepteurs Tf peut devenir une limite de la méthode, dans le cas où ce récepteur est trop peu ou n'est pas présent dans le compartiment étudié. Comme le montrent nos expériences et des résultats précédents (Cameron et al., 1991, *J. Cell Biol.*; Patton et al., 1992, *J. Cell Biol.*) le récepteur Tf est quasiment absent à l'AIS et dans l'axone qui sont au centre de ce travail de recherche, une autre méthode est donc nécessaire pour visualiser l'endocytose.

Lors de la CME, une partie du liquide extracellulaire est internalisé au sein de l'invagination formée depuis la membrane plasmique et les composés présents dans le liquide extracellulaire peuvent ainsi se retrouver internalisés, on parle alors d'endocytose de phase-fluide. L'endocytose de phase fluide est un phénomène surtout étudié dans le contexte de la macropinocytose (indépendante de la clathrine) mais il est également présent de façon passive lors de la CME, on parle alors de micropinocytose (Cousin & Smillie, 2021, *Exocytosis Endocytosis Methods Protoc.*; Saha et al., 2013, *Small*). Pour étudier la CME axonale, nous avons utilisé du dextran 10kDa, un polysaccharide soluble dont le poids moléculaire et les dimensions (10 kDa, rayon 2.3 nm) lui permettent d'être intégré à une CCV en formation Ballesteros & Swartz, 2020, *J. Vis. Exp.*; Chen et al., 2022, *Proc. Natl. Acad. Sci.*; Li et al., 2015, *Cell Biol. Int.*). Couplé à une sonde fluorescente fixable Alexa Fluor, ce marqueur de phase-fluide permet d'obtenir une visualisation du contenu extracellulaire internalisé dans le cytosol par micropinocytose. Il faut noter que dans les cas d'endocytose initiée mais non complétée à la membrane (lors de l'utilisation de Pitstop 2 ou lors d'une fixation en cours d'endocytose par exemple) le dextran fluorescent peut rester prisonnier d'un CCP en cours de formation mais toujours attachée à la membrane et contribuer ainsi au signal fluorescent de l'échantillon sans pour autant être passé dans le cytosol. Ce point particulier sera important pour interpréter au mieux les observations réalisées lors d'expériences utilisant ce cargo.

4.1.1.3 Endocytose de sonde pH-sensible pHrodo

Pour observer la dynamique temporelle de l'endocytose le long de l'axone de neurones vivants, un type de sonde fluorescente plus élaboré est nécessaire. En effet, avec du dextran dont la fluorescence est toujours présente, il serait compliqué de pouvoir distinguer le dextran fluorescent du milieu dans lequel les neurones sont observés du dextran qui a été endocyté par la cellule. Une sonde dont la fluorescence est directement conditionnelle à l'internalisation dans une vésicule est donc nécessaire (**Figure 4-1**). Nous avons utilisé du dextran couplé à une sonde pHrodo dont la fluorescence est sensible au pH et ne devient visible par acidification qu'une fois internalisée et transportée dans la voie de recyclage vésiculaire à la suite de la CME.

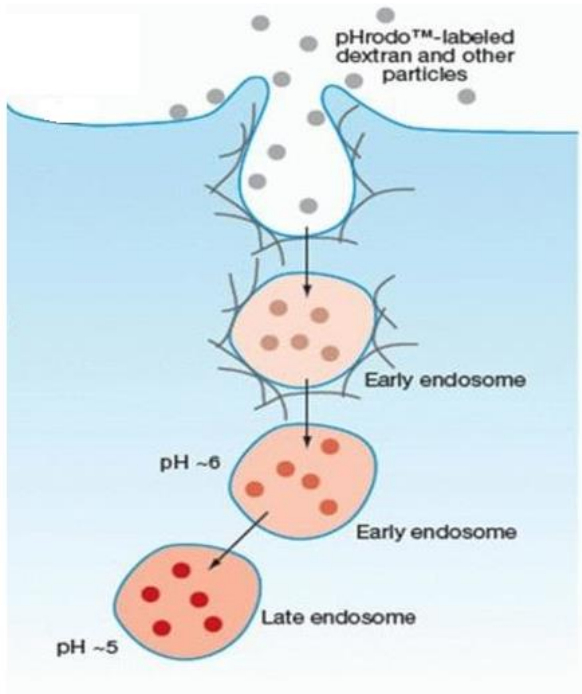

Figure 4-1 : Sonde fluorescente pHrodo. La fluorescence de la sonde est quasi-inactive à pH extracellulaire et brille de plus en plus intensément par la baisse du pH dans la voie de recyclage endosomal et de degradation lysosomale. Adapté depuis la documentation fabricant *pHrodo*^{TM} *Red and Green Dextran, 10000 MW, for Endocytosis*.

4.1.2 Perturbation de la CME

Pour perturber l'endocytose peu après l'initiation de l'assemblage de ses premières composantes moléculaires, nous avons utilisé du Pitstop 2, un composé inhibiteur qui bloque l'accessibilité du domaine terminal de la clathrine ciblé par le domaine *clathrin-box* d'AP2 (von Kleist et al., 2011, *Cell*) et le même domaine sur l'amphiphysine (Miele et al., 2004, *Nat. Struct. Mol. Biol.*), ce qui conduit à réduire drastiquement la dynamique d'assemblage de la clathrine et à quasiment « geler » l'endocytose (**Figure 4-2**). Sur des cellules non-neuronales en culture l'utilisation du Pitstop 2 a donné lieu à l'accumulation à la membrane de CCPs dont l'endocytose ne complète pas (von Kleist et al., 2011, *Cell*), in-vivo au calyx de Held de rats l'utilisation de Pitstop 2 a conduit à une diminution de la densité de vésicules récemment recyclées et d'endosomes immatures sans affecter la densité d'endosomes matures, mais en augmentant cependant leur volume (Paksoy et al., 2022, *Front. Synaptic Neurosci.*). Ce dernier résultat ajouté à d'autres (Delvendahl et al., 2016, *Neuron*; Dutta et al., 2012, *PloS One*; López-Hernández et al., 2022, *eLife*) suggère d'une part d'autres effets de Pitstop 2 plus en aval dans la voie de recyclage vésiculaire, et d'autre part une action sur les voies d'endocytose indépendantes de la clathrine mais intermédiées par AP2. Ces études sur les mécanismes de Pitstop 2 n'invalident pas son utilisation dans le cadre d'expériences fonctionnelles sur la CME, elles permettent cependant d'affiner le cadre d'interprétation des résultats lorsque nous l'utilisons dans nos expériences.

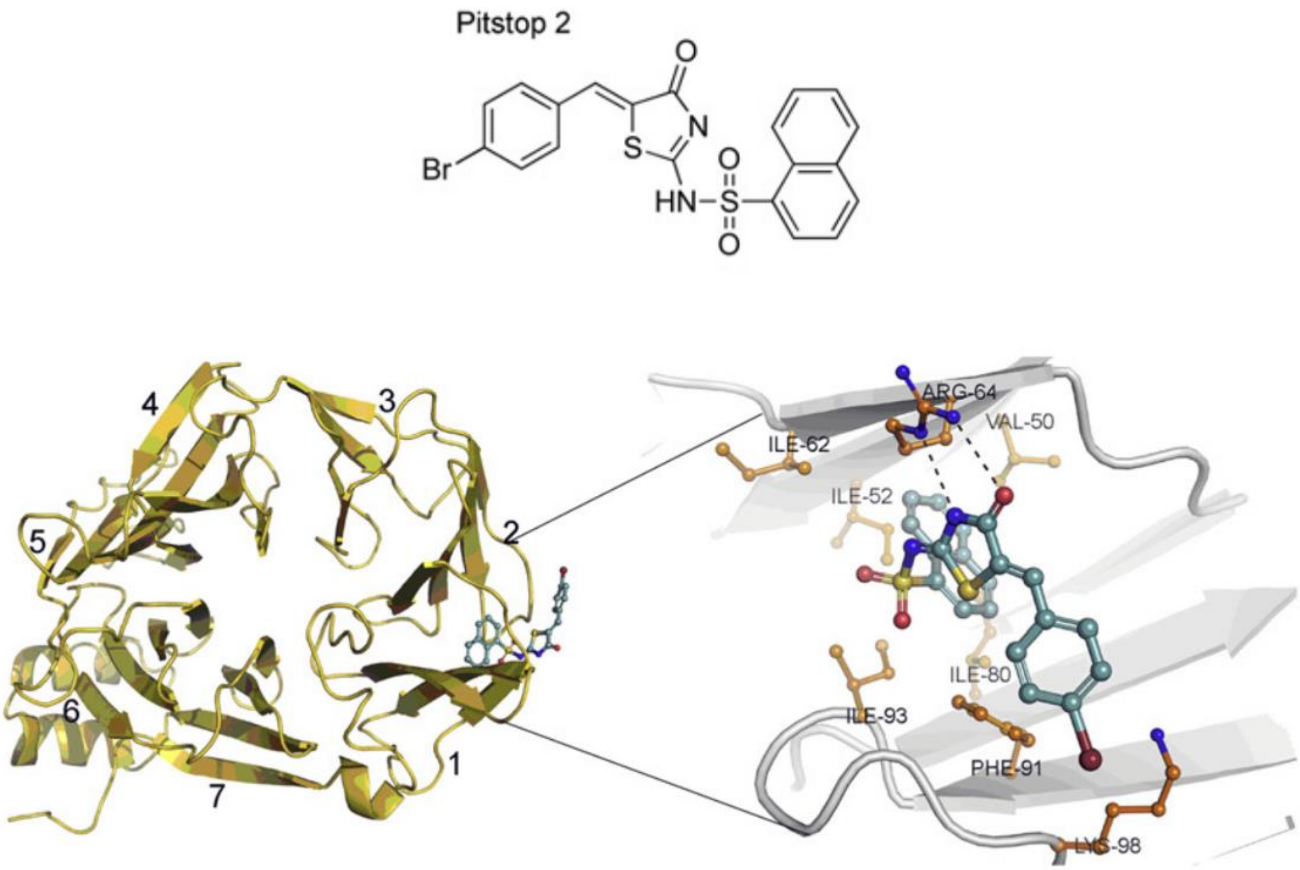

Figure 4-2 : Pitstop 2, molécule et action sur l'endocytose. En haut, on peut voir la structure moléculaire de Pitstop 2. En bas, la molécule de Pitstop 2 occupe le site « clathrin box » du complexe AP représenté en doré. Adapté de von Kleist et al., 2011, Cell.

4.1.3 Stimulation chimique de la CME axonale

Nos observations des CCP axonaux ont montré leur grande stabilité dans le temps en comparaison avec celles des compartiments dendritiques et somatiques, cependant nous observions l'endocytose du neurone sans stimulation extérieure. Récemment, les travaux de Fréal et al., 2023 ont suggéré la régulation par endocytose des récepteurs $Na_V1.2$ dans la partie la plus distale de l'AIS sous l'effet d'une stimulation chimique par du NMDA. Nous avons donc souhaité savoir si les CCP axonaux « inactives » que nous observions pouvaient effectivement endocyter lors d'une stimulation chimique de la transmission synaptique.

Nous avons adapté le protocole de stimulation NMDA issu de l'article mentionné pour réaliser une endocytose stimulée de la sonde dextran-AF555 à l'AIS, puis observé les résultats après fixation (*intact*, contenu total) ou unroofing puis fixation immédiate (*unroofed*, fraction membranaire uniquement, **Figure 4-3**).

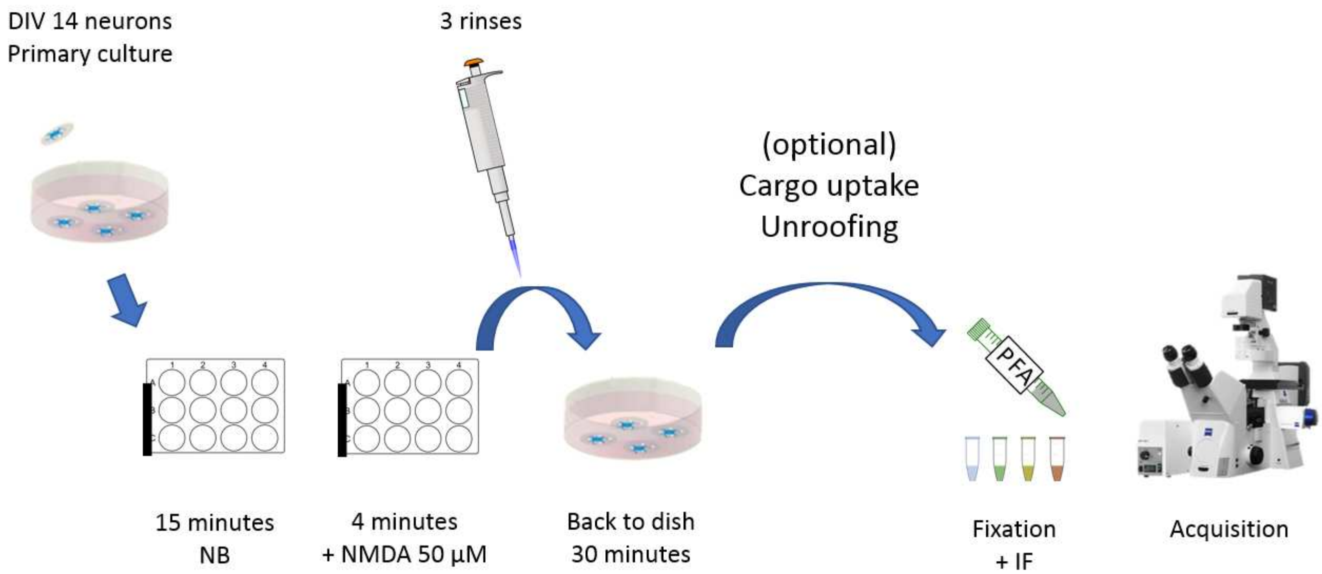

Figure 4-3 : Protocole de stimulation NMDA. Nous avons adapté le protocole présenté dans l'article Fréal et al., 2023 à nos cultures cellulaires et nos préparations d'échantillons. Nous avons aussi élaboré un protocole pour intégrer la stimulation NMDA à nos expériences en endocytose de cargo de phase fluide.

4.1.4 L'unroofing pour distinguer la composante membranaire et cytosolique

Pour déterminer plus précisément l'organisation de la clathrine et de l'endocytose dans l'axone, nous avons souhaité distinguer les assemblages en mailles de clathrine à la membrane de la composante cytosolique et éviter la superposition des membranes ventrales et dorsales en microscopie de fluorescence. Pour atteindre ce but, nous avons utilisé l'unroofing (**Figure 4-4**), une méthode qui consiste à retirer par sonication la membrane cellulaire non adhésive au support de culture, juste avant la fixation des cellules. Cette méthode nous permet de réaliser une observation directe de la seule membrane intracellulaire restante collée à la lamelle de culture.

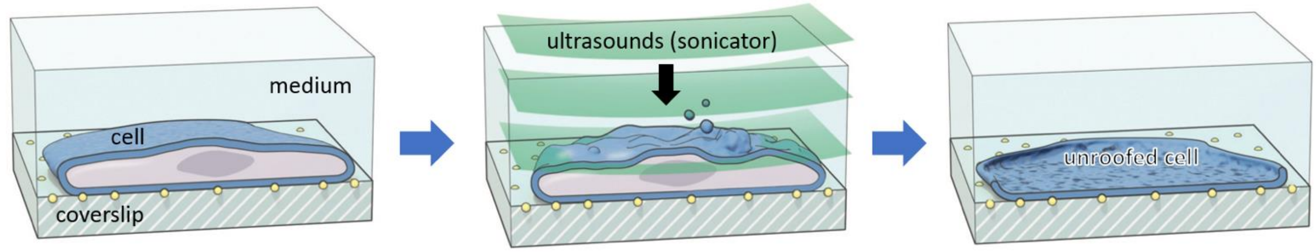

Figure 4-4 : Unroofing de cellule en culture par sonication. L'application d'ondes ultrasoniques en milieu liquide décape la membrane supérieure des cellules et laisse visible la face interne de la membrane adhésive coté substrat de culture. Adapté de S. Vassilopoulos.

4.1.5 Perturbation aigue du MPS avec des inhibiteurs chimiques

À la suite des observations en microscopie électronique qui ont conduit à cette thèse nous avions fait l'hypothèse d'une régulation de l'endocytose médiée par le MPS, MPS qui contrôlerait l'accès à la membrane plasmique. Pour explorer cette hypothèse sur les liens entre le MPS axonal et l'endocytose, nous avons utilisé des perturbations chimiques spécifiques de l'un ou l'autre.

Pour perturber l'actine afin d'observer si cela avait un effet sur l'endocytose, nous avons utilisé la swinholide A (**Figure 4-5**), une molécule qui stoppe l'élongation des filaments d'actine en séquestrant les monomères d'actine G et dépolymérise les filaments déjà assemblés (Spector et al., 1999, *Microsc. Res. Tech.*). Les latrunculines A et B ont été considérées, mais leur effet est uniquement de séquestrer les monomères sans dépolymériser les filaments déjà assemblés, de ce fait nous avons pu constater dans la littérature (Abouelezz et al., 2019, *Biol. Chem.*) et dans une étude précédente de l'équipe (Vassilopoulos et al., 2019, *Nat. Commun.*) qu'elles étaient sans effet pour perturber les anneaux d'actine du MPS à l'axone, et donc non pertinente dans le cadre de ces travaux.

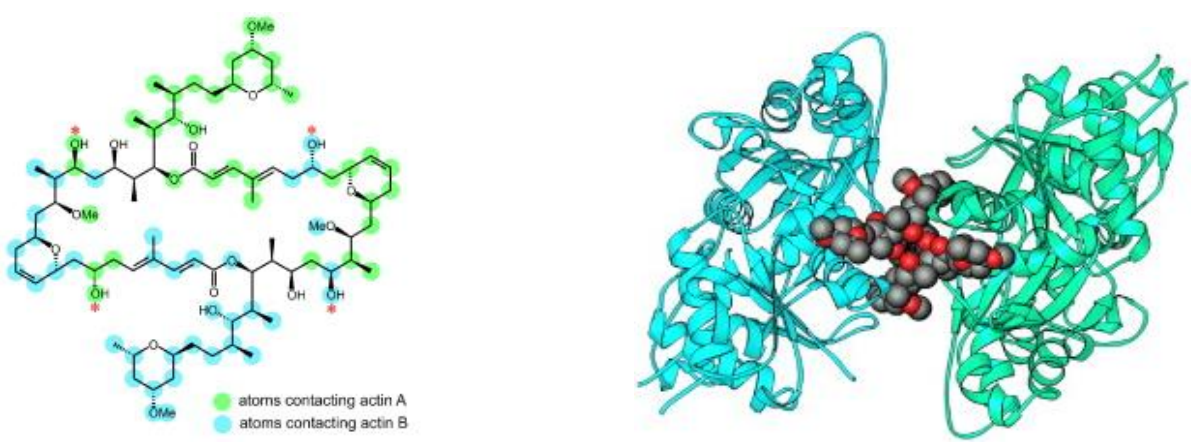

Figure 4-5 : Swinholide A, molécule et séquestration des monomères. La structure moléculaire est montrée à gauche et les sous-domaines impliqués dans la séquestration de chacun des 2 monomères d'actine sont indiqués en vert et en bleu, la représentation tridimensionnelle de la molécule ayant séquestré 2 monomères d'actine est montrée à droite. Adapté depuis Klenchin et al., 2005, Chem. Biol.

Pour agir sur les spectrines, nous avons utilisé de la diamide, un composé qui oxyde les groupements SH des cystéines des spectrines, ce qui provoque la formation de ponts disulfure et induit un repliement en anneau de celles-ci (**Figure 4-6**, Becker et al., 1986, *J. Biol. Chem.*; Borrelli et al., 1998, *J. Cell. Physiol.*; Ghisleni et al., 2020, *Nat. Commun.*). Cette modification de leur structure tertiaire entraine une diminution drastique de leur mobilité et entrave leur capacité à former l'assemblage périodique du MPS axonal.

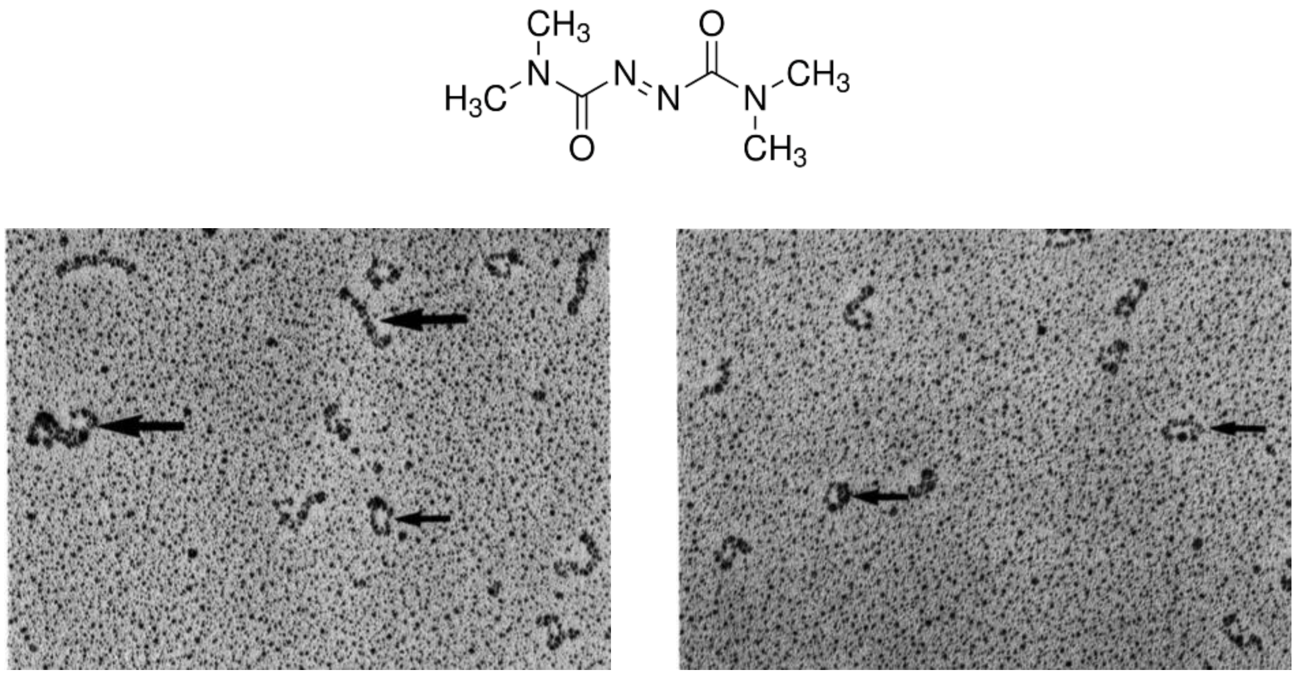

Figure 4-6 : Oxydation des spectrines par l'application de diamide. La molécule de diamide est montrée en haut. En bas, on on observe des spectrines purifiées en milieu non réducteur et acquises en PREM. La condition contrôle est montrée à gauche, ici les spectrines s'assemblent en majorité en dimères et prennent une conformation longitudinale (flèches épaisses), alors qu'à droite après un traitement de 10 µM de diamide les spectrines purifiées sont visibles uniquement sous forme d'oligomères circulaires indiqués par des flèches fines. Adapté depuis Becker et al., 1986, *J. Biol. Chem.*

Pour les travaux rapportés dans cette thèse, nous avons utilisé la swinholide A et la diamide pour observer si le fait d'endommager les composantes principales du MPS axonal conduisait à une modification de la densité de CCP axonaux et la quantité de cargos endocytés.

4.1.6 Perturbation à long terme du MPS avec des shRNA contre les spectrines

Même si l'usage de composés perturbant les phénomènes auxquels nous nous intéressons présente des avantages pratiques pour étudier la mécanistique d'un phénomène, il souffre néanmoins de des limites en matière de spécificité. En effet, la swinholide A cible de façon indifférenciée l'actine axonale du MPS et les autres structures d'actine présentes dans le neurone et la diamide oxyde les groupements sulfhydrile présents dans toute la cellule et pas uniquement ceux des spectrines, ce qui peut conduire à l'observation d'effets non-spécifiques. Pour cibler avec davantage de spécificité les spectrines, nous avons généré des vecteurs viraux et des plasmides codant pour des shRNA.

Les shRNA (*short hairpin RNA*) sont des ARN simple brin présentant deux régions complémentaire qui s'arrangent en une structure secondaire tige-boucle. Ils sont reconnus dans la cellule par le complexe protéique RISC, élément clé du système d'interférence ARN, lui-même un des nombreux système de régulation de l'expression génique utilisé chez les organismes eucaryotes. Une fois incorporée dans ce complexe, les ARNm complémentaires ou partiellement complémentaires de la séquence shRNA sont clivés puis dégradés par des exonucléases impliquées dans le contrôle qualité de la cellule (**Figure 4-7**). Cela entraine ainsi une diminution de l'expression de la protéine codée par ces ARNm (Lambeth & Smith, 2013, *SiRNA Des. Methods Protoc.*).

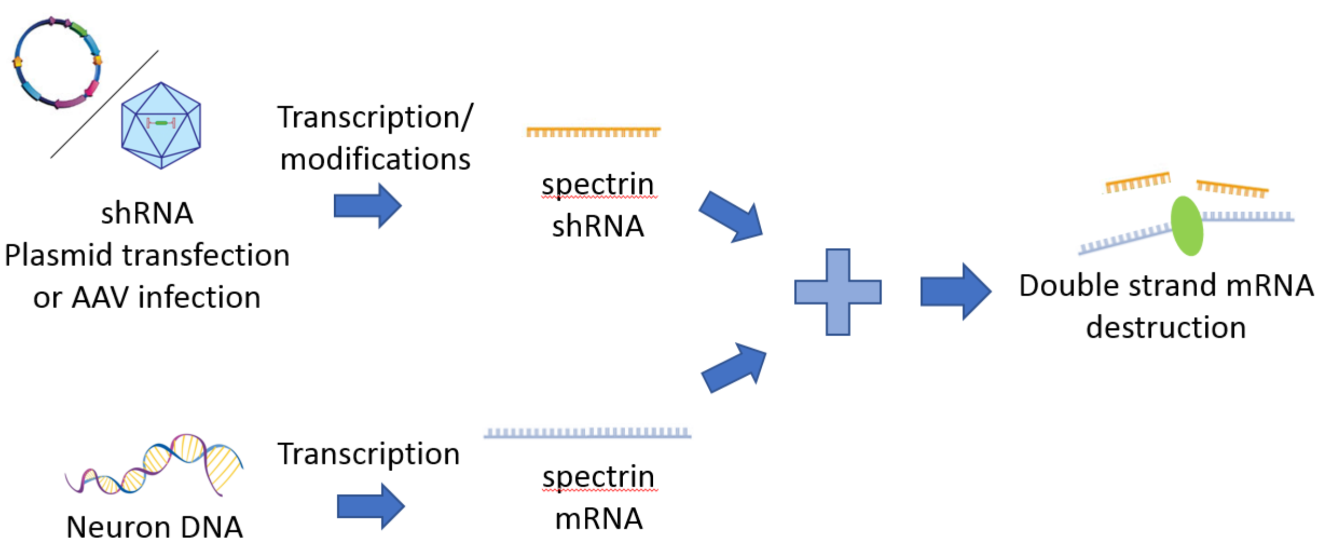

Figure 4-7 : Déplétion des spectrines par shRNA. Mécanismes utilisés pour diminuer l'expression de chacune ou plusieurs des spectrines de façon globale (AAV-shRNA) ou ponctuelle (plasmides shRNA) au sein d'un échantillon.

Nous avons utilisé des shRNA ciblant chacune des α2-, β2- et β4-spectrines, ou plusieurs d'entre elles combinées.

4.1.6.1 Transfection des shRNA par lipofection

Une des méthodes éprouvée pour faire exprimer un shRNA à une cellule est la lipofection. Elle consiste à intégrer au sein d'un plasmide la séquence que l'on souhaite faire exprimer puis à intégrer ces plasmides au sein de liposomes, des structures de lipides dont la charge positive réagit avec le plasmide et va former une enveloppe autour de ce dernier. Cette enveloppe lipidique permet aux plasmides de traverser la membrane plasmique et d'utiliser les mécanismes cellulaires pour être transcrits (**Figure 4-8**). Cette méthode présente la particularité de ne faire exprimer le transcrit que dans un nombre limité de cellules, ce qui peut être un avantage pour faire des comparaisons directes entre cellules transfectées et non transfectées dans une même culture cellulaire.

Par ailleurs la lipofection permet d'intégrer simultanément aux liposomes d'autres plasmides que le shRNA. Les protéines codées par ces plasmides seront surexprimées par la cellule en plus de leur expression endogène. Nous avons par exemple utilisé des protéines de fusion fluorescentes pour visualiser les composantes de l'endocytose (clathrin light-chain et AP2, GFP ou RFP) lors de l'application de shRNAs ciblant les spectrines.

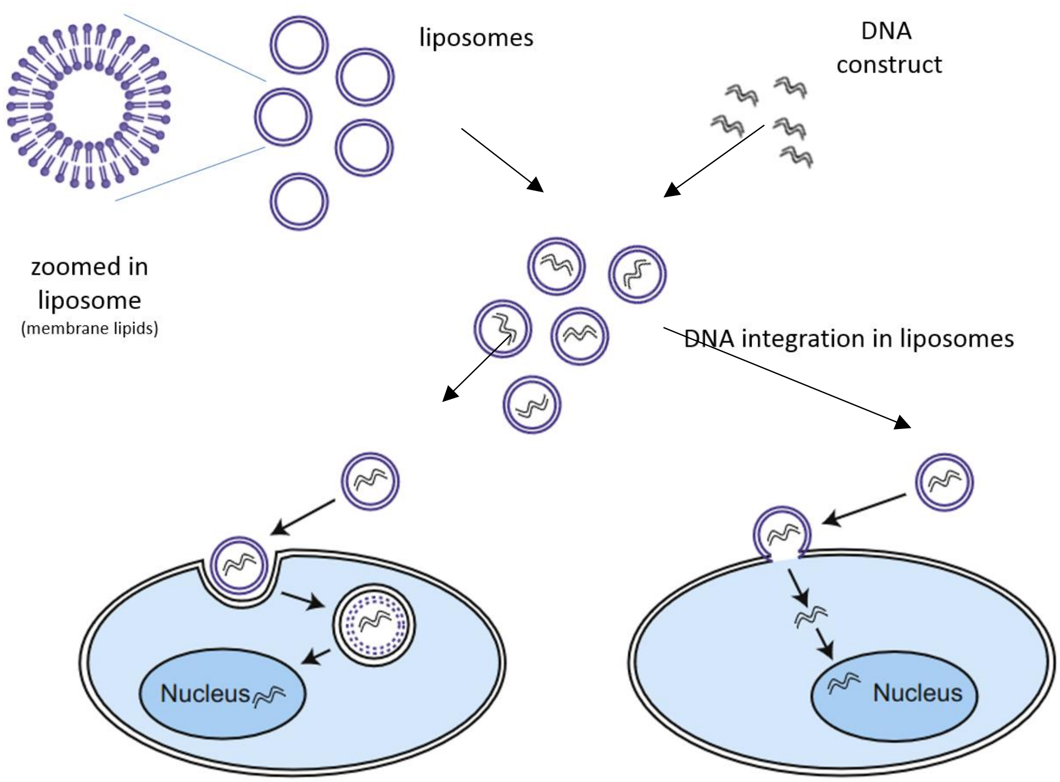

DNA construct delivery and translocation for translation

Figure 4-8 : Lipofection de plasmides. Les plasmides contenant la cassette ADN à exprimer sont intégrés dans des liposomes pouvant être endocytés avec ou sans fusion à la membrane plasmique et ainsi délivrer leur contenu dans le cytosol. Adapté de Carter & Shieh, 2015, Guide Res. Tech. Neurosci. Second Ed.

4.1.6.2 Infection par vecteur AAV-shRNA

Une autre méthode pour exprimer des shRNA dans une cellule est l'utilisation de vecteurs viraux adéno-associés (*adeno-associated virus* : AAV) dont le génome a été modifié pour intégrer la séquence codant le shRNA cible. Ces vecteurs ont la capacité d'entrer dans une grande diversité de types cellulaires, dont les neurones, en fonction du sérotype de leur enveloppe (Lambeth & Smith, 2013, *SiRNA Des. Methods Protoc.*). En faisant produire des constructions AAV-shRNA qui ciblent chacune des spectrines et en infectant des cultures de neurones en développement (DIV3), nous disposons d'un outil moléculaire pour réaliser un effet de plus long terme et plus proche de la physiologie de la cellule qu'une substance chimique. Cependant, cette perturbation à long-terme possède également des désavantages, car elle peut impacter le développement des neurones, provoquer des effets indirects, et être modifiée par des mécanisme de compensation.

4.1.7 Expression endogène d'une clathrine de fusion fluorescente

Les méthodes d'expression d'une protéine par transfection d'un plasmide dont l'ADN sera traduit par la cellule ont l'avantage de la simplicité d'usage expérimental, mais présentent des limites quant à la représentativité qu'elles donnent de la physiologie cellulaire. En effet, les plasmides porteurs d'ADN codant pour une protéine qui existent déjà dans la cellule présentent le risque de faire exprimer à la cellule une plus grande quantité de cette protéine que son niveau d'expression endogène, ce qui peut conduire à une déviation de la physiologie cellulaire. Pour pouvoir contourner ce biais potentiel, il est possible de développer des outils moléculaires basés sur la technologie CRISPR/Cas9 (Jinek et al., 2012, *Science*) grâce auxquels nous pouvons directement remplacer, dans l'ADN cellulaire, une séquence cible par une séquence modifiée de notre choix (*knock-in* : KI). Nous avons utilisé cette technique pour faire exprimer de façon endogène une clathrine fluorescente et observer la dynamique endogène de l'endocytose en microscopie sur cellule vivante.

4.2 Méthodes de microscopie

Les travaux rapportés par cette thèse ont utilisé un ensemble de méthode de microscopie optique et électronique après marquage de l'échafaudage périodique et des puits de clathrine, que nous allons brièvement présenter dans ce chapitre. En ce qui concerne l'organisation des différentes tâches, la culture de neurone, la préparation d'échantillons (incluant l'unroofing) et la microscopie de fluorescence ont été réalisé dans notre laboratoire à Marseille, puis les échantillons envoyés en express au laboratoire de Stéphane Vassilopoulos à Paris pour effectuer la préparation des répliques de platine et les acquisitions en microscopie électronique.

4.2.1 Méthodes d'immunocytochimie

4.2.1.1 Immunofluorescence

Pour la microscopie de fluorescence, nous avons utilisé les techniques devenues courantes en biologie d'immunomarquage par anticorps primaires spécifiques à la cible d'intérêt et secondaires couplées à un fluorophore (**Figure 4-9**), pour une introduction historique générale voir Childs, 2014, *Pathobiol. Hum. Dis.*, pour des protocoles généraux sur différents types d'échantillons voir Im et al., 2019, *Methods Mol. Biol. Clifton NJ.*

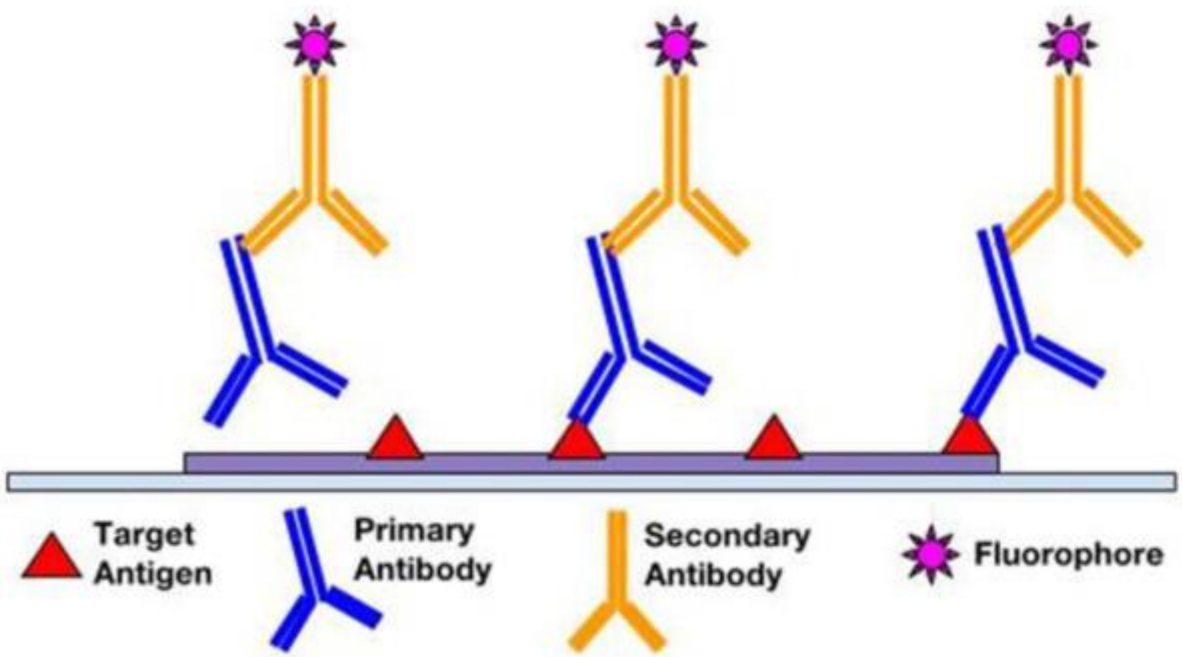

Figure 4-9 : Principe de l'immunofluorescence indirecte. Les anticorps primaires en bleu ciblent l'antigène d'intérêt (triangle rouge), puis des anticorps secondaires qui ciblent l'espèce de l'anticorps primaire et couplés à un fluorophore sont utilisés. Adapté depuis Im et al., 2019, Methods Mol. Biol. Clifton NJ.

4.2.1.2 Immunogold

En microscopie électronique sur réplique de platine (*platinum replica electron microscopy* PREM), une méthode alternative à la fluorescence est nécessaire pour pouvoir marquer et identifier des structures spécifiques. Pour cela, une méthode d'immunomarquage dont les prémisses restent les mêmes que précédemment est utilisée : la différence se situe au niveau du fluorophore qui est remplacé par une nanoparticule d'or. Ces particules ont la particularité d'être très denses en électrons, et donc facilement identifiables sur l'échantillon observé en microscopie électronique. Des exemples de PREM avec un marquage immunogold de la clathrine sont montrés dans Collins et al., 2011, *Curr. Biol. CB*, des marquages immunogold de l'actine et les spectrines sont visibles dans Vassilopoulos et al., 2019, *Nat. Commun.* (**Figure 4-10**)

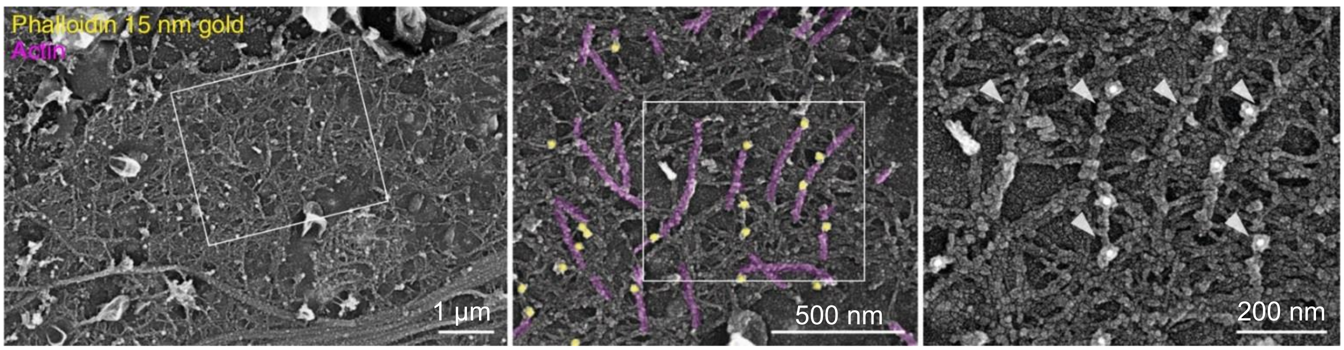

Figure 4-10 : Immunogold de l'actine axonale. A milieu un marquage en fausses couleurs montre les filament d'actine en magenta et l'immunomarquage en phalloïdine-gold en jaune. Sur le panneau de droite les flèches blanches pointent les filaments d'actine et les billes d'or sont identifiables en blanc, constrastant avec le reste de l'échantillon moins dense en électrons. Adapté depuis Vassilopoulos et al., 2019, Nat. Commun.

4.2.2 Microscopie super-résolue

Les structures étudiées dans ces travaux de thèse présentent des tailles moyennes souvent inférieure à la limite de la diffraction optique : 50 à 100 nm de diamètre pour un CCP, 190 nm de période pour le MPS d'actine-spectrine, une taille éventuellement inférieure pour les brins d'actine non assemblés en anneaux périodiques. Si nous souhaitons pouvoir observer l'organisation et les modifications à l'échelle intracellulaire, nous avons besoin d'utiliser des méthodes de microscopie qui permettent d'aller au-delà de la limite de la diffraction optique (environ 220 nm dans le visible avec les objectifs les plus performants, suivant la longueur d'onde). Dans les travaux rapportés ici, nous avons utilisé de la microscopie STORM et DNA-PAINT pour la caractérisation structurale des liens entre MPS et structures d'endocytose, et la microscopie SIM pour l'étude fonctionnelle et l'imagerie sur cellule vivante.

4.2.2.1 Microscopie SMLM : STORM et DNA-PAINT

Il existe plusieurs techniques de microscopie par localisation de particule unique (*single molecule localization microscopy* : SMLM, **Figure 4-11**) qui reposent toutes sur le même principe, discrétiser dans le temps l'information de localisation portée par les fluorophores. Cela est réalisé en plaçant l'échantillon dans des conditions dans lesquelles lors d'une séquence de plusieurs dizaines de millier d'images, à chaque image illuminée seule une infime proportion des fluorophores s'éclaireront, ce qui permet d'enregistrer des « spots » d'émission séparés spatialement les uns des autres. Ces spots d'émission suivent une fonction gaussienne d'étalement du point lumineux (*point-spread function* : PSF) caractérisée au préalable sur le système d'acquisition, et en ajustant la PSF sur chaque source unique, on peut alors retrouver le point central de cette source avec une précision théoriquement infinie (qui dépend néanmoins du nombre de photons émis). Dans la pratique, cette technique permet de résoudre des structures dont la taille est 10 fois inférieure à la limite de la diffraction, soit autour de 20 nanomètres. Pour une revue récente consulter Jimenez et al., 2020, *Methods*.

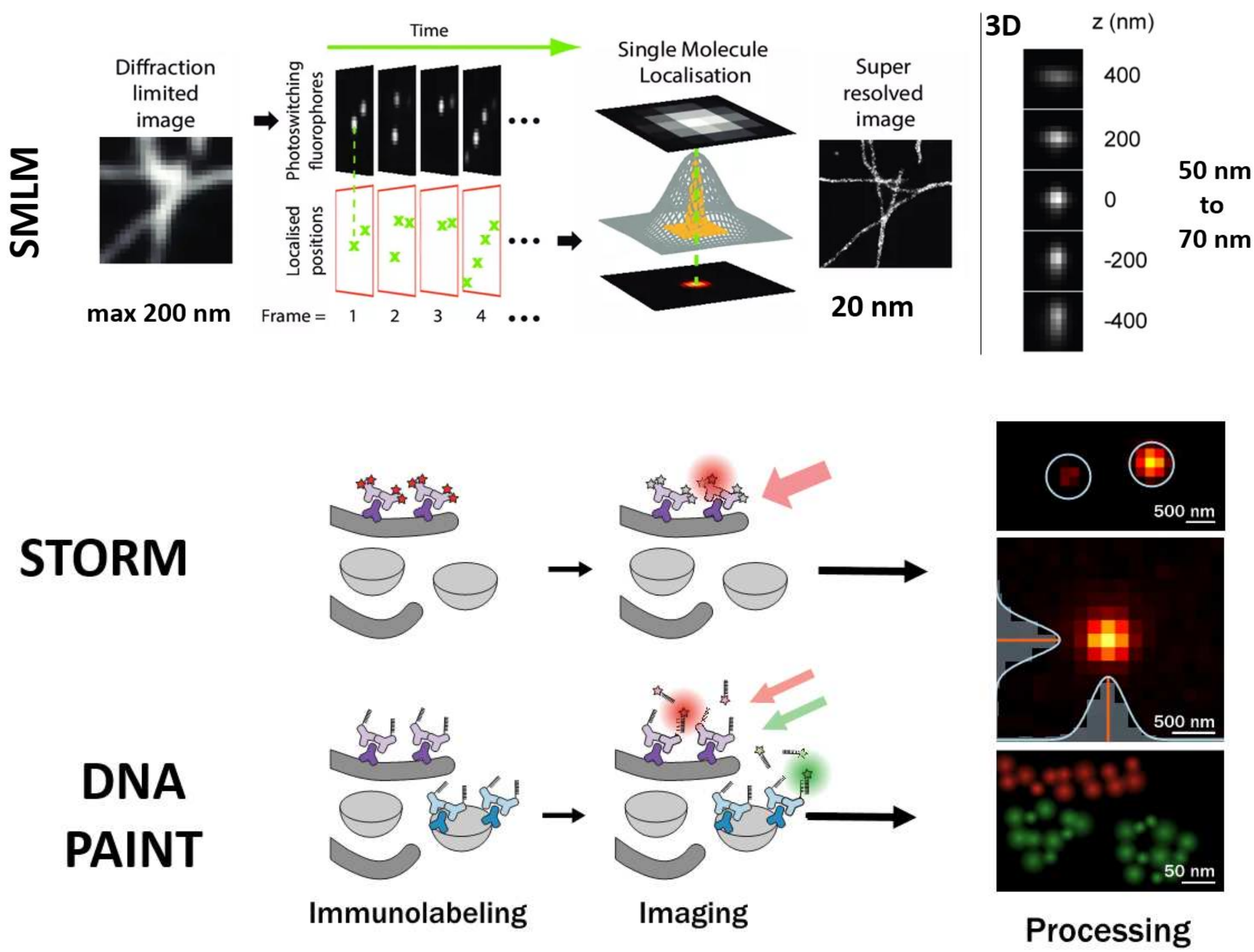

Figure 4-11 : Principe et applications du SMLM. Dans le panneau en haut à gauche le principe général du SMLM est présenté, on y voit l'étalement dans le temps et la détection de spots ponctuels de fluorescence, puis l'ajustement de la PSF sur chaque spot détecté pour retrouver la coordonnée super résolue et l'accumulation des localisations pour reconstruire l'image résolue latéralement à 20 nm. En haut à droite est présenté la déformation horizontale ou verticale de la PSF en fonction de la distance axiale au plan focal, ces déformations permettent par la suite de retrouver l'information de coordonnée en Z (Patel et al., 2017). Dans le panneau en bas à gauche on retrouve 2 applications concrètes du SMLM et les marquages fluorescents utilisés en STORM et en DNA-PAINT sont présentés. A droite dans la vignette du haut on voit la détection des spots de fluorescence, dan la vignette du milieu la localisation du centre de la PSF, dans la vignette du bas est illustrée une image super résolue en 2 couleurs après post-traitement. Adapté depuis Jimenez et al., 2020, Methods.

Le SMLM est un principe général implémenté en pratique par des méthodes spécifiques, dans ces travaux de thèse, j'ai utilisé les techniques SMLM *stochastic optical reconstruction microscopy* (STORM, Rust et al., 2006, *Nat. Methods*) et *DNA-point accumulation for imaging nanoscale topography* (Jungmann et al., 2010, *Nano Lett.*; 2014, *Nat. Methods*).

4.2.2.1.1 STORM

Cette technique consiste à placer l'échantillon biologique immuno-marqué en fluorescence de façon conventionnelle dans un milieu réducteur qui maintient dans l'état sombre la quasi-totalité des fluorophores et limite la proportion d'entre eux qui peut passer à l'état excité à chaque créneau temporel acquis par le microscope. Ce passage à l'état excité est stochastique, et en acquérant un séquence d'images de l'échantillon illuminé, on obtient un film sur lequel à chaque image seuls une dizaine à une vingtaine de fluorophores sont lumineux et bien distincts les uns des autres, et idéalement les fluorophores à l'état excité sont différents de l'image précédente. A partir du film de l'acquisition, un traitement algorithmique va identifier la localisation super résolue de chaque fluorophore excité en ajustant la PSF sur son spot d'émission puis en retrouvant la coordonnée centrale de la PSF ajustée, sur chacune des images du film. Enfin, le traitement algorithmique va regrouper les spots d'émissions appartenant manifestement au même fluorophore sur des images successives, puis générer une image finale unique reconstruite depuis toutes les images du film ainsi traitées (**Figure 4-12**).

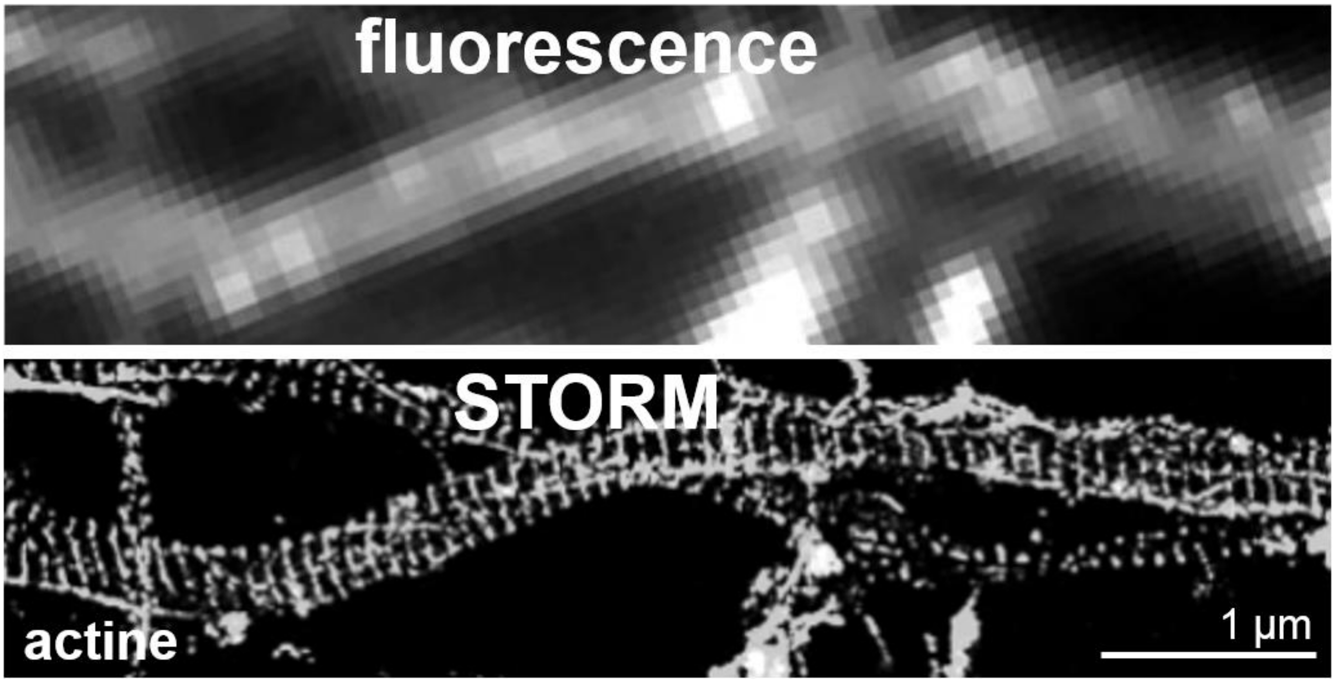

Figure 4-12 : Super résolution en STORM d'un axone marqué pour l'actine. En haut est montrée une acquisition de l'échantillon marqué pour l'actine en microscopie de fluorescence à champ large. En bas on peut voir le même échantillon reconstruit après une acquisition en STORM. Adapté depuis Xu et al., 2013, Science.

Avec cette technique, une résolution de 10 et 20 nm par pixel peut être obtenue, soit un ordre de grandeur au-delà de la limite de la diffraction optique, les techniques d'immunofluorescence sont les mêmes que pour des échantillons conventionnels, et l'échantillon est préservé en milieu liquide. La durée d'acquisition est « relativement » rapide pour du SMLM (15 ms/image) ce qui permet d'obtenir un film de 60 000 images en 15 minutes. Il est possible d'acquérir aussi l'information de profondeur avec une en ajoutant une lentille d'astigmatie sur le chemin lumineux, cette dernière va déformer la PSF sur l'axe horizontal ou vertical en fonction de la profondeur (**Figure 4-11**) et lors du traitement post-acquisition l'algorithme d'ajustement de la PSF sur les spots lumineux prendra en compte cette déformation pour resituer la position en Z du fluorophore émetteur. La résolution axiale ainsi obtenue varie entre 50 et 70 nm.

La limite principale du STORM est qu'il n'est réalisable qu'avec des fluorophores émettant dans le spectre rouge lointain, ce qui dans la pratique courante réduit son utilisation « simple » à un seul canal de fluorescence super-résolu. De nouvelles méthodes émergent toutefois pour séparer plusieurs fluorophores émettant dans différentes longueurs d'onde du rouge lointain et permettre plus d'un canal de fluorescence en STORM, on parle de techniques de démixage spectral (Friedl et al., 2023, *Cell Rep. Methods*). De façon plus secondaire un autre inconvénient en STORM est la durée d'acquisition et de post-traitement qui sont plus longues qu'en microscopie standard. Une façon de s'affranchir de la limite principale est d'utiliser une technique de SMLM permettant plus facilement des acquisitions multi-canaux, le DNA-PAINT.

4.2.2.1.2 DNA-PAINT

La technique de DNA-PAINT consiste à utiliser une autre méthode pour obtenir le clignotement des fluorophores. Ici les fluorophores liés aux anticorps secondaires dans les méthodes classiques d'immunofluorescence sont substitués par des séquences d'ADN simple brin d'une quinzaine de bases (*docking strand*), et des séquences d'ADN simple brin couplés aux fluorophores et partiellement complémentaires à celle des anticorps secondaires (*imaging strands*) sont placés dans le tampon d'imagerie (**Figure 4-13** et **Figure 4-14**).

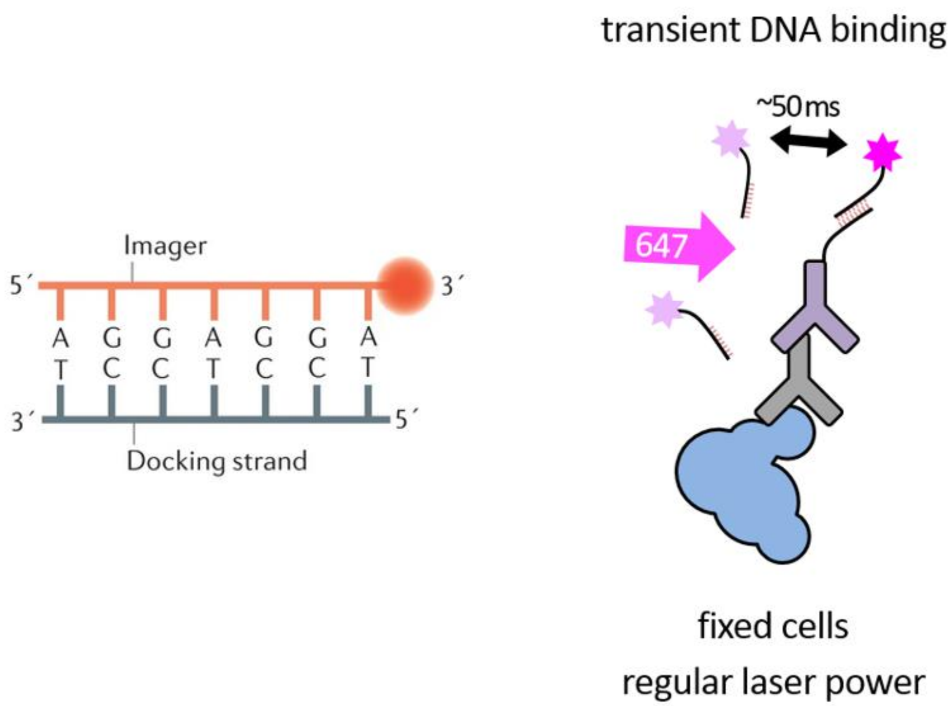

Figure 4-13 : Principe du DNA-PAINT. A gauche sont illustrés les brins d'ADN complémentaires dont le brin imageur est couplé à un fluorophore. A droite est présenté l'assemblage moléculaire pour l'immunomarquage en DNA-PAINT. Adapté depuis Schnitzbauer et al., 2017, Nat. Protoc. et C. Leterrier.

C'est la constante d'association/dissociation entre ces 2 séquences d'ADN qui détermine la durée d'exposition de chaque image, et la concentration des *imaging strands* doit être ajustée en conséquence afin d'obtenir une densité du marquage optimale pour le SMLM (typiquement 20 spots par image 512x512 pixels).

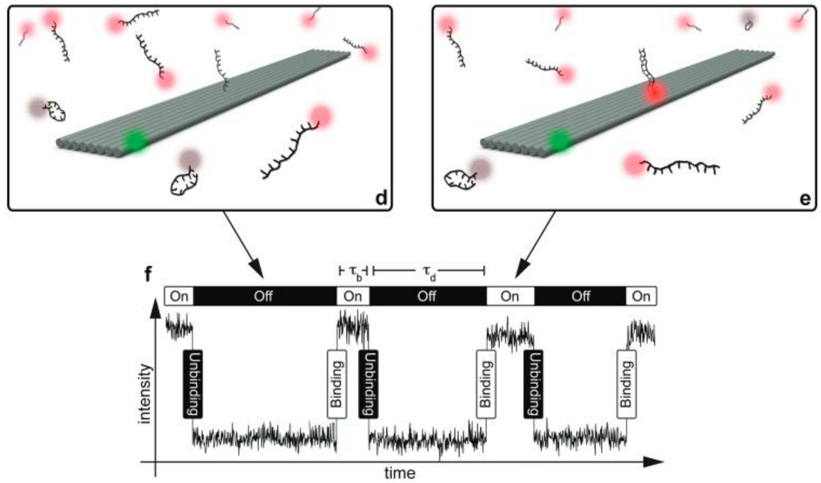

Figure 4-14 : Dynamique du DNA-PAINT. Lors de l'association transitoire par diffusion d'un simple brin ADN couplé à un fluorophore (à droite), l'intensité de fluorescence enregistrée au plan focal augmente drastiquement pendant la durée d'association (en bas). Adapté depuis Jungmann et al., 2010, Nano Lett.

L'intérêt principal de cette méthode est la possibilité d'obtenir des images super-résolues sur plusieurs canaux de fluorescence grâce à l'existence de plusieurs couples *docking/imaging strand*, soit en simultané (2 canaux, **Figure 4-15**) soit en séquentiel (2 canaux ou plus par Exchange-PAINT, Jungmann et al., 2014, *Nat. Methods*). Comme pour le STORM, l'information de profondeur peut être acquise en insérant une lentille d'astigmatie dans le chemin optique. Dans le cadre des travaux de cette thèse, le DNA-PAINT simultané m'a permis de produire des images super-résolues d'échantillons marqués pour la clathrine et les spectrines et ainsi pouvoir montrer l'exclusion mutuelle entre ces deux composantes.

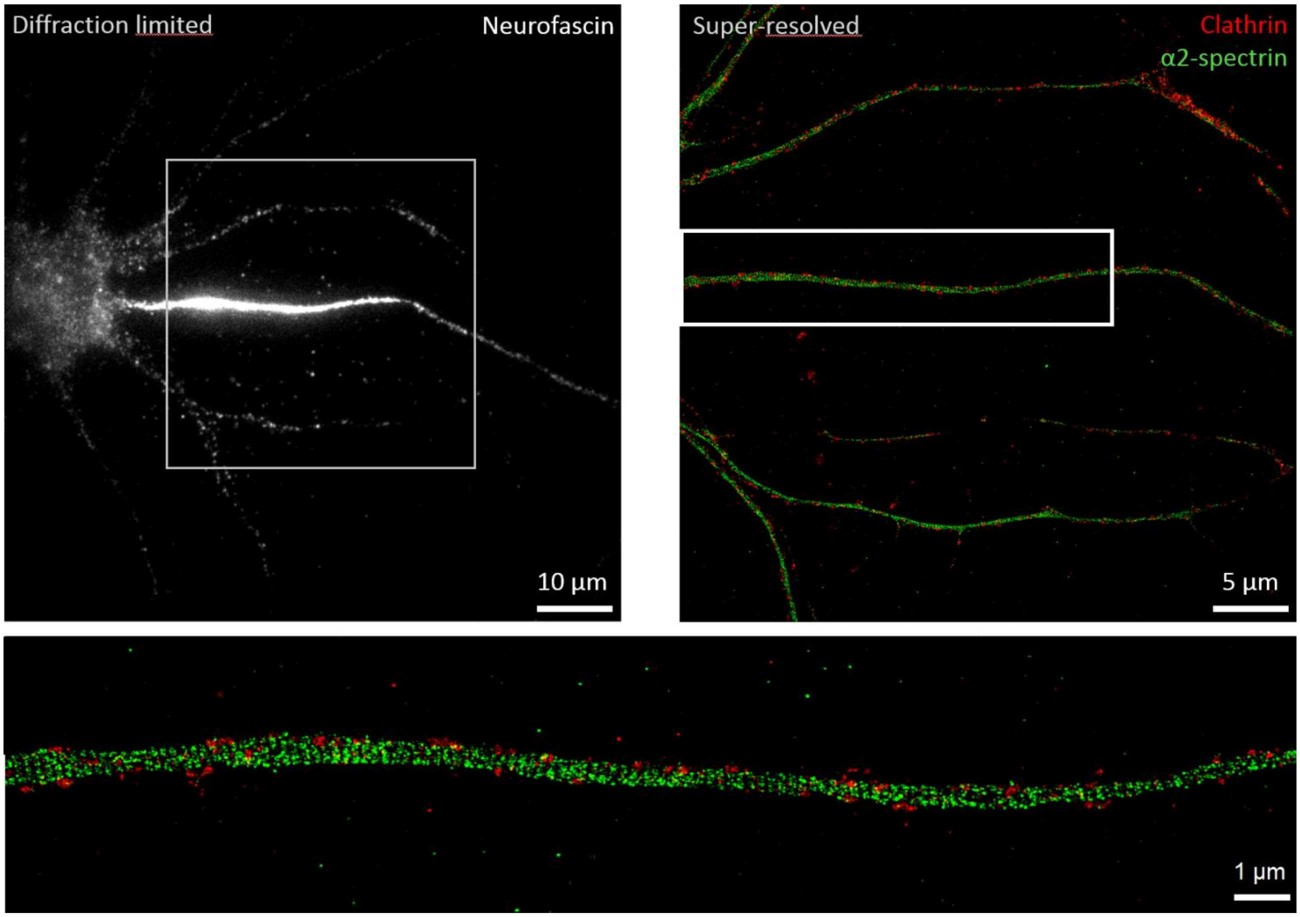

Figure 4-15 : Illustration pratique de DNA-PAINT 2 couleurs. A gauche on voit le champ large d'un neurone marqué pour la neurofascine (AIS), l'encadré blanc indique la zone d'acquisition en DNA-PAINT. A droite on voit l'image finale super-résolue en DNA-PAINT 2 couleurs, marquée pour la clathrine en rouge et l'α2-spectrine en vert, l'encadré indique la zone d'agrandissement pour l'image présentée en bas. En bas est montré un zoom de l'encadré précédent qui illustre la résolution accessible en DNA-PAINT 2 couleurs. On peut y noter la structure périodique de l'α2-spectrine.

L'avantage de pouvoir faire plusieurs canaux super-résolus en DNA-PAINT est contrebalancé par une complexité technique, un coût en réactifs et en temps plus élevé pour obtenir une image reconstruite utilisable. En effet, les brins *docking/imaging* ont un coût plus important que des anticorps secondaires conventionnellement utilisés, les ajustements de leur concentration pour obtenir une densité de spots par image optimale sont longs et difficilement répétables, et la constante d'association/dissociation des brins nécessite des durées d'exposition plus longues ce qui rallonge le temps d'acquisition (typiquement 45 minutes pour 2 canaux simultanés). Ces 2 méthodes sont donc utilisées de façon complémentaire suivant la question scientifique que l'on pose.

4.2.2.2 Microscopie SIM

La technique de *structured illumination microscopy* (SIM Gustafsson, 2000, *J. Microsc.*) consiste à moduler en phase et en orientation le faisceau d'illumination avec un motif périodique grâce à un miroir à commande numérique (*digital micro-mirror device* : DMD). Aux sites où l'illumination périodique interfère avec l'échantillon, des franges de moiré apparaissent et correspondent dans l'espace de Fourier à une fréquence 2 fois supérieure à celle de la résolution initiale de l'image (**Figure 4-16**). En combinant les différentes phases et orientations du motif de modulation pour un même champ illuminé, on peut acquérir une série d'images contenant chacune une partie de l'information de plus haute fréquence donnée par les interférences de Moiré, puis extraire algorithmiquement ces informations et les assembler pour reconstruire l'image finale super-résolue.

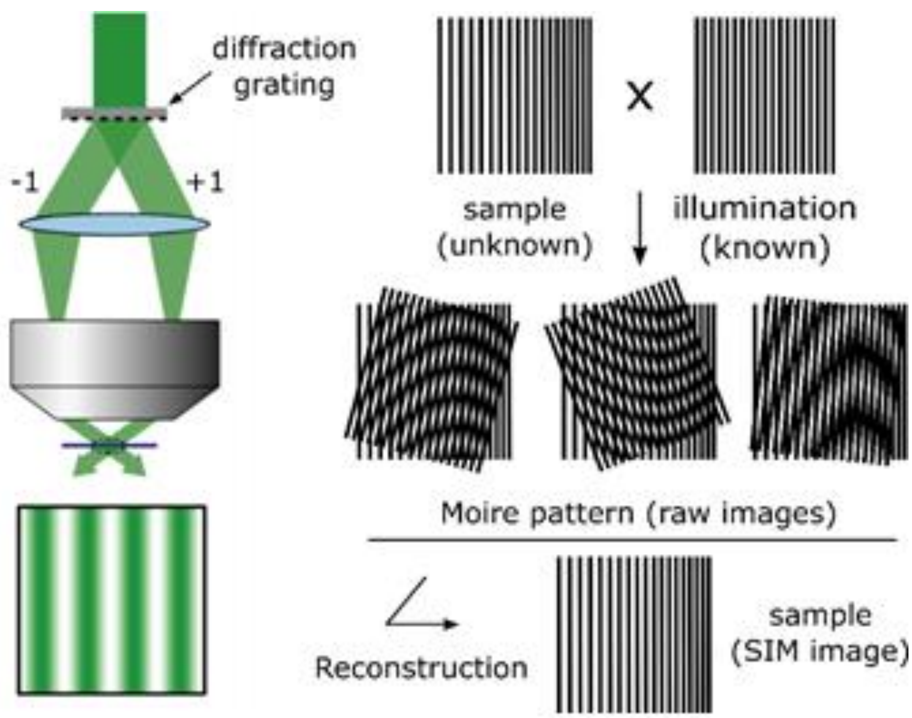

Figure 4-16 : Principe du gain de résolution en SIM. A gauche, modulation en phase et en orientation du faisceau d'illumination. A droite, interférences de Moiré entre l'illumination modulée et l'échantillon (C. Leterrier).

Le SIM est une méthode qui permet d'obtenir une résolution théoriquement doublée au-delà de la diffraction optique (reconstructions théoriquement résolues à 120 nm latéralement), sur des échantillons immuno-marqués et montés sur lames de façon conventionnelle, sur plusieurs canaux de fluorescence en un temps d'acquisition largement inférieur à celui des techniques multi-couleurs SMLM (quelques secondes), sans toutefois obtenir un niveau de résolution latérale équivalent à ces dernières. De plus, contrairement au SMLM la technique est compatible avec l'imagerie sur cellules vivantes, dans les limites du temps d'exposition nécessaire à l'acquisition des images modulées. Enfin, comme en microscopie conventionnelle, il est possible de réaliser des acquisitions d'images à différents plans focaux pour obtenir un assemblage 3D (*stacked* 2D-SIM), et même de moduler en plus le faisceau lumineux sur 3 plans focaux (3D-SIM, M. G. L. Gustafsson et al., 2008, *Biophys. J.*) afin de doubler également la résolution axiale lors de la reconstruction (250 nm).

Dans la pratique et comme illustré dans l'article principal associé à cette thèse, la résolution latérale de 120 nm du SIM permet ainsi de s'approcher suffisamment du critère d'échantillonnage de Shannon-Nyquist (Shannon, 1949, *Proc. IRE*) pour résoudre la périodicité du MPS (≈190 nm). Bien que super-résolue, la résolution optique du SIM n'atteint pas celle du SMLM, la technique est donc complémentaire et bien appropriée pour obtenir un gain de résolution lors d'observations fonctionnelles sur des structures subcellulaires. La limite principale en SIM est le nombre de photons nécessaires car pour chaque image finale, 9 images modulées auront dû être acquises pour chaque canal de fluorescence (15 images pour chaque plan en 3D-SIM). Ce n'est que rarement un problème sur des immunomarquages compte-tenu de la performance des fluorophores actuels, toutefois sur des protéines fluorescentes exprimées en transfection comme la GFP ou la mCherry, la quantité de fluorescence disponible peut devenir un facteur limitant, en particulier lors de l'acquisition de séries temporelles sur cellules vivantes, lors desquelles la phototoxicité est un paramètre de plus à prendre en compte pour l'illumination de l'échantillon.

4.2.2.3 Améliorations du rapport signal bruit par technique d'apprentissage profond

Pour dépasser la limite qui vient d'être évoquée lors de l'utilisation du SIM en imagerie sur cellules vivantes, de nouvelles techniques numériques ont été développées pour améliorer le rapport signal-bruit des acquisitions et pouvoir maintenir une puissance d'illumination compatible avec le vivant. La méthode CARE (*content-aware image restoration,* Weigert et al., 2018, *Nat. Methods*) est ainsi devenue un outil précieux pour l'étude fonctionnelle en microscopie (**Figure 4-17**). Le principe de cette méthode est d'entrainer un réseau profond de neurones artificiels à reconstruire une image au rapport signal-bruit élevé depuis une image bruitée, à partir de paires d'images du même échantillon fixé et éclairée à forte et faible intensité.

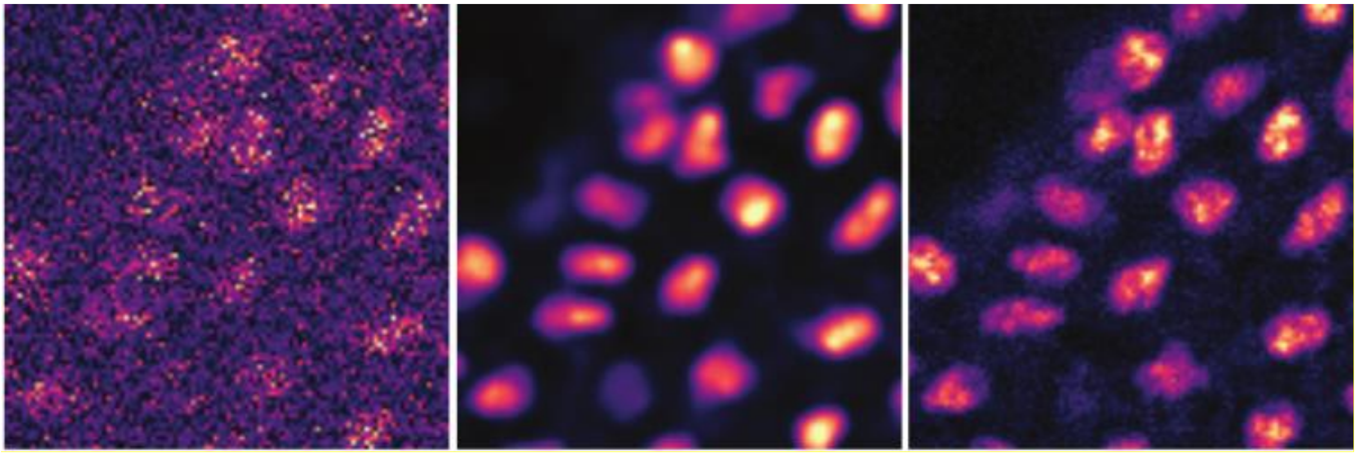

Figure 4-17 : Méthode d'amélioration du rapport signal-bruit CARE. Noyaux de cellules de ver plat marquées au RedDot1, à gauche échantillon faiblement illuminé, au milieu prédiction du réseau, à droite vérité terrain (adapté depuis Weigert et al., 2018, Nat. Methods).

Dans le contexte de cette thèse, j'ai utilisé le module *Enhance.ai* intégré dans le logiciel du microscope NIS Elements, qui met en œuvre un principe similaire à la méthode CARE. Les modèles (les pondérations du réseau produites par son entrainement) sont spécifiques des structures sur lesquelles le réseau a été entrainé, j'ai par exemple entrainé sur des paires d'images deux modèles distincts pour améliorer le rapport signal bruit des films sur neurones vivants exprimant la clathrine-mCherry et la β2-spectrine-GFP (Figure 4-18).

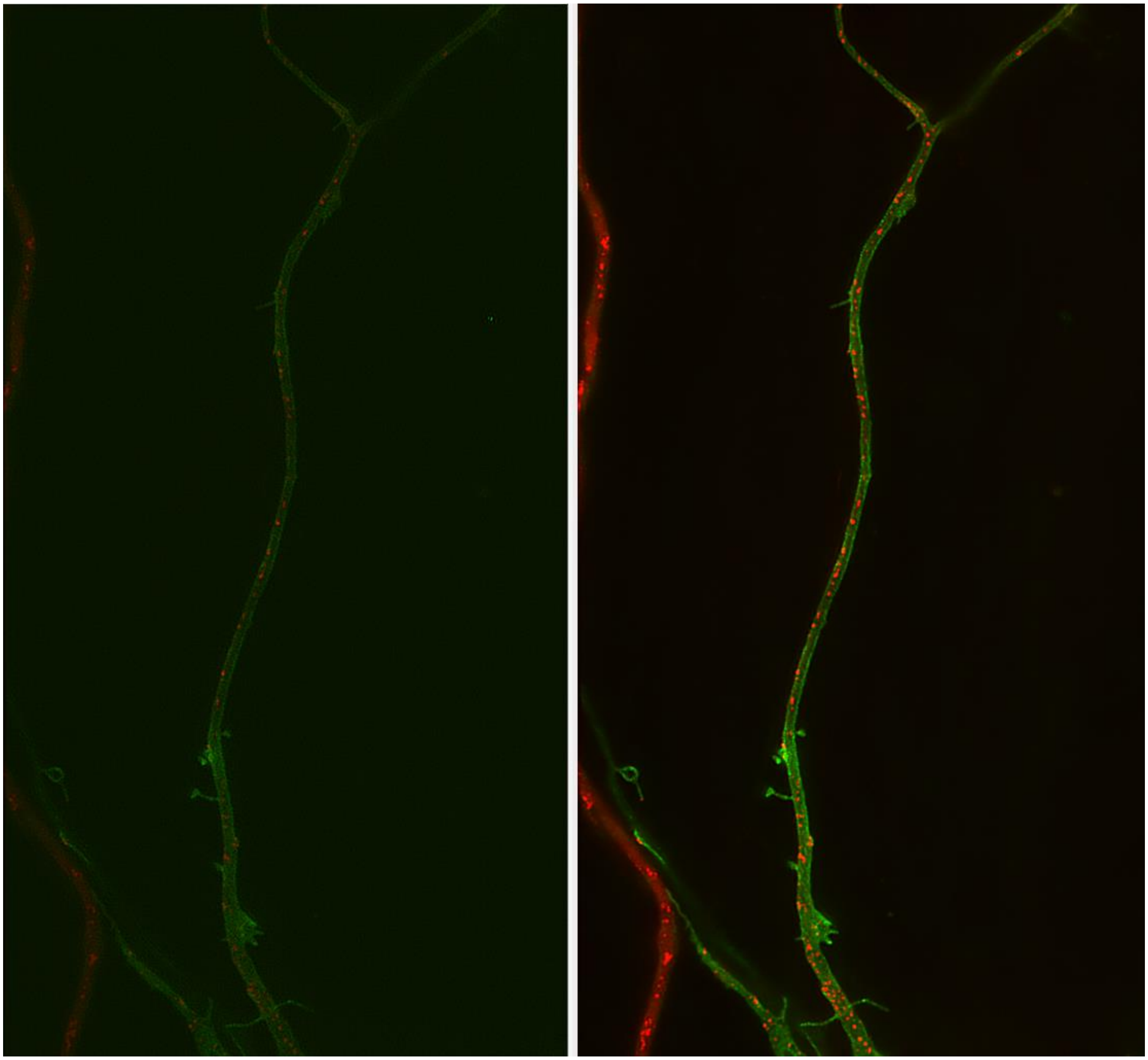

Figure 4-18 : Amélioration du rapport signal/bruit en utilisant des techniques basées sur le deep-learning. À gauche image originale à faible signal d'un neurone surexprimant la β2-spectrine-GFP et la clathrine-mCherry, à droite la même image après amélioration du rapport signal bruit en applicant un modèle de deep-learning restauratif n'ayant jamais vu l'original, entrainé spécifiquement entrainé sur le type de marquage présenté ici.

4.2.3 Microscopie électronique sur réplique de platine

Cette méthode consiste à déposer par évaporation sous vide un masque d'atomes de platine directement sur l'échantillon biologique fixé (**Figure 4-19**), puis le consolider avec un dépôt d'atomes de carbone, dissoudre le verre de la lamelle de culture à l'aide d'acide fluorhydrique, et enfin monter le masque ainsi obtenu sur une grille de microscopie électronique à transmission (Svitkina, 2017, *Int. J. Biochem. Cell Biol.*).

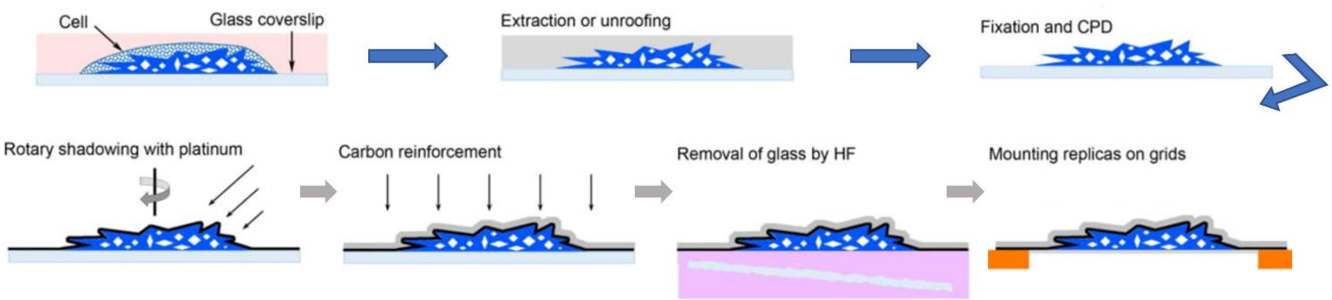

Figure 4-19 : Méthode PREM. La membrane plasmique supérieure de l'échantillon est retiré par des impulsions ultrasonique, puis l'échantillon est fixé, enrobé de platine puis de carbone. Le masque platine/carbone est alors préparé sur un support adapté à la microscopie électronique. Adapté depuis Svitkina, 2017, Int. J. Biochem. Cell Biol.

Dans le contexte de cette thèse, cette technique a été utilisée grâce à notre collaboration avec Stéphane Vassilopoulos et son équipe. Après unroofing des cultures neuronales, la PREM a permis de visualiser l'ultrastructure de la face interne de la membrane axonale, et faire le lien avec les observations en microscopie fluorescente.

Résultats

5 Article principal de thèse : « The actin-spectrin submembrane scaffold restricts endocytosis along proximal axons »

5.1 Commentaire

Dans les neurones, les avancées en microscopie super-résolue ont permis la mise au jour d'un maillage périodique sous-membranaire (MPS) d'actine-spectrine a ouvert de nouvelles perspectives sur l'organisation et le maintien de leurs compartiments spécialisés, l'axone en premier lieu ((Leterrier, 2021, *Curr. Opin. Neurobiol.*)). En contrepoint de ces avancées, malgré la présence de composants moléculaires associées à l'endocytose médiée par la clathrine (clathrin-mediated endocytosis : CME) à la membrane du tube axonal, les spécificités de la CME et de sa régulation dans l'axone en dehors des compartiments présynaptiques n'ont été que peu explorées.

Parmi les publications d'intérêt préexistantes sur ce sujet, l'article Jenkins et al., 2015, Sci Adv avait fait l'observation de structures mobile d'actine/spectrine qui viendraient freiner l'endocytose à la membrane latérale de cellules épithéliales en colonnes. Dans Zhou et al., 2019, Science, les auteurs font l'observation que déstabiliser la structure du MPS avec des perturbations chimiques ciblant l'actine ou des shRNA ciblant les spectrines conduit à inactiver la signalisation phospho-ERK (pERK) des transactivateurs membranaires (récepteurs CB1 et NCAM) de la voie de signalisation RTK. Par ailleurs, ils observent aussi un remodelage local du réseau de spectrines axonales lors de l'effection de la voie de signalisation pERK par un agoniste de CB1, l'utilisation simultanée de l'agoniste et d'un antagoniste de CB1 font disparaitre ce remodelage. Ainsi le désassemblage local du MPS de spectrines à la suite de l'effection des transactivateurs membranaires constituerait une boucle négative de régulation de la voie de signalisation pERK-RTK. Enfin, les auteurs font aussi l'observation annexe (figure supplémentaire 18) d'un accroissement de l'endocytose de récepteurs CB1 à l'axone et dans les dendrites lorsque le MPS de spectrines est endommagé via un shRNA spectrine.

Lors de la préparation de l'article Vassilopoulos et al., 2019, Nat Commun. impliquant notre équipe, l'observation informelle avait été faite d'une exclusion physique entre les puits à manteau de clathrine (*clathrin coated pits* : CCP) et la présence du MPS à la membrane plasmique axonale. Prises dans leur ensemble, ces observations dans différents modèles nous ont fait nous interroger sur l'existence possible d'un lien mécanistique et/ou fonctionnel entre la CME et le maillage périodique sous-membranaire (MPS) d'actine-spectrine du cytosquelette axonal. L'exploration de cette question a constitué la plus grande part de ce travail de thèse et ses résultats sont synthétisés dans l'article principal ci-après. Nous avons par la suite obtenu un financement ANR pour explorer ce sujet et c'est dans ce cadre que ces travaux se sont inscrits.

Enfin, dans les travaux reliés au sujet publiés après le commencement de mon doctorat, l'article de Ghisleni et al., 2020, Nat Commun suggère un rôle du MPS dans la régulation de phénomènes physiologiques comme la motilité cellulaire des fibroblastes et se termine sur l'observation de domaines d'exclusion membranaire entre d'une part la β2-spectrine et d'autre part la clathrine et AP2, 2 composantes majeures de la CME. Puis dans une proximité plus grande avec le sujet de l'article principal, on peut noter en particulier Eichel et al., 2022, Nature, dans lequel l'endocytose à l'AIS des récepteurs membranaires DMA-1 et TfR est étudiée dans les neurones PVD d'un modèle C. Elegans. Les auteurs tirent parti du fait que ces récepteurs sont fortement polarisés vers les dendrites et absents à l'axone pour créer des mutations qui vont abolir cette polarisation et induire la relocalisation d'une partie de ces récepteurs à l'AIS. Puis à l'aide de différentes sondes de ces récepteurs et de perturbateurs chimiques de l'endocytose, les auteurs y montrent que ces récepteurs dendritiques relocalisés à l'AIS y sont ensuite endocytés, que cette endocytose peut être bloquée par inhibition chimique ou par une mutation qui permet aux récepteurs de se lier à l'ankyrine G et être ainsi présentés à la membrane. Les auteurs de cette étude proposent que l'endocytose axonale ait pour fonction de maintenir la polarité dendrites/axone en retirant de la membrane de l'AIS les récepteurs qui y arrivent par diffusion depuis la membrane somato-dendritique.

Dans cet article, nous explorons sur des neurones les liens moléculaires et fonctionnels entre le MPS et les structures à manteaux de clathrine présentes à l'AIS en combinant des techniques de microscopie de fluorescence super-résolue et de microscopie électronique sur réplique de platine. Ces différentes modalités de visualisation nous permettent de montrer qu'à l'AIS, les CCPs se forment à la membrane plasmique dans des « clairières » de spectrine, des zones circulaires de 300 nm de diamètre dénuées de spectrine et délimitées par des filaments d'actine qui contactent parfois la CCPs. En utilisant des perturbations chimiques ou moléculaires des différents composants du MPS axonal nous montrons une augmentation de la formation des CCPs. Toutefois, en contraste avec cette abondance de CCPs à l'AIS, des expériences d'endocytose de cargo et de microscopie sur cellules vivantes révèlent que ces structures n'endocytent pas, sont quasiment statiques et restent assemblées à long-terme à la membrane plasmique. Pour élucider le lien entre la nature « inactive » des CCPs et la présence du MPS axonal, nous avons réalisé des expériences d'endocytose de cargo en ayant perturbé le MPS de spectrine, ce qui a conduit à un accroissement de la quantité de CCP sans accroissement de l'endocytose. Enfin, l'application d'une stimulation NMDA nous a permis de montrer que ces CCPs pouvaient endocyter dans certaines conditions d'excitabilité neuronale.

Ma contribution à ces travaux se retrouve dans les expériences sur neurones en culture primaire intacts et unroofés (Fig. 1, 2, 4, 5, 7), les observations en microscopie de fluorescence SIM (Fig. 1, 4, 5), STORM (Fig. 2), DNA-PAINT, la génération des particules moyennes (Fig. 1 et 5), la segmentation et la quantification des particules de clathrine et de dextran (Fig. 4 et 7), l'élaboration ou l'adaptation des protocoles d'endocytose de dextran et d'endocytose stimulée par de la NMDA (Fig. 7), la préparation d'échantillons de neurones unroofés en amont du processus de PREM, l'acquisition des images de neurones en microscopie SIM en amont de la microscopie corrélative SIM-PREM, la validation de l'effet des shRNA spectrines sur la périodicité du MPS des neurones (Fig. S4) les observations sur neurones vivants en SIM (non montrées). Tous les travaux sur cellules Rat2 ainsi que les réplications d'échantillons de neurones en PREM, leur observation et leur corrélation avec la microscopie fluorescente a été effectué par l'équipe collaboratrice sur ce projet (Satish Moparthi, Stéphane Vassilopoulos).

The actin-spectrin submembrane scaffold restricts endocytosis along proximal axons

Florian Wernert [1°], Satish Moparthi [2°], Jeanne Lainé [3], Gilles Moulay [2], Fanny Boroni-Rueda [1], Florence Pelletier [1], Nicolas Jullien [1], Sofia Benkhelifa-Ziyat [2], Marie-Jeanne Papandréou [1], Christophe Leterrier [1#*] and Stéphane Vassilopoulos [2#*]

[1] Aix Marseille Université, CNRS, INP UMR7051, NeuroCyto, 13005 Marseille, France.

[2] Sorbonne Université, INSERM, Institute of Myology, Centre of Research in Myology, UMRS 974, Paris, France.

[3] Sorbonne Université, Department of Physiology, Faculty of Medicine Pitié-Salpêtrière, Paris, France

° and #: these authors contributed equally

* Correspondence: christophe.leterrier@univ-amu.fr and s.vassilopoulos@institut-myologie.org

Abstract

Neuronal clathrin-mediated endocytosis has unique features in compartments such as dendrites and presynaptic boutons, but how membrane and extracellular components are internalized along the axon shaft remains poorly known. Here we focused on clathrin-coated structures and endocytosis along the axon initial segment (AIS), and their relationship to the periodic actin-spectrin scaffold that lines the axonal plasma membrane. Super-resolution optical microscopy, platinum replica electron microscopy, and their correlative combination on cultured hippocampal neurons reveal that in the AIS, clathrin-coated pits form on bare membrane patches, ~300 nm circular areas devoid of spectrin mesh and lined by actin filaments we termed "clearings". In fibroblasts and the proximal axon of neurons, spectrin depletion and drug-induced scaffold disorganization increase clathrin-coated pit formation. However, the presence of clathrin-coated pits at the AIS is not directly linked to actual endocytosis: using cargo uptake and live-cell imaging experiments, we find that most AIS clathrin-coated pits are long-lived and immobile within the spectrin mesh clearings. Direct perturbation of the spectrin scaffold as well as elevated neuronal activity could induce endocytosis downstream of clathrin pit formation, showing that spectrin clearings are structures responsible for regulated endocytosis at the AIS.

Introduction

Endocytosis is a ubiquitous cellular process that allows cells to interact with their environment by internalizing surface receptors and extracellular substances (Mukherjee et al., 1997). Differentiated cells such as neurons extensively rely on endocytosis for retrieving and transporting membrane and extracellular components to organize their complex and compartmented morphology, and sustain the synaptic vesicle cycle at the core of neuronal communication. This role explains the historical focus on presynapses as the main site of endocytosis in neurons, with a wealth of studies dissecting its molecular mechanisms and coupling to the converse process of exocytosis (Azarnia Tehran and Maritzen, 2022; Rizzoli, 2014). Neuronal endocytosis has also been extensively studied in dendrites, where it drives receptor internalization near postsynapses (Rosendale et al., 2017; Catsburg et al., 2022) and is the source of a complex endocytic trafficking network (Yap and Winckler, 2022).

Outside of presynapses, endocytosis in neurons is mainly achieved through clathrin-mediated endocytosis (Camblor-Perujo and Kononenko, 2022). Clathrin forms triskelia made of trimerized heavy chains and light chains that assemble via adaptor proteins to form a cage-like coat around a membrane invagination called clathrin-coated pit (CCP), before scission of the CCP neck releases a clathrin-coated vesicle. In neurons, CCPs are found at the plasma membrane of the cell body and dendrites as well as in the vicinity of the active zone in presynapses, strengthening the prevalent view that endocytosis mainly occurs in these compartments. By contrast, little is known about the nanoscale organization or even the existence of clathrin-mediated endocytosis along the axon shaft and at the axon initial segment (AIS), the specialized compartment that constitutes the most proximal part of the axon (Rasband, 2010; Leterrier, 2018). It was commonly assumed that little to no endocytosis could take place along the axon shaft (Parton et al., 1992), a view reinforced by the presence of a dense submembrane assembly of spectrins, ankyrin G and anchored membrane proteins at the AIS, and the discovery of a dense, periodic scaffold of actin rings connected by spectrin tetramers lining the axonal plasma membrane (Xu et al., 2013; Lorenzo et al., 2023; Leterrier, 2021).

We previously used super-resolution microscopy combined with platinum-replica electron microscopy (PREM) on unroofed neurons to reveal the ultrastructure of the periodic actin-spectrin scaffold and AIS submembrane components (Vassilopoulos et al., 2019). Despite the presence of this dense undercoat, PREM views showed numerous CCPs present along the AIS of mature neurons, which was surprising because studies at the time only detected endocytosis in the nascent AIS in developing neurons (Torii et al., 2020; Fréal et al., 2019) or under acute excitotoxic stress (Benned-Jensen et al., 2016). More recently, robust endocytic activity at the AIS was proposed as a mechanism for membrane protein sorting, allowing the retrieval of somatodendritic proteins when they enter into the axon (Eichel et al., 2022). This prompted us to focus on the detailed architecture of CCPs at the AIS, their endocytic function and their relationships with the actin-spectrin submembrane scaffold.

We used a combination of super-resolution microscopy and PREM to visualize the structural components of the AIS and proximal axon at nanoscale resolution. We show that in addition to the periodic scaffold, AIS spectrins together with actin form well-defined circular exclusion zones we termed "clearings", which allow CCPs to form on the bare plasma membrane area exposed at their center. Moreover, we demonstrate the role of the dense spectrin mesh in restricting the formation of these CCPs and their unusual stability, resulting in limited endocytosis of fluid phase markers at the AIS. Finally, we show that physiological stimulation of N-methyl-d-aspartate (NMDA) receptors releases this inhibition and triggers efficient endocytosis from AIS CCPs.

Results

Clathrin-coated pits are present in circular clearings of the actin-spectrin scaffold at the AIS

We first visualized the distribution of CCPs with regard to the spectrin mesh at the proximal axon of neurons after two weeks in culture labeled for α2-spectrin and for the AIS-spe-

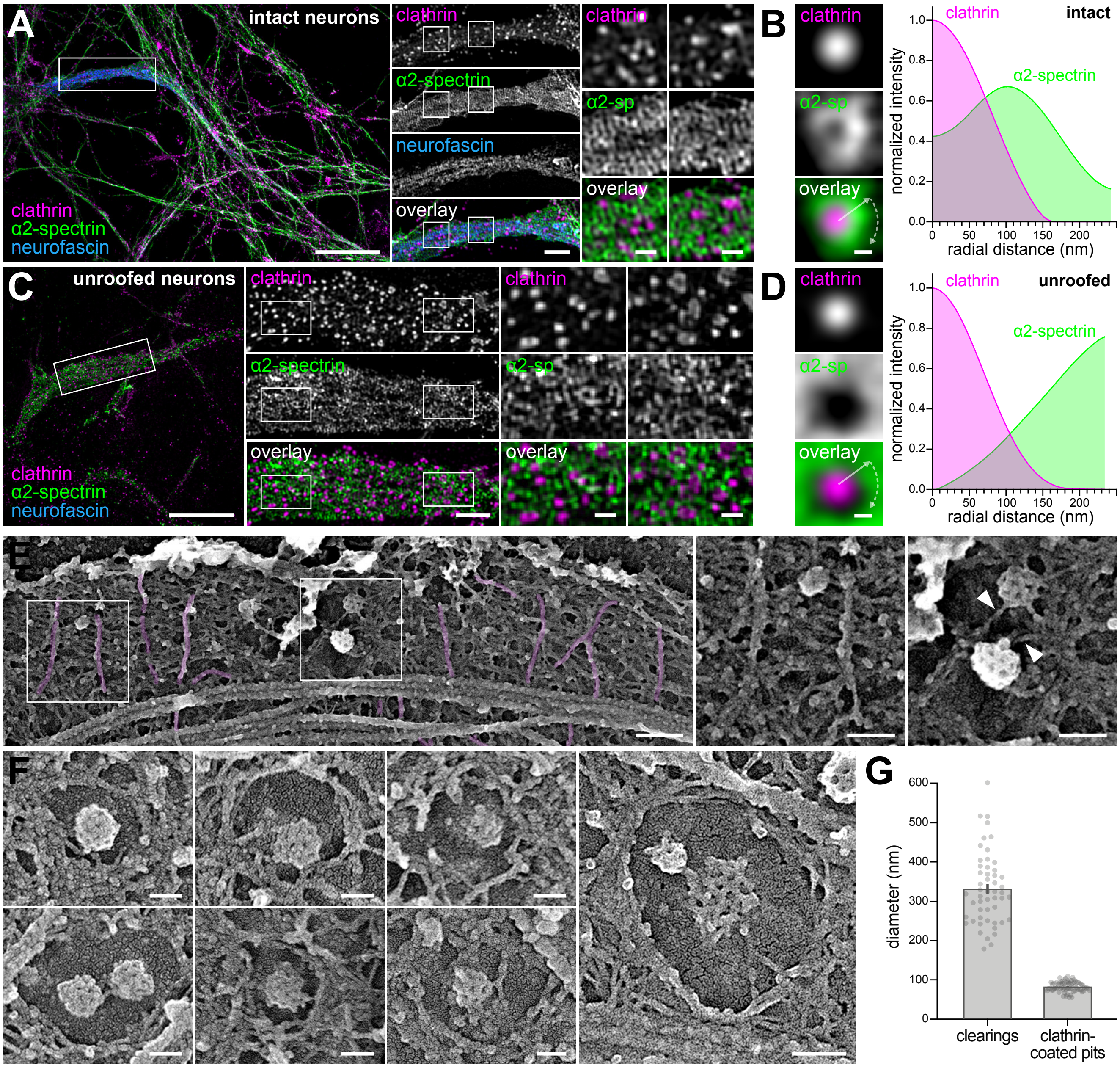

Figure 1: Clathrin-coated pits are present in clearings of the periodic spectrin scaffold at the AIS.
A. SIM image of a cultured hippocampal neuron at 14 div fixed and stained for clathrin (magenta, CCPs appear as clusters), α2-spectrin (green, ~190 nm-spaced bands are visible) and neurofascin (blue, labels the AIS). Scale bars, 10 µm (left image), 2 µm (center column), 0.5 µm (square zoomed images). B. Left, average images centered on CCPs for n=591 individual pits showing the distribution of clathrin (magenta on overlay) and α2-spectrin (green on overlay). Right, radial intensity profile corresponding to the average images on the left (gray arrow), showing how CCPs reside in an area devoid of α2-spectrin. Scale bar, 100 nm. C. SIM image of a neuron unroofed, fixed and stained for clathrin (magenta, CCPs appear as clusters), α2-spectrin (green, 190-nm bands are visible) and neurofascin (blue, labels the AIS). Central column shows zooms corresponding to the area highlighted in the left image, while square images on the right correspond to zooms on the areas highlighted in the central column. Scale bars, 10 µm (left image), 2 µm (center column), 0.5 µm (square zoomed images). D. Left, average images centered on CCPs for n=562 individual pits showing the distribution of clathrin (magenta on overlay) and α2-spectrin (green on overlay). Right, radial intensity profile corresponding to the average images on the left (gray arrow), showing how CCPs reside in an area devoid of α2-spectrin. Scale bar, 100 nm. E. PREM view of an unroofed proximal axon showing the presence of ~190 nm-spaced actin rings (magenta), the dense mesh of spectrins between actin rings, and CCPs that reside in "clearings" of the spectrin mesh. Right images show zooms of square areas highlighted on the left image corresponding to an actin rings-spectrin mesh area, and an area with two CCPs (with an actin filament contacting the pit, arrowheads). Scale bars, 200 nm (left image), 100 nm (square zoomed images). F. Gallery of additional PREM views showing CCPs found in circular areas of bare plasma membrane devoid of spectrin mesh ("clearings") along the proximal axon. Scale bars, 100 nm. G. Quantification of the diameter for spectrin mesh clearings (331 ± 13 nm, n=52) and for CCPs (83 ± 1.4 nm, n=75) from PREM views.

cific adhesion molecule neurofascin (Figure 1, A). We used Structured Illumination Microscopy (SIM), which resolves the 190-nm periodicity of the actin-spectrin scaffold as well as individual CCPs, and found that CCPs were present in areas devoid of α2-spectrin, as confirmed by the intensity profiles of averaged images centered on CCPs (Figure 1, B). The presence of CCPs in areas devoid of spectrin is also observed further along the axon and similarly observed when labeling the spectrin mesh for ß2-spectrin (Supporting Figure 1, A-C). To isolate the axonal plasma membrane and associated cortical cytoskeleton in a close-to-native state, without additional signal from intracellular compartments, we mechanically unroofed cultured hippocampal neurons using ultrasound (Figure 1, C). The presence of CCPs inside circular areas devoid of α2-spectrin was made clearer by the unroofing, with a distinct circular hole of α2-spectrin around CCPs seen on the average image (Figure 1, D).

We then produced platinum replicas of unroofed hippocampal neurons to visualize the ultrastructure of CCPs at the AIS by PREM. To identify the axonal process stemming from unroofed cell bodies, we located the characteristic fascicles of AIS microtubules (Figure 1, E). High-magnification PREM views of the axonal membrane-associated cytoskeleton revealed the presence of characteristic actin rings embedded in a dense spectrin mesh as previously described (Vassilopoulos et al., 2019), but also provided unique views of CCPs at the AIS, with their characteristic honeycomb pattern (Figure 1, E). In agreement with super-resolution fluorescence microscopy, CCPs formed on a patch of bare plasma membrane, forming a circular "clearing" of the actin-spectrin scaffold. These clearings were devoid of proteinaceous material, save for single actin filaments which reached the central CCPs (Figure 1, F). Spectrin clearings measured 330± 12 nm in diameter, while the CCPs in their center measured 83 ± 1.5 nm (mean ± SEM; Figure 1, G). While single actin filaments were found to interact with CCPs in all neuronal compartments, we only observed the circular clearings of the actin-spectrin scaffold in proximal axons, while they were absent from cell body and dendrites that lack such a dense undercoat (Supporting Figure 1, C).

Molecular organization of the CCPs and actin-spectrin clearings at the AIS

We next detailed the components and organization of the AIS CCPs and actin-spectrin clearings using Single Molecule Localization Microscopy (SMLM), alone and in correlation with PREM. 3D Stochastic Optical Reconstruction Microscopy (STORM) of clathrin in intact neurons revealed the presence of CCPs distributed circumferentially across the AIS (Figure 2, A-C). Point-Accumulation in Nanoscale Topography (PAINT) allowed us to simultaneously image CCPs and α2-spectrin in 3D at ~20 nm resolution (Figure 2, D-E). This confirmed the presence of CCPs in areas devoid of the spectrin mesh, both on in-plane views and transverse sections of the AIS (Figure 2, F). After unroofing, CCPs were only seen along the remaining ventral plasma membrane by 3D-STORM (Supporting Figure 2, A-C). In addition, we used 3D-PAINT to show that the adaptor protein complex AP2 colocalizes to CCPs along the AIS (Supporting Figure 2, D-F), as classically described (McMahon and Boucrot, 2011; Pearse and Robinson, 1990).

To further dissect the organization of the submembrane scaffold components around CCPs-containing clearings, we performed correlative STORM-PREM. After unroofing and fixation of neurons, we labeled a given component with Alexa Fluor 647 followed by STORM. We then produced platinum replicas of the same unroofed neurons and observed them by PREM (Vassilopoulos et al., 2019). We validated our correlative approach by using an anti-clathrin antibody to label CCPs at the AIS. The resulting overlays show how we can precisely correlate the 100-nm CCPs on both STORM and PREM images, although the anti-clathrin immunolabeling obscures the characteristic honeycomb pattern of the pits (Supporting Figure 2, G). We then stained the AIS-specific ß4-spectrin, localizing fluorescence clusters corresponding to the center of the spectrin tetramers within the dense mesh that surrounds CCP-containing clearings (Figure 2, G). We confirmed this localization using immunogold staining of ß4-spectrin, which similarly showed gold beads localized within the dense mesh (Figure 2, H). Turning to correlative STORM-PREM of actin, we observed fluorescent phalloidin delineating the 190 nm-spaced actin rings throughout the mesh, but also actin filaments along the circular border of the mesh clearings, as well as individual filaments contacting the CCPs (Fig.2, I). Indirect immunogold staining of actin filaments confirmed the presence of actin along the border of the clearings (Figure 2, J).

We also examined the nanoscale distribution of two more components of the actin-spectrin mesh in the AIS: the AIS master organizer ankyrin G (Rasband, 2010) and phospho-myosin light chain (pMLC) that decorates actin within the periodic scaffold (Berger et al., 2018; Costa et al., 2020). Correlative STORM-PREM and immunogold labeling showed that both proteins are present in the actin-spectrin mesh, including around the CCP-containing clearings (Supporting Figure 2, H-K). Altogether, our results indicate that in addition to forming a periodic actin-spectrin lattice, the AIS membrane-associated scaffold accommodates the presence of CCPs on the plasma membrane by forming stereotyped circular structures lined by actin filaments.

The sparse submembrane actin-spectrin mesh restricts clathrin-coated structure formation in non-neuronal cells

Spectrin tetramers form hexagonal lattices in erythrocytes and organize periodically between actin rings in axons (Leterrier and Pullarkat, 2022). In non-neuronal cells such as fibroblasts, loose disordered spectrin networks are found co-existing with denser erythroid-like hexagonal and neuron-like periodic arrays (Ghisleni et al., 2020, 2023). We thus decided to first assess the role of actin and spectrins in regulating clathrin-mediated endocytosis in Rat2 fibroblasts, which express α2- and ß2-spectrin that can be targeted using the same interfering RNA sequences as in rat hippocampal neurons. PREM views of unroofed fibroblasts showed abundant clathrin-coated structures (CCSs) at their inner surface, with more diverse clathrin structures than in neurons (Figure 3, A), ranging from flat to fully curved endocytic pits (Heuser, 1980; Moulay et al., 2020). Using immunogold labeling of α2- and ß2-spectrin, we found both spectrins localized on the cortical mesh in the vicinity of CCSs (Figure 3, B). We also noticed that α2- and ß2-spectrin directly associated with actin filaments surrounding fully-formed CCPs (Figure 3, B). Correlative super-resolution spinning disk microscopy-PREM confirmed this observation and also showed that α2- and ß2-spectrin could form polygonal networks with actin filaments surrounding CCPs (Figure 3, C). We next used siRNAs to deplete spectrins, resulting in a ~90% reduction of expression in fibroblasts (Supporting Figure 3, A-B) that did not affect the expression levels of clathrin heavy chain (Supporting Figure 3, C). PREM views of spectrin-depleted fibroblasts revealed a significant rise in the density of CCSs, which retained heterogeneous shapes (Figure 3, D): from 0.88 ± 0.09 CCS/µm² in control cells to 1.8 ± 0.16, 1.6 ± 0.14, and 1.3 ± 0.14 CCS/µm² for cells transfected with siRNA against α2-, ß2-, or α2- and ß2-spectrin, respectively (Figure 3, E). This suggests that the loose spectrin mesh found in non-neuronal cells can negatively regulate the formation of CCSs.

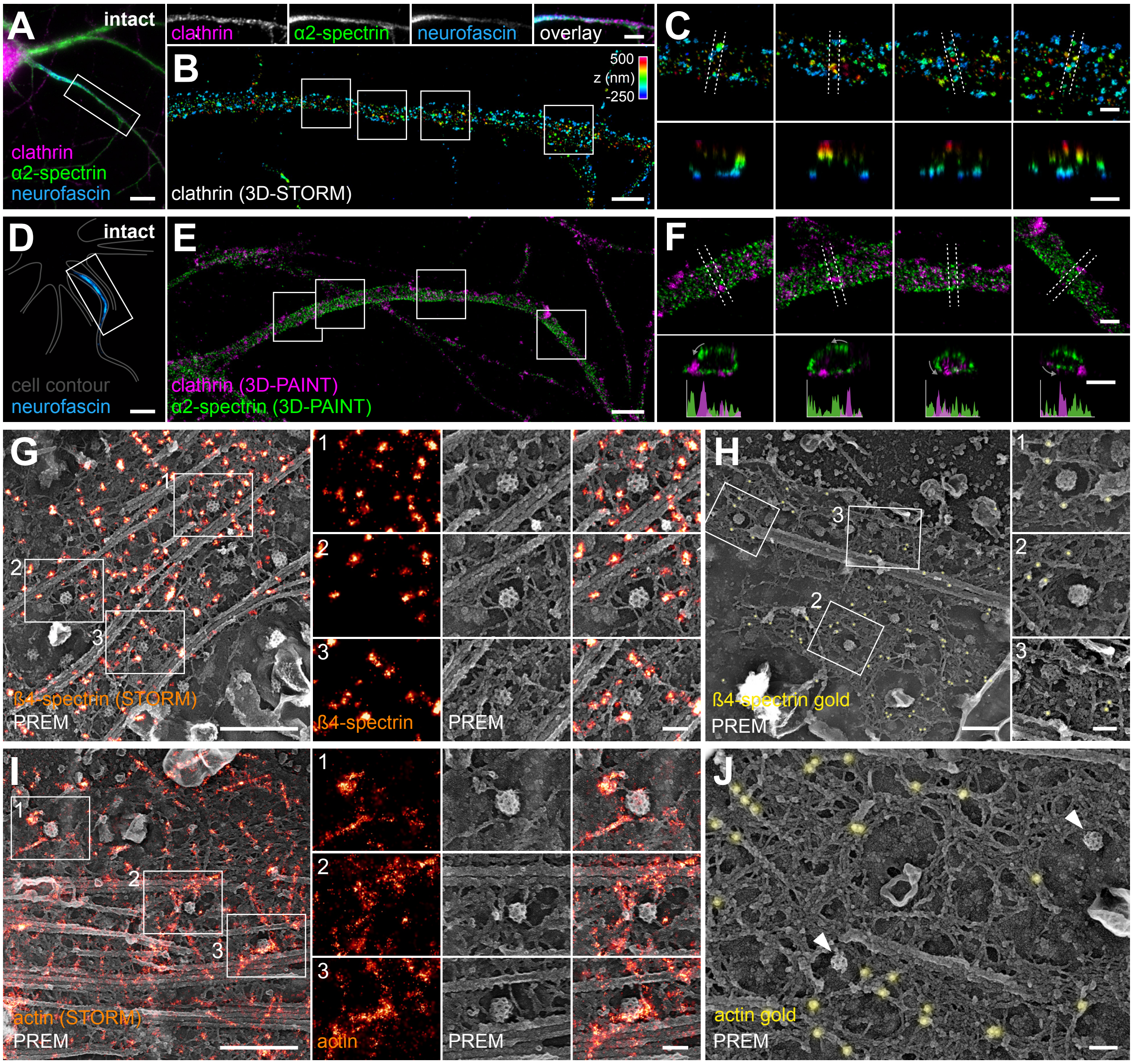

Figure 2: Molecular organization of the CCPs and actin-spectrin clearings at the AIS.
A. Widefield image of a neuron fixed and stained for clathrin (magenta), α2-spectrin (green) and neurofascin (blue). Line of images on the right are individual channels and overlays corresponding to the AIS area highlighted on the left image. Scale bars, 10 µm (left image), 5 µm (AIS images). B. 3D-STORM image of clathrin corresponding to the AIS area shown in A, color coded for depth. Scale bar, 2 µm. C. Zooms showing individual CCPs on XY images (top row, corresponding to areas highlighted in B) and corresponding XZ transverse sections (bottom row, taken between the lines highlighted on the XY images). Pits are mostly found at the plasma membrane, delineating the axon contour on transverse sections. Scale bars, 0.5 µm. D. Widefield image of a neuron fixed and stained for neurofascin (blue). The contour of the whole neuron (gray) is delineated. Scale bar, 10 µm. E. 2-color 3D-PAINT images of the AIS corresponding to the image in A with staining for clathrin (magenta) and α2-spectrin (green). Scale bar, 2 µm. F. Zooms showing individual CCPs (magenta) in clearing of the periodic α2-spectrin mesh (green) on XY images (top row, corresponding to areas highlighted in E) and corresponding XZ transverse sections (bottom row, taken between the lines highlighted on the XY images). Pits are mostly found at interruptions of the spectrin mesh delineating the axonal plasma membrane on transverse sections, as shown by intensity profiles along the sections (bottom graphs). Scale bars, 0.5 µm. G. Correlative STORM-PREM image of an unroofed AIS labeled for ß4-spectrin (orange). Right, zoomed images showing CCPs in spectrin mesh clearings, with spectrin encircling the bare membrane area. Scale bars, 500 nm (left image), 100 nm (zoomed images). H. PREM view of an unroofed AIS immunogold-labeled for ß4-spectrin (yellow). Right, zoomed images showing CCPs in spectrin mesh clearings, with 15 nm gold beads bound to the spectrin mesh around the bare membrane area. Scale bars, 500 nm (left image), 100 nm (zoomed images). I. Correlative STORM-PREM image of an unroofed AIS labeled for actin (orange). Right, zoomed images showing CCPs in spectrin mesh clearings. Scale bars, 5 µm (left image), 100 nm (zoomed images). J. PREM view of an unroofed AIS immunogold-labeled for actin (yellow) showing CCPs in spectrin mesh clearings (arrowheads), with 15 nm gold beads bound to the spectrin mesh around the bare membrane area. Scale bar, 100 nm.

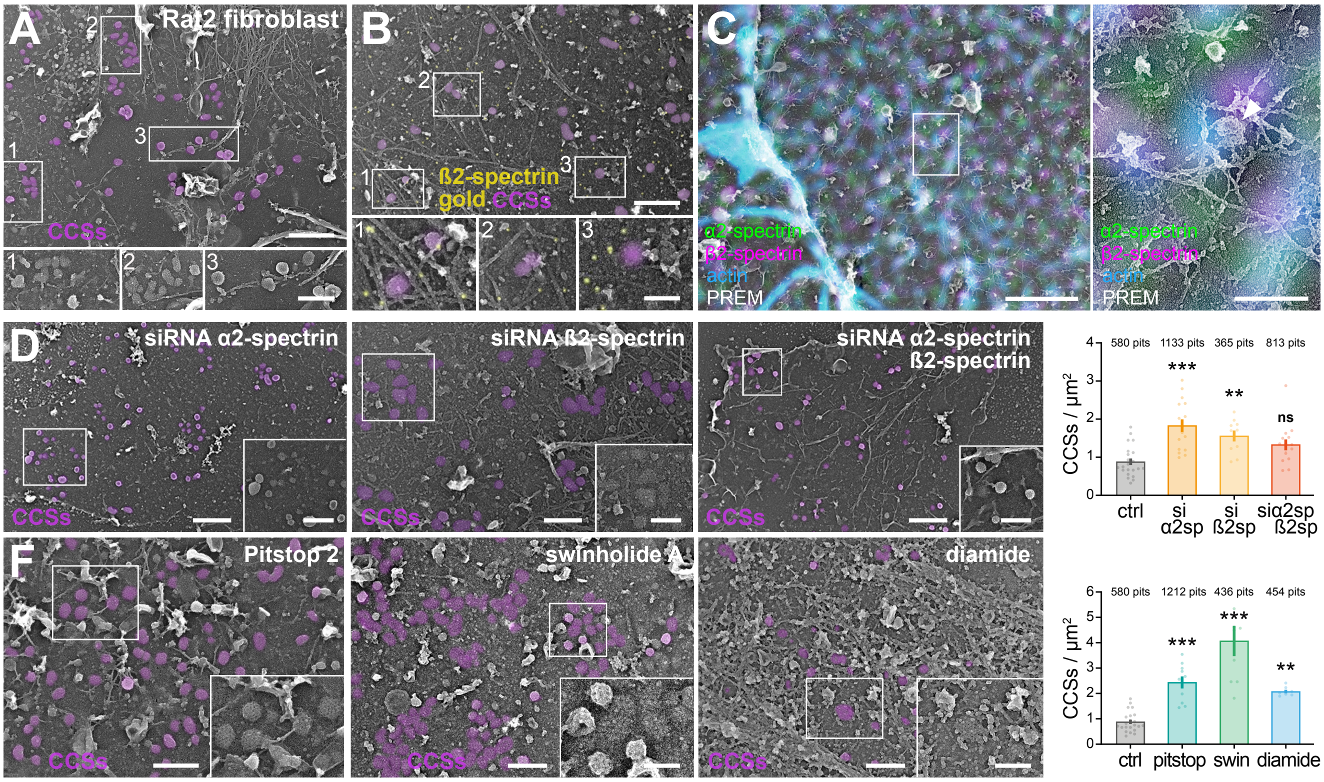

Figure 3: The sparse submembrane actin-spectrin mesh restricts clathrin-coated structure formation in non-neuronal cells.
A. PREM view of an unroofed Rat2 fibroblast showing the presence of CCSs (magenta). Bottom images are zooms of the highlighted areas in the top image. Scale bars, 2 µm (top image), 200 nm (bottom images). B. PREM view of an unroofed Rat2 fibroblast immunogold-labeled for ß2-spectrin (yellow), with CCSs colored in magenta. Bottom images are zooms of the highlighted areas in the top image. Spectrins are present along the membrane, sometimes appearing as rods. Scale bars, 2 µm (top image), 200 nm (bottom images). C. Correlative super-resolution spinning disk microscopy-PREM of an unroofed fibroblast labeled α2-spectrin (green), ß2-spectrin (magenta), and actin (blue). Right images show a zoom of the area highlighted on the overlayed left image, with the spectrins being found along the areas rich in actin filaments, encasing a CCP (arrowhead). Scale bars, 1 µm (main image), 200 nm (right images). D. PREM views of unroofed Rat2 fibroblasts after knockdown of α2-spectrin (left), ß2-spectrin (center), or both (right), with CCSs colored in magenta on the main image. Zoomed inset corresponds to the area highlighted on the main image. Scale bars, 5 µm (main images for siRNA against α2-spectrin and α2/ß2-spectrin), 2 µm (main image for siRNA against ß2-spectrin), 200 nm (insets). E. Effect of spectrins knockdown on the density of CCSs as quantified from PREM views of unroofed Rat2 fibroblasts (n=25, 16, 10, and 15 images for Ctrl, siRNA against α2, ß2, and α2/ß2-spectrin conditions, respectively). F. PREM views of unroofed Rat2 fibroblasts after treatment with swinholide A (100 nM 3h, disassembles actin, left), pitstop2 (30 µM 15 min, inhibits endocytosis, center), or diamide (500 µM 15 min, perturbs spectrins, right), with CCSs colored in magenta on the main image. Zoomed inset corresponds to the area highlighted on the main image. Scale bars, 1 µm (main images), 200 nm (insets). G. Effect of drugs on the density of CCSs as quantified from PREM views of unroofed Rat2 fibroblasts (n=25, 9, 10, and 7 images for Ctrl, swinholide A, pitstop2, and diamide conditions, respectively).

We next used drugs to target CCSs, actin filaments, or the spectrin mesh and assessed their effect on CCS density in fibroblasts. We used Pitstop 2, a drug that selectively blocks endocytic ligand association with the clathrin terminal domain, to inhibit receptor-mediated endocytosis (von Kleist et al., 2011). Pitstop 2 treatment (30 µM, 15 min) led to a strong increase in CCS density to 2.5 ± 0.24 CCS/µm^2 (Figure 3, F-G). To disassemble actin filaments including stable ones, we used swinholide A, which inhibits new filament assembly and disassembles existing ones (Vassilopoulos et al., 2019; Bubb et al., 1995). 100 nM swinholide A for 3h also caused a large increase in CCS density (to 4.1 ± 0.60 CCS/µm^2) with clathrin lattices at all degrees of curvature occupying vast areas of the cell surface (Figure 3, F-G). We finally used diamide, a drug that causes oxidation of spectrins and disruption of their submembrane arrangement (Wu et al., 2017). PREM views on unroofed fibroblasts revealed that 500 µM diamide for 15 min causes a drastic alteration of the spectrin mesh, with aggregation of the submembrane scaffold into clumps (Figure 3, F). This disorganized spectrin mesh also caused the appearance of more CCSs, with a density rising to 2.1 ± 0.07 CCS/µm^2 (Figure 3, G). Overall, perturbation of the actin-spectrin mesh increased the formation of CCSs at the membrane of non-neuronal cells.

The periodic submembrane actin-spectrin mesh restricts CCP formation at the AIS

If the sparse actin-spectrin mesh can inhibit the formation of CCSs in fibroblasts, the denser periodic actin-spectrin mesh should be able to tightly control this process at the AIS of neurons. To test this hypothesis, we knocked down α2- and/or ß4-spectrin in neuronal cultures using adeno-associated viruses (AAVs) expressing shRNA sequences. These AAVs could knock down spectrins efficiently, as shown by Western blots (Supporting Figure 3, E) and immunolabeling (Supporting Figure 4, A-D). In addition, AAV-expressed shRNAs against α2-spectrin, ß4-spectrin or a combination of both disorganized the periodic scaffold, as shown by the loss of periodic actin rings along the AIS and proximal axon (Supporting Figure 4, E-J). 3D-STORM showed that we could still unroof neurons depleted for both α2-spectrin and ß4-spectrin, revealing CCPs along the remaining ventral plasma membrane (Figure 4, A). PREM views of unroofed neurons depleted for α2- and/or ß4-spectrin showed a lack of submembrane spectrin mesh, with only isolated actin filament visible and the presence of numerous CCPs (Figure 4, B). Quantification confirmed that depletion of spectrins increased the density of

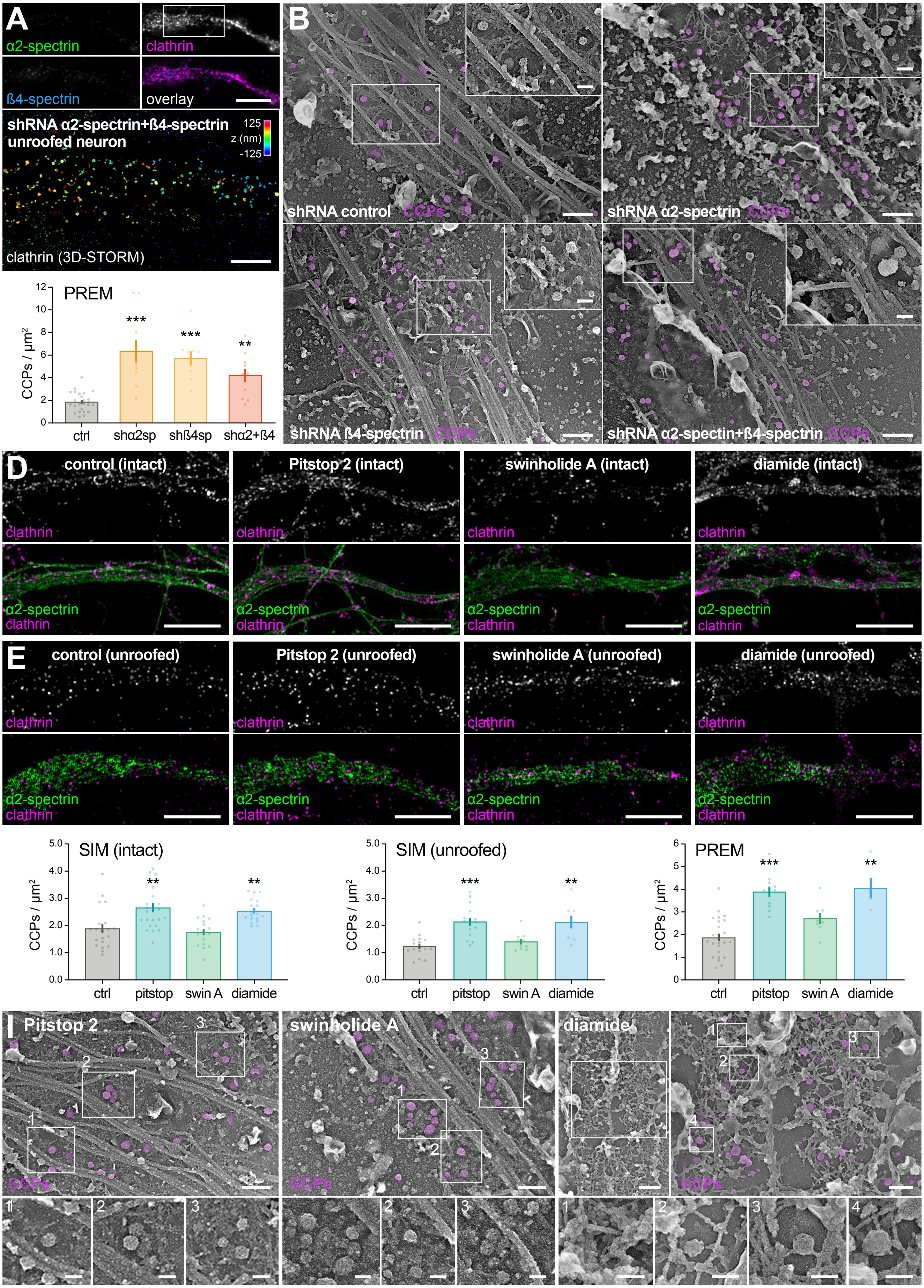

Figure 4: The periodic submembrane actin-spectrin mesh restricts CCP formation at the AIS.
See Legends on next page.

(< previous page) Figure 4: The periodic submembrane actin-spectrin mesh restricts CCP formation at the AIS.
A. Top, widefield image of the AIS of a neuron infected with an AAV expressing shRNAs against α2-spectrin and ß4-spectrin, unroofed, fixed and stained for clathrin (magenta on overlay), α2-spectrin (green on overlay) and neurofascin (blue overlay). Bottom, 3D-STORM image of clathrin corresponding to the AIS area shown on the top image, color coded for depth. Scale bar, 10 µm (top images), 2 µm (bottom image). B. PREM views of the unroofed proximal axon of neurons infected with AAVs expressing control shRNAs (top left) or targeted against α2-spectrin (top right), ß4-spectrin (bottom left) or α2-spectrin and ß4-spectrin (bottom right), with CCPs colored in magenta on the main image. Insets are zooms of the area highlighted on the main images. Scale bars, 1 µm (main images), 200 nm (insets). C. Effect of spectrins knockdown on the CCP density as quantified from PREM views of unroofed proximal axons (n=25, 10, 10, and 11 images for Ctrl, shRNA against α2, ß4, and α2/ß4-spectrin conditions, respectively). D. SIM images of the proximal axon of neurons treated with vehicle (0.1% DMSO 3h), swinholide A (100 nM 3h), Pitstop 2 (30 µM 45 min), or diamide (500 µM 45 min), fixed and stained for clathrin (magenta on overlay) and α2-spectrin (green on overlay). Scale bars, 5 µm. E. SIM images of the proximal axon of neurons treated with vehicle (0.1% DMSO 3h), swinholide A (100 nM 3h), Pitstop 2 (30 µM 45 min), or diamide (500 µM 45 min), unroofed and fixed, then stained for clathrin (magenta on overlay) and α2-spectrin (green on overlay). Scale bars, 5 µm. F. Effect of drugs on the density of CCPs along the AIS as quantified from SIM images of intact neurons (n=20, 18, 24, and 18 cells for Ctrl, swinholide A, Pitstop 2, and diamide conditions, respectively). G. Effect of drugs on the density of CCPs along the AIS as quantified from SIM images of unroofed neurons (n=16, 10, 16, and 9 cells for Ctrl, swinholide A, Pitstop 2, and diamide conditions, respectively). H. Effect of drugs on the density of CCPs along the AIS as quantified from PREM views of unroofed neurons (n=25, 8, 11, and 5 images for Ctrl, swinholide A, Pitstop 2, and diamide conditions, respectively). I. PREM views of the proximal axon of unroofed neurons after treatment with swinholide A (100 nM 3h), Pitstop 2 (30 µM 15 min), and diamide (500 µM 15 min), with CCPs colored in magenta on the main image. Zoomed insets correspond to the area highlighted on the main image. Scale bars, 500 nm (main images), 200 nm (insets).

CCPs in comparison with controls: from 1.9 ± 0.17 CCP/µm² in control neurons to 6.4 ± 1.0, 5.7 ± 0.61, and 4.2 ± 0.87 CCP/µm² at the AIS of neurons depleted for α2-, ß4-, or α2- and ß4-spectrin, respectively; (Figure 4, C). This demonstrates that the dense spectrin mesh indeed restricts the formation of CCPs at the AIS plasma membrane.

Next, we treated neuronal cultures with the same set of drugs that were used on fibroblasts to target CCP endocytosis (Pitstop 2), actin filaments (swinholide A) and spectrin mesh (diamide). In this case, we first evaluated the density of CCPs at the AIS of treated neurons using SIM of intact and unroofed neurons labeled for clathrin and α2-spectrin (Figure 4, D-E). Pitstop 2 treatment (30 µM for 45 min) resulted in an increase of the CCP density at the AIS compared to controls (from 1.9 ± 0.17 to 2.7 ± 0.17 CCP/µm² for intact neurons, 1.2 ± 0.09 to 2.1 ± 0.14 for unroofed neurons), whereas swinholide A (100 nM for 3h) did not significantly change the density of CCPs (1.8 ± 0.12 and 1.4 ± 0.10 CCP/µm² for intact and unroofed neurons, respectively; Figure 4, F-G). Diamide (500 µM for 45 min) resulted in a visibly patchier appearance of the α2-spectrin mesh at the AIS of unroofed neurons (Figure 4, E) and led to an increased density of CCPs (2.5 ± 0.10 and 2.12 ± 0.21 CCP/µm² for intact and unroofed neurons, respectively; Figure 4, F-G). Quantification of PREM views of treated and unroofed neurons confirmed these results, with Pitstop 2 and diamide A treatment resulting in an increased density of CCPs (from 1.9 ±017 for control to 3.9 ± 0.23, 2.7 ± 0.25, and 4.1 ± 0.44 CCP/µm² for Pitstop 2, swinholide A, and diamide, respectively; Figure 4, H). High-magnification PREM views also resolved the lack of actin filaments in swinholide A-treated neurons and the profound disorganization of the spectrin mesh into connected aggregates caused by diamide (Figure 4, I). Overall, perturbation experiments showed that while CCP formation seems less sensitive to actin disassembly in the AIS compared to fibroblasts. Disorganization of the spectrin mesh increases the density of CCPs at the AIS, suggesting that the disorganization of the periodic spectrin scaffold and its defined clearings makes the plasma membrane more accessible, resulting in the assembly of more CCPs.

Endocytic cargo concentrates in CCPs at the surface of the AIS

There is no direct correlation between the CCP density at the plasma membrane and the amount of endocytosis occurring in a cell: for example, Pitstop 2 treatment leads to more stalled CCPs and completely inhibits endocytosis (von Kleist et al., 2011), as we verified in Rat2 fibroblasts . Thus, beyond its effect on CCP density, we next sought to directly assess the extent of clathrin-mediated endocytosis after perturbation of the actin-spectrin submembrane scaffold. In fibroblast cells, fluorescent transferrin uptake is a straightforward way to assess clathrin-mediated endocytosis. We first verified that knockdown of α2- and/or ß2-spectrin using siRNAs in Rat2 cells does not downregulate the expression of the transferrin receptor by Western blot (Supporting Figure 3, D). Knockdown of α2- and/or ß2-spectrin, which increase the density of CCPs, also significantly increased the uptake of transferrin from a normalized transferrin fluorescence value of 1.0 ± 0.04 for control to 1.38 ± 0.07, 1.37 ± 0.10, and 1.89 ± 0.09 for knockdown of α2-, ß2-, or α2- and ß2-spectrin, respectively (Figure 5, A-B). By contrast, treatment of fibroblasts with Pitstop 2 and swinholide A, which also increase the density of CCPs, efficiently inhibited the endocytosis of fluorescent transferrin (down to 0.09 ± 0.004 for Pitstop 2 and 0.42 ± 0.04 for swinholide A; Figure 5, C).

We then aimed to assess endocytosis at the AIS of neurons by visualizing the uptake of fluorescent cargo. Incubation of neuronal cultures with fluorescent transferrin for up to 1h resulted in the accumulation of fluorescent puncta and tubules within the cell body and dendrites of neurons, but no endocytosed transferrin could be detected along the proximal axon (Figure 5, D). This is consistent with the literature and the reported absence of transferrin receptors from the axon (Cameron et al., 1991; Farías et al., 2012; Parton et al., 1992). To detect endocytic processes in all neuronal compartments independently of any specific receptor, we thus used fluorescent 10 kDa dextran as a fluid phase marker able to enter cells via clathrin-dependent and independent endocytosis (Li et al., 2015). After 5 to 30 min of incubation at 50 µg/mL, fluorescent dextran clusters were readily detected along the dendrites and the proximal axon (Figure 5, E). Close inspection of SIM images revealed that a fraction of these dextran clusters along the proximal axon of intact neurons were colocalized with CCPs, an observation confirmed by averaged images centered on CCPs, which showed the selective enrichment in dextran at CCPs (Figure 5, F). To verify that a significant proportion of dextran clusters were not found in endosomes, but trapped at the cell surface in CCPs after 30 min of dextran feeding, we un-

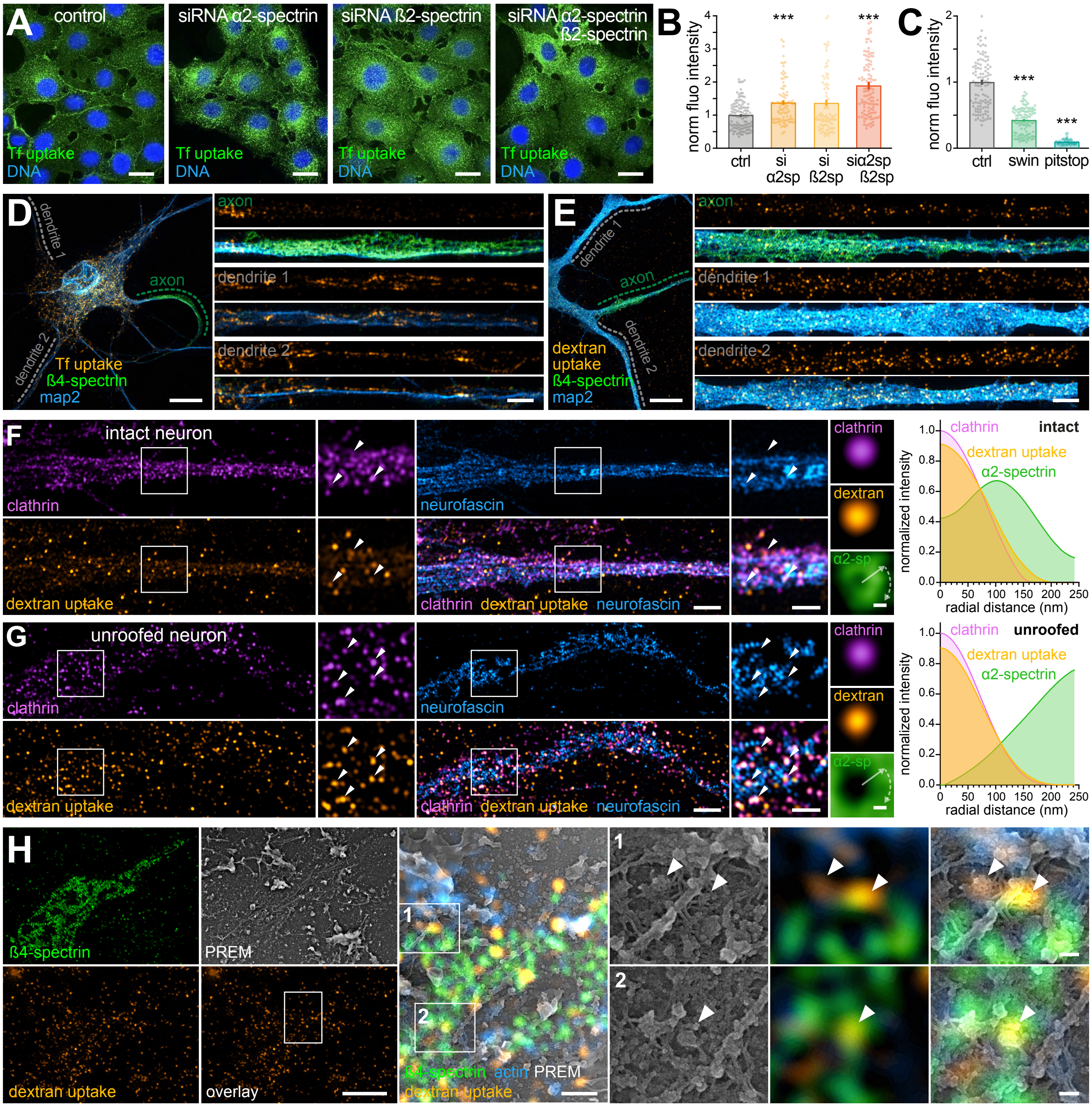

Figure 5 Endocytic cargo concentrates in CCPs at the surface of the AIS.
A. Super-resolution spinning disk microscopy images of transferrin-Alexa Fluor 488 uptake (Tf uptake, 20 µg/µL for 10 min, green) in Rat2 fibroblasts transfected with control siRNAs or against α2-spectrin, ß2-spectrin, or α2- and ß2-spectrin (from left to right), fixed and labeled with DAPI (blue). Scale bars, 10 µm. B. Effect of spectrins knockdown on the intensity of Tf uptake in Rat2 fibroblasts, as quantified from confocal images (n=115, 91, 87, and 113 images for Ctrl and siRNA against α2, ß2, and α2/ß2-spectrin, respectively). C. Effect of drugs on the intensity of Tf uptake in Rat2 fibroblasts, as quantified from spinning-disk confocal images (n=115, 116, and 70 images for Ctrl, swinholide A, and pitstop2, respectively). D. SIM image of a neuron fed for 1h with transferrin-Alexa Fluor 647 (orange), fixed, and stained for map2 (dendrites, blue) and ß4-spectrin (AIS, green). Images on the right are straightened zooms along the dendrites and axon highlighted on the main image. Tf uptake is detected along the dendrites, but absent from the AIS and proximal axon. Scale bar, 10 µm (main image), 2 µm (zooms). E. SIM image of a neuron fed for 30 min with dextran-Alexa Fluor 555 (orange), fixed, and stained for map2 (dendrites, blue) and ß4-spectrin (AIS, green). Images on the right are straightened zooms along the dendrites and axon highlighted on the main image. Dextran uptake is detected along the dendrites as well as along the AIS and proximal axon. Scale bar, 10 µm (main image), 2 µm (zooms). F. Left, SIM image of the AIS of a neuron fed with dextran-AF555 (yellow), fixed, and stained for clathrin (magenta) and neurofascin (blue). Some dextran clusters colocalize with CCPs (arrowheads). Right, average images (n=591 pits) centered on CCPs showing the distribution of dextran (orange), clathrin (magenta) and α2-spectrin (green). The graph shows the radial intensity profile corresponding to the average images, with the dextran clusters colocalizing with CCPs in an area devoid of α2-spectrin. Scale bars, 1 µm (AIS images), 100 nm (average images). G. Left, SIM image of the AIS of a neuron fed with dextran-AF555 (yellow), unroofed, fixed, and stained for clathrin (magenta) and neurofascin (blue). Most dextran clusters colocalize with CCPs (arrowheads). Right, average images (n=562 pits) centered on CCPs showing the distribution of dextran (orange), clathrin (magenta) and α2-spectrin (green). The graph shows the radial intensity profile corresponding to the average images (gray arrow), with dextran cluster colocalizing with CCPs in an area devoid of α2-spectrin. Scale bars, 1 µm (AIS images), 100 nm (average images). H. Correlative SIM-PREM image of the AIS of a neuron fed with dextran-AF555 (orange), unroofed, fixed, and stained for ß4-spectrin (green) and actin (blue). Zoomed overlays on the right show dextran clusters found at CCPs in areas devoid of spectrin labeling (arrowheads). Scale bars, 5 µm (isolated SIM channels), 2 µm (main overlay), 100 nm (zooms).

roofed neurons just before fixation to remove the intracellular compartments. SIM images showed that most of the dextran clusters now colocalized with CCPs after unroofing (Figure 5, G). We confirmed that a major population of dextran clusters were still present at CCPs after 30 min of feeding by obtaining correlative SIM-PREM images of unroofed neurons, which showed colocalization of fluorescent dextran clusters at CCPs on PREM views (Figure 5, H). These experiments suggest that despite the presence of a dense population of CCPs in spectrin mesh clearings along the AIS, these CCPs are not efficiently resulting in endocytosis, with endocytic marker clusters being found at the cell surface even after a prolonged incubation.

Live-cell super-resolution microscopy reveals that CCPs are static along the AIS and proximal axon

If CCPs are present at the AIS but rarely result in scission and conclusive endocytosis, they should be long-lived and seen as stable structures by live-cell imaging. To visualize the dynamics of CCPs together with the periodic actin-spectrin scaffold along the submembrane of the proximal axon, we used live-cell TIRF-SIM (Kner et al., 2009) of neurons transfected with clathrin light chain (CLC)-mCherry and EGFP-ß2-spectrin

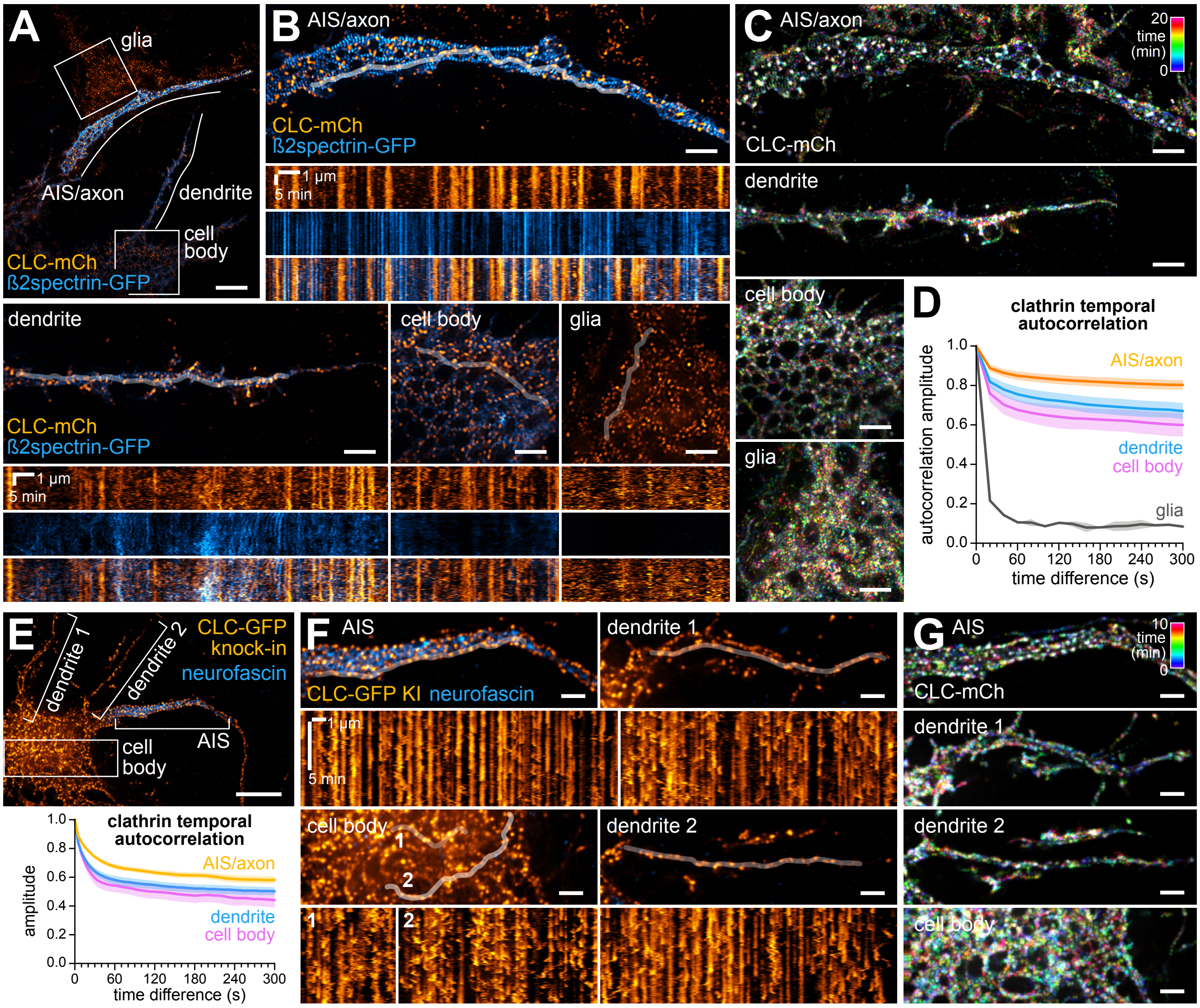

Figure 6: CCPs are static along the AIS and proximal axon.
A. Individual frame from Supplementary Movie 1 showing a neuron transfected with ß2spectrin-GFP (blue) and CLC-mCh (orange) and imaged by TIRF-SIM every 20s for 20 min. Scale bar, 5 µm. B. Zooms on areas highlighted in A, with corresponding kymographs (highlighted white lines) along the AIS and proximal axon (top), along a dendrite (bottom left), inside the cell body (bottom center) and a neighboring glial cell (bottom right). Spectrin bands appear as vertical lines spaced by 190 nanometers in blue, while static pits appear as vertical lines and dynamic pits as dots in orange. Scale bars, 2 µm (images), 1 µm (kymograph horizontal), 5 min (kymograph vertical). C. Time color-coded projection of the CLC-mCh channel for the neuronal compartments shown in the panels of B: static pits appear white, while dynamic pits are colored due to their transient appearance. Scale bars, 2 µm. D. Temporal autocorrelation of the clathrin dynamics from tracings within the different compartments of 3 neurons and one glia, showing the relative immobility of CLC in the axon (orange, n=5 tracings) compared to the dendrites (blue, n=5), cell body (magenta, n=4) and within a glial cell (gray, n=2). E. Individual frame from Supplementary Movie 2 showing a neuron with CLC endogenously tagged with GFP (orange), and extracellular staining for neurofascin highlighting the AIS (blue), imaged by SoRa spinning disk every 5s for 10 min. Scale bar, 10 µm. F. Zooms on areas highlighted in E, with corresponding kymographs (highlighted white lines) along the AIS (top left), along two dendrites (top and bottom right), and inside the cell body (bottom left). Static CCPs appear as vertical lines, with putative endocytic events appearing as discontinuities of characteristic J-shaped traces. Scale bars, 2 µm (image), 1 µm (kymograph horizontal), 5 min (kymograph vertical). G. Time color-coded projection of CLC-GFP for the neuronal compartments shown in the panels of B: static pits appear white, while dynamic pits are colored due to their transient appearance. Scale bars, 2 µm. H. Temporal autocorrelation of the clathrin dynamics from tracings within the different compartments of 2 neurons, showing the relative immobility of CLC in the axon (orange, n=5 tracings) compared to the dendrites (blue, n=9) and cell body (magenta, n=7).

(Figure 6, A; Supporting Movie 1). The ~110 nm lateral resolution of TIRF-SIM could clearly resolve individual CCPs and the 190-nm periodicity of ß2-spectrin along the AIS and proximal axon, and low intensity illumination coupled to deep learning-based denoising allowed to image for tens of frames every 20s. The resulting movie (Supporting Movie 1) and subsequent analysis with kymographs (static CCPs appear as vertical lines, Figure 6, B) or time-color coded projections (static CCPs appear as white dots, Figure 6, C) clearly showed the high stability of CCPs at the AIS compared to the dendrites and cell body of the same neuron, with most AIS CCPs being present across the 20 min of imaging. Temporal autocorrelation analysis of CLC-mCherry intensity profiles from movies of several neurons confirmed this visual impression, with a higher temporal persistence of CLC-mCherry at the AIS compared to the cell body and dendrites (Figure 6, D).

To confirm the specific stability of CCPs at the AIS of neurons, and avoid potential stabilizing effects of overexpressed clathrin or spectrin, we next used a modified AAV-mediated HiUGE strategy (Ogawa et al., 2023; Bingham et al., 2023) to endogenously tag clathrin light chain with EGFP in cultured hippocampal neurons (CLC-GFP KI), and imaged clathrin dynamics using super-resolution spinning disk microscopy (Figure 6, E; Supporting Movie 2). The enhanced temporal resolution (one frame every 5s for 10 min) allowed us to discern scission events for both static pits at the AIS (appearing as interruptions in the vertical traces on kymographs) and transient pits in dendrites (appearing as J-shaped traces in kymographs; Figure 6, F). Here again, kymographs and time color-coded projections (Figure 6, G) showed that endogenously-tagged CCPs were more stable at the AIS compared to dendrites and the cell body, an observation confirmed by temporal autocorrelation analysis of CLC-GFP KI from several neurons (Figure 6, H). Overall, these live-cell imaging experiments demonstrate that CCPs are specifically stabilized at the AIS of neurons, consistent with the restrained endocytic activity observed using dextran uptake.

Endocytosis at the AIS can be triggered by disassembling the spectrin mesh or elevating neuronal activity

At the AIS, CCPs that form in the clearings of the spectrin mesh thus appear to be "frozen", long-lived structures that do not readily engage in endocytosis. We then wanted to test if perturbation of the actin-spectrin mesh, in addition to increasing the density of CCPs by increasing membrane accessibility, could result in more endocytosis downstream of this increase. We treated neurons with drugs Pitstop 2, swinholide A, and diamide, combining treatments with a dextran uptake assay. Neurons were kept intact before fixation, labeling, and imaging by SIM (Figure 7, A and C) or unroofed before fixation (Figure 7, B and D). Inhibition of CCP scission with Pitstop 2 resulted in a decreased density of dextran clusters, while actin disassembly by swinholide A did not significantly change this density in intact neurons (from 0.66 ± 0.05 clusters/µm^2 in controls to 0.35 ± 0.04 clusters/µm^2 for Pitstop 2 and 0.52 ± 0.04 clusters/µm^2 for swinholide A in intact neurons; Figure 7, C). Both Pitstop 2 and swinholide A did not affect the density of surface dextran clusters after unroofing, suggesting that the decrease in intact neurons for Pitstop 2 was due to inhibited endocytosis (0.72 ± 0.08, 0.70 ± 0.05, 0.64 ± 0.07 for control, Pitstop 2 and swinholide A in unroofed neurons, respectively; Figure 7, D). Interestingly, diamide treatment resulted in an increased density of dextran clusters both in intact and unroofed neurons, indicating enhanced formation of CCPs and increased endocytosis after disorganization of the spectrin mesh at the AIS (0.97 ± 0.07 and 1.19 ± 0.16 clusters/µm^2 after diamide treatment in intact and unroofed neurons, respectively; Figure 7, C-D). Disorganization of the actin-spectrin mesh thus allows for the formation of more CCPs at the AIS membrane, and results in increased endocytosis.

Beyond drug induced perturbations, we finally wondered if a more physiological signal would be able to trigger long-lived AIS CCPs to engage in more efficient endocytosis. It was recently shown that a brief application of NMDA triggered increased neuronal activity and long-term depression (LTD), in turn causing structural AIS plasticity driven by $Na_V1.2$ voltage-gated sodium channel endocytosis along the distal AIS (Fréal et al., 2023). We reasoned that this upregulated AIS endocytosis could result from a rearrangement of the actin-spectrin mesh and engagement of CCPs into conclusive endocytosis. Neurons were stimulated with NMDA (50 µM, 4 min) before a 30-minute dextran uptake period in the absence of NMDA. Quantification of CCP and dextran cluster densities from SIM images of intact and unroofed neurons (Figure 7, G-H) showed that NMDA stimulation modestly increased the density of CCPs at the AIS compared to controls (from 2.01 ± 0.07 to 2.30 ± 0.05, from 1.18 ±0.04 to 1.61 ± 0.05 CCP/µm^2, control to NMDA in intact and unroofed neurons, respectively; Fig. 7, E-F). By contrast, NMDA stimulation induced a significant increase in dextran cluster density in intact neurons (from 0.91 ± 0.05 to 1.40 ± 0.07 clusters/µm^2 for control and NMDA, respectively; Figure 7, E), whereas it did not change the detected density of surface dextran clusters (from 0.95 ± 0.06 to 0.98 ± 0.06 clusters/µm^2 for control and NMDA, respectively; Figure 7, F). This suggests that NMDA stimulation can trigger endocytosis from existing CCPs at the AIS membrane. We next visualized the submembrane ultrastructure of NMDA-treated neurons with PREM. High-magnification images of unroofed proximal axons presented a partial disorganization of the spectrin mesh with a more clustered appearance compared to control, and the presence of CCPs with normal morphology (Figure 7, I). We observed an increased presence of branched actin filaments surrounding CCPs within enlarged spectrin clearings, suggesting a role of these filaments in engaging CCPs toward conclusive endocytosis. Quantification of CCP density showed a modest increase in CCPs density along the AIS, consistent with the SIM data (from 1.87 ± 0.17 CCP/µm^2 in controls to 2.54 ± 0.11 CCP/µm^2 after NMDA stimulation; Figure 7, J). Elevated activity is thus able to stimulate endocytosis at the AIS, by unlocking the engagement of long-lived CCPs.

Discussion

The AIS and proximal axon are neuronal compartments where endocytosis has long been overlooked. Our experiments combining super-resolution optical and electron microscopy with genetic and pharmacological perturbations provide compelling evidence that the AIS contains a population of CCPs with unique properties, allowing endocytosis to be tightly controlled by the AIS submembrane scaffold.

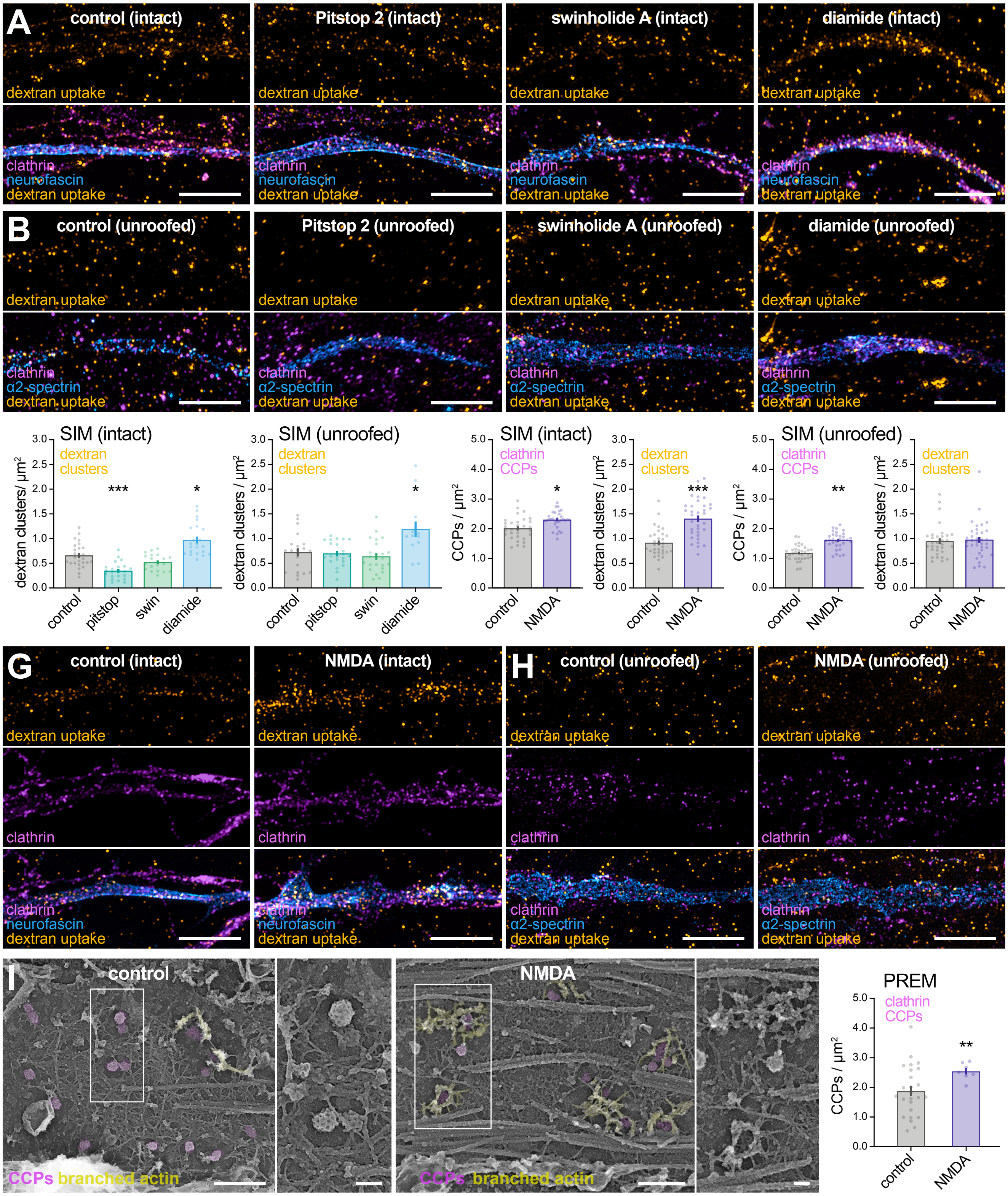

Figure 7: Endocytosis at the AIS can be triggered by disassembling the spectrin mesh or elevating neuronal activity.
A. SIM images of the AIS of neurons treated with vehicle (0.1% DMSO 3h), swinholide A (100 nM 3h), Pitstop 2 (30 µM 45 min), or diamide (500 µM 45 min), fed with dextran-AF555 (yellow), fixed, and stained for clathrin (magenta) and neurofascin (blue). Scale bars, 5 µm. B. SIM images of the AIS of neurons treated with vehicle (0.1% DMSO 3h), swinholide A (100 nM 3h), Pitstop 2 (30 µM 45 min), and diamide (500 µM 45 min), fed with dextran-AF555 (yellow), unroofed, fixed, and stained for clathrin (magenta) and neurofascin (blue). Scale bars, 5 µm. C. Effect of drugs on the density of dextran clusters density along the AIS as quantified from SIM images of intact neurons (n=26, 20, 22, and 22 cells for Ctrl, swinholide A, Pitstop 2, and diamide conditions, respectively). D. Effect of drugs on the density of dextran clusters density along the AIS as quantified from SIM images of unroofed neurons (n=21, 23, 23, and 13 cells for Ctrl, swinholide A, Pitstop 2, and diamide conditions, respectively). E. Effect of NMDA-mediated elevation of activity on the CCPs (left graph) and dextran clusters (right graph) density along the AIS as quantified from SIM images of intact neurons (n=31, 31, 32, and 34 cells for Ctrl CCPs, NMDA CCPs, Ctrl dextran, and NMDA dextran conditions, respectively). F. Effect of NMDA-mediated elevation of activity on the CCPs (left graph) and dextran clusters (right graph) density along the AIS as quantified from SIM images of unroofed neurons (n=33, 32, 32, and 35 cells for Ctrl CCPs, NMDA CCPs, Ctrl dextran, and NMDA dextran conditions, respectively). G. SIM images of the AIS of neurons treated with vehicle (0.1% DMSO), or NMDA (50 µm 4 min followed by 30 min rest), fed with dextran-AF555 (yellow), fixed, and stained for clathrin (magenta) and neurofascin (blue). Scale bars, 5 µm. H. SIM images of the AIS of neurons treated with vehicle (0.1% DMSO), or NMDA (50 µm 4 min followed by 30 min rest), fed with dextran-AF555 (yellow), unroofed, fixed, and stained for clathrin (magenta) and neurofascin (blue). Scale bars, 5 µm. I. PREM views of the proximal axon of unroofed neurons after treatment with vehicle or NMDA, with CCPs colored in magenta and branched actin surrounding CCPs colored in yellow on the main image. Zoomed Inset corresponds to the area highlighted on the main image. Scale bars, 1 µm (main images), 200 nm (insets). J. Effect of NMDA-mediated elevation of activity on the density of CCPs along the AIS as quantified from PREM views of unroofed neurons (n=25 and 7 images for Ctrl and NMDA conditions, respectively).

We discovered that in the AIS, CCPs form on bare areas of the plasma membrane that are precisely delimited by a circular clearing of the actin-spectrin undercoat. These ~300 nm clearings are scattered across the inner surface of the AIS and proximal axon, inserted within the previously described periodic scaffold of actin rings connected by spectrin tetramers (Vassilopoulos et al., 2019). They exhibit a specific organization: actin filaments are present at the border of the clearings, crosslinked by spectrins and ankyrin that form an outer polygonal arrangement. In addition, a single actin filament is often seen to enter the clearing and contact the central CCP. We propose that clearings are structures that allow the formation of CCPs by providing access to the AIS plasma membrane. The necessity for CCPs to form in membrane areas devoid of spectrins was previously shown by diffraction-limited fluorescent microscopy in spectrin-dense regions of fibroblasts (Ghisleni et al., 2020), and along the lateral membrane of epithelial cells (Jenkins et al., 2015) – it makes all the more sense along axons where the spectrin mesh is particularly dense.

This organization of CCPs in clearings defined by the submembrane spectrin scaffold immediately suggests that this scaffold can control the formation of CCPs by defining the location and density of these clearings. This inhibitory role of submembrane spectrins on CCP formation and subsequent endocytosis was proposed for fibroblasts (Ghisleni et al., 2020) and it was shown that endocytosis was negatively controlled by the ankyrin/spectrin domains at the lateral membrane of epithelial cells (Jenkins et al., 2015). Here, we demonstrate that spectrin knockdown or disorganization directly upregulates CCP formation and endocytosis in fibroblasts and along the AIS in neurons, establishing the spectrin mesh as an insulating layer restricting endocytic processes. Beyond the AIS, the periodic actin-spectrin scaffold is likely to regulate endocytosis along the whole axon, as shown by the enhanced endocytosis of cannabinoid receptors after activation in neurons depleted for ß2-spectrin, part of the distal axon periodic scaffold (Zhou et al., 2019).

Our results suggest that another layer of regulation is present besides the insulating effect of the spectrin mesh. We found that CCPs that do form in mesh clearings along the AIS are unusually long-lived and do not readily engage in conclusive endocytosis, accumulating cargoes at the AIS surface. Actin has been shown to be important for the late stages of clathrin-mediated endocytosis (Loebrich, 2014), as confirmed by the presence of numerous stalled CCPs in fibroblasts after swinholide A treatment. What could explain the “frozen” property of CCPs at the AIS? We speculate that the dense spectrin mesh could prevent the polymerization of actin around pits, impeding the progression of CCPs toward scission and conclusive endocytosis.

These two layers of regulation allow us to explain the observed effects of different perturbations on CCP formation and endocytosis at the AIS: swinholide A disassemble actin structures, but cannot fully disassemble the periodic spectrin scaffold at the AIS (Vassilopoulos et al., 2019). In addition, it does not induce the accumulation of low-curvature clathrin-coated structures by blocking the late stage of endocytosis like in fibroblasts, as this block is already occurring at the AIS in control conditions and neurons do not form flat clathrin lattices (Moulay et al., 2020). Depletion of the spectrin mesh by knockdown and its disorganization by diamide increase the accessible membrane area and increase the number of CCPs, while releasing actin from the submembrane mesh that can help CCPs to engage in conclusive endocytosis, resulting in more internalized cargo. Finally, NMDAR activation is a more subtle and physiological intervention that does not profoundly alter the spectrin mesh, but could allow the formation of branched actin interacting with CCPs, resulting in the engagement of existing CCPs into conclusive endocytosis (Engqvist-Goldstein et al., 2004; Vassilopoulos et al., 2014).

What could be the functional relevance of this tight regulation of endocytosis at the AIS by the submembrane spectrin scaffold? Firstly, static CCPs could help sequester membrane proteins that do not bind to AIS-specific scaffolds like ankyrin G, priming them for a low but continuous process of endocytic retrieval and degradation as a sorting mechanism (Eichel et al., 2022). Secondly, the presence of pre-arranged, static endocytic spots in the dense spectrin mesh likely facilitates the rearrangement of AIS membrane proteins that are bound to the remarkably stable ankyrin/spectrin scaffold (Brachet et al., 2010): endocytosis of sodium channels or neurofascin during morphological plasticity (Fréal et al., 2023) would only require detachment from ankyrin G – a process likely to be phosphorylation-dependent (Tuvia et al., 1997; Bréchet et al., 2008) – and diffusion to the nearest CCP. An “unfreezing” mechanism such as the one we evidenced after NMDA treatment would thus trigger efficient endocytosis from these CCPs, allowing to modify the AIS length or position (Yamada and Kuba, 2016).

Overall, our results support a model where CCPs form in newly-described structures, “clearings” of the actin-spectrin mesh along the AIS, and are then stabilized as long-lived structures with moderate endocytic activity at steady-state. Efficient endocytosis can be triggered by physiological signals, allowing to rearrange the AIS membrane content or internalize extracellular components. We look forward to further explore the mechanisms and roles of this regulated process, which is likely to have important physiological and pathological implications for neuronal organization and function.

Acknowledgments

We would like to acknowledge funding by the Agence Nationale pour la Recherche (ANR-20-CE16-021-03 to C.L. and S.V., ANR-21-CE13-0018-01 to SV), Fédération pour la Recherche sur le Cerveau (AOE 16 “Espoir en tête” 2021) to C.L., Sorbonne Université, INSERM, Association Institut de Myologie core funding to S.V. We would like to thank the Neuro-Cellular Imaging Service and Nikon Center for Neuro-NanoImaging at INP, with funding from CPER-FEDER (PlateForme NeuroTimone PA0014842), the Institut Marseille Imaging and NeuroMarseille for complementary equipment funding from Excellence Initiative of Aix-Marseille University – A*MIDEX, a French “Investissements d’Avenir” program (AMX-19-IET-002), and NeuroSchool for end-of-PhD funding. We would also like to thank the IBPS electron microscopy platform (Sorbonne University, Paris, France) and the MyoVector facility from the Institute of Myology (Paris, France). We would like to thank Subhojit Roy and Marc Bitoun for insightful discussions, as well as Damaris Lorenzo for the gift of the EGFP-ß2-spectrin plasmid.

Author Contributions

Conceptualization: C.L., S.V.; Methodology: F.W., S.M., J.L., N.J., C.L., S.V.; Formal analysis: F.W., S.M., C.L., S.V.; Investigation: F.W., S.M., J.L., G.M., F.B.-R., F.P., S.B.-Z., M.-J.P., C.L., S.V.; Resources: N.J.; Writing-Original Draft: S.M., C.L., S.V.; Writing-Review and Editing: F.W., S.M., J.L., M.-J.P., C.L., S.V.; Visualization: F.W., S.M., C.L, S.V.; Supervision, Project Administration: C.L., S.V.; Funding acquisition: C.L., S.V.

Methods

Animals and neuronal cultures

The use of Wistar rats followed the guidelines established by the European Animal Care and Use Committee (86/609/CEE) and was approved by the local ethics committee (agreement D13-055-8). Rat hippocampal neurons were cultured following the Banker method, above a feeder glia layer (Kaech and Banker, 2006). Rapidly, 12 or 18 mm-diameter round #1.5H coverslips were affixed with paraffin dots as spacers, then treated with poly-L-lysine (Sigma-Aldrich #P2636). Hippocampi from E18 rat pups were dissected and homogenized by trypsin treatment followed by mechanical trituration and seeded on the coverslips at a density of 4,000-8,000 cells/cm^2 for 3h in serum-containing plating medium. Coverslips were then transferred, cells down, to petri dishes containing confluent glia cultures conditioned in B27-supplemented (Thermo Fisher Scientific #17504044) neurobasal medium (NB, Thermo Fisher Scientific #21103049), and cultured in these dishes for up to 4 weeks. For this work, neurons were fixed at 13-16 days in vitro (div), a stage where they exhibit a periodic actin/spectrin scaffold along virtually all axons (Xu et al., 2013).

Fibroblast cultures and siRNA-mediated knockdown of spectrins

Rat2 fibroblasts were seeded on 18-mm glass coverslips to 80 % confluency in DMEM containing 10 % FCS, and they were incubated overnight at 37°C. Prior to transfection, cells were washed in PBS. Complexes of Lipofectamine 3000 (Thermo Fisher Scientific) and siRNA (corresponding to the shRNA sequences detailed below) were then introduced to the cells following the manufacture protocol (Thermo Fisher Scientific). The cells were left to incubate for 48 hours.

The validation of siRNAs knock-down in fibroblasts was performed by Western blot. Rat2 cultures were lysed in a buffer (50 mM Tris-HCl, pH 7.5, 0.15 M NaCl, 1 mM EDTA, 1% NP-40) supplemented with a protein inhibitor cocktail 1:100 (Sigma-Aldrich). Samples denatured by 3 min boiling in Laemmli buffer were separated by electrophoresis on 4-12% bis-acrylamide gel (Thermo Fisher Scientific), then transferred to 0.45 µm nitrocellulose membranes (Thermo Fisher Scientific) and labeled with a primary antibody then a secondary antibody coupled to horseradish peroxidase (Trueblot immunoglobulin G HRP, Rockland). Proteins in samples were detected using Immobilon Western Chemiluminescent HRP Substrate (Sigma-Aldrich) and image acquisition was performed on a G-Box (Ozyme). The following primary antibodies were used to validate siRNA knock-down in fibroblasts: anti-α2-spectrin (mouse IgG2b clone D8B7, Biolegend #803201, 1:1000), anti-β2-spectrin (BD Biosciences #612563, mouse IgG1 against residues 2101–2189 of human β2-spectrin, 1:100), anti-clathrin (rabbit polyclonal anti-CHC, Abcam #ab21679, 1:1000), anti-TfR (mouse IgG1, Invitrogen #13-6800, 1:1000); anti-GADPH (mouse IgG1, Santa Cruz #sc-47724, 1:1000) was used as a loading control.

Plasmid constructs and neuronal culture transfection

Transfections were performed using the following constructs: clathrin-GFP and clathrin-mCherry plasmids were a gift from Subhojit Roy (Ganguly et al., 2021). The EGFP-β2-spectrin plasmid was a gift from Damaris Lorenzo (Cousin et al., 2021). The spectrin-silencing shRNA plasmids were constructed in the pRFP-C-RS backbone (Origene). These plasmids allow cloning and expression of shRNA under a U6 promoter and co-expression of the TurboRFP red fluorescent protein under the control of a CMV promoter. Insertion of the shRNA sequences was performed using the SLIC technique using overlapping single strand oligonucleotides (Jeong et al., 2012).

The sequences for each shRNA were:
α2-spectrin: **g**ATCAGTTTGTGGAAGAAACTTtcaagagAAGTTTCTTCCACAAACTGAT
β2-spectrin: **g**CAGAAGAGATCTCCAACTACAtcaagagTGTAGTTGGAGATCTCTTCTG
β4-spectrin: **g**CACTGGATAGCCGAGAAGGtcaagagCCTTCTCGGCTATCCAGTG
Luc (negative control): **g**CGCTGAGTACTTCGAAATGTCtcaagagGACATTTCGAAGTACTCAGCG

(First g in bold-lowercase: additional g for efficient U6 transcription, underscore-lowercase: shRNA loop. A shRNA directed against the luciferase coding sequence was used as negative control).

Plasmid constructs (0.25 to 0.5 µg) per 18-mm coverslip were incubated with 1 µL of Lipofectamine 3000 (Thermo Fisher Scientific #L3000001) in 50 µL NB for 20 min at room temperature for liposomes to form, before being added to 10 div cultured hippocampal neurons, coverslips flipped cells up in FB12 dishes containing preheated NB. Neurons were incubated for 30 min at 37°C with 5% CO_2. After incubation, the neurons were returned to their origin culture dishes and left incubating for 2.5 to 3 days before imaging.

AAV production and titration

AAV viral vectors were prepared by triple transfection in HEK-293 cells using polyethyleneimine transfection agent: pSMD2 AAV vector plasmid containing the shRNA sequences detailed above, pXX6 plasmid coding for the viral sequences essential for AAV production, and p0009 plasmid coding for serotype 9 capsid. Vector particles were purified on an iodixanol gradient and concentrated on Amicon Ultra-15 100K columns (Merck-Millipore). The AAV vectors were titrated as vg per milliliter by quantitative real-time PCR using ITR2 (inverted terminal repeats) specific primers at a 60°C annealing temperature (forward 5′-CTCCATCACTAGGGGTTCCTTG-3′ and reverse 5′-GTAGATAAGTAGCATGGC-3′) and the MGB Taqman probe 5′-TAGTTAATGATTAACCC-3.

AAV infection for shRNA-mediated knockdown in neuronal cultures

Spectrin-silencing shRNAs in adeno-associated virus vectors (AAV) were produced and titrated by the AAV production service of Institut de Myologie (Paris). Vectors identifiers AAV9-U6SCR (p05.1 Origen scrambled sequence GAGAGCCAGATTCAATCTGACGACTATGG), AAV9-U6beta4 /

p10.1 (Hedstrom et al., 2007), AAV9-U6alpha2 / p09.1 (Galiano et al., 2012), AAV9-U6-shRNA-α2+ß4-spectrin / p11.1 (both combined) targeted respectively no protein (scrambled control), β4-spectrin, α2-spectrin, α2- and β4-spectrin. The validation of shRNAs knock-down in neurons was performed by Western blot. Cells infected with an AAV-shRNAs were resuspended in a loading buffer with DTT, diluted to 50% in ultrapure water. The samples were then heated to 90°C for 3 min. After extensive washes, samples were resolved by 7.5% sodium dodecyl sulfate–polyacrylamide gel electrophoresis, and immunoprobed with one of anti-α2-spectrin (Biolegend #803201, mouse IgG2b clone D8B7, 1:1000), anti-β2-spectrin (BD Biosciences #612563, mouse IgG1 against residues 2101–2189 of human β2-spectrin, 1:100), anti-β4-spectrin Cter (from Matthew Rasband, Baylor College of Medicine Austin TX, rabbit against residues 2237-2236, 1:100), an anti-α tubulin (Sigma-Aldrich #T5168, mouse IgG1 clone B-5-1-2, 1:1500) was used as control. The shRNAs effect on the periodicity of the axonal actin-spectrin scaffold was evaluated by fluorescence intensity quantification and autocorrelation of intensity profiles along axonal segments (https://github.com/cleterrier/Process_Profiles).

Endogenous clathrin tagging (knock-in)

We used a rat optimized version of the HiUGE method (Gao et al., 2019; Ogawa et al., 2023), with an adapted Donor Recognition Sequence (DRS) GCGATCGTAATCACCCGAGT-GGG. We used the homologous sequence of the protospacer used by Gao et al. to cut the clathrin light chain A subunit gene (Clta).as close as possible to the stop codon (5 nucleotides before):

Mouse, Gao et al : …-GGCTCTTCAGTGCACCA-**GGG**
Rat, this study: *GGT*-GGCTCTTCAaTGCACCA-**GGG**

In italics: Additional nucleotides in 5' to have a 20-nucleotide length protospacer sequence. In bold the PAM sequence on the Clta gene. In lowercase the nucleotide that differs from the mouse sequence.

AAVs were produced by the standard triple transfection in HEK293T in the AAV9/PHP.S serotype. Small scale AAV preparations were obtained by mild lysis of HEK cells 3 days post transfection in a citrate buffer (38.1 mM citric acid, 74.8 mM $NaHCO_3$, 75 mM NaCl, 100 mM MgCl, pH 5) and neutralized subsequently with Tris-HCl pH 9.5. AAV particles were titrated by qPCR with an improved version of the Addgene SYBR green method. In brief, we used a linearized AAV plasmid as standard instead of a supercoiled plasmid and we incorporated a proteinase K step after the DNAse treatment. We usually obtained titers between 10^{11} and 10^{12} part/mL. Hippocampal neurons were triply infected after plating at 0 div and at a density of 12,000 cells/cm^2 with 10^9 AAV particles for each 3 different AAVs: Mecp2-Cas9 AAV, clathrin-Cter sgRNA AAV and DRSR2-EGFP-ORF1 Cter HiUGE payload.

Pharmacological treatments

Treatments were applied on neurons and fibroblasts in their original culture medium at 37°C, 5% CO_2. Dimethyl sulfoxide (DMSO) 0.1% (from pure DMSO, Sigma-Aldrich #D2650) was used as a control vehicle, Pitstop 2 30 µM (from 30 mM stock in DMSO, Abcam #120687) was applied for 15 min (45 min in neuron feeding experiments), swinholide A 100 nM (from 100 µM stock in DMSO, Sigma-Aldrich #S9810) was applied for 3h, diamide 500 µM (from 1M stock in ultrapure water, Sigma-Aldrich #D3648) was applied for 15 min (45 min in neuron feeding experiments). All stock solutions were stored at −20°C. For NMDA stimulation, 14 div neurons were first incubated 15 min in 500 µL of uncomplemented neurobasal medium (NB) in a 12 wells plate at 37°C 5% CO_2, then NMDA (from 50 mM stock in ultrapure water, Sigma-Aldrich #M3262), diluted to 100 µM in preheated NB, was added to the wells for a final concentration of 50 µM NMDA. For control experiments, NB without NMDA was used. After 4 min, neurons were gently washed 3 times with 500 µL NB, then returned to their original complemented medium and incubated for 30 min. Neurons were then either fixed and stained as described in the immunocytochemistry section or incubated with an endocytosis probe before as described in the uptake assays section.

Unroofing and fixation of fibroblasts and neuronal cultures

Unroofing was performed by sonication as previously described (Heuser, 2000). Coverslips were quickly rinsed three times in Ringer+Ca (155 mM NaCl, 3 mM KCl, 3 mM NaH_2PO_4, 4.5 mM HEPES, 10 mM glucose, 2 mM $CaCl_2$, 1 mM $MgCl_2$, pH 7.2), then immersed 10s in Ringer-Ca (155 mM NaCl, 3 mM KCl, 3 mM NaH_2PO4, 4.5 mM HEPES, 10 mM glucose, 3 mM EGTA, 5 mM $MgCl_2$, pH 7.2) containing 0.5 mg/mL poly-L-lysine, then quickly rinsed in Ringer-Ca then unroofed by scanning the coverslip with rapid (2-5s) sonicator pulses at the lowest deliverable power in KHMgE buffer (70 mM KCl, 30 mM HEPES, 5 mM $MgCl_2$, 3 mM EGTA, pH 7.2). Unroofed cells were immediately fixed in 4% PFA in KHMgE for 10 min for epifluorescence microscopy, SIM and SMLM, for 45 min for PREM of immunogold-labeled samples, and for 15 min for PREM, correlative SIM-PREM and SMLM-PREM. After fixation and rinses, all neuronal samples for PREM were placed in individual sealed transport wells containing 5 mL of KHMgE with 2% glutaraldehyde and shipped immediately the following day. Samples for correlative light microscopy-PREM were immunolabeled and imaged immediately and kept in KHMgE with 2% sodium azide (Sigma-Aldrich #08591) at 4°C for a maximum of 1.5 days before being shipped in the same manner.

Fluorescence immunocytochemistry

Fluorescence immunocytochemistry of neuronal cultures for widefield microscopy, SIM and SMLM was performed as in published protocols (Jimenez et al., 2020). Cells were fixed using 4% PFA in PEM buffer (80 mM PIPES pH 6.8, 5 mM EGTA, 2 mM $MgCl_2$) for 10 min at room temperature (RT). After rinses in 0.1 M phosphate buffer (PB), neurons were blocked for 2-3h at RT in immunocytochemistry buffer (ICC: 0.22% gelatin, 0.1% Triton X-100 in PB), and incubated with primary antibodies diluted in ICC overnight at 4°C. After rinses in ICC, neurons were incubated with secondary antibodies diluted in ICC for 1h at RT and rinsed. Actin staining was then performed by incubating in fluorescent phalloidin at 0.5 µM for either 1h at RT or overnight at 4°C. Stained coverslips were kept in PB + 0.02% sodium azide at 4°C until imaging by SMLM. For widefield microscopy and SIM, coverslips were mounted in ProLong Glass (Thermo Fisher Scientific #P36980).

Immunofluorescence of unroofed neurons for correlative SIM-PREM was performed using a fast protocol, beginning with 3 rinses in KHMgE buffer, then 30 min blocking in detergent-free buffer (DFB: KHMgE, 1% BSA), 30 min primary antibodies incubation at RT, 3 DFB rinses with 5 min incubation between them, 30 min secondary antibodies incubation at RT, 3 DFB rinses as before, then a KHMgE rinse, keeping the unused coverslips in KHMgE at 4°C until acquired in SIM.

Immunogold labeling of unroofed samples was performed in the same detergent-free solution: samples were blocked for 30 min, incubated for 90 min with the primary antibodies diluted to 1:20, rinsed, incubated two times 20 min with the gold-coupled secondary antibodies, then rinsed.

Antibodies labeling, probes and other reagents

Rabbit polyclonal anti β4-spectrin antibody (against residues 2237–2256 of human β4-spectrin, 1:500 dilution for immunofluorescence IF, 1:20 for immunogold IG) was a gift from Matthew Rasband (Baylor College of Medicine, Austin, TX). Mouse monoclonal anti β2-spectrin (against residues 2101–2189 of human β2-spectrin, 1:100 for IF) was from BD Biosciences (#612563). Mouse monoclonal anti α2s-spectrin (clone D8B7, 1 :100 for IF) was from Biolegend (#803201). Rabbit polyclonal anti 480-kDa ankyrin G (residues 2735–2935 of rat 480-kDa ankyrin G, 1:300 for IF, 1:100 for IG) was a gift from Vann Bennett (Duke University, Durham, NC). Rabbit anti phospho-myosin light chain 2 Thr18/Ser19 (pMLC, 1:50 for IF, 1:20 for IG) was from Cell Signaling Technologies (#3674). Chicken anti-map2 (against residues 2-314 of human map2, 1:1000 for IF) was from Synaptic Systems (#188006). Chicken anti pan-neurofascin (against residues 25-1031 of rat neurofascin, 1:400 for IF) was from R&D System (#AF3235). Rabbit polyclonal anti-clathrin heavy chain (against residues 1650 to C-terminus of human clathrin heavy chain, IF 1:150) was from Abcam (#ab21679). Mouse monoclonal anti-clathrin light chain (clone X22, 1:100 for IF) was from Thermo Fisher Scientific (#MA1-065); we also used clone CON.1 (1:1000 for IF) from Sigma-Aldrich (#c1985). Mouse monoclonal anti-AP2 (1:100 for IF) was from Abcam (#ab2730).

Secondary antibodies and reagents

Donkey and goat anti-rabbit, anti-mouse, and anti-chicken secondary antibodies conjugated to Alexa Fluor 488, 555, and 647 were from Life Technologies or Jackson ImmunoResearch (1:200-1:400 for IF). Goat anti-rabbit and anti-mouse secondary antibodies conjugated to DNA-PAINT handles were obtained from Massive Photonics (MASSIVE-sdAB 2-PLEX). Goat anti-rabbit and anti-mouse secondary antibodies conjugated to gold nanobeads were from Aurion (15 nm gold, #815011 and #815022, respectively, 1:20 for IG) or Jackson ImmunoResearch (18 nm gold, #111-215-144 and #115-215-146, respectively, 1:15 for IG). For light microscopy, we used Alexa Fluor 488 and Alexa Fluor 647 Plus-conjugated phalloidin from Thermo Fisher Scientific (#A12379 and #A2287, respectively) and Atto488-conjugated phalloidin (#AD48881) from Atto-Tec. For immunogold labeling of actin, unroofed neurons were fixed with 2% PFA in KHMgE, then quenched for 10 min in KHMgE, 100 mM glycine, and 100 mM NH4Cl. After blocking in KHMgE, 1% BSA, they were incubated with phalloidin-Alexa Fluor 488 (0.5 µM) for 45 min, then immunolabeled using an anti-Alexa Fluor 488 primary antibody and a gold coupled goat anti-rabbit secondary antibody as described above for immunogold labeling. Paraformaldehyde (PFA, #15714, stock 32% in water) was from Electron Microscopy Sciences, and glutaraldehyde (#G5882, stock 25% in water) was from Sigma-Aldrich.

Transferrin and dextran uptake assays

For pulse-chase uptake assay of transferrin internalization in rat fibroblasts, cells were cultured on 12-mm glass coverslips in DMEM and 10% FCS to 80% confluency. Transferrin from human serum conjugated to Alexa Fluor 488 (Thermo Fisher Scientific #T3342) was used at 20 µg/mL for 10 min at 37°C. Cells were acid-stripped (0.2 M Na_2HPO_4, 0.1 M citric acid), rinsed three times in PBS, and then fixed in 4 % paraformaldehyde (PFA) for 20 min. Glass slides were mounted with coverslips using Vectashield containing DAPI (Vector Laboratories #H-1200). Regions of interest were defined based on the cell shape. Individual cells were manually outlined and corrected total cell fluorescence = integrated density - (area of selected cell × mean fluorescence of background readings) was calculated using Fiji imaging software.

For transferrin uptake experiments in neurons, cells that were incubated for 1h in uncomplemented Neurobasal medium, then Alexa-Fluor-647-conjugated transferrin was used (Thermo Fisher Scientific, #T23366) diluted at 1:50 in the same medium and incubated for 1h at 37°C and 5% CO_2. After incubation, the cells were quickly rinsed 3 times with pre-heated medium and fixed with PFA 4% in PEM buffer. For dextran uptake experiments, the same procedure was used, with Alexa Fluor 555-conjugated dextran 10 kDa (Thermo Fisher Scientific #D34679) diluted at 50 µg/mL and incubated for 30 min at 37°C and 5% CO_2 before rinses and fixation.

Live-cell imaging probes and AIS staining

All live-cell experiments were performed in live-cell imaging medium (Hibernate E low fluorescence, Brainbits/Thermo Fisher Scientific #NC0285514) supplemented with 3% glucose, 2% B27, and 0.5mM L-glutamine). Live-cell AIS staining was performed using a mouse anti-neurofascin antibody targeting an extracellular epitope (NeuroMab clone A12/18, #75-172) conjugated with CF647 (Mix-N-Stain CF647 antibody labeling kit, Sigma-Aldrich #MX647S50) following the manufacturer protocol. The conjugate was diluted to 1:50 and incubated for 10 min at 37°C and 5% CO_2 before proceeding to SIM.

Structured illumination microscopy

SIM of neurons was performed on an N-SIM-S microscope (Nikon Instruments). The N-SIM system uses an inverted Nikon Eclipse Ti2-E microscope with a perfect focus system 4, an integrated Nikon laser launch with 405, 488, 561, and 640 nm solid-state excitation lasers, a 100X NA 1.49 oil objective (SR HP Apo TIRF), a Mad City Labs Nanodrive piezo stage and a Hamamatsu Fusion BT CMOS camera. On fixed cells, after locating a neuron of interest using low-intensity illumination, an image was acquired in 2D-SIM/TIRF-SIM (9 images per image) or 3D-SIM (15 images per z plane) mode. Reconstruction was performed using the N-SIM module in the NIS-Elements software (AR 5.30.05), resulting in a ~120 nm lateral (all modalities) and ~250 nm axial resolution (for 3D-SIM).

For live-cell SIM, live-cell imaging medium was used, and the stage was kept at 37°C by a Tokay Hit STX heater. TIRF-SIM movies were captured at a frequency of 0.05 Hz for 15 to 20 min, alternating the 488- and 561-nm illumination to image ß2-spectrin-GFP and CLC-mCherry, respectively. Movies were processed using a deep-learning based denoising module (Enhance.ai in NIS-Elements software, Nikon) using a model trained from 20 pairs of fixed samples imaged at low (10%-20%) and high (100%) laser intensities. Neurons used for training were transfected with CLC-mCherry and EGFP-β2-spectrin, then fixed and mounted in live-cell imaging medium.

For super-resolved spinning disk microscopy of Rat2 fibroblasts, images were acquired using a Nikon Ti2 microscope, driven by Metamorph (Molecular Devices), equipped with a motorized stage and a Yokogawa CSU-W1 spinning disk head coupled with a Prime 95 sCMOS camera (Photometrics) equipped with a 100X oil-immersion objective lens. Super-resolution images were obtained using the LiveSR module (Gataca Systems). DAPI, Alexa Fluor 488, Alexa Fluor 568 and Alexa Fluor 647 were sequentially excited. Z-series from the top to the bottom of fibers were sequentially collected for each channel with a step of 0.1-0.3 µm between each plane.

Live-cell super-resolved spinning-disk imaging of endogenously-tagged clathrin-EGFP in neurons was performed on a Yokogawa CSU-W1 spinning disk microscope equipped with 405, 488, 561, and 640 nm solid-state excitation lasers, a SoRa pixel reassignment module, a Ti2-E stand (Nikon), a 60X NA 1.49 oil objective, and a Fusion BT sCMOS camera (Hamamatsu). Live-cell imaging medium was used, and the stage was kept at 37°C by a stage enclosure (Okolab). After capturing a single image of the neurofascin live-cell staining using 647-nm laser excitation, super-resolved images of clathrin-GFP were obtained using 488-nm laser excitation, with the SoRa module 4X magnification lens and a camera binning of 2x2 at a frequency of 0.2 Hz. Movies were processed using a pre-trained deep-learning based denoising module embedded in the NIS-Elements software (Denoise.ai, Nikon).

SMLM: STORM and PAINT

Both STORM and DNA-PAINT acquisitions were performed on an N-STORM microscope (Nikon Instruments). The N-STORM system uses an Agilent MLC-400B laser launch with 405 nm (50 mW maximum fiber output power), 488 nm (80 mW), 561 mW (80 mW), and 647 nm (125 mW) solid-state lasers, a 100X NA 1.49 objective, and an Ixon DU-897 camera (Andor). After locating an axon using low-intensity epifluorescence illumination, followed by either a STORM or DNA-PAINT acquisition using laser illumination in HiLo (grazing angle) configuration. An astigmatic lens was added to the light path to achieve 3D imaging. For STORM, stained coverslips were mounted in a silicone chamber filled with STORM buffer (Smart Buffer Kit; Abbelight), and 30,000-60,000 images (256 × 256 pixels, 15 ms exposure time) were acquired at 100% 647-nm laser power. Reactivation of fluorophores was performed during acquisition by increasing illumination with the 405-nm laser. For DNA-PAINT, stained coverslips were mounted in a Ludin chamber filled with imaging buffer (Massive Photonics). Imaging strands conjugated to Atto565 and Atto655 (Massive Photonics) were added from a starting concentration of 0.1 nM each, then adjusted to optimize blinking density. 30,000-45,000 images (256x256, 40 ms exposure time) were acquired at 25-50% laser power for 561 nm, 60-100% laser power for 647 nm by alternating frames with 561-nm and 647-nm laser excitation.

For STORM and DNA-PAINT images, acquired stacks were processed using DECODE (Speiser et al., 2021). Briefly, PSFs were modeled using spline fitting in SMAP (Li et al., 2018) and used to simulate sequences of blinking events using characteristics (photon number range and lifetime distribution) inferred from real acquisition data from the N-STORM microscope. A PyTorch model was trained to infer the 3D coordinates and uncertainty of the simulated blinking events and then applied to the experimental acquired sequence (Speiser et al., 2021). The resulting localizations (fitted blinking events) were filtered based on uncertainty, and drift during acquisition was corrected in 3D using a redundant cross-correlation algorithm (Wang et al., 2014) implemented as an independent module of SMAP (Ries, 2020). After translation of the coordinate files, image reconstructions were performed using the ThunderSTORM ImageJ plugin (Ovesný et al., 2014) in Fiji software. Custom scripts and macros were used to translate coordinate files, as well as automate image reconstruction for whole images at 16 nm/pixel for visualization and at 8 nm/pixel for cluster analysis (https://github.com/cleterrier/ChriSTORM).

PREM

Adherent plasma membranes from rat hippocampal neurons and rat fibroblasts grown on glass coverslips were disrupted by sonication (Heuser, 2000). Unroofed cells were fixed and processed as described previously (Vassilopoulos et al., 2019). Cells were sequentially treated with 0.5% OsO_4, 1% tannic acid, and 1% uranyl acetate prior to graded ethanol dehydration and hexamethyldisilane substitution (Sigma-Aldrich). Dried samples were rotary-shadowed with 2 nm of platinum and 6 nm of carbon using a high vacuum sputter coater (Leica Microsystems). The resultant platinum-replica was floated off the glass with hydrofluoric acid (5%), washed several times with distilled water, and picked up on 200 mesh formvar/carbon-coated EM grids. Images were captured using a digital camera (Xarosa) and the grids were mounted on an eccentric side-entry goniometer stage of a transmission electron microscope running at 120 kV (Jeol). Images were adjusted for brightness and contrast in Adobe Photoshop (Adobe) and presented in inverted contrast. Tomograms were created by acquiring images with 5° increments at tilt angles up to 20° relative to the sample plane. In Photoshop, layers were used to stack images on top of one another to align them.

Correlative SIM-PREM/SMLM-PREM microscopy

Unroofed and stained samples were imaged by SIM and an objective-style diamond scriber (Leica) was used to engrave a 1 mm circle around the imaged area. Low-magnification, 10x and 40x phase and fluorescence images were taken as a reference for relocation. After the acquisition session, samples were stored, shipped and platinum replicated as described in the PREM section. After replica generation and prior to its release, the coated surface of each coverslip was scratched with a needle to make an EM grid sized region of interest containing the engraved circle. Grids were imaged with low-magnification EM to relocate the region that was previously imaged by SIM or SMLM, and high magnification EM views were taken from the corresponding axonal region. The SIM or SMLM reconstructions were mapped and aligned by affine transformation to the corresponding high-magnification EM view using the eC-CLEM plugin in ICY software (Paul-Gilloteaux et al., 2017).

Data quantification and analysis

Clathrin pits and dextran clusters segmentation (SIM data)

Clathrin and dextran clusters were segmented using a custom script in Fiji (Schindelin et al., 2012). After manually delineating ROIs corresponding to the proximal axon on a stack of SIM images, fluorescence within each axon ROI was thresholded (threshold levels were determined by the Moments method for clathrin and dextran intact, Otsu method for clathrin and dextran unroofed, eventually fine-tuned manually). Thresholded areas were then segmented using the StarDist plugin in Fiji

(Schmidt et al., 2018), with a baseline threshold of 0.5, eventually fine-tuned manually (other StarDist parameters were: StarDist2D Versatile model, normalize bottom 0.1 top 99.8, overlap threshold 0.33). Only the clusters inside the axon ROI or overlapping it by more than half their area were kept, and segmented aggregates of several clusters were removed. The remaining clusters were quantified for area within Fiji and the quantifications exported to a CSV file for each image. The particles CSV files were analyzed in a dedicated JupyterLab notebook, pooling the experiments per condition, and performing particle area, count, density, and pixel-occupation averages.

Average image of clathrin pits and dextran clusters

The ROI sets for clusters obtained after the segmentation of SIM images were used to generate average intensity plots of clathrin pits and dextran clusters. 15x15 pixels centered areas were extracted from each ROI and averaged over all ROIs for each channel. The radial average fluorescence profile for each channel was obtained from the averaged image using the Radial Profile Extended ImageJ plugin.

Live-cell temporal autocorrelation and kymographs

Live-cell imaging movies were corrected for drift using the Image Stabilization plugin and for bleaching by histogram matching, both in Fiji. Line ROIs were traced on the axon, dendrites, and cell body using NeuronJ (Meijering et al., 2004) on the maximum projection of the movie frames. These line ROIs (360-390 nm line thickness) were used to generate kymographs using the KymoResliceWide plugin (https://github.com/ekatrukha/KymoResliceWide). In addition, the intensity profile along thick line ROIs was used to calculate a temporal correlation profile with the ImageCorrelationJ plugin, comparing the image similarity between all pairs of frames distant by 1, 2, …, (n-1) frames within an n-frames movie (https://www.gcsca.net/IJ/ImageCorrelationJ.html). Temporal correlation profiles were averaged for ROIs of the same type (axon, dendrite, cell body), resulting in an average temporal correlation profile for this compartment.

Particle quantification by PREM

Clathrin structures were manually delineated on unroofed PM pictures using ImageJ. Each object was classified as a CCP by the observer and the object area was measured. On each image, the total membrane area was also measured to calculate the object density (object count normalized by membrane area).

Statistics

Individual measurement points (n) from independent experiments (N) were pooled. Intensity profiles, graphs, and statistical analyses were generated using Prism. On bar graphs, dots (if present) are averages of each independent experiment, bars or horizontal lines represent the mean, and vertical lines are the SEM unless otherwise specified. Significances were tested using one-way, non-parametric ANOVA with Kruskal-Wallis post-hoc significance testing between selected conditions. In Figures, the results of the post-hoc significance are indicated as follows: ns or ns, non-significant; *, $p < 0.05$; **, $p < 0.01$; ***, $p < 0.001$.

References

Azarnia Tehran, D., and T. Maritzen. 2022. Endocytic proteins: An expanding repertoire of presynaptic functions. Current Opinion in Neurobiology. 73:102519. doi:10.1016/j.conb.2022.01.004.

Benned-Jensen, T., R.K. Christensen, F. Denti, J.-F. Perrier, H.B. Rasmussen, and S.-P. Olesen. 2016. Live Imaging of Kv7.2/7.3 Cell Surface Dynamics at the Axon Initial Segment: High Steady-State Stability and Calpain-Dependent Excitotoxic Downregulation Revealed. J Neurosci. 36:2261–2266. doi:10.1523/JNEUROSCI.2631-15.2016.

Berger, S.L., A. Leo-Macias, S. Yuen, L. Khatri, S. Pfennig, Y. Zhang, E. Agullo-Pascual, G. Caillol, M.-S. Zhu, E. Rothenberg, C.V. Melendez-Vasquez, M. Delmar, C. Leterrier, and J.L. Salzer. 2018. Localized Myosin II Activity Regulates Assembly and Plasticity of the Axon Initial Segment. Neuron. 97:555-570.e6. doi:10.1016/j.neuron.2017.12.039.

Bingham, D., C.E. Jakobs, F. Wernert, F. Boroni-Rueda, N. Jullien, E.-M. Schentarra, K. Friedl, J. Da Costa Moura, D.M. van Bommel, G. Caillol, Y. Ogawa, M.-J. Papandréou, and C. Leterrier. 2023. Presynapses contain distinct actin nanostructures. Journal of Cell Biology. 222:e202208110. doi:10.1083/jcb.202208110.

Brachet, A., C. Leterrier, M. Irondelle, M.-P. Fache, V. Racine, J.-B. Sibarita, D. Choquet, and B. Dargent. 2010. Ankyrin G restricts ion channel diffusion at the axonal initial segment before the establishment of the diffusion barrier. J Cell Biol. 191:383–395. doi:10.1083/jcb.201003042.

Bréchet, A., M.-P. Fache, A. Brachet, G. Ferracci, A. Baude, M. Irondelle, S. Pereira, C. Leterrier, and B. Dargent. 2008. Protein kinase CK2 contributes to the organization of sodium channels in axonal membranes by regulating their interactions with ankyrin G. J Cell Biol. 183:1101–1114. doi:10.1083/jcb.200805169.

Bubb, M.R., I. Spector, A.D. Bershadsky, and E.D. Korn. 1995. Swinholide A is a microfilament disrupting marine toxin that stabilizes actin dimers and severs actin filaments. J Biol Chem. 270:3463–3466. doi:10.1074/jbc.270.8.3463.

Camblor-Perujo, S., and N.L. Kononenko. 2022. Brain-specific functions of the endocytic machinery. The FEBS Journal. 289:2219–2246. doi:10.1111/febs.15897.

Cameron, P.L., T.C. Südhof, R. Jahn, and P. De Camilli. 1991. Colocalization of synaptophysin with transferrin receptors: implications for synaptic vesicle biogenesis. Journal of Cell Biology. 115:151–164. doi:10.1083/jcb.115.1.151.

Catsburg, L.A., M. Westra, A.M. van Schaik, and H.D. MacGillavry. 2022. Dynamics and nanoscale organization of the postsynaptic endocytic zone at excitatory synapses. eLife. 11:e74387. doi:10.7554/eLife.74387.

Costa, A.R., S.C. Sousa, R. Pinto-Costa, J.C. Mateus, C.D. Lopes, A.C. Costa, D. Rosa, D. Machado, L. Pajuelo, X. Wang, F. Zhou, A.J. Pereira, P. Sampaio, B.Y. Rubinstein, I. Mendes Pinto, M. Lampe, P. Aguiar, and M.M. Sousa. 2020. The membrane periodic skeleton is an actomyosin network that regulates axonal diameter and conduction. eLife. 9:e55471. doi:10.7554/eLife.55471.

Cousin, M.A., B.A. Creighton, K.A. Breau, R.C. Spillmann, E. Torti, S. Dontu, S. Tripathi, D. Ajit, R.J. Edwards, S. Afriyie, J.C. Bay, K.M. Harper, A.A. Beltran, L.J. Munoz, L. Falcon Rodriguez, M.C. Stankewich, R.E. Person, Y. Si, E.A. Normand, A. Blevins, A.S. May, L. Bier, V. Aggarwal, G.M.S. Mancini, M.A. Van Slegtenhorst, K. Cremer, J. Becker, H. Engels, S. Aretz, J.J. MacKenzie, E. Brilstra, K.L.I. Van Gassen, R.H. Van Jaarsveld, R. Oegema, G.M. Parsons, P. Mark, I. Helbig, S.E. McKeown, R. Stratton, B. Cogne, B. Isidor, P. Cacheiro, D. Smedley, H.V. Firth, T. Bierhals, K. Kloth, D. Weiss, C. Fairley, J.T. Shieh, A. Kritzer, P. Jayakar, E. Kurtz-Nelson, R.A. Bernier, T. Wang, E.E. Eichler, I.M.B.H. Van De Laar, A. McConkie-Rosell, M.T. McDonald, J. Kemppainen, B.C. Lanpher, L.E. Schultz-Rogers, L.B. Gunderson, P.N. Pichurin, G. Yoon, M. Zech, R. Jech, J. Winkelmann, Undiagnosed Diseases Network, Genomics England Research Consortium, A.S. Beltran, M.T. Zimmermann, B. Temple, S.S. Moy, E.W. Klee, Q.K.-G. Tan, and D.N. Lorenzo. 2021. Pathogenic SPTBN1 variants cause an autosomal dominant neurodevelopmental syndrome. Nat Genet. 53:1006–1021. doi:10.1038/s41588-021-00886-z.

Eichel, K., T. Uenaka, V. Belapurkar, R. Lu, S. Cheng, J.S. Pak, C.A. Taylor, T.C. Südhof, R. Malenka, M. Wernig, E. Özkan, D. Perrais, and K. Shen. 2022. Endocytosis in the axon initial segment maintains neuronal polarity. Nature. 609:128–135. doi:10.1038/s41586-022-05074-5.

Engqvist-Goldstein, Å.E.Y., C.X. Zhang, S. Carreno, C. Barroso, J.E. Heuser, and D.G. Drubin. 2004. RNAi-mediated Hip1R Silencing Results in Stable Association between the Endocytic Machinery and the Actin Assembly Machinery. MBoC. 15:1666–1679. doi:10.1091/mbc.e03-09-0639.

Farías, G.G., L. Cuitino, X. Guo, X. Ren, M. Jarnik, R. Mattera, and J.S. Bonifacino. 2012. Signal-mediated, AP-1/clathrin-dependent sorting of transmembrane receptors to the somatodendritic domain of hippocampal neurons. Neuron. 75:810–823. doi:10.1016/j.neuron.2012.07.007.

Fréal, A., N. Jamann, J. Ten Bos, J. Jansen, N. Petersen, T. Ligthart, C.C. Hoogenraad, and M.H.P. Kole. 2023. Sodium channel endocytosis drives axon initial segment plasticity. Sci Adv. 9:eadf3885. doi:10.1126/sciadv.adf3885.

Fréal, A., D. Rai, R.P. Tas, X. Pan, E.A. Katrukha, D. van de Willige, R. Stucchi, A. Aher, C. Yang, A.F.M. Altelaar, K. Vocking, J.A. Post, M. Harterink, L.C. Kapitein, A. Akhmanova, and C.C. Hoogenraad. 2019. Feedback-Driven Assembly of the Axon Initial Segment. Neuron. 104:305-321.e8. doi:10.1016/j.neuron.2019.07.029.

Galiano, M.R., S. Jha, T.S.-Y. Ho, C. Zhang, Y. Ogawa, K.-J. Chang, M.C. Stankewich, P.J. Mohler, and M.N. Rasband. 2012. A distal axonal cytoskeleton forms an intra-axonal boundary that controls axon initial segment assembly. Cell. 149:1125–1139. doi:10.1016/j.cell.2012.03.039.

Ganguly, A., R. Sharma, N.P. Boyer, F. Wernert, S. Phan, D. Boassa, L. Parra, U. Das, G. Caillol, X. Han, J.R. Yates, M.H. Ellisman, C. Leterrier, and S. Roy. 2021. Clathrin packets move in slow axonal transport and deliver functional payloads to synapses. Neuron. 109:2884-2901.e7. doi:10.1016/j.neuron.2021.08.016.

Gao, Y., E. Hisey, T.W.A. Bradshaw, E. Erata, W.E. Brown, J.L. Courtland, A. Uezu, Y. Xiang, Y. Diao, and S.H. Soderling. 2019. Plug-and-Play Protein Modification Using Homology-Independent Universal Genome Engineering. Neuron. 103:583-597.e8. doi:10.1016/j.neuron.2019.05.047.

Ghisleni, A., M. Bonilla-Quintana, M. Crestani, A. Fukuzawa, P. Rangamani, and N. Gauthier. 2023. Mechanically induced topological transition of spectrin regulates its distribution in the mammalian cortex. bioRxiv. 2023.01.02.522381. doi:10.1101/2023.01.02.522381.

Ghisleni, A., C. Galli, P. Monzo, F. Ascione, M.-A. Fardin, G. Scita, Q. Li, P. Maiuri, and N.C. Gauthier. 2020. Complementary mesoscale dynamics of spectrin and acto-myosin shape membrane territories during mechanoresponse. Nat Commun. 11:5108. doi:10.1038/s41467-020-18825-7.

Hedstrom, K.L., X. Xu, Y. Ogawa, R. Frischknecht, C.I. Seidenbecher, P. Shrager, and M.N. Rasband. 2007. Neurofascin assembles a specialized extracellular matrix at the axon initial segment. J Cell Biol. 178:875–886. doi:10.1083/jcb.200705119.

Heuser, J. 1980. Three-dimensional visualization of coated vesicle formation in fibroblasts. J Cell Biol. 84:560–583. doi:10.1083/jcb.84.3.560.

Heuser, J. 2000. The production of “cell cortices” for light and electron microscopy. Traffic. 1:545–552. doi:10.1034/j.1600-0854.2000.010704.x.

Jenkins, P.M., M. He, and V. Bennett. 2015. Dynamic spectrin/ankyrin-G microdomains promote lateral membrane assembly by opposing endocytosis. Sci Adv. 1:e1500301. doi:10.1126/sciadv.1500301.

Jeong, J.-Y., H.-S. Yim, J.-Y. Ryu, H.S. Lee, J.-H. Lee, D.-S. Seen, and S.G. Kang. 2012. One-step sequence- and ligation-independent cloning as a rapid and versatile cloning method for functional genomics studies. Appl Environ Microbiol. 78:5440–5443. doi:10.1128/AEM.00844-12.

Jimenez, A., K. Friedl, and C. Leterrier. 2020. About samples, giving examples: Optimized Single Molecule Localization Microscopy. Methods. 174:100–114. doi:10.1016/j.ymeth.2019.05.008.

Kaech, S., and G. Banker. 2006. Culturing hippocampal neurons. Nat Protoc. 1:2406–2415. doi:10.1038/nprot.2006.356.

Kner, P., B.B. Chhun, E.R. Griffis, L. Winoto, and M.G.L. Gustafsson. 2009. Super-resolution video microscopy of live cells by structured illumination. Nat Methods. 6:339–342. doi:10.1038/nmeth.1324.

Leterrier, C. 2018. The Axon Initial Segment: An Updated Viewpoint. J Neurosci. 38:2135–2145. doi:10.1523/JNEUROSCI.1922-17.2018.

Leterrier, C. 2021. Putting the axonal periodic scaffold in order. Curr Opin Neurobiol. 69:33–40. doi:10.1016/j.conb.2020.12.015.

Leterrier, C., and P.A. Pullarkat. 2022. Mechanical role of the submembrane spectrin scaffold in red blood cells and neurons. J Cell Sci. 135:jcs259356. doi:10.1242/jcs.259356.

Li, L., T. Wan, M. Wan, B. Liu, R. Cheng, and R. Zhang. 2015. The effect of the size of fluorescent dextran on its endocytic pathway. Cell Biol Int. 39:531–539. doi:10.1002/cbin.10424.

Loebrich, S. 2014. The role of F-actin in modulating Clathrin-mediated endocytosis: Lessons from neurons in health and neuropsychiatric disorder. Communicative & Integrative Biology. 7:e28740. doi:10.4161/cib.28740.

Lorenzo, D.N., R.J. Edwards, and A.L. Slavutsky. 2023. Spectrins: molecular organizers and targets of neurological disorders. Nat Rev Neurosci. 24:195–212. doi:10.1038/s41583-022-00674-6.

McMahon, H.T., and E. Boucrot. 2011. Molecular mechanism and physiological functions of clathrin-mediated endocytosis. Nat Rev Mol Cell Biol. 12:517–533. doi:10.1038/nrm3151.

Meijering, E., M. Jacob, J.-C.F. Sarria, P. Steiner, H. Hirling, and M. Unser. 2004. Design and validation of a tool for neurite tracing and analysis in fluorescence microscopy images. Cytometry A. 58:167–176. doi:10.1002/cyto.a.20022.

Moulay, G., J. Lainé, M. Lemaître, M. Nakamori, I. Nishino, G. Caillol, K. Mamchaoui, L. Julien, F. Dingli, D. Loew, M. Bitoun, C. Leterrier, D. Furling, and S. Vassilopoulos. 2020. Alternative splicing of clathrin heavy chain contributes to the switch from coated pits to plaques. J Cell Biol. 219:e201912061. doi:10.1083/jcb.201912061.

Mukherjee, S., R.N. Ghosh, and F.R. Maxfield. 1997. Endocytosis. Physiological Reviews. 77:759–803. doi:10.1152/physrev.1997.77.3.759.

Ogawa, Y., B.C. Lim, S. George, J.A. Oses-Prieto, J.M. Rasband, Y. Eshed-Eisenbach, H. Hamdan, S. Nair, F. Boato, E. Peles, A.L. Burlingame, L. Van Aelst, and M.N. Rasband. 2023. Antibody-directed extracellular proximity biotinylation reveals that Contactin-1 regulates axo-axonic innervation of axon initial segments. Nat Commun. 14:6797. doi:10.1038/s41467-023-42273-8.

Ovesný, M., P. Křížek, J. Borkovec, Z. Švindrych, and G.M. Hagen. 2014. ThunderSTORM: a comprehensive ImageJ plug-in for PALM and STORM data analysis and super-resolution imaging. Bioinformatics. 30:2389–2390. doi:10.1093/bioinformatics/btu202.

Parton, R.G., K. Simons, and C.G. Dotti. 1992. Axonal and dendritic endocytic pathways in cultured neurons. J Cell Biol. 119:123–137. doi:10.1083/jcb.119.1.123.

Paul-Gilloteaux, P., X. Heiligenstein, M. Belle, M.-C. Domart, B. Larijani, L. Collinson, G. Raposo, and J. Salamero. 2017. eC-CLEM: flexible multidimensional registration software for correlative microscopies. Nat Methods. 14:102–103. doi:10.1038/nmeth.4170.

Pearse, B.M., and M.S. Robinson. 1990. Clathrin, adaptors, and sorting. Annu Rev Cell Biol. 6:151–171. doi:10.1146/annurev.cb.06.110190.001055.

Rasband, M.N. 2010. The axon initial segment and the maintenance of neuronal polarity. Nat Rev Neurosci. 11:552–562. doi:10.1038/nrn2852.

Ries, J. 2020. SMAP: a modular super-resolution microscopy analysis platform for SMLM data. Nat Methods. 17:870–872. doi:10.1038/s41592-020-0938-1.

Rizzoli, S.O. 2014. Synaptic vesicle recycling: steps and principles. The EMBO Journal. 33:788–822. doi:10.1002/embj.201386357.

Rosendale, M., D. Jullié, D. Choquet, and D. Perrais. 2017. Spatial and Temporal Regulation of Receptor Endocytosis in Neuronal Dendrites Revealed by Imaging of Single Vesicle Formation. Cell Rep. 18:1840–1847. doi:10.1016/j.celrep.2017.01.081.

Schindelin, J., I. Arganda-Carreras, E. Frise, V. Kaynig, M. Longair, T. Pietzsch, S. Preibisch, C. Rueden, S. Saalfeld, B. Schmid, J.-Y. Tinevez, D.J. White, V. Hartenstein, K. Eliceiri, P. Tomancak, and A. Cardona. 2012. Fiji: an open-source platform for biological-image analysis. Nat Methods. 9:676–682. doi:10.1038/nmeth.2019.

Schmidt, U., M. Weigert, C. Broaddus, and G. Myers. 2018. Cell Detection with Star-Convex Polygons. In Medical Image Computing and Computer Assisted Intervention – MICCAI 2018. A.F. Frangi, J.A. Schnabel, C. Davatzikos, C. Alberola-López, and G. Fichtinger, editors. Springer International Publishing, Cham. 265–273.

Speiser, A., L.-R. Müller, P. Hoess, U. Matti, C.J. Obara, W.R. Legant, A. Kreshuk, J.H. Macke, J. Ries, and S.C. Turaga. 2021. Deep learning enables fast and dense single-molecule localization with high accuracy. Nat Methods. 18:1082–1090. doi:10.1038/s41592-021-01236-x.

Torii, T., Y. Ogawa, C.-H. Liu, T.S.-Y. Ho, H. Hamdan, C.-C. Wang, J.A. Oses-Prieto, A.L. Burlingame, and M.N. Rasband. 2020. NuMA1 promotes axon initial segment assembly through inhibition of endocytosis. J Cell Biol. 219:e201907048. doi:10.1083/jcb.201907048.

Tuvia, S., T.D. Garver, and V. Bennett. 1997. The phosphorylation state of the FIGQY tyrosine of neurofascin determines ankyrin-binding activity and patterns of cell segregation. Proc Natl Acad Sci U S A. 94:12957–12962. doi:10.1073/pnas.94.24.12957.

Vassilopoulos, S., C. Gentil, J. Lainé, P.-O. Buclez, A. Franck, A. Ferry, G. Précigout, R. Roth, J.E. Heuser, F.M. Brodsky, L. Garcia, G. Bonne, T. Voit, F. Piétri-Rouxel, and M. Bitoun. 2014. Actin scaffolding by clathrin heavy chain is required for skeletal muscle sarcomere organization. J. Cell Biol. 205:377–393. doi:10.1083/jcb.201309096.

Vassilopoulos, S., S. Gibaud, A. Jimenez, G. Caillol, and C. Leterrier. 2019. Ultrastructure of the axonal periodic scaffold reveals a braid-like organization of actin rings. Nat Commun. 10:5803. doi:10.1038/s41467-019-13835-6.

von Kleist, L., W. Stahlschmidt, H. Bulut, K. Gromova, D. Puchkov, M.J. Robertson, K.A. MacGregor, N. Tomilin, A. Pechstein, N. Chau, M. Chircop, J. Sakoff, J.P. von Kries, W. Saenger, H.-G. Kräusslich, O. Shupliakov, P.J. Robinson, A. McCluskey, and V. Haucke. 2011. Role of the Clathrin Terminal Domain in Regulating Coated Pit Dynamics Revealed by Small Molecule Inhibition. Cell. 146:471–484. doi:10.1016/j.cell.2011.06.025.

Wang, Y., J. Schnitzbauer, Z. Hu, X. Li, Y. Cheng, Z.-L. Huang, and B. Huang. 2014. Localization events-based sample drift correction for localization microscopy with redundant cross-correlation algorithm. Opt Express. 22:15982–15991. doi:10.1364/OE.22.015982.

Wu, X.-T., L.-W. Sun, X. Yang, D. Ding, D. Han, and Y.-B. Fan. 2017. The potential role of spectrin network in the mechanotransduction of MLO-Y4 osteocytes. Sci Rep. 7:40940. doi:10.1038/srep40940.

Xu, K., G. Zhong, and X. Zhuang. 2013. Actin, spectrin, and associated proteins form a periodic cytoskeletal structure in axons. Science. 339:452–456. doi:10.1126/science.1232251.

Yamada, R., and H. Kuba. 2016. Structural and Functional Plasticity at the Axon Initial Segment. Front Cell Neurosci. 10:250. doi:10.3389/fncel.2016.00250.

Yap, C.C., and B. Winckler. 2022. Spatial regulation of endosomes in growing dendrites. Developmental Biology. 486:5–14. doi:10.1016/j.ydbio.2022.03.004.

Zhou, R., B. Han, C. Xia, and X. Zhuang. 2019. Membrane-associated periodic skeleton is a signaling platform for RTK transactivation in neurons. Science. 365:929–934. doi:10.1126/science.aaw5937.

Supporting Material

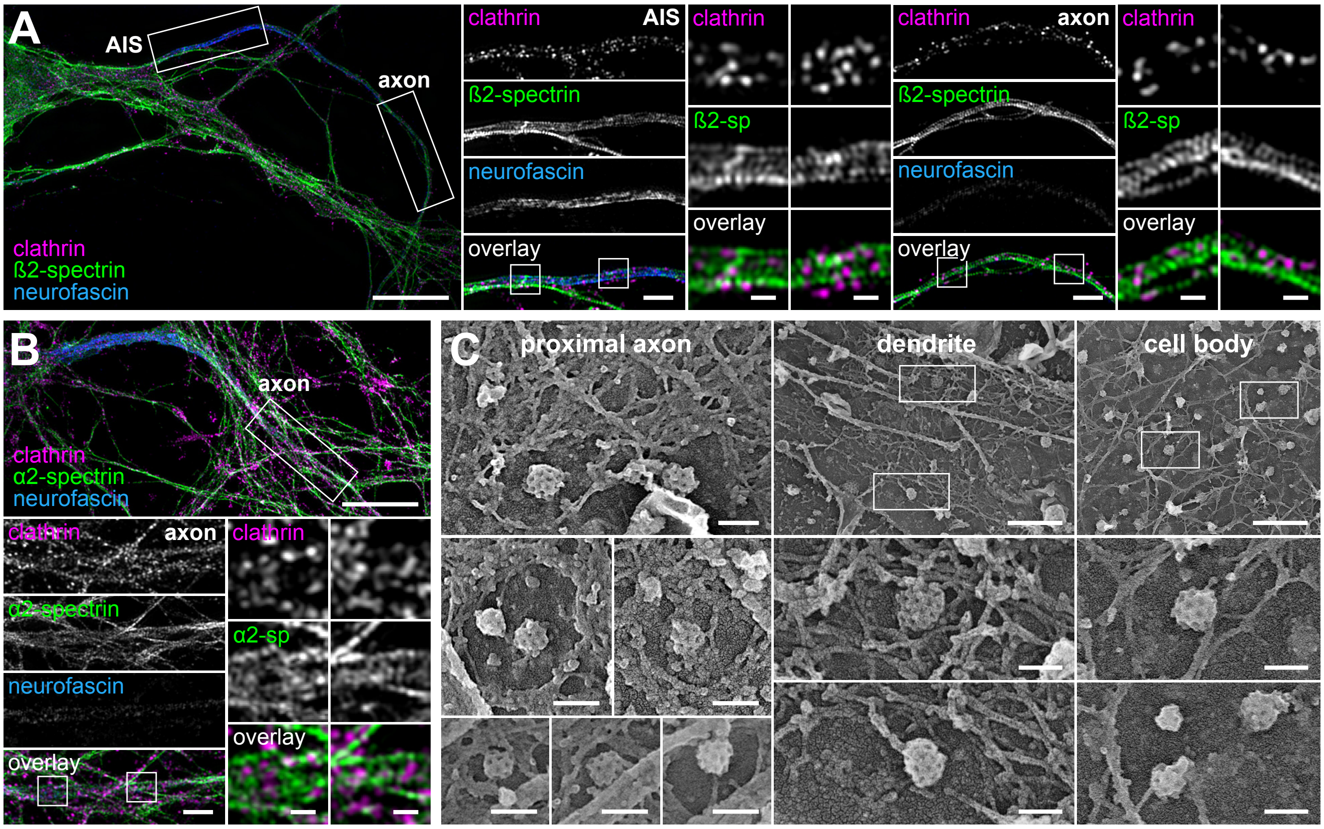

Supporting Figure 1: Clearings of the periodic spectrin mesh encase CCPs along the AIS and proximal axon, but not in the dendrites or cell body of neurons.
A. SIM image of a cultured hippocampal neuron at 14 div fixed and stained for clathrin (magenta, pits appear as clusters), ß2-spectrin (green, ~190 nm-spaced bands are visible) and neurofascin (blue, labels the AIS). Zooms show portions of the AIS (center panels) and axon proper after the AIS (right panels). Scale bars, 10 µm (left image), 2 µm (center column), 0.5 µm (square zoomed images). B. Same SIM image as in Fig. 1A of a cultured hippocampal neuron at 14 div fixed and stained for clathrin (magenta), α2-spectrin (green) and neurofascin (blue), with a zoom on the axon proper (bottom panels). Scale bars, 10 µm (top image), 2 µm (bottom left panels), 0.5 µm (bottom right square zoomed images). C. Left, PREM views showing CCPs found along the proximal axon in circular areas devoid of the actin-spectrin scaffold (left), or along dendrites (center) and in the cell body (right) where the submembrane scaffold is sparser. Scale bars, 100 nm.

Supporting Figure 2: Molecular organization of CCPs, ankyrin G and pMLC along AIS. (next page >)
A. Widefield image of a neuron unroofed, fixed and stained for clathrin (magenta), α2-spectrin (green) and neurofascin (blue). Line of images on the right are individual channels and overlays corresponding to the AIS area highlighted on the left image. Scale bars, 10 µm (left image), 5 µm (AIS images). B. 3D-STORM image of clathrin corresponding to the AIS area shown in A, color coded for depth. Scale bar, 2 µm. C. Zooms showing individual CCPs on XY images (top row, corresponding to areas highlighted in B) and corresponding XZ transverse sections (bottom row, taken between the lines highlighted on the XY images). Pits are found along the remaining ventral plasma membrane after unroofing. Scale bars, 0.5 µm. D. Widefield image of a neuron fixed and stained for neurofascin (blue). The contour of the whole neuron is delineated (gray). Scale bar, 10 µm. E. 2-color 3D-PAINT images of the AIS corresponding to the image in D with staining for clathrin (magenta) and AP2 (green). Scale bar, 2 µm. F. Zooms showing individual CCPs immunolabeled for clathrin heavy chain (magenta) and AP2 (green) on XY images (top row, corresponding to areas highlighted in E) and corresponding XZ transverse sections (bottom row, taken between the lines highlighted on the XY images). Both CHC and AP2 colocalize at CCPs. Scale bars, 0.5 µm. G. Correlative STORM-PREM image of an unroofed AIS immunolabeled for clathrin (orange). Right, zoomed images showing CCPs in spectrin mesh clearings. Scale bars, 500 nm (left image), 100 nm (zoomed images). H. Correlative STORM-PREM image of an unroofed AIS immunolabeled for ankyrin G (ankG, orange). Right, zoomed images showing CCPs in spectrin mesh clearings. Scale bars, 500 nm (left image), 100 nm (zoomed images). I. PREM view of an unroofed AIS immunogold-labeled for ß4-spectrin (orange), showing CCPs in spectrin mesh clearings, with 15 nm gold beads bound to the spectrin mesh around the bare membrane area. Scale bar, 200 nm (zoomed images). J. Correlative STORM-PREM image of an unroofed AIS labeled for pMLC (orange). Right, zoomed images showing CCPs in spectrin mesh clearings. Scale bars, 5 µm (left image), 100 nm (zoomed images). K. PREM view of an unroofed AIS immunogold-labeled for pMLC (yellow), showing CCPs in spectrin mesh clearings, with 15 nm gold beads bound to the spectrin mesh around the bare membrane area. Scale bar, 200 nm.

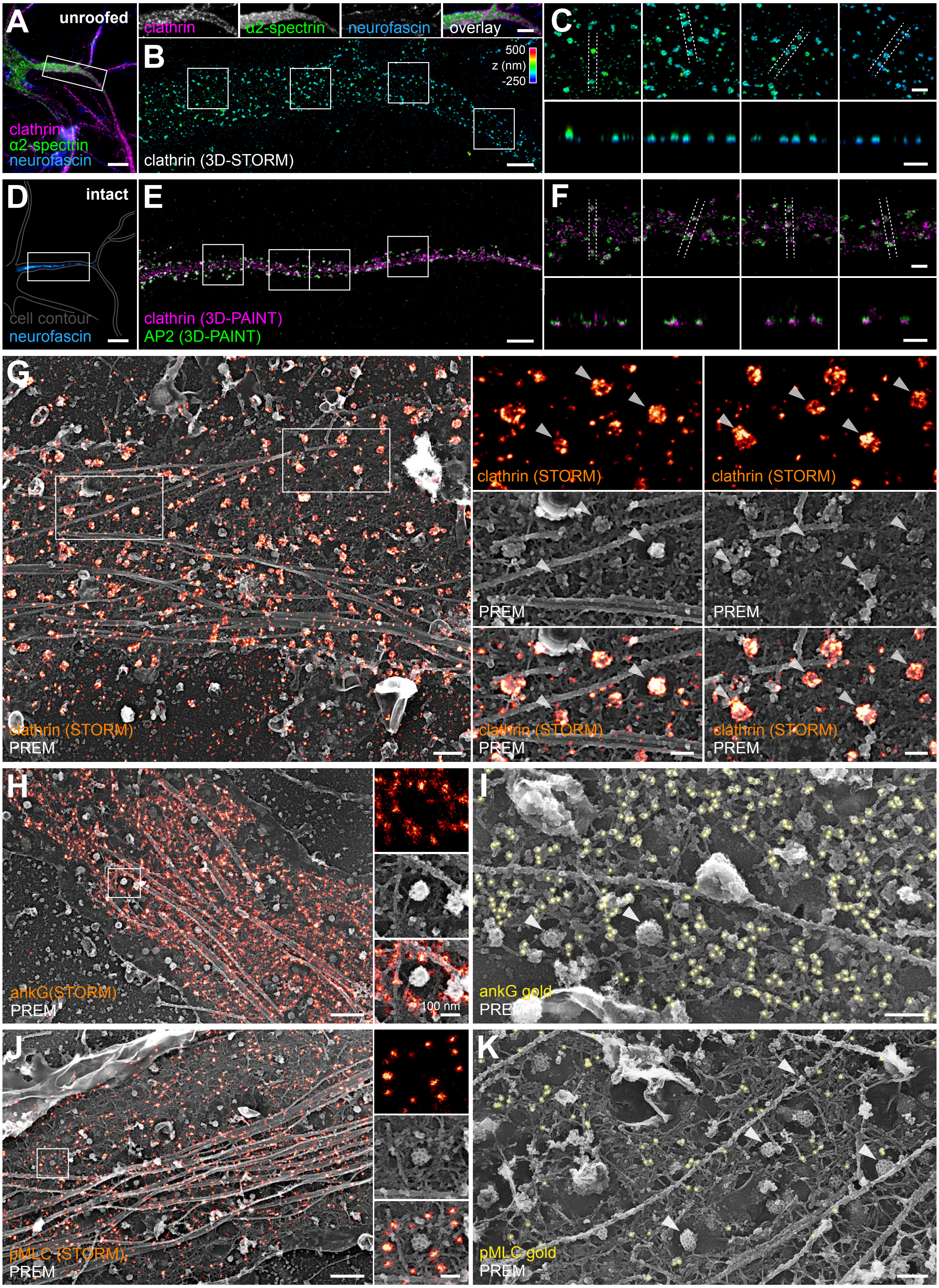

Supporting Figure 2: Molecular organization of CCPs, ankyrin G and pMLC along AIS.
See Legends on previous page.

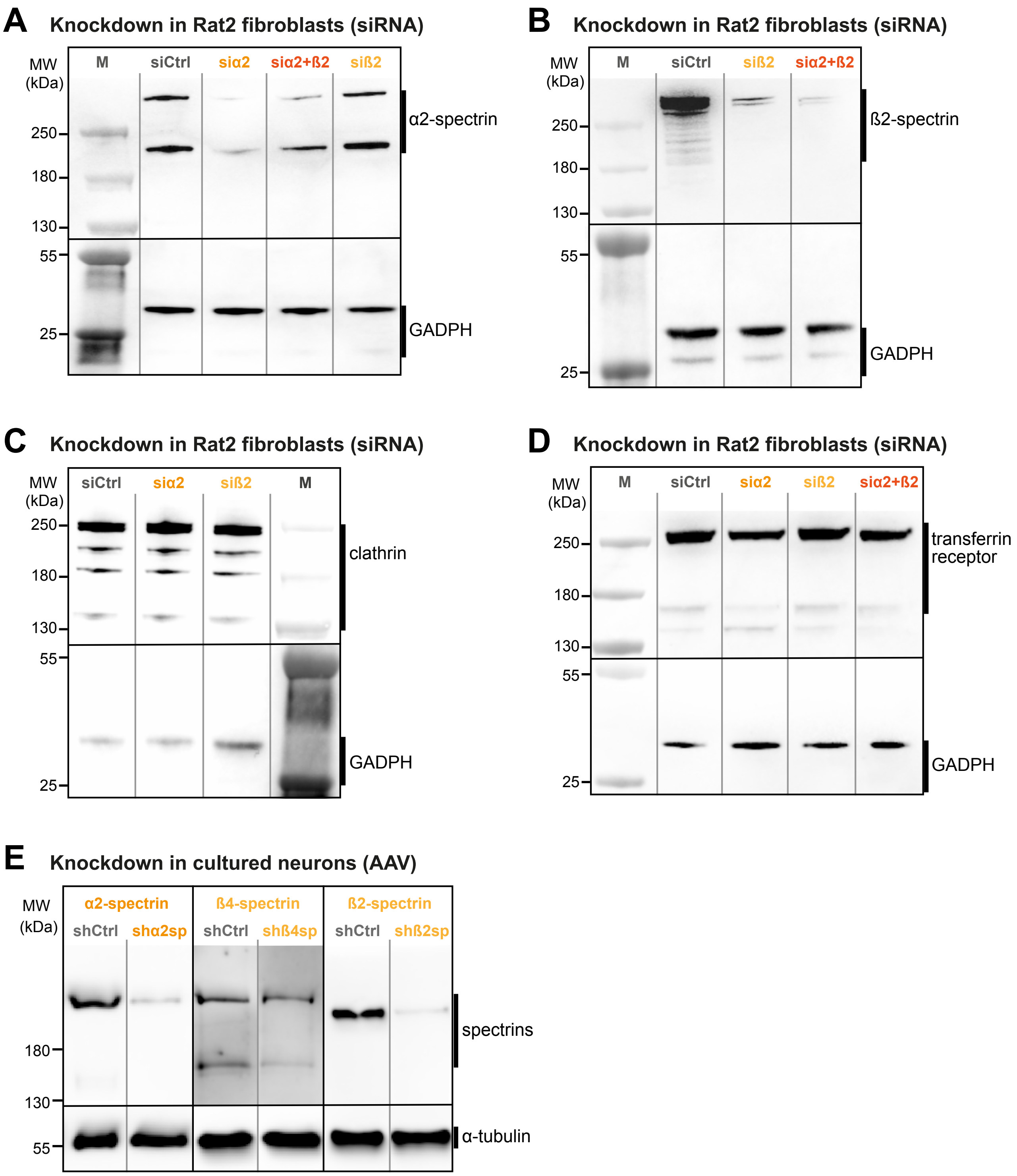

Supporting Figure 3: siRNA and shRNA knockdown efficiency assessed by Western blot.
A. Western blot of lysates from Rat2 fibroblasts transfected with control, α2-spectrin, α2+ß2-spectrin, or ß2-spectrin siRNAs probed for α2-spectrin (top), with GADPH as a loading control (bottom). B. Western blot of lysates from Rat2 fibroblasts transfected with control, ß2-spectrin, or α2+ß2-spectrin siRNAs probed for ß2-spectrin (top), with GADPH as a loading control (bottom). C. Western blot of lysates from Rat2 fibroblasts transfected with control, α2-spectrin, or ß2-spectrin siRNAs probed for clathrin (top), with GADPH as a loading control (bottom). Clathrin levels are unaffected by the knockdown of α2 and/or ß2-spectrin. D. Western blot of lysates from Rat2 fibroblasts transfected with control, α2-spectrin, ß2-spectrin, or α2+ß2-spectrin siRNAs probed for transferrin receptor (TfR, top), with GADPH as a loading control (bottom). TfR levels are unaffected by the knockdown of α2 or ß2-spectrin. E. Western blots of lysates from hippocampal neurons infected with control, α2-spectrin, ß4-spectrin, or ß2-spectrin shRNA AAVs probed for α2-spectrin, ß4-spectrin, or ß2-spectrin, respectively. α-tubulin is used as a loading control (bottom).

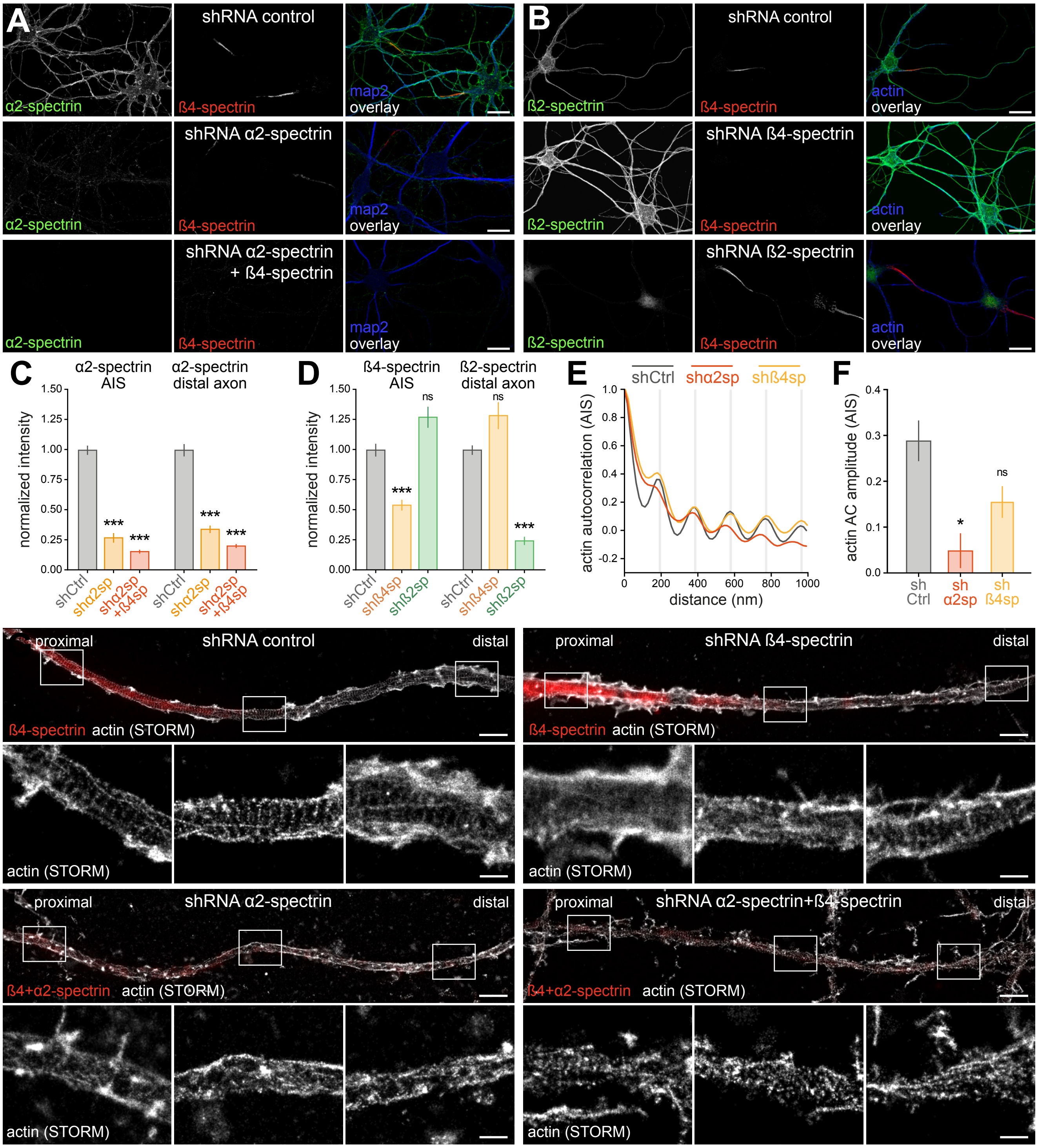

Supporting Figure 4: Effect of spectrin knockdown in neurons assessed by immunolabeling and STORM.
A. Epifluorescence images of cultured neurons infected with control, α2-spectrin, or α2+ß4-spectrin shRNA AAVs, fixed and stained for α2-spectrin (green), ß4-spectrin (red) and map2 (blue). Scale bars, 20 µm. B. Epifluorescence images of cultured neurons infected with control, ß4-spectrin, or ß2-spectrin shRNA AAVs, fixed and stained for ß2-spectrin (green), ß4-spectrin (red) and map2 (blue). Scale bars, 20 µm. C. Quantification of the normalized staining intensity for α2-spectrin at the AIS (left) and distal axon (right) in neurons infected with control, α2-spectrin, or α2+ß4-spectrin shRNA AAVs, showing the efficient knockdown of α2-spectrin in both compartments. D. Quantification of the normalized staining intensity for ß4-spectrin at the AIS (left) and ß2-spectrin in the distal axon (right) in neurons infected with control, ß4-spectrin, or ß2-spectrin shRNA AAVs, showing the selective knockdown of each ß-spectrin in the AIS and distal axon. E. Autocorrelation curves from intensity profiles traced along the AIS of neurons infected with control, α2-spectrin, or ß4-spectrin shRNA AAVs, fixed, stained for actin using phalloidin-Alexa Fluor 647, and imaged by STORM (see G-J). Oscillations demonstrating the 190-nm periodicity (actin rings) are attenuated in α2-spectrin and ß4-spectrin knocked-down neurons. F. Quantification of the autocorrelation amplitude (first valley to first peak) on the graph in E, showing lower values in α2-spectrin and ß4-spectrin knocked-down neurons. G. Image of the AIS of a neuron infected with a control shRNA AAV, fixed, and stained for ß4-spectrin (red, epifluorescence image) and actin (gray, STORM image). Bottom zooms show the actin rings in the proximal, middle, and distal portions of the axon shown. Scale bar, 500 nm. H. Image of the proximal axon of a neuron infected with a ß4-spectrin shRNA AAV, fixed, and stained for ß4-spectrin (red, epifluorescence image) and actin (gray, STORM image). Bottom zooms show the selective perturbation of the actin rings in the proximal portion of the axon shown. Scale bar, 500 nm. I. Image of the proximal axon of a neuron infected with a α2-spectrin shRNA AAV, fixed, and stained for α2+ß4-spectrin (red, epifluorescence image) and actin (gray, STORM image). Bottom zooms show the perturbation of the actin rings in the proximal, middle, and distal portions of the axon shown. Scale bar, 500 nm. J. Image of the proximal axon of a neuron infected with an α2+ß4-spectrin shRNA AAV, fixed, and stained for α2+ß4-spectrin (red, epifluorescence image) and actin (gray, STORM image). Bottom zooms show the perturbation of the actin rings in the proximal, middle, and distal portions of the axon shown. Scale bar, 500 nm.

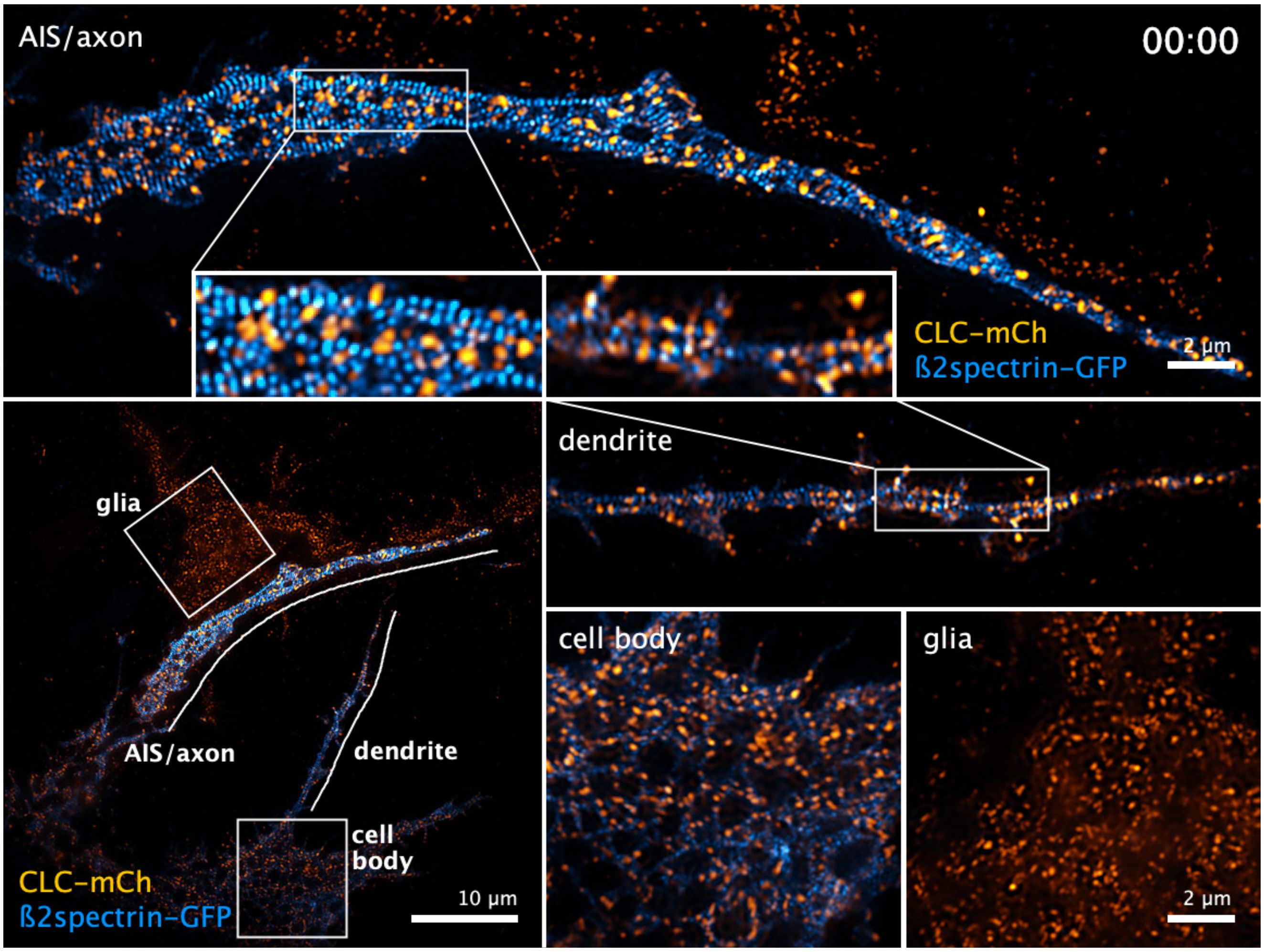

Supporting Movie 1: Dynamics of neuronal CCPs and the axonal periodic scaffold by live-cell TIRF-SIM.
Hippocampal neuron in culture transfected at 10 div with clathrin light chain-mCherry (CLC-mCh, orange) and EGFP-ß2-spectrin (ß2spectrin-GFP, blue) and imaged at 13 div by 2-color TIRF-SIM (one frame every 20s for 20 min, 61 frames total). Reconstructed TIRF-SIM images were denoised using a supervised deep-learning model trained on pairs of low and high SNR images of fixed cells expressing the same constructs (Enhance.ai). Bottom left, full-field view of the transfected neuron with highlighted areas corresponding to the AIS/proximal axon (top), dendrite (middle right), cell body (bottom center), and a neighboring glia only transfected with CLC-mCh (bottom left). Further zooms detail the dynamic of CCPs within the AIS and along the dendrite. CCPs are more stable at the AIS, being present throughout the 20-minute movie, whereas they appear more dynamic in the dendrites and cell body, and very dynamic in the glial cell.

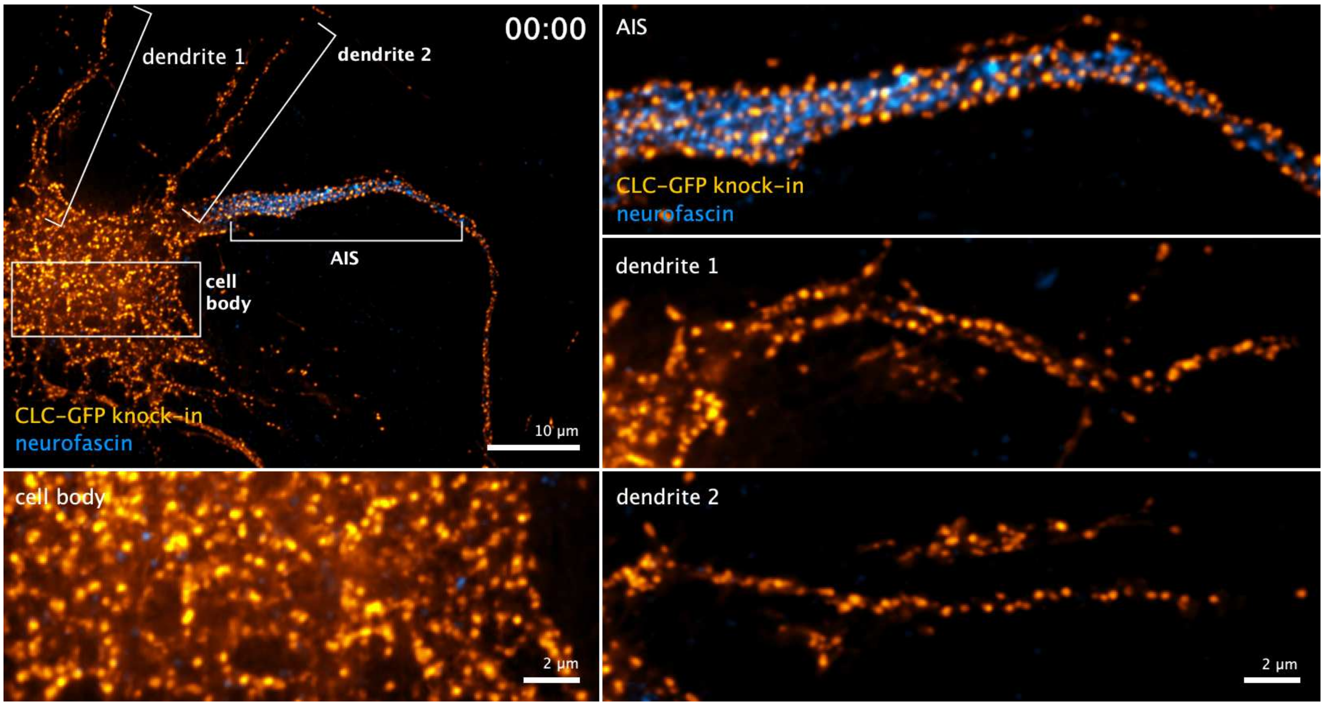

Supporting Movie 2: Dynamics of neuronal CCPs using super-resolved imaging of endogenously-tagged clathrin.
Hippocampal neuron in culture infected with AAVs targeting the endogenous tagging of clathrin light chain with EGFP at its C-terminus (CLC-GFP knock-in, orange), labeled for the AIS using an anti-neurofascin antibody targeting an extracellular epitope (blue), and imaged at 14 div using SoRa super-resolved spinning disk microscopy (one frame every 5s for 10 m, 121 images total). Raw images were denoised using a built-in deep-learning module trained on a dataset of confocal images (Denoise.ai). Top left, full-field view of the transfected neuron with highlighted areas corresponding to the AIS/proximal axon (top right), two dendrites (middle right and bottom right), and the cell body (bottom left). CCPs are more stable at the AIS compared to the dendrites and cell body.

6 Collaboration à l'article Ganguly et al., Neuron 2021 : « Clathrin packets move in slow axonal transport and deliver functional payloads to synapses »

6.1 Commentaire

Lors de mes premiers mois en doctorat, j'ai eu l'occasion de collaborer avec l'équipe de Subhojit Roy (Roy Lab, UC San Diego) sur les travaux qui ont conduit à la publication de l'article "Clathrin packets move in slow axonal transport and deliver functional payload to synapses" Ganguly et al., 2021, Neuron. Le point de départ de cette étude fut l'observation dans le laboratoire de Subhojit Roy de particules de clathrine mobiles dans le tube axonal. Ces particules de clathrine étaient mobiles latéralement, toutefois leurs profils d'intensité fluorescente ne semblaient pas indiquer une activité endocytique. À partir de ces observations initiales, nos équipes ont collaboré pour caractériser ces structures et la dynamique de leur transport, découvrir leurs partenaires moléculaires et tester fonctionnellement leur activité endocytique et enfin révéler leur rôle dans le recyclage vésiculaire présynaptique.

Cette étude a d'abord permis de caractériser la dynamique du transport axonal de clathrine vers les présynapses, puis de mettre au jour que ce transport est lent et s'effectue via le réseau de microtubules axonales, dans le sens antérograde et rétrograde, avec un faible biais dans le sens antérograde. Puis, elle a mis en relief que ce transport se fait avec les partenaires d'assemblage et de désassemblage des manteaux de clathrine nécessaires à la CME présynaptique, et qu'il semble destiné à former des réserves de clathrine présynaptique. Aux présynapses, la mobilité de la clathrine contraste fortement avec son transport axonal lent, elle est échangée rapidement entre les boutons présynaptiques, et la déplétion artificielle en clathrine des boutons laisse apparaitre une diminution drastique de la CME présynaptique. Cette étude montre donc l'importance capitale de la clathrine et de son transport lent aux synapses dans le maintien du recyclage vésiculaire présynaptique et par conséquent pour la transmission du signal entre neurones.

Dans ces travaux, ma contribution a d'abord consisté à identifier les paquets de transport de clathrine axonaux et les distinguer des puits à manteau de clathrine membranaire sur les images DNA-PAINT 3D 2 couleurs de notre équipe. J'ai développé des routines d'analyse pour objectiver les observations dans le logiciel de visualisation 3D ChimeraX (Goddard et al., 2018, *Protein Sci. Publ.*

Protein Soc.), avec ces routines j'ai pu caractériser les tailles et les densités moyennes des paquet de transport. Cette partie de ma contribution est présentée dans le panneau C de la figure 3 de l'article ci-après. Par la suite, toujours sur des données DNA-PAINT 3D 2 couleurs sur ChimeraX, j'ai contribué à caractériser les structures de clathrine présentes aux présynapses et à quantifier clathrine et présynapses en nombre et en taille. Cette autre partie de ma contribution est visible dans les panneaux A à F de la figure 5 de l'article ci-après.

Neuron

Article

Clathrin packets move in slow axonal transport and deliver functional payloads to synapses

Graphical abstract

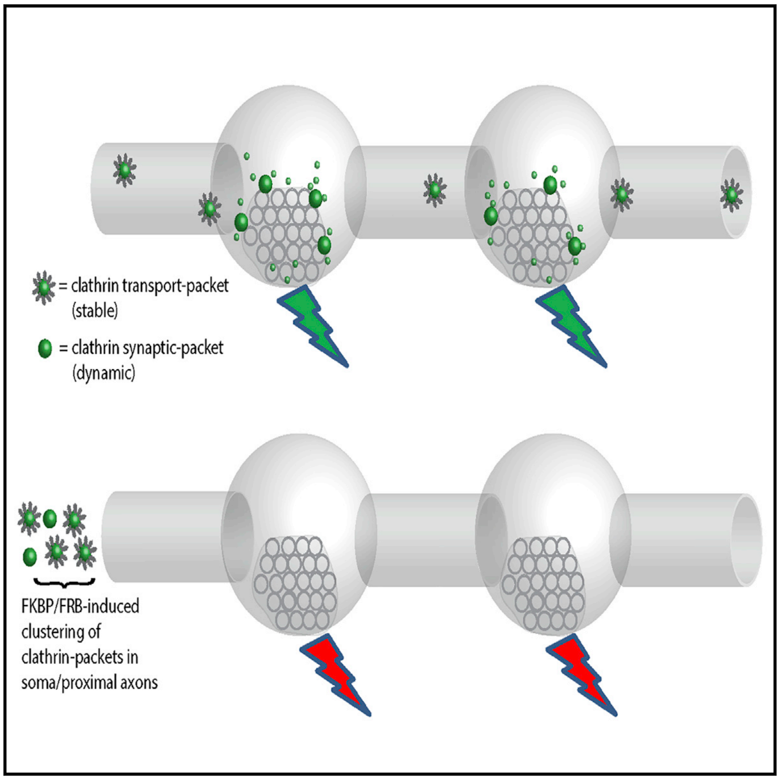

Authors

Archan Ganguly, Rohan Sharma, Nicholas P. Boyer, ..., Mark H. Ellisman, Christophe Leterrier, Subhojit Roy

Correspondence

sroy@ucsd.edu

In brief

Clathrin helps maintain synaptic homeostasis, but it's unclear how it gets to synapses. Ganguly and Sharma et al. show that clathrin assembles into stable transport packets in axons that are trapped upon reaching synapses, where packets radially organize around synaptic vesicle clusters. Synaptic clathrin packets are dynamic, and their depletion impairs synaptic function.

Highlights

- Clathrin moves as stable "transport packets" in axons with overall anterograde bias
- Stable clathrin packets switch to a dynamic state upon reaching synapses
- Synaptic clathrin packets are radially organized around synaptic vesicle clusters
- Depletion of synaptic clathrin packets impairs synaptic vesicle recycling

Ganguly et al., 2021, Neuron *109*, 2884–2901
September 15, 2021 © 2021 Elsevier Inc.
https://doi.org/10.1016/j.neuron.2021.08.016

CellPress

Neuron

Article

Clathrin packets move in slow axonal transport and deliver functional payloads to synapses

Archan Ganguly,[1,6,7] Rohan Sharma,[1,7] Nicholas P. Boyer,[1] Florian Wernert,[2] Sébastien Phan,[3,4] Daniela Boassa,[3,4] Leonardo Parra,[1] Utpal Das,[1,3] Ghislaine Caillol,[2] Xuemei Han,[5] John R. Yates III,[5] Mark H. Ellisman,[3,4] Christophe Leterrier,[2] and Subhojit Roy[1,3,8,*]

[1]Department of Pathology, University of California, San Diego, La Jolla, CA, USA
[2]Aix Marseille Université, CNRS, INP UMR7051, NeuroCyto, Marseille, France
[3]Department of Neurosciences, University of California, San Diego, La Jolla, CA, USA
[4]National Center for Microscopy and Imaging Research, University of California, San Diego, La Jolla, CA, USA
[5]Department of Cell Biology, The Scripps Research Institute, La Jolla, CA, USA
[6]Present address: Department of Pharmacology and Physiology, University of Rochester Medical Center, Rochester, NY, USA
[7]These authors contributed equally
[8]Lead contact
*Correspondence: sroy@ucsd.edu
https://doi.org/10.1016/j.neuron.2021.08.016

SUMMARY

In non-neuronal cells, clathrin has established roles in endocytosis, with clathrin cages enclosing plasma membrane infoldings, followed by rapid disassembly and reuse of monomers. However, in neurons, clathrin is conveyed in slow axonal transport over days to weeks, and the underlying transport/targeting mechanisms, mobile cargo structures, and even its precise presynaptic localization and physiologic role are unclear. Combining live imaging, photobleaching/conversion, mass spectrometry, electron microscopy, and super-resolution imaging, we found that unlike in dendrites, where clathrin cages rapidly assemble and disassemble, in axons, clathrin and related proteins organize into stable "transport packets" that are unrelated to endocytosis and move intermittently on microtubules, generating an overall slow anterograde flow. At synapses, multiple clathrin packets abut synaptic vesicle (SV) clusters, and clathrin packets also exchange between synaptic boutons in a microtubule-dependent "superpool." Within synaptic boundaries, clathrin is surprisingly dynamic, continuously exchanging between local clathrin assemblies, and its depletion impairs SV recycling. Our data provide a conceptual framework for understanding clathrin trafficking and presynaptic targeting that has functional implications.

INTRODUCTION

The cytosolic protein clathrin is an established player in endocytosis. During this process, soluble clathrin is recruited to the inner plasma membrane, forming clathrin-coated pits and vesicles. After vesicle internalization, the clathrin coat is rapidly removed by uncoating proteins, and the released clathrin monomers are reused for subsequent rounds of endocytosis. Clathrin-mediated endocytosis (CME) has been studied for over forty years, and a host of adapters and regulators are known. Clathrin also plays roles in sorting of intracellular membranes, although this is less studied (Jung and Haucke, 2007; Dittman and Ryan, 2009; McMahon and Boucrot, 2011; Traub and Bonifacino, 2013).

In neurons, clathrin synthesized in cell bodies is transported into axons, enriching at presynapses, and previous *in vivo* pulse-chase radiolabeling studies have established that clathrin is conveyed in slow axonal transport, taking days to weeks in reaching axon terminals (Black et al., 1991; de Waegh and Brady, 1989; Elluru et al., 1995; Garner and Lasek, 1981; Gower and Tytell, 1987). Slow transport is a poorly defined rate-class carrying cytosolic (or soluble) and cytoskeletal proteins to the axon tips and presynaptic terminals, unlike fast vesicular cargoes that are rapidly transported in minutes to hours (for review, see Maday et al., 2014; Roy, 2014, 2020). Although radiolabeling techniques established the overall movement of clathrin in slow transport, these methods could not visualize the movement, and many questions remain.

How can clathrin undergo organized slow axonal transport, given the ephemeral nature of cytoplasmic clathrin assemblies? Indeed, previous studies in cultured hippocampal neurons showed rapid on/off behavior of GFP:clathrin puncta in dendrites, lasting only for seconds, consistent with CME (Blanpied et al., 2002; Rosendale et al., 2017). While clathrin may organize into longer-lasting assemblies for slow transport, no such structures have been described. How is clathrin targeted to presynapses and retained there? What is its nanoscale organization at synapses? What is the dynamic behavior of clathrin at the synapse, and can this offer insight into function? Though clathrin is involved in retrieving SVs from the presynaptic plasma membrane (Heuser and Reese, 1973; Royle and Lagnado, 2010; Saheki and De Camilli, 2012), newer studies argue that clathrin acts downstream of endocytosis—in the regeneration of new SVs (Chanaday et al., 2019; Chanaday and Kavalali, 2018; Milosevic, 2018; Watanabe et al., 2014)—and a better understanding of the precise localization and dynamic behavior of clathrin may offer a fresh perspective.

Recent studies from us and others using cultured neurons as a model system to visualize and manipulate slow axonal transport have begun to offer some answers about mechanisms (Chakrabarty et al., 2019; Ganguly et al., 2017; Scott et al., 2011; Tang et al., 2013; Twelvetrees et al., 2016). Here, we report previously unknown long-lasting axonal assemblies of clathrin and associated proteins that are unrelated to endocytosis and specialized for cargo delivery. We also found a striking radial organization of clathrin around—but not within—SV clusters, and a microtubule-dependent clathrin superpool that may be distinct from the known actin-dependent SV superpool (Darcy et al., 2006). Though the transported axonal clathrin packets are stable, surprisingly, they become dynamic upon entering synaptic boundaries—exchanging clathrin molecules with local synaptic clathrin—and depletion of clathrin packets from boutons impairs SV recycling. Collectively, the data advocate new models for trafficking and targeting of clathrin and related proteins, with implications for synaptic function.

RESULTS

Discrete clathrin transport packets move intermittently in slow axonal transport

Although the overall appearance of clathrin puncta in cultured neurons seems similar in somatodendritic and axonal compartments by immunostaining (Figure 1A), their dynamics were different. To visualize clathrin in living neurons, we used GFP (or mCherry) tagged to the N terminus of clathrin light chain A (CLC), a structurally and functionally active fusion protein (Gaidarov et al., 1999) that has been used in other studies (Blanpied et al., 2002; Mueller et al., 2004; Pelassa et al., 2014; Rosendale et al., 2017; Zhao and Keen, 2008). All live imaging of axons was performed between 8 and 10 days *in vitro* (DIV), and synapses were imaged between 13 and 21 DIV—a time when synapses are established in our cultures. As reported previously (Blanpied et al., 2002; Rosendale et al., 2017), GFP:CLC showed largely on/off dynamics in dendrites, reflecting transient recruitment of clathrin molecules to coated pits (see kymographs in Figure 1B; also see Video S1). However, axonal GFP:CLC particles were long-lasting, and ~40% were motile, moving with an overall anterograde bias (Figures 1C–1E; see also Figure S1A and Video S2). Where visible, moving clathrin particles did not colocalize with transported vesicles (Figure S1B). To distinguish moving axonal clathrin structures from dendritic clathrin-coated pits and other endocytosis-related clathrin structures, here we call them clathrin "transport packets."

Previously, we developed an assay to visualize the anterogradely biased transport of cytosolic cargoes moving in slow transport ("intensity-center shift assay"; see Roy et al., 2011; Scott et al., 2011). Here, cultured neurons are transfected with photoactivatable (or photoconvertible) probes tagged to the cytosolic protein of interest, and a discrete region of interest (ROI) in the axon shaft is photoactivated/photoconverted (schematic in Figure 1F). Thereafter, a line is drawn along the long axis of the axon, including the photoactivated/photoconverted ROI, and the intensity center (or centroid) shift of the fluorescence in the ROI is monitored over time. While untagged photoactivatable GFP (PAGFP) rapidly diffuses without any centroid shift, cytosolic proteins disperse with a slow anterogradely biased centroid shift, consistent with slow transport (Chakrabarty et al., 2019; Ganguly et al., 2017; Scott et al., 2011; Tang et al., 2012, 2013; Twelvetrees et al., 2016). A kymograph from these experiments is shown in Figure 1G, along with the ensuing raw and ensemble data (Figures 1H and 1I). Note that PAGFP:CLC—but not soluble, untagged PAGFP—has an overall anterograde bias with a predicted average rate of ~0.006 μm/s or ~0.5 cm/day, in line with overall rates of slow transport in radiolabeling studies (Garner and Lasek, 1981). Similar results were obtained with a photoconversion assay, in which we first visualized green Dendra2:CLC puncta in axons and then photoconverted them to red (Figure 1J). Collectively, the data indicate that the intermittent movement of axonal clathrin transport packets generates an overall anterograde bias of the clathrin population, conveyed at rates consistent with slow axonal transport.

Motility of clathrin transport packets is independent of endocytosis

The persistent and biased movement of the transport packets suggest that clathrin is conveyed as a unique structure that is specialized for axonal transport, with no role in endocytosis. To test this idea, we asked if inhibition of endocytosis would also affect the motility of axonal transport packets. First, we globally suppressed endocytosis in cultured neurons using Dynasore, a small-molecule inhibitor of dynamin (Das et al., 2013; Macia et al., 2006). We also specifically inhibited clathrin-dependent endocytosis with CHC-T7-Hub, a clathrin heavy-chain dominant-negative mutant known to disrupt clathrin-dependent endocytosis (Bennett et al., 2001). As reported previously in non-neuronal cells, the CHC-T7-Hub mutant attenuated receptor-mediated endocytosis in cultured hippocampal neurons (Figures S2A and S2B). The on/off dynamics of GFP:CLC in dendrites was essentially abolished in neurons treated with Dynasore (Figure 2A) or transfected with the CHC-T7-Hub mutant (Figures S2C and S2D). Interestingly, however, neither Dynasore nor the CHC-T7-Hub mutant had any effect on the mobility of axonal clathrin transport packets (Figures 2B–2D). Since the motility of individual clathrin transport packets generates the overall anterogradely biased flow of the axonal clathrin population (see Figure 1H), a prediction is that endocytosis inhibition would not interfere with the slow transport of clathrin. Indeed, neither Dynasore nor the CHC-T7-Hub mutant had any effect on the biased transit of PAGFP:CLC in axons (Figure 2E). Previous studies suggest that the slow transport of synapsin and dynein is microtubule dependent (Scott et al., 2011; Twelvetrees et al., 2016). Low levels of the microtubule-disrupting drug nocodazole (at a concentration that blocks vesicle transport; see

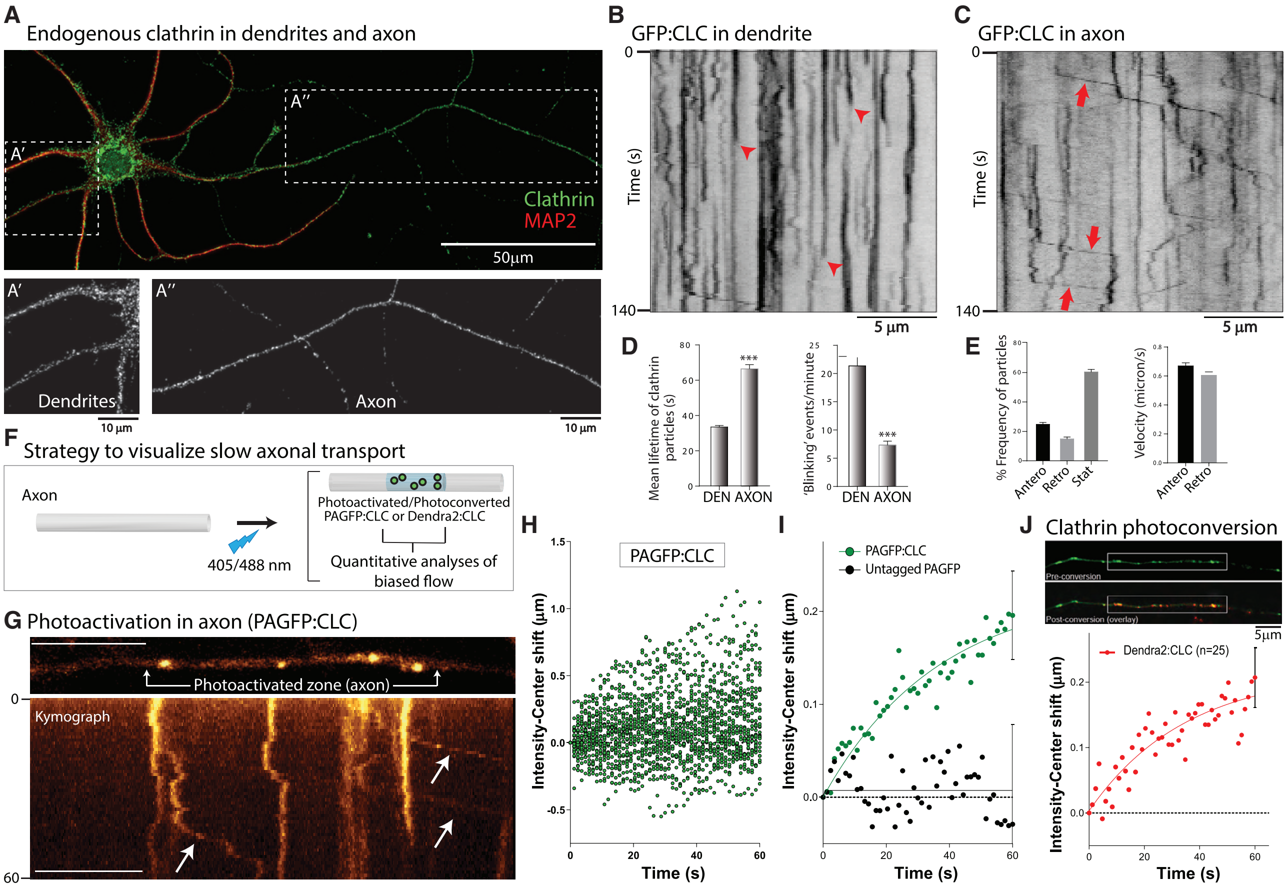

Figure 1. Differential dynamics of clathrin in dendrites and axons

(A) Clathrin and MAP2 immunostaining in cultured hippocampal neurons. Note punctate clathrin in both somatodendritic (A') and axonal (A'') compartments.

(B) Kymograph of GFP:CLC in a dendrite. Note abrupt appearance and disappearance of fluorescence (red arrowheads), indicating assembly/disassembly of clathrin in coated pits (CME). Scale bars, 5 µm.

(C) Kymograph of GFP:CLC in an axon. Note rapid, infrequent, and anterogradely biased movement of clathrin particles (some marked by red arrows; more examples in Figure S1A). Scale bars, 5 µm.

(D) Mean lifetimes of GFP:CLC particles as determined from kymographs were significantly higher in axons, while "blinking events"—representing clathrin assembly/disassembly and receptor-mediated endocytosis—are much lower in axons, compared to dendrites (1,113 particles from 22 dendrites and 403 particles from 41 axons were analyzed; data were pooled from 3 independent experiments; ***$p < 0.0001$).

(E) About 40% of the axonal GFP:CLC particles were mobile, with a larger fraction of particles moving anterogradely (460 anterograde and 263 retrograde events were analyzed from 41 axons; data were combined from 3 independent experiments).

(F) Strategy for analyzing biased axonal transport of clathrin in axons (see Results for details).

(G) Kymograph from a photoactivation (PAGFP:CLC) experiment. Note anterograde movement of photoactivated clathrin particles (arrows). Scale bars, 10 µm.

(H) Raw data of intensity-center shifts from all PAGFP:CLC experiments in axons. Note anterograde drift of datapoints (38 neurons from 3 separate cultures were analyzed).

(I) Ensemble data showing mean intensity-center shift of PAGFP:CLC and PAGFP-only in axons, with fitted curves. While there is an overall anterograde bias of PAGFP:CLC, there is no bias with untagged PAGFP-only (10 neurons from 2 separate cultures were analyzed for PAGFP-only).

(J) Neurons were transfected with Dendra2:CLC, axonal clathrin particles were identified by green fluorescence, and intensity-center shifts of photoconverted (red) particles were analyzed. Note anterograde shift of the particles (25 neurons from 3 separate cultures were analyzed). Scale bars, 5 µm.

Figure S2F) also inhibited movement of clathrin transport packets (Figure 2F). Taken together, the data indicate that axonal clathrin transport packets are unique conveyance structures, unrelated to endocytosis.

Structure of axonal clathrin transport packets

What do the transport packets look like? To visualize the ultrastructure of axonal clathrin, we tagged clathrin to APEX, an engineered peroxidase that acts as an electron microcopy (EM) tag by catalyzing the polymerization and local deposition of diaminobenzidine (DAB), subsequently recruiting electron-dense osmium for EM contrast (Martell et al., 2012). Cultured neurons were transfected with APEX-GFP:CLC and fixed and incubated with DAB and H_2O_2 (see schematic in Figure 3A and STAR methods). Transfected neurons were visualized by GFP fluorescence and DAB staining, dendrites and axons were identified by morphology, and the same neurons and processes were visualized by EM tomography (see Figure S3 and STAR methods). As

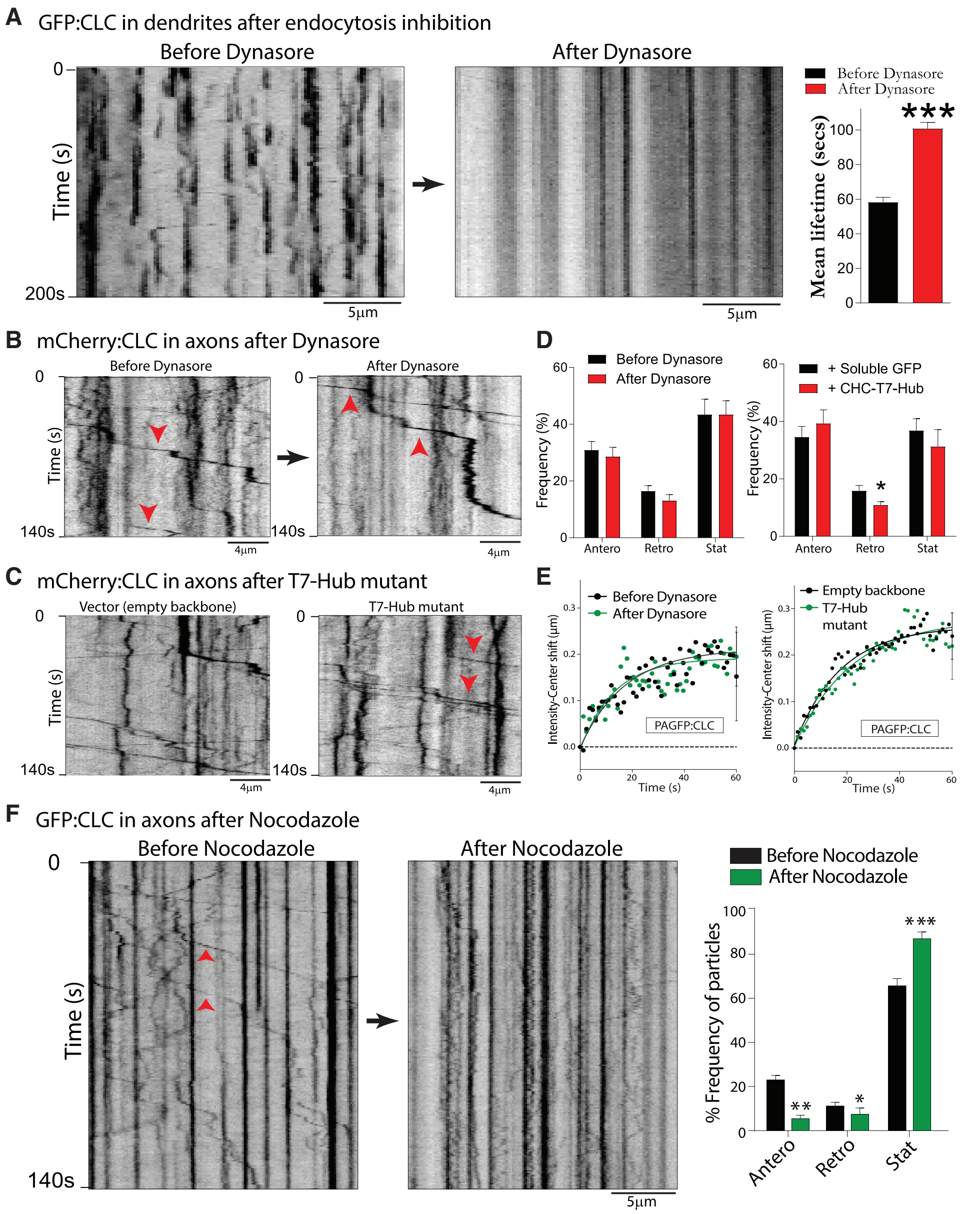

Figure 2. Motility of axonal clathrin transport packets is independent of endocytosis, but dependent on microtubules

(A) Kymographs of GFP:CLC from a dendrite before and after endocytosis inhibition (Dynasore). Note that blinking events—reflecting endocytosis—are abolished after drug treatment. GFP:CLC fluorescence lifetimes are quantified on the right (~150–250 particles from 10 neurons were analyzed; data from three separate cultures; ***$p < 0.0001$). Scale bars, 5 µm.

(B) Kymographs of mCherry:CLC from same axon before and after Dynasore. Note that vectorial movement of clathrin transport packets (some marked by arrowheads) continues after drug treatment. Scale bars, 4 µm.

(C) Kymographs of axonal mCherry:CLC from neurons transfected with a dominant-negative clathrin mutant (T7-Hub) that specifically interferes with clathrin-dependent endocytosis (see Figure S2) or control. Note that vectorial movement of clathrin transport packets (some marked by arrowheads) are similar in the two groups. Scale bars, 4 µm.

(D) Quantification of all mCherry:CLC axonal transport data, with and without endocytosis inhibition, global or clathrin dependent. (~140–170 motile particles were analyzed from 10–12 neurons; data from 2–3 separate cultures; *$p < 0.01$.)

(E) Ensemble intensity-center shift data (PAGFP:CLC slow transport assay) from neurons treated with Dynasore or co-transfected with the T7-Hub mutant. Note that inhibiting global—or clathrin-dependent—endocytosis has no effect on the slow anterograde bias of the clathrin population in axons (20–30 axons from two and four separate cultures were analyzed).

(F) Kymographs of GFP:CLC dynamics from the same axon before and after treatment with 10 µg/mL nocodazole for 30 min; quantification on right. Note that motility of the clathrin transport packets is attenuated after drug treatment. Scale bars, 5 µm (**$p < 0.01$. **$p < 0.001$, ***$p < 0.0001$).

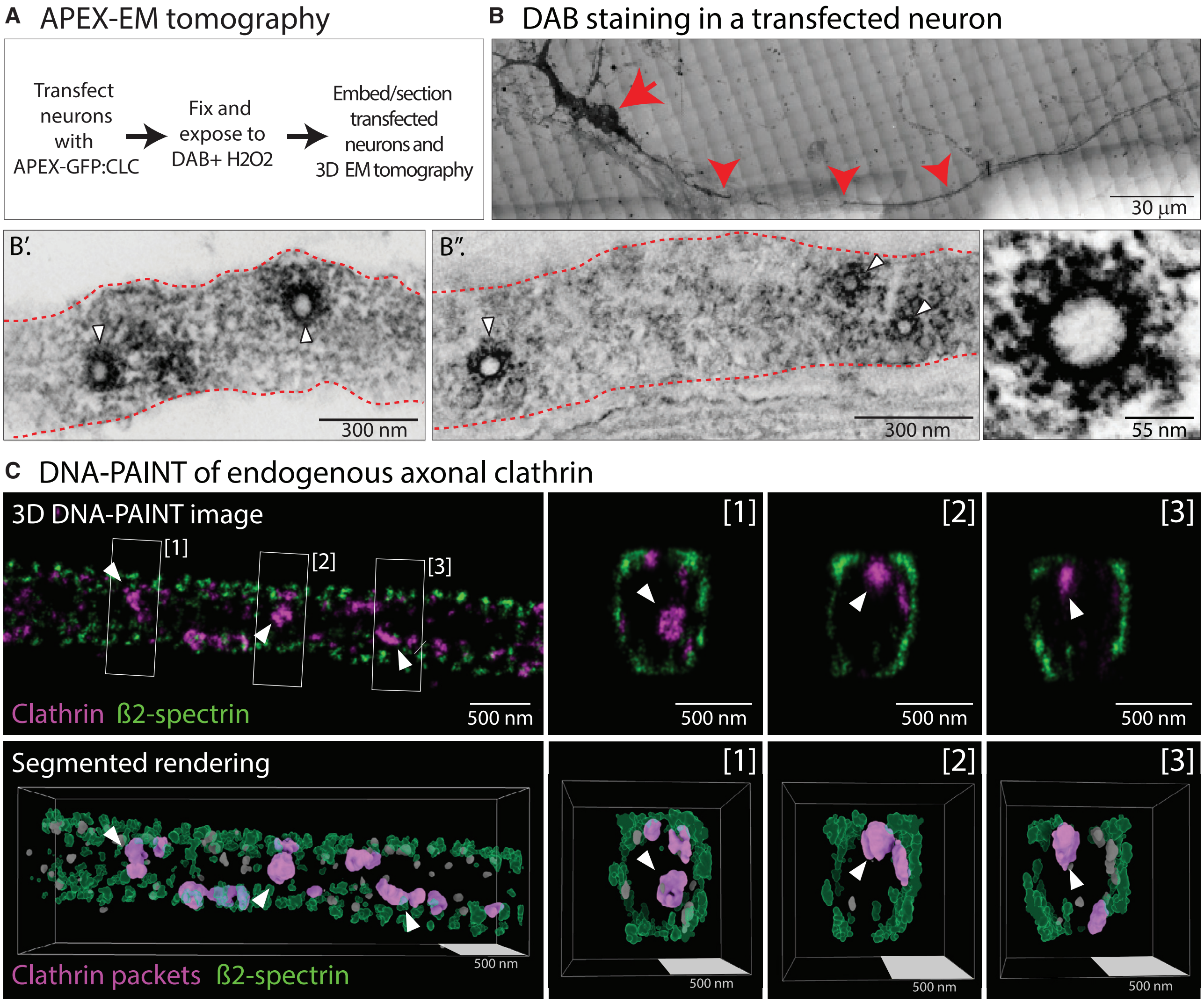

Figure 3. Ultrastructure and super-resolution imaging of axonal clathrin transport packets

(A) Strategy to visualize clathrin by APEX labeling and EM tomography.

(B) A DAB-stained neuron identified on gridded membrane (soma and axon marked by arrow and arrowhead, respectively; see also STAR methods and Figure S3). Scale bars, 30 μm.

(B' and B'') EM of the axon above (a single plane of tomogram shown). Note clathrin-coated structures in the axon shaft (white arrowheads), with average diameters of ~50 nm (spherical core). Representative 3D EM from three separate cultures (see STAR methods for more details). Scale bar (lower left) for B' represents 300 nm, B'' represents 300 nm, and lower right represents 55 nm.

(C) DNA-PAINT of endogenous clathrin in the axon shaft. Top panels: β2-spectrin (green, to mark axonal boundaries) and clathrin heavy chain (magenta). An XY image is shown on the left, along with three Z-slices on right (1–3). Bottom panels: Segmented rendering from 3D-PAINT images (small excluded particles are in gray). Equivalent sphere diameters for the clathrin particles marked by arrowheads: 79, 70, and 70 nm for particles highlighted in 1, 2, and 3, respectively. Scale bars, 500 nm.

expected, coated pits and coated vesicles were seen in soma and dendrites (Figure S2B). However, axons contained intact clathrin-coated structures that were inside the axon shaft, with no association with the axonal plasma membrane, as seen by EM tomography (Figures 3B–3B''; see also 3D view in Video S3). The diameters of these clathrin structures as determined by EM were ~50 nm and ~125 nm (inner spherical core and outer diameter including spokes, respectively), consistent with previous cryo-EM studies of clathrin-coated vesicles (Heymann et al., 2013).

We also used DNA-PAINT, a single-molecule-based super-resolution microscopy technique (Jungmann et al., 2014), to visualize the nanoscale organization of endogenous clathrin along axons. Axonal boundaries were determined by visualizing β2-spectrin, a component of the submembrane periodic axonal scaffold (for review, see Leterrier et al., 2017). Unlike the tedious APEX EM imaging process involving light/EM correlation of transfected axons, DNA-PAINT allowed us to visualize and characterize a large number (> 500) of axonal clathrin structures. From 3D multicolor DNA-PAINT images of clathrin and β2-

spectrin, we generated 3D renderings for the segmentation and measurement of axonal clathrin particles, some of which are likely to be mobile transport packets (Figure 3C). The average equivalent diameter of clathrin heavy-chain-labeled packets was 43.3 ± 0.5 nm (mean ± SEM; 1,294 packets), consistent with the core size of the structures seen in our EM data, and the average density was 7.6 ± 0.5 packets/μm of axon (82 rendered axonal segments). Interestingly, most clathrin packets seen by super-resolution imaging were close to the β2-spectrin sheath, suggesting associations with the submembrane actin/spectrin scaffold (see cross-sections of axons in Figure 3C and Video S4). Given that the majority of axonal clathrin particles are immobile at any given time, we speculate that this may reflect anchoring of clathrin assemblies to the periodic actin/spectrin lattice.

Composition of axonal clathrin transport packets

To define the composition of axonal clathrin, we immunoprecipitated (IP) clathrin from mouse sciatic axon fractions, followed by MudPIT-MS (multidimensional protein identification technology-mass spectrometry; Liao et al., 2008; Yates et al., 2009); see protocol in Figure S4A. A diverse group of cytosolic proteins were identified (Figure 4A; see Table S1 for a full list, which has also been submitted to the database PRIDE: PXD027857), and as expected, clathrin was one of the most abundant proteins (Figure 4B). We identified 115 proteins, and many were cytosolic proteins that are known to be enriched at synapses (Wilhelm et al., 2014). Network analyses showed that the axonal clathrin interactome contained many cytoskeleton-associated proteins such as actin isoforms and myosins (Figure 4A, dashed circle). Actin and clathrin have established anatomic and functional links in non-neuronal cells (for review, see Kaksonen et al., 2006). Previously, using a probe for filamentous actin (GFP tagged to the calponin homology domain of utrophin, GFP:Utr-CH), we found that axon shafts have focal actin "hotspots" every ~3–4 μm along their length, where actin assembles and disassembles continuously, and that these foci serve as a nidus for nucleation of actin filaments that elongate bidirectionally along the axon shaft ("actin trails"; see Ganguly et al., 2015). Interestingly, simultaneous imaging of GFP:Utr-CH and GFP:CLC showed that there was a striking colocalization of actin hotspots and stationary clathrin in axons, though the actin foci were much more short-lived, as expected (Figures 4C and S4B).

Network analyses also revealed that axonal clathrin was associated with proteins known to disassemble clathrin-coated pits (such as GAK, Hsc70, synaptojanin), as well as those linked to clathrin pit formation (dynamin, AP-complex); see Figure 4A. The presence of both assembly and disassembly proteins in MS datasets is intriguing, as the transported clathrin structure is clearly discrete. To test if candidate assembly/disassembly proteins from the MS dataset are indeed co-transported with clathrin, we visualized the transport of mCherry:CLC with GFP fusions labeling actin, GAK, AP180, and dynamin, using simultaneous two-color live imaging. A significant fraction of GAK was also co-transported with clathrin (Figure 4D). Like clathrin, the dynamics of GAK in dendrites was also very different from axons. As shown in the kymograph in Figure S4C, foci of GFP:GAK typically coincided with clathrin disassembly in dendrites, very different from the mixture of stationary and motile GAK particles seen in axons. Quantification showed that significant amounts of GAK, AP180, and dynamin were co-transported with clathrin (Figure 4E). In previous proteomic studies, we identified Hsc70 as a regulator of the slow axonal transport of synapsin (Ganguly et al., 2017). However, pharmacologic or genetic inhibition of Hsc70 had no effect on the axonal GFP:CLC motility (Figure S4D), suggesting that the mechanistic basis for the transport of the two slow-component cargoes, clathrin and synapsin, is different. Indeed, synapsin has an anterogradely biased diffusion-like flow in axons (Scott et al., 2011; Tang et al., 2013), while clathrin is conveyed as discrete, stable packets.

Nanoscale organization of synaptic clathrin

Clathrin is strongly enriched at presynaptic boutons and terminals, though its precise synaptic function has been controversial in recent years (Chanaday et al., 2019; Milosevic, 2018; Watanabe et al., 2013). Using light microscopy, we noticed that the presynaptic localization of clathrin was not homogeneous, like the classical vesicular or cytosolic synaptic markers synaptophysin or synapsin, but appeared as multiple puncta within a bouton. To pinpoint the spatial relationship of endogenous presynaptic clathrin to synaptic vesicle clusters, we first visualized synapses and adjacent axons at nanometer resolution in 3D, with two-color DNA-PAINT, using antibodies to clathrin and synapsin (the latter to label SV clusters; see STAR methods for details). In the cropped axon and *en passant* bouton shown in Figure 5A (entire image in Figure S5A), note that multiple clathrin particles (magenta) are abutting the SV cluster (green). 3D views (Figure 5B and Video S4) unequivocally show that clathrin particles are circumferentially organized around SVs and rarely seen deep within the SV cluster. Segmented rendering of the super-resolution data showed that each presynapse contains ~4–12 clathrin particles (Figure 5C) that were on average ~43 nm in equivalent diameter (Figure 5D), consistent with the size of clathrin assemblies seen in axon shafts. The morphologic similarities between the axonal and presynaptic clathrin particles suggest that they are related to transport packets, and hereafter we refer to them as "synaptic clathrin packets." The large number of synaptic clathrin packets visualized by DNA-PAINT (> 1,200 packets from > 100 synapses) also allowed us to explore their correlation with SV clusters. The total volume of all clathrin packets at a given synapse correlated with volume of the SV cluster (Figure 5E), suggesting putative links between clathrin levels and SV pools. Taken together, the data suggest that motile axonal transport packets are targeted to presynapses, where they radially organize around SVs.

Though we were not able to confidently visualize the APEX-EM signal at synapses due to high background, we analyzed immuno-gold EM datasets collected by Dr. Tao-Cheng at NINDS/NIH (also see Tao-Cheng, 2020). As shown in the representative images (Figure 5F), immuno-gold particles were mostly seen around—and not within—SV clusters, and some gold particles were associated with vesicular structures resembling endosomes and cisternae (asterisk in Figure 5F, subpanel 2). Coated vesicles are rarely seen at synapses, as reported by previous EM studies (Heuser and Reese, 1973; Kononenko et al., 2014; Petralia et al., 2003; Tao-Cheng, 2020). Taken together, the super-

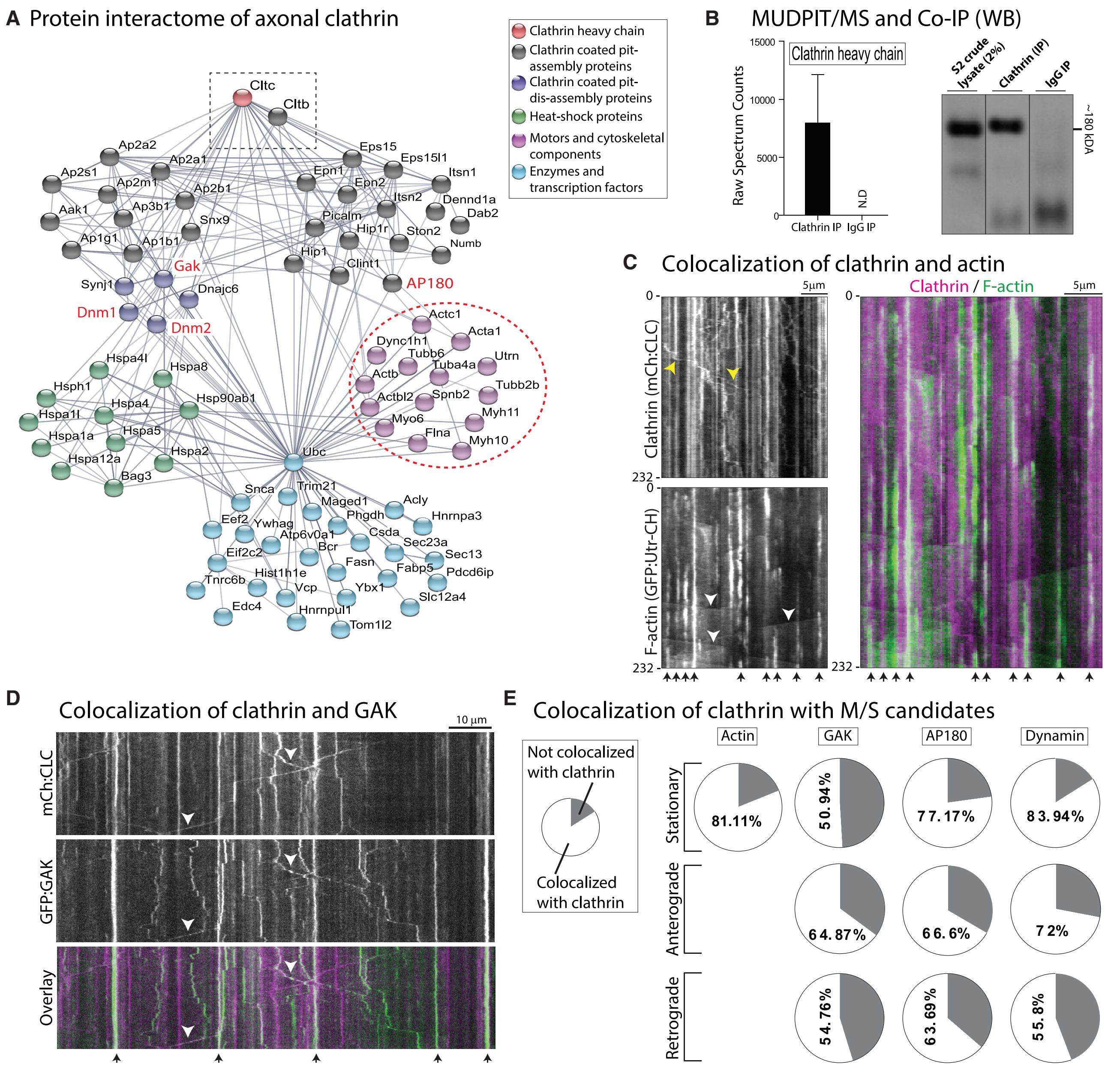

Figure 4. The axonal clathrin interactome

(A) An interactome of clathrin-associated proteins (clathrin marked by dashed rectangle), grouped into functional clusters. The "actin hub" (dashed circle) was of particular interest as previous studies have established mechanistic links between clathrin and actin (see also Results).

(B) High clathrin spectrum counts in MS data, confirmed by western blots showing clathrin in IP fractions.

(C) Kymographs from axons of neurons co-transfected with mCherry:CLC and a GFP-tagged probe for F-actin (GFP:Utr-CH). Note extensive colocalization of stationary clathrin and actin (arrowheads at the bottom, merged kymograph on right). Moving clathrin particles and "actin trails" are marked on the kymographs by yellow and white arrowheads, respectively. Time in seconds is marked on the left of the kymographs, and scale bar on upper right. Scale bars, 5 μm.

(D) Kymographs from axons of neurons co-transfected with mCherry:CLC and GFP:GAK. Note colocalization of stationary particles (arrowheads at the bottom of kymographs), and co-transported clathrin and GAK particles (arrowheads). Time in seconds is marked on the left of the kymographs, and scale bar on upper right. Scale bars, 10 μm.

(E) Quantification of kinetic data from simultaneous imaging of of clathrin with candidates from MS data (GAK, AP180, and dynamin). Note that a substantial amount of clathrin particles were co-transported with GAK, AP180, and dynamin (~140–340 particles were analyzed from 12–19 neurons; data from 2–3 separate cultures).

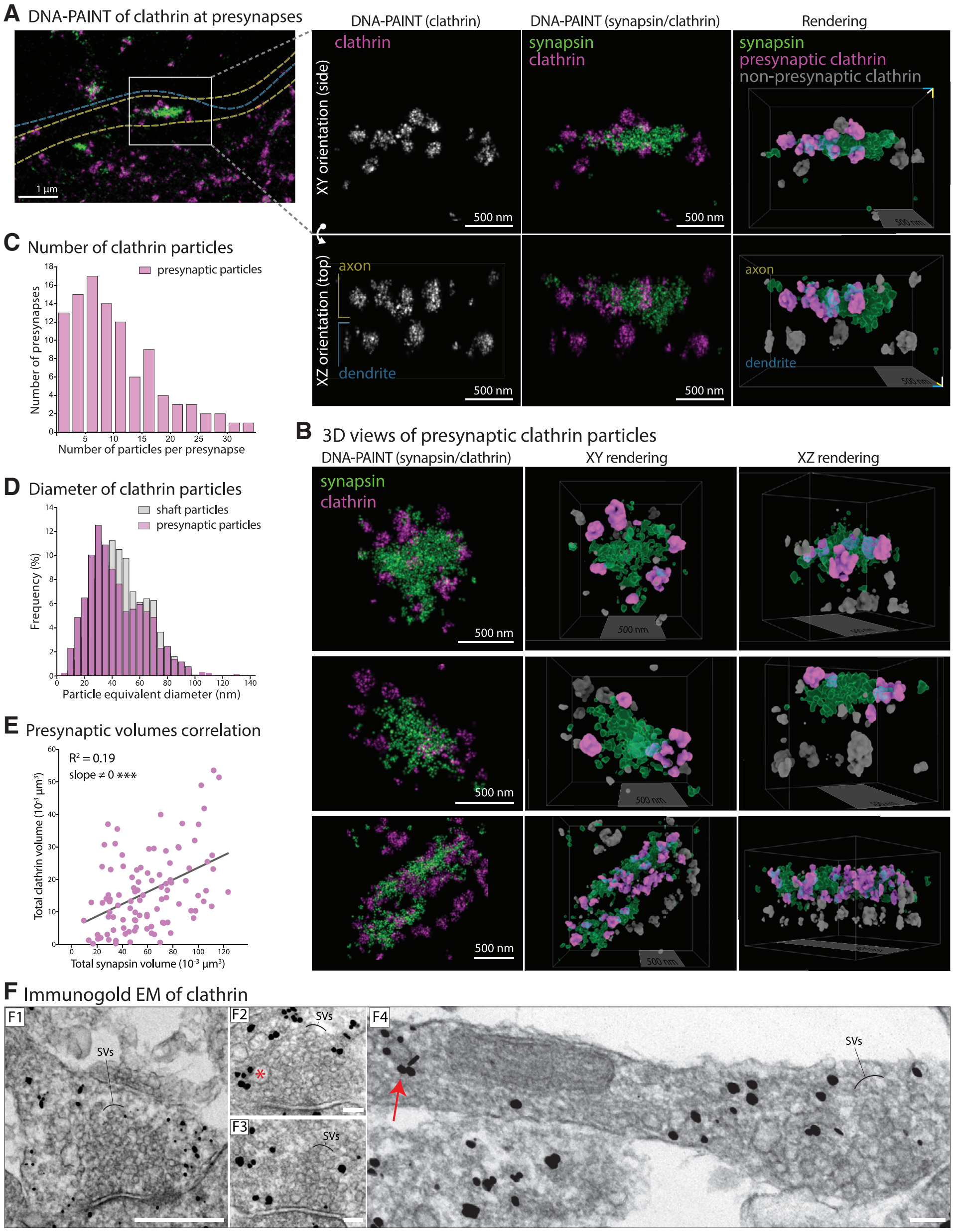

Figure 5. The nanostructure of clathrin at the presynapses

(A) Left: DNA-PAINT of endogenous clathrin (magenta) and synapsin (green, SV marker) at an *en passant* bouton. Outline of a dendrite (blue dashed line) and axon (yellow dashed line) are shown (see full image in Figure S5A); scale bars, 1 μm. Right: 3D views of rectangular inset with XY and XZ (rotated) views, along with 3D rendering and segmentation (extreme right panels). The rendered view shows presynaptic clathrin in magenta, non-presynaptic clathrin in gray, and synapsin in green. Note clathrin particles abutting the presynaptic SV cluster. See also Video S4. Scale bars, 500 nm.

(B) 3D views of more presynapses showing DNA-PAINT image and segmented rendering (see also Video S4). Scale bars, 500 nm.

(C) Histogram of segmented presynaptic clathrin particles per presynapse (1,261 clathrin particles from 102 synapses analyzed).

(D) Overlaid histograms showing frequency distribution of presynaptic clathrin particle diameters (1,261 particles from 3 independent experiments), compared to clathrin particle diameters in axon shaft (685 particles from 3 independent experiments).

(E) Total clathrin volume (cumulative of all clathrin particles) at a given bouton correlated with the total volume of synapsin.

(F) Immuno-gold EM of clathrin (silver enhancement of nanogold particles). F1-F4: Note most particles are located at the periphery of SV clusters, and some are associated with cisternae that may be endosomes (red asterisk in F2 for example). F4 shows a segment of an axon with presynapse, and red arrow marks a coated structure resembling an axonal transport packet. Note that the labeling is specific for clathrin; see also Figure S5B. Scale bar (lower right) for F1 is 500 nm and for F2, F3, and F4 is 100 nm. F1-F4: photo courtesy from Jung-Hwa Tao-Cheng (NINDS/NIH).

resolution and immuno-EM data, along with previous studies, indicate that endogenous synaptic clathrin localizes at the periphery of SV clusters, and the majority of synaptic clathrin is not in the form of coated vesicles.

Clathrin packets are captured and immobilized at synapses

To explore the dynamics of synaptic clathrin, we first visualized GFP:CLC at synapses with relatively high temporal resolution (5 frames/s). Motile clathrin particles rapidly moved between boutons (average velocity 0.54 μm/s) and were often trapped at synapses (kymographs in Figures 6A and S6A). A "pass/trap analysis" (see Figure S6B and STAR methods) indicated that ~60% of the moving particles were retained at boutons for at least a minute (129 particles analyzed from 19 neurons, 3 separate cultures). Within a bouton, clathrin particles moved back and forth, seemingly constrained by the synaptic boundary, though they could exit (Figure 6A'). Single synaptic GFP:CLC particles could be tracked for only a few seconds, suggesting instability (see photoconversion data later). Next, we used FRAP to bleach GFP:CLC in a single bouton and visualized fluorescence recovery over time, reflecting the entry of unbleached fluorescent molecules from adjacent boutons/axons into the bleached zone. As shown in Figure 6B, there was a slow recovery of fluorescence over several minutes, and particles were frequently seen to enter the bleached bouton (best seen in Video S5). Interestingly, FRAP of GFP:CLC fluorescence at boutons was qualitatively very different from GFP:synapsin. While recovery of clathrin was largely due to entry of discrete fluorescent structures—and was somewhat stochastic—synapsin FRAP was gradual and diffuse (Figures 6C and S6C). Also, clathrin mobility in presynaptic boutons decreased over time in our cultures (Figure S6D), likely due to synaptic maturation, reminiscent of the on/off behavior of GFP:CLC in dendrites, which also decreases with time (Blanpied et al., 2002).

Fluorescence recovery of a freely diffusing molecule is expected to be complete (see FRAP of soluble, untagged GFP in boutons, Figure 6D inset), and incomplete recovery reflects a bound, immobile pool that was unable to enter the bleached zone (Lippincott-Schwartz et al., 2003). Though FRAP of both clathrin and synapsin was incomplete, clathrin had a much larger immobile fraction (Figures 6D, 6E, and S6E). A previous study in *C. elegans* found that endophilin, a soluble protein involved in endocytosis, showed diffusion-like mobility between synapses that was blocked when SV recycling was perturbed (Bai et al., 2010); suggesting that the trafficking endophilin pool was generated locally after SV recycling. Though the diffusion-like kinetics of endophilin is very different from the particle movement of clathrin, it is possible that the inter-synaptic movement of clathrin is also dependent on endocytosis, and that the clathrin packets are locally generated at the synapse. To test this, we performed clathrin FRAP experiments before and after adding Dynasore. Dynasore did not attenuate FRAP of clathrin, and unexpectedly, there was an increase in clathrin motility (Figure 6F). One possibility is that blocking endocytosis might decrease the usage of clathrin packets at synapses, allowing more packets to shuttle between synapses (perhaps also increasing their synaptic capture). Indeed, after Dynasore treatment, there was an increase in the number of clathrin packets exchanging between boutons, i.e., exported from one synapse and captured at another (Figure 6G). Collectively, the data suggest that the "superpool clathrin packets" are related to trafficking and not generated at synapses following endocytosis. The increase in the synaptic capture after Dynasore also suggests that synaptic targeting of clathrin may be independent of its function at the synapse.

The morphology and dynamics of synaptic clathrin puncta suggest that axonal transport and subsequent presynaptic "trapping" of a discrete number of transport packets may be the basis of clathrin enrichment at boutons. To further explore morphologic similarities between the transported clathrin and the clathrin localized at synapses, we asked if the total fluorescence of clathrin at individual boutons was an aggregate of integer multiples of axonal puncta/transport packets. Overlaid histogram distributions of GFP:CLC fluorescence intensities in axons (green) and presynapses (red) are shown in Figure 6H (left). Note that while GFP:CLC axonal intensities occupy a single peak, synaptic GFP:CLC intensities are distributed as multiple peaks of higher intensities. Figure 6H (middle) shows predicted fluorescence peaks of synaptic clathrin if they were integer multiples of the axonal intensity peak (assumed as "x1"). From this analysis, single boutons are predicted to contain ~4–8+ clathrin packets (Figure 6H, right). A similar distribution of axonal and synaptic fluorescence was also seen for endogenous clathrin (Figure S6F). Collectively, the data are consistent with a model in which synaptic enrichment of clathrin is largely due to clathrin packets shipped by slow axonal transport.

Dynamics of synaptic clathrin packets

Next, we used photoconvertible clathrin to determine the fate of synaptic clathrin. Neurons were transfected with Dendra2:CLC (green to red photoconversion), and synaptic clathrin was identified by constitutive green fluorescence (see STAR methods for details). Dendra2:CLC in a single bouton was photoconverted to red, and both green (stable) and red (photoconverted) fluorescence was monitored over time. Photoconverted clathrin particles moved out of the synapse into the flanking axons and were often trapped at adjacent boutons (Figure 7A; see also Video S6). Pass/trap analysis showed that ~67% of moving particles were trapped (see Figure S6B and STAR methods for details; 46 particles analyzed from 14 neurons; 3 separate cultures). The overall dispersion of clathrin from photoconverted boutons, determined by decay of red fluorescence over time, is shown in Figure 7B. Previous studies have described a mobile vesicle superpool spanning multiple synaptic boutons and flanking axons, composed of vesicles that are available to synapses during stimulation (Darcy et al., 2006; Krueger et al., 2003; Staras et al., 2010), and pharmacologic experiments suggest that the SV superpool is actin dependent (Darcy et al., 2006; Ratnayaka et al., 2011). Though the kinetics of the clathrin particles in and around synapses resemble the vesicle superpool, interestingly, the peri-synaptic motility of photoconverted Dendra2:CLC particles was microtubule—and not actin—dependent (Figures 7C and 7D).

To explore the dynamics of individual synaptic packets, we photoconverted a single Dendra-2:CLC packet within a bouton and visualized both stable (green) and photoconverted (red)

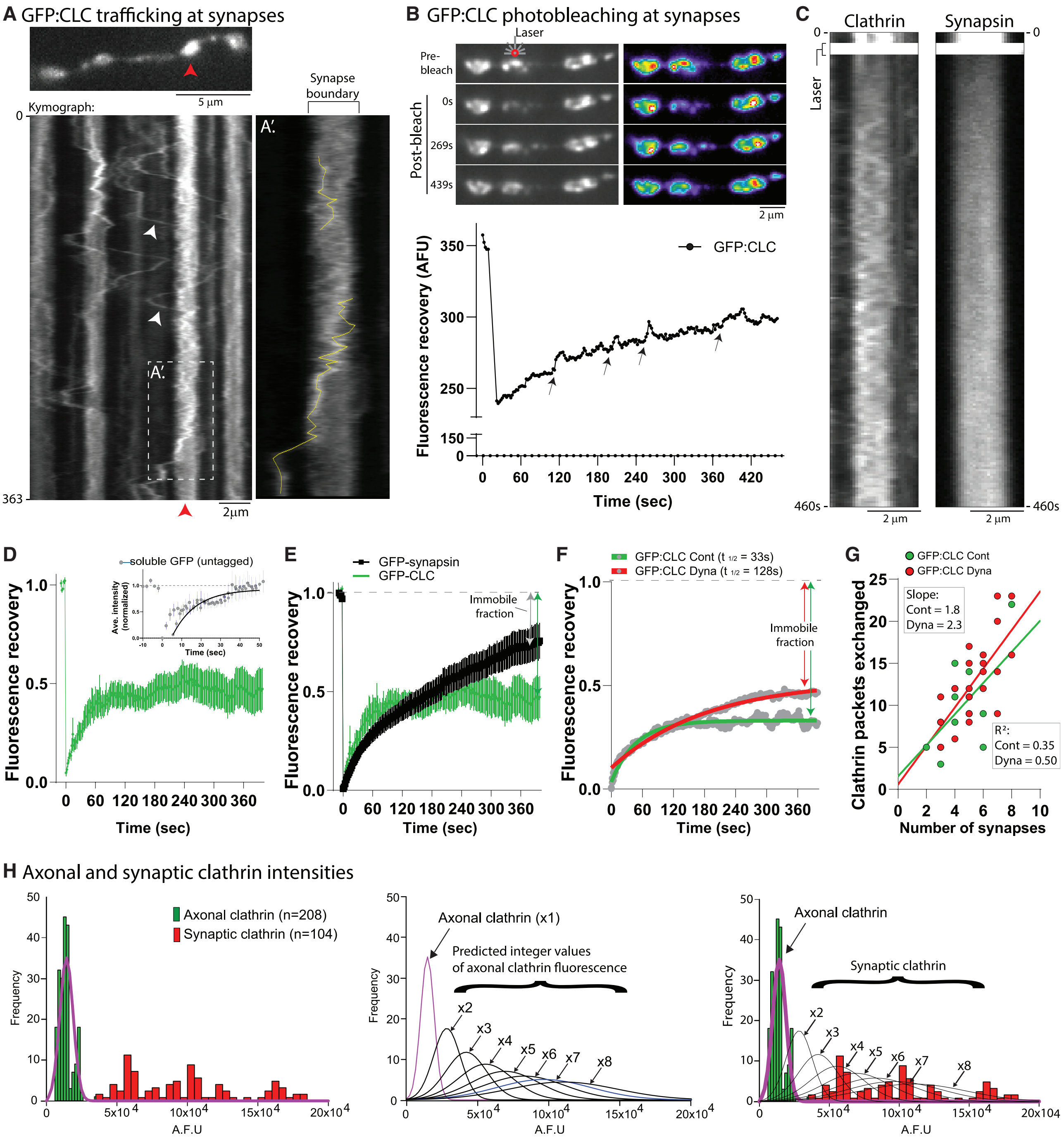

Figure 6. Transported clathrin packets are captured and immobilized at presynapses

(A) Rapid imaging of GFP:CLC around boutons, with first frame on top and kymograph at bottom. Note that clathrin particles are rapidly transported between boutons and often localize to synapses (white arrowheads, targeting to synapse marked by red arrowhead). (A') is a zoom of the boxed region in kymograph showing trajectories of two particles. Scale bar for upper left, 5 μm; lower left, 2 μm.

(B) GFP:CLC was bleached in a single bouton and fluorescence recovery was monitored over time, as shown in the time-series grayscale and pseudocolor heatmap images. Note gradual recovery of fluorescence over time, also evident in the FRAP curve below (small arrowheads point to transient peaks due to particle entry into bleached bouton; see also Video S5). Scale bars, 2 μm.

(C) Bouton kymographs from FRAP of GFP:CLC and GFP:synapsin. Note that while fluorescence recovery of clathrin is particulate, the rise of synapsin fluorescence is diffusive. Scale bars, 2 μm.

(D) Bouton FRAP recovery of GFP:CLC was incomplete, suggesting an immobile pool of clathrin (FRAP of soluble, untagged GFP in boutons recovered completely, inset). For GFP:CLC, 12 neurons were analyzed from 3 separate cultures.

(legend continued on next page)

fluorescence by live imaging. Given the stability of the axonal transport packets, we expected that the fluorescence would be stable in the photoconverted synaptic packet as well. Surprisingly, however, the photoconverted synaptic packet lost fluorescence over tens of seconds, while the other clathrin packets within the same bouton—identified by the stable green fluorescence—gained fluorescence over the same time frame (Figure 7E and Video S7; more examples in Figures S7A and S7A'). Clathrin exchange between synaptic packets was not seen in boutons from neurons fixed with paraformaldehyde (Figure S7B). To quantify the aggregate data from these experiments, we compared the change of fluorescence in the photoconverted packet in a bouton to that of the non-converted ("dark") packets within the same bouton (see basic principle in Figure 7F schematic). If there was exchange, fluorescence would be lost from the photoconverted packet, and there would be a gain of fluorescence in the "dark" regions. As shown in in the graphs in Figure 7F, fluorescence was lost from photoconverted packets in living neurons (left red bar) and gained in the non-photoconverted dark regions (left black bar). However, in fixed boutons, fluorescence was not lost from the photoconverted packet (right red bar, Figure 7F), and there was little change of fluorescence in the non-photoconverted dark regions of the synapse (right black bar, Figure 7F). Occasionally in axons, there was a mechanical dispersion of the axonal fluorescence due to other moving axonal packets that happened to cross the field of view (see Figure S7C for an example). A side-by-side comparison of synaptic and axonal Dendra2:CLC photoactivation is shown in Figure S7D. Collectively, the data suggest that though synaptic clathrin packets are derived from axonal packets, the packets become much more dynamic upon arriving at synapses.

Physiologic role of clathrin packets

Do the clathrin transport/synaptic packets have a physiologic role at synapses? To address this, we designed a system to sequester clathrin packets in the neuronal soma—depleting them from synapses—and then examined SV recycling in the clathrin-depleted boutons using FM4-64, a red styryl dye that is selectively endocytosed into rapidly recycling SVs and has been widely used to evaluate synaptic function (Gaffield and Betz, 2006). Though previous studies have used shRNAs to deplete clathrin over several days, clathrin is required for Golgi formation (Radulescu et al., 2007) and essential for survival (Bazinet et al., 1993). Thus, we sought a more acute knockdown of clathrin, and also a method that visibly depleted the packets from synapses. Toward this, we used the FKBP-Rapalog-FRB heterodimerization system, in which proteins fused to FKBP or FRB dimerize upon adding Rapalog (Belshaw et al., 1996; Bentley et al., 2015; Kapitein et al., 2010; Robinson et al., 2010). We tagged FRB to GFP:CLC (FRB-GFP:CLC), and FKBP to the dynein-binding fragment of BicD2 (BicD2-FKBP ± Tdtomato tag), a dynein cargo adaptor that moves cargoes toward the minus end of microtubules (Dienstbier and Li, 2009).

In our system, Rapalog would induce dimerization of GFP:CLC-labeled clathrin packets and BicD2, transporting them toward the minus end of axonal microtubules and into the neuronal soma, thus depleting clathrin packets from boutons (see schematic in Figure 8A). Figure 8B shows examples of neurons transfected with FRB-GFP:CLC and Tdt:BicD2-FKBP, with or without Rapalog. Note sequestration of GFP:CLC in neuronal cell bodies and its depletion from synapses after incubation with Rapalog (Figure 8C, quantified in Figure 8D). Importantly, almost all of the transfected FRB-GFP:CLC co-assembles with endogenous axonal clathrin (Figures S8A and S8B); thus sequestering FRB-GFP:CLC leads to a depletion of *all* synaptic clathrin in these experiments, including endogenous clathrin (see Figure 8E). Neurons appeared healthy with normal axonal and dendritic arborizations after FKBP/FRB/Rapalog-mediated clathrin sequestration for up to 10 h, and a live/dead assay (Liljebäck et al., 2019) showed no toxicity (Figure S8C).

Next we evaluated SV recycling in the clathrin-depleted boutons using FM-uptake protocols that specifically label the recycling pool (Cousin et al., 2018; see Figure 8F and STAR methods; for discussion of various synaptic pools, see Denker and Rizzoli, 2010). Incubation with Dynasore led to ∼75% decrease in FM uptake (Figure S8D), and as shown in Figure 8G, there was also a significant reduction in FM-dye uptake in the Rapalog-treated neurons (quantified in Figure 8H, similar changes were seen at room temperature as well as 37°C; see Figure S8E). Interestingly, though Rapalog treatment for 10 h led to a greater attenuation of synaptic clathrin when compared to the 5 h Rapalog treatment (see Figures 8D, 8E, and 8G, left graph), the extent of FM attenuation was similar at both 5 h and 10 h time points, suggesting that there may be a finite pool of synaptic clathrin that participates in function, and the remainderacts as a reservoir to help maintain homeostatic protein levels at this locale. Taken together, the data suggest that clathrin packets at the synapse are involved in maintaining SV recycling.

(E) Comparison of GFP:CLC and GFP:synapsin bouton FRAP. Note that clathrin has a larger immobile pool than synapsin (12–14 neurons from 2 or 3 separate cultures were analyzed).

(F) Blocking endocytosis with Dynasore attenuated the immobile fraction of GFP:CLC in bouton-FRAP experiments (i.e., increased mobility of clathrin packets), indicating that FRAP recovery was not due to clathrin on newly generated endosomes at adjacent synapses (11–15 neurons from 3 separate cultures for each condition). For each experiment, the same coverslip was evaluated before/after Dynasore to minimize variability.

(G) More GFP:CLC particles exchanged between synapses after Dynasore treatment (moved from one synapse into another and stayed there for at least a minute). ~200–400 particles moving between ~100 synapses (16–21 neurons per condition) were analyzed.

(H) Integers of axonal clathrin packets localize to synapses. Left: Histogram showing distribution of GFP:CLC intensities in axons and synapses. Note that while axonal clathrin intensities are tightly clustered in a single peak (green), synaptic intensities are distributed as multiple peaks of fluorescence (red). Middle: Mean fluorescence of axonal clathrin was considered as 1x, and hypothetical integer multiple curves were generated (fitted curves shown). Right: Axonal and synaptic GFP:CLC fluorescence data were overlaid with the curves shown in the middle panel. Note that data predict that the synaptic clathrin fluorescence is composed of 4–8+ integer multiples of axonal fluorescence (100–200 particles were analyzed from 3 separate cultures).

Key for kymographs: elapsed time in seconds on left or right and scale bar on lower right (laser illumination also marked).

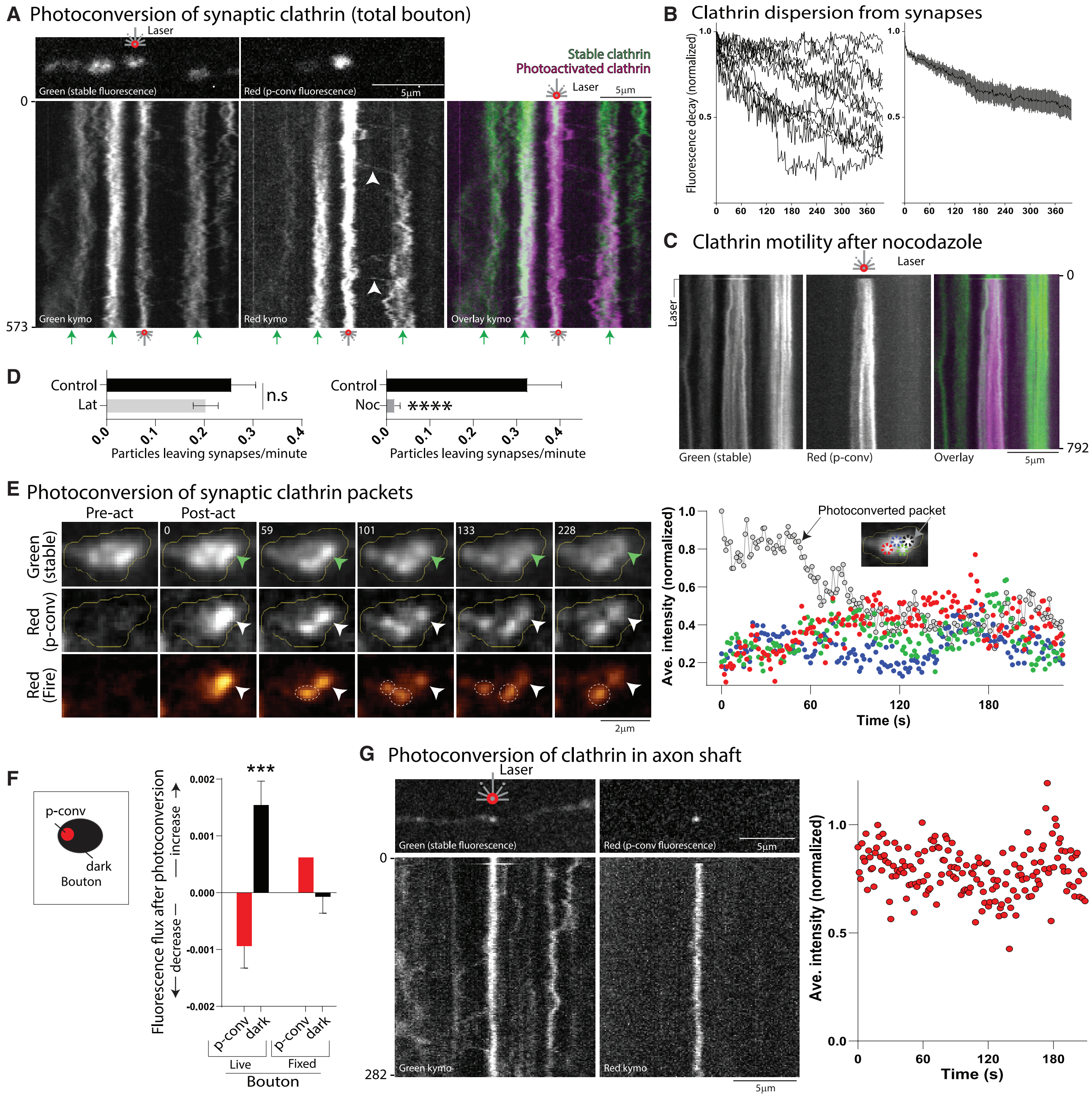

Figure 7. Dynamics of synaptic clathrin packets

(A) First post-photoconverted frames (above) and kymographs (below) from photoconversion of Dendra2:CLC at a single bouton. Photoconverted bouton is marked by red laser symbol and non-photoconverted boutons by small green arrows at bottom. Note that over time, fluorescent clathrin particles leave the single photoactivated bouton and are immobilized at adjacent boutons (white arrowheads in middle kymograph).

(B) Decay of photoconverted Dendra2:CLC red fluorescence from single boutons (raw and ensemble data; 13 neurons from 2 separate cultures).

(C) Nocodazole (10 μg/mL for 40 min) attenuated export of synaptic clathrin particles in single-bouton photoconversion experiments, whereas latrunculin (100 nM for 15 min) had no significant effect.

(D) Quantificaton of data from (C)—15–20 neurons from 2 or 3 separate cultures analyzed for each control- and drug-treated group.

(E) Left: Dendra2:CLC was photoconverted in a single synaptic clathrin packet (arrowhead, elapsed time in seconds on top left). Note that after photoconversion (middle and bottom panels), the photoconverted packet lost fluorescence, while there was an increase of fluorescence in adjacent packets (identified by stable green fluorescence, some marked by dashed circles in bottom panel). Right: Quantification of intensities in individual packets (normalized to highest post-conversion intensity). Colors in graph correspond to the colors of circles marking packets in inset image. Black dashed circle marks the green clathrin packet that was photoconverted to red. Note reciprocal fluctuations in photoconverted and non-photoconverted packets. Scale bars, 2 μm.

(legend continued on next page)

DISCUSSION

Our main findings are: (1) clathrin and related proteins are conveyed in axons as stable coated structures (transport packets), moving intermittently on microtubules with an overall slow anterograde bias; (2) at synapses, most clathrin assemblies (synaptic packets) localize to the periphery of SV clusters, and despite morphologic similarities with transport packets, most synaptic packets lack a conventional coat; (3) mobile clathrin packets shuttle between synapses in a microtubule-dependent superpool, and a significant fraction (~60%) of the moving clathrin is captured at boutons; (4) though axonal clathrin packets are stable, single synaptic clathrin packets can exchange with other neighboring packets within a bouton; and (5) depletion of synaptic clathrin packets impairs SV recycling.

A model for trafficking and presynaptic targeting of clathrin

The most straightforward model emerging from our data is that clathrin and related proteins are synthesized in the neuronal soma, where they are packaged into stable coated structures that are dedicated for transport—with no role in endocytosis. Transport packets move intermittently on microtubules and are conveyed to synapses with an overall anterograde bias in slow axonal transport. Upon reaching the synapse, the conventional coat on the packets is disrupted—perhaps due to the high concentration of uncoating proteins like Hsc70 at this locale (Ganguly et al., 2017)—allowing clathrin to dynamically exchange with other local packets. Thus, at synapses, clathrin molecules would either be associated with a synaptic packet or exchange between local packets. This metastable state would provide a labile local pool of clathrin that could be rapidly recruited for synaptic function, as needed. In this hypothetical model, clathrin would undergo a seamless transition from transport to function upon reaching the synapse, simply by dynamically shedding the coat on the transport carrier.

Despite the dynamic exchange, our experiments strongly suggest that the synaptic clathrin is not freely diffusible as commonly believed. For instance, in photoconversion experiments (Figure 7A), we only saw discrete clathrin particles leave boutons, and incubation with nocodazole—which stalled the mobility of the synaptic clathrin packets—did not lead to a loss of clathrin from the stalled structures over time (Figure 7C), which would be predicted if this clathrin was freely diffusible. However, the precise structures on which the synaptic clathrin localizes are still unclear, though immuno-EM data suggest that some of the clathrin may be on cisternae/endosomes (Figure 5F). Our MS data and two-color live imaging also suggest that many proteins related to endocytosis are co-transported with clathrin, so once the transport packets reach the synapse, perhaps they too would be available for performing their functions. Thus, conceptually, our model may have broad consequences for neuronal form and function.

Synapses have integer multiples of clathrin transport packets (Figure 6G), which is also consistent with our working model wherein clathrin trafficking and targeting are interconnected events. However, EM suggests that while axonal clathrin packets are coated, most of the synaptic clathrin lacks a conventional coat. Previous studies have shown that clathrin-coated vesicles are infrequent in resting hippocampal synapses—for example, in a recent detailed study, only ~5–10 coated vesicles were seen per 100 presynaptic profiles (Tao-Cheng, 2020)—but it is clear that clathrin is abundant at synapses, obvious by routine immunostaining. Our live-imaging, super-resolution, and EM data provide some clarity on this issue, showing that most of the synaptic clathrin (1) is organized into discrete structures, and not as free monomers, and (2) does not resemble conventional clathrin-coated vesicles. Another prediction of our model is that during transport, the stable clathrin on axonal transport packets would not be functionally available, which might be a way of preventing unwanted endocytosis along the axon shaft.

Clathrin transport packets: a carrier for slow axonal transport

Though the phenomenon of cytosolic slow transport is established, the nature of transported cargoes has been puzzling. In previous imaging studies of other slow-component cargoes (like synapsin and CamKII), we saw transient mobile structures—lasting for a few seconds at best—that appeared to contribute to the overall anterograde movement (Roy, 2014; Scott et al., 2011), but the exact cargo structure remained unclear. The discrete nature of axonal clathrin enabled us to examine the cargo structure at a nanoscale level by 3D EM and super-resolution imaging, and clathrin is probably the first cytosolic cargo to be characterized in detail. Based on the overlapping of radiolabeled "peaks" in axons, previous studies hypothesized that common mechanisms were involved in slow transport (for review, see Roy, 2014, 2020). However, the synaptic dynamics of two slow transport cargoes, clathrin and synapsin, is very different (Figure 6C), and an emerging theme in slow transport is the diversity in the nature and mechanisms of movement (Roy, 2020).

The structure of an axonal transport packet resembles clathrin-coated vesicles. However, coated vesicles are thought to be transient intermediates that deliver endocytosed vesicles and their contents either to Golgi/endosomes or back to the plasma membrane (for review, see Paraan et al., 2020), while the transport packets are long lasting structures that are

(F) Quantification of fluorescence change after single-packet photoconversion in boutons. Schematic on left shows general principle of quantifying photoconverted and non-photoconverted (dark) regions; see STAR methods for details. Note loss of intensity from photoconverted packet within bouton (red bar, left), with a corresponding gain in adjacent non-converted regions (black bar, left). Similar reciprocal changes in fluorescence were not seen after fixing the neurons, though the photoactivation still occurred as expected (red/black middle bars; 6 neurons from 1 culture for fixed boutons and 10 cells from 2 separate cultures for live boutons).

(G) Photoconversion of single Dendra2:CLC clathrin packet in axon. Note no change in fluorescence, quantified on right (8 neurons from 2 separate cultures analyzed). Scale bars, 5 μm.

Time in seconds on left or right of kymograph and scale bar on upper right. ****$p < 0.0001$, ***$p < 0.001$. See Figure S7 for more examples.

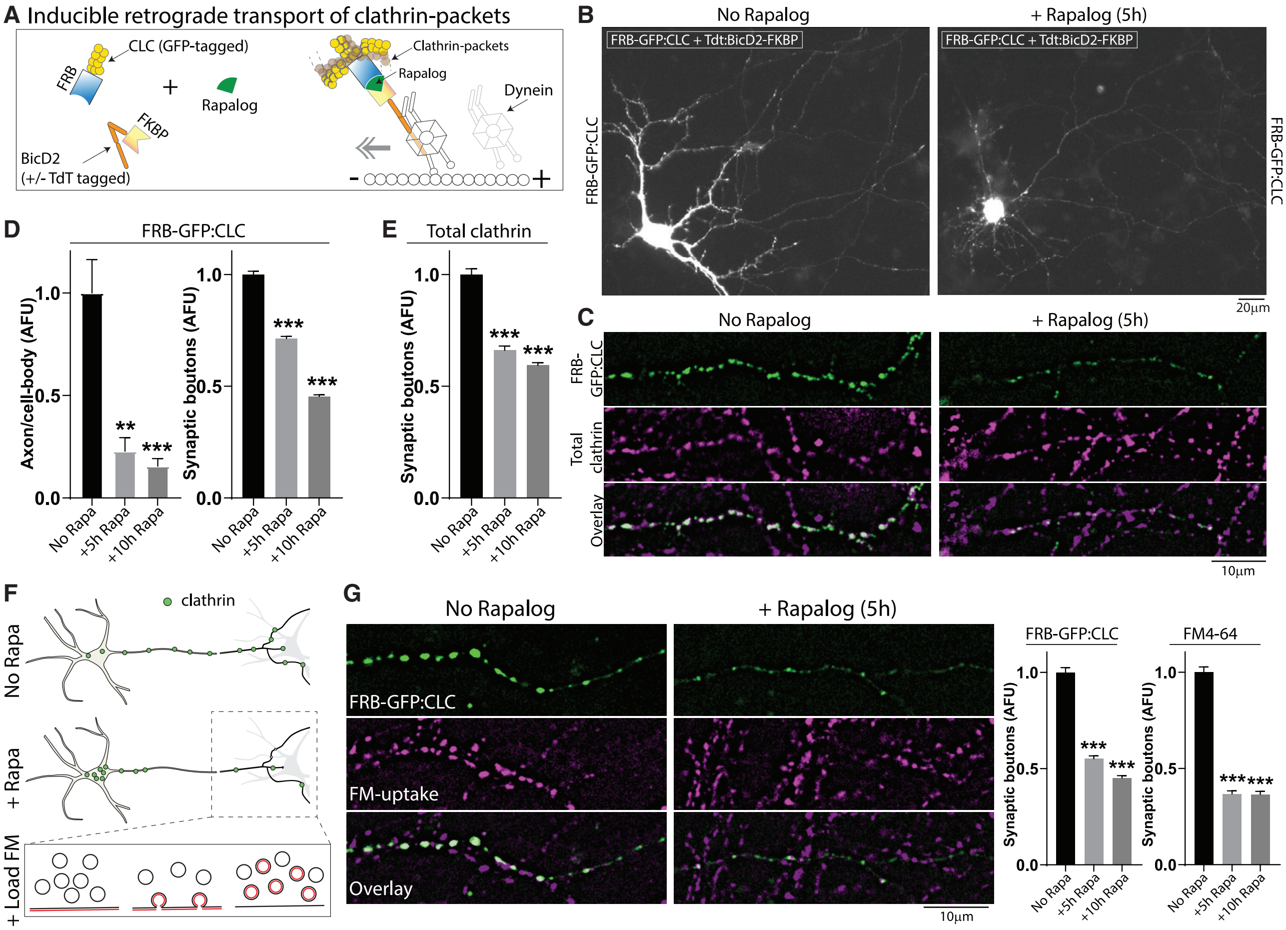

Figure 8. Depletion of synaptic clathrin packets impairs function

(A) Principle: GFP:CLC was tagged to FRB, and the dynein adaptor BicD2 was tagged to FKBP (+/− TdTomato). Upon adding Rapalog, FKBP and FRB—along with clathrin and BicD2—would dimerize, transporting clathrin packets into the soma and depleting them from synapses.

(B) Representative images showing clustering of FRB-GFP:CLC in cell bodies after Rapalog treatment (constructs used on top left of images). Also note that transfected FRB-GFP:CLC extensively colocalizes with endogenous clathrin (Figure S8). Scale bars, 20 μm.

(C) Representative images showing that upon Rapalog treatment, both tagged and endogenous clathrin is depleted from boutons, quantified in (D) and (E); ~900–1800 boutons were analyzed for each condition from 3 separate coverslips. Scale bars, 10 μm.

(F) Schematic showing plan of FM-dye uptake experiments (to evaluate SV recycling) in clathrin-depleted boutons.

(G) Representative images (left) and quantification (right) showing the reduction of both clathrin and FM uptake in Rapalog-treated neurons at room temperature (~600–950 boutons were analyzed for each condition from 3 separate cultures). Similar results were seen at 37°C; see Figure S8E. $^{**}p < 0.01$, $^{***}p < 0.001$. Scale bars, 10 μm.

delivered to distal synapses. Though previous studies in non-neuronal cells have described motile coated intermediates in the cytoplasm (Keyel et al., 2004; Puertollano et al., 2003; Rappoport and Simon, 2003; Rappoport et al., 2003a, 2003b), these seem different from the axonal transport packets. First, the intermediates are described as large, pleomorphic tubulovesicular aggregates (Polishchuk et al., 2006; Puertollano et al., 2003), different from the ~40–50 nm uniform-sized structures we see in the axon (Figure 3). Also, the clathrin in these moving intermediates is reported to "cycle on and off"—eventually fusing with early or late endosomes (Puertollano et al., 2003)—which is also different from the stable structures we see in axons. However, it is possible that the transported clathrin packet is a stable form of specialized coated vesicle dedicated to slow transport.

Alternatively, the transported structure might represent clathrin assemblies that are not around vesicles. Indeed, the lumens of clathrin transport packets do not appear electron dense (see Figure 3B''), though cryo-EM might be conclusive. Interestingly, "clathrin baskets"—clathrin cages with no vesicles inside—are routinely isolated from biochemical fractionations of bovine brains (Nandi et al., 1982) and, in fact, comprise ~80% of the clathrin structures isolated in these preparations (Heymann et al., 2013). Clathrin baskets are thought to be artifacts, assembled in the homogenate during biochemical isolation (Heymann et al., 2013). However, given the long-lasting coated transport packets we describe here, and the large combined relative volumes that axons must occupy in brain homogenate preparations, it is conceivable that clathrin baskets are actually axonal transport packets. One caveat in our experiments is that our APEX-EM experiments cannot distinguish between transported and stationary clathrin in the axon.

Mechanistic implications of clathrin trafficking and targeting

The movement of clathrin between presynaptic boutons resembles SV superpools that are thought to be an extension of local SV pools (Staras et al., 2010). However, while the SV superpool is dependent on actin dynamics, the "clathrin superpool" depends on microtubules (Figure 7D) and may be a distinct superpool conveying endocytic (and perhaps other slow-component) proteins. Interestingly, the mobility of clathrin particles is also different from the soluble diffusive motion of endophilin (Bai et al., 2010), so it seems likely that there are many components to the superpool. Substantial evidence from our live-imaging, photobleaching, and photoconversion experiments supports the view that trafficking clathrin packets are captured at synapses (Figures 6 and 7) and that their depletion causes functional deficits (Figure 8); thus, it seems reasonable that the trafficking pool is critical for synaptic function. We posit that at any given synapse, multiple synaptic clathrin packets may act as local reservoirs that are "poised" to provide functional clathrin molecules that would be locally available in the vicinity of SVs, thus speeding up SV recycling. Some studies suggest that clathrin may be locally translated at axons and synapses (Biever et al., 2020; Shigeoka et al., 2016), and our experiments do not exclude a possible role for local translation, though it is clear that axonal transport is a major route for synaptic delivery of clathrin. The function of clathrin at synapses has been controversial in recent years, and clathrin has been proposed to play roles in SV biogenesis, particularly at physiologic temperatures (Delvendahl et al., 2016; Soykan et al., 2017; Watanabe et al., 2013). In that context, our key experiments were done at ~37°C, though our experiments cannot directly distinguish between the different models. Finally, the behavior of synaptic clathrin resembles the movement of soluble molecules within liquid condensates and may be conceptually related to the contemporary idea that SV clusters have fluid-like properties (Milovanovic et al., 2018). Interestingly, recent studies in non-neuronal cells indicate that CME also relies on the formation of liquid condensates (Day et al., 2021; Witkowska and Haucke, 2021), and future experiments focused on these issues might bring more clarity.

STAR★METHODS

Detailed methods are provided in the online version of this paper and include the following:

SUPPLEMENTAL INFORMATION

Supplemental information can be found online at https://doi.org/10.1016/j.neuron.2021.08.016.

ACKNOWLEDGMENTS

This work was supported by a NIH grant to S.R. (R01NS075233), a CNRS ATIP grant to C.L. (ATIP2016), NIH grants to D.B. (R01GM086197) and M.H.E. (P41 GM103412) supporting the National Center for Microscopy and Imaging Research, and NIH grants to J.R.Y. (P41 GM103533 and R01 MH100175). The authors thank Titus Jung for proteomic data handling and various investigators for generously sharing constructs (listed in STAR methods).

AUTHOR CONTRIBUTIONS

S.R. conceived the project. A.G., R.S., and S.R. designed most of the experiments and analyzed the data. C.L., F.W., and G.C. designed and performed the DNA-PAINT experiments and data analyses. A.G. performed the live-imaging experiments in axons and dendrites and analyzed most of the ensuing data. Electron microscopy/analysis was performed by A.G., with assistance from D.B. and S.P. at NCMIR, led by M.H.E. Samples for mass spectrometry were prepared by A.G.; experiments were performed by X.H. under the supervision of J.R.Y.; and ensuing data were analyzed by X.H. and A.G. R.S. performed the synaptic live imaging, photo-manipulation, FKBP/FRB/FM uptake, and live/dead assay experiments; analyzed the ensuing data; and helped analyze some of the axonal transport data. N.P.B. designed strategies to analyze the photo-manipulation experiments and performed most of the ensuing analyses, with assistance from R.S. and S.R. L.P. helped with neuronal cultures, and U.D. and L.P. designed and generated constructs. S.R. wrote the manuscript, with contributions from C.L., R.S., and A.G.

DECLARATION OF INTERESTS

The authors declare no competing interests.

Received: March 1, 2020
Revised: June 10, 2021
Accepted: August 13, 2021
Published: September 15, 2021

REFERENCES

Applewhite, D.A., Barzik, M., Kojima, S., Svitkina, T.M., Gertler, F.B., and Borisy, G.G. (2007). Ena/VASP proteins have an anti-capping independent function in filopodia formation. Mol. Biol. Cell *18*, 2579–2591.

Bai, J., Hu, Z., Dittman, J.S., Pym, E.C., and Kaplan, J.M. (2010). Endophilin functions as a membrane-bending molecule and is delivered to endocytic zones by exocytosis. Cell *143*, 430–441.

Bazinet, C., Katzen, A.L., Morgan, M., Mahowald, A.P., and Lemmon, S.K. (1993). The Drosophila clathrin heavy chain gene: clathrin function is essential in a multicellular organism. Genetics *134*, 1119–1134.

Belshaw, P.J., Ho, S.N., Crabtree, G.R., and Schreiber, S.L. (1996). Controlling protein association and subcellular localization with a synthetic ligand that induces heterodimerization of proteins. Proc. Natl. Acad. Sci. USA *93*, 4604–4607.

Bennett, E.M., Chen, C.Y., Engqvist-Goldstein, A.E., Drubin, D.G., and Brodsky, F.M. (2001). Clathrin hub expression dissociates the actin-binding protein Hip1R from coated pits and disrupts their alignment with the actin cytoskeleton. Traffic *2*, 851–858.

Bentley, M., Decker, H., Luisi, J., and Banker, G. (2015). A novel assay reveals preferential binding between Rabs, kinesins, and specific endosomal subpopulations. J. Cell Biol. *208*, 273–281.

Biever, A., Glock, C., Tushev, G., Ciirdaeva, E., Dalmay, T., Langer, J.D., and Schuman, E.M. (2020). Monosomes actively translate synaptic mRNAs in neuronal processes. Science *367*, eaay4991. https://doi.org/10.1126/science.aay4991.

Black, M.M., Chestnut, M.H., Pleasure, I.T., and Keen, J.H. (1991). Stable clathrin: uncoating protein (hsc70) complexes in intact neurons and their axonal transport. J. Neurosci. *11*, 1163–1172.

Blanpied, T.A., Scott, D.B., and Ehlers, M.D. (2002). Dynamics and regulation of clathrin coats at specialized endocytic zones of dendrites and spines. Neuron *36*, 435–449.

Boyer, N.P., McCormick, L.E., Menon, S., Urbina, F.L., and Gupton, S.L. (2020). A pair of E3 ubiquitin ligases compete to regulate filopodial dynamics and axon guidance. J. Cell Biol. *219*, e201902088.

Burkel, B.M., von Dassow, G., and Bement, W.M. (2007). Versatile fluorescent probes for actin filaments based on the actin-binding domain of utrophin. Cell Motil. Cytoskeleton *64*, 822–832.

Bushlin, I., Petralia, R.S., Wu, F., Harel, A., Mughal, M.R., Mattson, M.P., and Yao, P.J. (2008). Clathrin assembly protein AP180 and CALM differentially control axogenesis and dendrite outgrowth in embryonic hippocampal neurons. J. Neurosci. *28*, 10257–10271.

Chakrabarty, N., Dubey, P., Tang, Y., Ganguly, A., Ladt, K., Leterrier, C., Jung, P., and Roy, S. (2019). Processive flow by biased polymerization mediates the slow axonal transport of actin. J. Cell Biol. *218*, 112–124.

Chanaday, N.L., and Kavalali, E.T. (2018). Optical detection of three modes of endocytosis at hippocampal synapses. eLife *7*, e36097.

Chanaday, N.L., Cousin, M.A., Milosevic, I., Watanabe, S., and Morgan, J.R. (2019). The Synaptic Vesicle Cycle Revisited: New Insights into the Modes and Mechanisms. J. Neurosci. *39*, 8209–8216.

Cousin, M.A., Gordon, S.L., and Smillie, K.J. (2018). Using FM dyes to monitor clathrin-mediated endocytosis in primary neuronal culture. Clathrin-Mediated Endocytosis (Humana Press), pp. 239–249.

Darcy, K.J., Staras, K., Collinson, L.M., and Goda, Y. (2006). Constitutive sharing of recycling synaptic vesicles between presynaptic boutons. Nat. Neurosci. *9*, 315–321.

Das, U., Scott, D.A., Ganguly, A., Koo, E.H., Tang, Y., and Roy, S. (2013). Activity-induced convergence of APP and BACE-1 in acidic microdomains via an endocytosis-dependent pathway. Neuron *79*, 447–460.

Day, K.J., Kago, G., Wang, L., Richter, J.B., Hayden, C.C., Lafer, E.M., and Stachowiak, J.C. (2021). Liquid-like protein interactions catalyse assembly of endocytic vesicles. Nat. Cell Biol. *23*, 366–376.

de Waegh, S., and Brady, S.T. (1989). Axonal transport of a clathrin uncoating ATPase (HSC70): a role for HSC70 in the modulation of coated vesicle assembly in vivo. J. Neurosci. Res. *23*, 433–440.

Delvendahl, I., Vyleta, N.P., von Gersdorff, H., and Hallermann, S. (2016). Fast, Temperature-Sensitive and Clathrin-Independent Endocytosis at Central Synapses. Neuron *90*, 492–498.

Denker, A., and Rizzoli, S.O. (2010). Synaptic vesicle pools: an update. Front. Synaptic Neurosci. *2*, 135.

Dienstbier, M., and Li, X. (2009). Bicaudal-D and its role in cargo sorting by microtubule-based motors. Biochem. Soc. Trans. *37*, 1066–1071.

Dittman, J., and Ryan, T.A. (2009). Molecular circuitry of endocytosis at nerve terminals. Annu. Rev. Cell Dev. Biol. *25*, 133–160.

Elluru, R.G., Bloom, G.S., and Brady, S.T. (1995). Fast axonal transport of kinesin in the rat visual system: functionality of kinesin heavy chain isoforms. Mol. Biol. Cell *6*, 21–40.

Gaffield, M.A., and Betz, W.J. (2006). Imaging synaptic vesicle exocytosis and endocytosis with FM dyes. Nat. Protoc. *1*, 2916–2921.

Gaidarov, I., Santini, F., Warren, R.A., and Keen, J.H. (1999). Spatial control of coated-pit dynamics in living cells. Nat. Cell Biol. *1*, 1–7.

Ganguly, A., and Roy, S. (2014). Using photoactivatable GFP to track axonal transport kinetics. Methods Mol. Biol. *1148*, 203–215.

Ganguly, A., Tang, Y., Wang, L., Ladt, K., Loi, J., Dargent, B., Leterrier, C., and Roy, S. (2015). A dynamic formin-dependent deep F-actin network in axons. J. Cell Biol. *210*, 401–417.

Ganguly, A., Han, X., Das, U., Wang, L., Loi, J., Sun, J., Gitler, D., Caillol, G., Leterrier, C., Yates, J.R., 3rd, and Roy, S. (2017). Hsc70 chaperone activity is required for the cytosolic slow axonal transport of synapsin. J. Cell Biol. *216*, 2059–2074.

Garner, J.A., and Lasek, R.J. (1981). Clathrin is axonally transported as part of slow component b: the microfilament complex. J. Cell Biol. *88*, 172–178.

Gerrow, K., Romorini, S., Nabi, S.M., Colicos, M.A., Sala, C., and El-Husseini, A. (2006). A preformed complex of postsynaptic proteins is involved in excitatory synapse development. Neuron *49*, 547–562.

Gitler, D., Xu, Y., Kao, H.T., Lin, D., Lim, S., Feng, J., Greengard, P., and Augustine, G.J. (2004). Molecular determinants of synapsin targeting to presynaptic terminals. J. Neurosci. *24*, 3711–3720.

Goddard, T.D., Huang, C.C., Meng, E.C., Pettersen, E.F., Couch, G.S., Morris, J.H., and Ferrin, T.E. (2018). UCSF ChimeraX: Meeting modern challenges in visualization and analysis. Protein Sci. *27*, 14–25.

Gower, D.J., and Tytell, M. (1987). Axonal transport of clathrin-associated proteins. Brain Res. *407*, 1–8.

Heuser, J.E., and Reese, T.S. (1973). Evidence for recycling of synaptic vesicle membrane during transmitter release at the frog neuromuscular junction. J. Cell Biol. *57*, 315–344.

Heymann, J.B., Winkler, D.C., Yim, Y.I., Eisenberg, E., Greene, L.E., and Steven, A.C. (2013). Clathrin-coated vesicles from brain have small payloads: a cryo-electron tomographic study. J. Struct. Biol. *184*, 43–51.

Jimenez, A., Friedl, K., and Leterrier, C. (2020). About samples, giving examples: Optimized Single Molecule Localization Microscopy. Methods *174*, 100–114.

Jung, N., and Haucke, V. (2007). Clathrin-mediated endocytosis at synapses. Traffic *8*, 1129–1136.

Jungmann, R., Avendaño, M.S., Woehrstein, J.B., Dai, M., Shih, W.M., and Yin, P. (2014). Multiplexed 3D cellular super-resolution imaging with DNA-PAINT and Exchange-PAINT. Nat. Methods *11*, 313–318.

Kaksonen, M., Toret, C.P., and Drubin, D.G. (2006). Harnessing actin dynamics for clathrin-mediated endocytosis. Nat. Rev. Mol. Cell Biol. *7*, 404–414.

Kapitein, L.C., Schlager, M.A., van der Zwan, W.A., Wulf, P.S., Keijzer, N., and Hoogenraad, C.C. (2010). Probing intracellular motor protein activity using an inducible cargo trafficking assay. Biophys. J. *99*, 2143–2152.

Keyel, P.A., Watkins, S.C., and Traub, L.M. (2004). Endocytic adaptor molecules reveal an endosomal population of clathrin by total internal reflection fluorescence microscopy. J. Biol. Chem. *279*, 13190–13204.

Kononenko, N.L., Puchkov, D., Classen, G.A., Walter, A.M., Pechstein, A., Sawade, L., Kaempf, N., Trimbuch, T., Lorenz, D., Rosenmund, C., et al. (2014). Clathrin/AP-2 mediate synaptic vesicle reformation from endosome-like vacuoles but are not essential for membrane retrieval at central synapses. Neuron *82*, 981–988.

Kremer, J.R., Mastronarde, D.N., and McIntosh, J.R. (1996). Computer visualization of three-dimensional image data using IMOD. J. Struct. Biol. *116*, 71–76.

Krueger, S.R., Kolar, A., and Fitzsimonds, R.M. (2003). The presynaptic release apparatus is functional in the absence of dendritic contact and highly mobile within isolated axons. Neuron *40*, 945–957.

Lawrence, A., Bouwer, J.C., Perkins, G., and Ellisman, M.H. (2006). Transform-based backprojection for volume reconstruction of large format electron microscope tilt series. J. Struct. Biol. *154*, 144–167.

Leterrier, C., Dubey, P., and Roy, S. (2017). The nano-architecture of the axonal cytoskeleton. Nat. Rev. Neurosci. *18*, 713–726.

Liao, L., Park, S.K., Xu, T., Vanderklish, P., and Yates, J.R., 3rd (2008). Quantitative proteomic analysis of primary neurons reveals diverse changes in synaptic protein content in fmr1 knockout mice. Proc. Natl. Acad. Sci. USA *105*, 15281–15286.

Liljebäck, H., Quach, M., Carlsson, P.-O., and Lau, J. (2019). Fewer Islets Survive from a First Transplant than a Second Transplant: Evaluation of Repeated Intraportal Islet Transplantation in Mice. Cell Transplant. *28*, 1455–1460.

Lippincott-Schwartz, J., Altan-Bonnet, N., and Patterson, G.H. (2003). Photobleaching and photoactivation: following protein dynamics in living cells. Nat. Cell Biol. *Suppl* (*Suppl*), S7–S14.

Liu, S.H., Marks, M.S., and Brodsky, F.M. (1998). A dominant-negative clathrin mutant differentially affects trafficking of molecules with distinct sorting motifs in the class II major histocompatibility complex (MHC) pathway. J. Cell Biol. *140*, 1023–1037.

Macia, E., Ehrlich, M., Massol, R., Boucrot, E., Brunner, C., and Kirchhausen, T. (2006). Dynasore, a cell-permeable inhibitor of dynamin. Dev. Cell *10*, 839–850.

Maday, S., Twelvetrees, A.E., Moughamian, A.J., and Holzbaur, E.L. (2014). Axonal transport: cargo-specific mechanisms of motility and regulation. Neuron *84*, 292–309.

Martell, J.D., Deerinck, T.J., Sancak, Y., Poulos, T.L., Mootha, V.K., Sosinsky, G.E., Ellisman, M.H., and Ting, A.Y. (2012). Engineered ascorbate peroxidase as a genetically encoded reporter for electron microscopy. Nat. Biotechnol. *30*, 1143–1148.

Massol, R.H., Boll, W., Griffin, A.M., and Kirchhausen, T. (2006). A burst of auxilin recruitment determines the onset of clathrin-coated vesicle uncoating. Proc. Natl. Acad. Sci. USA *103*, 10265–10270.

Mastronarde, D.N. (2005). Automated electron microscope tomography using robust prediction of specimen movements. J. Struct. Biol. *152*, 36–51.

McDonald, W.H., Tabb, D.L., Sadygov, R.G., MacCoss, M.J., Venable, J., Graumann, J., Johnson, J.R., Cociorva, D., and Yates, J.R., 3rd (2004). MS1, MS2, and SQT-three unified, compact, and easily parsed file formats for the storage of shotgun proteomic spectra and identifications. Rapid Commun. Mass Spectrom. *18*, 2162–2168, 2168.g.

McMahon, H.T., and Boucrot, E. (2011). Molecular mechanism and physiological functions of clathrin-mediated endocytosis. Nat. Rev. Mol. Cell Biol. *12*, 517–533.

Milosevic, I. (2018). Revisiting the Role of Clathrin-Mediated Endoytosis in Synaptic Vesicle Recycling. Front. Cell. Neurosci. *12*, 27.

Milovanovic, D., Wu, Y., Bian, X., and De Camilli, P. (2018). A liquid phase of synapsin and lipid vesicles. Science *361*, 604–607.

Mueller, V.J., Wienisch, M., Nehring, R.B., and Klingauf, J. (2004). Monitoring clathrin-mediated endocytosis during synaptic activity. J. Neurosci. *24*, 2004–2012.

Nandi, P.K., Irace, G., Van Jaarsveld, P.P., Lippoldt, R.E., and Edelhoch, H. (1982). Instability of coated vesicles in concentrated sucrose solutions. Proc. Natl. Acad. Sci. USA *79*, 5881–5885.

Paraan, M., Mendez, J., Sharum, S., Kurtin, D., He, H., and Stagg, S.M. (2020). The structures of natively assembled clathrin-coated vesicles. Sci. Adv. *6*, a8397.

Patterson, G.H., and Lippincott-Schwartz, J. (2002). A photoactivatable GFP for selective photolabeling of proteins and cells. Science *297*, 1873–1877.

Pelassa, I., Zhao, C., Pasche, M., Odermatt, B., and Lagnado, L. (2014). Synaptic vesicles are "primed" for fast clathrin-mediated endocytosis at the ribbon synapse. Front. Mol. Neurosci. *7*, 91.

Peng, J., Kim, M.J., Cheng, D., Duong, D.M., Gygi, S.P., and Sheng, M. (2004). Semiquantitative proteomic analysis of rat forebrain postsynaptic density fractions by mass spectrometry. J. Biol. Chem. *279*, 21003–21011.

Perez-Riverol, Y., Xu, Q.W., Wang, R., Uszkoreit, J., Griss, J., Sanchez, A., Reisinger, F., Csordas, A., Ternent, T., Del-Toro, N., et al. (2016). PRIDE Inspector Toolsuite: Moving Toward a Universal Visualization Tool for Proteomics Data Standard Formats and Quality Assessment of ProteomeXchange Datasets. Mol. Cell. Proteomics *15*, 305–317.

Petralia, R.S., Wang, Y.X., and Wenthold, R.J. (2003). Internalization at glutamatergic synapses during development. Eur. J. Neurosci. *18*, 3207–3217.

Phan, S., Boassa, D., Nguyen, P., Wan, X., Lanman, J., Lawrence, A., and Ellisman, M.H. (2017). 3D reconstruction of biological structures: automated procedures for alignment and reconstruction of multiple tilt series in electron tomography. Adv. Struct. Chem. Imaging *2*, 8.

Polishchuk, R.S., San Pietro, E., Di Pentima, A., Teté, S., and Bonifacino, J.S. (2006). Ultrastructure of long-range transport carriers moving from the trans Golgi network to peripheral endosomes. Traffic *7*, 1092–1103.

Puertollano, R., van der Wel, N.N., Greene, L.E., Eisenberg, E., Peters, P.J., and Bonifacino, J.S. (2003). Morphology and dynamics of clathrin/GGA1-coated carriers budding from the trans-Golgi network. Mol. Biol. Cell *14*, 1545–1557.

Radulescu, A.E., Siddhanta, A., and Shields, D. (2007). A role for clathrin in reassembly of the Golgi apparatus. Mol. Biol. Cell *18*, 94–105.

Rappoport, J.Z., and Simon, S.M. (2003). Real-time analysis of clathrin-mediated endocytosis during cell migration. J. Cell Sci. *116*, 847–855.

Rappoport, J.Z., Taha, B.W., Lemeer, S., Benmerah, A., and Simon, S.M. (2003a). The AP-2 complex is excluded from the dynamic population of plasma membrane-associated clathrin. J. Biol. Chem. *278*, 47357–47360.

Rappoport, J.Z., Taha, B.W., and Simon, S.M. (2003b). Movement of plasma-membrane-associated clathrin spots along the microtubule cytoskeleton. Traffic *4*, 460–467.

Ratnayaka, A., Marra, V., Branco, T., and Staras, K. (2011). Extrasynaptic vesicle recycling in mature hippocampal neurons. Nat. Commun. *2*, 531.

Robinson, M.S., Sahlender, D.A., and Foster, S.D. (2010). Rapid inactivation of proteins by rapamycin-induced rerouting to mitochondria. Dev. Cell *18*, 324–331.

Rosendale, M., Jullié, D., Choquet, D., and Perrais, D. (2017). Spatial and Temporal Regulation of Receptor Endocytosis in Neuronal Dendrites Revealed by Imaging of Single Vesicle Formation. Cell Rep. *18*, 1840–1847.

Roy, S. (2014). Seeing the unseen: the hidden world of slow axonal transport. Neuroscientist *20*, 71–81.

Roy, S. (2020). Finding order in slow axonal transport. Curr. Opin. Neurobiol. *63*, 87–94.

Roy, S., Yang, G., Tang, Y., and Scott, D.A. (2011). A simple photoactivation and image analysis module for visualizing and analyzing axonal transport with high temporal resolution. Nat. Protoc. *7*, 62–68.

Royle, S.J., and Lagnado, L. (2010). Clathrin-mediated endocytosis at the synaptic terminal: bridging the gap between physiology and molecules. Traffic *11*, 1489–1497.

Saheki, Y., and De Camilli, P. (2012). Synaptic vesicle endocytosis. Cold Spring Harb. Perspect. Biol. *4*, a005645.

Schindelin, J., Arganda-Carreras, I., Frise, E., Kaynig, V., Longair, M., Pietzsch, T., Preibisch, S., Rueden, C., Saalfeld, S., Schmid, B., et al. (2012). Fiji: an open-source platform for biological-image analysis. Nat. Methods *9*, 676–682.

Scott, D.A., Das, U., Tang, Y., and Roy, S. (2011). Mechanistic logic underlying the axonal transport of cytosolic proteins. Neuron *70*, 441–454.

Sharma, R., Gulia, R., and Bhattacharyya, S. (2019). Analysis of ubiquitination and ligand-dependent trafficking of group I mGluRs. Methods Cell Biol. *149*, 107–130.

Shigeoka, T., Jung, H., Jung, J., Turner-Bridger, B., Ohk, J., Lin, J.Q., Amieux, P.S., and Holt, C.E. (2016). Dynamic Axonal Translation in Developing and Mature Visual Circuits. Cell *166*, 181–192.

Song, B.D., Yarar, D., and Schmid, S.L. (2004). An assembly-incompetent mutant establishes a requirement for dynamin self-assembly in clathrin-mediated endocytosis in vivo. Mol. Biol. Cell *15*, 2243–2252.

Soykan, T., Kaempf, N., Sakaba, T., Vollweiter, D., Goerdeler, F., Puchkov, D., Kononenko, N.L., and Haucke, V. (2017). Synaptic Vesicle Endocytosis Occurs on Multiple Timescales and Is Mediated by Formin-Dependent Actin Assembly. Neuron *93*, 854–866.e854.

Staras, K., Branco, T., Burden, J.J., Pozo, K., Darcy, K., Marra, V., Ratnayaka, A., and Goda, Y. (2010). A vesicle superpool spans multiple presynaptic terminals in hippocampal neurons. Neuron *66*, 37–44.

Tabb, D.L., McDonald, W.H., and Yates, J.R., 3rd (2002). DTASelect and Contrast: tools for assembling and comparing protein identifications from shotgun proteomics. J. Proteome Res. *1*, 21–26.

Tang, Y., Das, U., Scott, D.A., and Roy, S. (2012). The slow axonal transport of alpha-synuclein–mechanistic commonalities amongst diverse cytosolic cargoes. Cytoskeleton (Hoboken) *69*, 506–513.

Tang, Y., Scott, D., Das, U., Gitler, D., Ganguly, A., and Roy, S. (2013). Fast vesicle transport is required for the slow axonal transport of synapsin. J. Neurosci. *33*, 15362–15375.

Tao-Cheng, J.H. (2020). Stimulation-induced differential redistributions of clathrin and clathrin-coated vesicles in axons compared to soma/dendrites. Mol. Brain *13*, 141.

Traub, L.M., and Bonifacino, J.S. (2013). Cargo recognition in clathrin-mediated endocytosis. Cold Spring Harb. Perspect. Biol. *5*, a016790.

Twelvetrees, A.E., Pernigo, S., Sanger, A., Guedes-Dias, P., Schiavo, G., Steiner, R.A., Dodding, M.P., and Holzbaur, E.L. (2016). The Dynamic Localization of Cytoplasmic Dynein in Neurons Is Driven by Kinesin-1. Neuron *90*, 1000–1015.

Wang, L., Das, U., Scott, D.A., Tang, Y., McLean, P.J., and Roy, S. (2014). α-synuclein multimers cluster synaptic vesicles and attenuate recycling. Curr. Biol. *24*, 2319–2326.

Washburn, M.P., Wolters, D., and Yates, J.R., 3rd (2001). Large-scale analysis of the yeast proteome by multidimensional protein identification technology. Nat. Biotechnol. *19*, 242–247.

Watanabe, S., Rost, B.R., Camacho-Pérez, M., Davis, M.W., Söhl-Kielczynski, B., Rosenmund, C., and Jorgensen, E.M. (2013). Ultrafast endocytosis at mouse hippocampal synapses. Nature *504*, 242–247.

Watanabe, S., Trimbuch, T., Camacho-Pérez, M., Rost, B.R., Brokowski, B., Söhl-Kielczynski, B., Felies, A., Davis, M.W., Rosenmund, C., and Jorgensen, E.M. (2014). Clathrin regenerates synaptic vesicles from endosomes. Nature *515*, 228–233.

Wilhelm, B.G., Mandad, S., Truckenbrodt, S., Kröhnert, K., Schäfer, C., Rammner, B., Koo, S.J., Claßen, G.A., Krauss, M., Haucke, V., et al. (2014). Composition of isolated synaptic boutons reveals the amounts of vesicle trafficking proteins. Science *344*, 1023–1028.

Witkowska, A., and Haucke, V. (2021). Liquid-like protein assemblies initiate endocytosis. Nat. Cell Biol. *23*, 301–302.

Xu, T., Park, S.K., Venable, J.D., Wohlschlegel, J.A., Diedrich, J.K., Cociorva, D., Lu, B., Liao, L., Hewel, J., Han, X., et al. (2015). ProLuCID: An improved SEQUEST-like algorithm with enhanced sensitivity and specificity. J. Proteomics *129*, 16–24.

Yates, J.R., Ruse, C.I., and Nakorchevsky, A. (2009). Proteomics by mass spectrometry: approaches, advances, and applications. Annu. Rev. Biomed. Eng. *11*, 49–79.

Zhao, Y., and Keen, J.H. (2008). Gyrating clathrin: highly dynamic clathrin structures involved in rapid receptor recycling. Traffic *9*, 2253–2264.

STAR★METHODS

KEY RESOURCES TABLE

REAGENT or RESOURCE	SOURCE	IDENTIFIER
Antibodies		
Anti-Clathrin heavy chain antibody	Abcam	Cat#ab21679; RRID:AB_2083165
Chicken polyclonal anti-GFP antibody	Abcam	Cat#ab13970; RRID:AB_300798
Anti-rabbit Alexa Fluor 594	Invitrogen	Cat#A11037; RRID:AB_2534095
Anti-Chicken Alexa Fluor 488	Invitrogen	Cat#A11039; RRID:AB_142924
polyclonal chicken anti-Map2	Abcam	Cat# ab5392; RRID:AB_2138153
monoclonal mouse anti β2-spectrin	BD Bioscience	Cat#612563; RRID:AB_399854
Anti-Clathrin mouse monoclonal antibody	Affinity Bioreagents	Cat#MA1-065; RRID:AB_2083179
Anti-Mouse IgG	Abcam	Cat#ab190475; RRID:AB_2827162
monoclonal mouse anti-synapsin	Synaptic Systems	Cat#106-001; RRID:AB_887805
Anti-rabbit D2 (Ultivue Kit)	Ultivue	Cat#Ultivue-2
Anti-mouse D2 (Ultivue Kit)	Ultivue	Cat#Ultivue-2
Chemicals, peptides, and recombinant proteins		
Dynasore	Abcam	Cat#ab120192
Latrunculin A	Life Technologies	Cat#L12370
Nocodazole	Millipore-Sigma	Cat#487928-10MG
Swinholide A	Millipore-Sigma	Cat#574776-10UG
A/C heterodimerizer	Takara	Cat#635056
FM4-64	Invitrogen	Cat#T13320
Advasep-7	Millipore-Sigma	Cat#A3723
HBSS	GIBCO	Cat#14025092
6-cyano-7-nitroquinoxaline-2,3-dione CNQX	Tocris Biosciences	Cat#1045
D,L-2-amino-5-phosphonovaleric acid AP5	Tocris Biosciences	Cat#106
VER155008	Tocris Biosciences	Cat#3803
Lipofectamine 2000	Life Technologies	Cat#11668-019
ProFection Mammalian Transfection System	Promega	Cat#E1200
B27 supplement	GIBCO	Cat#17504044
Glutamax	GIBCO	Cat#35050061
Neurobasal A	GIBCO	Cat#10888022
poly-D-lysine	Sigma	Cat#P0899
Hibernate-E low fluorescence medium	Brainbits	Cat#HE-lf
0.25% Trypsin–EDTA	Invitrogen	Cat#25200072
Fetal bovine serum	Hyclone	Cat#SH30071.03
Hemin chloride	Millipore-Sigma	Cat#3741
Sodium cacodylate trihydrate	Millipore-Sigma	Cat#C4945
Diaminobenzidine (DAB)	Millipore-Sigma	Cat#D8001
Osmium Tetraoxide (4% aqueous solution)	Electron Microscopy Sciences	Cat#19150
Paraformaldehyde (16% aqueous solution)	Electron Microscopy Sciences	Cat#15710
Glutaraldehyde (25% aqueous solution)	Electron Microscopy Sciences	Cat#16220
Durcupan ACM, Epoxy Resin (Kit)	Electron Microscopy Sciences	Cat#14040
Tris (2-carboxyethyl) phosphine hydrochloride	Sigma-Aldrich	Cat# 75259

(*Continued on next page*)

Continued

REAGENT or RESOURCE	SOURCE	IDENTIFIER
Iodo-acetamide	Sigma-Aldrich	Cat#144-48-9
Protease inhibitor cocktail	Sigma-Aldrich	Cat#P8340
Dynabeads Co-Immunoprecipitation Kit	ThermoFisher Scientific	Cat#14321D
1.4 nm Nanogold secondary antibody	Nanoprobes	Cat#2001
HQ silver enhancement kit	Nanoprobes	Cat#2012-45ML
Critical commercial assays		
Live-or-Dye NucFix Red	Biotium	Cat#32010-T
Deposited data		
Proteomics Data	This Paper; ProteomeXchange Consortium (PRIDE database) (Perez-Riverol et al., 2016)	Table S1; PXD027857 (https://www.ebi.ac.uk/pride/)
Experimental models: Organisms/strains		
Mouse: CD1	Charles River Laboratories	Cat#022-CD1
Recombinant DNA		
GFP:CLC	Gaidarov et al.,1999	N/A
pUC57-APEX	Martell et al., 2012	Addgene Plasmid #40306
Dendra2-Lifeact-7	Dendra2-Lifeact-7 was a gift from Michael Davidson	Addgene plasmid #54694
Dendra2:CLC	This paper	N/A
PAGFP-C1	Patterson and Lippincott-Schwartz, 2002	Addgene plasmid #11910
PAGFP:CLC	This paper	N/A
CHC-T7-Hub	Liu et al., 1998	N/A
T7-empty backbone	Liu et al., 1998	N/A
GFP:Utr-CH	Burkel et al., 2007	Addgene Plasmid #26737
synaptophysin:mCh	Gerrow et al., 2006	N/A
pBa-Flag-BicD2-FKBP	Bentley et al., 2015	Addgene Plasmid #64206
pBa- Flag-tdTM-BicD2-FKBP	Bentley et al., 2015	Addgene Plasmid #64205
pBa-FRB-3myc-Rab5a	Bentley et al., 2015	Addgene Plasmid #64209
FRB-GFP:CLC	This paper	N/A
GFP:synapsin-1a	Gitler et al., 2004	N/A
EGFP-AP180	Bushlin et al., 2008	N/A
GAK-GFP	Massol et al., 2006	N/A
pEGFP-C1-Dynamin	Song et al., 2004	Addgene Plasmid #34680
CLC:mCherry	This paper	N/A
pEGFP-N1	Clonetech	Cat#6085-1
Software and algorithms		
GraphPad Prism	GraphPad Software, La Jolla, CA, USA	Version 7.00; www.graphpad.com; RRID:SCR_002798
Fiji ImageJ	Schindelin et al., 2012	https://imagej.net/Fiji; RRID:SCR_002285
MetaMorph Version 7.10	Molecular Devices	https://www.moleculardevices.com/products/cellular-imaging-systems/acquisition-and-analysis-software/metamorph-microscopy; RRID:SCR_002368
Adobe Illustrator	Adobe	https://www.adobe.com/products/illustrator/free-trial-download.html; RRID:SCR_010279
RawXtract version 1.9.9	McDonald et al., 2004	http://fields.scripps.edu/downloads.php

(*Continued on next page*)

Continued		
REAGENT or RESOURCE	SOURCE	IDENTIFIER
N-STORM software	Nikon; Jungmann et al., 2014	https://www.microscope.healthcare.nikon.com/products/super-resolution-microscopes/n-storm-super-resolution; RRID:SCR_018302
ChimeraX software	Goddard et al., 2018	https://www.rbvi.ucsf.edu/chimerax/; RRID:SCR_015872
ThunderSTORM	Jimenez et al., 2020	https://github.com/zitmen/thunderstorm; RRID:SCR_016897

RESOURCE AVAILABILITY

Lead contact

Further information and requests for resources and reagents should be directed to and will be fulfilled by the lead contact, Subhojit Roy (sroy@ucsd.edu).

Materials availability statement

Plasmids generated in this study are available from the Lead Contact without restriction.

Data and code availability

The MUDPIT-MS data are available in the supplemental information. Microscopy data reported in this paper will be shared by the lead contact upon request.
This paper does not report original code.
Any additional information required to reanalyze the data reported in this paper is available from the lead contact upon request.

EXPERIMENTAL MODEL AND SUBJECT DETAILS

Animals

CD1 pups obtained from Charles River Laboratories (Cat#022-CD1) were used for preparing primary hippocampal cultures. Wistar rats were obtained from Janvier labs (France).

Primary cell cultures

For most experiments, hippocampal cultures were obtained from brains of postnatal (P0–P1) CD-1 mice and plated on MatTek glass-bottom dishes as described previously in detailed published protocols (Ganguly and Roy, 2014; Roy et al., 2011), in accordance with University of California guidelines. Briefly, MatTek dishes were coated with 100 μl of 1 mg/mL poly-d-lysine for 2 h at RT, washed thrice with ddH_2O, and air-dried before plating. Hippocampi from P0–P1pups were dissected in ice-cold dissection buffer (HBSS, 4.44 mM d-glucose, and 6.98 mM HEPES) and incubated in 0.25% Trypsin–EDTA at 37°C for 15 min. Following this, neurons were dissociated in plating media (10% FBS and 90% Neurobasal/B27; Life Technologies) by trituration. Neurons were plated at a density of 50,000 cells/100 μl (for FM4-64 experiments and clathrin imaging at *en-passant* boutons) and at 25,000 cells/100 μl (for all other experiments) of plating media. Neurons were maintained in Neurobasal/B27 media (supplemented with 2% B27 and 1% GlutaMAX) in an incubator at 37°C and 5% CO_2 for 7–9 d before transfection. All the experiments on neuronal cultures were performed between 8-21 DIV. E18 rat hippocampal cultures were used for the DNA-PAINT experiments following standard protocols, and guidelines established by the European Animal Care and Use Committee (86/609/CEE) and local ethics committee (agreement D13-055-8) were followed.

METHOD DETAILS

DNA constructs, pharmacologic agents, neuronal cultures, transfections, and immunocytochemistry

The GFP:CLC (Gaidarov et al.,1999), pUC57-APEX (Martell et al., 2012) and Dendra2 constructs were obtained from Addgene [from the laboratories of Drs. James H. Keen (Thomas Jefferson University, PA), Alice Ting (Stanford University, CA) and Michael Davidson (Florida State University, Tallahassee, FL), respectively]. The PAGFP:CLC construct was subcloned from the PAGFP backbone (Patterson and Lippincott-Schwartz, 2002), a gift from Dr. George Patterson (NIH/NIBIB) and Jennifer Lippincott-Schwartz (Janelia Farms Research Campus, Ashburn VA), by standard cloning. CHC-T7-Hub and T7-empty backbone (Liu et al., 1998) was a gift from Dr. Frances Brodsky (UCL, London, UK). The GFP:Utr-CH (Burkel et al., 2007), and synaptophysin:mCherry constructs (Gerrow et al.,

2006) were gifts from Drs. William Bement (University of Wisconsin, Madison, WI) and Leon Lagnado (University of Sussex, Sussex, England, UK) respectively. pBa-Flag-BicD2-FKBP and pBa- Flag-tdTM-BicD2-FKBP constructs were from Gary Banker (Oregon Health & Science University, Portland, OR). FRB-GFP:CLC was generated by inserting GFP:CLC in pFRB-3myc-Rab5a plasmid by replacing Rab5a (Bentley et al., 2015). GFP:synapsin-1a (Gitler et al., 2004) was a gift from George Augustine (Nanyang University, Singapore). EGFP-AP180 (Bushlin et al., 2008), GAK-GFP (Massol et al., 2006) and pEGFP-C1-Dynamin (Song et al., 2004) were kindly gifted by Drs. Pamela Yao (National Institute on Aging-National Institutes of Health, Baltimore, Maryland), Tomas Kirchhausen Harvard Medical School, Boston, MA and Sandra Schmid (University of Texas Southwestern Medical Center, Dallas, Texas) respectively. Dynasore, Latrunculin A (Life Technologies) and nocodazole were dissolved in DMSO and used at a final concentration of 80 μM, 100 nm and 10 μg/mL respectively. Swinholide A and Rapamycin analog A/C heterodimerizer (Takara) were dissolved in ethanol and used at a final concentration of 100 nM respectively. The stocks of FM4-64 (Invitrogen), Advasep-7, Live-or-Dye NucFix Red (Biotium) were prepared in DMSO and used at a final concentration of 10 μM, 1 mM and 0.1x in PBS (manufacturers' protocol) respectively. The glutamate receptor antagonists 6-cyano-7-nitroquinoxaline-2,3-dione (CNQX, TOCRIS bioscience), and D,L-2-amino-5-phosphonovaleric acid (AP5, TOCRIS bioscience) were used at 10 μM and 50 μM concentration respectively. Unless otherwise noted, all drugs were purchased from Millipore-Sigma and added to Hibernate E media (see below) prior to imaging. The Hsc70-D10N and control Hsc70 constructs were from N. Lamarche-Vane (McGill University, Montreal, Canada). The Hsc70 inhibitor VER155008 (Cat#3803; Tocris Biosciences) was dissolved in DMSO and used at a working concentration of 100 μM.

Neurons were transfected with the indicated fluorescent constructs (0.8 μg DNA for clathrin constructs, 1.2 μg of all others) at 7–9 DIV with either Lipofectamine 2000 (Life Technologies) or Calcium phosphate transfection kit (Promega) (Sharma et al., 2019). Live imaging of axons was performed between 8-10 DIV, and boutons were imaged between 13-21 DIV. As dictated by the experiment, neurons were co-transfected with soluble-GFP/soluble -mCherry/synaptophysin:DsRed to identify axons/dendrites/boutons. GFP:CLC transfected neurons selected for imaging had punctate clathrin appearance in dendrites, and axon regions imaged were more than 150 μm from the neuronal cell body. Boutons were selected > 150 μm away from the soma on the basis of varicosities in the intensity along the axon and other morphological features typical of synapses (Wang et al., 2014).

For immunostaining, neurons were fixed in 4% paraformaldehyde/sucrose solution in 1x PBS for 10 min at room temperature, followed by extraction in 0.2% Triton X-100 for 10 min, and blocking in 1% bovine serum albumin/5% FBS for 2 h at room temperature. To label endogenous clathrin, neurons were incubated overnight at 4∘C with rabbit polyclonal antibody against clathrin heavy chain at 1:500 dilution. After washing the primary antibody with 1x PBS, neurons were blocked again for 30 min at room temperature, and incubated in goat-rabbit Alexa Fluor 594 (1:500) for 1 h. for some experiments, GFP:CLC transfected neurons was stained with primary chicken polyclonal anti-GFP antibody (1:500) and secondary Alexa Fluor 488 (1:500). All primary and secondary antibodies were purchased from Abcam.

Live imaging, photobleaching, photoactivation, and photoconversion experiments

Most single-color live imaging experiments for axonal trafficking were performed on an Olympus IX81 inverted motorized epifluorescence microscope equipped with a CoolSNAP *HQ2* camera (Photometrics). Two-color live imaging was done either by simultaneous imaging of green/red channels using the Dual Cam imaging device (Photometrics) attached to two CoolSNAP *HQ2* cameras (Olympus IX81), or by rapid sequential excitation of green/red LEDs (SPECTRA-X) on an inverted epifluorescence microscope (Eclipse Ti-E; Nikon) equipped with CFI Plan Apochromat VC 100 × oil (NA 1.40; Nikon) objective, and an electron-multiplying charge-coupled device camera (QuantEM:512SC; Photometrics). A multi–band-pass filter (Chroma Technology Corp.) was inserted into the emission light path, and GFP/RFP images were obtained with precise subpixel registration. Before live imaging, neurons were transferred to Hibernate media (Brainbits), supplemented with 2% B27, 2mM Glutamax, 0.4% D-glucose, 37.5 mM NaCl (Ganguly et al., 2017; Roy et al., 2011; Scott et al., 2011), and maintained at 35.5°C to 37°C for the duration of the experiments (Precision Control, Weatherstation or a heated stage chamber, model STEV; World Precision Instrument, Inc.). Axons were identified by morphology, and only neurons with unambiguous morphology were selected for imaging (Roy et al., 2011; Scott et al., 2011). For experiments in Figure 1, GFP:CLC, neurons were either imaged every 0.7 s for several minutes, or PAGFP:CLC was photoactivated with 405 nm LED light for 1 s, and imaged every 1.2 s. Dendra2:CLC was photoconverted by 405 nm LED light for 3 s, and imaged every 1.2 s. Synaptophysin:GFP was imaged using the stream acquisition function (MetaMorph) at 5 frames/s (with no time interval between images). For imaging *en passant* boutons, 13-21 DIV neurons were co-transfected with synaptophysin:dsRed/sol-mCherry and GFP:CLC/GFP:Synapsin, and boutons were identified based on size of the synaptic vesicle cluster and morphology (Wang et al., 2014). Boutons along the primary axon, > 150 μm from the soma and < 7um apart from the each other were selected for imaging. Additionally, for the GFP:CLC live imaging of *en-passant* boutons and intervening axonal-segments, boutons expressing > 2 clathrin packets were selected and imaged at every 0.2 s (rapid imaging) for several minutes.

The clathrin photoactivation and photoconversion experiments in Figure 1 were done using a setup that has been described previously in detail (Roy et al., 2011). All other photobleaching and photoconversion experiments were done on the Nikon set-up described above, using Andor Mosaic3 Digital Micromirror Device (DMD) attached to a 405 nm diode laser (450 mW). All synaptic photobleaching and photoconversion experiments were done on DIV-13-14 neurons – a time when synapses are established in our post-natal cultures. For photobleaching, *en passant* boutons were bleached using the 405 nm laser (5 consecutive pulses of 1.5 s each), and imaged at every 2 s for several minutes. For photoconversion, Dendra2:CLC at boutons was photoconverted by pulsing the 405 nm laser for 1 s, and boutons were imaged at 2 s time-intervals for several minutes. For the single clathrin packet experiments, boutons were imaged every 1 s for several minutes. All movies were analyzed using kymographs generated with a built-in function in MetaMorph (Molecular Devices, LLC). Photoactivation and photoconversion data was analyzed using the intensity-center/bin-center shift method described previously in several publications from our group (Chakrabarty et al., 2019; Ganguly et al., 2017; Roy et al., 2011; Scott et al., 2011; Tang et al., 2013). All statistical analysis was performed using Graph Pad Prism (Graph Pad Software, San Diego, CA).

Rapamycin-inducible FKBP-FRB dimerizer and FM4-64 assays

Primary hippocampal neurons were co-transfected with the FRB-GFP:CLC and FKBP-BicD2 (+/− Tdtomato-tagged) constructs. Experiments were performed on 9-15 DIV neurons. Live neurons were incubated with 100 nM Rapalog for indicated times. Subsequently, neurons were either used for FM4-64 uptake assay or fixed for immunocytochemistry. Viability of neurons was evaluated using dead cell stain (Live-or-Dye NucFix Red), following the manufacturers' protocol. In brief, after the FKBP-FRB experiment, live neurons were incubated with the stain (0.1x in PBS) for 10 min at 37 ◦C. Thereafter, neurons were washed with PBS and imaged in HELF media at 37 ◦C. For positive controls, neurons were treated with 0.01% Triton for 1 min before staining. For the FM4-64 uptake assay, we used a protocol specifically optimized to evaluate CME (Cousin et al., 2018). Briefly, neurons were washed with imaging buffer (2.5 mM KCl, 136 mM NaCl, 1.3 mM MgCl2, 2 mM CaCl2, 10 mM glucose, 10 mM HEPES) followed by 30 s incubation in high potassium stimulation buffer (50 mM KCl, 86 mM NaCl, 1.3 mM MgCl2, 2 mM CaCl2, 10 mM glucose, 10 mM HEPES) containing 10 μM FM4-64. Thereafter, neurons were washed with imaging buffer containing 10 μM FM4-64 for 90 s. Finally, neurons were washed with Imaging buffer containing 1mM Advasep-7 for 2 min and imaged. All experiments were done at room temperature, with pH of all buffers adjusted to 7.4, and supplemented with 10 μM CNQX, 50 μM DAP-5. For some experiments, neurons were pre-incubated with 80 μM Dynasore before FM4-64 uptake.

Biochemical fractionation, western blotting and immuno-precipitation from mouse sciatic nerves

In vivo biochemical assays were adapted from protocols described earlier by (Das et al., 2013; Ganguly et al., 2017; Scott et al., 2011; Tang et al., 2012). Briefly, sciatic nerves were dissected from 6-8-wk-old mouse CD1 (WT) mouse. 64 sciatic nerves were pooled for each round of immune-precipitation (IP) and crushed in liquid nitrogen using a motor pestle and then homogenized in nondenaturing buffer (1X IP buffer, Invitrogen Dynabeads Co-Immunoprecipitation Kit [ThermoFisher Scientific, USA]) using 18 G and 23 G needles in the presence of protease inhibitor cocktail (Sigma-Aldrich). The resulting homogenate was centrifuged at 1,000 g for 20 min at 4þC to obtain a nuclear pellet (P1) and a post-nuclear supernatant (S1). The S1 supernatant was then centrifuged at 10,200 g for 20 min at 4þC to obtain a crude synaptosomal fraction (P2) and synaptosome-depleted fraction (S2). IP was performed using the DynaBeads Co-Immunoprecipitation kit (14321D; Thermo Fisher Scientific). After centrifugation, the S2 fraction was divided equally and incubated with 10.5 mg anti–Clathrin-Heavy-Chain antibody (ab21679; Abcam, Cambridge MA) and anti-Mouse IgG (ab190475; Abcam, Cambridge MA) for overnight coupling with magnetic beads at 37°C. All following washes were performed as per the manufacturer's protocol. The S2 fraction was incubated with the antibody-coupled beads for 35 min at 4°C on a rotor. After the final wash, 3 mg beads from each fraction were subjected to 2D gel electrophoresis on a 4%–12% gradient SDS-page gel and then probed with the anti–Clathrin-Heavy-Chain antibody to determine the efficacy of immunoprecipitation. The remaining 7.5 mg of S2 fraction lysate beads were then used for MudPIT-MS analysis. Two independent repeats were performed with sciatic nerve axons S2 lysate.

Protein identification through MudPIT-MS analysis and *in silico* data analysis

Overall steps in MudPIT-MS protocols were identical to our previous studies (Ganguly et al., 2017). Briefly, beads coated with the clathrin heavy chain antibody (or mouse IgG) were dissolved in 100 μL of 8 M urea in 100 mM Tris, pH 8.5, followed by reduction and alkylation in 10 mM Tris (2-carboxyethyl) phosphine hydrochloride (Sigma) and 55 mM iodo-acetamide (Sigma-Aldrich), respectively. This was followed by digestion in trypsin (Promega; incubated at 37°C overnight in the dark) and magnetic bead removal by a magnetic separator. The resulting protein digest was acidified in formic acid followed by centrifugation at 14,000 rpm for 10 min. Thereafter, the supernatant was pressure loaded onto a 250 μm inner diameter–fused silica capillary column (Polymicro Technologies). This column was fitted with a Kasil frit packed with 2.5 cm of 5 μm Partisphere strong cation exchange resin (Whatman) and 2.5 cm of 5 μm C18 resin (Phenomenex). After desalting, this biphasic column was connected to a 100 μm inner diameter-fused silica capillary (Polymicro Technologies) analytical column with a 3 μm pulled tip packed with 10 cm of 3 μm C18 resin (Phenomenex). The entire three-phase column was then laced in line with a 1,200 quaternary HPLC pump (Agilent Technologies) and analyzed using a modified 12-step separation described previously (Washburn et al., 2001). As peptides were eluted from the microcapillary column, they were electrosprayed directly into a hybrid LTQ Orbitrap Velos mass spectrometer (Thermo Fisher Scientific). A cycle consisted of one full-scan mass spectrum (300–1,600 m/z) followed by 20 data-dependent collision-induced dissociation tandem MS spectra. The application of mass spectrometer scan functions and HPLC solvent gradients was controlled by the Xcalibur data system (Thermo Fisher Scientific). Tandem MS spectra were extracted using RawXtract (version 1.9.9; (McDonald et al., 2004) and searched with the ProLuCID algorithm (Xu et al., 2015) against a mouse UniProt database concatenated to a decoy database in which the sequence for each entry in the original database was reversed (Peng et al., 2004). The ProLuCID search was performed using semi-enzyme specificity and static modification of cysteine because of carboxyam-idomethylation (57.02146). ProLuCID search results were assembled and filtered using the DTA Select algorithm (version 2.0; (Tabb et al., 2002)). The protein identification false positive rate was kept below 1%, and all peptide–spectra matches had < 10 ppm mass error.

For selection of peptides from the raw MudPIT data, peptides were subjected to the following selection criteria. First, the same peptide fragment had to appear in both rounds of the co-immunoprecipitation, followed by the criteria that the total raw spectrum count from both rounds for the peptide should be > 30. Finally, only peptides with combined spectrum counts twenty-fold or higher than the combined spectrum counts from IgG coupled beads were selected. Only peptides that meet all three criteria were included in the final list (**Table S1**). The identification of peptides and gene names was performed using the Uniprot database (https://www.uniprot.org/). For generation of the clathrin protein interaction map from the S2 fraction all known interactions from experimental data were determined from the String protein interaction database (http://www.string-db.org).

Sample preparation, data acquisition and data processing for electron tomography

For EM, mouse hippocampal neurons were plated at a density of 25,000 cells/100 μl in wells of gridded MatTek dishes coated with poly-D-lysine. DIV 9-10 neurons were transfected with APEX:GFP:CLC using lipofectamine 2000 as described previously (Ganguly et al., 2017). 6-8 h before transfection, 7 μM Hemin chloride (Sigma-Aldrich) was added to the culture medium and kept in the medium until the fixation step (below). 12-16 h after transfection, transfected neurons were identified based on the GFP signal, and corresponding grid numbers were noted. Following this, neurons were fixed for 5 min at room temperature, and then 60 min on ice in 2.5% glutaraldehyde in 0.1M sodium cacodylate buffer (pH 7.4). After washes in cacodylate buffer and a quenching step in 20mM glycine, cells were incubated with freshly prepared DAB (25.24 mM) and 0.03% H_2O_2 for 25-30 min. Neurons were then washed in 0.1M cacodylate buffer and post-fixed with 1% osmium tetroxide for 30 min on ice. The neurons were washed with ddH_2O and then dehydrated and embedded in Durcupan epoxy resin. After curing, the coverslip from the bottom of the MatTek dish was removed gently, and grid numbers with transfected neurons were sawed out and mounted on a dummy acrylic block for sectioning. Ultra-thin (70 nm) and semi-thin sections (200 nm) were cut using a diamond knife (Diatome). To improve stability of specimens under the beam of the EM for tomography, these sections were coated with carbon on both sides. Colloidal gold particles (5 nm and 10 nm diameter) were deposited on each side of the sections to serve as fiducial markers.

Ultra-thin sections were imaged on the JOEL 120 kV while the EM tomogram data were obtained from distal axonal regions (> 150 μm from the cell body) of transfected neurons using a FEI Titan high base microscope operated at 300 kV and micrographs were produced using a 4K × 4K Gatan CCD camera (US4000). Both microscope and detector were controlled by the Serial EM software package (Mastronarde, 2005) which managed the automated tilt series acquisition. Technical details of how the sections of the tomogram were acquired, image series were aligned properly, and its 3D representations were created have been described by (Phan et al., 2017). Briefly, sections were tilted every 1þ from -60° to $+60^\circ$, aligned properly using colloidal gold particles as fiducial markers and final high-quality 3D representations were built from the projection sets using a custom written non-linear bundle adjustment scheme in TxBR (Lawrence et al., 2006). 3D tomograms were visualized in IMOD (Kremer et al., 1996) and only axon regions with clathrin organelles which do not open to the surface were selected for representative images. EM tomograms were performed on APEX-GFP:CLC transfected neurons from three separate cultures. At least 2-3 independent transfected neurons from each experiment were imaged. 8 axons and 9 dendrites were imaged in total, with tomograms for at least 3 ROIs acquired for each transfected axon and dendrite. A total of 62 coated-pits were identified from tomograms of dendrites, and 17 clathrin coated structures were identified in tomograms from axons. For immuno-EM experiments, a mouse monoclonal antibody against clathrin (clone X22, 1:200-500; Affinity Bioreagents) was used. Detailed procedures including preparation, fixation and immunogold labeling are described in Tao-Cheng, 2020.

DNA-PAINT imaging and image analysis

Rat hippocampal neurons were cultured on 18 mm coverslips at a density of 6,000/cm from embryonic day 18 pups following established guidelines of the French Animal Care and Use Committee (French Law 2013-118 of 1st February 2013) and approval of the local ethics committee (agreement 2019041114431531-V2 #20242). To selectively label identified axons, neurons in some experiments were transfected the day before fixation with actin-GFP using Lipofectamine 2000 according to the manufacturer's instructions. After 9 to 13 DIV, neurons were fixed at RT in phosphate buffer (PB) 0.1M pH 7.3 containing 4% paraformaldehyde and 4% sucrose for 10 min, followed by permeabilization and blocking in incubation buffer (IB): 0.22% gelatin, 0.1% Triton in PB 0.1M pH 7.3 at RT for 2 h, and incubated overnight at 4°C with primary antibody in IB: polyclonal chicken anti-Map2 (Abcam #53392, 1:1000), polyclonal rabbit anti-clathrin heavy chain (Abcam #21679, 1:150) and monoclonal mouse anti β2-spectrin (for axon shaft images, BD Bioscience 612563, 1:150) or monoclonal mouse anti-synapsin (Synaptic Systems #106-001, 1:500. After rinses, neurons were incubated with secondary antibodies, including anti-rabbit D2 and anti-mouse D2 DNA-coupled secondary antibodies for DNA-PAINT (Ultivue) at RT for 1 h.

DNA-PAINT imaging (Jungmann et al., 2014) was performed on an N-STORM microscope (Nikon Instruments) in imaging buffer with 0.25-1 nM Imager-650 and nM Imager-560 (Ultivue). The sample was alternatively illuminated at 647 nm and 561 nm (full laser power) and 20,000-30,000 images of each channel were acquired at 25-33 Hz. DNA-PAINT acquisitions were processed using the N-STORM software followed by post-processing; filtering and image reconstruction at 4 or 12 nm/pixel with the ThunderSTORM Fiji plugin (Jimenez et al., 2020). For 3D rendering, localizations were density-filtered (50 nm 3D radius) before reconstruction of individual presynapses as of 4-nm voxel stacks. Stacks where then 3D Gaussian-smoothened and imported into ChimeraX software (Goddard et al., 2018). After surface thresholding and smoothing (default values), 3D rendering images and movies were exported as images and movies. Clathrin particles were segmented using the Segger plugin and their volume measured. Volume V in μm3 was converted in equivalent sphere diameter D in nm using [D = 1000*2*V(^1/3)*3/(4*π)] for graphing. For presynaptic clathrin particles, only particles contacting or apposed to the synapsin cluster were counted and measured.

QUANTIFICATION AND STATISTICAL ANALYSIS

FRAP Quantification

FRAP data were analyzed as previously described (Applewhite et al., 2007; Boyer et al., 2020). Background fluorescence values were subtracted from all data at each time point, and photobleaching was estimated by fitting an exponential decay function ($F = F_0 \times e^{-kt}$, where F is fluorescence, F_0 is initial fluorescence, k is the decay time constant, and t is time) to the fluorescence of an unbleached control region in the same image. Fluorescence curves were normalized between cells by subtracting the fluorescence immediately after bleaching (time = 0), and then dividing by the average of the 5 pre-bleach fluorescence time points. Fluorescence recovery half-time and immobile fraction were calculated from an inverse exponential decay ($F = A \times (1 - e^{-\tau t})$, where F is fluorescence, A is the recovery plateau fluorescence, τ is the recovery time constant, and t is time) fit to the average fluorescence recovery curve for each protein or treatment. Photobleaching curves were fit to the data using the Solver add-in of Microsoft Excel 2013, and fluorescence recovery curves were fit using GraphPad Prism.

Statistical Analyses

Datasets were tested for normality using the Shapiro-Wilk W test with α set at 0.05. Pairwise comparisons were made using a Student's t test only when both groups being compared were found to be normally distributed: in all other cases, a Mann-Whitney nonparametric U test was used. Correlation of clathrin to synapsin volume at synapses was performed using a Pearson's test. All three-group comparisons contained non-normally distributed data; therefore, nonparametric Kruskal-Wallis tests were used for all three-group comparisons. Post hoc pairwise comparisons were performed with Mann-Whitney nonparametric U tests and were corrected for multiple comparisons using the Benjamini-Krieger-Yekutieli two-stage step-up method. No pre-hoc sample size estimates were determined prior to experiments. Details of experimental design are described in the experiment specific subsections of Method details section. All the data are presented as mean ± SEM. The values of n and what n represents are included in the legends of the respective figures.

Neuron, Volume *109*

Supplemental information

Clathrin packets move in slow axonal transport and deliver functional payloads to synapses

Archan Ganguly, Rohan Sharma, Nicholas P. Boyer, Florian Wernert, Sébastien Phan, Daniela Boassa, Leonardo Parra, Utpal Das, Ghislaine Caillol, Xuemei Han, John R. Yates III, Mark H. Ellisman, Christophe Leterrier, and Subhojit Roy

SUPPLEMENTARY INFORMATION

- 8 supp figs
- 1 supp table

Supp Fig. 1 is related to main Fig. 1
Supp Fig. 2 is related to main Fig. 2
Supp Fig. 3 is related to main Fig. 3
Supp Fig. 4 is related to main Fig. 4
Supp Fig. 5 is related to main Fig. 5
Supp Fig. 6 is related to main Fig. 6
Supp Fig. 7 is related to main Fig. 7
Supp Fig. 8 is related to main Fig. 8

Figure S1, related to Figure 1

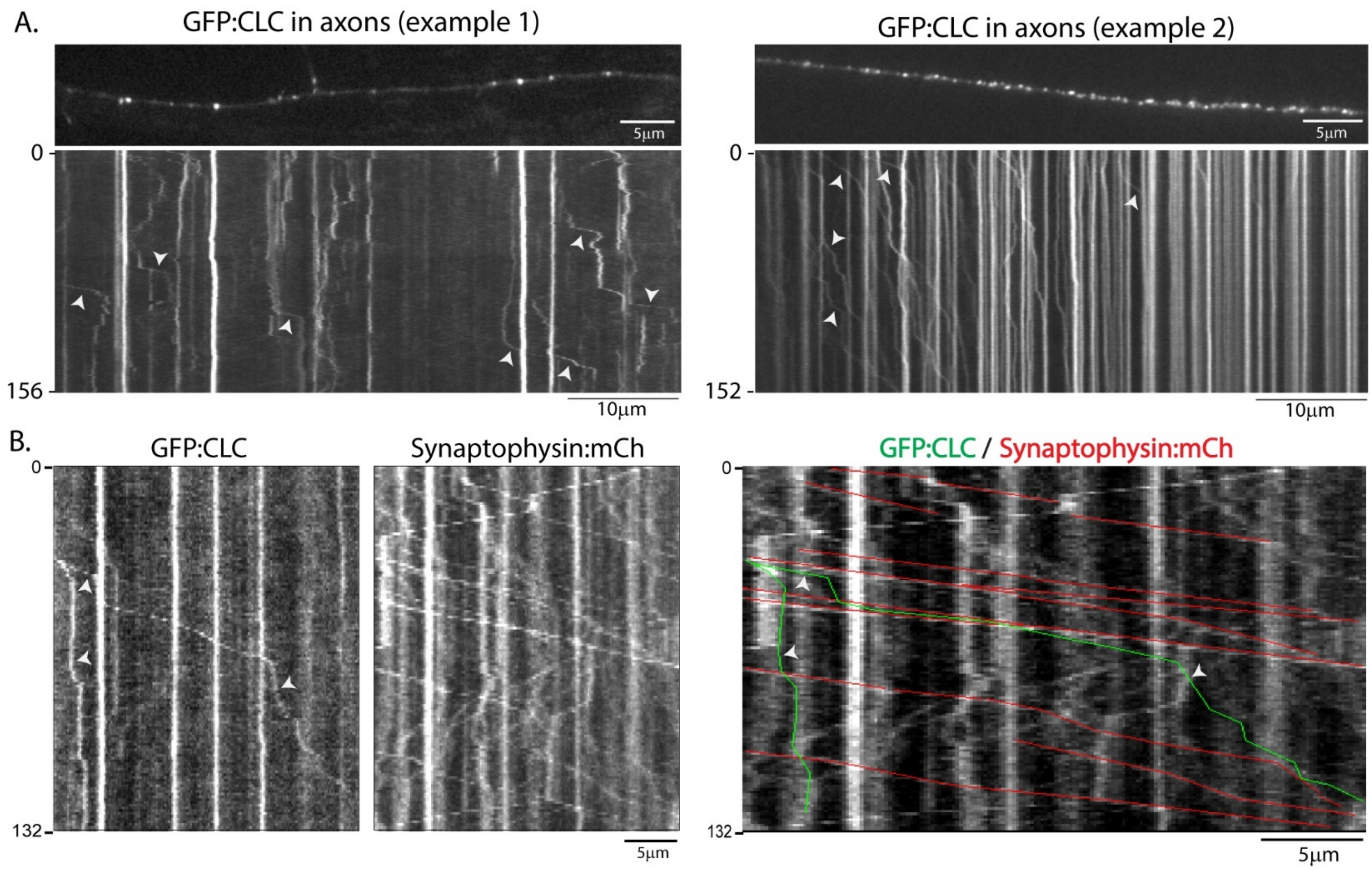

<u>Figure S1:</u> Axonal clathrin dynamics.

(A) Two examples of GFP:CLC dynamics in axons (image of axon on top, kymograph at bottom). Unlike dendrites, blinking (on/off) dynamics are rare in axons, and a fraction of particles move intermittently (arrowheads). Example 1 shows an axon with lower density of clathrin particles and example 2 shows an axon with higher particle density. Note that stationary and moving particles are seen in both cases.

(B) Kymographs from dual-imaging of GFP:CLC and synaptophysin:mCherry (left), with overlaid tracks (right). The movement of clathrin transport-packets was much less frequent than the fast transport of synaptophysin-vesicles. Though the extensive movement of synaptophysin made definitive conclusions difficult, we could see clear instances where clathrin-packets were transported independently of synaptophysin – see overlaid clathrin (green) and synaptophysin (red) tracks in kymograph below.

Time in seconds to the left of kymographs, and scale bar on lower right.

Figure S2, related to Figure 2

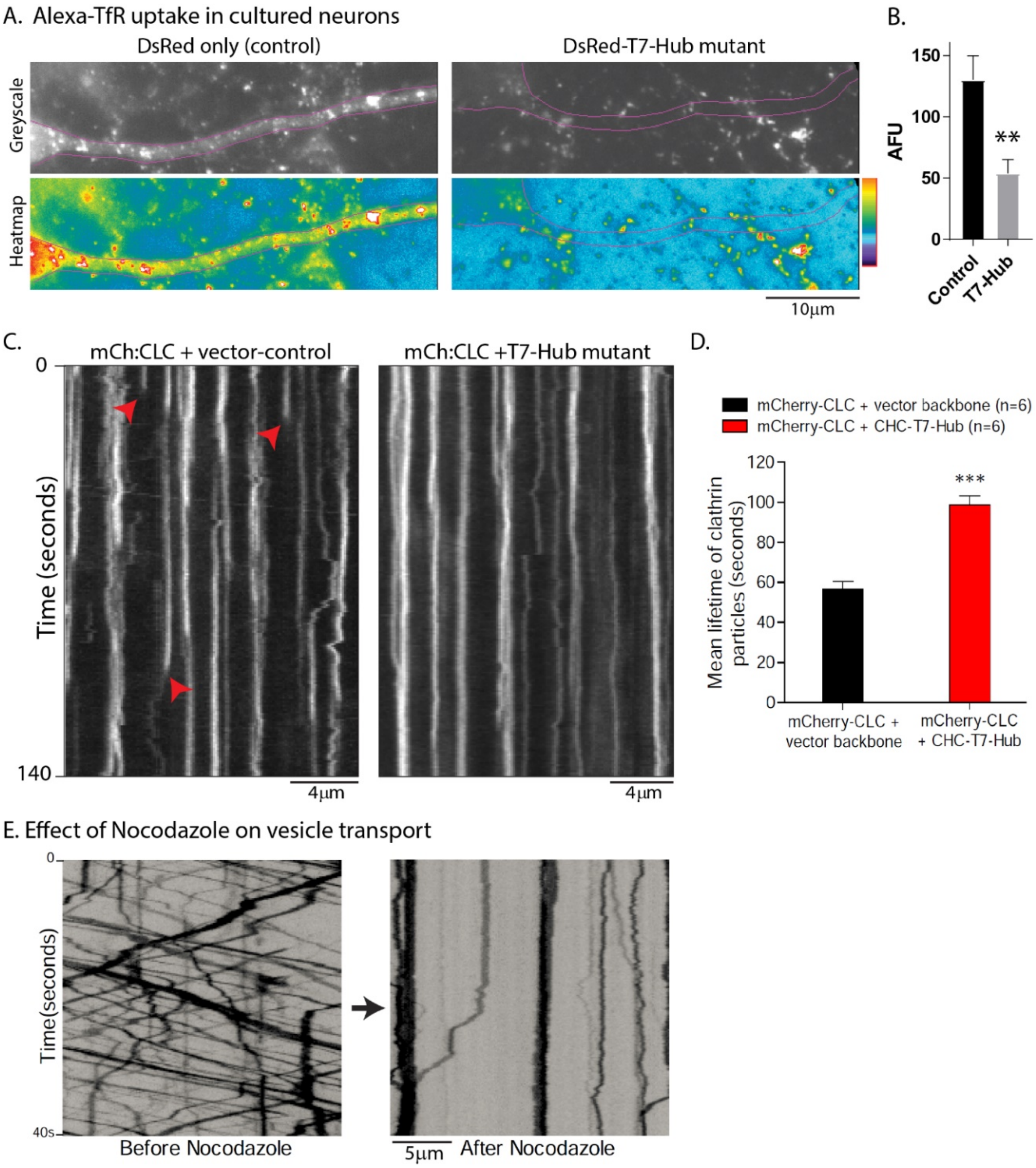

Figure S2: The clathrin T7-Hub mutant blocks receptor mediated endocytosis.

(A) Neurons were transfected with T7-Hub mutant (DsRed-tagged) or vector-control (DsRed-only), and Alexa-488-transferrin uptake into the transfected neurons was analyzed. As evident in the representative greyscale images (above) and pseudocolor heatmaps (below), the T7-Hub mutant attenuates transferrin-uptake. Data quantified in (B), 5-6 neurons per condition, from one culture; $**p<0.001$.

(C) Kymographs showing dynamics of mCh:CLC in dendrites co-transfected with the T7-Hub mutant (or vector control). Note that the blinking of clathrin fluorescence – due to receptor mediated endocytosis, some marked by arrowheads – is essentially abolished in the T7-Hub transfected neurons.

(D) Quantification of mCh:CLC lifetime in dendrites (100-150 particles from 6 dendrites were analyzed; $***p<0.0001$).

(E) Kymographs showing movement of the pan-vesicle marker NPYss:mCherry (see Ganguly et al., 2015) in an axon before and after 10μg/ml Nocodazole for 30 min. Note complete stoppage of vesicle transport after adding the microtubule depolymerizing agent.

Time in seconds to the left of kymographs, and scale bar on lower right.

Figure S3, related to Figure 3

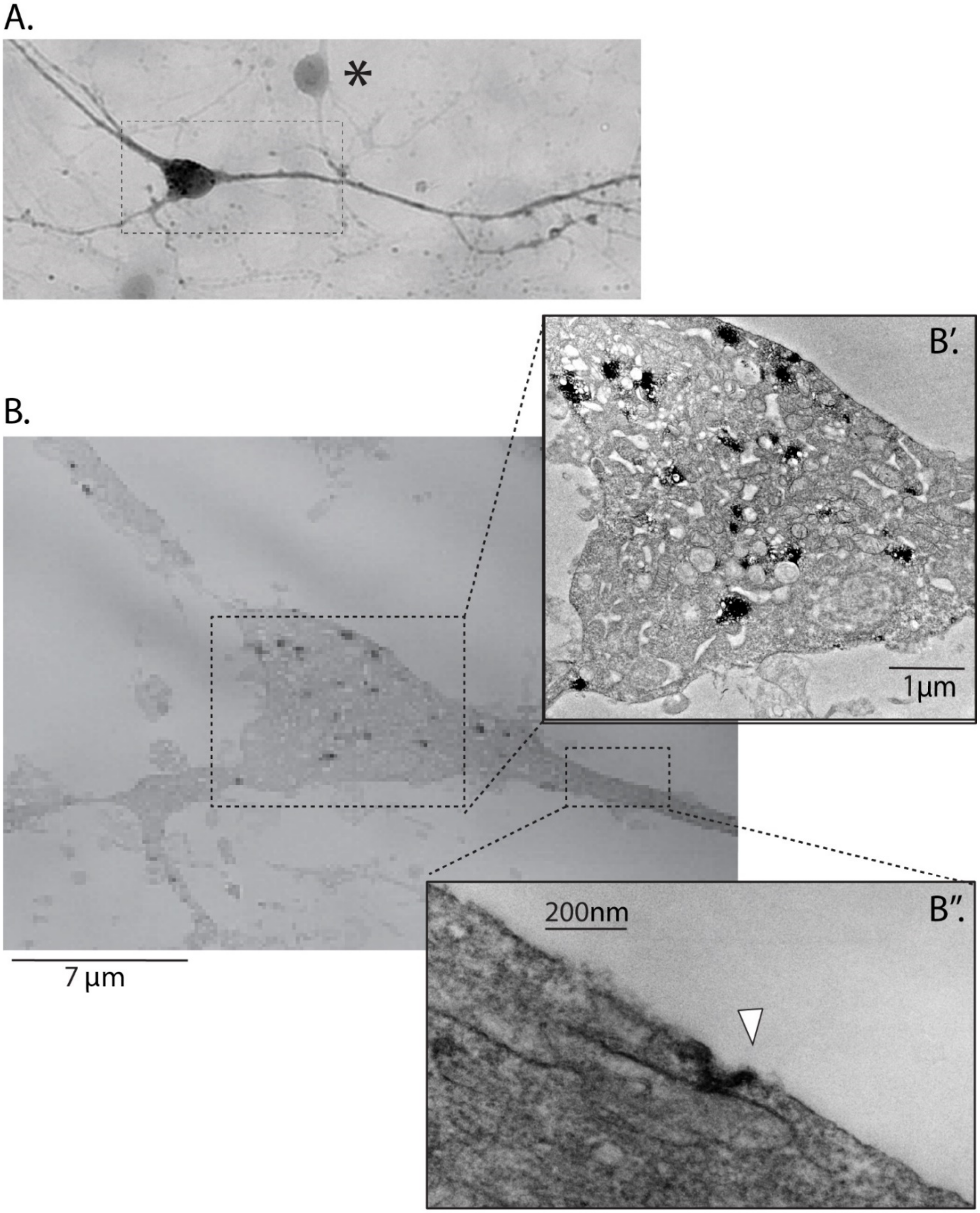

__Figure S3:__ **Apex-clathrin labeling and EM.**

(A) Neurons were transfected with Apex:GFP:CLC and processed for EM. Gridded coverslips were used to identify transfected neurons for EM processing, as described in methods. The DAB signal from an Apex:GFP:CLC transfected neuron is shown, along with an adjacent un-transfected neuron (marked with an asterisk).

(B) EM of rectangular region from (A), dark signals represent clathrin. Note that many clathrin structures are seen in the somatodendritic region (B'), some clearly representing coated clathrin pits (B'').

Figure S4, related to Figure 4

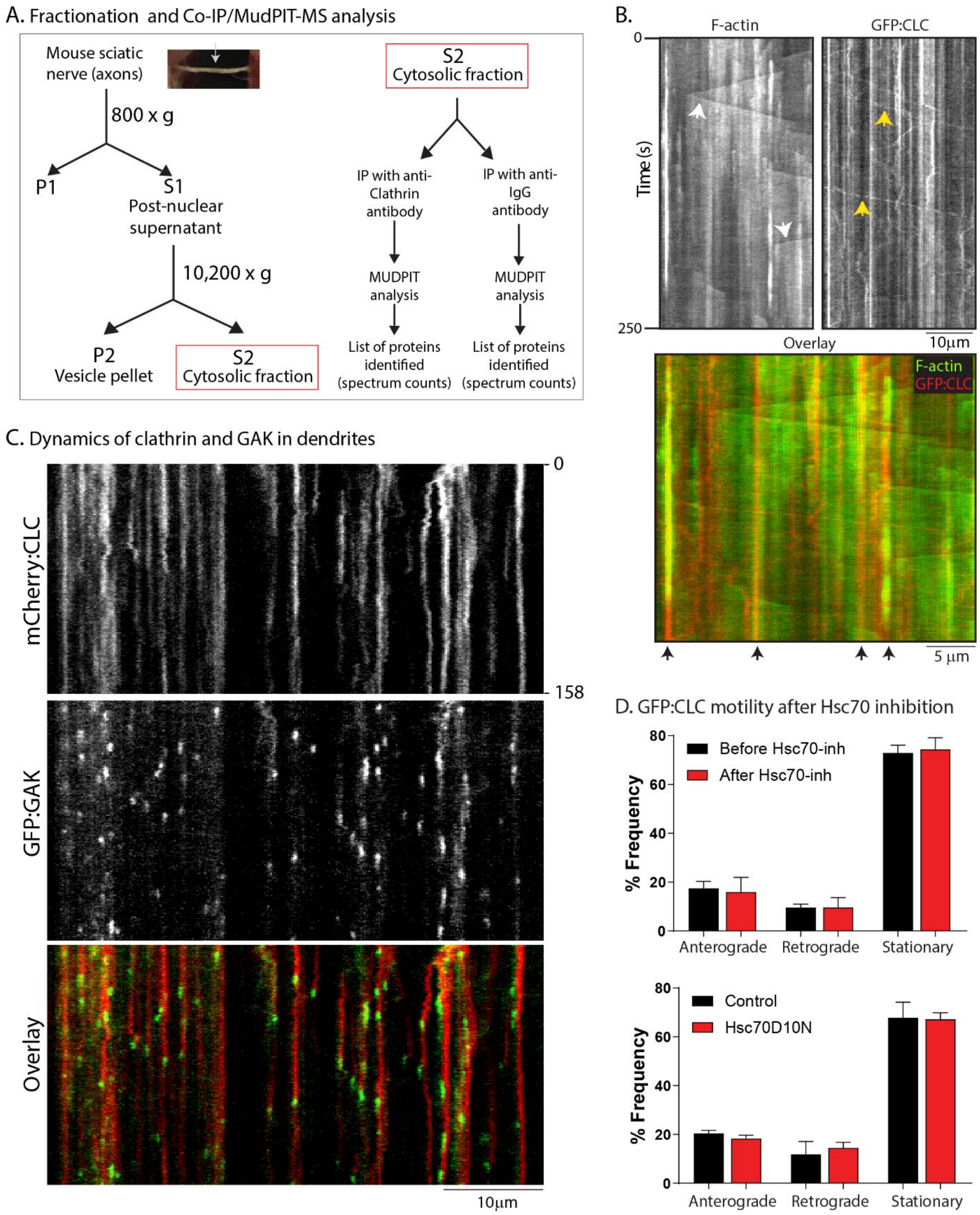

Figure S4: Composition of axonal clathrin packets.

(A) Schematic for fractionation and Mudpit-MS. Clathrin was immunoprecipitated from cytosolic (S2) sciatic nerve fractions (dissected from mice, see inset picture and arrow), and associating proteins were identified by MS.

(B) Kymographs from two-color imaging of GFP:Utr-CH (labeling F-actin) and mCh:CLC – some 'actin trails' and clathrin transport-packets are marked by white and yellow arrowheads respectively. On the overlaid red/green kymographs on right, note that many stationary clathrin particles are colocalized with F-actin (black arrowheads, bottom).

(C) Simultaneous two-color imaging of mCherry:CLC and GFP:GAK in dendrites. Note that GAK particles only appear in kymographs when clathrin is disassembled, consistent with the role of GAK as a protein that dis-assembles clathrin cages. Also note that this behavior of GAK is very different from its dynamics in axons, where many GAK particles colocalize with clathrin and are intermittently transported (**Fig. 4D**).

(D) Quantification of GFP:CLC particle dynamics in axons before and after pharmacologic inhibition of Hsc70 with a small-molecule (VER155008); or genetic interference of Hsc70 function using a dominant-negative construct (Hsc70D10N). Note that motility of clathrin is unchanged after Hsc70 inhibition.

Figure S5, related to Figure 5

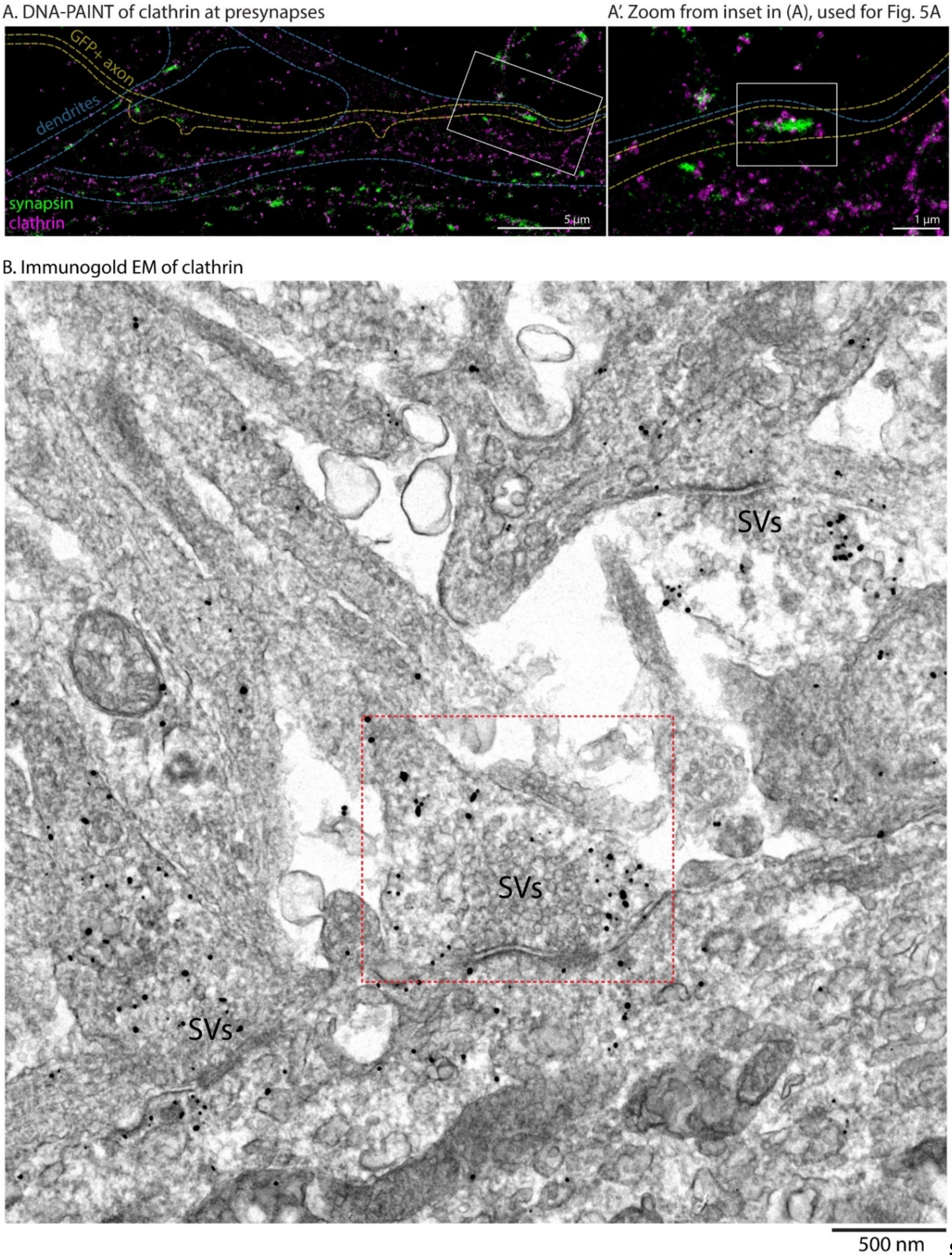

Supplementary

Figure S5: Supplements super-resolution and immuno-EM data shown in Fig. 5.

(A) DNA-PAINT: Larger field of view showing axons and dendrites corresponding to the bouton shown in **Fig. 5A**. Blue dashed lines represent dendrites (identified by MAP2 staining), and dashed yellow lines represent an axon (identified by Actin:GFP transfection). A' shows the actual image shown in **Fig. 5A**.

(B) Immuno-EM of clathrin - Large field of view showing synapses and neurites around the synapse showed in **Fig. 5F1** (dashed red box marks ROI used in figure). Note that the immuno-gold particles do not bind to many other structures (tubulo-vesicular organelles, mitochondria, cytoskeletal structures, cytoplasmic matrix, etc.) and appears specific for clathrin.

Figure S6, related to Figure 6

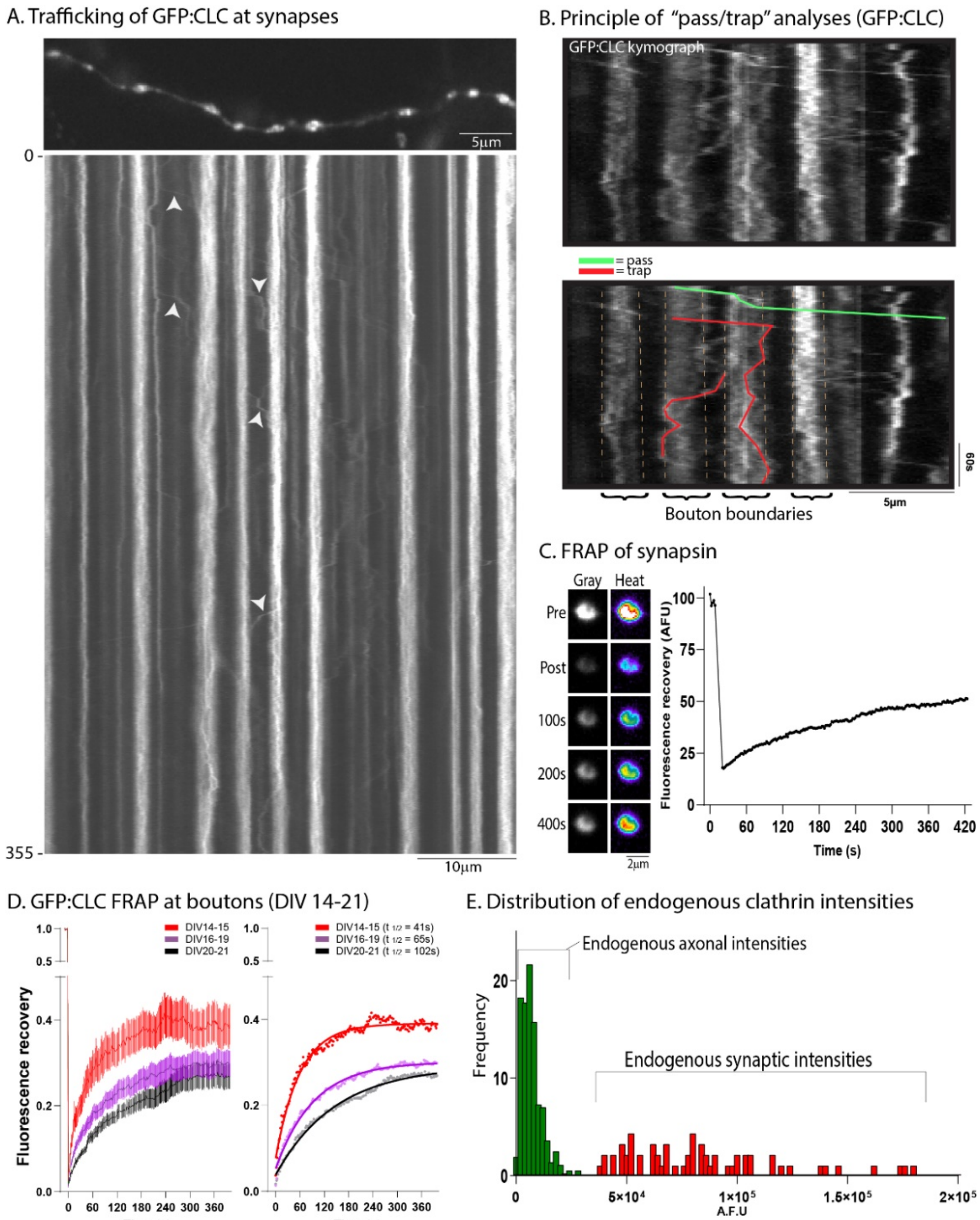

<u>Figure S6:</u> Trafficking and synaptic targeting of clathrin particles.

(A) Image (top) and kymograph (bottom) of GFP:CLC trafficking in presynaptic boutons (varicosities) and flanking axons. Note that many clathrin particles are exchanged between boutons. Elapsed time on left, and scale-bar on lower right of kymograph.

(B) Principle of "pass/trap analysis" to quantify moving clathrin particles trapped at boutons. Moving GFP:CLC (or Dendra2:CLC) particles that did not re-emerge from boutons after 60 seconds were considered trapped. Green and red lines show examples of passing and trapped GFP:CLC particles. Time/scalebar on lower right.

(C) Time-series grayscale and heatmap images of a bouton containing GFP:synapsin that was photobleached, with corresponding FRAP curve on right (time in seconds shown on left of images). Note the relatively smooth, gradual rise of GFP:synapsin fluorescence after photobleaching.

(D) FRAP-curves of GFP:CLC from boutons of neurons cultured for 14-21 days in vitro (DIV). Note that there is an earlier flattening of the FRAP-curves with increasing DIV – suggesting a larger immobile pool with age in cultures – likely reflecting synaptic maturity over time (data from 34 neurons, 5 separate cultures for DIV14-15; 51 neurons, 10 separate cultures for DIV16-19; and 44 neurons, 6 separate cultures for DIV20-21). All clathrin photobleaching and photoconversion experiments in main figures were done on DIV 13-14 neurons.

(E) Intensity distributions (histograms) of endogenous clathrin in axons and synapses, determined by immunostaining cultures with antibody to clathrin heavy chain (to mark synapses, see methods; 355 axonal particles and 92 synapses were analyzed from 2 separate cultures).

Figure S7, related to Figure 7

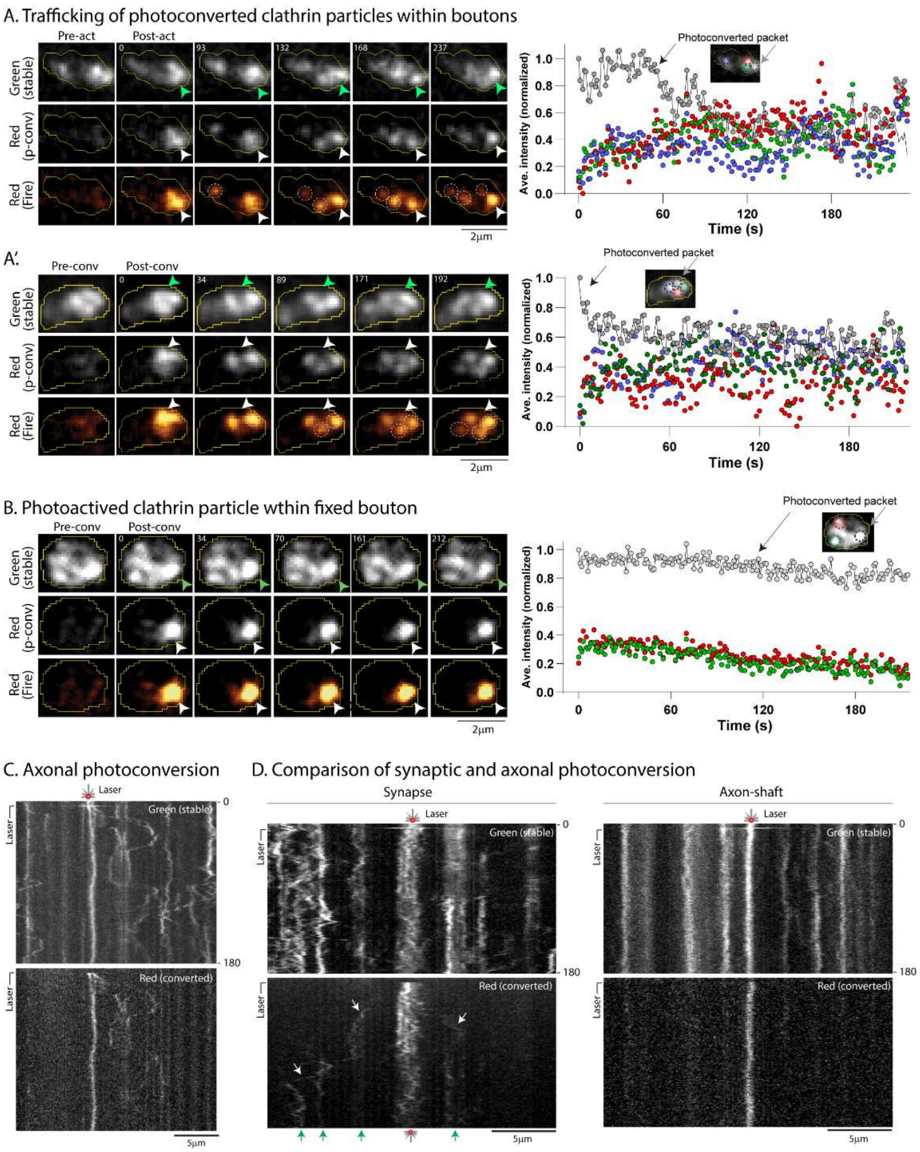

<u>Figure S7:</u> Photoconversion of single clathrin packets in synapses and axons.

(A, A') Photoconversion of single clathrin-packets (Dendra2:CLC) at presynaptic boutons – two more examples. **<u>Left</u>**: Dendra2:CLC was photoconverted in a single synaptic clathrin-packet (arrowhead, elapsed time in seconds on top left). Note that after photoconversion (middle and bottom panels), the photoconverted packet lost fluorescence, while there was an increase of fluorescence in adjacent packets, identified by stable green fluorescence (some marked by dashed circles in bottom panel). **<u>Right</u>**: Quantification of intensities in individual packets (normalized to highest post-conversion intensity). Colors in graph correspond to the colors of circles marking packets in inset-image. Note reciprocal fluctuations in photoconverted and non-photoconverted packets.

(B) Same experiment as above, but in fixed NEURONS. Note that while the Dendra2:CLC synaptic packet could be photoconverted, there was little to no loss of fluorescence from this packet, or gain of fluorescence in the other local clathrin packets.

(C) Kymographs from photoactivation of single Dendra2:CLC axonal packets. In this example, note that moving clathrin particles caused some disruption of the photoconverted clathrin, but there was no appreciable loss of clathrin molecules from the photoconverted axonal packet. Also note that the time-scale of dispersion in this case – seconds – is very different from the slower exchange of clathrin molecules at the synapse (over tens of seconds to minutes).

(D) A side by side comparison of synaptic and axonal Dendra2:CLC photoconversion. In the kymographs of photoconverted (red) fluorescence, note that in the case of synapses, single particles of clathrin emerged from the laser-illuminated bouton, and were trapped at adjacent boutons (white arrowheads on kymograph; green arrowheads at bottom mark the positions of non-activated boutons, as determined by the stable green fluorescence). On the other hand, no dispersion of fluorescence was seen when a single axonal clathrin-packet was photoconverted.

Key for kymographs: elapsed time in seconds on right and scale-bar on lower right (laser illumination also marked).

Figure S8, related to Figure 8

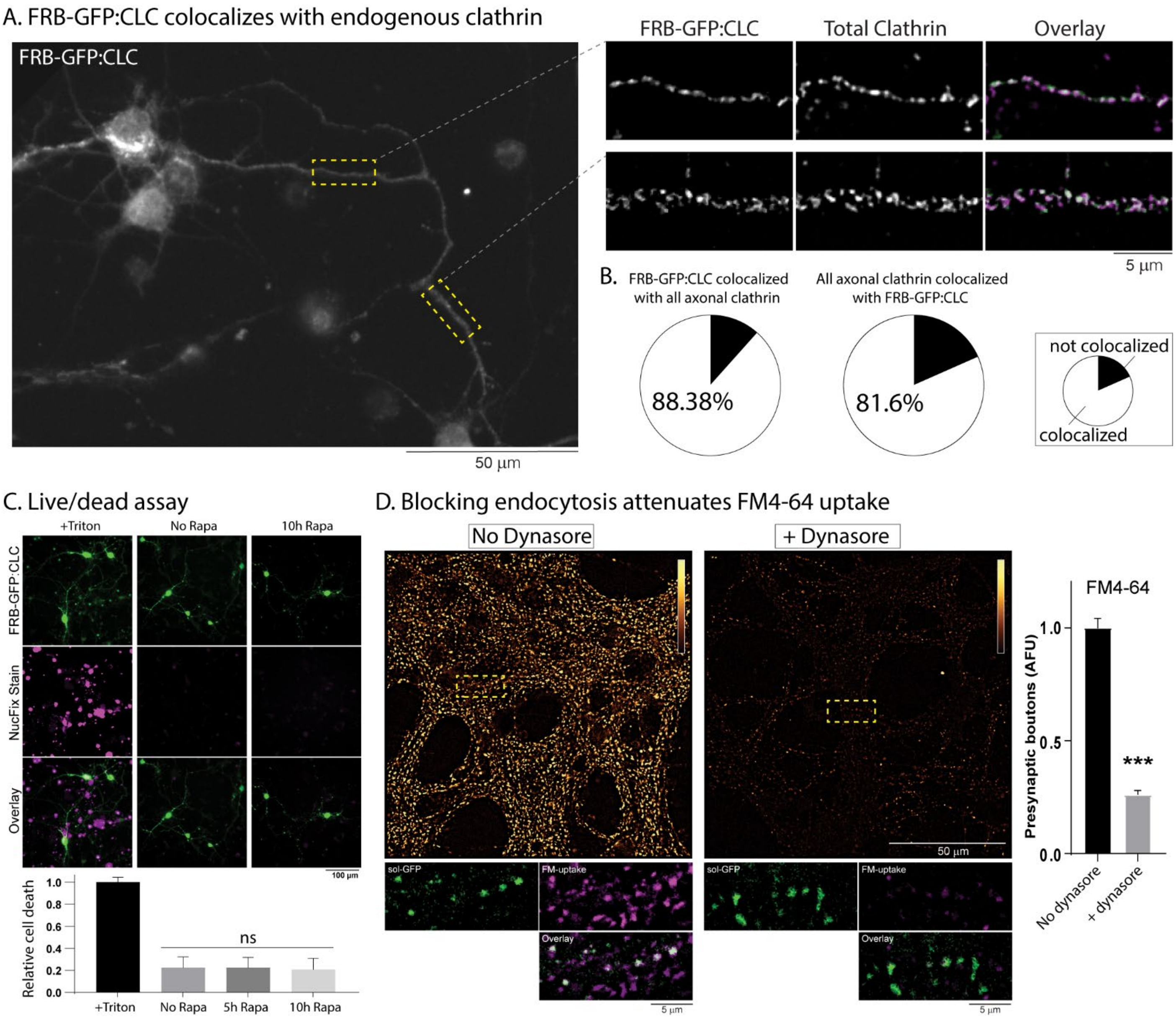

Figure S8: **Transfected FRB-GFP:CLC co-assembles with endogenous clathrin.**

(A) Neurons were transfected with FRB-GFP:CLC and immunostained with an antibody recognizing the clathrin heavy-chain (see 'methods"). In the insets magnified in A', note the extensive colocalization of transfected FRB-GFP:CLC with endogenous clathrin.

(B) Colocalization analysis indicates that the majority of transfected FRB-GFP:CLC (~ 80-90%) co-assembles with the endogenous clathrin in axons (~250 particles were analyzed from 10 neurons).

(C) Live/dead assay with NucFix stain (see "Methods") was validated in FRB-GFP:CLC transfected neurons by treating the cells with 0.01% Triton for one minute (left panel). Note that there was no staining above baseline after addition of Rapalog; quantified at bottom (12-16 fields of neurons were imaged for each condition from two separate cultures).

(D) Blocking endocytosis by Dynasore led to an attenuation of the FM4-64 dye uptake, as shown in the representative images on left (zoom from boxed regions shown below) and quantification of the data on right. For quantification, boutons were identified by varicosities in neurons transiently transfected with soluble GFP (~240-310 synapses were analyzed for each condition from 3 coverslips).

Table S1. Proteins associated with clathrin - MUDPIT data (related to Fig. 4)

Protein Families	UniProtKB ID (from MudPIT)	Gene IDs	Organism
ATP citrate synthase	Q3V117	Acly	Mus musculus (Mouse)
Actin	P68134, P60710, Q8BFZ3, P68033	Acta1, Actb, Actbl2, Actc1	Mus musculus (Mouse)
Argonaute	Q8CJG0	Ago2	Mus musculus (Mouse)
Ahnak2	E9PYB0	Ahnak2	Mus musculus (Mouse)
Adaptor Related Protein Complex	Q8CC13, Q8CBB7, Q3UHJ0, P17426, P17427, Q9DBG3, P84091, P62743, Q9Z1T1	Ap1b1, Ap1g1, Aak1, Ap2a1, Ap2a2, Ap2b1, Ap2m1, Ap2s1 , Ap3b1	Mus musculus (Mouse)
V-ATPase	Q9Z1G4	Atp6v0a1	Mus musculus (Mouse)
Bag3	Q9JLV1	Bag3	Mus musculus (Mouse)
Bcr	Q6PAJ1	Bcr	Mus musculus (Mouse)
Bmp	Q91Z96	Bmp2k	Mus musculus (Mouse)
Calcoco	Q8CGU1	Calcoco1	Mus musculus (Mouse)
Ccdc	D3YZP9	Ccdc6	Mus musculus (Mouse)
Clint1	Q5SUH7	Clint1	Mus musculus (Mouse)
Clathrin	Q6IRU5, Q68FD5	Cltb, Cltc	Mus musculus (Mouse)
Alpha-crystallin	P23927	Cryab	Mus musculus (Mouse)
Casein	P19228, Q02862	Csn1s1, Csn1s2a	Mus musculus (Mouse)
Dab2	P98078	Dab2	Mus musculus (Mouse)
Connecdenn	Q8K382	Dennd1a	Mus musculus (Mouse)
Dynamin	P39053, P39054	Dnm1, Dnm2	Mus musculus (Mouse)
Dynein	Q9JHU4	Dync1h1	Mus musculus (Mouse)
Edc	Q3UJB9	Edc4	Mus musculus (Mouse)
Eef	P58252	Eef2	Mus musculus (Mouse)
Epsin	Q80VP1, Q5NCM5	Epn1, Epn2	Mus musculus (Mouse)
Eps	P42567, Q60902	Eps15, Eps15l1	Mus musculus (Mouse)
Fatty acid binding protein	Q05816	Fabp5	Mus musculus (Mouse)
Fatty Acid Synthase	P19096	Fasn	Mus musculus (Mouse)
Fcho	Q3UQN2	Fcho2	Mus musculus (Mouse)
Fibrinogen A	E9PV24	Fga	Mus musculus (Mouse)
Filamin A	Q8BTM8	Flna	Mus musculus (Mouse)
Gak	Q99KY4	Gak	Mus musculus (Mouse)
Gulp1	Q8K2A1	Gulp1	Mus musculus (Mouse)
H1	P15864, P43274	H1-2, H1-4	Mus musculus (Mouse)
Hip1	Q8VD75, Q6ZQ77	Hip1, Hip1r	Mus musculus (Mouse)
Hnrnp	Q8BG05, Q8VDM6	Hnrnpa3, Hnrnpul1	Mus musculus (Mouse)
Heat shock proteins	Q80TZ3, Q71LX8, Q8K0U4, Q61696, P16627,P17156, Q3U2G2, P48722, P20029, Q504P4, Q61699	Dnajc6, Hsp90ab1, Hspa12a, Hspa1a, Hspa1l, Hspa2, Hspa4, Hspa4l, Hspa5, Hspa8, Hsph1	Mus musculus (Mouse)
Intersectin	E9Q0N0, B2RR82	Itsn1, Itsn2	Mus musculus (Mouse)
Kcp	Q3U492	Kcp	Mus musculus (Mouse)
Lactate Dehydrogenase	P16125	Ldhb	Mus musculus (Mouse)
Lrp1	Q91ZX7	Lrp1	Mus musculus (Mouse)
Maged1	Q9QYH6	Maged1	Mus musculus (Mouse)
Map7	A2AG50	Map7d2	Mus musculus (Mouse)
Myosin	Q3UH59, Q69ZX3, E9Q174	Myh10, Myh11, Myo6	Mus musculus (Mouse)
Numb	Q9QZS3, O08919	Numb, Numbl	Mus musculus (Mouse)
Osbp	D3YTT6	Osbpl3	Mus musculus (Mouse)
Pdcd	Q9WU78	Pdcd6ip	Mus musculus (Mouse)
Phgdh	Q61753	Phgdh	Mus musculus (Mouse)
Picalm	Q7M6Y3	Picalm	Mus musculus (Mouse)
Pik3	Q61194	Pik3c2a	Mus musculus (Mouse)
Prune	Q52KR3	Prune2	Mus musculus (Mouse)
Periaxin	O55103	Prx	Mus musculus (Mouse)
Reps	O54916, B9EI38	Reps1, Reps2	Mus musculus (Mouse)
Rundc3a	O08576	Rundc3a	Mus musculus (Mouse)
Sec Faily	Q9D1M0, E9QAT4, Q01405	Sec13, Sec16a, Sec23a	Mus musculus (Mouse)
Sh3d19	Q91X43	Sh3d19	Mus musculus (Mouse)
Slc12a4	Q9JIS8	Slc12a4	Mus musculus (Mouse)
Snap91	Q61548	Snap91	Mus musculus (Mouse)
Alpha-synuclein	O55042	Snca	Mus musculus (Mouse)
Sorting nexin	Q91VH2	Snx9	Mus musculus (Mouse)
Sos1	Q62245	Sos1	Mus musculus (Mouse)
Spectrin Beta	Q62261	Sptbn1	Mus musculus (Mouse)
Stambpl1	Q76N33	Stambpl1	Mus musculus (Mouse)
Ston2	E9PXP7	Ston2	Mus musculus (Mouse)
Synj1	D3Z656	Synj1	Mus musculus (Mouse)
Tfg	Q9Z1A1	Tfg	Mus musculus (Mouse)
Tnrc6b	Q8BKI2	Tnrc6b	Mus musculus (Mouse)
Tom1l2	Q5SRX1	Tom1l2	Mus musculus (Mouse)
Trim21	Q3U7K7	Trim21	Mus musculus (Mouse)
Tubulin	P68368, Q9CWF2, Q922F4	Tuba4a, Tubb2b, Tubb6	Mus musculus (Mouse)
Ubiquitin C	P0CG50	Ubc	Mus musculus (Mouse)
Utrophin	E9Q6R7	Utrn	Mus musculus (Mouse)
Vcp	Q01853	Vcp	Mus musculus (Mouse)

Ybx	P62960, Q9JKB3	Ybx1, Ybx3	Mus musculus (Mouse)
Ywhag	P61982	Ywhag	Mus musculus (Mouse)
FLJ45252 homolog	Q6PIU9	FLJ45252 homolog	Mus musculus (Mouse)

7 Collaboration à l'article Bingham et al. JCB 2023 : « Presynapses contain distinct actin nanostructures »

7.1 Commentaire

Pendant ma 3^{e} année de doctorat, j'ai eu l'occasion d'apporter ma contribution aux travaux de recherche d'un autre doctorant dans l'équipe (Bingham et al., 2023, *J. Cell Biol.*), ses travaux de thèse portaient sur le rôle de l'actine dans l'organisation et la physiologie présynaptique. L'organisation et les rôles de l'actine aux présynapses est un sujet au long cours dans la communauté scientifique car son étude présente beaucoup d'obstacles techniques devant être contournés. Un obstacle majeur est présenté par la densité d'actine dans les compartiments postsynaptiques qui viennent masquer les structures de densité plus faibles à la présynapse lors d'un marquage de l'actine sur des neurones en culture. De plus, la taille d'un bouton présynaptique dans les neurones du système nerveux central est déjà particulièrement petite (quelques centaines de nanomètres de diamètre) et nous cherchons à observer des structures sub-synaptiques distinctes à l'intérieur de ce petit compartiment (Campbell et al., 2020, *Eneuro*; X. Yang & Specht, 2019, *Front. Mol. Neurosci.*).

Enfin, les synapses des neurones présents sur un substrat de culture présentent un grand nombre d'orientations, ce qui complique encore la tâche d'identification de structures d'actine communes à toutes les présynapses.

Grâce à la mise en œuvre de techniques de microscopie super-résolue sur un modèle de présynapses induites par billes et au développement d'un marquage endogène de l'actine non global à un échantillon, nous avons pu montrer l'existence d'une distribution différenciée de l'actine dans les présynapses, puis mettre en évidence 3 structures d'actine présynaptiques à la morphologie et aux rôles putatifs distincts.

Jusqu'à présent, la littérature concernant le rôle de l'actine dans les présynapse montre des résultats contradictoires. Selon les études et les méthodes, l'actine serait promotrice ou inhibitrice du recyclage vésiculaire, ou uniquement un échafaudage du bouton présynaptique. Ces résultats contrastés suggèrent que différents types de structures d'actine sont présentes aux présynapses, chacune avec des rôles distincts.

Dans ce travail, nous avons caractérisé la distribution hétérogène de l'actine dans 2 classes de synapses, puis identifié 3 types de structures d'actine présynaptique en utilisant des méthodes de microscopie super-résolues dans un modèle de présynapses induites par billes. Par la suite nous avons pu montrer l'existence de ces structures au sein de synapses glutamatergiques comme GABAergiques et l'usage de perturbations chimiques nous a permis d'identifier les nucléateurs d'actine à l'origine de chacune des structures. Puis nous avons confirmé la présence et le rôle de ces structures sur des synapses naturelles en faisant exprimer de façon endogène une fusion actine-Halotag. Enfin, l'expression endogène d'une fusion actine-FLAG dans une proportion limitée des neurones d'un échantillon a permis de retrouver ces structures sur des synapses naturelles orientées de façon similaires aux synapses induites sur bille.

Dans ces travaux, j'ai évalué qualitativement les différentes acquisitions de présynapses dans le logiciel de visualisation de particules 3D ChimeraX (UC San Francisco). Sur la base des notes d'observation prises pour chacune de ces observations qualitatives, j'ai défini des classes de structures d'actine que j'observais de façon récurrente au travers des échantillons. Sur la base de ce premier jeu de classes de structures, j'ai quantifié leur présence et qualifié leur modifications en fonction des types de traitements appliqués dans les expériences présentées dans les figures 6 à 8. Nous avons par la suite raffiné ce modèle pour aboutir aux 3 catégories rails/corrals/mesh dont le modèle d'organisation est présenté dans la figure 10.

JCB Journal of Cell Biology

ARTICLE

Presynapses contain distinct actin nanostructures

Dominic Bingham[1], Channa Elise Jakobs[1], Florian Wernert[1], Fanny Boroni-Rueda[1], Nicolas Jullien[1], Eva-Maria Schentarra[1], Karoline Friedl[1,2], Julie Da Costa Moura[1], Danique Michelle van Bommel[1], Ghislaine Caillol[1], Yuki Ogawa[3], Marie-Jeanne Papandréou[1], and Christophe Leterrier[1]

The architecture of the actin cytoskeleton that concentrates at presynapses remains poorly known, hindering our understanding of its roles in synaptic physiology. In this work, we measure and visualize presynaptic actin by diffraction-limited and super-resolution microscopy, thanks to a validated model of bead-induced presynapses in cultured neurons. We identify a major population of actin-enriched presynapses that concentrates more presynaptic components and shows higher synaptic vesicle cycling than their non-enriched counterparts. Pharmacological perturbations point to an optimal actin amount and the presence of distinct actin structures within presynapses. We directly visualize these nanostructures using Single Molecule Localization Microscopy (SMLM), defining three distinct types: an actin mesh at the active zone, actin rails between the active zone and deeper reserve pools, and actin corrals around the whole presynaptic compartment. Finally, CRISPR-tagging of endogenous actin allows us to validate our results in natural synapses between cultured neurons, confirming the role of actin enrichment and the presence of three types of presynaptic actin nanostructures.

Introduction

In the human brain and nervous system, hundreds of trillions (~10^{14}) of synapses ensure fast communication between neurons (DeWeerdt, 2019; Cano-Astorga et al., 2021). Chemical synapses are intricate assemblies connecting the emitting neuron, usually from a presynapse located along the axon, to the receiving neuron, typically along its dendrites. Following calcium elevation, synaptic vesicles fuse at the presynaptic active zone, releasing neurotransmitters through the synaptic cleft (Südhof, 2021). Since their discovery by pioneering electron microscopy (EM) works in the middle of the 20th century (Sotelo, 2020), the architecture of presynapses and their diversity have been progressively unraveled. Decades of studies have defined the presence and role of hundreds of specific synaptic proteins, culminating in elaborate molecular models of the presynaptic compartment (Wilhelm et al., 2014). Presynaptic boutons and terminals exhibit unique molecular specialization and structural plasticity, yet the detailed arrangement of the presynaptic cytoskeleton supporting these processes remains poorly known compared with their postsynaptic counterpart. This is particularly true for actin, despite its prominent enrichment in both pre- and postsynapses (Cingolani and Goda, 2008; Gentile et al., 2022).

The presence of actin at presynapses has been recognized from early EM studies, but its precise organization was difficult to pinpoint because of the challenging size, lability, and low contrast of actin filaments in EM preparations (Papandréou and Leterrier, 2018; Leterrier, 2021a). Short actin filaments are seen within the cytomatrix of the active zone, contacting closely apposed synaptic vesicles that form the readily releasable pool (RRP, Hirokawa et al., 1989; Li et al., 2010). Actin filaments are also present deeper in the presynapse, where they are found around or within the vesicle clusters of the reserve pool, which can be mobilized by prolonged or intense stimulation (Landis and Reese, 1983; Siksou et al., 2007). Actin also forms larger structures between the periphery of the active zone, where endocytosis occurs for synaptic vesicle recycling, and the reserve pool (Bloom et al., 2003; Shupliakov et al., 2002; Del Signore et al., 2021; Ogunmowo et al., 2023). The overall view of presynaptic actin organization from EM studies points to the existence of different nanostructures (Dillon and Goda, 2005) but is still too fragmented for a comprehensive architectural model to emerge. Fluorescence optical microscopy can provide much better throughput and molecular specificity to visualize presynaptic components, but its limited spatial resolution (~250 nm) precludes obtaining details within the ~1 μm presynaptic bouton. Fortunately, super-resolution microscopy techniques can bypass this limitation, easily reaching resolutions down to tens of nanometers in fixed samples (Jacquemet et al., 2020).

[1]CNRS, INP UMR7051, NeuroCyto, Aix Marseille Université, Marseille, France; [2]Abbelight, Cachan, France; [3]Department of Neuroscience, Baylor College of Medicine, Houston, TX, USA.

Correspondence to Marie-Jeanne Papandréou: marie-jeanne.papandreou@univ-amu.fr; Christophe Leterrier: christophe.leterrier@univ-amu.fr.

Single Molecule Localization Microscopy (SMLM) techniques, such as Stochastic Optical Reconstruction Microscopy (STORM; Rust et al., 2006) or DNA-Point Accumulation in Nanoscale Topography (PAINT; Jungmann et al., 2014) work by localizing single emitters in "blinking" samples, progressively building an image from single fluorophore coordinates with a resolution down to 10–15 nm (Lelek et al., 2021). At the presynapse, SMLM has been used to delineate the organization of specific components, but the organization of presynaptic actin has not been addressed so far (Dani et al., 2010; Carvalhais et al., 2021; Nosov et al., 2020; Glebov et al., 2017). This is likely due to the challenge of densely labeling presynaptic actin (Reshetniak and Rizzoli, 2019) and distinguishing it from the high concentration and dense meshwork of postsynaptic actin that is evident in platinum-replica EM images of synapses (Korobova and Svitkina, 2010).

This lack of a comprehensive view of the presynaptic actin architecture keeps us from understanding the roles of actin in presynaptic physiology and its functions in the various steps of the synaptic vesicle cycle. The diversity of synaptic types studied cannot alone explain the large span of different and often contradictory results on presynaptic functions obtained after perturbation of the actin cytoskeleton (Cingolani and Goda, 2008; Rust and Maritzen, 2015; Wu and Chan, 2022). Applications of drugs that perturb actin assembly have led to reduced, unchanged, or elevated vesicular release depending on the model, drug, and experimental conditions used, leading to a number of conclusions on a driving, resisting, or merely the scaffolding role of presynaptic actin in the synaptic vesicle cycle (Morales et al., 2000; Cole et al., 2000; Li and Murthy, 2001; Sakaba and Neher, 2003; Sankaranarayanan et al., 2003; Bleckert et al., 2012; Rampérez et al., 2019). A plausible explanation of these contrasted results is that distinct actin structures co-exist within presynapses that have different functions in the synaptic vesicle cycle, with a net effect dependent on the precise experimental conditions (Cingolani and Goda, 2008; Papandréou and Leterrier, 2018). This further highlights the need to directly visualize and identify these presynaptic actin nanostructuresto generate meaningful hypotheses on their function.

In this work, we thus aimed at delineating and characterizing the presynaptic actin nanostructures. We first set up and validated a bead-induced model of presynapses in cultured hippocampal neurons that allowed us to distinguish presynaptic actin by both diffraction-limited and super-resolution microscopy. We could characterize the actin enrichment in a dominant subpopulation of induced presynapses and its effect on the presynapse composition and cycling activity. We assessed the effect of acute perturbations and modulations of the actin cytoskeleton on presynapses, validating induced presynapses against natural synapses in the same cultures. We then used super-resolution STORM and PAINT to directly visualize presynaptic actin nanostructures, demonstrating the existence of three main types of actin assemblies likely responsible for distinct functions within induced presynapses. Finally, we used CRISPR-tagging of endogenous actin to confirm the role of actin enrichment and the presence of three types of actin nanostructures within natural synapses between neurons.

Results

Bead-induced presynapses allow isolating presynaptic actin for imaging and quantification

The gold standard reagent to label filamentous actin in fixed neurons is fluorescent phalloidin (Melak et al., 2017). It provides a dense labeling of actin filaments, allowing for both quantification of the amount of actin on diffraction-limited images, and visualization of the nanoscale actin structures in super-resolution microscopy (Jimenez et al., 2020; Lavoie-Cardinal et al., 2020). However, phalloidin stains all neurons in a fixed culture, labeling both the presynaptic and postsynaptic actin at synapses. As postsynapses are highly enriched in actin, notably within the dendritic spine heads (Allison et al., 1998), their close apposition hides the lower amount of presynaptic actin (Zhang and Benson, 2002; Fig. S1). This is true not only for diffraction-limited images, where pre- and post-synapses are not resolved (Fig. S1, A and D), but also for STORM images, where despite their better resolution, the highly enriched dendrites and spines mask the presynaptic actin structures (Fig. S1, B, C, E, and F). In neurons after 9–10 d in culture, this is true for both excitatory (VGLUT-positive) synapses contacting spines and filopodia and inhibitory (VGAT-positive) synapses opposed to the actin-rich dendritic shaft (Fig. S1, D–F).

To visualize the specific enrichment and organization of presynaptic actin, we turned to a validated model of presynaptic induction using polylysine-coated beads. As discovered more than 40 yr ago (Burry, 1980), polylysine-coated beads seeded on neuronal cultures will induce the formation of presynaptic compartments within tens of minutes after contacting axons, whereas non-coated beads fail to attach or don't induce presynaptic specializations (Lucido et al., 2009). These induced specializations show that the structural hallmark of presynapses, including synaptic vesicle pools, are enriched in presynaptic protein components and are competent for vesicular release (Burry, 1980; Burry et al., 1986; Lucido et al., 2009). They form by inducing recruitment of heparan sulfate proteoglycans harbored by neurexins (Zhang et al., 2018) and have been used to dissect the mechanism of presynapse formation, in particular the need for local axonal translation (Taylor et al., 2013; Batista et al., 2017).

We thus seeded neurons after 7–8 d in vitro (div) with 3–5 μm-diameter polylysine-coated beads to induce isolated presynapses. After 48 h, we fixed and immunolabeled neurons for presynaptic markers to check for presynaptic induction (Fig. 1). Fluorescence images show beads readily inducing the concentration of presynaptic components when contacting axons: scaffold proteins bassoon and synapsin (Fig. 1, A and B) as well as synaptic vesicle proteins synaptophysin and vamp2 (Fig. 1, C and D). 80 ± 2.3% of axon-contacting beads induce such presynaptic components accumulation (S+ population, mean ± SEM, Fig. 1 G), whereas 20 ± 2.3% of beads do not result in visible presynaptic specialization along the contacted axon (S− population; see all statistics and tests for significance in Data S1). We next assessed if the induced presynaptic specializations were competent for vesicular cycling. We first used an antibody against an extracellular epitope of synaptotagmin that accumulates in presynapses either during constitutive cycling via a

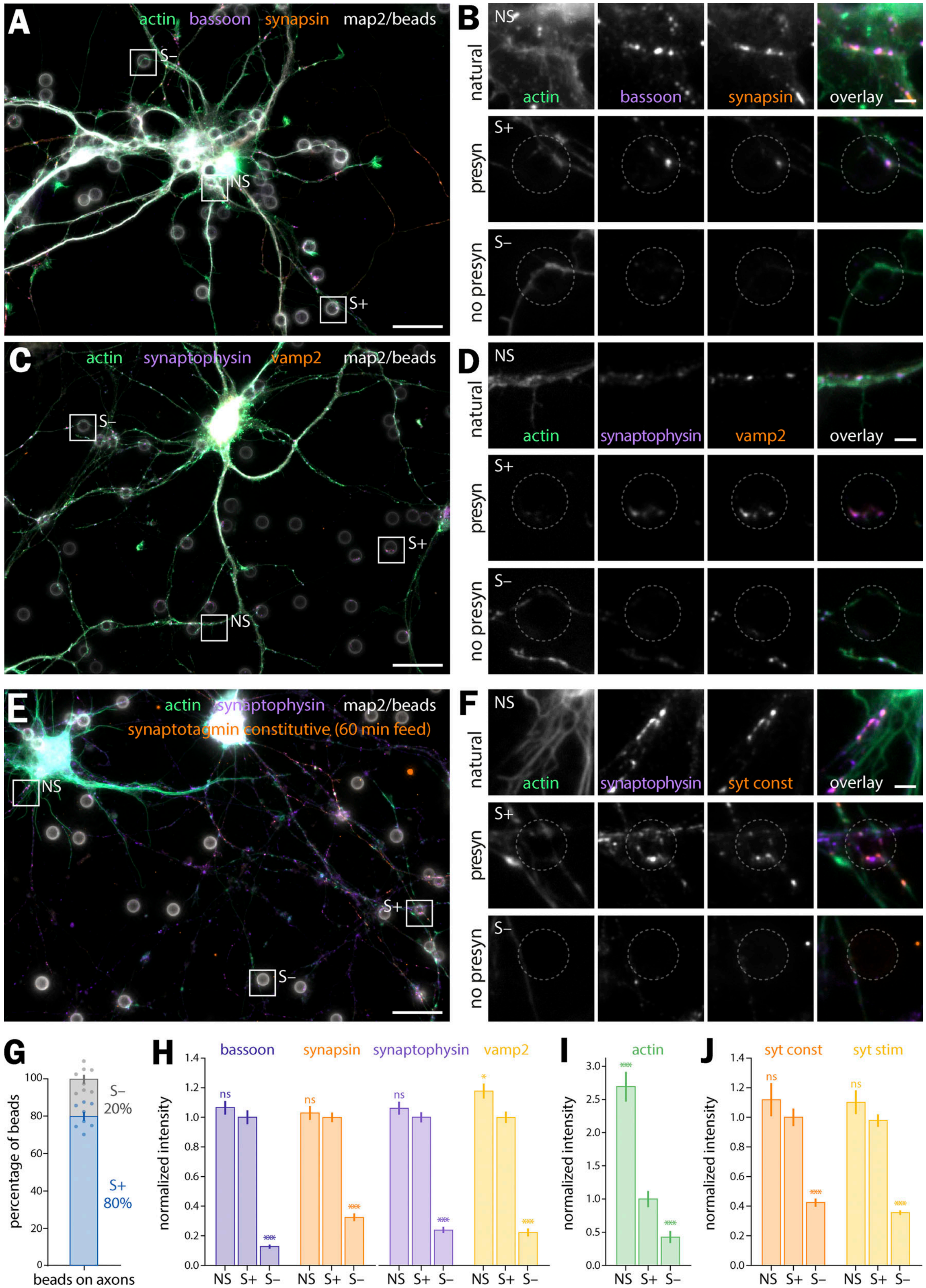

Figure 1. **Polylysine-coated beads induce functional presynaptic specializations at axon-bead contacts. (A)** Widefield fluorescence image of cultured neurons seeded with polylysine-coated beads (gray) after 8 div and fixed 48 h later at 10 div, labeled for actin (green), bassoon (purple), synapsin (orange), and map2 (gray). **(B)** Zooms corresponding to the areas highlighted in A: top row, natural synapse at axon-dendrite contact (NS); middle row, induced presynapse at an axon-bead contact (S+); bottom row, axon-bead contact with no induced presynapse (S−). The position of the bead is indicated by the dashed gray circle. **(C)** Widefield fluorescence image of cultured neurons 2 d after bead seeding at 8 div, labeled for actin (green), synaptophysin (purple), vamp2 (orange), and map2 (gray). **(D)** Zooms corresponding to the natural synapse, S+ and S− axon-bead contacts highlighted in C. **(E)** Widefield fluorescence image of cultured

neurons 2 d after bead seeding at 8 div, labeled for actin (green), synaptophysin (purple), map2 (gray), and feeding with anti-synaptotagmin antibody (syt) during constitutive vesicular cycling (orange). **(F)** Zooms corresponding to the natural synapse (NS), S+, and S− axon-bead contacts highlighted in E. Scale bars for A, C, and E: 20 µm; for B, D, and F: 2 µm. **(G)** Quantification of the proportion of S+ (blue) and S− (gray) axon-bead contacts. **(H)** Quantification of the labeling intensity for bassoon (dark purple), synapsin (orange), synaptophysin (purple), and vamp2 (yellow) at natural synapses (NS), induced presynapses at axon-bead contacts (S+) and axon-bead contacts devoid of presynapse (S−), normalized to the intensity at S+ contacts. **(I)** Quantification of the labeling intensity for actin at natural synapses (NS), induced presynapses at axon-bead contacts (S+) and axon-bead contacts devoid of presynapse (S−), normalized to the intensity at S+ contacts. **(J)** Quantification of the labeling intensity after syt feeding for constitutive (orange) and stimulated (KCl-induced, yellow) vesicular cycling at natural synapses (NS), induced presynapses at axon-bead contacts (S+), and axon-bead contacts devoid of presynapse (S−), normalized to the intensity at S+ contacts. Significance signs on graphs compare to the value for the same labeling in bead-induced presynapses (S+, normalized to 1.0). See Data S1 file for detailed statistics.

prolonged incubation or during stimulated cycling via a short incubation together with KCl (Kraszewski et al., 1995; Fig. S2 A). In our bead-seeded cultures, the anti-synaptotagmin antibody readily labels bead-induced presynaptic specializations in both the constitutive (Fig. 1, E and F) and stimulated (Fig. S2, B and C) versions of the assay. We also used the styryl dye FM1-43 to label cycling synaptic vesicles in living neurons (Gaffield and Betz, 2006), loading and then releasing the FM dye using two successive short KCl incubations (Fig. S2 D). FM dye readily accumulates in most enlarged contacts between axons and beads (as visualized using the live-cell actin probe SiR-actin; Lukinavičius et al., 2014) and is released after the second stimulation (Fig. S2, E and F).

In these 9–10 div neurons 48 h after beads seeding, we quantitatively assessed the enrichment of presynaptic components at axon–bead contacts where a presynaptic specialization has developed (S+) compared with the ones where it did not happen (S−), and to "natural" synapses between axons and dendrites in the same culture (NS, Fig. 1 H). Intensity measurements at axon–bead contacts show that induced presynaptic specializations S+ contain 3.1–7.7 times more bassoon, synapsin, synaptophysin, and vamp2 than non-presynaptic contacts S−. This enrichment is similar to natural synapses NS (Fig. 1 H), whereas natural synapses have a 2.7 times higher actin intensity due to the presence of dendritic and postsynaptic actin (Fig. 1 I). In addition, we measured vesicular cycling at axon–bead contacts using the anti-synaptotagmin (syt) antibody feeding assay: induced presynaptic specializations accumulate 2.4–2.7 times more syt antibody than non-presynaptic contacts and similar accumulation of natural synapses (Fig. 1 J). This was confirmed using FM1-43 loading experiments, where bead-induced presynapses had similar staining intensities to natural synapses after loading and release of the dye (Fig. S2 G). In conclusion, we confirmed that the bead-seeding model robustly induces isolated, functional presynapses in cultured hippocampal neurons, making it a valid model to discriminate presynaptic actin enrichment and organization.

Actin is enriched in a major subpopulation of induced presynapses, which shows higher accumulation of presynaptic components and higher synaptic cycling

We next focused on the actin content at induced presynapses (Fig. 2). A majority of axon–bead contacts where a presynaptic specialization was induced (labeled S+ in Fig. 1) show visible enrichment in actin compared with the nearby axon shaft after phalloidin staining (Fig. 2, A–D) and were labeled "actin +" (A+), whereas a minority of induced presynapses do not show actin enrichment and were labeled "actin −" (A−). A+ and A− induced presynapses are often found along the same axon arborization, suggesting it is not dependent on a cell-wide state (Fig. 2, A–D). Quantitatively, 67 ± 2.8% of all S+ induced presynapses are A+ (actin-enriched), corresponding to 53 ± 2.1% of all axon-bead contacts (Fig. 2 E). We measured the intensity of presynaptic components clusters at A+, A−, and S− axon–bead contacts to compare the accumulation of components in each type of contact (Fig. 2 F). In all quantifications, we normalized the cluster intensities to the dominant A+ population. By definition, actin intensity is much lower in A− than in A+ presynapses, similar to non-presynaptic contacts S− (0.25 ± 0.03 and 0.29 ± 0.03, respectively; Fig. 2 F). The intensity of presynaptic component clusters in A− presynapses is significantly below that of A+ presynapses (below 1 after normalizing to A+ presynapses: 0.74 ± 0.03 for bassoon; 0.66 ± 0.03 for synaptophysin; 0.70 ± 0.03 for synapsin; 0.65 ± 0.03 for vamp2; Fig. 2 F). Altogether, two-thirds of induced presynapses are specifically enriched in actin, and this enrichment is associated with a 30–50% enrichment in all presynaptic components assessed.

We then explored what are the factors for this selective enrichment of actin at induced presynapses. First, we tested if the maturity of seeded neurons could have an effect on actin enrichment (Fig. S3). We seeded neurons during the third week in culture (polylysine beads seeded at 14 div and fixation at 16 div) instead of the second week. Classification of axon-bead contacts into A+, A−, and S−, and quantification of presynaptic clusters intensities show similar results to neurons seeded with beads between 8 and 10 d (Fig. S3, A–F, see Data S1 for precise values and statistics). This shows that the maturation stage of neurons is not a key factor in the development of induced presynapses and that second-week neurons are as competent as third-week ones for developing isolated presynapses. We then assessed if the ∼30% proportion of induced presynapses that are not enriched in actin (A−) is due to a lack of synaptic maturation 48 h after bead seeding. We thus compared neurons seeded at 6 div and incubated with beads for 48 h (endpoint 8 div) or 96 h (endpoint 10 div, Figs. S4 and S6). We found that induced presynapses had levels of presynaptic components similar to natural presynapses at both time points (Fig. S6 A). The proportion of A− induced presynapses was similar after 48 and 96 h (Fig. S4 E), and in both conditions, A+ induced presynapses showed a similar 30–50% enrichment in presynaptic components and synaptic vesicle cycling (Fig. S4 F). This shows that synaptic maturation is not a factor for the existence of the A+ and A−

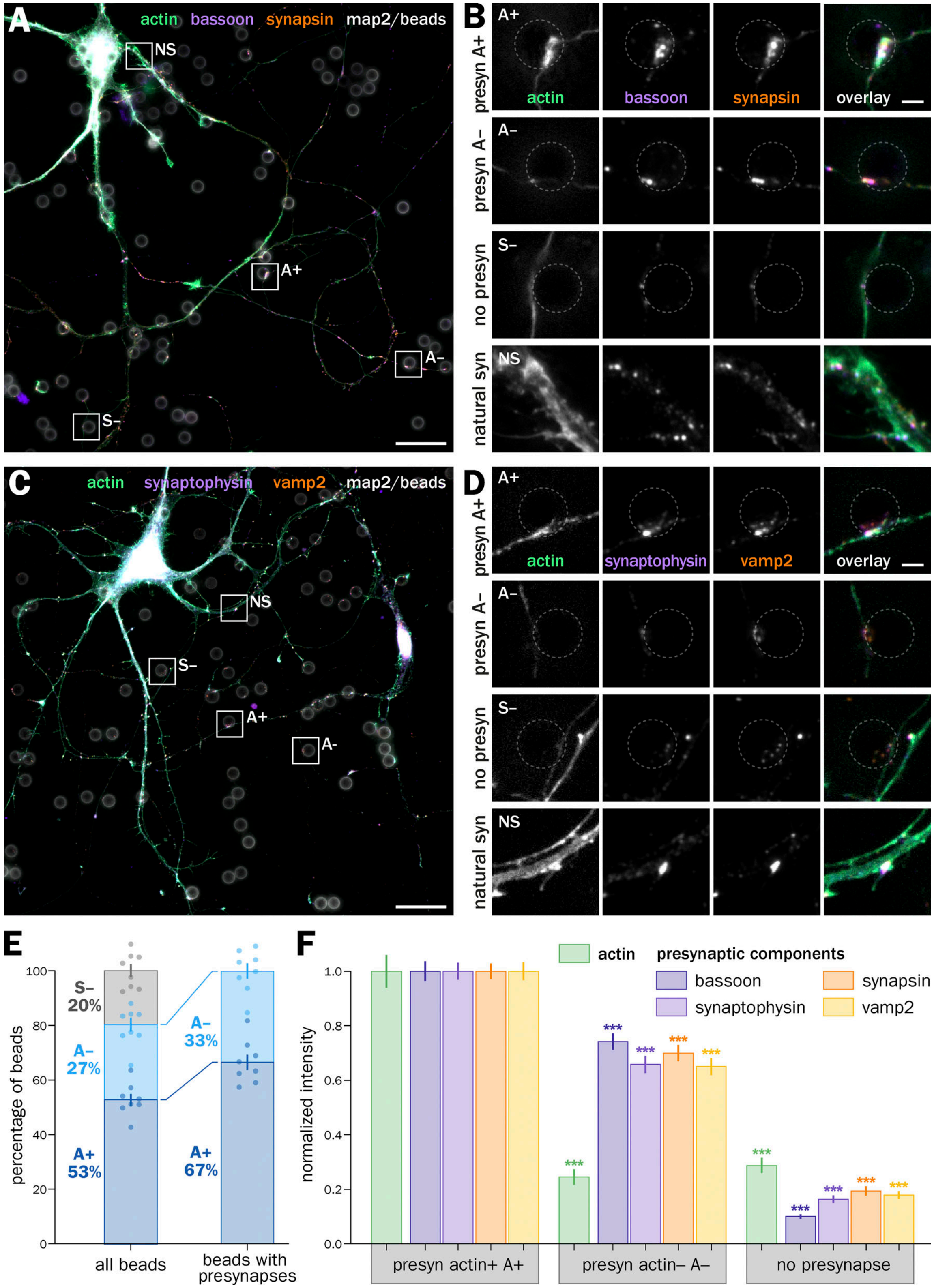

Figure 2. **A major proportion of bead-induced presynapses is enriched in actin and concentrates more presynaptic components than non-enriched induced presynapses. (A)** Widefield fluorescence image of cultured neurons 2 d after bead seeding at 8 div, labeled for actin (green), bassoon (purple), synapsin (orange), and map2 (gray). **(B)** Zooms corresponding to the areas highlighted in A: top row, actin-enriched induced presynapse at an axon-bead contact (A+); second row, induced presynapse at an axon-bead contact with no actin enrichment (A−); third row, axon-bead contact with no induced presynapse (S−); bottom row, natural synapse at axon-dendrite contact (NS). **(C)** Widefield fluorescence image of cultured neurons 2 d after bead seeding at 8 div, labeled for actin (green), synaptophysin (purple), vamp2 (orange), and map2 (gray). **(D)** Zooms corresponding to the A+, A−, S− axon-bead contacts and natural synapses (NS) highlighted in C. Scale bars in A and C: 20 µm; B and D: 2 µm. **(E)** Quantification of the proportion of A+ (dark blue), A− (blue), and S− (gray)

axon-bead contacts. **(F)** Quantification of the labeling intensity for actin (green), bassoon (dark purple), synaptophysin (purple), synapsin (orange), and vamp2 (yellow) at actin-enriched presynapses (A+), induced presynapses with no actin enrichment (A−), and axon-bead contacts devoid of presynapse (S−), normalized to the intensity at A+ presynapses. Significance signs on graphs compare to the value for the same labeling in actin-enriched presynapses (A+, normalized to 1.0). See Data S1 file for detailed statistics.

populations of induced presynapses and their distinct accumulation of presynaptic components.

Next, we tested if the proportion of A+ and A− induced presynapses is different between presynapses induced along axons from excitatory (glutamatergic) and inhibitory (GABAergic) neurons. In cultures of embryonic rat hippocampal neurons, only 6% of neurons are GABAergic (Benson et al., 1994), but their synapses represent between 20% and 40% of all synapses (Harms and Craig, 2005; Danielson et al., 2021). We labeled bead-seeded neurons using markers for glutamatergic (VGLUT) and GABAergic (VGAT) presynapses (Fig. S5, A–D) and measured the proportion of A+ vs. A− induced presynapses as well as the intensity of presynaptic component clusters in each population. Actin-enriched presynapses are similarly dominant in the two synapse types (Fig. S5 E). In both types, actin enrichment is associated with a higher accumulation of presynaptic components (including VGLUT and VGAT), with normalized cluster intensities below 1 for the A− presynapses (Fig. S5 F). In addition, we verified that bead-induced presynapses had similar presynaptic component levels as natural synapses in the same cultures (Fig. S6, C and D), except that actin was 2.2 and 1.8 times higher at natural synapses for glutamatergic and GABAergic synapses, respectively, due to the presence of postsynaptic actin (Fig. S6 E). This shows that selective actin enrichment is similar in excitatory- and inhibitory-induced presynapses, suggesting a general phenomenon that does not depend on the presynapse type.

Finally, we assessed whether actin enrichment in induced presynapses is associated with a difference in synaptic vesicle cycling. It has been shown that actin was involved in activating silent synapses after stimulation, suggesting that non-enriched presynapses could even be silent in our cultures (Yao et al., 2006). We used the syt antibody feeding assay (Fig. S2 A) to measure the constitutive and stimulated vesicular cycling at actin-enriched and non-enriched induced presynapses while monitoring the synaptophysin accumulation in the same experiment (Fig. 3, A–D). A+ presynapses showed a 20–40% more intense syt accumulation than A− presynapses, with the A−normalized intensity of syt clusters being below 1 for both constitutive and stimulated versions of the assay (0.71 ± 0.06 for constitutive cycling and 0.72 ± 0.03 for stimulated cycling; Fig. 3 E). We confirmed these results using FM1-43 staining experiments in living neurons co-stained with SiR-actin to reveal the actin enrichment at induced presynapses, measuring FM1-43 intensity after dye loading and release by two successive short KCl incubations (Fig. 3 F). Actin-enriched presynapses A+ could accumulate more FM1-43 than non-actin enriched ones A− that had a lower normalized intensity (0.72 ± 0.07), while the intensity level after dye release was similarly low (0.38 ± 0.03 for A+ and 0.33 ± 0.04 for A− after release, normalized to the loaded A+ intensity; Fig. 3 G). Thus, lack of actin enrichment is not associated with silent presynapses, but actin-enriched induced presynapses tend to have a significantly higher vesicular cycling activity.

Both acute disassembly and over-stabilization of actin content lower the accumulation of presynaptic components and vesicular cycling in presynapses

To test if actin enrichment was responsible for the higher accumulation of presynaptic components and higher cycling rate of A+ presynapses, we perturbed actin using drugs able to either disassemble and sever actin filaments (swinholide A; Spector et al., 1999) or inhibit their depolymerization and overstabilize them (cucurbitacin E; Sörensen et al., 2012). We used acute perturbations with strong drugs to avoid indirect effects from impacting other aspects of neuronal physiology (Fig. 4; Vassilopoulos et al., 2019). 1 h treatment with 1 μM swinholide A (swin) results in the near-complete disappearance of filamentous actin at induced presynapses, as evidenced by comparing phalloidin staining between the control and swin conditions (Fig. 4, A and B), and all treated presynapses were classified as A− and the normalized intensity dropped to 0.02 ± 0.01 **Q:1** (Fig. 4 D). Conversely, phalloidin staining is strongly elevated after a 3 h treatment with 5 μM cucurbitacin E (cuc; Fig. 4 C), which caused all treated presynapses to be classified as A+, and a rise of the normalized intensity to 7.3 ± 0.43 (Fig. 4 E).

We then measured the accumulation of presynaptic components and vesicular cycling after swin and cuc treatments. Swin treatment decreased the accumulation of all labeled components to values very similar to those from untreated A− presynapses (normalized intensities of 0.69 ± 0.03 for bassoon, 0.74 ± 0.03 for synaptophysin, 0.67 ± 0.03 for synapsin, and 0.61 ± 0.03 for vamp2; Fig. 4 D). In addition, actin disassembly by swin also reduced the vesicular cycling in both constitutive and KCl-stimulated assays to values similar to control A− presynapses (syt normalized intensities of 0.79 ± 0.04 for constitutive and 0.71 ± 0.03 for stimulated; Fig. 4 D). Interestingly, elevated polymerization and stabilization of actin by cuc also reduced the accumulation of presynaptic components and vesicular cycling at induced presynapses to values similar to untreated A− presynapses (normalized intensities of 0.83 ± 0.04 for bassoon, 0.86 ± 0.04 for synaptophysin, 0.68 ± 0.02 for synapsin, 0.89 ± 0.03 for vamp2, 0.77 ± 0.08 for syt constitutive, and 0.69 ± 0.04 for syt stimulated; Fig. 4 E).

This drop in presynaptic component clustering and vesicular cycling after both swin and cuc treatments suggests that an optimal level of presynaptic actin enrichment is needed to ensure their efficient functioning. To further confirm the validity of these findings, we measured the accumulation of presynaptic components and the amount of vesicular cycling in natural synapses (dendrite-axon contact) on the same images as the bead-induced presynapses. Actin disassembly by swin and

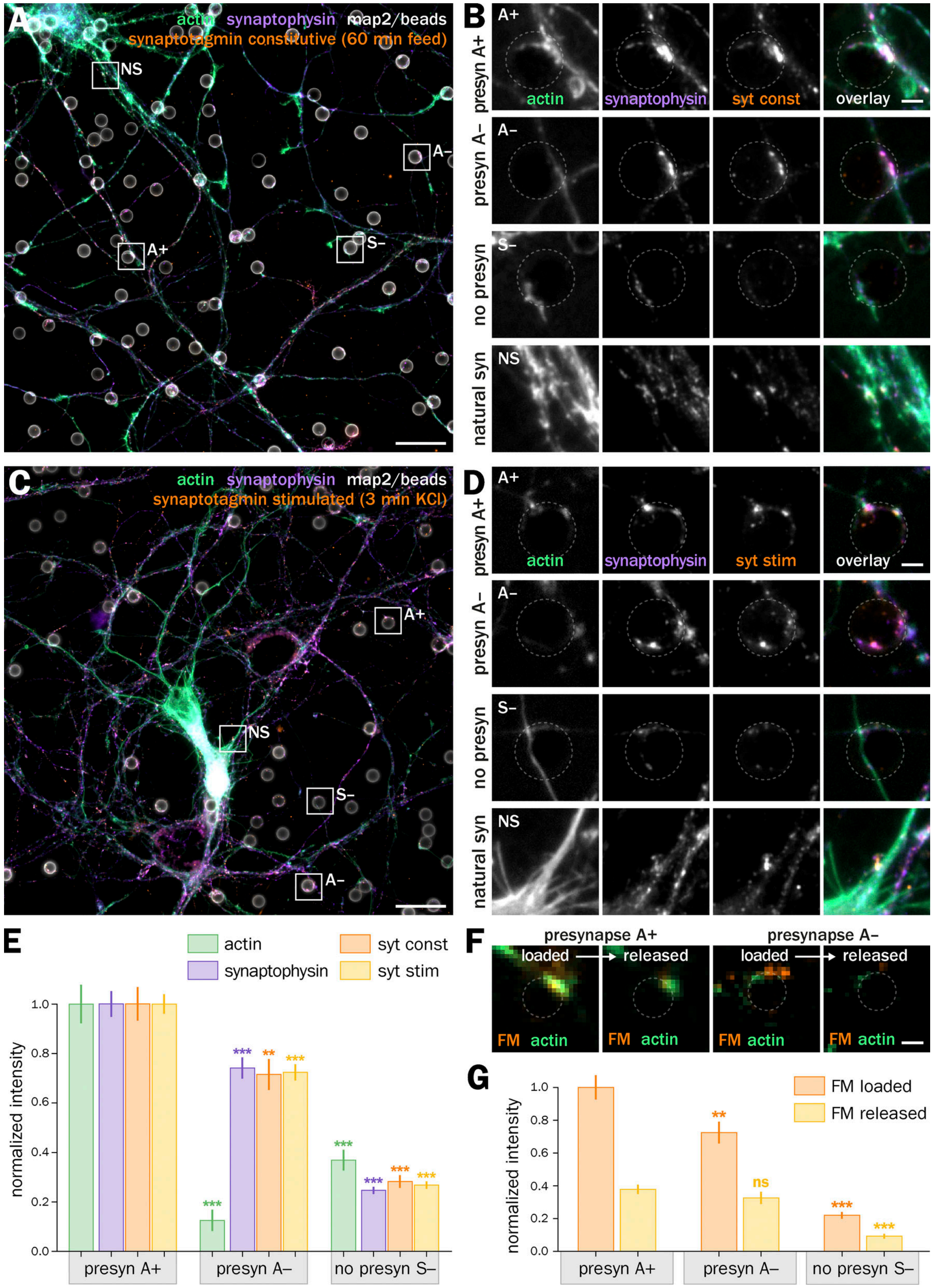

Figure 3. **Actin-enriched induced presynapses have a higher vesicular cycling than non-enriched induced presynapses. (A)** Widefield fluorescence image of cultured neurons 2 d after bead seeding at 8 div, labeled for actin (green), synaptophysin (purple), map2 (gray), and feeding with anti-synaptotagmin antibody (syt) during constitutive cycling (orange). **(B)** Zooms corresponding to the A+, A–, S– axon-bead contacts and natural synapses (NS) highlighted in B. **(C)** Widefield fluorescence image of cultured neurons 2 d after bead seeding at 8 div, labeled for actin (green), synaptophysin (purple), and map2 (gray) and feeding with anti-synaptotagmin antibody (syt) during KCl-stimulated vesicular cycling (orange). **(D)** Zooms corresponding to the A+, A–, S– axon-bead contacts and natural synapses (NS) highlighted in C. Scale bars in A and C, 20 µm; B and D, 2 µm. **(E)** Quantification of the labeling intensity for actin (green), synaptophysin (purple), and after syt feeding for constitutive (orange) and stimulated (yellow) vesicular cycling at actin-enriched presynapses (A+), induced

presynapses with no actin enrichment (A−), and axon-bead contacts devoid of presynapse (S−), normalized to the intensity at A+ presynapses. **(F)** Zooms on axon-bead contacts of living neurons stained with SiR-actin (green) and loaded with FM1-43 (orange, left image) before release (right image). Left two images show an A+ presynapse, right images show an A− presynapse. Scale bar, 2 µm. **(G)** Quantification of the FM staining intensity after loading (orange) and release (yellow) in A+ and A− induced presynapses as well as axon-bead contacts devoid of a presynapse (S−). Significance signs on graphs compare to the value for the same labeling condition in actin-enriched presynapses (normalized to 1.0 for A+ in E, normalized to 1.0 for the A+ in loading condition in G). See Data S1 file for detailed statistics.

overstabilization by cuc leads to a 10–40% drop in presynaptic component accumulation and vesicular cycling, in line with the effects observed in bead-induced presynapses (Fig. S6, F–J).

Inhibition of actin nucleators results in different effects on actin and presynaptic components in induced presynapses, suggesting action on distinct presynaptic actin structures

The fact that both actin disassembly and overstabilization lead to a less efficient vesicular cycling is consistent with the idea that distinct actin structures coexist within a presynapse and can have opposing effects on presynaptic function. To address this hypothesis more finely, we used drugs that target distinct actin filament nucleation mechanisms: CK666 inhibits Arp2/3-mediated branched actin nucleation (Nolen et al., 2009), whereas SMIFH2 inhibits the nucleation of linear actin structures mediated by formins (Rizvi et al., 2009). We thus evaluated the effect of CK666 and SMIFH2 treatments on actin-enriched induced presynapses (A+; Fig. 5, A–C). 1 h treatment with 50 µM CK666 results in a contrasted modulation of presynaptic components (Fig. 5 D): total filamentous actin in A+ presynapses is not significatively affected (normalized intensity of 0.95 ± 0.04), indicating a shift of actin polymerization toward other nucleation mechanisms. Scaffold proteins bassoon and synapsin are downregulated (0.89 ± 0.04 for bassoon and 0.77 ± 0.04 for synapsin), whereas synaptic vesicle proteins and vesicular cycling are not significantly affected (1.04 ± 0.05 for synaptophysin, 1.07 ± 0.04 for vamp2, 1.05 ± 0.09 for syt constitutive, and 1.08 ± 0.07 for syt stimulated). We further tested the effect of CK666 on presynaptic scaffold protein Munc13 and synaptic vesicle proteins syntaxin and SV2 and measured a reduction in the accumulation of SV2 and Munc13, but not syntaxin, in bead-induced presynapses after CK666 treatment (Fig. S7, F–H). Treatment with 30 µM SMIFH2 for 1 h results in a significantly higher amount of actin in A+ presynapses (normalized intensity 1.35 ± 0.06), but this compensation is associated with a general downregulation of presynaptic components (0.86 ± 0.04 for bassoon, 0.71 ± 0.03 for synaptophysin, 0.80 ± 0.05 for synapsin, and 0.89 ± 0.04 for vamp2) and a significant drop of vesicular cycling (0.55 ± 0.03 for syt constitutive and 0.72 ± 0.04 for syt stimulated, Fig. 5 D).

By contrast, CK666 has no effect on induced presynapses non-enriched in actin and SMIFH2 has a limited effect on synapsin and synaptophysin content, as well as KCl-stimulated cycling (Fig. S7 D). Here again, we verified the effects found on induced presynapses by quantifying the effect of CK666 and SMIFH2 on natural synapses in the same neuronal culture (Fig. S7, A–C, E, and I). The same treatments resulted in small variations for presynaptic components' accumulation, suggesting a tighter control or higher stability of the presynaptic compartment in natural synapses. Of note, vesicular cycling is strongly affected by inhibiting formins with SMIFH2, similar to induced presynapses (Fig. S7 E). Overall, the effect of CK666 and SMIFH2 on induced presynapses content and function reveals some insight into the role of different actin structures: small, contrasted effects of inhibiting Arp2/3 likely result from the inhibition of several different branched Arp2/3-dependent actin structures, whereas the global downregulation observed with SMIFH2 suggests the presence of linear, formin-dependent actin structures that favor synaptic cycling.

STORM of actin at induced presynapses reveals three types of nanostructures

At this point, these inferred distinct actin structures remain undiscernible due to the small size of the presynapses and the limited resolution of diffraction-limited fluorescence microscopy. We thus used STORM to directly visualize actin nanostructures within induced presynapses with a lateral resolution of around 15 nm (Fig. 6; Leterrier et al., 2015). In contrast to natural axon-dendrite synapses (Fig. 6, A and B, top), STORM clearly resolves presynaptic actin at axon–bead presynapses (Fig. 6, A and B, bottom and Fig. 6 C). The 190-nm spaced actin rings found along the axon shaft (Leterrier, 2021b; Vassilopoulos et al., 2019) usually stop at the presynaptic bouton, confirming previous results suggesting that boutons are devoid of the axonal actin/spectrin periodic scaffold (He et al., 2016; Sidenstein et al., 2016). However, it is sometimes possible to see a continuity of the periodic scaffold along the membrane dorsal to the presynaptic contact, consistent with the idea that en-passant boutons are laterally adjacent to a continuous axonal shaft. In addition, the vicinity of presynapses often shows fine longitudinal actin bundles, reminiscent of the actin trails that can transport actin and presynaptic components between adjacent boutons (Fig. 6 C; Ganguly et al., 2015; Chenouard et al., 2020).

Within induced presynapses themselves, STORM allowed us to delineate distinct nanostructures that we could classify into three types (Fig. 6 D): a small, often faint cluster of actin mesh at the bead contact, corresponding to the localization of the active zone (in red on Fig. 6 D); linear actin rails often connecting the active zone to deeper compartments within the bouton (green on Fig. 6 D); and larger, branched structures surrounding the whole presynapse (synapsin-positive area) that we called actin corrals (in cyan on Fig. 6 D). Similar to natural presynapses, induced presynapses show significant variability in size, shape, and architecture. Despite this, the three types of presynaptic actin structures (mesh, rails, and corrals) were consistently identified in most of the >90 presynapses imaged by STORM in control conditions (Fig. 6 E). To refine the relationship between actin and presynaptic components, we performed three-color

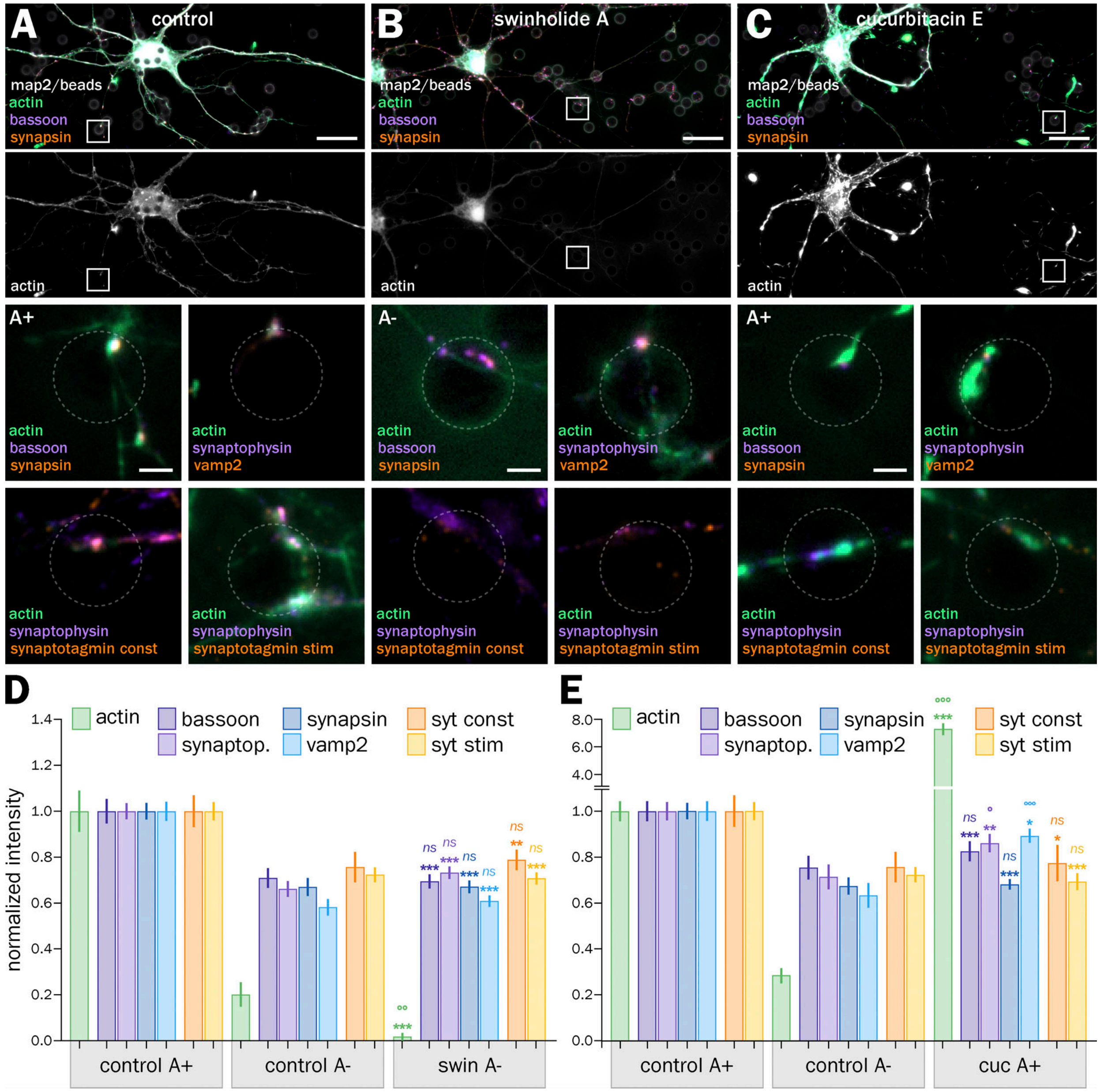

Figure 4. **Acute actin disassembly and over-stabilization lower the accumulation of presynaptic components at induced presynapses. (A)** Top, widefield fluorescence image of cultured neurons 2 d after bead seeding at 8 div, control treated with vehicle (DMSO) for 1 h and labeled for actin (green), bassoon (purple), synapsin (orange), and map2 (gray). Bottom, panels showing A+ presynapses labeled for actin, presynaptic components, and after syt feeding. The first panel is a zoom of the area highlighted in the top image. **(B)** Top, widefield fluorescence image of cultured neurons 2 d after bead seeding at 8 div, treated with 1 µM swinholide A (swin) for 1 h, and labeled for actin (green), bassoon (purple), synapsin (orange), and map2 (gray). Bottom, panels showing A− presynapses labeled for actin, presynaptic components, and after syt feeding. The first panel is a zoom of the area highlighted in the top image. **(C)** Top, widefield fluorescence image of cultured neurons 2 d after bead seeding at 8 div, treated with 5 µM cucurbitacin E (cuc) for 3 h, and labeled for actin (green), bassoon (purple), synapsin (orange), and map2 (gray). Bottom, panels showing A+ presynapses labeled for actin, presynaptic components, and after syt feeding. The first panel is a zoom of the area highlighted in the top image. Scale bars on large images in A–C, 20 µm; on zoomed images, 2 µm. **(D)** Quantification of the labeling intensity for actin (green), bassoon (dark purple), synaptophysin (purple), synapsin (dark blue), vamp2 (blue), and after syt feeding for constitutive (orange), and stimulated (yellow) vesicular cycling at actin-enriched presynapses (A+) and induced presynapses with no actin enrichment (A−) in the control condition, and at A− presynapses after swin treatment. **(E)** Quantification of the labeling intensity for actin (green), bassoon (dark purple), synaptophysin (purple), synapsin (dark blue), vamp2 (blue), and after syt feeding for constitutive (orange), and stimulated (yellow) vesicular cycling at actin-enriched presynapses (A+) and induced presynapses with no actin enrichment (A−) in the control condition, and at A+ presynapses after cuc treatment. Significance signs (bottom: *, ns) on graphs compare to the value for the same labeling in the control condition for A+ presynapses (normalized to 1.0); significance signs (top: °, *ns*) compare to the value for the same labeling in the control condition for A− presynapses. See Data S1 file for detailed statistics.

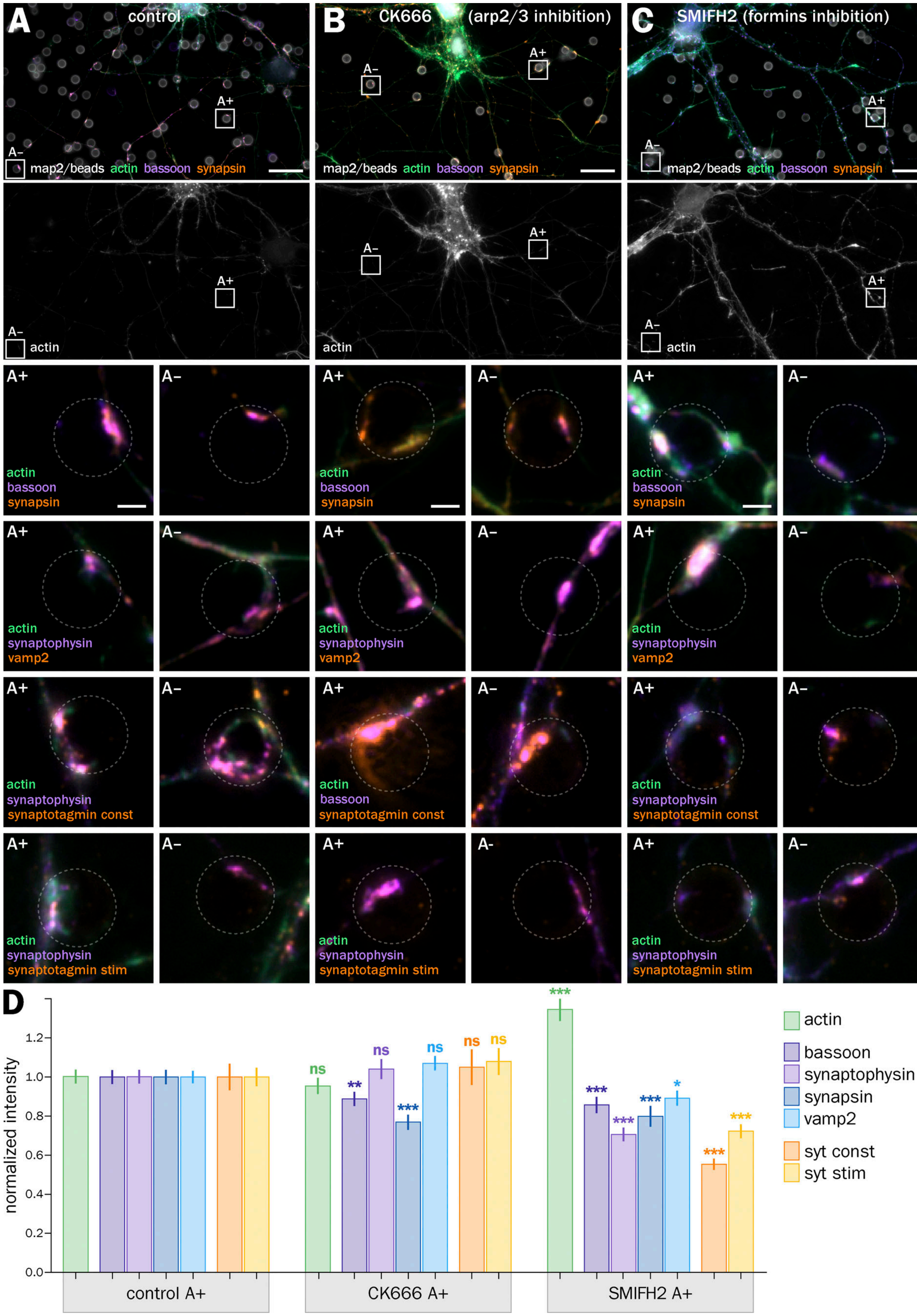

Figure 5. **Arp2/3 and formins inhibitors have distinct effects on actin and presynaptic components at induced presynapses. (A)** Top, widefield fluorescence image of cultured neurons 2 d after bead seeding at 8 div, control-treated with vehicle (DMSO) for 1 h and labeled for actin (green), bassoon (purple),

and map2 (gray). Bottom, panels showing A+ and A− presynapses labeled for actin, presynaptic components, and after syt feeding. The top panels are zooms of the areas highlighted in the top image. **(B)** Top, widefield fluorescence image of cultured neurons 2 d after bead seeding at 8 div, treated with 50 µM CK666 (Arp2/3 inhibitor) for 1 h, and labeled for actin (green), bassoon (purple), and map2 (gray). Bottom, panels showing A+ and A− presynapses labeled for actin, presynaptic components, and after syt feeding. The top panels are zooms of the areas highlighted in the top image. **(C)** Top, widefield fluorescence image of cultured neurons 2 d after bead seeding at 8 div, treated with 30 µM SMIFH2 (formins inhibitor) for 3 h, and labeled for actin (green), bassoon (purple), and map2 (gray). Bottom, panels showing A+ and A− presynapses labeled for actin, presynaptic components and after syt feeding. Top panels are zooms of the areas highlighted in the top image. Scale bars on large images in A–C, 20 µm; on zoomed images, 2 µm. **(D)** Quantification of the labeling intensity for actin (green), bassoon (dark purple), synaptophysin (purple), synapsin (dark blue), vamp2 (blue), and after syt feeding for constitutive (orange), and stimulated (yellow) vesicular cycling at actin-enriched presynapses (A+) in the control condition, and after CK666 or SMIFH2 treatment. Significance signs on graphs compare to the value for the same labeling in the control condition for A+ presynapses (normalized to 1.0). See Data S1 file for detailed statistics.

STORM/PAINT acquisition, imaging actin with STORM before performing two-color DNA-PAINT (Jimenez et al., 2020) for ß2-spectrin, which forms rings along the axon shaft, and synapsin, which delineates the pools of synaptic vesicles. This confirmed that the spectrin submembrane scaffold stops at the bouton and that the actin corral encases the synaptic vesicle cluster, with rails pointing to the active zone (Fig. 7 A).

As our diffraction-limited experiment revealed two populations of actin-enriched (A+) and non-enriched (A−) induced presynapses (see Fig. 2), we next assessed the difference between these two types at the nanoscale by imaging A+ and A− induced presynapses with STORM. Both A+ and A− induced presynapses contain the three types of actin nanostructures (mesh, rails, and corrals), and actin enrichment at the diffraction-limited level corresponds to the presence of larger actin corrals at the periphery of the presynapse (Fig. 7 B). To quantify this, we blindly scored the presence of actin mesh, rails, and corrals within each A+ and A− induced presynapse by visual inspection of high-resolution 3D-STORM images (see Materials and methods). This confirmed that most A+ and A− induced presynapses contain an actin mesh (86% and 82%, respectively), rails (57% and 73%, with the faint rails more visible in A− presynapses with smaller corrals), and corrals (93% and 91%, Fig. 7 C). Measuring the size of the mesh and corrals from images showed that corrals are indeed significantly larger in A+ than in A− induced presynapses (0.23 ± 0.05 µm² vs. 0.10 ± 0.01 µm²; Fig. 7 D). We next assessed if the three types of actin nanostructures are present in excitatory and inhibitory presynapses induced by coated beads (see Fig. S5). Anti-VGLUT and -VGAT antibodies revealed no qualitative difference in actin nanoarchitecture between these two types of induced presynapses, most of which contain actin mesh, rails, and corrals (Fig. 7, E and F).

Presynaptic actin nanostructures are distinctly dependent on arp2/3 and formins nucleators

The nanoscale texture of the mesh and corrals suggest that they are made of branched actin filaments, while the rails are made of linear filaments, and could be differentially dependent on Arp2/3 and formins-mediated actin nucleation. To test this, we performed 3D-STORM of induced presynapses after a short treatment of bead-seeded cultures with CK666 (50 µM, 1 h) and SMIFH2 (30 µM, 1 h) and blindly scored the presence of actin mesh, rails, and corrals (Fig. 8, A–C). Inhibition of Arp2/3-mediated branched actin nucleation with CK666 resulted in a lower proportion of presynapses containing actin mesh (from 71% to 62% of presynapses) and actin corrals (from 69% to 62%), whereas it led to slightly more presynapses with actin rails (from 46% to 54%; Fig. 8 D). Inhibition of formins-mediated linear actin nucleation minimally elevated meshes and corrals (71–78% and 69–72%, respectively), but led to a drop in the proportion of presynapses containing actin rails (46–33%). These effects of treatments are quite small and the semiquantitative evaluation precludes assessing their significance. To confirm the distinct dependence of presynaptic actin nanostructures on different actin nucleators, we imaged actin together with the Arp2/3 complex at the nanoscale using two-color spectral demixing STORM (Friedl et al., 2023 *Preprint*). Within bead-induced presynapses, we could resolve the Arp2/3 complexes as discrete puncta that are associated with the actin mesh and corrals, but not along the actin rails (Fig. 8 E). Overall, these experiments suggest that the actin mesh and corrals are Arp2/3-dependent, while the actin rails rely on formin-mediated nucleation, confirming that they are indeed distinct structures.

CRISPR-tagging of endogenous actin confirms actin enrichment and organization into distinct nanostructures within natural presynapses

Finally, we aimed at verifying our findings on natural presynapses—formed between an axon and a dendrite or cell body. To obtain a high labeling density of actin in a small subset of neurons in culture, we implemented the HiUGE method (Gao et al., 2019) to insert small peptide tags at the aminoterminus of endogenous ß-actin via CRISPR-mediated recombination. We used an optimized triple-AAV infection method to obtain a good knock-in efficiency in our rat hippocampal cultures (Ogawa et al., 2023 *Preprint*). We first devised a HA tag knock-in and verified that the insertion of a small tag allowed us to selectively label actin in a small subset of neurons, with a similar organization to unlabeled actin and without impairing neuronal growth or morphology for several weeks in culture (Fig. 9 A). We could follow individual axons from knocked-in neurons and visualize presynapses as well as probe synaptic vesicle cycling along these identified axons (Fig. 9, B and C). Like the bead-induced presynapses, a majority (75 ± 1.5%) of these natural presynapses were enriched in actin compared with the nearby axon shaft. Moreover, the actin-enriched (A+) presynapses exhibited a ∼40% higher synaptophysin content compared with non-enriched (A−) ones (synaptophysin intensity in A− presynapses 0.78 ± 0.06, normalized to the A+ intensity) and a ∼50% higher level of vesicular cycling (syt feeding intensity in A− presynapses 0.67 ± 0.09, Fig. 9 D). These figures were very

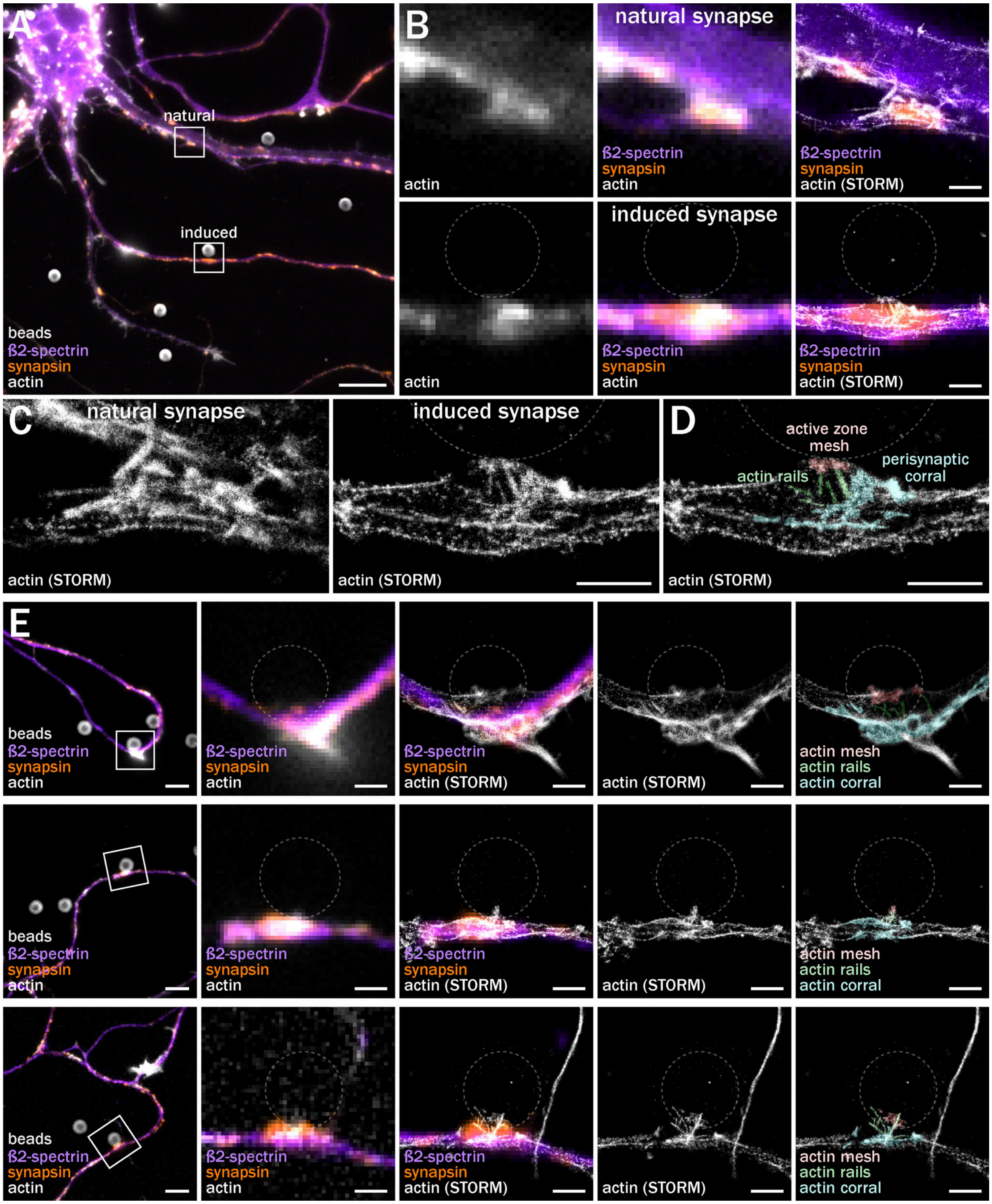

Figure 6. **STORM visualizes distinct actin nanostructures at induced presynapses. (A)** Widefield fluorescence image of cultured neurons 2 d after bead seeding at 8 div, labeled for ß2-spectrin (purple), synapsin (orange), and actin (gray). **(B)** Zooms on a natural synapse at an axon–dendrite contact (top row) and on an induced presynapse at an axon–bead contact (bottom row), corresponding to the highlighted areas in A. Left columns are widefield images of actin (gray), middle channels are overlays of widefield images of ß2-spectrin (purple), synapsin (orange), and actin (gray); right columns are overlays of widefield images of ß2-spectrin (purple) and synapsin (orange) with the STORM image of actin (gray). **(C)** Zoomed STORM images of the natural synapse (left) and bead-induced presynapse (right). **(D)** Same image as C, left, with color highlighting of presynaptic actin structures: active zone mesh (red), actin rails (green), perisynaptic corral (blue). **(E)** Additional representative images of bead-induced presynapses. The first column shows the widefield image of ß2-spectrin (purple), synapsin (orange) and actin (gray). The second column is a zoom of the highlighted area in the first image. The third column shows an overlay of widefield images of ß2-spectrin (purple) and synapsin (orange) with the STORM image of actin (gray). The fourth column is the isolated STORM image of actin (gray). The fifth column is the STORM image of actin with highlighted presynaptic actin structures: active zone mesh (red), actin rails (green), and perisynaptic corral (blue). Scale bars in A, 10 µm; in B–D, 1 µm; in E, 5 µm (first column) and 1 µm (other columns).

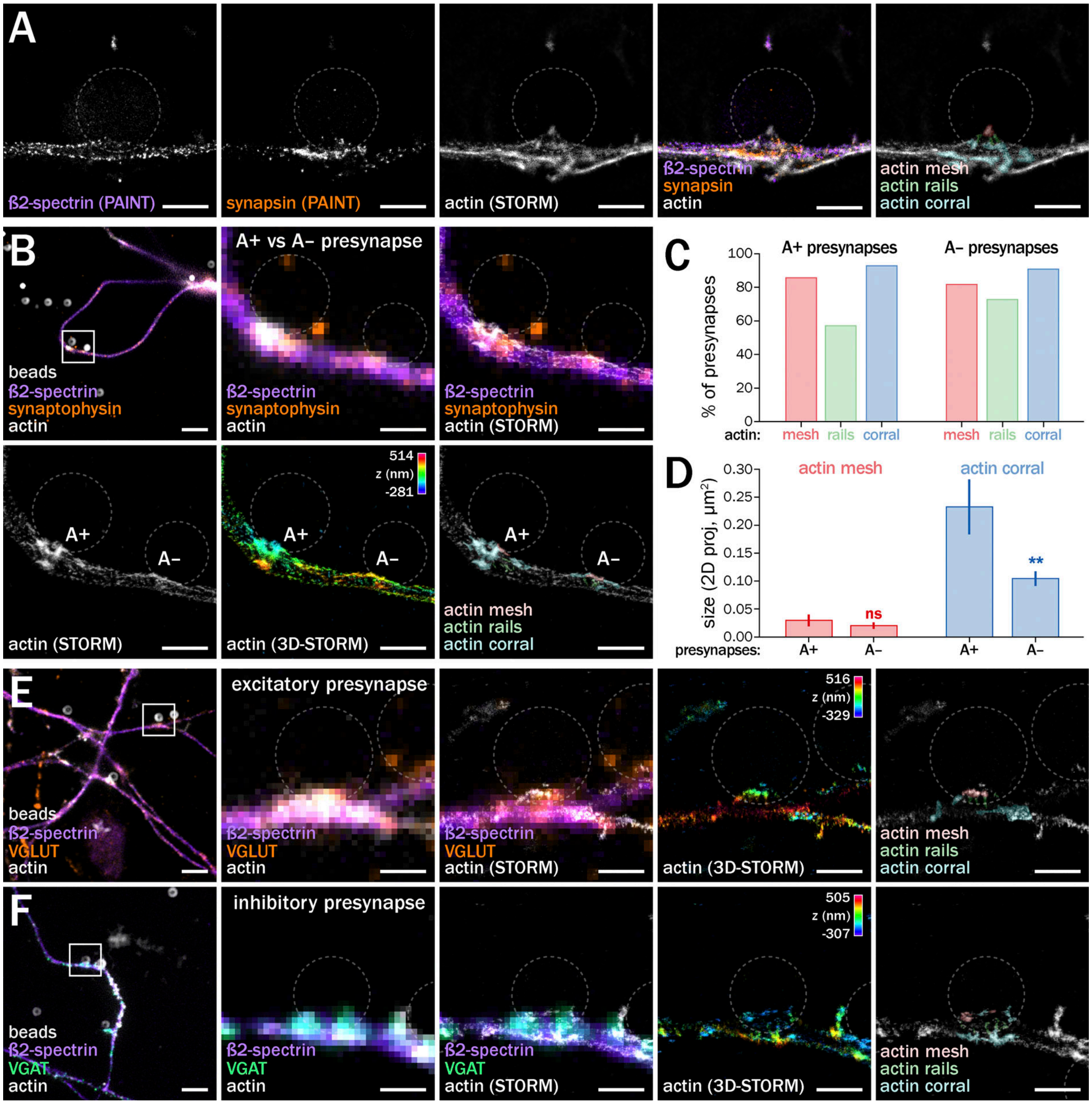

Figure 7. **Actin mesh, rails, and corrals are present in various types of induced presynapses. (A)** Three-color SMLM image of a bead-induced presynapse labeled for ß2-spectrin (DNA-PAINT image), synapsin (DNA-PAINT image), and actin (STORM image). The fourth column is an overlay of the three channels, while the fifth column shows the actin STORM image with highlighted presynaptic actin structures. **(B)** Actin nanostructures in A+ and A− induced presynapses along the same axon. The top-left panel shows the widefield image of ß2-spectrin (purple), synaptophysin (orange), and actin (gray). The top-center panel is a zoom of the highlighted area in the first image. The top-right panel shows an overlay of widefield images of ß2-spectrin (purple) and synaptophysin (orange) with the STORM image of actin (gray). The bottom-left panel is the isolated STORM image of actin (gray). The bottom-center panel is the isolated 3D-STORM image of actin, color-coded for depth (with Z scale in the top right corner). The bottom-right panel is the STORM image of actin with highlighted presynaptic actin structures in the A+ and A− induced presynapses: active zone mesh (red), actin rails (green), perisynaptic corral (blue). **(C)** Semi-quantitative assessment of the frequency of identification for presynaptic actin structures: actin mesh (red), rails (green), and corral (blue) from A+ and A− induced presynapses. **(D)** Quantification of the size of the mesh (red) and corral (blue) on 2D-projected STORM images of A+ and A− induced presynapses. Significance signs on the graph compare to the value of a given nanostructure size between A+ and A− synapses. See Data S1 file for detailed statistics. **(E)** Actin nanostructures in an identified bead-induced glutamatergic presynapse. First column shows the widefield image of ß2-spectrin (purple), VGLUT (orange) and actin (gray). The second column is a zoom of the highlighted area in the first image. The third column shows an overlay of widefield images of ß2-spectrin (purple) and VGLUT (orange) with the STORM image of actin (gray). The fourth column is 3D-STORM image of actin, color-coded for depth (with Z scale in the top right corner). The fifth column is the STORM image of actin with highlighted presynaptic actin structures: active zone mesh (red), actin rails (green), perisynaptic corral (blue). **(F)** Actin nanostructures in an identified bead-induced GABAergic presynapse. The first column shows the widefield image of ß2-spectrin (purple), VGAT (green), and actin (gray). The second column is a zoom of the highlighted area in the first image. The third column shows an overlay of widefield images of ß2-spectrin (purple) and VGAT (green) with the STORM image of actin (gray). The fourth column is 3D-STORM image of actin, color-coded for depth (with Z scale in the top right corner). The fifth column is the STORM image of actin with highlighted presynaptic actin structures: active zone mesh (red), actin rails (green), and perisynaptic corral (blue). Scale bars in A, 1 µm; in B, 5 µm (top left panel) and 1 µm (other panels); in E and F, 5 µm (left column panels) and 1 µm (other panels).

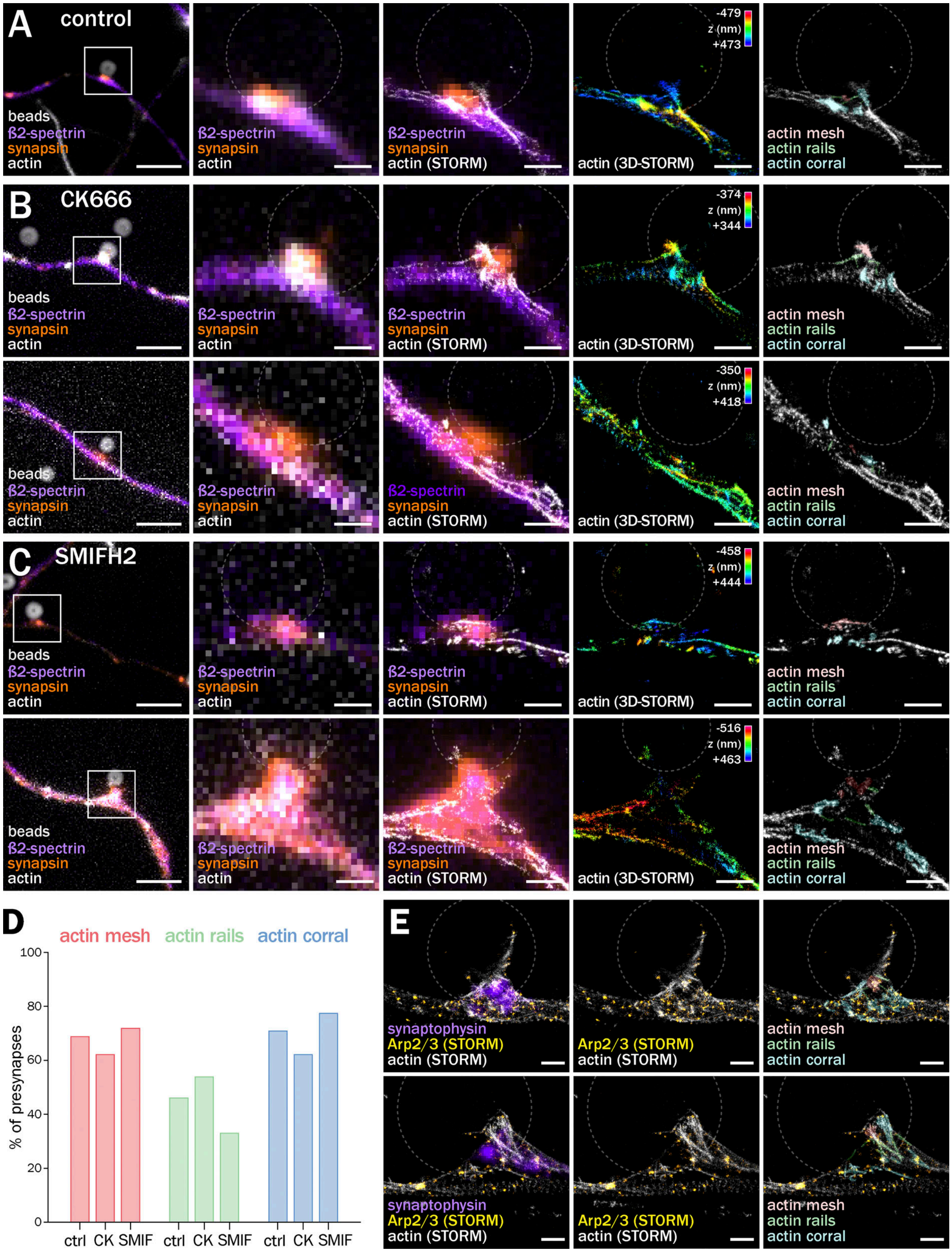

Figure 8. **Presynaptic actin nanostructures are distinctly dependent on Arp2/3 and formins. (A–C)** Images of induced presynapses from cultured neurons 2 d after bead seeding at 8 div. The first column shows a widefield image of ß2-spectrin (purple), synapsin (orange), and actin (gray). The second column is a zoom of the highlighted area in the first column image. The third column shows an overlay of widefield images of ß2-spectrin (purple) and synapsin (orange) with the STORM image of actin (gray). The fourth column is the isolated 3D-STORM image of actin, color-coded for depth (with Z scale in the top right corner). The fifth column is the STORM image of actin with highlighted presynaptic actin structures: active zone mesh (red), actin rails (green), perisynaptic corral (blue). **(A)** Representative examples from neuronal cultures treated with DMSO for 1 h (control condition). **(B)** Two examples after treatment with 50 µM

CK666 for 1 h. **(C)** Two examples after treatment with 30 µM SMIFH2 for 1 h. **(D)** Semi-quantitative assessment of the frequency of identification for presynaptic actin structures: actin mesh, rails, and corrals, from all the presynapses imaged in the control condition (ctrl) or after treatment with CK666 (CK) or SMIFH2 (SMIF). **(E)** Two-color STORM images of actin and Arp2/3 (anti-p34 antibody) at two representative bead-induced presynapses. The first column shows an overlay of the widefield image of synaptophysin (purple) with the STORM images of actin (gray) and Arp2/3 (yellow). The second column shows the overlayed STORM images of actin (gray) and Arp2/3 (yellow). The third column adds highlighted presynaptic actin structures: active zone mesh (red), actin rails (green), and perisynaptic corral (blue) to the image in the second column. Scale bars in A–C, 5 µm (first column) and 1 µm (other columns); in E, 1 µm.

similar to bead-induced presynapses (see Figs. 2 and 3), confirming our key findings that a majority of presynapses are enriched in actin and that enrichment correlates with higher presynapse component accumulation and vesicular cycling.

We next optimized the endogenous actin-tagging strategy to obtain high-quality SMLM images and reveal the nanoarchitecture of actin within natural presynapses. The best results were obtained with the ALFA tag (Götzke et al., 2019; Fig. 10, A and B). To obtain a high-enough number of localizations for good structural imaging of presynaptic actin using STORM, we labeled the ALFA tag with primary and secondary antibodies, visualizing actin rings along the axon shaft and presynapses formed on the dendrites and cell body of unlabeled neurons (Fig. 10 C). Antibody labeling led to more punctate labeling than phalloidin. Nonetheless, when these presynapses were oriented sideways, we could identify the three nanostructures previously observed within bead-induced presynapses: a small mesh at the central point of the presynapse

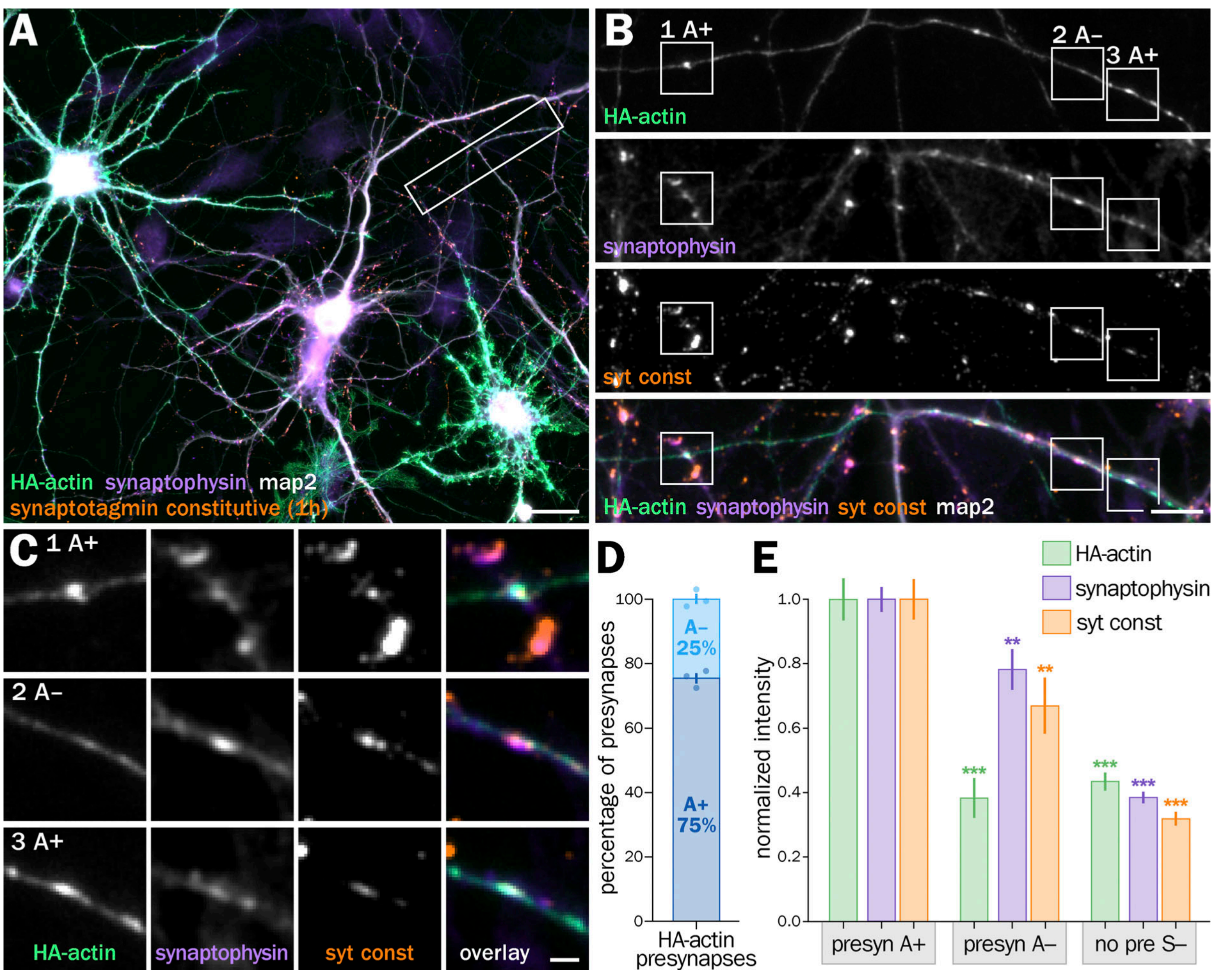

Figure 9. **Revealing presynaptic actin enrichment in natural synapses and its role using CRISPR-tagging of endogenous actin. (A)** Widefield fluorescence image of cultured neurons infected after plating with CRISPR AAVs for the knock-in of an HA tag on endogenous actin, fed with a synaptotagmin antibody for 1 h (orange) and fixed at 9 div, then labeled for HA (green), synaptophysin (purple), and map2 (gray). **(B)** Zooms corresponding to the area highlighted in A showing isolated channels and overlay of the axon of a HA-actin knocked-in neuron forming actin-enriched A+ (1 and 3) and non-enriched A– (2) presynapses. **(C)** Zooms on individual presynapses highlighted in B. **(D)** Quantification of the proportion of A+ (dark blue) and A– (blue) presynapses along the axons of HA-actin neurons. **(E)** Quantification of the labeling intensity for HA-actin (green), synaptophysin (purple), and constitutive synaptotagmin feeding (orange) at HA-actin-enriched presynapses (A+), induced presynapses with no actin enrichment (A–), and axon shafts contacts devoid of presynapse (S–), normalized to the intensity at A+ presynapses. Significance signs on graphs compare to the value for the same labeling in A+ presynapses (normalized to 1.0).

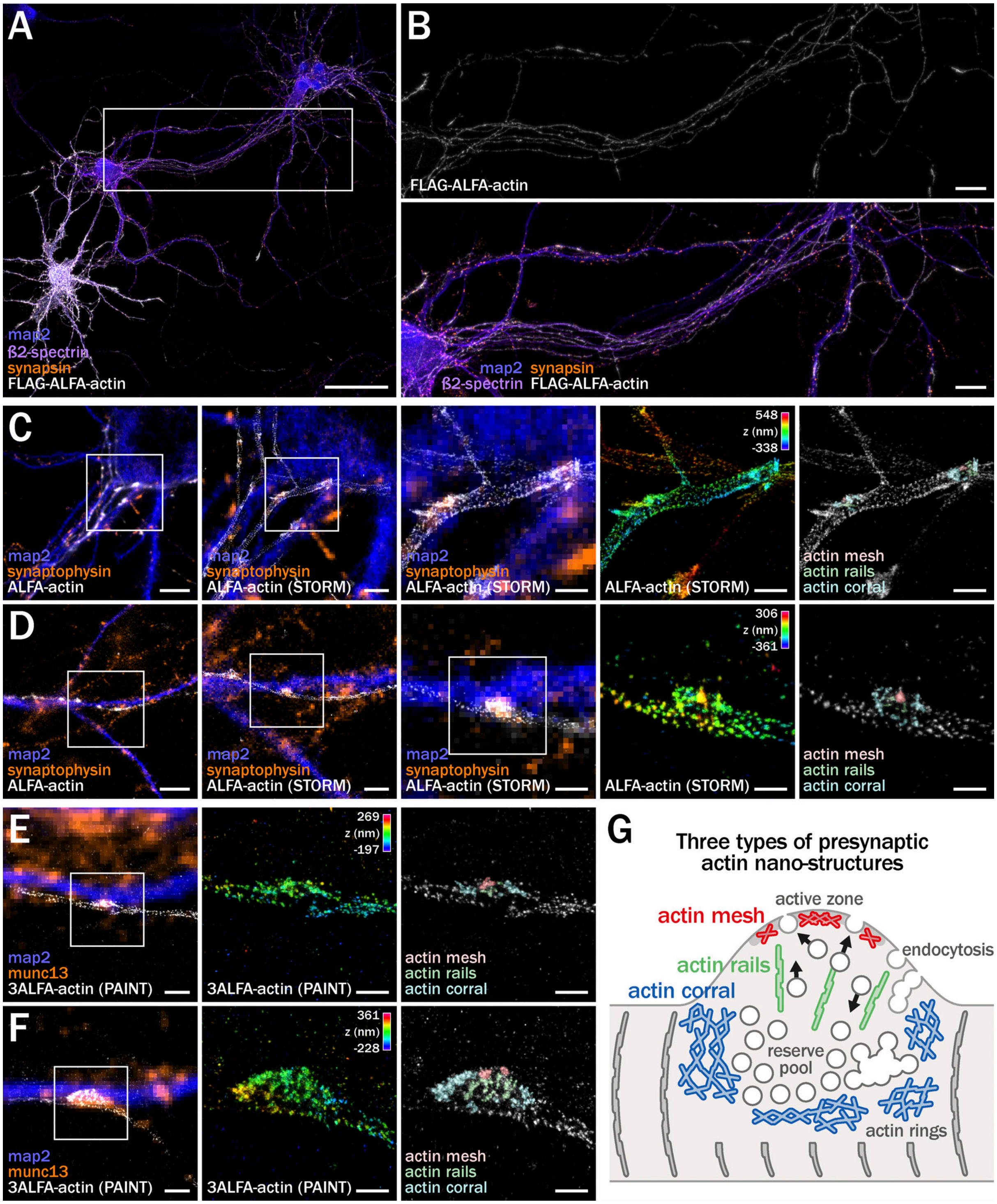

Figure 10. **Actin mesh, rails and corrals are present in natural presynapses. (A)** Widefield fluorescence image of cultured neurons infected after plating with CRISPR AAVs for the knock-in of a FLAG-ALFA tag on endogenous actin, fixed at 9 div and labeled for FLAG (gray), ß2-spectrin (purple), map2 (blue), and synapsin (orange). **(B)** Zooms corresponding to the area highlighted in A showing the FLAG-ALFA-actin isolated channel and overlay for the axon arborization of a FLAG-ALFA-actin knocked-in neuron forming presynapses on nearby neurons. **(C and D)** STORM images of actin nanostructures in the presynapses of ALFA-actin knock-in neurons labeled for ALFA using primary and secondary antibodies. The first column shows the widefield image of map2 (blue), synaptophysin (orange), and ALFA-actin (gray). The second and third columns are zooms of the highlighted areas, showing an overlay of widefield images of map2 (blue) and synaptophysin (orange) with the STORM image of ALFA-actin (gray). Fourth column is 3D-STORM image of ALFA-actin, color-coded for depth (with Z scale in the top right corner). Fifth column is the STORM image of ALFA-actin with highlighted presynaptic actin structures: active zone mesh (red), actin rails (green), perisynaptic corral (blue). **(E and F)** DNA-PAINT images of actin nanostructures in the presynapses of 3ALFA-actin knock-in neurons labeled for ALFA using an anti-ALFA nanobody. The first column shows the overlay of the widefield image of map2 (blue) and synaptophysin (orange) with the PAINT image of 3ALFA-actin (gray). The second column is 3D-STORM image of 3ALFA-actin, color-coded for depth (with Z scale in the top right corner). The third column is the

PAINT image of 3ALFA-actin with highlighted presynaptic actin structures: active zone mesh (red), actin rails (green), perisynaptic corral (blue). Scale bars in A, 50 µm; in B, 10 µm; in C, 5 µm (first panel), 2 µm (second panel), 1 µm (other panels); in D, 5 µm (first panel), 2 µm (second panel), 1 µm (third panel), 0.5 µm (fourth and fifth panels); in E and F, 1 µm (first column), 0.5 µm (second and third columns). **(G)** Cartoon summarizing the identified presynaptic actin nanostructures and their putative role: the branched actin mesh at the active zone where vesicles are exocytosed; linear actin rails (green) help vesicles move between the exocytosis, endocytosis zones, and intracellular pools; the perisynaptic actin corral (blue) scaffolds the vesicular pool.

close to the dendrite, linear rails inside the presynaptic protein cluster, and larger actin corrals at the presynapse periphery (Fig. 10, C and D). To further validate these findings using smaller probes than primary and secondary antibodies, we used a triple-ALFA tag together with an anti-ALFA nanobody coupled to a DNA docking strand and performed 3D-PAINT of knocked-in actin at natural presynapses. These images also showed that natural presynapses contain the actin mesh, rails, and corrals (Fig. 10, E and F), confirming our findings on bead-induced presynapses.

Discussion

In this work, we addressed a long-standing gap in our understanding of neuronal architecture by delineating and characterizing the presence of actin nanostructures within presynapses. We first made presynaptic actin visible by inducing isolated presynapses on polylysine-coated beads. This revealed that around two-thirds of presynapses are enriched in actin, an enrichment associated with a higher accumulation of presynaptic components (scaffolds and synaptic vesicle-associated proteins), and an elevated rate of constitutive and stimulated vesicular cycling. This 30–50% strengthening of presynapses depends on a set level of actin enrichment, as it disappears after both disassembly or over-stabilization of axonal actin. Acute modulation of actin assembly by Arp2/3 and formins inhibitors results in more subtle effects on presynaptic component accumulation and vesicular cycling, suggesting that they target distinct actin structures within presynapses. We were able to directly visualize these presynaptic actin structures using super-resolution SMLM in bead-induced presynapses, revealing that presynaptic actin forms three main types of nanostructures: an Arp2/3-dependent actin mesh at the active zone, formin-sensitive actin rails between the active zone and the deeper presynapse containing the reserve pool of synaptic vesicles, and Arp2/3-dependent dense, branched actin corrals surrounding the whole presynaptic compartment. Finally, we confirmed these results in natural presynapses using CRISPR-mediated tagging of endogenous actin. This first comprehensive view of presynaptic actin architecture provides a structural basis for its multiple previously proposed functions and will foster new hypotheses on the role of actin at presynapses (Fig. 10 G).

Visualizing the arrangement of actin within presynapses presents several challenges. Brain mammalian synapses are usually small and packed with a high density of components, with actin being the most abundant one (Wilhelm et al., 2014). In addition, actin filaments are hard to optimally preserve and not readily visible on classic EM thin sections (Papandréou and Leterrier, 2018). Finally, the close apposition of an even greater amount of postsynaptic actin makes optical fluorescence approaches, even super-resolutive ones, challenging (see Fig. S1). Selective labeling of presynaptic actin using over-expressed probes such as LifeAct-GFP is possible (Reshetniak and Rizzoli, 2019), but avoiding perturbative effects requires very low labeling densities, below what is necessary to resolve the fine organization of actin filaments. To benefit from the high density of actin labeling provided by fluorescent phalloidin without interference from the postsynaptic side, we used a validated model of bead-induced presynapses (Lucido et al., 2009). We have confirmed that bead-induced presynapses concentrate all tested presynaptic components and are competent for synaptic vesicle cycling using anti-synaptotagmin antibody feeding and FM1-43 staining experiments. We have carefully verified that experiments that do not involve measuring actin content, such as presynaptic component accumulation and vesicular cycling after pharmacological treatments, give similar results in bead-induced presynapses and natural (axon-dendrite) presynapses present in the same neuronal cultures. Finally, we have used a complementary strategy of endogenous actin knock-in to confirm our key finding in natural presynapses.

Being able to specifically visualize presynaptic actin, we first found that a major subpopulation of presynapses is enriched in actin and that these actin-enriched presynapses are structurally and functionally stronger than the non-enriched presynapses. Numerous studies have examined the role of actin at presynapses, with a large variability in results and conclusions (Cingolani and Goda, 2008; Papandréou and Leterrier, 2018; Wu and Chan, 2022). Among them, actin disassembly has been shown to impact immature synapses (5–6 div) but not established synapses in mature neurons (12–16 div; Zhang and Benson, 2001). Here, we have induced presynapses between 8 and 10 div when neurons are fully competent for presynapse formation. In addition, presynapses form within minutes after bead contact (Suarez et al., 2013), allowing them to maturate over 48 h after seeding in our experiments. We further verified that incubating more mature neurons, as well as incubating them with beads for up to 96 h, generate the same proportions of actin-enriched and non-enriched presynapses, suggesting that these two populations of presynapses are unlikely to be at a transient developmental stage of maturation. Actin has also been shown to drive activity-induced unsilencing of presynaptically non-functional synapses in 7–11 div neurons (Yao et al., 2006; Shen et al., 2006). In bead-induced presynapses, we did not see such a clear on/off difference in vesicular cycling between actin-enriched and non-enriched presynapses. However, the absence of actin enrichment is associated with lower presynaptic content and less constitutive and stimulated cycling. In addition, acutely disassembling actin brings actin-enriched presynapses to the component and cycling levels of non-enriched ones. It would be interesting to determine which stages of the vesicular cycle are regulated by actin enrichment, as well as if the selective actin enrichment is induced by an existing nucleator concentration, or can be influenced by the activity patterns at each presynapse. Indeed, in the light of more recent studies (Glebov et al., 2017; O'Neil et al., 2021), the interplay between neuronal activity, the concentration and organization of presynaptic actin, and the resulting regulation of presynaptic strength is a key question for future studies.

In bead-induced presynapses, we visualized the nanoscale organization of actin with the resolution required to discern distinct structures. Optimized SMLM consistently revealed the presence of three main actin nanostructures: an active zone mesh, rails between the active zone and the deeper reserve pools, and corrals around the whole presynaptic compartment. Importantly, we validated the generality of these nanostructures: they are present in both actin-enriched and non-enriched induced presynapses, the difference being the size of the actin corrals, and are present in both excitatory and inhibitory presynaptic specializations. Using endogenous actin tagging, we could finally detect these three types of actin nanostructures in natural presynapses between axons and dendrites.

We further determined that the presynaptic actin nanostructure has a distinct dependency on Arp2/3 and formins, which could explain why inhibition of these actin nucleators has distinct effects on presynaptic content and vesicular cycling, with further variations depending on the presynaptic component assessed. The nanoscale association of Arp2/3 with the presynaptic actin mesh and corrals is in line with its recently described role in presynaptic plasticity (O'Neil et al., 2021). Of note, the strong effect of formins inhibition is likely partly due to a reduction of intersynaptic vesicle trafficking by actin trails (Ganguly et al., 2015; Chenouard et al., 2020). It should also be kept in mind that the formins inhibitor SMIFH2 can inhibit non-muscular myosin II (NMII) activity partially. While SMIFH2 is three to six times less potent on NMII than on formins, NMII is implicated in the synaptic vesicle cycle (Peng et al., 2012; Chandrasekar et al., 2013). However, NMII is differentially implicated in constitutive and evoked release (Peng et al., 2012), a selective effect we do not see when applying SMIFH2 to induced presynapses. Finally, formins implication in the synaptic vesicle cycle has been confirmed independently of SMIFH2 by knockdown of the formin mDia1 (Soykan et al., 2017).

This direct visualization brings together decades of scattered EM observation and structural speculations from perturbation experiments (Dillon and Goda, 2005), allowing for functional hypotheses. The presence of branched actin at the active zone (Hirokawa et al., 1989) could have a resistive effect on exocytosis and define exocytic sites (Aunis and Bader, 1988; Morales et al., 2000); the actin rails (Siksou et al., 2007) might allow myosin-mediated trafficking of vesicles between the reserve pool and the readily releasable pool at the active zone (Maschi et al., 2018; Sakaba and Neher, 2003); and the perisynaptic branched actin corrals (Li et al., 2010) could help in constraining, shaping, or retaining components of the reserve pool (Sankaranarayanan et al., 2003). Each of these nanostructures could also have a role in the retrieval of new synaptic vesicles via endocytosis, in particular, the actin corrals: presynaptic endocytosis has been shown to involve actin at the periphery of the active zone, where corrals are localized (Bloom et al., 2003; Shupliakov et al., 2002; Del Signore et al., 2021). A recent study using STED microscopy confirmed the presence of perisynaptic actin corrals, proposing that they confine excess membrane from exocytosed vesicles within the presynaptic area, allowing for fast compensatory endocytosis near the corrals (Ogunmowo et al., 2023).

Isolated presynapses in culture are undoubtedly a reductionist approach to the myriad of processes influencing synapse physiology in vivo, but they have allowed us to uniquely isolate and reveal core principles of presynaptic actin organization. Multiple additional layers are added to further shape the presynaptic actin architecture through maturation and plasticity. Feedback mechanisms from the postsynaptic compartments, such as cannabinoid regulation of the presynaptic architecture (McFadden et al., 2018 *Preprint*) or neuroligin-driven strengthening of presynaptic scaffolds (Wittenmayer et al., 2009), are absent from our experimental model. This also prevents further refinements, like the formation of cross-synaptic nanocolumns that align the release machinery to the clusters of postsynaptic receptors (Tang et al., 2016)—although it should be noted that recent works hint at a primary role of the presynaptic side in organizing nanocolumns (Ramsey et al., 2021). Our study provides the first comprehensive visualization of presynaptic actin structures at the nanoscale, replacing the inferred cartoons of past studies with experimental data. We look forward to this structural insight to help revisit functional hypotheses and elaborate new ones toward a better understanding of actin's multiple roles at presynapses.

Materials and methods

Animals, cell culture, and polylysine-coated bead treatment

All procedures were in agreement with the guidelines established by the European Animal Care and Use Committee (86/609/CEE) and were approved by the local ethics committee (agreement G13O555). Experiments were performed on pregnant female Wistar rats (Janvier labs). Animals were sacrificed by decapitation and embryo brains were used for primary neuronal cell culture.

Rat hippocampal neurons were cultured following the Banker method above a feeder glia layer (Kaech and Banker, 2006). Rapidly, 18-mm diameter round, #1.5H coverslips were affixed with paraffine dots as spacers and then treated with poly-L-lysine. Hippocampi from E18 rat pups were dissected, homogenized by trypsin treatment followed by mechanical trituration, and seeded on the coverslips at a density of 6,000 cells/cm^2 for 3 h in a serum-containing plating medium (MEM with 10% fetal bovine serum, 0.6% added glucose, 0.08 mg/ml sodium pyruvate, and 100 UI/ml penicillin-streptomycin). Coverslips were then transferred, cells down, to Petri dishes containing confluent glia cultures conditioned in NB+ medium (Neurobasal medium supplemented with 2% B-27, 100 UI/ml penicillin/streptomycin and 2.5 µg/ml amphotericin) and cultured in these dishes for up to 16 d at 37°C, 5% CO_2. For most bead-induced presynapse experiments (except Fig. S3), neurons were cultured for 8 d in vitro (8 div) before the addition of beads (6 div for the comparison between 48 and 96 h of bead induction). Poly-D-lysine beads are prepared as follows: 30 million of 3 or 4.5-µm aliphatic amine latex beads (A3736 or A37370, respectively; Thermo Fisher Scientific) were incubated with poly-D-lysine (P7405, 63 µg/ml; Sigma-Aldrich) in Dulbecco's phosphate buffered saline (PBS; Thermo Fisher Scientific) for 3 h at room temperature with rotary agitation. Beads were then washed twice in sterile water and once with NB+ medium. Beads were resuspended in NB+ medium and added dropwise to the neurons at a concentration of 3 million beads/coverslip, neurons facing up. After 3 h, the coverslips were then flipped back, neurons facing the astrocytes for 2 d before further treatments.

Pharmacological treatments and anti-synaptotagmin vesicular cycling assays

Neurons at 10 div were treated 1 h with 1 µM swinholide A (Sigma-Aldrich), 3 h with 5 µM cucurbitacin E (Sigma-Aldrich), 1 h with 50 µM CK666 (Bio-Techne), or 1 h with 30 µM SMIFH2 (Bio-Techne). Drugs were directly added to the culture medium and controls included the same amount of dimethyl sulfoxide (DMSO) that was originally used to dissolve the drugs. Neurons were rinsed three times with PBS prior to fixation.

Vesicular cycling assays were performed using an antibody directed to an extracellular epitope of synaptotagmin 1 (syt, clone 604.2; Synaptic Systems) that was fed to neurons just before fixation. For assaying constitutive cycling, neurons were incubated with the syt antibody at 1.6 µg/µl in HBS medium (NaCl 136 mM, HEPES 10 mM, *D*-glucose 10 mM, $CaCl_2$ 2 mM, $MgCl_2$ 1.3 mM) for 1 h at 37°C, 5% CO_2. For assaying stimulated cycling, neurons were treated with the syt antibody in an HBS medium supplemented with 50 mM KCl for 3 min at room temperature. Cells were then washed three times with PBS before fixation.

FM1-43 experiments on living cells

Neurons at 10 div were incubated for 1 h at 37°C, 5% CO_2 in NB+ medium containing 100 nM SiR-actin (Spirochrome). Neurons were then incubated in an HBS medium for 10 min at 37°C. Following this incubation, the neurons were transferred to a live-cell imaging chamber (Life Imaging Services) containing HBS medium and placed at 37°C in the incubated chamber of an epifluorescence/TIRF microscope (Zeiss). HBS medium was then exchanged for HBS/KCL medium containing APV at 50 µM, CNQX at 25 µM, and FM1-43 (SynaptoGreen-C4; Biotium) at 5 µM for 180 s at 37°C. HBS/KCL medium was then changed back to HBS medium after three 1-min 30-s rinses with HBS medium. Neurons were then left to recover for 15 min in an HBS medium. Green (FM1-43) and far-red (SiR-actin) channel epifluorescence images were taken using a 40X objective for several fields of view selected for the presence of a number of beads induced. FM1-43 release was achieved following an additional 3-min incubation with HBS/KCl medium with APV/CNQX, followed by three rinses with HBS medium every 1 min 30 s, and 15 min recovery in HBS medium. After release, images of the same preselected fields of view were then acquired using the same settings as the post-loading images.

Immunocytochemistry and sample preparation

Neurons at 9–10 div were fixed and stained similarly to published procedures (Jimenez et al., 2020). Fixation used 4% PFA in PEM buffer (PIPES 80 mM, $MgCl_2$ 2 mM, EGTA 5 mM, pH 6.8) for 10 min at room temperature. After rinses in 0.1 M phosphate buffer (TpO4), neurons were blocked for 1 h in immunochemistry buffer (ICC: TpO4, gelatin 0.22%, Triton 0.1%) and incubated with primary antibodies diluted in ICC overnight at 4°C. Primary antibodies used are chicken anti-map2 (1:1,000, ab5392, RRID:AB_2138153; Abcam), mouse anti-ß2-spectrin (1:150, #612563, RRID:AB_399854; BD Bioscience), guinea pig anti-synaptophysin (1:400, 101 004, RRID:AB_1210382; Synaptic Systems), rabbit anti-synapsin (1:1,000, ab1543P, RRID:AB_90757; Merck), mouse anti-bassoon (1:200, clone SAP7F407, ab82958, RRID:AB_1860018; Abcam), mouse anti-vamp2 (1:200, clone 69.1, 104 211, RRID:AB_887811; Synaptic Systems), guinea pig anti-VGLUT (1:500, 135 304, RRID:AB_887878; Synaptics Systems), rabbit anti-VGAT (1:1,000, 131 003, RRID:AB_887869; Synaptic Systems), mouse anti-syntaxin1 (1:200, 110 011, RRID:AB_887844; Synaptic Systems), guinea pig anti-SV2A (1:300, 119 004, RRID:AB_10894884; Synaptic Systems), rabbit anti-munc13-1 (1:400, 126 103, RRID:AB_887733; Synaptic Systems), mouse anti-p34 Arc (1:300, 306 011, RRID:AB_887756; Synaptic Systems), rat anti-HA (1:200, clone 3F10, 11867423001, RRID:AB_390918; Roche), mouse anti-FLAG (1:500, clone M2, F3215, RRID:AB_259529; Sigma-Aldrich), and mouse anti-ALFA (1:200, N1582; Nanotag). After rinses in ICC, corresponding secondary antibodies conjugated to Alexa Fluor 488, 555, or 647 (Thermo Fisher Scientific), CF680 (Biotium), or DyLight 405 (Rockland) diluted in ICC (1:200–1:400) were incubated for 1 h at room temperature. Secondary antibodies were rinsed and neurons were incubated with Alexa Fluor 647-conjugated phalloidin (A2287, ∼500 nM in TpO4; Thermo Fisher Scientific), Alexa Fluor 647 Plus-conjugated phalloidin (A30107, ∼165 nM in TpO4; Thermo Fisher Scientific), or Atto 488-conjugated phalloidin (#AD488-81, ∼500 nM in TpO4; Atto-Tec) for 1 h 30 min at room Q:2 temperature or overnight at 4°C. For epifluorescence imaging, coverslips were mounted in Prolong Glass containing fluorescent phalloidin (1:10 of the staining concentration). Alternatively, after the rinsing steps, stained coverslips were kept in PB + 0.02% sodium azide and fluorescent phalloidin at 4°C before STORM imaging.

CRISPR-mediated tagging of endogenous actin

A rat-optimized HiUGE methodology (Gao et al., 2019) was used to tag endogenous actin in cultured neurons. The necessary components were delivered via co-infection with three AAVs: gRNA, Cas9 protein (Mecp2-Cas9), and donor tag (Ogawa et al., 2023 *Preprint*). Different tags were designed and integrated into the donor plasmid to target in-frame fusion at the amino terminus of ß-actin, which is better tolerated than a carboxyterminal fusion (Nagasaki et al., 2017). Table S1 details the resulting DNA and amino-acid sequences after the insertion of the tags.

AAVs were produced by the NeuroTools facility (INT, Marseille) or using the following protocol: HEK 293T cells were plated in 12-well plates (200,000 cells/well in DMEM medium supplemented with 10% FBS). After 24 h, cells were transfected with the three AAV plasmids (see above), helper plasmid (Cat #240071; Agilent Technologies), and serotype PHP.S (plasmid #103006; Addgene, a gift from Viviana Gradinaru) using Lipofectamin 3000 (Invitrogen). The medium was exchanged the
Q:3 next day, reducing FBS concentration to 2%. 48 h later, cells were trypsinized and lysed in citrate lysis buffer (38 mM citric acid, 75 mM sodium citrate, 75 mM sodium chloride, and 100 mM magnesium chloride, pH 5). The cell lysate was centrifuged at 10,000 × g for 10 min and mixed with 10% vol/vol of 2 M Tris-HCl (pH 9.5). AAVs were titrated with a SYBR Green-qPCR procedure (Aurnhammer et al., 2012).

Hippocampal neurons were infected at 0 div: 3 h after plating at a density of 12,000 cells/cm^2, the coverslips were transferred to the wells of a 12-well plate containing conditioned NB+ medium. Around 1.10^9 particles of each of the three AAVs (Cas9, gRNA, and donor tag) were mixed in 100 µl conditioned NB+ medium and deposited dropwise in each well before returning the plate to 37°C, 5° CO_2. 48 h later (2 div), the coverslips were transferred, cells down, to Petri dishes containing confluent glia cultures conditioned in NB+ medium. Neurons were cultured until 9 div before being fixed and stained for fluorescence microscopy.

Epifluorescence microscopy

Diffraction-limited epifluorescence images were obtained using an Axio-Observer upright microscope (Zeiss) equipped with a 40X NA 1.4 or 63X NA 1.4 objective and an Orca-Flash4.0 camera (Hamamatsu) controlled by Zen software (Zeiss). Appropriate hard-coated filters and dichroic mirrors were used for each fluorophore. A thin Z-stack of 3–10 slices spaced out by 0.2 µm was acquired to include the signal from all neuronal processes within the whole field of view. For illustration of the images, image editing was performed using Fiji (Schindelin et al., 2012), and it included projection using the Extended Depth of Field plugin (Forster et al., 2004), linear contrast adjustment, and gamma adjustment (0.7–0.9) to highlight the faint actin labeling
Q:4 along axons. In the case of different treatment conditions labeled for the same targets, the contrast settings were kept constant for each channel across the different conditions/treatments.

SMLM: STORM and PAINT

For single-color SMLM, we used STORM. STORM was performed on an N-STORM microscope (Nikon Instruments). Stained coverslips were mounted in a silicone chamber filled with STORM buffer (Smart Buffer Kit; Abbelight). The N-STORM system uses an Agilent MLC-400B laser launch with 405 nm (50 mW maximum fiber output power), 488 nm (80 mW), 561 mW (80 mW), and 647 nm (125 mW) solid-state lasers, a 100X NA 1.49 objective, and an Ixon DU-897 camera (Andor). After locating an area with bead synapses using low-intensity illumination, a TIRF image was acquired, followed by a STORM acquisition. 30,000–60,000 images (256 × 256 pixels, 15 ms exposure time) were acquired at full 647 nm laser power. Reactivation of fluorophores was performed during acquisition by increasing illumination with the 405 nm laser. When imaging actin, 30 nM phalloidin-Alexa Fluor 647 was added to the STORM buffer to mitigate actin unbinding during imaging (Jimenez et al., 2020). For three-color SMLM (Fig. 7 A), we used STORM in combination with DNA-PAINT (Jimenez et al., 2020). Neurons were labeled using rabbit anti-synapsin and mouse anti-ß2-spectrin primary antibodies (see above), then anti-rabbit and anti-mouse secondary antibodies coupled to distinct PAINT DNA strands, as well as phalloidin-Alexa Fluor 647 for actin. Imaging was done sequentially, first for actin in STORM buffer (60,000 frames at 67 Hz), then for two immunostained proteins in PAINT buffer (0.1 M phosphate buffer saline, 500 mM NaCl, 5% dextran sulfate, pH 7.2) supplemented with 0.12–0.25 nM of PAINT imagers strands coupled to Atto565 and Atto650 (Metabion, two times 40,000 frames of alternating 561 and 647 nm excitation at 30 Hz). For single-color DNA-PAINT of 3ALFA-actin (Fig. 10, E and F), a custom nanobody conjugated with an F3 DNA-PAINT strand and an Alexa-488 fluorophore (1: 200; Massive Photonics) was incubated together with the secondary antibodies for co-stained targets before being imaged using an Atto643-coupled imaging strand (0.1–1 nM) with 647 nm excitation for 100,000 frames at 30 Hz.

For 2D STORM and DNA-PAINT images, the N-STORM software (Nikon Instruments) was used for the localization of single fluorophore activations and corrected for drift using cross-correlation. For two-color PAINT acquisitions using alternating 561 and 647 nm excitation, lateral chromatic aberration correction was corrected within the N-STORM software using polynomial warping calibrated on sub-diffraction beads. The list of localizations was then exported as a text file. For 3D STORM and DNA-PAINT images, acquired stacks were processed using DECODE (Speiser et al., 2021). Briefly, PSF were Q:5
modeled using spline fitting in SMAP (Li et al., 2018) and used to simulate sequences of blinking events using characteristics (photon number range and lifetime distribution) inferred from real acquisition data from the N-STORM microscope. A Pytorch model was trained to infer the 3D coordinates and uncertainty of the simulated blinking events and then applied to the experimental acquired sequences (Speiser et al., 2021). The resulting localizations (fitted blinking events) were filtered based on uncertainty, and drift during acquisition was corrected in 3D using a redundant cross-correlation algorithm (Wang et al., 2014) implemented as an independent module of SMAP (Ries, 2020). After translation of the coordinate files obtained from N-STORM or DECODE/SMAP, image reconstructions were performed using the ThunderSTORM ImageJ plugin (Ovesný et al., 2014) in Fiji software. Custom scripts and macros were used to translate coordinate files, as well as automate image reconstruction for whole images at 16 nm/pixel and detailed zooms at 4 nm/pixel (https://github.com/cleterrier/ChriSTORM). For visualization of faint actin structures, the local contrast of monochrome (2D) or z-colored (3D) reconstructed images was enhanced using the Contrast Limited Adaptive Histogram Equalization (CLAHE) plugin.

For two-color STORM images (Fig. 8 E), a SAFe360 module (Abbelight) mounted on a Nikon Ti2 stand (Nikon), equipped with a LC4Cc laser combiner (Oxxius) and a 100X NA 1.49 objective, was used to perform spectral-demixing STORM (Friedl et al., 2023 *Preprint*). The sample, labeled for actin using Alexa Fluor 647 Plus-phalloidin and for Arp2/3 (p34 Arc) using a CF680-conjugated secondary antibody, was placed in STORM buffer and illuminated using a 640 nm laser (500 mW). Emitted fluorescence was split by a 700 nm dichroic toward two Flash v3 cameras (Hamamatsu). Separation of Alexa Fluor 647 and CF680 fluorescence was performed by demixing blinking events, resulting in two-channel coordinates files that were further processed and rendered using custom scripts and macros similar to single-color images (https://github.com/cleterrier/ChriSTORM).

Epifluorescence image analysis

Intensity quantifications were performed on the maximum projection of the raw data with no further adjustment (see below). Linear regions of interest (ROIs) were traced along an axon using the NeuronJ plugin in Fiji software, encompassing an axon–bead contact. Tracings were then translated into ImageJ ROIs. The ROI was then refined to the presynaptic cluster using the ProFitFeat script (available at https://github.com/cleterrier/Measure_ROIs/blob/master/Pro_Feat_Fit.js), restricting the ROI to the segment with an intensity above 50% of the maximum intensity point along the line ROI. The background-corrected intensities within these ROIs were then measured for each labeled channel. Induced presynapses were categorized as "actin-enriched" (A+) or "non-enriched" (A−) by visual inspection, comparing their actin staining level to neighboring axon shaft, as a simple threshold value was not adapted to local variation in actin staining. For natural synapses, ROIs were traced along the axon at axon–dendrite contacts where presynaptic proteins were visibly accumulated, and fluorescence intensities were measured for each labeled channel as described above.

STORM image analysis

To obtain the best STORM images with an interpretable pattern of actin staining, we carefully selected induced presynapses where the bead made a single "touch" contact on one side of a well-isolated, continuous axon. We avoided situations where the bead would deform the contacted axon, as well as axons crossing or bundling. We generated a high-magnification image (4 nm/pixel) for each bead-induced presynapse image. Actin structures present on the reconstructed image were scored as present, non-present, or not determined when their presence or absence could not be reliably determined by at least two experimenters in order to reduce bias (Fig. 7 C and Fig. 8 D). We used the following criteria to define the three types of presynaptic actin nanostructures:

- actin mesh: a small cluster of actin opposed to the bead contact and within the presynaptic marker cluster
- actin rails: linear structures within the presynaptic marker cluster
- actin corrals: large actin clusters at the periphery or just outside of the presynaptic marker cluster.

The size of the actin mesh and corrals (Fig. 7 D) was determined from manual outlines on 2D projection images in ImageJ.

Data presentation and statistical analysis

The Data S1 file recapitulates the statistics for all quantifications shown as graphs in the figures. Individual measurement points (number *n*) from independent experiments (number N) were pooled. All experiments were replicated between two- and eight-times using bead-seeded neurons from different cultures. Intensity profiles, graphs, and statistical analyses were generated using Prism. On bar graphs, dots (if present) are averages of each independent experiment, bars or horizontal lines represent the mean, and vertical lines are the SEM unless otherwise specified. Significances were tested using one-way, non-parametric ANOVA with Šídák post-hoc significance testing between selected conditions. All differences and variations mentioned in the text are significant unless specified as non-significant. In Data S1 and in figures, the results of the post-hoc significance are indicated as follows: ns or *ns*, non-significant; * or °, P < 0.05; ** or °°, P < 0.01; *** or °°°, P < 0.001.

Online supplemental material

Fig. S1 shows that postsynaptic actin impedes the visualization of presynaptic content and organization in hippocampal neurons, even using state-of-the-art super-resolution microscopy. Fig. S2 shows optical methods to assess vesicular cycling at bead-induced presynapses. Fig. S3 shows presynapses induced 48 h after seeding more mature, 14-div neurons show a similar proportion of actin enrichment and with similar presynaptic content. Fig. S4 shows presynapses induced for 48 and 96 h show a similar proportion of actin enrichment with similar presynaptic content. Fig. S5 shows that bead-induced inhibitory and excitatory presynapses show similar actin and presynaptic component content distribution. Fig. S6 shows induced presynapses are similar to natural presynapses between 48 and 96 h after bead seeding and between inhibitory and excitatory presynapses; acute actin perturbation effect on the accumulation of presynaptic components is similar at natural synapses and induced presynapses. Fig. S7 shows that acute actin nucleators' inhibition effect on the accumulation of presynaptic components is similar at natural synapses and induced presynapses; effect of CK666 on additional presynaptic components. Table S1 shows sequences of the inserted tags for endogenous tagging of rat ß-actin. Data S1 shows a spreadsheet file containing the statistics (mean, SEM, number of points, number of independent experiments, significance tests) for all values shown in figures and supplementary figures.

Data availability

The data are available from the corresponding authors upon reasonable request.

Acknowledgments

We would like to thank the Neuro-Cellular Imaging Service and Nikon Center for Neuro-NanoImaging at INP, funded by CPER-FEDER (PlateForme NeuroTimone PA0014842), the Fédération pour la Recherche sur le Cerveau (AOE 16 “Espoir en tête” 2021), and the Institut Marseille Imaging (A*MIDEX, AMX-19-IET-002). We also thank the NeuroVir facility at the Timone Neuroscience Institute (CNRS-AMU UMR 7289) for AAV production. We would like to thank Subhojit Roy for insightful discussions, Archan Ganguly for the initial help in setting up the bead-induced presynapse model, and Javier De Felipe for pointers on the total number of synapses in the brain.

This work has received support from the Centre National de la Recherche Scientifique ATIP program (AO 2016 to C. Leterrier), Fondation pour la Recherche Médicale (EQ202103012966 to C. Leterrier), A*MIDEX (ICN PhD Program, Q:6 ANR-11-IDEX-0001-02 grant) funded by the French Government “Investissements d’Avenir” program (Pépinière to M-J. Papandréou, NeuroSchool PhD program to D. Bingham, Q:7 Master funding to NvB), and the Institut NeuroMarseille (A*MIDEX, AMX-19-IET-002).

Author contributions: Conceptualization: M.-J. Papandréou and C. Leterrier. Data curation: D. Bingham and C. Leterrier. Formal analysis: D. Bingham, C.E. Jakobs, F. Wernert, M.-J. Papandréou, and C. Leterrier. Funding acquisition: M.-J. Papandréou and C. Leterrier. Investigation: D. Bingham, C.E. Jakobs, F. Boroni-Rueda, N. Jullien, E. Schentarra, K. Friedl, J. Da Costa Moura, Danique Michelle van Bommel, Ghislaine Caillol, Marie-Jeanne Papandréou, and Christophe Leterrier. Methodology: Dominic Bingham, Channa Elise Jakobs, Fanny Boroni-Rueda, Nicolas Jullien, Eva Schentarra, Karoline Friedl, Julie Da Costa Moura, D. Michelle van Bommel, G. Caillol, Y. Ogawa, M.-J. Papandréou, and C. Leterrier. Project administration: M.-J. Papandréou and C. Leterrier. Resources: Y. Ogawa. Software: C. Leterrier. Supervision: M.-J. Papandréou and C. Leterrier. Visualization: D. Bingham, C.E. Jakobs, F. Wernert, E. Schentarra, K. Fried, M.-J. Papandréou, and C. Leterrier. Writing—original draft: C. Leterrier. Writing—review and editing: D. Bingham, C.E. Jakobs, F. Wernert, N. Jullien, E. Schentarra, K. Friedl, D. Michelle van Bommel, M.-J. Papandréou, and C. Leterrier.

Disclosures: All authors have completed and submitted the ICMJE Form for Disclosure of Potential Conflicts of Interest. K. Friedl reported “Employee of Abbelight.” No other disclosures were reported.

Submitted: 19 August 2022
Revised: 7 June 2023
Accepted: 25 July 2023

References

Allison, D.W., V.I. Gelfand, I. Spector, and A.M. Craig. 1998. Role of actin in anchoring postsynaptic receptors in cultured hippocampal neurons: Differential attachment of NMDA versus AMPA receptors. *J. Neurosci.* 18:2423–2436. https://doi.org/10.1523/jneurosci.18-07-02423.1998

Aunis, D., and M.F. Bader. 1988. The cytoskeleton as a barrier to exocytosis in secretory cells. *J. Exp. Biol.* 139:253–266. https://doi.org/10.1242/jeb.139.1.253

Aurnhammer, C., M. Haase, N. Muether, M. Hausl, C. Rauschhuber, I. Huber, H. Nitschko, U. Busch, A. Sing, A. Ehrhardt, and A. Baiker. 2012. Universal real-time PCR for the detection and quantification of adeno-associated virus serotype 2-derived inverted terminal repeat sequences. *Hum. Gene Ther. Methods.* 23:18–28. https://doi.org/10.1089/hgtb.2011.034

Batista, A.F.R., J.C. Martínez, and U. Hengst. 2017. Intra-axonal synthesis of SNAP25 is required for the formation of presynaptic terminals. *Cell Rep.* 20:3085–3098. https://doi.org/10.1016/j.celrep.2017.08.097

Benson, D.L., F.H. Watkins, O. Steward, and G. Banker. 1994. Characterization of GABAergic neurons in hippocampal cell cultures. *J. Neurocytol.* 23: 279–295. https://doi.org/10.1007/bf01188497

Bleckert, A., H. Photowala, and S. Alford. 2012. Dual pools of actin at presynaptic terminals. *J. Neurophysiol.* 107:3479–3492. https://doi.org/10.1152/jn.00789.2011

Bloom, O., E. Evergren, N. Tomilin, O. Kjaerulff, P. Löw, L. Brodin, V.A. Pieribone, P. Greengard, and O. Shupliakov. 2003. Colocalization of synapsin and actin during synaptic vesicle recycling. *J. Cell Biol.* 161: 737–747. https://doi.org/10.1083/jcb.200212140

Burry, R.W. 1980. Formation of apparent presynaptic elements in response to poly-basic compounds. *Brain Res.* 184:85–98. https://doi.org/10.1016/0006-8993(80)90588-0

Burry, R.W., R.H. Ho, and W.D. Matthew. 1986. Presynaptic elements formed on polylysine-coated beads contain synaptic vesicle antigens. *J. Neurocytol.* 15:409–419. https://doi.org/10.1007/bf01611725

Cano-Astorga, N., J. DeFelipe, and L. Alonso-Nanclares. 2021. Three-Dimensional synaptic organization of layer III of the human temporal neocortex. *Cereb. Cortex.* 31:4742–4764. https://doi.org/10.1093/cercor/bhab120

Carvalhais, L.G., V.C. Martinho, E. Ferreiro, and P.S. Pinheiro. 2020. Unraveling the nanoscopic organization and function of central mammalian presynapses with super-resolution microscopy. *Front. Neurosci.* 14: 578409. https://doi.org/10.3389/fnins.2020.578409

Chandrasekar, I., J.E. Huettner, S.G. Turney, and P.C. Bridgman. 2013. Myosin II regulates activity dependent compensatory endocytosis at central synapses. *J. Neurosci.* 33:16131–16145. https://doi.org/10.1523/jneurosci.2229-13.2013

Chenouard, N., F. Xuan, and R.W. Tsien. 2020. Synaptic vesicle traffic is supported by transient actin filaments and regulated by PKA and NO. *Nat. Commun.* 11:5318. https://doi.org/10.1038/s41467-020-19120-1

Cingolani, L.A., and Y. Goda. 2008. Actin in action: The interplay between the actin cytoskeleton and synaptic efficacy. *Nat. Rev. Neurosci.* 9:344–356. https://doi.org/10.1038/nrn2373

Cole, J.C., B.R. Villa, and R.S. Wilkinson. 2000. Disruption of actin impedes transmitter release in snake motor terminals. *J. Physiol.* 525:579–586. https://doi.org/10.1111/j.1469-7793.2000.t01-2-00579.x

Dani, A., B. Huang, J. Bergan, C. Dulac, and X. Zhuang. 2010. Superresolution imaging of chemical synapses in the brain. *Neuron.* 68:843–856. https://doi.org/10.1016/j.neuron.2010.11.021

Danielson, E., K. Perez de Arce, B. Cimini, E.-C. Wamhoff, S. Singh, J.R. Cottrell, A.E. Carpenter, and M. Bathe. 2021. Molecular diversity of glutamatergic and GABAergic synapses from multiplexed fluorescence imaging. *Eneuro.* 8:ENEURO.0286-20.2020. https://doi.org/10.1523/eneuro.0286-20.2020

DeWeerdt, S. 2019. How to map the brain. *Nature.* 571:S6–S8. https://doi.org/10.1038/d41586-019-02208-0

Dillon, C., and Y. Goda. 2005. The actin cytoskeleton: Integrating form and function at the synapse. *Annu. Rev. Neurosci.* 28:25–55. https://doi.org/10.1146/annurev.neuro.28.061604.135757

Forster, B., D.V.D. Ville, J. Berent, D. Sage, and M. Unser. 2004. Extended depth-of-focus for multi-channel microscopy images: A complex wavelet approach. 2004 2nd Ieee Int Symposium Biomed Imaging Nano Macro Ieee Cat 04ex821. IEEE, Manhattan, NY. 660–663. https://doi.org/10.1109/isbi.2004.1398624

Friedl, K., A. Mau, V. Caorsi, N. Bourg, S. Lévêque-Fort, and C. Leterrier. 2023. Robust and fast multicolor single molecule localization microscopy using spectral separation and demixing. *bioRxiv*. https://doi.org/10.1101/2023.01.23.525017(PreprintpostedJanuary232023)

Gaffield, M.A., and W.J. Betz. 2006. Imaging synaptic vesicle exocytosis and endocytosis with FM dyes. *Nat. Protoc.* 1:2916–2921. https://doi.org/10.1038/nprot.2006.476

Ganguly, A., Y. Tang, L. Wang, K. Ladt, J. Loi, B. Dargent, C. Leterrier, and S. Roy. 2015. A dynamic formin-dependent deep F-actin network in axons. *J. Cell Biol.* 210:401–417. https://doi.org/10.1083/jcb.201506110

Gao, Y., E. Hisey, T.W.A. Bradshaw, E. Erata, W.E. Brown, J.L. Courtland, A. Uezu, Y. Xiang, Y. Diao, and S.H. Soderling. 2019. Plug-and-Play protein modification using homology-independent universal genome engineering. *Neuron*. 103:583–597.e8. https://doi.org/10.1016/j.neuron.2019.05.047

Gentile, J.E., M.G. Carrizales, and A.J. Koleske. 2022. Control of synapse structure and function by actin and its regulators. *Cells*. 11:603. https://doi.org/10.3390/cells11040603

Glebov, O.O., R.E. Jackson, C.M. Winterflood, D.M. Owen, E.A. Barker, P. Doherty, H. Ewers, and J. Burrone. 2017. Nanoscale structural plasticity of the active zone matrix modulates presynaptic function. *Cell Rep*. 18: 2715–2728. https://doi.org/10.1016/j.celrep.2017.02.064

Götzke, H., M. Kilisch, M. Martínez-Carranza, S. Sograte-Idrissi, A. Rajavel, T. Schlichthaerle, N. Engels, R. Jungmann, P. Stenmark, F. Opazo, and S. Frey. 2019. The ALFA-tag is a highly versatile tool for nanobody-based bioscience applications. *Nat. Commun*. 10:4403. https://doi.org/10.1038/s41467-019-12301-7

Harms, K.J., and A.M. Craig. 2005. Synapse composition and organization following chronic activity blockade in cultured hippocampal neurons. *J. Comp. Neurol*. 490:72–84. https://doi.org/10.1002/cne.20635

He, J., R. Zhou, Z. Wu, M.A. Carrasco, P.T. Kurshan, J.E. Farley, D.J. Simon, G. Wang, B. Han, J. Hao, et al. 2016. Prevalent presence of periodic actin-spectrin-based membrane skeleton in a broad range of neuronal cell types and animal species. *Proc. Natl. Acad. Sci. USA*. 113:6029–6034. https://doi.org/10.1073/pnas.1605707113

Hirokawa, N., K. Sobue, K. Kanda, A. Harada, and H. Yorifuji. 1989. The cytoskeletal architecture of the presynaptic terminal and molecular structure of synapsin 1. *J. Cell Biol*. 108:111–126. https://doi.org/10.1083/jcb.108.1.111

Jacquemet, G., A.F. Carisey, H. Hamidi, R. Henriques, and C. Leterrier. 2020. The cell biologist's guide to super-resolution microscopy. *J. Cell Sci*. 133: jcs240713. https://doi.org/10.1242/jcs.240713

Jimenez, A., K. Friedl, and C. Leterrier. 2020. About samples, giving examples: Optimized single molecule localization microscopy. *Methods*. 174: 100–114. https://doi.org/10.1016/j.ymeth.2019.05.008

Jungmann, R., M.S. Avendaño, J.B. Woehrstein, M. Dai, W.M. Shih, and P. Yin. 2014. Multiplexed 3D cellular super-resolution imaging with DNA-PAINT and Exchange-PAINT. *Nat. Methods*. 11:313–318. https://doi.org/10.1038/nmeth.2835

Kaech, S., and G. Banker. 2006. Culturing hippocampal neurons. *Nat. Protoc*. 1:2406–2415. https://doi.org/10.1038/nprot.2006.356

Korobova, F., and T. Svitkina. 2010. Molecular architecture of synaptic actin cytoskeleton in hippocampal neurons reveals a mechanism of dendritic spine morphogenesis. *Mol. Biol. Cell*. 21:165–176. https://doi.org/10.1091/mbc.e09-07-0596

Kraszewski, K., O. Mundigl, L. Daniell, C. Verderio, M. Matteoli, and P. De Camilli. 1995. Synaptic vesicle dynamics in living cultured hippocampal neurons visualized with CY3-conjugated antibodies directed against the lumenal domain of synaptotagmin. *J. Neurosci*. 15:4328–4342. https://doi.org/10.1523/jneurosci.15-06-04328.1995

Landis, D.M., and T.S. Reese. 1983. Cytoplasmic organization in cerebellar dendritic spines. *J. Cell Biol*. 97:1169–1178. https://doi.org/10.1083/jcb.97.4.1169

Lavoie-Cardinal, F., A. Bilodeau, M. Lemieux, M.-A. Gardner, T. Wiesner, G. Laramée, C. Gagné, and P. De Koninck. 2020. Neuronal activity remodels the F-actin based submembrane lattice in dendrites but not axons of hippocampal neurons. *Sci. Rep*. 10:11960. https://doi.org/10.1038/s41598-020-68180-2

Lelek, M., M.T. Gyparaki, G. Beliu, F. Schueder, J. Griffié, S. Manley, R. Jungmann, M. Sauer, M. Lakadamyali, and C. Zimmer. 2021. Single-molecule localization microscopy. *Nat. Rev. Methods Primers*. 1:39. https://doi.org/10.1038/s43586-021-00038-x

Leterrier, C. 2021a. A pictorial history of the neuronal cytoskeleton. *J. Neurosci*. 41:11–27. https://doi.org/10.1523/jneurosci.2872-20.2020

Leterrier, C. 2021b. Putting the axonal periodic scaffold in order. *Curr. Opin. Neurobiol*. 69:33–40. https://doi.org/10.1016/j.conb.2020.12.015

Leterrier, C., J. Potier, G. Caillol, C. Debarnot, F. Rueda Boroni, and B. Dargent. 2015. Nanoscale architecture of the axon initial segment reveals an organized and robust scaffold. *Cell Rep*. 13:2781–2793. https://doi.org/10.1016/j.celrep.2015.11.051

Li, Y., M. Mund, P. Hoess, J. Deschamps, U. Matti, B. Nijmeijer, V.J. Sabinina, J. Ellenberg, I. Schoen, and J. Ries. 2018. Real-time 3D single-molecule localization using experimental point spread functions. *Nat. Methods*. 15:367–369. https://doi.org/10.1038/nmeth.4661

Li, Y.-C., W.-Z. Bai, L. Zhou, L.-K. Sun, and T. Hashikawa. 2010. Nonhomogeneous distribution of filamentous actin in the presynaptic terminals on the spinal motoneurons. *J. Comp. Neurol*. 518:3184–3192. https://doi.org/10.1002/cne.22374

Li, Z., and V.N. Murthy. 2001. Visualizing postendocytic traffic of synaptic vesicles at hippocampal synapses. *Neuron*. 31:593–605. https://doi.org/10.1016/s0896-6273(01)00398-1

Lucido, A.L., F. Suarez Sanchez, P. Thostrup, A.V. Kwiatkowski, S. Leal-Ortiz, G. Gopalakrishnan, D. Liazoghli, W. Belkaid, R.B. Lennox, P. Grütter, et al. 2009. Rapid assembly of functional presynaptic boutons triggered by adhesive contacts. *J. Neurosci*. 29:12449–12466. https://doi.org/10.1523/jneurosci.1381-09.2009

Lukinavičius, G., L. Reymond, E. D'Este, A. Masharina, F. Göttfert, H. Ta, A. Güther, M. Fournier, S. Rizzo, H. Waldmann, et al. 2014. Fluorogenic probes for live-cell imaging of the cytoskeleton. *Nat. Methods*. 11: 731–733. https://doi.org/10.1038/nmeth.2972

Maschi, D., M.W. Gramlich, and V.A. Klyachko. 2018. Myosin V functions as a vesicle tether at the plasma membrane to control neurotransmitter release in central synapses. *Elife*. 7:e39440. https://doi.org/10.7554/eLife.39440

McFadden, M.H., H. Xu, Y. Cui, R.A. Piskorowski, C. Leterrier, D. Zala, L. Venance, V. Chevaleyre, and Z. Lenkei. 2018. Actomyosin-mediated nanostructural remodeling of the presynaptic vesicle pool by cannabinoids induces long-term depression. *bioRxiv*. https://doi.org/10.1101/444950(PreprintpostedOctober162018)

Melak, M., M. Plessner, and R. Grosse. 2017. Actin visualization at a glance. *J. Cell Sci*. 130:525–530. https://doi.org/10.1242/jcs.189068

Morales, M., M.A. Colicos, and Y. Goda. 2000. Actin-dependent regulation of neurotransmitter release at central synapses. *Neuron*. 27:539–550. https://doi.org/10.1016/s0896-6273(00)00064-7

Nagasaki, A., S. T Kijima, T. Yumoto, M. Imaizumi, A. Yamagishi, H. Kim, C. Nakamura, and T. Q P Uyeda. 2017. The position of the GFP tag on actin affects the filament formation in mammalian cells. *Cell Struct. Funct*. 42: 131–140. https://doi.org/10.1247/csf.17016

Nolen, B.J., N. Tomasevic, A. Russell, D.W. Pierce, Z. Jia, C.D. McCormick, J. Hartman, R. Sakowicz, and T.D. Pollard. 2009. Characterization of two classes of small molecule inhibitors of Arp2/3 complex. *Nature*. 460: 1031–1034. https://doi.org/10.1038/nature08231

Nosov, G., M. Kahms, and J. Klingauf. 2020. The decade of super-resolution microscopy of the presynapse. *Front. Synaptic Neurosci*. 12:32. https://doi.org/10.3389/fnsyn.2020.00032

Ogawa, Y., B.C. Lim, S. George, J.A. Oses-Prieto, J.M. Rasband, Y. Eshed-Eisenbach, S. Nair, F. Boato, E. Peles, A.L. Burlingame, et al. 2023. Antibody-directed extracellular proximity biotinylation reveals Contactin-1 regulates axo-axonic innervation of axon initial segments. *bioRxiv*. https://doi.org/10.1101/2023.03.06.531378(PreprintpostedMarch062023)

Ogunmowo, T.H., H. Jing, S. Raychaudhuri, G.F. Kusick, Y. Imoto, S. Li, K. Itoh, Y. Ma, H. Jafri, M.B. Dalva, et al. 2023. Membrane compression by synaptic vesicle exocytosis triggers ultrafast endocytosis. *Nat. Commun*. 14:2888. https://doi.org/10.1038/s41467-023-38595-2

O'Neil, S.D., B. Rácz, W.E. Brown, Y. Gao, E.J. Soderblom, R. Yasuda, and S.H. Soderling. 2021. Action potential-coupled Rho GTPase signaling drives presynaptic plasticity. *Elife*. 10:e63756. https://doi.org/10.7554/eLife.63756

Ovesný, M., P. Křížek, J. Borkovec, Z. Svindrych, and G.M. Hagen. 2014. ThunderSTORM: A comprehensive ImageJ plug-in for PALM and STORM data analysis and super-resolution imaging. *Bioinformatics*. 30: 2389–2390. https://doi.org/10.1093/bioinformatics/btu202

Papandréou, M.-J., and C. Leterrier. 2018. The functional architecture of axonal actin. *Mol. Cell. Neurosci*. 91:151–159. https://doi.org/10.1016/j.mcn.2018.05.003

Peng, A., Z. Rotman, P.-Y. Deng, and V.A. Klyachko. 2012. Differential motion dynamics of synaptic vesicles undergoing spontaneous and activity-evoked endocytosis. *Neuron*. 73:1108–1115. https://doi.org/10.1016/j.neuron.2012.01.023

Rampérez, A., D. Bartolomé-Martín, A. García-Pascual, J. Sánchez-Prieto, and M. Torres. 2019. Photoconversion of FM1-43 reveals differences in synaptic vesicle recycling and sensitivity to pharmacological disruption of actin dynamics in individual synapses. *ACS Chem. Neurosci*. 10: 2045–2059. https://doi.org/10.1021/acschemneuro.8b00712

Ramsey, A.M., A.-H. Tang, T.A. LeGates, X.-Z. Gou, B.E. Carbone, S.M. Thompson, T. Biederer, and T.A. Blanpied. 2021. Subsynaptic positioning of AMPARs by LRRTM2 controls synaptic strength. *Sci. Adv*. 7: eabf3126. https://doi.org/10.1126/sciadv.abf3126

Reshetniak, S., and S.O. Rizzoli. 2019. Interrogating synaptic architecture: Approaches for labeling organelles and cytoskeleton components. *Front. Synaptic Neurosci*. 11:23. https://doi.org/10.3389/fnsyn.2019.00023

Ries, J. 2020. SMAP: A modular super-resolution microscopy analysis platform for SMLM data. *Nat. Methods*. 17:870–872. https://doi.org/10.1038/s41592-020-0938-1

Rizvi, S.A., E.M. Neidt, J. Cui, Z. Feiger, C.T. Skau, M.L. Gardel, S.A. Kozmin, and D.R. Kovar. 2009. Identification and characterization of a small molecule inhibitor of formin-mediated actin assembly. *Chem. Biol.* 16: 1158–1168. https://doi.org/10.1016/j.chembiol.2009.10.006

Rust, M.B., and T. Maritzen. 2015. Relevance of presynaptic actin dynamics for synapse function and mouse behavior. *Exp. Cell Res.* 335:165–171. https://doi.org/10.1016/j.yexcr.2014.12.020

Rust, M.J., M. Bates, and X. Zhuang. 2006. Sub-diffraction-limit imaging by stochastic optical reconstruction microscopy (STORM). *Nat. Methods*. 3: 793–795. https://doi.org/10.1038/nmeth929

Sakaba, T., and E. Neher. 2003. Involvement of actin polymerization in vesicle recruitment at the calyx of held synapse. *J. Neurosci.* 23:837–846. https://doi.org/10.1523/jneurosci.23-03-00837.2003

Sankaranarayanan, S., P.P. Atluri, and T.A. Ryan. 2003. Actin has a molecular scaffolding, not propulsive, role in presynaptic function. *Nat. Neurosci.* 6:127–135. https://doi.org/10.1038/nn1002

Schindelin, J., I. Arganda-Carreras, E. Frise, V. Kaynig, M. Longair, T. Pietzsch, S. Preibisch, C. Rueden, S. Saalfeld, B. Schmid, et al. 2012. Fiji: An open-source platform for biological-image analysis. *Nat. Methods*. 9: 676–682. https://doi.org/10.1038/nmeth.2019

Shen, W., B. Wu, Z. Zhang, Y. Dou, Z.R. Rao, Y.R. Chen, and S. Duan. 2006. Activity-induced rapid synaptic maturation mediated by presynaptic cdc42 signaling. *Neuron*. 50:401–414. https://doi.org/10.1016/j.neuron.2006.03.017

Shupliakov, O., O. Bloom, J.S. Gustafsson, O. Kjaerulff, P. Low, N. Tomilin, V.A. Pieribone, P. Greengard, and L. Brodin. 2002. Impaired recycling of synaptic vesicles after acute perturbation of the presynaptic actin cytoskeleton. *Proc. Natl. Acad. Sci. USA*. 99:14476–14481. https://doi.org/10.1073/pnas.212381799

Sidenstein, S.C., E. D'Este, M.J. Böhm, J.G. Danzl, V.N. Belov, and S.W. Hell. 2016. Multicolour multilevel STED nanoscopy of actin/spectrin organization at synapses. *Sci. Rep.* 6:26725. https://doi.org/10.1038/srep26725

Del Signore, S.J., C.F. Kelley, E.M. Messelaar, T. Lemos, M.F. Marchan, B. Ermanoska, M. Mund, T.G. Fai, M. Kaksonen, and A.A. Rodal. 2021. An autoinhibitory clamp of actin assembly constrains and directs synaptic endocytosis. *Elife*. 10:e69597. https://doi.org/10.7554/eLife.69597

Siksou, L., P. Rostaing, J.-P. Lechaire, T. Boudier, T. Ohtsuka, A. Fejtová, H.-T. Kao, P. Greengard, E.D. Gundelfinger, A. Triller, and S. Marty. 2007. Three-dimensional architecture of presynaptic terminal cytomatrix. *J. Neurosci.* 27:6868–6877. https://doi.org/10.1523/jneurosci.1773-07.2007

Sörensen, P.M., R.E. Iacob, M. Fritzsche, J.R. Engen, W.M. Brieher, G. Charras, and U.S. Eggert. 2012. The natural product cucurbitacin E inhibits depolymerization of actin filaments. *ACS Chem. Biol.* 7:1502–1508. https://doi.org/10.1021/cb300254s

Sotelo, C. 2020. The history of the synapse. *Anat. Rec.* 303:1252–1279. https://doi.org/10.1002/ar.24392

Soykan, T., N. Kaempf, T. Sakaba, D. Vollweiter, F. Goerdeler, D. Puchkov, N.L. Kononenko, and V. Haucke. 2017. Synaptic vesicle endocytosis occurs on multiple timescales and is mediated by formin-dependent actin assembly. *Neuron*. 93:854–866.e4. https://doi.org/10.1016/j.neuron.2017.02.011

Spector, I., F. Braet, N.R. Shochet, and M.R. Bubb. 1999. New anti-actin drugs in the study of the organization and function of the actin cytoskeleton. *Microsc. Res. Tech.* 47:18–37. https://doi.org/10.1002/(sici)1097-0029(19991001)47:1<18:aid-jemt3>3.0.co;2-e

Speiser, A., L.-R. Müller, P. Hoess, U. Matti, C.J. Obara, W.R. Legant, A. Kreshuk, J.H. Macke, J. Ries, and S.C. Turaga. 2021. Deep learning enables fast and dense single-molecule localization with high accuracy. *Nat. Methods*. 18:1082–1090. https://doi.org/10.1038/s41592-021-01236-x

Suarez, F., P. Thostrup, D. Colman, and P. Grütter. 2013. Dynamics of presynaptic protein recruitment induced by local presentation of artificial adhesive contacts. *Dev. Neurobiol.* 73:98–106. https://doi.org/10.1002/dneu.22037

Südhof, T.C. 2021. The cell biology of synapse formation. *J. Cell Biol.* 220: e202103052. https://doi.org/10.1083/jcb.202103052

Tang, A.-H., H. Chen, T.P. Li, S.R. Metzbower, H.D. MacGillavry, and T.A. Blanpied. 2016. A trans-synaptic nanocolumn aligns neurotransmitter release to receptors. *Nature*. 536:210–214. https://doi.org/10.1038/nature19058

Taylor, A.M., J. Wu, H.-C. Tai, and E.M. Schuman. 2013. Axonal translation of β-catenin regulates synaptic vesicle dynamics. *J. Neurosci.* 33: 5584–5589. https://doi.org/10.1523/jneurosci.2944-12.2013

Vassilopoulos, S., S. Gibaud, A. Jimenez, G. Caillol, and C. Leterrier. 2019. Ultrastructure of the axonal periodic scaffold reveals a braid-like organization of actin rings. *Nat. Commun.* 10:5803. https://doi.org/10.1038/s41467-019-13835-6

Wang, Y., J. Schnitzbauer, Z. Hu, X. Li, Y. Cheng, Z.-L. Huang, and B. Huang. 2014. Localization events-based sample drift correction for localization microscopy with redundant cross-correlation algorithm. *Opt. Express*. 22:15982–15991. https://doi.org/10.1364/oe.22.015982

Wilhelm, B.G., S. Mandad, S. Truckenbrodt, K. Kröhnert, C. Schäfer, B. Rammner, S.J. Koo, G.A. Claßen, M. Krauss, V. Haucke, et al. 2014. Composition of isolated synaptic boutons reveals the amounts of vesicle trafficking proteins. *Science*. 344:1023–1028. https://doi.org/10.1126/science.1252884

Wittenmayer, N., C. Körber, H. Liu, T. Kremer, F. Varoqueaux, E.R. Chapman, N. Brose, T. Kuner, and T. Dresbach. 2009. Postsynaptic Neuroligin1 regulates presynaptic maturation. *Proc. Natl. Acad. Sci. USA*. 106: 13564–13569. https://doi.org/10.1073/pnas.0905819106

Wu, L.-G., and C.Y. Chan. 2022. Multiple roles of actin in exo- and endocytosis. *Front. Synaptic Neurosci.* 14:841704. https://doi.org/10.3389/fnsyn.2022.841704

Yao, J., J. Qi, and G. Chen. 2006. Actin-dependent activation of presynaptic silent synapses contributes to long-term synaptic plasticity in developing hippocampal neurons. *J. Neurosci.* 26:8137–8147. https://doi.org/10.1523/jneurosci.1183-06.2006

Zhang, P., H. Lu, R.T. Peixoto, M.K. Pines, Y. Ge, S. Oku, T.J. Siddiqui, Y. Xie, W. Wu, S. Archer-Hartmann, et al. 2018. Heparan sulfate organizes neuronal synapses through neurexin partnerships. *Cell*. 174: 1450–1464.e23. https://doi.org/10.1016/j.cell.2018.07.002

Zhang, W., and D.L. Benson. 2001. Stages of synapse development defined by dependence on F-actin. *J. Neurosci.* 21:5169–5181. https://doi.org/10.1523/jneurosci.21-14-05169.2001

Zhang, W., and D.L. Benson. 2002. Developmentally regulated changes in cellular compartmentation and synaptic distribution of actin in hippocampal neurons. *J. Neurosci. Res.* 69:427–436. https://doi.org/10.1002/jnr.10313

Supplemental material

https://doi.org/10.1083/jcb.202208110

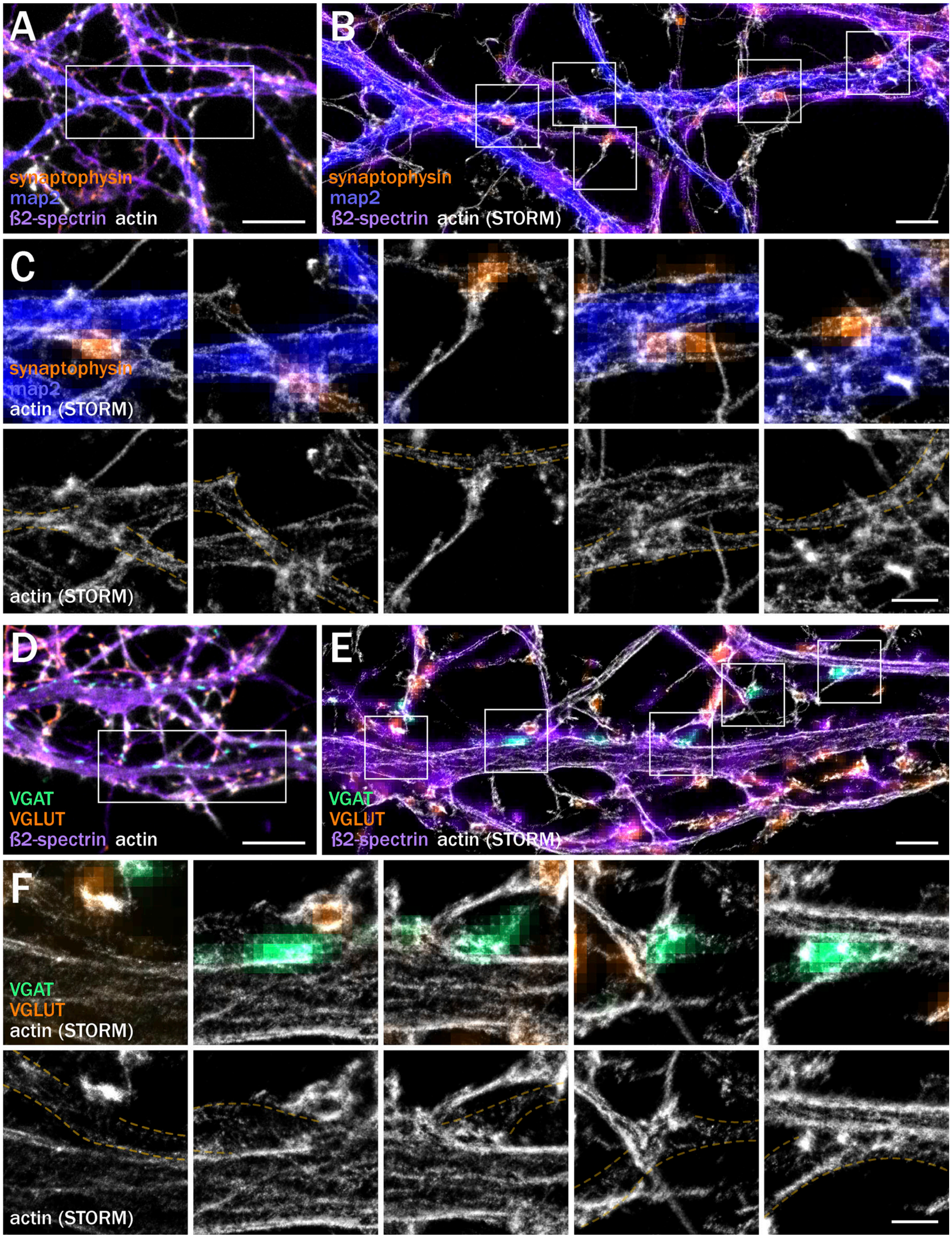

Figure S1. **Postsynaptic actin impedes the visualization of presynaptic content and organization in hippocampal neurons, even using state-of-the-art super-resolution microscopy. (A–C)** Images of neurons after 9 d in vitro (div), stained for synaptophysin (purple), map2 (blue), ß2-spectrin (purple), and actin (gray). **(A)** Widefield image. **(B)** Zooms from the highlighted area in A, overlaying the widefield image of synaptophysin, map2, and ß2-spectrin with the STORM image of actin. **(C)** Zooms from the highlighted area in B, with the top row showing overlayed widefield image of synaptophysin and map2 with the STORM image of actin (gray) and bottom showing the isolated actin STORM image with axon shaft highlighted in orange dashed lines. **(D–F)** Images of neurons after 9 div, stained for VGAT (green), VGLUT (orange), ß2-spectrin (purple), and actin (gray). **(C)** Widefield image. **(D)** Widefield image. **(E)** Zoom from the highlighted area in D, overlaying widefield images of VGAT, VGLUT, and ß2-spectrin with the STORM image of actin. F, zooms from the highlighted areas in E, with the top row showing overlayed widefield image of VGAT and VGLUT with the STORM image of actin (gray) and the bottom showing the isolated actin STORM image with axon shaft highlighted in orange dashed lines. Scale bars for A and D, 10 µm; for B and E, 2 µm; for C and F, 0.5 µm.

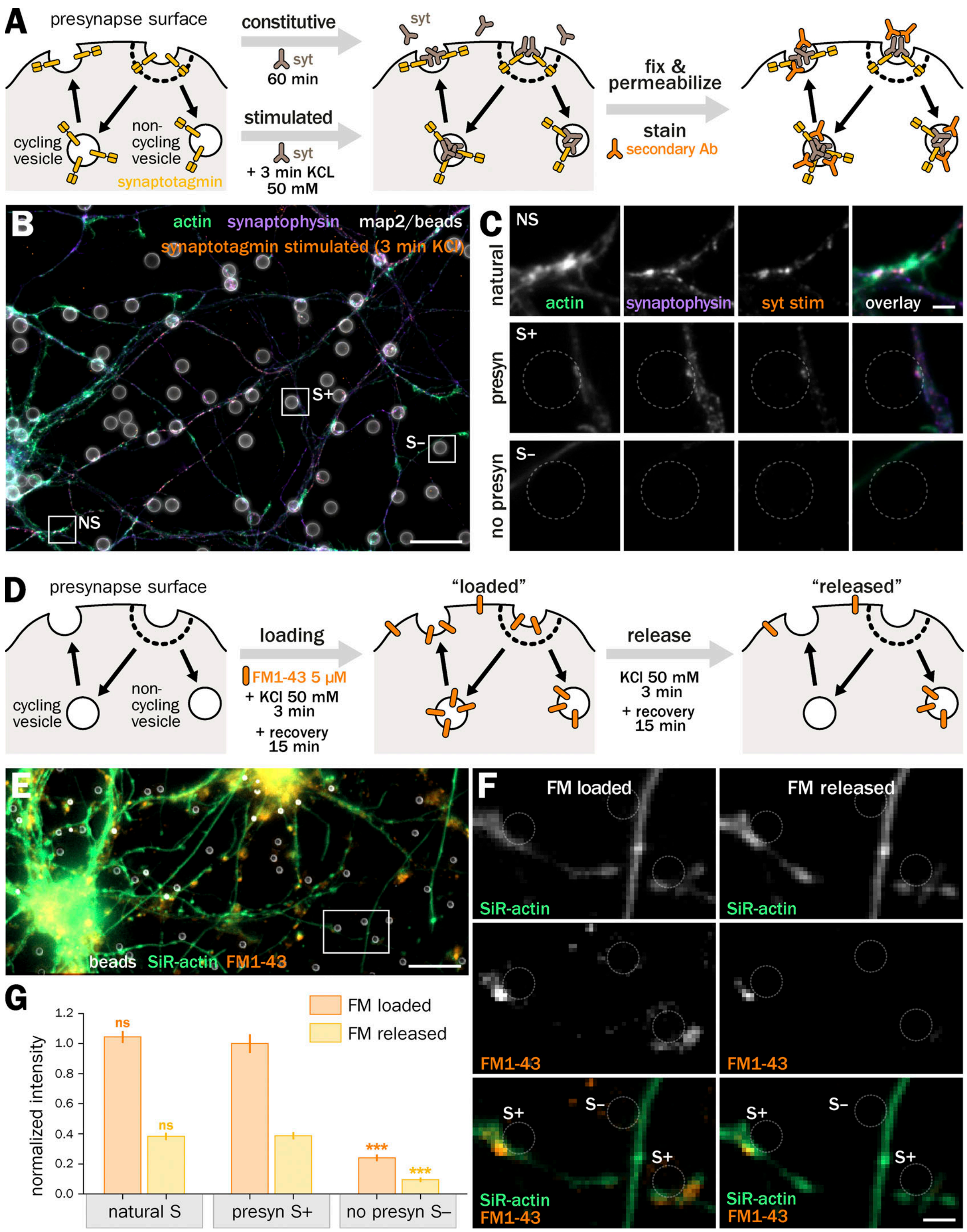

Figure S2. **Optical methods to assess vesicular cycling at bead-induced presynapses. (A–C)** Anti-synaptotagmin (syt) antibody feeding experiments to assess the cycling activity of presynapses. **(A)** Cartoon of the anti-syt feeding experiments. Living neurons are incubated with the syt antibody (orange) directed against an extracellular epitope of synaptotagmin (yellow), either for 60 min to measure constitutive cycling, or for 3 min in the presence of 50 mM KCl to measure stimulated cycling. Neurons are then fixed and the syt antibody is revealed with a secondary antibody (green). **(B)** Widefield fluorescence image of cultured neurons 2 d after bead seeding at 8 div, labeled for actin (green), synaptophysin (purple), map2 (gray), and feeding with anti-synaptotagmin antibody (syt) during a 3-min incubation with KCl (stimulated cycling). **(C)** Zooms corresponding to the natural synapse (NS), S+, and S− axon-bead contacts highlighted in B. Scale bars for B, 20 µm; for C, 2 µm. **(D–G)** FM1-43 dye loading/release experiment to assess the cycling activity of presynapses. **(D)** Cartoon of the FM1-43 experiment. Living neurons are first loaded with FM1-43 using a 3-min incubation in 50 mM KCl followed by 15 min of recovery, then images of the "loaded" time point are taken. FM1-43 is then released using a second 3-min incubation with 50 mM KCl and 15-min recovery, before images are taken of the "released" time point. **(E)** Widefield fluorescence image of cultured neurons 2 d after bead seeding at 8 div, labeled for actin using SiR (green) after loading with FM1-43 (orange). **(F)** Zooms corresponding to area highlighted in E, showing the images obtained after loading (left column) and release (right column) of FM1-43. Beads are indicated by dashed-line circles labeling the induced presynapses (S+) and axon-bead contact with no presynapse (S−). Scale bars for B, 20 µm; for C, 5 µm. **(G)** Quantification of the FM staining intensity after loading (orange) and release (yellow) in natural synapses (NS) and bead-induced presynapses (S+) as well as axon-bead contacts devoid of a presynapse (S−). Significance signs on the graph compare to the value for the same labeling condition in bead-induced presynapses (S+, normalized to 1.0 for the loading condition). See Data S1 file for detailed statistics.

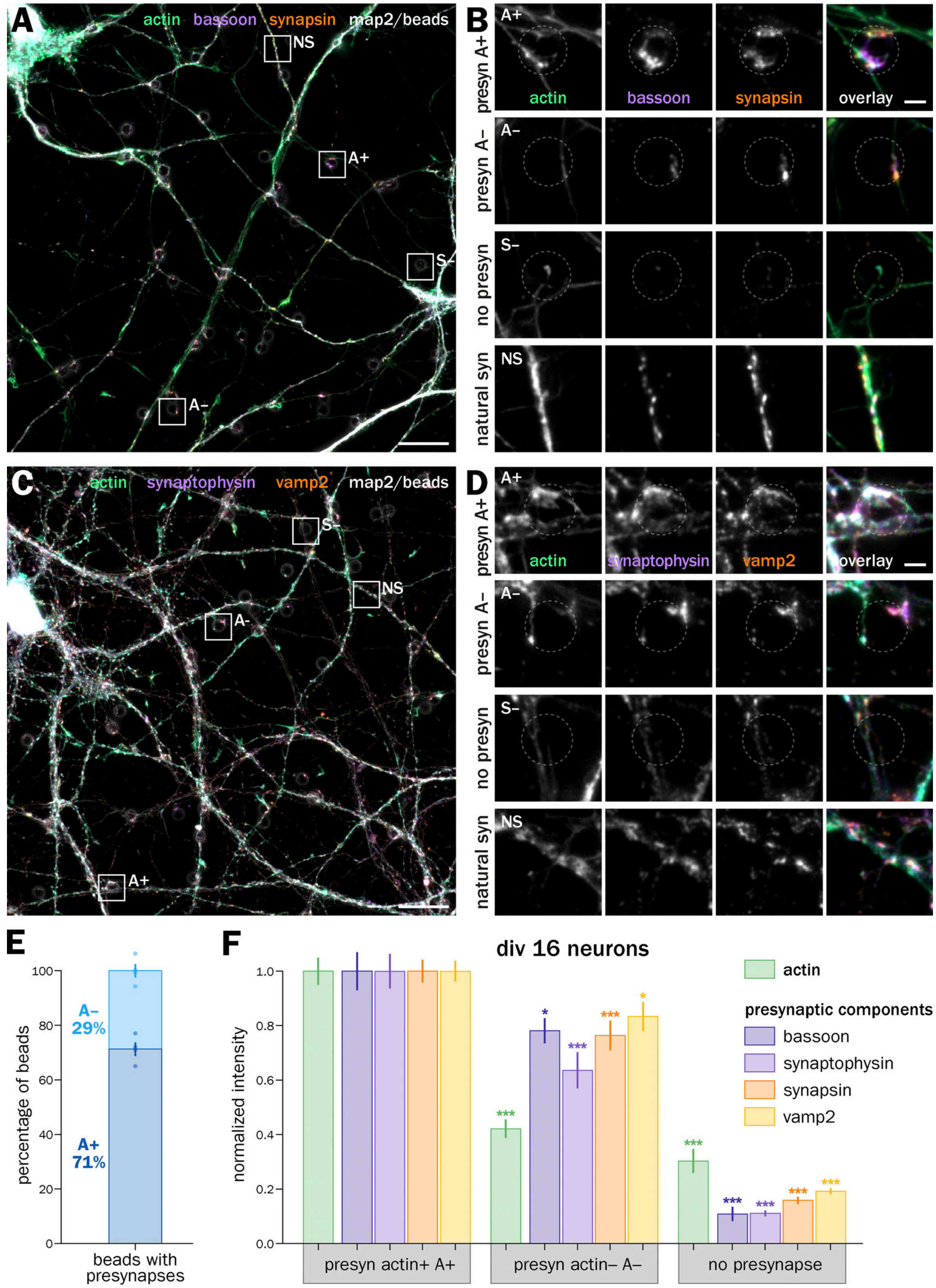

Figure S3. **Presynapses induced 48 h after seeding more mature, 14-div neurons show a similar proportion of actin enrichment and with similar presynaptic content. (A)** Widefield fluorescence image of cultured neurons 2 d after bead seeding at 14 div, labeled for actin (green), bassoon (purple), synapsin (orange), and map2 (gray). **(B)** Zooms corresponding to the areas highlighted in A: top row, actin-enriched induced presynapse at an axon-bead contact (A+); second row, induced presynapse at an axon-bead contact with no actin enrichment (A–); third row, axon-bead contact with no induced presynapse (S–); bottom row, natural synapse at axon-dendrite contact (NS). **(C)** Widefield fluorescence image of cultured neurons 2 d after bead seeding at 14 div, labeled for actin (green), synaptophysin (purple), vamp2 (orange), and map2 (gray). **(D)** Zooms corresponding to the A+, A–, S– axon-bead contacts and natural synapses (NS) highlighted in C. Scale bars in A and C: 20 µm; B and D: 2 µm. **(E)** Quantification of the proportion of A+ (dark blue) and A– (blue) at axon-bead contacts that resulted in an induced presynapse. **(F)** Quantification of the labeling intensity for actin (green), bassoon (dark purple), synaptophysin (purple), synapsin (orange), and vamp2 (yellow) at actin-enriched presynapses (A+), induced presynapses with no actin enrichment (A–), and axon-bead contacts devoid of presynapse (S–), normalized to the intensity at A+ presynapses. Significance signs on graphs compare to the value for the same labeling in bead-induced presynapses (S+, normalized to 1.0). See Data S1 file for detailed statistics.

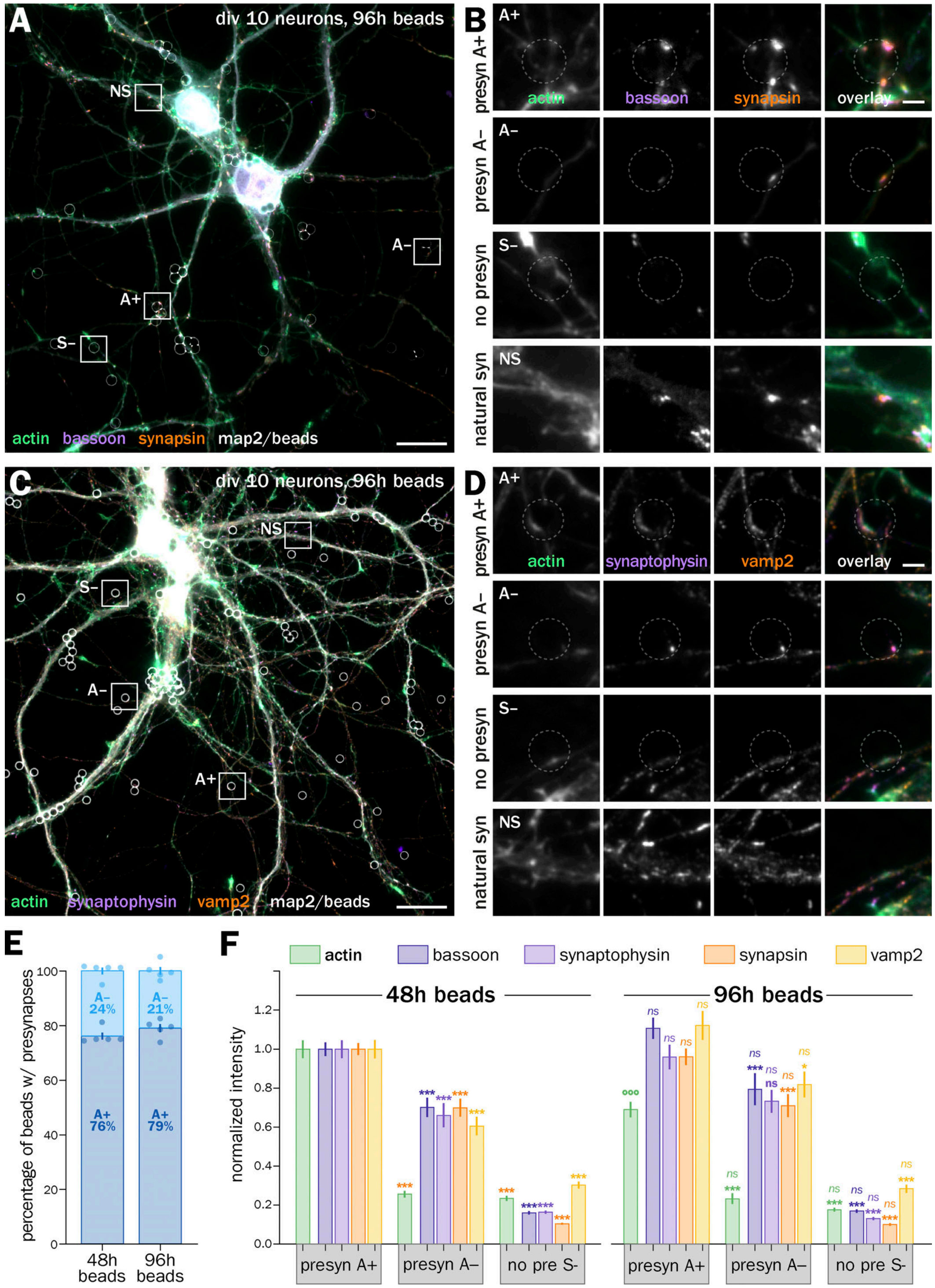

Figure S4. **Presynapses induced for 48 and 96 h show a similar proportion of actin enrichment with similar presynaptic content. (A)** Widefield fluorescence image of cultured neurons 96 h after bead seeding at 6 div, labeled for actin (green), bassoon (purple), synapsin (orange), and map2 (gray). **(B)** Zooms corresponding to the areas highlighted in A: top row, actin-enriched induced presynapse at an axon-bead contact (A+); second row, induced presynapse at an axon-bead contact with no actin enrichment (A−); third row, axon-bead contact with no induced presynapse (S−); bottom row, natural synapse at axon-dendrite contact (NS). **(C)** Widefield fluorescence image of cultured neurons 96 h after bead seeding at 6 div, labeled for actin (green), synaptophysin (purple), vamp2 (orange), and map2 (gray). **(D)** Zooms corresponding to the A+, A−, S− axon-bead contacts and natural synapses (NS) highlighted in C. Scale bars in A and C: 20 µm; B and D: 2 µm. **(E)** Quantification of the proportion of A+ (dark blue) and A− (blue) at axon-bead contacts that resulted in an induced presynapse for neurons after 48 and 96 h incubation with beads. **(F)** Quantification of the labeling intensity for actin (green), bassoon (dark purple), synaptophysin (purple), synapsin (orange), and vamp2 (yellow) at actin-enriched presynapses (A+), induced presynapses with no actin enrichment (A−), and axon-bead contacts devoid of presynapse (S−), 48 h (left), and 96 h (right) after bead seeding, normalized to the intensity of A+ presynapses after 48 h. Significance signs on graphs (bottom: *, ns) compare to the value for the labeling on bead-induced presynapses (S+, normalized to 1.0 at 48 h); significance signs (top: °, *ns*) compare to the value for the same labeling and type of induced presynapse (A+ or A−) between 48 and 96 h. See Data S1 file for detailed statistics.

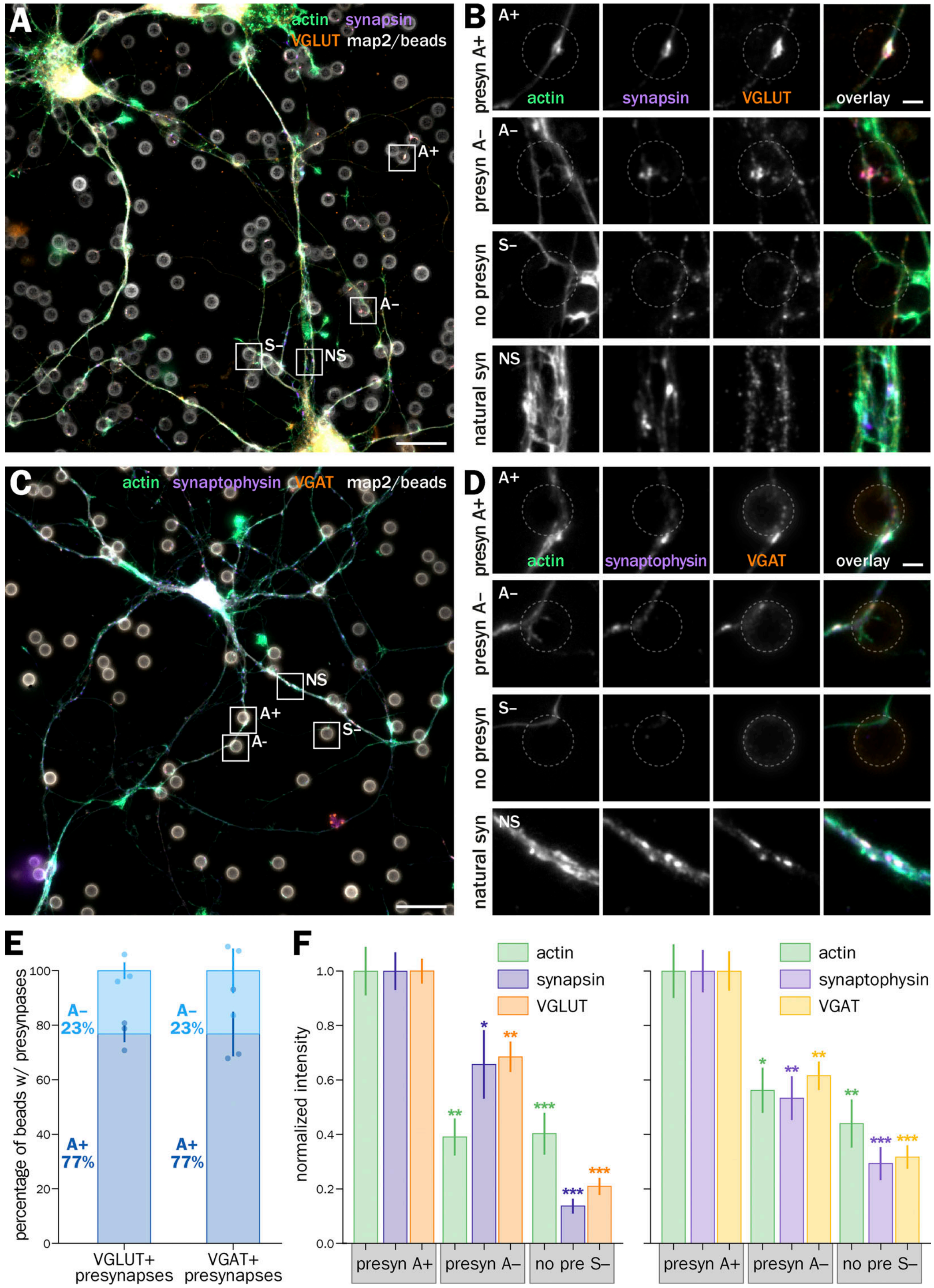

Figure S5. **Bead-induced inhibitory and excitatory presynapses show similar actin and presynaptic component content distribution. (A)** Widefield fluorescence image of cultured neurons 2 d after bead seeding at 8 div, labeled for actin (green), synapsin (purple), VGLUT (orange), and map2 (gray). **(B)** Zooms corresponding to the areas highlighted in A: top row, actin-enriched induced presynapse at an axon-bead contact (A+); second row, induced presynapse at an axon-bead contact with no actin enrichment (A−); third row, axon-bead contact with no induced presynapse (S−); bottom row, natural synapse at axon-dendrite contact (NS). **(C)** Widefield fluorescence image of cultured neurons 2 d after bead seeding at 8 div, labeled for actin (green), synaptophysin (purple), VGAT (orange), and map2 (gray). **(D)** Zooms corresponding to the A+, A−, S− axon-bead contacts and natural synapses (NS) highlighted in C. Scale bars in A and C: 20 µm; B and D: 2 µm. **(E)** Quantification of the proportion of A+ (dark blue) and A− (blue) at axon-bead contacts that resulted in an induced VGLUT-positive (left bar) and VGAT-positive (right bar) presynapse. **(F)** Left graph, quantification of the labeling intensity for actin (green), synapsin (dark purple), and VGLUT (orange) at actin-enriched presynapses (A+), induced presynapses with no actin enrichment (A−), and axon-bead contacts devoid of presynapse (S−), normalized to the intensity at A+ presynapses. Right graph, quantification of the labeling intensity for actin (green), synaptophysin (purple), and VGAT (yellow) at A+ and A− induced presynapses as well as S− axon bead contacts. Significance signs on graphs compare to the value for the same labeling in actin-enriched presynapses (A+, normalized to 1.0). See Data S1 file for detailed statistics.

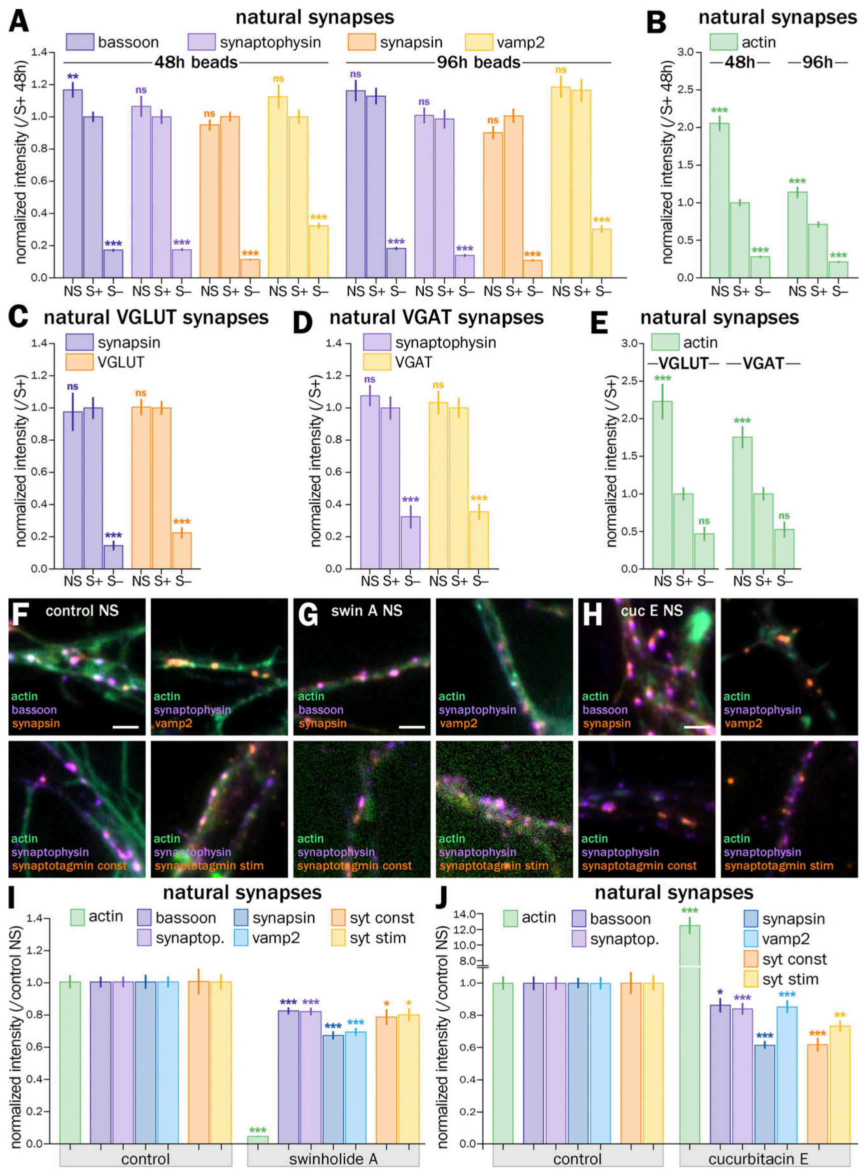

Figure S6. **Induced presynapses are similar to natural presynapses between 48 and 96 h after bead seeding and between inhibitory and excitatory presynapses; acute actin perturbation effect on the accumulation of presynaptic components is similar at natural synapses and induced presynapses.** **(A)** Quantification of the labeling intensity for bassoon (dark purple), synaptophysin (purple), synapsin (orange), and vamp2 (yellow) at natural synapses (NS), induced presynapses at axon-bead contacts (S+) and axon-bead contacts devoid of presynapse (S–) 48 h (left) or 96 h (right) after bead seeding, normalized to the intensity at S+ contacts after 48 h. **(B)** Quantification of the labeling intensity for actin at natural synapses (NS), induced presynapses at axon-bead contacts (S+), and axon-bead contacts devoid of presynapse (S–) 48 h (left) or 96 h (right) after bead seeding, normalized to the intensity at S+ contacts after 48 h. **(C)** Quantification of the labeling intensity for synapsin (dark purple) and VGLUT (orange) at excitatory natural synapses (NS), induced presynapses at axon-bead contacts (S+), and axon-bead contacts devoid of presynapse (S–), normalized to the intensity at S+ contacts. **(D)** Quantification of the labeling intensity for synaptophysin (purple) and VGAT (yellow) at inhibitory natural synapses (NS), induced presynapses at axon-bead contacts (S+) and axon-bead contacts devoid of presynapse (S–), normalized to the intensity at S+ contacts. **(E)** Quantification of the labeling intensity for actin at natural synapses (NS), induced presynapses at axon-bead contacts (S+), and axon-bead contacts devoid of presynapse (S–), normalized to the intensity at S+ contacts for excitatory (left) or inhibitory (right) presynapses. Significance signs on graphs A–E compare to the value for the same labeling in bead-induced presynapses (S+, normalized to 1.0). **(F–H)** Representative images of natural presynapses in control condition (F) or after treatment with swinholide A (G) or cucurbitacine E (H) labeled for actin, bassoon, and synapsin (green, purple, and orange respectively, top-left image); actin, synaptophysin, and vamp2 (green, purple and orange respectively, top-right image); actin, synaptophysin and constitutive feeding with anti-synaptotagmin antibody (green, purple and orange respectively, bottom-left image); actin, synaptophysin, and stimulated feeding with anti-synaptotagmin antibody (green, purple, and orange, respectively, bottom-right image). Zooms are taken from the images shown in Fig. 4, A–C. Scale bars, 2 µm. **(I)** Quantification of the labeling intensity for actin (green), bassoon (dark purple), synaptophysin (purple), synapsin (dark blue), vamp2 (blue), and after syt feeding for constitutive (orange) and stimulated (yellow) vesicular cycling at natural synapses in the control condition and after swinholide A treatment, normalized to control natural synapses. **(J)** Quantification of the labeling intensity for actin (green), bassoon (dark purple), synaptophysin (purple), synapsin (dark blue), vamp2 (blue), and after syt feeding for constitutive (orange) and stimulated (yellow) vesicular cycling at natural synapses in the control condition and after cucurbitacin E treatment, normalized to control natural synapses. Significance signs on graphs I and J compare to the value for the same labeling in the control condition for natural synapses (normalized to 1.0). See Data S1 file for detailed statistics.

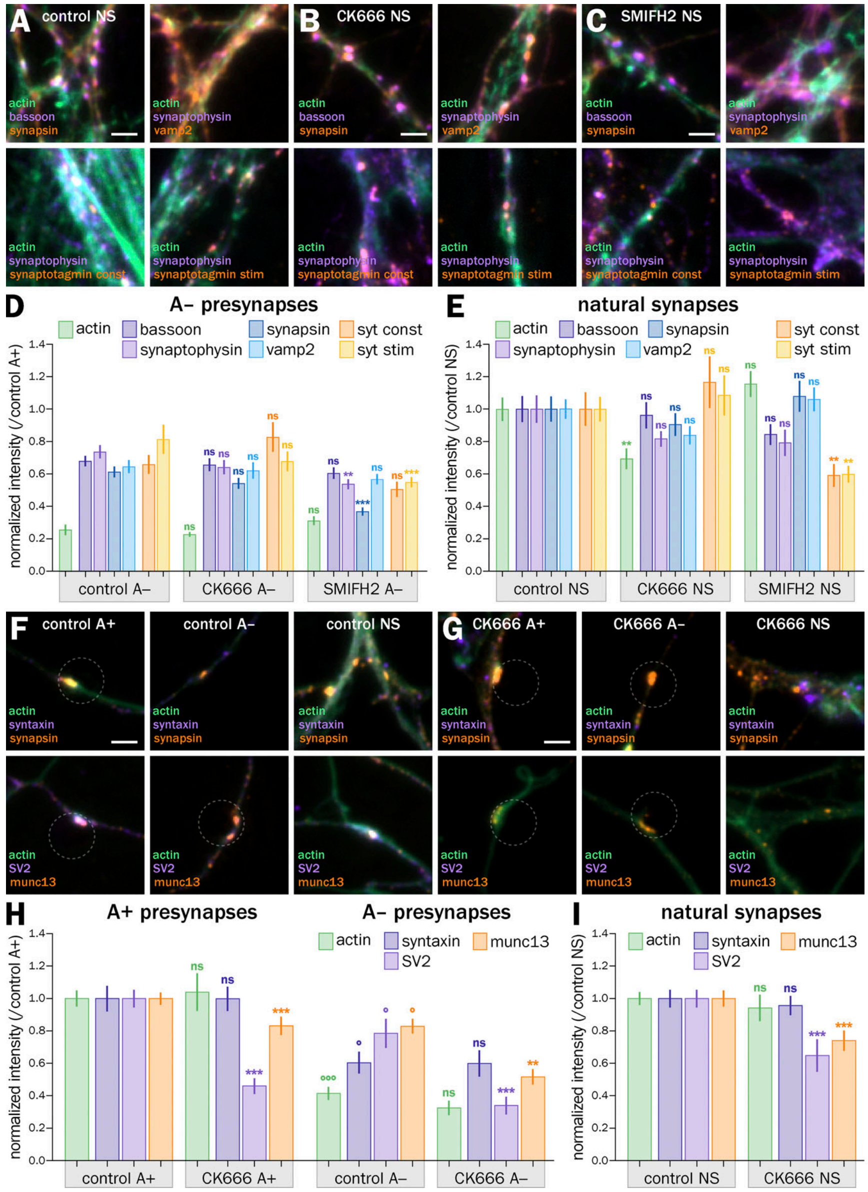

Figure S7. **Acute actin nucleators inhibition effect on the accumulation of presynaptic components is similar at natural synapses and induced presynapses; effect of CK666 on additional presynaptic components. (A–C)** Representative images of natural presynapses in control condition (A) or after treatment with CK666 (B) or SMIFH2 (C) labeled for actin, bassoon, and synapsin (green, purple, and orange respectively, top-left image); actin, synaptophysin, and vamp2 (green, purple and orange respectively, top-right image); actin, synaptophysin and constitutive feeding with anti-synaptotagmin antibody (green, purple, and orange, respectively, bottom-left image); actin, synaptophysin and stimulated feeding with anti-synaptotagmin antibody (green, purple, and orange, respectively, bottom-right image). Zooms are taken from the images shown in Fig. 5, A–C. Scale bars, 2 µm. **(D)** Quantification of the labeling intensity for actin (green), bassoon (dark purple), synaptophysin (purple), synapsin (dark blue), vamp2 (blue), and after syt feeding for constitutive (orange), and stimulated (yellow) vesicular cycling at induced presynapses devoid of actin enrichment (A–) in the control condition and after CK666 or SMIFH2 treatment, normalized to control A+ presynapses. Significance signs on graph compare to the value for the same labeling in the control condition for A– presynapses (normalized to 1.0). **(E)** Quantification of the labeling intensity for actin (green), bassoon (dark purple), synaptophysin (purple), synapsin (dark blue), vamp2 (blue), and after syt feeding for constitutive (orange), and stimulated (yellow) vesicular cycling at natural synapses in the control condition and after CK666 or SMIFH2 treatment, normalized to control natural synapses. Significance signs on the graph compare to the value for the same labeling in the control condition for natural synapses (normalized to 1.0). **(F and G)** Representative images of induced and natural presynapses in the control condition (F) or after treatment with CK666 (G) labeled for actin, syntaxin, and synapsin (green, purple, and orange respectively, top row); actin, SV2 and munc13 (green, purple, and orange, respectively, bottom row). Scale bars, 2 µm. **(H)** Quantification of the labeling intensity for actin (green), syntaxin (dark purple), SV2 (purple), synaptophysin (dark blue) and munc13 (orange), at induced presynapses enriched in actin (A+) or devoid of actin enrichment (A–), in the control condition and after CK666 treatment, normalized to control A+ presynapses. Significance signs (bottom: *, ns) on graphs compare to the value for the same measurement in the control condition for the same type of presynapse (A+ or A–, normalized to 1.0); significance signs (top: °, *ns*) compare to the value for the same measurement in the control condition for A+ presynapses. **(I)** Quantification of the labeling intensity for actin (green), syntaxin (dark purple), SV2 (purple), synaptophysin (dark blue), and munc13 (orange), at natural presynapses (NS), in the control condition and after CK666, normalized to control natural synapses. Significance signs on graphs I and J compare to the value for the same labeling in the control condition for natural synapses (normalized to 1.0). See Data S1 file for detailed statistics.

Provided online are Table S1 and Data S1. Table S1 shows sequences of the inserted tags for endogenous tagging of rat ß-actin. Data S1 shows spreadsheet file containing the statistics (mean, SEM, number of points, number of independent experiments, significance tests) for all values shown in figures and supplementary figures.

Discussion

L'initiation du potentiel d'action à l'AIS et le cycle d'endo-exocytose présynaptique sont deux éléments majeurs dans la transmission du signal nerveux. En contraste des nombreuses études sur ces deux phénomènes, seules quelques références dans la littérature ont rapporté des interactions possibles entre composants du cytosquelette et l'endocytose (Ghisleni et al., 2020, *Nat. Commun.*; Jenkins et al., 2015, *Sci. Adv.*; Zhou et al., 2019, *Science*), ainsi que la présence de composants de l'endocytose dans les compartiments axonaux non-synaptiques (Eichel et al., 2022, *Nature*; Ganguly et al., 2021, *Neuron*; Zhou et al., 2019, *Science*). Pourtant la présence en densité importante de composants de l'endocytose dans l'AIS et les indices d'une organisation des CCPs en relation avec les éléments du MPS axonal restent encore peu explorés à ce jour.

Dans l'article principal de cette thèse, nous proposons une étude inédite des mécanismes moléculaires associés à la CME dans l'AIS et des liens qu'ils entretiennent avec le MPS. L'association de la visualisation d'immunomarquages spécifiques en microscopie de fluorescence super-résolue et de l'ultrastructure riche en contexte de la PREM nous permettent de montrer l'existence à l'axone proximal d'une population dense de puits de clathrine dits « inactifs » puis de caractériser leur relation d'exclusion avec des zones sous-membranaires dénuées de spectrines dites « clairières ».

Au travers d'expériences d'endocytose de cargos, puis d'expression endogène d'une clathrine fluorescente observée sur neurones vivants, nous montrons qu'en situation physiologique ces CCPs axonaux sont immobiles dans leur immense majorité, en contraste avec la dynamique des structures de clathrine observées dans les dendrites et au soma dans les mêmes conditions.

Enfin l'application d'un protocole de LTD induite par une stimulation au NMDA rend ces CCPs de l'AIS capables d'endocytose et nous renseigne sur leur rôle de régulation dans des situations d'excitotoxicité.

Mis en perspective de la littérature existante à ce jour, nous pouvons noter que les travaux de l'article principal supportent l'hypothèse de spectrines qui agissent comme une barrière physique sous-membranaire s'opposant à une endocytose conclusive. L'existence de domaines d'exclusion (*clairières* dans l'article principal, *void patches* dans Ghisleni et al. 2020) entre les composants de l'endocytose et les spectrines au sein de types cellulaires distincts morphologiquement et fonctionnellement tels que les neurones du SNC (article principal), les membranes latérales des cellules épithéliales en colonne (Jenkins et al., 2015, *Sci. Adv.*) et les fibroblastes (Ghisleni et al., 2020, *Nat Commun* et dans l'article principal) pointe vers la possibilité d'un mécanisme général en mesure de maintenir les équilibres physiologiques de différents types cellulaires. Nos approches expérimentales s'additionnent à celles des articles susmentionnés et viennent ainsi enrichir le faisceau de preuves soutenant l'idée d'un mécanisme général de régulation de l'endocytose par le maillage d'actine-spectrines du MPS.

Plus en détails, l'étude de Zhou et al., 2019, *Science* est effectuée dans un modèle de neurone en culture similaire au notre et présente des observations dans le tube axonal distal. Les auteurs observent la transactivation de la signalisation RTK via l'effection des RCPG membranaires CB1 ou NCAM et la redistribution spatiale des composants de cette voie de signalisation relativement au MPS. Ils proposent ainsi que lors de l'effection de ces RCPG par leur agoniste, le MPS puisse jouer un rôle de plateforme organisatrice de la signalisation RCPG-pERK-RTK en regroupant les différents composants moléculaires de cette signalisation au centre des tétramères de spectrines, possiblement fixées aux ankyrines B. De plus les auteurs mentionnent un possible mécanisme d'auto-régulation négative dans l'activation de la voie pERK-RTK, par un désassemblage du MPS sous l'effet de la calpaine activée lors de l'effection de cette voie. La calpaine est une protéase qui désassemble les spectrines, ce qui a pour effet d'augmenter l'endocytose des RCPG. Ce désassemblage présenté dans la figure 4 de leur article se présente cependant à une échelle spatiale différente de nos observations sur les clairières de spectrines. Dans Zhou et al., il s'agit de larges patchs de spectrines de 10 à 20 tétramères de long qui disparaissent de façon réversible sur une échelle temporelle d'une à trois heures, il s'agit donc sans doute d'un phénomène distinct des clairières de spectrines présentées dans l'article principal de cette thèse, et il y aurait un intérêt certain à caractériser les contours de ces 2 phénomènes et leurs éventuelles interactions dans les études à venir. Enfin leur figure additionnelle S18 montre un résultat directement comparable au notre, lors de la déplétion de la β2-spectrine ils observent qu'après effection par son agoniste, le récepteur CB1 est endocyté dans des proportions bien plus importantes que dans la condition contrôle, non seulement dans l'axone mais aussi dans le compartiment somato-dendritique.

Enfin les travaux de Eichel et al., 2022, *Nature* présentent un intérêt certain pour nous car ils sont réalisés à l'AIS d'un modèle vivant C. Elegans. Dans ces travaux, les auteurs s'appuient sur des manipulations moléculaires qui relocalisent à l'axone des récepteurs polarisés vers les dendrites, puis observent leur endocytose axonale par CME. Au même titre qu'ils présentent un intérêt car réalisés dans un modèle in vivo, le paradigme expérimental de ces travaux rapproche l'axone d'une identité fonctionnelle dendritique ce qui rend la généralité de leurs résultats dans un contexte physiologique d'axone difficile à estimer. Les interactions entre la CME et le MPS axonal ont sans doute besoin d'être davantage explorées et mieux caractérisées avant de pouvoir intégrer les observations de modèles expérimentaux aussi distincts au sein d'un modèle général cohérent.

Durant l'exploration des liens entre MPS et CME, nous avons régulièrement eu à arbitrer entre méthodes expérimentales générales et spécifiques, de mise en œuvre aisée ou ardue. À titre d'exemple, les questions se sont posées d'étudier la CME liée à un récepteur spécifique ou sous son aspect le plus général avec un marqueur de phase fluide, de perturber les phénomènes observés avec des méthodes de déplétion ou avec des perturbateurs chimiques, de composer entre la simplicité des observations en microscopie sur échantillons fixés ou la résolution temporelle offerte par les expériences en microscopie sur neurones vivants, et encore beaucoup d'autres alternatives. De ce fait, parmi les pistes expérimentales initiées durant cette thèse, toutes n'ont pas pu être menées à leur conclusion et intégrées dans l'article principal. Ainsi, si les expérimentations sur l'organisation de la clathrine lors d'un KD des différentes spectrines (validées Fig. S4) ont pu nous montrer des différences de densité, de distribution et de taille des CCP (visibles en PREM Fig. 4 B et C), nos expériences pour observer les corrélats fonctionnels de ces différences en imagerie sur neurones vivants ont montré une différence dans la dynamique des différents shRNA comparés au contrôle. Sur des neurones transfectés pour exprimer la clathrine-GFP, en condition sh-β4-spectrine, nous avons pu observer une augmentation de la mobilité latérale des CCP de l'AIS, en condition sh-α2-β4-spectrine une quasi-immobilité des CCP ainsi qu'une densité plus faible que sur les contrôles. L'observation additionnelle a été faite d'une diminution fréquente de la largeur de l'AIS dans cette dernière condition sh-α2-β4-spectrine, additionnée à l'observation d'un stress cellulaire d'intensité moyenne pour le sh-β4-spectrine et importante pour le sh-α2-β4-spectrine. Au regard du stress cellulaire manifeste, l'interprétation de la part de ces résultats à attribuer uniquement à l'effet de déplétion des spectrines nous a semblé présenter trop de facteurs confondants pour conclure.

Par ailleurs, nous avons souhaité mieux caractériser les CCP dites « inactives » afin de déterminer si elles étaient capables de capturer un cargo et le conserver à la membrane extracellulaire sans l'endocyter. Dans ce but nous avons réalisé des expériences sur neurones vivants en les exposant simultanément au dextran couplé avec un fluorophore et au dextran à fluorescence sensible au pH dans une autre longueur d'onde de fluorescence (**Figure 7-1**). Nous souhaitions pouvoir déterminer au mieux la dynamique d'endocytose et une capture extracellulaire éventuelle des cargos. Toutefois les outils disponibles « sur l'étagère » pour réaliser cette expérience étaient limités car non couplés entre eux, et les résultats ainsi difficilement interprétables. Idéalement il nous aurait fallu réaliser ou faire réaliser une sonde unique présentant à la fois une fluorescence intrinsèque sur une longueur d'onde et une fluorescence sensible au pH sur un autre canal, puis réaliser des acquisitions sur neurones vivants exposés à cette sonde afin de pouvoir suivre le parcours d'un cargo, de sa présence dans le milieu extracellulaire jusqu'à son internalisation dans un compartiment plus acide du neurone. Coupler ces expériences à un marquage endogène de la clathrine ou des spectrines aurait permis d'élucider la dynamique temporelle complète de l'interaction d'un point de vue fonctionnel.

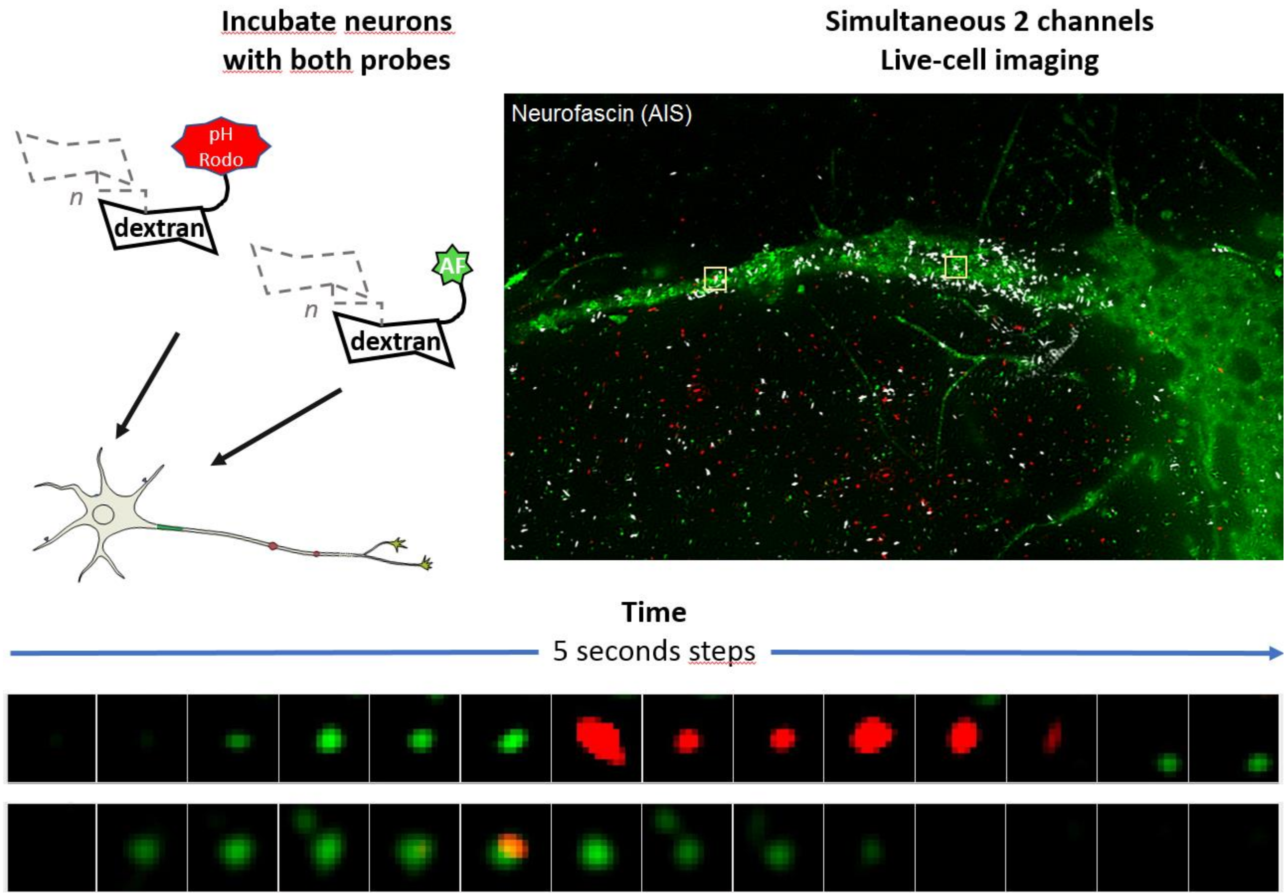

Figure 7-1 : Visualisation des composantes intracellulaire et totale de l'endocytose. En haut à gauche est présenté le schéma expérimental avec deux cargos dextran en simultané, l'un porte un fluorophore Alexa Fluor toujours actif en vert, l'autre porte une sonde sensible au pH pHrodo dont la fluorescence n'est activée que lors d'une endocytose effective. En haut à droite est montré l'image d'épifluorescence d'un neurone vivant ayant été incubé avec ces deux sondes, ainsi qu'avec un immunomarquage d'un épitope extracellulaire de la neurofascine pour indiquer l'AIS, montré ici en blanc. En bas, en microscopie TIRF-SIM, les images successives de 2 zones d'intérêt de l'AIS montrant une co-occurrence du marquage des deux sondes (acquisition simultanée des canaux de fluorescence des deux sondes à 0.2 Hz). La durée totale présentée s'étend sur 65 secondes.

Dans le but d'être généraux nous avons utilisé le dextran 10kDa comme cargo de phase fluide afin de rapporter la CME à l'AIS indifféremment du récepteur endocyté. Pour être plus complets, d'autres travaux pourraient étudier l'endocytose de récepteurs spécifiques à l'AIS, les travaux de Fréal et al., 2023 montrent une endocytose de canaux Nav 1.2 à l'AIS distal lors d'une LTD induite par stimulation

NMDA (adapté Fig. 7 de l'article principal), ces travaux pourraient être étendus à d'autres récepteurs ou canaux, avec pour limite principale que l'endocytose à l'AIS semble être dépendante de l'activité neuronale. Un protocole de LTD induite par stimulation électrique permettrait également de consolider les résultats d'endocytose axonale sous l'effet de l'activité synaptique par une autre méthode. Il serait également souhaitable d'avoir une approche complémentaire à l'unroofing pour réaliser une expérience produisant un effet complémentaire à ce dernier en matière de séparation des composantes membranaire et cytosolique. Une possibilité à envisager serait de réaliser des expériences d'endocytose suivie de *stripping* des anticorps (Arancibia-Cárcamo et al., 2006, *Molecular Methods in Ionotropic Receptor Biology*) ou de *quenching* de la fluorescence (Liao-Chan et al., 2015, *PLOS ONE*) pour éliminer la composante membranaire et ne conserver ainsi que la visualisation de la composante effectivement endocytée.

Pour renforcer le lien fonctionnel des observations faites dans l'article principal et pouvoir adresser la question du séquencement temporel entre la formation des clairières de spectrines, la formation des CCPs et l'endocytose effective, il serait souhaitable d'observer les spectrines en microscopie SMLM à la suite du protocole de LTD stimulée par NMDA présenté en figure 7. Des observations structurelles des spectrines après chacun des traitements pourraient également éclairer les interprétations des observations faites sur la clathrine dans la figure 4 de l'article principal. Des observations complémentaires de la présence et la dynamique éventuelle de la dynamine aux CCPs inactives donneraient des indices quant aux mécanismes moléculaires impliqués dans la régulation de la CME par le MPS. Un élément de preuve supplémentaire de poids serait d'observer l'effet d'une surexpression des spectrines sur la dynamique des CCPs dans les dendrites où celles-ci endocytent activement (voir Fig. 7 de l'article principal). Rappelons que nous avons mentionné dans l'introduction que surexprimer les spectrines par transfection ou dépléter l'ankyrine B conduisait à l'organisation du MPS dendritique suivant un motif périodique similaire à celui des axones (J. He et al., 2016, *Proc. Natl. Acad. Sci.*; Zhong et al., 2014, *eLife*). Coupler la surexpression des spectrines à l'expression endogène de clathrine fluorescente dans une expérience d'endocytose forcée via une LTD NMDA et observée en imagerie sur neurones vivants permettrait de déterminer au mieux la séquence complète des interactions. On pourrait s'attendre à ce que les spectrines rendues ainsi périodiques aux dendrites freinent la dynamique de l'endocytose de ce compartiment dans des proportions comparables à nos observations à l'AIS.

Pour des travaux futurs, il serait particulièrement intéressant de mettre en perspective les résultats de l'article principal et ceux de l'article contribué (Ganguly et al., 2021, *Neuron*). En effet, dans ces deux articles sont rapportés deux nouvelles observations bien distinctes liées à la clathrine et l'endocytose. Dans l'article principal nous observons une densité importante de CCP inactives à l'AIS, dans l'article contribué est observée une densité importante de paquets de transport de clathrine dans le tube axonal, on peut ainsi s'interroger sur l'existence d'un lien entre ces deux phénomènes qui impliquent le même acteur moléculaire dans deux compartiments axonaux aux propriétés distinctes. Dans nos observations en microscopie sur neurones vivants à l'AIS, nous observons une densité importante de CCPs inactives et nous n'avons observé que de façon anecdotique des paquets de transport, il est cependant tout à fait possible que la forte densité de CCPs inactives masque le signal des paquets de transport. De plus, la résolution temporelle que nous avions définie pour la microscopie sur cellules vivantes était destinée à pouvoir capturer des événements d'endocytose, mais possiblement trop lente pour capturer le mouvement d'un paquet de transport de clathrine. L'hypothèse que les CCPs inactives à l'AIS constituent une réserve de clathrine mobilisable sous forme de paquets de transport lors de l'activation synaptique est envisageable lorsque les observations de ces deux articles sont mises en perspective. Une expérience de stimulation chimique ou électrique sur un neurone exprimant de façon endogène une clathrine fluorescente et observé sur un champ incluant à la fois l'AIS et le tube distal pourrait être particulièrement éclairante et être compatible avec les observations de redistribution de la clathrine axonale aux synapses sous l'effet d'une dépolarisation chimique rapportées dans Tao-Cheng, 2020, *Mol Brain*. Une autre possibilité serait que les paquets de transport de clathrine au déplacement axonal antérograde soient dirigés en direction des synapses dès leur biosynthèse cellulaire, et que la composante rétrograde des paquets de clathrine vienne redistribuer la clathrine périsynaptique et des paquets inactifs de l'AIS.

Enfin, si nos observations indiquent une endocytose à l'AIS en situation de LTD induite par NMDA, le mécanisme de signalisation à l'origine de cette activation des CCPs inactives est à ce jour indéterminé. Dans les travaux de l'article principal, nous avons fréquemment fait l'observation d'un filament unique d'actine contactant le CCP au milieu de la clairière de spectrine, nous observons aussi une baisse drastique de l'endocytose du récepteur Tf dans les fibroblastes lors de la dépolymérisation de l'actine par la swinholide A (Fig. 5 de l'article principal). Le rôle de ce filament d'actine est donc à envisager lors de l'étude du mécanisme moléculaire à l'œuvre pour « débloquer » les CCPs inactives de l'AIS. De plus, des observations restent nécessaires pour déterminer la dynamique d'apparition/maintien/disparition des clairières de spectrines et les mettre en lien avec la dynamique des CCPs et de l'endocytose à l'AIS, bien que la résolution spatiale et temporelle nécessaire pour observer ce phénomène est aux limites de ce que permettent les techniques de microscopie à ce jour.

Comme nous avons pu en faire le constat au travers des travaux rapportés et mis en perspectives dans cette thèse, par-delà les connaissances canoniques sur l'endocytose médiée par la clathrine, l'exploration des mécanismes et structures associées à ses composants moléculaires est encore loin d'être épuisée. Les avancées technologiques en microscopie et les outils moléculaires dont nous tirons parti dans nos travaux nous permettent de poser un regard nouveau sur l'AIS et l'endocytose au travers d'observations et d'expériences inenvisageables il y a à peine une décennie et devenues des standards expérimentaux aujourd'hui. Sans pouvoir préjuger des avancées futures, il est certain que la progression continue des méthodes de microscopie parait prometteuse pour observer des phénomènes aux limites de ce qui est possible aujourd'hui et répondre au questionnement resté ouvert sur la dynamique éventuelle de l'apparition et disparition des clairières de spectrine. La disponibilité de sondes performantes et d'une résolution spatiale et temporelle suffisante serait également très désirable pour élucider la participation possible de l'actine dans un phénomène aussi dynamique que l'endocytose. Enfin, la possibilité d'explorer ces phénomènes dans des modèles in vivo nous permettrait de mieux étendre ces découvertes de l'échelle cellulaire jusqu'à la physiologie et la pathologie d'un individu.

Bibliographie et références

Abouelezz, A., Micinski, D., Lipponen, A., & Hotulainen, P. (2019). Sub-membranous actin rings in the axon initial segment are resistant to the action of latrunculin. *Biological Chemistry*, *400*(9), 1141‑1146. https://doi.org/10.1515/hsz-2019-0111

Almeida-Souza, L., Frank, R. A. W., García-Nafría, J., Colussi, A., Gunawardana, N., Johnson, C. M., Yu, M., Howard, G., Andrews, B., Vallis, Y., & McMahon, H. T. (2018). A Flat BAR Protein Promotes Actin Polymerization at the Base of Clathrin-Coated Pits. *Cell*, *174*(2), 325-337.e14. https://doi.org/10.1016/j.cell.2018.05.020

Arancibia-Cárcamo, I. L., Fairfax, B. P., Moss, S. J., & Kittler, J. T. (2006). Studying the Localization, Surface Stability and Endocytosis of Neurotransmitter Receptors by Antibody Labeling and Biotinylation Approaches. In J. T. Kittler & S. J. Moss (Éds.), *The Dynamic Synapse : Molecular Methods in Ionotropic Receptor Biology*. CRC Press/Taylor & Francis. http://www.ncbi.nlm.nih.gov/books/NBK2552/

Arnold, D. B., & Gallo, G. (2014). Structure meets function : Actin filaments and myosin motors in the axon. *Journal of Neurochemistry*, *129*(2), 213‑220. https://doi.org/10.1111/jnc.12503

Avinoam, O., Schorb, M., Beese, C. J., Briggs, J. A. G., & Kaksonen, M. (2015). Endocytic sites mature by continuous bending and remodeling of the clathrin coat. *Science*, *348*(6241), 1369‑1372. https://doi.org/10.1126/science.aaa9555

Ballesteros, A., & Swartz, K. J. (2020). Dextran Labeling and Uptake in Live and Functional Murine Cochlear Hair Cells. *Journal of Visualized Experiments*, *156*, 60769. https://doi.org/10.3791/60769

Bär, J., Kobler, O., van Bommel, B., & Mikhaylova, M. (2016). Periodic F-actin structures shape the neck of dendritic spines. *Scientific Reports*, *6*(1), 37136. https://doi.org/10.1038/srep37136

Barlan, K., & Gelfand, V. I. (2017). Microtubule-Based Transport and the Distribution, Tethering, and Organization of Organelles. *Cold Spring Harbor Perspectives in Biology*, *9*(5), a025817. https://doi.org/10.1101/cshperspect.a025817

Becker, P. S., Cohen, C. M., & Lux, S. E. (1986). The effect of mild diamide oxidation on the structure and function of human erythrocyte spectrin. *Journal of Biological Chemistry*, *261*(10), 4620‑4628. https://doi.org/10.1016/S0021-9258(17)38547-2

Bingham, D., Jakobs, C. E., Wernert, F., Boroni-Rueda, F., Jullien, N., Schentarra, E.-M., Friedl, K., Da Costa Moura, J., van Bommel, D. M., Caillol, G., Ogawa, Y., Papandréou, M.-J., &

Leterrier, C. (2023). Presynapses contain distinct actin nanostructures. *Journal of Cell Biology*, *222*(10), e202208110. https://doi.org/10.1083/jcb.202208110

Blanpied, T. A., Scott, D. B., & Ehlers, M. D. (2002). Dynamics and Regulation of Clathrin Coats at Specialized Endocytic Zones of Dendrites and Spines. *Neuron*, *36*(3), 435‑449. https://doi.org/10.1016/S0896-6273(02)00979-0

Borrelli, M. J., Stafford, D. M., Rausch, C. M., Bernock, L. J., Freeman, M. L., Lepock, J. R., & Corry, P. M. (1998). Diamide-induced cytotoxicity and thermotolerance in CHO cells. *Journal of Cellular Physiology*, *177*(3), 483‑492. https://doi.org/10.1002/(SICI)1097-4652(199812)177:3<483::AID-JCP11>3.0.CO;2-H

Boulant, S., Kural, C., Zeeh, J.-C., Ubelmann, F., & Kirchhausen, T. (2011). Actin dynamics counteract membrane tension during clathrin-mediated endocytosis. *Nature Cell Biology*, *13*(9), 1124‑1131. https://doi.org/10.1038/ncb2307

Cameron, P. L., Südhof, T. C., Jahn, R., & De Camilli, P. (1991). Colocalization of synaptophysin with transferrin receptors : Implications for synaptic vesicle biogenesis. *The Journal of Cell Biology*, *115*(1), 151‑164. https://doi.org/10.1083/jcb.115.1.151

Campbell, C., Lindhartsen, S., Knyaz, A., Erisir, A., & Nahmani, M. (2020). Cortical Presynaptic Boutons Progressively Engulf Spinules as They Mature. *Eneuro*, *7*(5), ENEURO.0426-19.2020. https://doi.org/10.1523/ENEURO.0426-19.2020

Carroll, R. C., Beattie, E. C., von Zastrow, M., & Malenka, R. C. (2001). Role of ampa receptor endocytosis in synaptic plasticity. *Nature Reviews Neuroscience*, *2*(5), 315‑324. https://doi.org/10.1038/35072500

Carter, M., & Shieh, J. (2015). Chapter 11—Gene Delivery Strategies. In M. Carter & J. Shieh (Éds.), *Guide to Research Techniques in Neuroscience (Second Edition)* (p. 239‑252). Academic Press. https://doi.org/10.1016/B978-0-12-800511-8.00011-3

Chakrabarty, N., Dubey, P., Tang, Y., Ganguly, A., Ladt, K., Leterrier, C., Jung, P., & Roy, S. (2018). Processive flow by biased polymerization mediates the slow axonal transport of actin. *Journal of Cell Biology*, *218*(1), 112‑124. https://doi.org/10.1083/jcb.201711022

Chanaday, N. L., Cousin, M. A., Milosevic, I., Watanabe, S., & Morgan, J. R. (2019). The Synaptic Vesicle Cycle Revisited : New Insights into the Modes and Mechanisms. *Journal of Neuroscience*, *39*(42), 8209‑8216. https://doi.org/10.1523/JNEUROSCI.1158-19.2019

Chen, Y., Hu, S., Wu, X., Xie, Z., Wang, Y., Wang, B., Li, X., Pei, Y., Gu, Y., Huang, K., Huo, J., Wei, A., Bi, C., Lu, Z., Song, Q., Xu, H., Kang, X., Shao, S., Long, J., … Wang, C. (2022). Synaptotagmin-1 is a bidirectional Ca $^{2+}$ sensor for neuronal endocytosis. *Proceedings of the National Academy of Sciences*, *119*(20), e2111051119. https://doi.org/10.1073/pnas.2111051119

Childs, G. V. (2014). History of Immunohistochemistry. In L. M. McManus & R. N. Mitchell (Éds.), *Pathobiology of Human Disease* (p. 3775‑3796). Academic Press. https://doi.org/10.1016/B978-0-12-386456-7.07401-3

Chuang, D.-M., & Costa, E. (1979). Evidence for internalization of the recognition site of β-adrenergic receptors during receptor subsensitivity induced by (-)-isoproterenol. *Proceedings of the National Academy of Sciences of the United States of America*, *76*(6), 3024‑3028.

Cocucci, E., Aguet, F., Boulant, S., & Kirchhausen, T. (2012). The first five seconds in the life of a clathrin-coated pit. *Cell*, *150*(3), 495‑507. https://doi.org/10.1016/j.cell.2012.05.047

Collins, A., Warrington, A., Taylor, K. A., & Svitkina, T. (2011). Structural Organization of the Actin Cytoskeleton at Sites of Clathrin-Mediated Endocytosis. *Current biology : CB*, *21*(14), 1167‑1175. https://doi.org/10.1016/j.cub.2011.05.048

Cousin, M. A., & Smillie, K. J. (2021). Monitoring Activity-Dependent Bulk EndocytosisEndocytosis in Primary Neuronal CultureCulturesUsing Large Fluorescent DextransDextrans. In F. Niedergang, N. Vitale, & S. Gasman (Éds.), *Exocytosis and Endocytosis : Methods and Protocols* (p. 101‑111). Springer US. https://doi.org/10.1007/978-1-0716-1044-2_7

Danglot, L., & Galli, T. (2007). What is the function of neuronal AP-3? *Biology of the Cell*, *99*(7), 349‑361. https://doi.org/10.1042/BC20070029

Das, J., Tiwari, M., & Subramanyam, D. (2021). Clathrin Light Chains : Not to Be Taken so Lightly. *Frontiers in Cell and Developmental Biology*, *9*, 774587. https://doi.org/10.3389/fcell.2021.774587

Delvendahl, I., Vyleta, N. P., von Gersdorff, H., & Hallermann, S. (2016). Fast, temperature-sensitive and clathrin-independent endocytosis at central synapses. *Neuron*, *90*(3), 492‑498. https://doi.org/10.1016/j.neuron.2016.03.013

D'Este, E., Kamin, D., Göttfert, F., El-Hady, A., & Hell, S. W. (2015). STED Nanoscopy Reveals the Ubiquity of Subcortical Cytoskeleton Periodicity in Living Neurons. *Cell Reports*, *10*(8), 1246‑1251. https://doi.org/10.1016/j.celrep.2015.02.007

D'Este, E., Kamin, D., Velte, C., Göttfert, F., Simons, M., & Hell, S. W. (2016). Subcortical cytoskeleton periodicity throughout the nervous system. *Scientific Reports*, *6*(1), 22741. https://doi.org/10.1038/srep22741

Doherty, G. J., & McMahon, H. T. (2009). Mechanisms of Endocytosis. *Annual Review of Biochemistry*, *78*(1), 857‑902. https://doi.org/10.1146/annurev.biochem.78.081307.110540

Dominguez, R., & Holmes, K. C. (2011). Actin Structure and Function. *Annual Review of Biophysics*, *40*(1), 169‑186. https://doi.org/10.1146/annurev-biophys-042910-155359

Dubey, S., Bhembre, N., Bodas, S., Veer, S., Ghose, A., Callan-Jones, A., & Pullarkat, P. (2020). The axonal actin-spectrin lattice acts as a tension buffering shock absorber. *eLife*, *9*, e51772. https://doi.org/10.7554/eLife.51772

Dutta, D., Williamson, C. D., Cole, N. B., & Donaldson, J. G. (2012). Pitstop 2 is a potent inhibitor of clathrin-independent endocytosis. *PloS One*, *7*(9), e45799. https://doi.org/10.1371/journal.pone.0045799

Ehrlich, M., Boll, W., Van Oijen, A., Hariharan, R., Chandran, K., Nibert, M. L., & Kirchhausen, T. (2004). Endocytosis by random initiation and stabilization of clathrin-coated pits. *Cell*, *118*(5), 591‑605. https://doi.org/10.1016/j.cell.2004.08.017

Eichel, K., Uenaka, T., Belapurkar, V., Lu, R., Cheng, S., Pak, J. S., Taylor, C. A., Südhof, T. C., Malenka, R., Wernig, M., Özkan, E., Perrais, D., & Shen, K. (2022). Endocytosis in the axon initial segment maintains neuronal polarity. *Nature*, *609*(7925), 128‑135. https://doi.org/10.1038/s41586-022-05074-5

Ferguson, S. S., Downey, W. E., Colapietro, A. M., Barak, L. S., Ménard, L., & Caron, M. G. (1996). Role of beta-arrestin in mediating agonist-promoted G protein-coupled receptor internalization. *Science (New York, N.Y.)*, *271*(5247), 363‑366. https://doi.org/10.1126/science.271.5247.363

Ferron, F., Rebowski, G., Lee, S. H., & Dominguez, R. (2007). Structural basis for the recruitment of profilin–actin complexes during filament elongation by Ena/VASP. *The EMBO Journal*, *26*(21), 4597‑4606. https://doi.org/10.1038/sj.emboj.7601874

Fréal, A., Jamann, N., Bos, J. T., Jansen, J., Petersen, N., Ligthart, T., Hoogenraad, C. C., & Kole, M. H. P. (2023). *Sodium channel endocytosis drives axon initial segment plasticity* (p. 2022.11.09.515770). bioRxiv. https://doi.org/10.1101/2022.11.09.515770

Friedl, K., Mau, A., Boroni-Rueda, F., Caorsi, V., Bourg, N., Lévêque-Fort, S., & Leterrier, C. (2023). Assessing crosstalk in simultaneous multicolor single-molecule localization microscopy. *Cell Reports Methods*, *3*(9), 100571. https://doi.org/10.1016/j.crmeth.2023.100571

Ganguly, A., Sharma, R., Boyer, N. P., Wernert, F., Phan, S., Boassa, D., Parra, L., Das, U., Caillol, G., Han, X., Yates, J. R., Ellisman, M. H., Leterrier, C., & Roy, S. (2021). Clathrin packets move in slow axonal transport and deliver functional payloads to synapses. *Neuron*, *109*(18), 2884-2901.e7. https://doi.org/10.1016/j.neuron.2021.08.016

Ganguly, A., Tang, Y., Wang, L., Ladt, K., Loi, J., Dargent, B., Leterrier, C., & Roy, S. (2015). A dynamic formin-dependent deep F-actin network in axons. *Journal of Cell Biology*, *210*(3), 401‑417. https://doi.org/10.1083/jcb.201506110

Ghisleni, A., Galli, C., Monzo, P., Ascione, F., Fardin, M.-A., Scita, G., Li, Q., Maiuri, P., & Gauthier, N. C. (2020). Complementary mesoscale dynamics of spectrin and acto-myosin shape membrane territories during mechanoresponse. *Nature Communications*, *11*, 5108. https://doi.org/10.1038/s41467-020-18825-7

Goddard, T. D., Huang, C. C., Meng, E. C., Pettersen, E. F., Couch, G. S., Morris, J. H., & Ferrin, T. E. (2018). UCSF ChimeraX : Meeting modern challenges in visualization and analysis. *Protein Science: A Publication of the Protein Society*, *27*(1), 14‑25. https://doi.org/10.1002/pro.3235

Goodson, H. V., & Jonasson, E. M. (2018). Microtubules and Microtubule-Associated Proteins. *Cold Spring Harbor Perspectives in Biology*, *10*(6). https://doi.org/10.1101/cshperspect.a022608

Greene, B., Liu, S. H., Wilde, A., & Brodsky, F. M. (2000). Complete reconstitution of clathrin basket formation with recombinant protein fragments : Adaptor control of clathrin self-assembly. *Traffic (Copenhagen, Denmark)*, *1*(1), 69‑75. https://doi.org/10.1034/j.1600-0854.2000.010110.x

Guček, A., Vardjan, N., & Zorec, R. (2012). Exocytosis in Astrocytes : Transmitter Release and Membrane Signal Regulation. *Neurochemical Research*, *37*(11), 2351‑2363. https://doi.org/10.1007/s11064-012-0773-6

Gustafsson, M. G. (2000). Surpassing the lateral resolution limit by a factor of two using structured illumination microscopy. *Journal of Microscopy*, *198*(Pt 2), 82‑87. https://doi.org/10.1046/j.1365-2818.2000.00710.x

Gustafsson, M. G. L., Shao, L., Carlton, P. M., Wang, C. J. R., Golubovskaya, I. N., Cande, W. Z., Agard, D. A., & Sedat, J. W. (2008). Three-Dimensional Resolution Doubling in Wide-Field Fluorescence Microscopy by Structured Illumination. *Biophysical Journal*, *94*(12), 4957‑4970. https://doi.org/10.1529/biophysj.107.120345

Hammarlund, M., Jorgensen, E. M., & Bastiani, M. J. (2007). Axons break in animals lacking β-spectrin. *The Journal of Cell Biology*, *176*(3), 269‑275. https://doi.org/10.1083/jcb.200611117

Han, B., Zhou, R., Xia, C., & Zhuang, X. (2017). Structural organization of the actin-spectrin–based membrane skeleton in dendrites and soma of neurons. *Proceedings of the National Academy of Sciences*, *114*(32), E6678‑E6685. https://doi.org/10.1073/pnas.1705043114

He, J., Zhou, R., Wu, Z., Carrasco, M. A., Kurshan, P. T., Farley, J. E., Simon, D. J., Wang, G., Han, B., Hao, J., Heller, E., Freeman, M. R., Shen, K., Maniatis, T., Tessier-Lavigne, M., & Zhuang, X. (2016). Prevalent presence of periodic actin–spectrin-based membrane skeleton in a broad range of neuronal cell types and animal species. *Proceedings of the National Academy of Sciences*, *113*(21), 6029‑6034. https://doi.org/10.1073/pnas.1605707113

He, K., Song, E., Upadhyayula, S., Dang, S., Gaudin, R., Skillern, W., Bu, K., Capraro, B. R., Rapoport, I., Kusters, I., Ma, M., & Kirchhausen, T. (2020). Dynamics of Auxilin 1 and GAK in clathrin-mediated traffic. *Journal of Cell Biology*, *219*(3), e201908142. https://doi.org/10.1083/jcb.201908142

Herrmann, H., & Aebi, U. (2016). Intermediate Filaments : Structure and Assembly. *Cold Spring Harbor Perspectives in Biology*, *8*(11), a018242. https://doi.org/10.1101/cshperspect.a018242

Heuser, J. (1980). Three-dimensional visualization of coated vesicle formation in fibroblasts. *Journal of Cell Biology*, *84*(3), 560‑583. https://doi.org/10.1083/jcb.84.3.560

Heuser, J. E., & Reese, T. S. (1973). EVIDENCE FOR RECYCLING OF SYNAPTIC VESICLE MEMBRANE DURING TRANSMITTER RELEASE AT THE FROG NEUROMUSCULAR JUNCTION. *The Journal of Cell Biology*, *57*(2), 315‑344.

Hlushchenko, I., Koskinen, M., & Hotulainen, P. (2016). Dendritic spine actin dynamics in neuronal maturation and synaptic plasticity. *Cytoskeleton*, *73*(9), 435‑441. https://doi.org/10.1002/cm.21280

Hohmann, T., & Dehghani, F. (2019). The Cytoskeleton—A Complex Interacting Meshwork. *Cells*, *8*(4), 362. https://doi.org/10.3390/cells8040362

Im, K., Mareninov, S., Diaz, M. F. P., & Yong, W. H. (2019). An introduction to Performing Immunofluorescence Staining. *Methods in molecular biology (Clifton, N.J.)*, *1897*, 299‑311. https://doi.org/10.1007/978-1-4939-8935-5_26

Isaac, J. T., Nicoll, R. A., & Malenka, R. C. (1995). Evidence for silent synapses : Implications for the expression of LTP. *Neuron*, *15*(2), 427‑434. https://doi.org/10.1016/0896-6273(95)90046-2

Jackson, C. B., Farzan, M., Chen, B., & Choe, H. (2022). Mechanisms of SARS-CoV-2 entry into cells. *Nature Reviews Molecular Cell Biology*, *23*(1), 3‑20. https://doi.org/10.1038/s41580-021-00418-x

Jalilian Tehrani, M. H., & Barnes Jr., E. M. (1993). Identification of GABAA/Benzodiazepine Receptors on Clathrin-Coated Vesicles from Rat Brain. *Journal of Neurochemistry*, *60*(5), 1755‑1761. https://doi.org/10.1111/j.1471-4159.1993.tb13400.x

Jenkins, P. M., He, M., & Bennett, V. (2015). Dynamic spectrin/ankyrin-G microdomains promote lateral membrane assembly by opposing endocytosis. *Science Advances*, *1*(8), e1500301. https://doi.org/10.1126/sciadv.1500301

Jimenez, A., Friedl, K., & Leterrier, C. (2020). About samples, giving examples : Optimized Single Molecule Localization Microscopy. *Methods*, *174*, 100‑114. https://doi.org/10.1016/j.ymeth.2019.05.008

Jinek, M., Chylinski, K., Fonfara, I., Hauer, M., Doudna, J. A., & Charpentier, E. (2012). A Programmable Dual-RNA–Guided DNA Endonuclease in Adaptive Bacterial Immunity. *Science*, *337*(6096), 816‑821. https://doi.org/10.1126/science.1225829

Johnsen, K. B., Burkhart, A., Thomsen, L. B., Andresen, T. L., & Moos, T. (2019). Targeting the transferrin receptor for brain drug delivery. *Progress in Neurobiology*, *181*, 101665. https://doi.org/10.1016/j.pneurobio.2019.101665

Jungmann, R., Avendaño, M. S., Woehrstein, J. B., Dai, M., Shih, W. M., & Yin, P. (2014). Multiplexed 3D cellular super-resolution imaging with DNA-PAINT and Exchange-PAINT. *Nature Methods*, *11*(3), 313‑318. https://doi.org/10.1038/nmeth.2835

Jungmann, R., Steinhauer, C., Scheible, M., Kuzyk, A., Tinnefeld, P., & Simmel, F. C. (2010). Single-Molecule Kinetics and Super-Resolution Microscopy by Fluorescence Imaging of Transient Binding on DNA Origami. *Nano Letters*, *10*(11), 4756‑4761. https://doi.org/10.1021/nl103427w

Kaksonen, M., & Roux, A. (2018). Mechanisms of clathrin-mediated endocytosis. *Nature Reviews Molecular Cell Biology*, *19*(5), 313‑326. https://doi.org/10.1038/nrm.2017.132

Kapitein, L. C., & Hoogenraad, C. C. (2011). Which way to go? Cytoskeletal organization and polarized transport in neurons. *Molecular and Cellular Neuroscience*, *46*(1), 9‑20. https://doi.org/10.1016/j.mcn.2010.08.015

Kawabata, H. (2019). Transferrin and transferrin receptors update. *Free Radical Biology & Medicine*, *133*, 46‑54. https://doi.org/10.1016/j.freeradbiomed.2018.06.037

Kirchhausen, T. (2000). Clathrin. *Annual Review of Biochemistry*, *69*, 699‑727. https://doi.org/10.1146/annurev.biochem.69.1.699

Kirchhausen, Tom, Owen, D., & Harrison, S. C. (2014). Molecular Structure, Function, and Dynamics of Clathrin-Mediated Membrane Traffic. *Cold Spring Harbor Perspectives in Biology*, *6*(5), a016725. https://doi.org/10.1101/cshperspect.a016725

Klenchin, V. A., King, R., Tanaka, J., Marriott, G., & Rayment, I. (2005). Structural Basis of Swinholide A Binding to Actin. *Chemistry & Biology*, *12*(3), 287‑291. https://doi.org/10.1016/j.chembiol.2005.02.011

Korobova, F., & Svitkina, T. (2010). Molecular Architecture of Synaptic Actin Cytoskeleton in Hippocampal Neurons Reveals a Mechanism of Dendritic Spine Morphogenesis. *Molecular Biology of the Cell*, *21*(1), 165‑176. https://doi.org/10.1091/mbc.e09-07-0596

Lambeth, L. S., & Smith, C. A. (2013). Short Hairpin RNA-Mediated Gene Silencing. In D. J. Taxman (Éd.), *siRNA Design : Methods and Protocols* (p. 205‑232). Humana Press. https://doi.org/10.1007/978-1-62703-119-6_12

Lavoie-Cardinal, F., Bilodeau, A., Lemieux, M., Gardner, M.-A., Wiesner, T., Laramée, G., Gagné, C., & De Koninck, P. (2020). Neuronal activity remodels the F-actin based submembrane lattice in dendrites but not axons of hippocampal neurons. *Scientific Reports*, *10*(1), 11960. https://doi.org/10.1038/s41598-020-68180-2

Lei, W., Omotade, O. F., Myers, K. R., & Zheng, J. Q. (2016). Actin Cytoskeleton in Dendritic Spine Development and Plasticity. *Current opinion in neurobiology*, *39*, 86‑92. https://doi.org/10.1016/j.conb.2016.04.010

Leterrier, C. (2021). Putting the axonal periodic scaffold in order. *Current Opinion in Neurobiology*, *69*, 33‑40. https://doi.org/10.1016/j.conb.2020.12.015

Li, L., Wan, T., Wan, M., Liu, B., Cheng, R., & Zhang, R. (2015). The effect of the size of fluorescent dextran on its endocytic pathway. *Cell Biology International*, *39*(5), 531‑539. https://doi.org/10.1002/cbin.10424

Liao, D., Zhang, X., O'Brien, R., Ehlers, M. D., & Huganir, R. L. (1999). Regulation of morphological postsynaptic silent synapses in developing hippocampal neurons. *Nature Neuroscience*, *2*(1), 37‑43. https://doi.org/10.1038/4540

Liao-Chan, S., Daine-Matsuoka, B., Heald, N., Wong, T., Lin, T., Cai, A. G., Lai, M., D'Alessio, J. A., & Theunissen, J.-W. (2015). Quantitative Assessment of Antibody Internalization with Novel Monoclonal Antibodies against Alexa Fluorophores. *PLOS ONE*, *10*(4), e0124708. https://doi.org/10.1371/journal.pone.0124708

Liu, C.-H., Seo, R., Ho, T. S.-Y., Stankewich, M., Mohler, P. J., Hund, T. J., Noebels, J. L., & Rasband, M. N. (2020). β spectrin-dependent and domain specific mechanisms for Na+ channel clustering. *eLife*, *9*, e56629. https://doi.org/10.7554/eLife.56629

Loerke, D., Mettlen, M., Yarar, D., Jaqaman, K., Jaqaman, H., Danuser, G., & Schmid, S. L. (2009). Cargo and Dynamin Regulate Clathrin-Coated Pit Maturation. *PLoS Biology*, *7*(3), e1000057. https://doi.org/10.1371/journal.pbio.1000057

López-Hernández, T., Takenaka, K.-I., Mori, Y., Kongpracha, P., Nagamori, S., Haucke, V., & Takamori, S. (2022). Clathrin-independent endocytic retrieval of SV proteins mediated by the clathrin adaptor AP-2 at mammalian central synapses. *eLife*, *11*, e71198. https://doi.org/10.7554/eLife.71198

Lorenzo, D. N., Badea, A., Zhou, R., Mohler, P. J., Zhuang, X., & Bennett, V. (2019). βII-spectrin promotes mouse brain connectivity through stabilizing axonal plasma membranes and enabling axonal organelle transport. *Proceedings of the National Academy of Sciences*, *116*(31), 15686‑15695. https://doi.org/10.1073/pnas.1820649116

Lorenzo, D. N., Edwards, R. J., & Slavutsky, A. L. (2023). Spectrins : Molecular organizers and targets of neurological disorders. *Nature Reviews Neuroscience*. https://doi.org/10.1038/s41583-022-00674-6

Malenka, R. C., & Nicoll, R. A. (1997). Silent Synapses Speak Up. *Neuron*, *19*(3), 473‑476. https://doi.org/10.1016/S0896-6273(00)80362-1

May, R. C. (2001). The Arp2/3 complex : A central regulator of the actin cytoskeleton. *Cellular and Molecular Life Sciences CMLS*, *58*(11), 1607‑1626. https://doi.org/10.1007/PL00000800

McMahon, H. T., & Boucrot, E. (2011). Molecular mechanism and physiological functions of clathrin-mediated endocytosis. *Nature Reviews. Molecular Cell Biology*, *12*(8), 517‑533. https://doi.org/10.1038/nrm3151

Merrifield, C. J., Feldman, M. E., Wan, L., & Almers, W. (2002). Imaging actin and dynamin recruitment during invagination of single clathrin-coated pits. *Nature Cell Biology*, *4*(9), 691‑698. https://doi.org/10.1038/ncb837

Merrifield, C. J., & Kaksonen, M. (2014). Endocytic Accessory Factors and Regulation of Clathrin-Mediated Endocytosis. *Cold Spring Harbor Perspectives in Biology*, *6*(11), a016733. https://doi.org/10.1101/cshperspect.a016733

Miele, A. E., Watson, P. J., Evans, P. R., Traub, L. M., & Owen, D. J. (2004). Two distinct interaction motifs in amphiphysin bind two independent sites on the clathrin terminal domain beta-propeller. *Nature Structural & Molecular Biology*, *11*(3), 242‑248. https://doi.org/10.1038/nsmb736

Moulay, G., Lainé, J., Lemaître, M., Nakamori, M., Nishino, I., Caillol, G., Mamchaoui, K., Julien, L., Dingli, F., Loew, D., Bitoun, M., Leterrier, C., Furling, D., & Vassilopoulos, S. (2020). Alternative splicing of clathrin heavy chain contributes to the switch from coated pits to plaques. *The Journal of Cell Biology*, *219*(9), e201912061. https://doi.org/10.1083/jcb.201912061

Neukirchen, D., & Bradke, F. (2011). Neuronal polarization and the cytoskeleton. *Seminars in Cell & Developmental Biology*, *22*(8), 825‑833. https://doi.org/10.1016/j.semcdb.2011.08.007

Paksoy, A., Hoppe, S., Dörflinger, Y., Horstmann, H., Sätzler, K., & Körber, C. (2022). Effects of the clathrin inhibitor Pitstop-2 on synaptic vesicle recycling at a central synapse in vivo. *Frontiers in Synaptic Neuroscience*, *14*, 1056308. https://doi.org/10.3389/fnsyn.2022.1056308

Papandréou, M.-J., & Leterrier, C. (2018). The functional architecture of axonal actin. *Molecular and Cellular Neuroscience*, *91*, 151‑159. https://doi.org/10.1016/j.mcn.2018.05.003

Park, S. Y., & Guo, X. (2014). Adaptor protein complexes and intracellular transport. *Bioscience Reports*, *34*(4), e00123. https://doi.org/10.1042/BSR20140069

Patel, L., Gustafsson, N., Lin, Y., Ober, R., Henriques, R., & Cohen, E. (2017). *A hidden Markov model approach to characterizing the photo-switching behavior of fluorophores* (p. 223875). bioRxiv. https://doi.org/10.1101/223875

Patton, R. G., Simons, K., & Dotti, C. G. (1992). Axonal and Dendritic Endocytic Pathways in Cultured Neurons. *The Journal of Cell Biology*, *119*.

Paul, A. S., & Pollard, T. D. (2009). Review of the mechanism of processive actin filament elongation by formins. *Cell Motility*, *66*(8), 606‑617. https://doi.org/10.1002/cm.20379

Pearse, B. M. F. (1975). Coated vesicles from pig brain : Purification and biochemical characterization. *Journal of Molecular Biology*, *97*(1), 93‑98. https://doi.org/10.1016/S0022-2836(75)80024-6

pHrodo^{TM} Red and Green Dextran, 10,000 MW, for Endocytosis. (s. d.). Consulté 23 novembre 2023, à l'adresse https://www.thermofisher.com/order/catalog/product/fr/en/P35368

Pinto-Costa, R., & Sousa, M. M. (2020). Profilin as a dual regulator of actin and microtubule dynamics. *Cytoskeleton*, *77*(3‑4), 76‑83. https://doi.org/10.1002/cm.21586

Pollard, T. D. (2016). Actin and Actin-Binding Proteins. *Cold Spring Harbor Perspectives in Biology*, *8*(8), a018226. https://doi.org/10.1101/cshperspect.a018226

Pollard, T. D., & Goldman, R. D. (2018). Overview of the Cytoskeleton from an Evolutionary Perspective. *Cold Spring Harbor Perspectives in Biology*, *10*(7), a030288. https://doi.org/10.1101/cshperspect.a030288

Qian, Z.-M., & Ke, Y. (2019). Brain iron transport. *Biological Reviews*, *94*(5), 1672‑1684. https://doi.org/10.1111/brv.12521

Qu, Y., Hahn, I., Webb, S. E. D., Pearce, S. P., & Prokop, A. (2017). Periodic actin structures in neuronal axons are required to maintain microtubules. *Molecular Biology of the Cell*, *28*(2), 296‑308. https://doi.org/10.1091/mbc.e16-10-0727

Rauch, C., & Farge, E. (2000). Endocytosis Switch Controlled by Transmembrane Osmotic Pressure and Phospholipid Number Asymmetry. *Biophysical Journal*, *78*(6), 3036‑3047. https://doi.org/10.1016/S0006-3495(00)76842-1

Redlingshöfer, L., & Brodsky, F. M. (2021). Antagonistic regulation controls clathrin-mediated endocytosis : AP2 adaptor facilitation vs restraint from clathrin light chains. *Cells & Development*, *168*, 203714. https://doi.org/10.1016/j.cdev.2021.203714

Redlingshöfer, L., McLeod, F., Chen, Y., Camus, M. D., Burden, J. J., Palomer, E., Briant, K., Dannhauser, P. N., Salinas, P. C., & Brodsky, F. M. (2020). Clathrin light chain diversity regulates membrane deformation in vitro and synaptic vesicle formation in vivo. *Proceedings of the National Academy of Sciences*, *117*(38), 23527‑23538. https://doi.org/10.1073/pnas.2003662117

Rizzoli, S. O., & Betz, W. J. (2005). Synaptic vesicle pools. *Nature Reviews Neuroscience*, *6*(1), 57‑69. https://doi.org/10.1038/nrn1583

Robinson, M. S. (2004). Adaptable adaptors for coated vesicles. *Trends in Cell Biology*, *14*(4), 167‑174. https://doi.org/10.1016/j.tcb.2004.02.002

Robinson, M. S. (2015). Forty Years of Clathrin-coated Vesicles. *Traffic*, *16*(12), 1210‑1238. https://doi.org/10.1111/tra.12335

Rottner, K., Faix, J., Bogdan, S., Linder, S., & Kerkhoff, E. (2017). Actin assembly mechanisms at a glance. *Journal of Cell Science*, *130*(20), 3427‑3435. https://doi.org/10.1242/jcs.206433

Rust, M. J., Bates, M., & Zhuang, X. (2006). Stochastic optical reconstruction microscopy (STORM) provides sub-diffraction-limit image resolution. *Nature methods*, *3*(10), 793‑795. https://doi.org/10.1038/nmeth929

Sabatini, B. L., & Regehr, W. G. (1999). Timing of Synaptic Transmission. *Annual Review of Physiology*, *61*(1), 521‑542. https://doi.org/10.1146/annurev.physiol.61.1.521

Saha, K., Kim, S. T., Yan, B., Miranda, O. R., Alfonso, F. S., Shlosman, D., & Rotello, V. M. (2013). Surface Functionality of Nanoparticles Determines Cellular Uptake Mechanisms in Mammalian Cells. *Small*, *9*(2), 300‑305. https://doi.org/10.1002/smll.201201129

Schnitzbauer, J., Strauss, M. T., Schlichthaerle, T., Schueder, F., & Jungmann, R. (2017). Super-resolution microscopy with DNA-PAINT. *Nature Protocols*, *12*(6), 1198‑1228. https://doi.org/10.1038/nprot.2017.024

Shannon, C. E. (1949). Communication in the Presence of Noise. *Proceedings of the IRE*, *37*(1), 10‑21. https://doi.org/10.1109/JRPROC.1949.232969

Sochacki, K. A., Heine, B. L., Haber, G. J., Jimah, J. R., Prasai, B., Alfonzo-Méndez, M. A., Roberts, A. D., Somasundaram, A., Hinshaw, J. E., & Taraska, J. W. (2021). The structure and spontaneous curvature of clathrin lattices at the plasma membrane. *Developmental Cell*, *56*(8), 1131-1146.e3. https://doi.org/10.1016/j.devcel.2021.03.017

Sochacki, K. A., & Taraska, J. W. (2019). From Flat to Curved Clathrin : Controlling a Plastic Ratchet. *Trends in Cell Biology*, *29*(3), 241‑256. https://doi.org/10.1016/j.tcb.2018.12.002

Sohn, R. H., & Goldschmidt-Clermont, P. J. (1994). Profilin : At the crossroads of signal transduction and the actin cytoskeleton. *BioEssays*, *16*(7), 465‑472. https://doi.org/10.1002/bies.950160705

Spector, I., Braet, F., Shochet, N. R., & Bubb, M. R. (1999). New anti-actin drugs in the study of the organization and function of the actin cytoskeleton. *Microscopy Research and Technique*, *47*(1), 18‑37. https://doi.org/10.1002/(SICI)1097-0029(19991001)47:1<18::AID-JEMT3>3.0.CO;2-E

Stricker, J., Falzone, T., & Gardel, M. (2010). Mechanics of the F-actin Cytoskeleton. *Journal of biomechanics*, *43*(1), 9. https://doi.org/10.1016/j.jbiomech.2009.09.003

Südhof, T. C. (2004). The Synaptic Vesicle Cycle. *Annual Review of Neuroscience*, *27*(1), 509‑547. https://doi.org/10.1146/annurev.neuro.26.041002.131412

Svitkina, T. M. (2017). Platinum replica electron microscopy : Imaging the cytoskeleton globally and locally. *The International Journal of Biochemistry & Cell Biology*, *86*, 37‑41. https://doi.org/10.1016/j.biocel.2017.03.009

Tao-Cheng, J.-H. (2020). Stimulation-induced differential redistributions of clathrin and clathrin-coated vesicles in axons compared to soma/dendrites. *Molecular Brain*, *13*(1), 141. https://doi.org/10.1186/s13041-020-00683-5

Tehrani, M. H. J., & Barnes Jr., E. M. (1991). Agonist-Dependent Internalization of γ-Aminobutyric AcidA/Benzodiazepine Receptors in Chick Cortical Neurons. *Journal of Neurochemistry*, *57*(4), 1307‑1312. https://doi.org/10.1111/j.1471-4159.1991.tb08295.x

ter Haar, E., Harrison, S. C., & Kirchhausen, T. (2000). Peptide-in-groove interactions link target proteins to the β-propeller of clathrin. *Proceedings of the National Academy of Sciences of the United States of America*, *97*(3), 1096‑1100.

Titus, M. A. (2018). Myosin-Driven Intracellular Transport. *Cold Spring Harbor Perspectives in Biology*, *10*(3), a021972. https://doi.org/10.1101/cshperspect.a021972

Vassilopoulos, S., Gibaud, S., Jimenez, A., Caillol, G., & Leterrier, C. (2019). Ultrastructure of the axonal periodic scaffold reveals a braid-like organization of actin rings. *Nature Communications*, *10*, 5803. https://doi.org/10.1038/s41467-019-13835-6

von Kleist, L., Stahlschmidt, W., Bulut, H., Gromova, K., Puchkov, D., Robertson, M. J., MacGregor, K. A., Tomilin, N., Pechstein, A., Chau, N., Chircop, M., Sakoff, J., von Kries, J. P., Saenger, W., Kräusslich, H.-G., Shupliakov, O., Robinson, P. J., McCluskey, A., & Haucke, V. (2011). Role of the Clathrin Terminal Domain in Regulating Coated Pit Dynamics Revealed by Small Molecule Inhibition. *Cell*, *146*(3), 471‑484. https://doi.org/10.1016/j.cell.2011.06.025

von Zastrow, M., & Kobilka, B. K. (1992). Ligand-regulated internalization and recycling of human beta 2-adrenergic receptors between the plasma membrane and endosomes containing transferrin receptors. *Journal of Biological Chemistry*, *267*(5), 3530‑3538. https://doi.org/10.1016/S0021-9258(19)50762-1

Watanabe, S., Rost, B. R., Camacho-Pérez, M., Davis, M. W., Söhl-Kielczynski, B., Rosenmund, C., & Jorgensen, E. M. (2013). Ultrafast endocytosis at mouse hippocampal synapses. *Nature*, *504*(7479), 242‑247. https://doi.org/10.1038/nature12809

Weigert, M., Schmidt, U., Boothe, T., Müller, A., Dibrov, A., Jain, A., Wilhelm, B., Schmidt, D., Broaddus, C., Culley, S., Rocha-Martins, M., Segovia-Miranda, F., Norden, C., Henriques, R., Zerial, M., Solimena, M., Rink, J., Tomancak, P., Royer, L., … Myers, E. W. (2018). Content-aware image restoration : Pushing the limits of fluorescence microscopy. *Nature Methods*, *15*(12), 1090‑1097. https://doi.org/10.1038/s41592-018-0216-7

Xu, K., Zhong, G., & Zhuang, X. (2013). Actin, Spectrin, and Associated Proteins Form a Periodic Cytoskeletal Structure in Axons. *Science*, *339*(6118), 452‑456. https://doi.org/10.1126/science.1232251

Yang, R., Walder-Christensen, K. K., Lalani, S., Yan, H., García-Prieto, I. D., Álvarez, S., Fernández-Jaén, A., Speltz, L., Jiang, Y.-H., & Bennett, V. (2019). Neurodevelopmental mutation of giant ankyrin-G disrupts a core mechanism for axon initial segment assembly. *Proceedings of the National Academy of Sciences of the United States of America*, *116*(39), 19717‑19726. https://doi.org/10.1073/pnas.1909989116

Yang, X., & Specht, C. G. (2019). Subsynaptic Domains in Super-Resolution Microscopy : The Treachery of Images. *Frontiers in Molecular Neuroscience*, *12*, 161. https://doi.org/10.3389/fnmol.2019.00161

Yin, L.-M., Schnoor, M., & Jun, C.-D. (2020). Structural Characteristics, Binding Partners and Related Diseases of the Calponin Homology (CH) Domain. *Frontiers in Cell and Developmental Biology*, *8*, 342. https://doi.org/10.3389/fcell.2020.00342

Yuan, A., Rao, M. V., Veeranna, & Nixon, R. A. (2017). Neurofilaments and Neurofilament Proteins in Health and Disease. *Cold Spring Harbor Perspectives in Biology*, *9*(4), a018309. https://doi.org/10.1101/cshperspect.a018309

Zhong, G., He, J., Zhou, R., Lorenzo, D., Babcock, H. P., Bennett, V., & Zhuang, X. (2014). Developmental mechanism of the periodic membrane skeleton in axons. *eLife*, *3*, e04581. https://doi.org/10.7554/eLife.04581

Zhou, R., Han, B., Xia, C., & Zhuang, X. (2019). Membrane-associated periodic skeleton is a signaling platform for RTK transactivation in neurons. *Science (New York, N.Y.)*, *365*(6456), 929‑934. https://doi.org/10.1126/science.aaw5937

Tables des figures